

Università degli Studi di Milano

Dipartimento di Chimica

Doctorate in Chemistry

XXXIV Cycle

CHIM-01



INHERENT CHIRALITY AT WORK FOR APPLICATIONS IN CHIRAL ELECTROCHEMISTRY, CHIROPTICS AND SPINTRONICS.

Supervisor: Prof. Patrizia Romana Mussini

Co-supervisors: Dott. Serena Arnaboldi, PhD

Prof. Tiziana Benincori

School Director: Prof. Daniele Passarella

Sara Grecchi

R12230

Academic Year 2021/2022

SUMMARY

Chapter 1	11
Introduction	11
1.1 Strategies and approaches reported in the literature to modify electrode surfaces with chiral molecules	17
1.1.1 <i>Weak points of the proposed strategy</i>	24
1.2 Advanced chiral molecular media for enantioselective electrochemistry and electroanalysis	27
<i>Implementing chirality in traditional solvent + supporting electrolyte media</i> ..	27
<i>Implementing chirality in ionic liquid (IL) media</i>	28
<i>Chiral LCs(CLCs) and chiral ionic LCs (CILCs)</i>	31
<i>Chiral deep eutectic solvents (DESs)</i>	32
1.3 Advanced applications of chiral molecular selectors: sensing electrochemical devices	35
1.3.1 <i>Bipolar electrochemistry with chiral conducting polymers</i>	35
1.3.2 <i>Magneto-electrochemistry experiments with chiral molecules</i>	39
1.4 The power of inherently chiral molecular selectors.....	43
1.5 Targets and guidelines of the present three-year thesis research work....	49
Chapter 2	53
Details on the techniques employed	53
2.1 Voltammetry	53
2.1.1 <i>Cyclic Voltammetry (CV)</i>	55
<i>Electrooligomerization of conductive polymers</i>	58
2.1.2 <i>Differential Pulse Voltammetry (DPV)</i>	59
Chapter 3	61
Inherently chiral monomers	61
and oligomer films	61

3.1 General experimental setup for the electrochemical measurements: characterization and electrooligomerization of the monomers	65
3.2 Result and discussion for the inherently chiral monomers exploited	67
3.2.1 <i>“Inherently chiral” bi-naphthyl systems with different wings: modulating functional properties and performance as chiral selectors</i>	67
a) <i>Experimental conditions for CV measurements: electrochemical characterization and enantiorecognition experiments</i>	68
b) <i>CV electrochemical characterizations of the bi-naphthyl systems</i>	68
c) <i>Enantioselection tests towards the enantiomers of DOPA</i>	71
3.2.2 <i>“Inherently chiral” monomers and oligomer films based on a 2,2’- biindole core with phenyl spacer</i>	75
a) <i>Experimental conditions for CV electrochemical characterization, electrodeposition and DPV or CV enantioselection tests</i>	76
b) <i>Circular Dichroism spectra of 1, 2 and 3</i>	77
c) <i>CV electrochemical characterizations of 1, 2 and 3 monomers</i>	78
d) <i>Electrooligomerization ability of 1, 2 and 3 monomers</i>	80
e) <i>Enantioselection tests on different chiral electroactive probes, also of pharmaceutical interest</i>	82
3.2.3 <i>Cobalt(III)-containing penta-dentate “Helmet”-type phthalogens ..</i>	93
a) <i>Experimental protocols for CV characterizations and enantioselection tests</i>	94
b) <i>CV electrochemical characterization</i>	94
c) <i>Enantioselection tests, using enantiopure Helmet CoPc both as chiral selector to modify the WE and as chiral probe.....</i>	103
3.2.4 <i>Electrodeposition of inherently chiral films: morphological and functional properties as a function of the operating conditions</i>	107

<i>a) Experimental set-up and conditions for: CV electrochemical characterization, electrodeposition protocol, enantioselection tests, AFM and HR LDI measurements.....</i>	108
<i>b) CV electrochemical characterizations of the inherently chiral BT₂T₄, BT₂(T₃)₂ and BT₂T₆ monomers</i>	110
<i>c) Electrooligomerization ability of BT₂T₄, BT₂(T₃)₂ and BT₂T₆ in ACN on GC working electrode</i>	116
<i>d) Studying the influence of the supporting electrolyte, changing the dimension of both the cation and the anion</i>	118
<i>e) The importance of the working electrode surface: ultra-flat vs no-flat ITO</i>	120
<i>f) LDI analysis of the films composition obtained at different electrodeposition cycles on ultra-flat ITO electrode.....</i>	123
<i>g) AFM measurements: a comparison of the film morphology obtained at different cycle numbers on ultra-flat ITO electrode</i>	126
<i>h) Enantioselection tests on electrodes modified with oligo-BT₂T₄ as a function of both the number of deposition cycles and the supporting electrolyte</i>	136
<i>i) Enantioselection tests on electrodes modified with oligo-BT₂T₆ as a function of the number of deposition cycles in TBAPF₆.....</i>	145
<i>3.2.5 A family of “inherently chiral” bisindole systems with N,N’ functionalization: modulating functional properties and performances as chiral selectors</i>	149
<i>a) Experimental section</i>	150
<i>b) Redox features of the three inherently chiral monomers</i>	151
<i>c) Inherently chiral oligomer films formation</i>	154
<i>d) Enantioselection experiments.....</i>	154

e) <i>Attenuated Total Reflectance (ATR)</i>	169
3.2.6 <i>Widening the scope of “inherently chiral” electrodes: enantiodiscrimination of chiral electroactive probes with planar stereogenicity</i>	173
a) <i>Experimental section</i>	174
b) <i>Electrochemical investigation of the redox features of the planar ferrocenyl family as racemates</i>	174
c) <i>Separation of the ferrocenyl chiral probes into pure enantiomers by chiral HPLC and CD spectra</i>	182
3.2.7 <i>Self-standing inherently chiral membranes: potentiometric tests in an ISE-like setup</i>	189
a) <i>Electrosynthesis and peeling-off of the inherently chiral membrane and implementation in an ISE-like setup</i>	190
b) <i>Electrosynthesis, HR LDI and ECD spectra of membranes</i>	192
c) <i>Potentiometric membrane tests in a classical ISE-like setup</i>	196
Chapter 4	205
Chiral media	205
4.1 <i>General Experimental setup for the electrochemical measurements: characterization of the chiral selectors and enantioselection tests</i>	209
4.2 <i>Result and discussion for the (inherently) chiral media</i>	213
4.2.1 <i>Chiral biobased ionic liquids with cations or anions including bile acid building blocks as chiral selectors in voltammetry</i>	213
a) <i>Thermal analysis: TGA and DSC features</i>	215
b) <i>Electrochemical properties of the CIL family</i>	219
c) <i>Enantiodiscrimination tests</i>	221
4.2.2 <i>Enantioselective electrooligomerization of an inherently chiral monomer</i>	225

a) <i>Experimental conditions for the electrooligomerization of the BT₂T₄ monomer</i>	225
b) <i>Enantioselective electrodeposition of enantiopure or racemic BT₂T₄ in achiral BMIMNTf₂</i>	226
c) <i>Enantioselective electrodeposition of enantiopure or racemic BT₂T₄ in BMIMNTf₂ + [NopolMIm]Mes</i>	226
4.2.3 <i>Chiral Tweezers and chiral moieties</i>	229
a) <i>Thermal analysis of the new tweezers: assessing CIL nature and stability</i>	232
b) <i>Voltammetry study of the whole chiral tweezer family and of some related molecules</i>	239
I. <i>Tweezers with N⁺ alkyl salt terminals</i>	240
II. <i>Neutral tweezers and tweezer moieties</i>	246
c) <i>Highlighting chirality properties with electronic circular dichroism</i>	250
d) <i>Features of two chiral probe candidates</i>	253
e) <i>Enantiodiscrimination experiments</i>	257
4.2.4 <i>Natural or artificial selector? Looking for an ideal chiral selector</i>	259
4.2.5 <i>Inherently chiral ionic liquid based on a 3,3'-bypiridine scaffold</i> .	261
4.2.6 <i>2,12-Diaza[6]helicene: an efficient non-conventional stereogenic scaffold for enantioselective electrochemical interphases</i>	269
a) <i>Resolution of the enantiomers by HPLC and CD spectra</i>	270
b) <i>Electrochemical characterizations of 2,12-diaza[6]helicene, N-ethyl-2,12-diaza[6]helicene-2-ium and N,N'-diethyl-2,12-diaza[6]helicene-2,12-dium salts</i>	272
c) <i>Chiral discrimination experiments</i>	276
4.2.7 <i>(N-Hex-Ind)₂Ph₂T₄ as low concentration chiral additive</i>	281

a) <i>Experimental conditions for enantiodiscrimination tests</i>	281
b) <i>Enantiodiscrimination tests: selector implemented as inherently chiral additive in ionic liquid</i>	282
4.2.8 <i>A family of inherently chiral QUINAP derivatives</i>	283
4.2.9 <i>Chiral Deep Eutectic Solvents (DES): a novel, effective tool for enantiodiscrimination in electroanalysis</i>	285
a) <i>Natural-based chiral task-specific deep eutectic solvents: DES A, DES G and DES U</i>	286
b) <i>New natural DESs with different HBA and HBD, also in different ratios</i> ..	301
Chapter 5	313
Advanced application in magnetochemistry experiments	313
a) <i>Experimental procedures</i>	314
b) <i>Magnetochemistry experiments</i>	317
c) <i>Effect of the chiral film thickness on the shift of the Fe(III)/Fe(II) peak potential in magnetochemistry experiments</i>	321
d) <i>Effect of the magnet distance on the shift of Fe(III)/Fe(II) peak potentials in magnetochemistry experiments</i>	321
e) <i>"Control" magnetochemistry experiments with achiral PEDOT as thin film on ITO electrode</i>	324
f) <i>Tentative explanation of the observed phenomenon</i>	325
g) <i>Other experiments changing the inherently chiral monomer and the support</i>	332
Chapter 6	337
Conclusion and Perspective	337

6.1 A comparison between the two approaches proposed in this thesis project: advantages and disadvantages of using chiral media or modified electrode surfaces	337
6.2 A Global critical insight: towards common guidelines.....	343
References	349
List of Publications	367
List of attendant conferences and doctorate school.	370
Chapter 7	373
Gallery	373
1. Electrochemical characterization of the bi-naphthyl systems.....	373
2. Electrochemical characterization of the inherently chiral family with phenyl spacer.....	374
3. Electrochemical characterization of terazosin in pH4 buffer solution....	376
4. Electrochemical characterization of lansoprazole in NaOH 0.1 M + buffer pH 4 (ratio 3:2).....	377
5. Electrochemical characterization of clopidogrel in buffer pH 4.....	377
6. Electrochemical characterization of ramosetron in buffer pH 4	377
7. Electrochemical characterization of BT ₂ T ₄ and BT ₂ (T ₃) ₂ in DCM.....	378
8. Electrochemical characterization of BT ₂ T ₄ , BT ₂ T ₆ and BT ₂ (T ₃) ₂ in ACN	378
9. Electrochemical characterization of the inherently chiral family EN-OH, EN-OCH ₃ and EN-Et	379
10. Electrochemical characterization of NSAIDs	382
11. Electrochemical characterizations of planar stereogenicity ferrocenes .	382
12. DSC features of CILs with chiral cations 1a-c (left column, from top to bottom) and 2a-c	385
13. DSC features of CILs with chiral anions 3a-d	386

14. Scan rate effect on the CV reduction patterns of the five salts with chiral cation.....	387
15. Scan rate effect on the CV reduction patterns of the three salts with chiral anion.....	387
16. CV tests of chiral electroactive probe enantiomers (R)-Fc and (S)-Fc in achiral commercial ionic liquid with no chiral additives.....	388
17. Thermal analyses of the new tweezers.....	389
18. CV enantioselection tests with racemic ferrocene in bulk (R)-3mO ₂ NTf ₂	397
19. CV enantioselection tests with racemic ferrocene in bulk (R)-3mO ₂ NTf ₂	398
20. DSC thermograms.....	398
21. EIS equivalent circuit fitting on experimental data	400
22. Enantiodiscrimination examples with mixed solutions of (R)- and (S)- enantiomer on C SPE and Au SPE cells	401
Chapter 8.....	403
Acknowledgments.....	403

*The shell of the Nautilus
is a symbol and expression of chirality in nature
and defines the mathematical language of beauty.*

*The Nautilus is a nocturnal creature that
spends most of his life in the depths of the ocean,
belongs to the mother-of-pearl family,
grows throughout life and has therefore become
a symbol of expansion and renewal.*

The word originates from the Greek and literally means "sailor".

*The shell has remained relatively unchanged for 450 million years
and dates back to the era of the dinosaurs,
in fact, often the Nautilus is also called "living fossil".*

Chapter 1

Introduction

Chirality (from the Greek word χείρ, which means hand) and chiral molecules constitute a key aspect of modern chemistry and chemical technologies, in fact the enantiomeric purity of various compounds is important (and plays a crucial role) in many different fields, such as in food science, pesticide analysis, environment monitoring, and especially in the pharmaceutical field.

Enantiomers are non-superimposable mirror physical systems, and they present the same physico-chemical properties (*i.e.* melting and boiling points). The enantiomers of chiral molecules (regardless of their natural or artificial origin) can present different biological activity. An example is provided by the enantiomers of limonene, which present different smells: the (*S*)-enantiomer in lemon and the (*R*)-one in oranges (Figure 1). We are able to distinguish them due to our nasal receptors (constituted by chiral molecules) that recognize the difference.

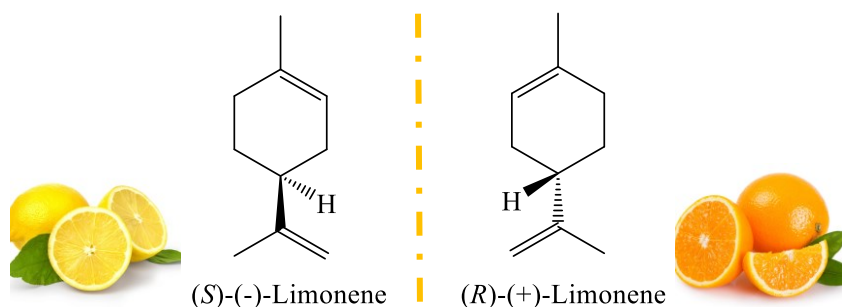


Figure 1. Molecular structures of (*S*)-(-)- and (*R*)-(+)-Limonene.

Moreover, in the human body, the enantiomers can exhibit similar, different or opposite behaviours and for this reason many drugs are often produced in enantiopure form, because only one enantiomer induces the desirable effect and

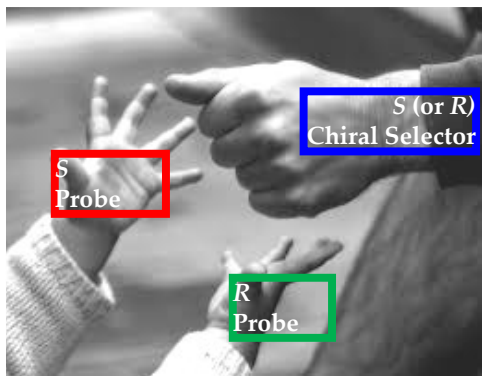
may interact satisfactorily, while the other one may not be active or induce side effects.

Some examples are reported below:

- DOPA (L- or D-3,4-dihydroxyphenylalanine), which is an α -amino acid used in the treatment of Parkinson's disease, is provided as single enantiomer (the L- one), since the D-form is inactive [1];
- thalidomide, which is one of the most notorious drugs, used as racemate, in the 1950s to relieve morning sickness in pregnant women and responsible for a tragic global medical disaster of limb malformations [2];
- ketoprofen, one of the propionic acid class of nonsteroidal anti-inflammatory drugs (NSAIDs), also including ibuprofen and naproxen, with analgesic and antipyretic effects; the therapeutically relevant mechanism of action for these therapeutic agents has been found only for the (*S*)-enantiomers [3];
- L-Methionine, which is a well-known amino acid, used to detect brain tumour, while D-methionine does not present this ability.

The separation and determination of enantiomers is currently performed most commonly by high-performance chromatographic and electro-migrating techniques, but the possibility to employ electrochemistry for chiral analysis presents many advantages including, for example: low cost, high sensitivity, the easy signal transduction, the ability to carry out *in situ* measurements, without previously separation steps and finally the possibility to minimize the use and generation of toxic and polluting substances, thus reducing the risks for the environment. Thus, the electrochemical discrimination of the enantiomers of chiral electroactive molecules, in both analytical and synthetic applications, is a field of high applicative interest and attractive potentialities, especially if the typical electrochemical advantage of fine control/modulation through the electrode potential can be exploited for enantiomer discrimination.

This can be achieved by the suitable choice of an appropriate chiral electrode surface or medium. In fact, enantioselective electrochemistry necessarily implies the electron transfer process to take place in asymmetric conditions (using chiral electrode surfaces or chiral media), since the enantiomers of a chiral molecule have identical physico-chemical properties and therefore the same electrochemical behaviour, except when interacting in a diastereoisomeric context (Figure 2); it is worthwhile mentioning that diastereoisomers are indeed energetically different and in electrochemistry can result in peak potential separation even in the absence of a chiral selector.



energetically different diastereomeric situations
electrochemically recognizable (e.g. ΔI or ΔE)



Figure 2. Diastereoisomeric interactions between probe and selector.

The development of artificial and intelligent selectors is particularly interesting, on account of the virtually unlimited range of tailored structures possible, and they should present the following features:

1. discrimination of probe enantiomers in terms of the largest possible peak potential differences, to achieve enantioselective electrochemical processes for both analytical and preparative purposes (while in this respect current differences are less useful);

2. equal availability of the selector in both enantiomer configurations, so that the first electron transfer (ET) can correspond to the preferred target enantiomer (especially for preparative purposes);
3. linear dynamic range for currents, possibly with low Limit of Detection (LOD), to complement enantiodiscrimination with quantitative analysis and enantiomeric excess estimation (particularly for analytical purposes);
4. general applicability to many probes and operating protocols;
5. reproducibility and stability, as well as robustness;
6. easy, fast and low-cost preparation;
7. little selector quantity required, and/or possibility of recycling.

To achieve the highest degree of selectivity it is possible to work in two different ways (Figure 3): the first one involves the use of electrode surfaces modified with chiral selectors (Figure 3a), the second one involves the use of chiral media or achiral media implemented with chiral selectors (Figure 3b).

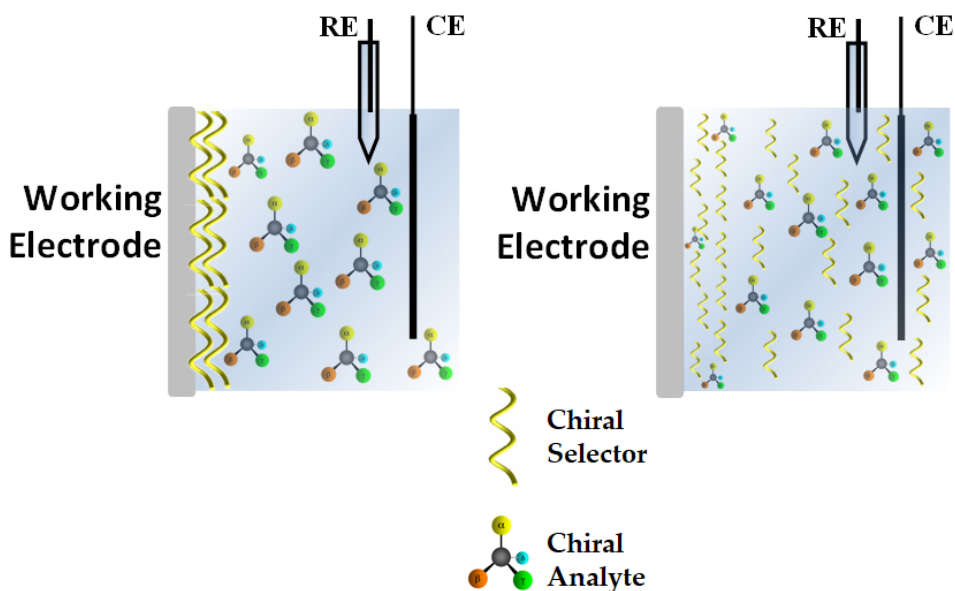


Figure 3. The two different approaches for chiral electrochemistry, using (a) modified chiral electrode surfaces and (b) chiral media.

- (a) Concerning the first approach, the modification of electrode surface can be performed with: chiral metal (or metal oxide), chiral conducting polymers (mostly with stereocenters localized in "pendants" attached to the conjugated backbone, or based on monomers including other stereogenic elements (like atropisomeric or helicoidal ones), or grown in asymmetric environments/matrices, or under magnetopolarization, or with chiral counteranions, or with chiral dopants/entrapped chiral selectors), molecularly imprinted polymers (MIP) obtained with chiral template, chiral self-assembled monolayers (SAMs), bio-based selectors (polysaccharide, enzyme, *etc.*), chiral ionophores incorporated in a membrane, and many others.
- (b) Instead, concerning the use of chiral media, in literature is reported a small number of examples, using chiral supporting electrolytes, media with dissolved chiral selectors/receptors/mediators, magnetic fields (employed to induce asymmetric conditions in electropolymerization/deposition), liquid crystals (with very little quantity of chiral additives).

Some examples reported in literature for both these approaches will be discussed in detail in the next paragraphs, in fact an increasing number of strategies and tools have been proposed to endow the electrochemical interphase with chirality, to achieve enantiodiscrimination in analytical and/or preparative applications.

1.1 Strategies and approaches reported in the literature to modify electrode surfaces with chiral molecules

Over the years, the study of chiral selectors has mainly focused on the development and modification of electrode surfaces, in which the electron transfer can take place above and/or inside the chiral film, depending on the charge, porosity, reciprocal dimensions, time scale, acid/base interactions, *etc.*

In particular, the use of polymers with chiral pendants, external to the main skeleton of the molecule, was very popular. Unfortunately, in many cases the discrimination was in terms of current intensity rather than in potential one. Instead in the last years, bio-organic compounds become the predominantly used material; moreover, the number of works in which it is possible to observe a separation in terms of peak potential (rather than in current intensity) is increasing.

A very wide range of strategies was explored in analytical experiments in the last few years, such as, for example:

1. the use of chiral imprinted mesoporous Ni surfaces with a lyotropic liquid crystalline phase and (*S*)-/(*R*)-phenylethanol as chiral compound (simultaneously present) [4] (Figure 4). When metallic nickel is grown around this soft template, mesoporous channels and chiral imprinted cavities are obtained after removal of the template. The mesoporous Ni surfaces thus achieved are able to discriminate between the two enantiomers of the templating probe, although in terms of current rather than potential differences [4] (Figure 4).

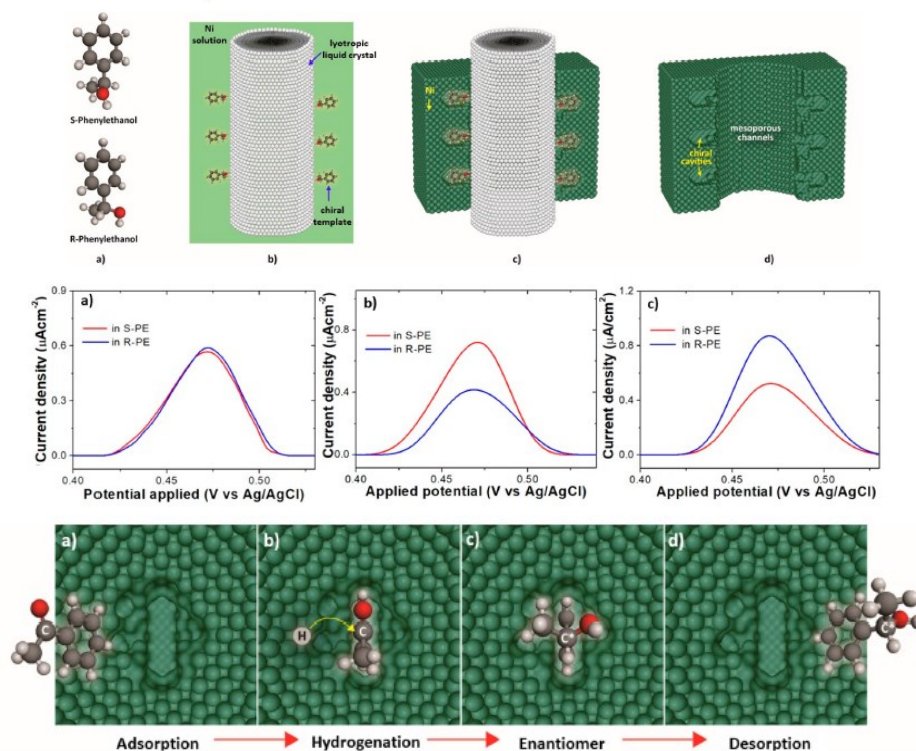


Figure 4. Enantiodiscrimination of (*S*)- and (*R*)-phenylethanol with chiral imprinted mesoporous Ni surfaces [4].

However, mesoporous metals show low stability [5], resulting in an important disadvantage for potential applications. A recent work [6] presents a strategy to overcome this limitation by using nanostructured platinum-iridium alloys, realized by the co-electrodeposition from Pt and Ir salts in the simultaneous presence of a chiral compound and a lyotropic liquid crystal as asymmetric template and mesoporegen, respectively. The alloys enable a remarkable discrimination between chiral compounds and greatly improved enantioselectivity when used for asymmetric electrocatalysis (>95% *ee*), combined with high electrochemical stability (Figure 5).

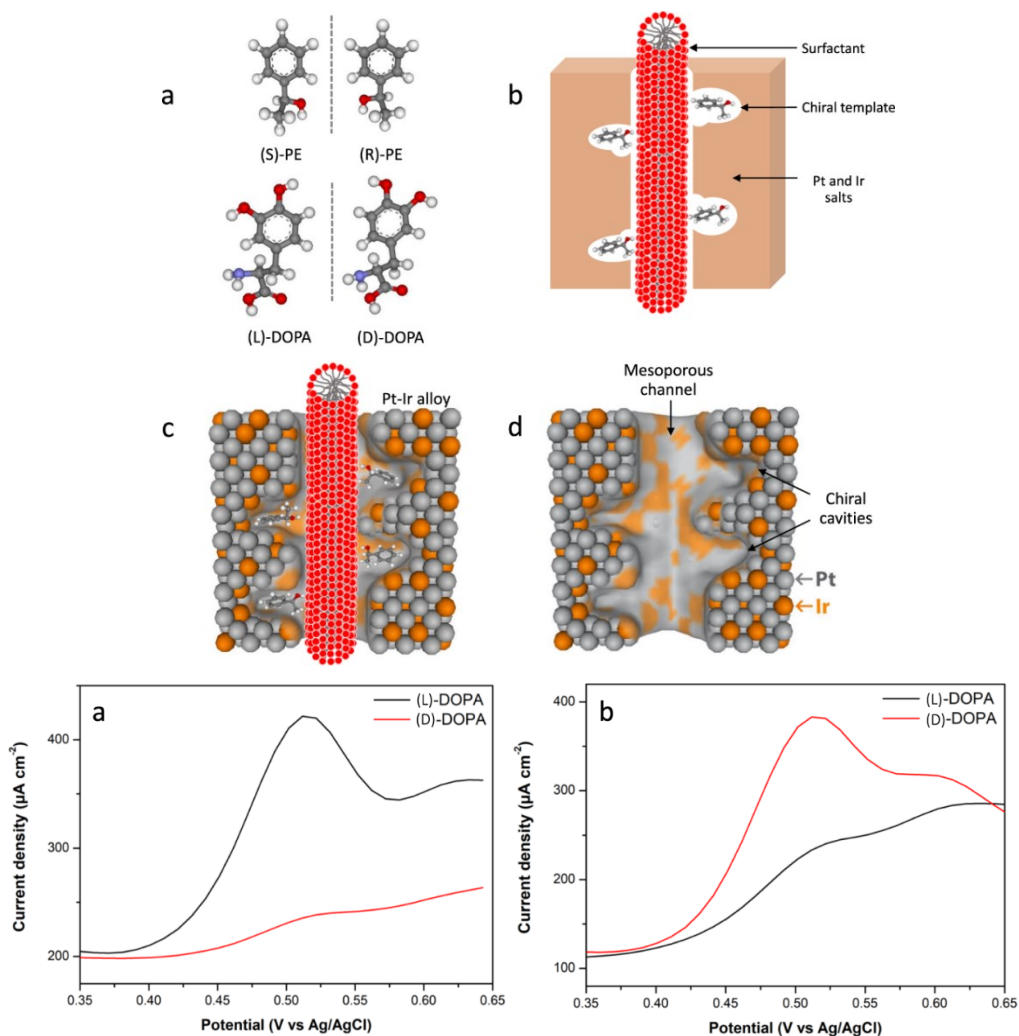


Figure 5. Synthesis of chiral-imprinted mesoporous Pt-Ir alloys (top) and enantioselection tests with the enantiomers of DOPA (bottom) [6].

2. The use of electrodes modified with macroporous carbon embedded with a sulfato- β -cyclodextrin (MPC-SCD). In particular, consistently with MPC featuring macroporous nanostructures, SCD could enter into MPC cavities through adsorption. The resulting structure was used to modify a glassy carbon electrode (GCE), and then to discriminate Tyr enantiomers through differential pulse voltammetry (DPV) experiments. Again, a difference in peak current was

achieved, although a slight potential difference can also be observed [7] (Figure 6).

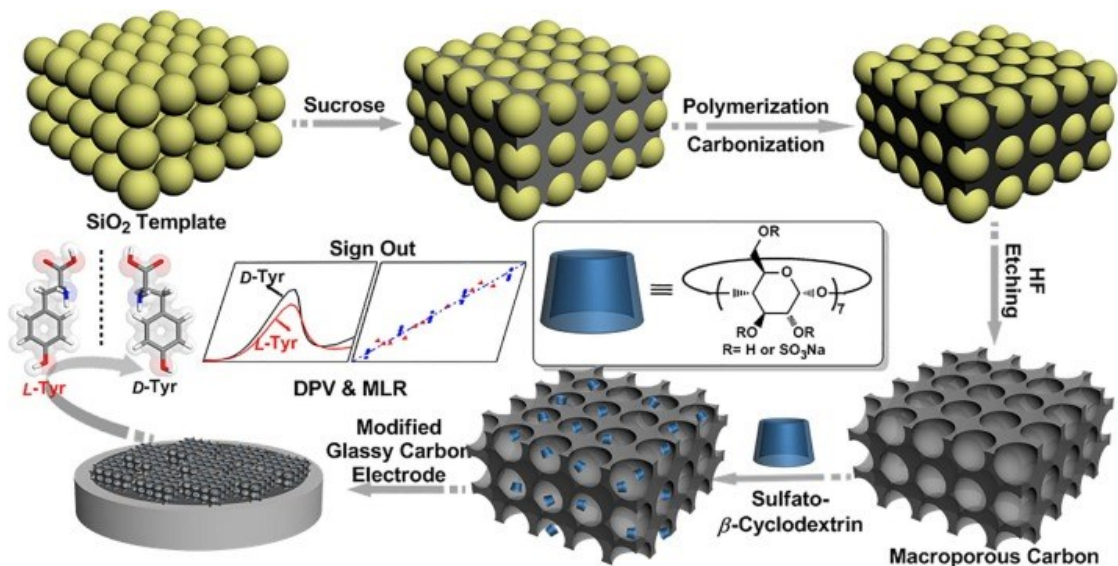


Figure 6. Enantiodiscrimination of Tyr enantiomers by using an electrode modified with macroporous carbon embedded with sulfato- β -cyclodextrin [7].

3. To overcome the problem of the recognition of non-electroactive molecules, an interesting approach is the functionalization of the working electrode surface with a thin layer that is able to act as achiral host for a suitable chiral selector (guest). When the chiral electroactive selector interacts with the non-electroactive chiral probe, its ability to access the guest layer is modulated by the probe configuration, resulting in different electrochemical signals in the presence of the L- and D- probe configurations (Figure 7). In particular, a literature example reported the use of hydrophobic cyclobis-(paraquat-p-phenylene) as the host. Concurrently, a supramolecular interaction was established among such host, a (*S,S*)-Fc derivative, as electroactive chiral selector able to coordinate with different non-electroactive amino acids (like threonine, histidine, glutamine, and leucine). This approach yielded a potential difference of ~ 100 mV in the case of the threonine enantiomers [8].

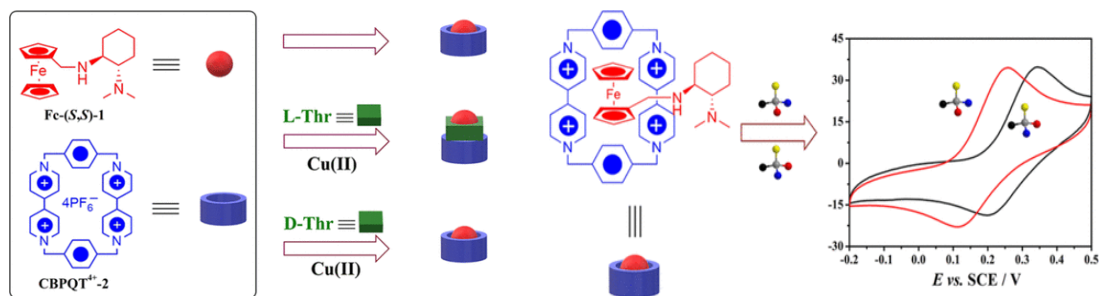


Figure 7. An approach based on host/electroactive chiral selector/non-electroactive chiral probe, resulting in a difference in peak potential for the chiral selector in the presence of the two chiral probe enantiomers [8].

4. Another strategy is based on the use of chiral nanoparticles (Nps, like nanocubes [9] or nanotubes [10]) that can form chiral coordination cages for enantioselective applications. In the cited paper [9], the synthesized Nps have a double helix chiral structure. A potential difference of ~ 90 mV is obtained for the detection of L- vs D- valine with chiral nanocubes [9] (Figure 8a) while in the case of chiral nanotubes a difference of ~ 24 mV is observed for the enantiomers of Tyr and ~ 62 mV for the enantiomers of Trp [10] (Figure 8b).

5. Chiral Molecularly Imprinted Polymers (CMIPs) are advantageous tools in both the separation and sensor fields [11]. There is a very large number of chemical and electrochemical analytical protocols, which use CMIPs as chiral selectors, including the case of modified carbon paste working electrode (CPE) applied for the detection of four β -blockers [12], as well as a highly sensitive and selective MIP sensor based on modification of a glassy carbon electrode (GCE) with prussian blue (PB)-porous carbon (PC)-CNTs hybrids and applied to recognition of cysteine enantiomers [13]. In these articles conductive MIPs were prepared by electropolymerization methods and the elution of templates was performed by a simple overoxidation/dedoping process leading to a “gate effect” that was used for the enantioseparation.

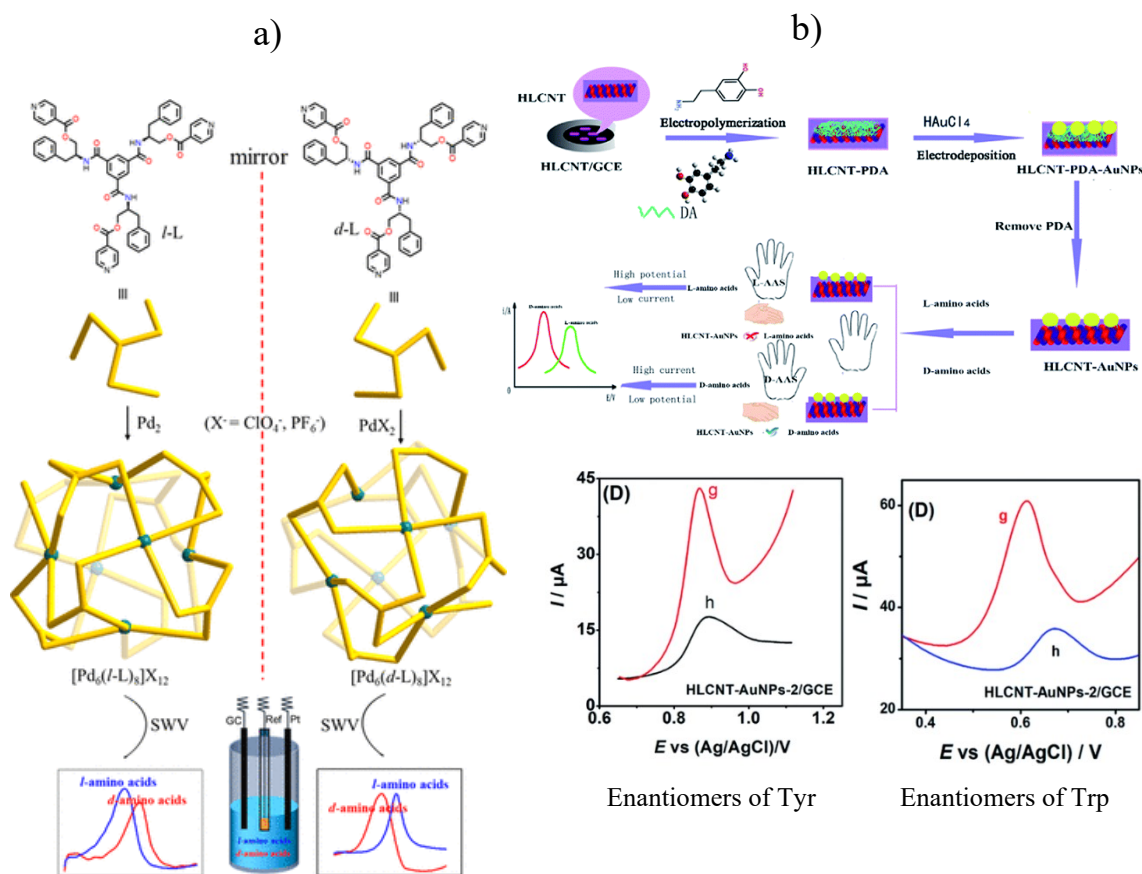


Figure 8. Formation and application of nanocubes (a) [9] and nanotubes (b) [10] for electrochemical sensing.

6. Another MIP, obtained by modifying the electrode with reduced graphene oxide on which a membrane consisting of chitosan is first deposited and then template with propranolol, was applied for the discrimination of the two enantiomers of propranolol (Figure 9) [14]. The electrode modified with the reduced graphene oxide alone results in small potential differences between the enantiomers of propranolol, which can be justified by the active material presenting many stereocenters; moreover, by templating it with the enantiomers of propranolol, even greater differences are observed.

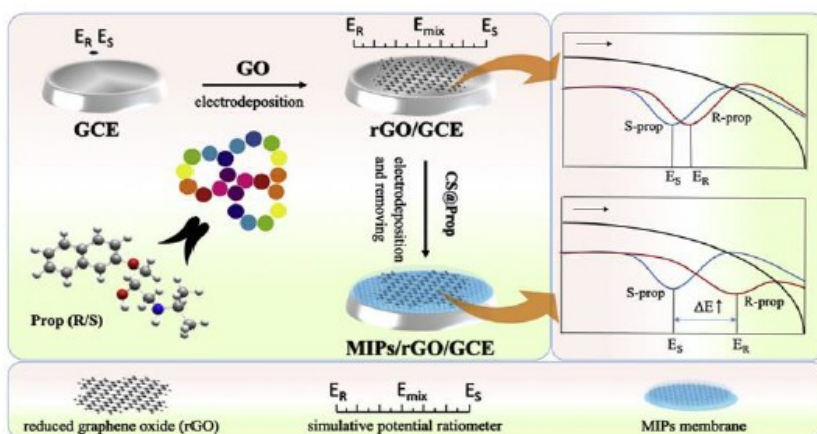


Figure 9. Schematic illustration for the realization of the MIP (left side) and enantioselection measurements (right side) [14].

7. Also, β -cyclodextrin, a bio-organic compound (in particular, a polysaccharide of natural origin), which presents many cavities, is able to interact with chiral probes. For example, in a recent literature case [15], the electrode surface was modified with graphene oxide on which β -cyclodextrin was deposited. The enantioselection measurements were then performed using the enantiomers of tryptophan as probes and obtaining differences in terms of both current and peak potential (~ 48 mV) (Figure 10).

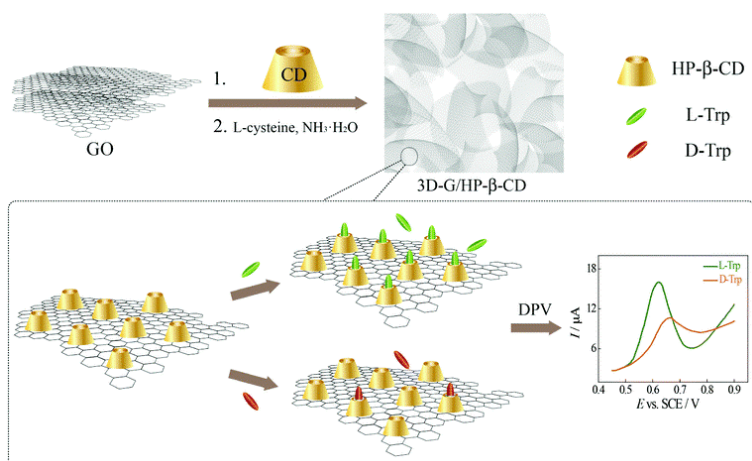


Figure 10. Sensor based on graphene oxide and β -cyclodextrin, and measurements for the enantioselection of tryptophan enantiomers [15].

8. Also many nanomaterials are used, like a type of "Single Walled Carbon Nanotubes" (SWCNTs) applied for the enantioselection of DOPA enantiomers [16]. Unfortunately, the results obtained show differences only in terms of current intensity (Figure 11).

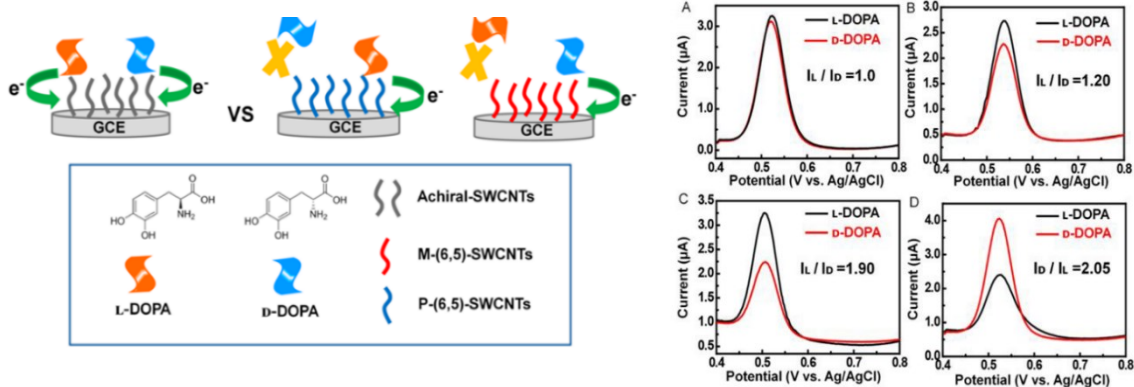


Figure 11. Illustration of the modification of a glassy carbon (GCE) electrode with left-handed or right-handed SWCNTs (left side) and DPV measurements of DOPA enantiomers (right side) [16].

1.1.1 Weak points of the proposed strategy

Many kinds of modified chiral electrode surfaces have been proposed in literature, as reported above. Unfortunately, many of them have one or more critical points including, for example:

- poor or labile enantioselectivity, difference in current intensity without potential separation, or too small peak potential differences. Notably, non-fully enantioselective sensors in terms of current, or mass, or conductivity, or potentiometric response (*i.e.*, responding X% to one enantiomer probe and Y% to the other one) could be applied to detection and management of a given enantiomer only provided that the presence of its antipode be *a priori* excluded.

- Actually, a problem common to most approaches, even attractive and successful, with only a few exceptions, consists in the difficulty to detect or manage both enantiomers when they are both present (or when it cannot be *a priori* excluded). Even sensors approaching full enantioselectivity in current or mass or potentiometric response (*i.e.*, responding 100% to one enantiomer probe and 0% to the other one) can offer outstanding detection and quantification of one molecule antipode even in the presence of the opposite enantiomer, but for the same reason cannot account for the presence and concentration of the antipode (unless two specular sensors be employed concurrently).
- Applicability to a single probe and/or a single probe enantiomer only (not general applications to many probes).
- Preparation procedures and/or operating protocols often appear sophisticated and expensive, and/or lacking robustness and/or reproducibility. Furthermore, most of them could hardly be applied to preparative experiments, which could explain the limited number of preparative studies so far available; actually, chiral electrosynthesis, in spite of its perspective importance, appears far from being mature. For example, many molecular films can be labile/fragile, and the elegant and conceptually simple chiral metal surfaces, offering by CV neat differentiation between probe enantiomers, are very difficult to prepare and manage.

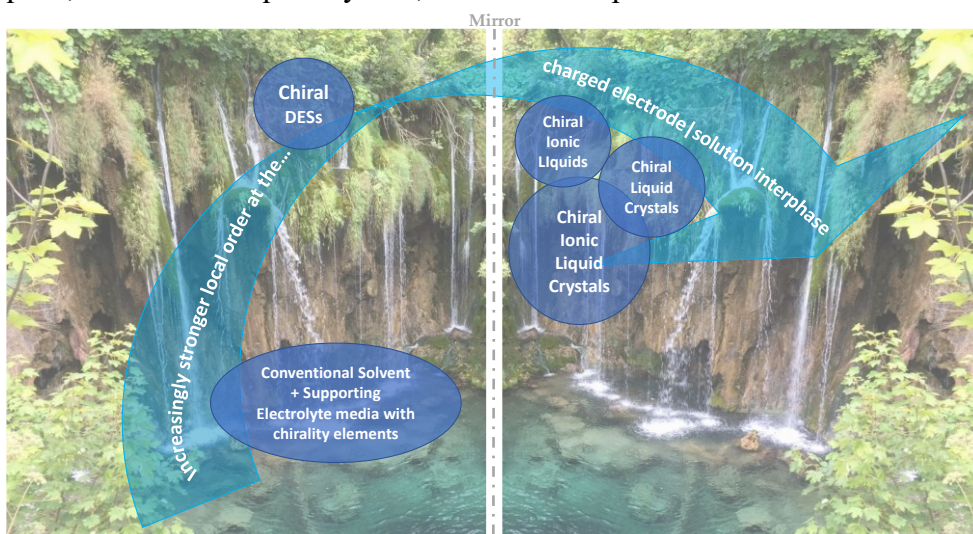
A weak point possibly connected with several of the above problems (in particular, weak and/or labile chirality manifestations) is that the chirality source is not intrinsic to the whole selector, but either localized (for instance, in oligo/polymer films, on stereocenters usually located in external “pendants” rather than in the main electroactive chain; in molecular selectors, on one or more

stereocenters; in composite materials, on stereocenter(s) of the chiral selector included in the hybrid material) or external (for example, from external molecular templating agents in molecularly imprinted materials, like polymers, metal films and composites, or from a magnetic field or a chiral electropolymerization medium, for asymmetrically grown inorganic and molecular films).

In this context, most desirable is the development of a low-cost and easy-to-prepare artificial chiral electrode material, stable and capable of discrimination of a wide variety of antipode pairs. A major breakthrough can come by the use of “inherently chiral” molecular materials, either as electrode surfaces or media (see later on chapter 1.4).

1.2 Advanced chiral molecular media for enantioselective electrochemistry and electroanalysis

Chirality has been implemented at the electrochemical interphase, not only at the electrode surface side (as reported in Chapter 1.1) but also on the medium side. Recently, the attractiveness of this latter approach has remarkably increased on account of the increasing availability of advanced chiral molecular media with intrinsic attractive features for electrochemical applications, such as chiral ionic liquids, chiral ionic liquid crystals, and chiral deep eutectic solvents.



Implementing chirality in traditional solvent + supporting electrolyte media

In traditional organic solvent + supporting electrolyte media, chirality can be implemented in the solvent, in the supporting electrolyte, or in additives [17,18-21]; however, there are not many examples involving chiral solvents/cosolvents [17,18], and instead a number of early electrosynthetic studies exploited chiral supporting electrolytes [17,18]. The observed enantiomeric excesses in the products, although modest in most cases, are consistent with the reacting molecules undergoing the electrode process in a double-layer-like interphase implemented with chirality in terms of chiral cations or chiral anions from the

supporting electrolyte [18]. More recent studies of preparative or synthetic character have chirality implemented in dissolved additives which can be involved in the electrode process playing the role of receptors/mediators/catalysts/auxiliaries [17,18-21].

Implementing chirality in ionic liquid (IL) media

ILs are molecular salts which are liquid at low temperature (*e.g.* below 100 °C) and particularly at room temperature (Room Temperature Ionic Liquids, RTILs) [22]. In many cases chiral ionic liquids (CILs) include ammonium, pyridinium, imidazolium, benzimidazolium, or phosphonium cations with alkyl chains in combination with anions such as BF_4^- , PF_6^- , or bistriflimidate (an anion used to lower the melting point), but a wide variety have been proposed, with many possibilities of structure/property modulation, also including tasks specific, polymeric, magnetic, and chiral ILs [22]. They have become popular solvents on account of their advantageous features, with respect to traditional organic solvents, such as low vapor pressure, chemical and thermal stability, non-flammability, and modulable features [22-24].

From the electrochemical point of view, ILs are even more attractive, because they can act both as solvent and supporting electrolyte with wide potential windows, and possibility of tuning charge/mass transport as well as electron transfer processes by their molecular design [22-25].

Very important is the possibility to achieve a highly controlled electrochemical interphase exploiting the peculiar order of ILs at a charged surface [22, 26- 32], consisting in compact and regular ion multilayer structures, tunable by the electrode potential, much stronger with respect to classical double/diffuse layer structures of normal solvent + supporting electrolyte systems, and extending at a quite larger distance from the electrode surface [26,33-35].

Attractively, IL interphases have local features similar to bulk liquid crystal (LC) ones (see later on), widely modulable through IL design and by the local presence of additives, including water; while, importantly, transition from IL structure to classical double layer only takes place at pretty high water mole fractions [36,37]. Effective enantiodiscrimination was achieved in many fields such as synthesis, catalysis, chromatography, spectroscopy, resolution/extraction [38]. However, notwithstanding the high and steadily increasing number of CIL applications [39,40,41-47] as chiral selectors in potential-driven separation techniques such as capillary electrophoresis/electrokinetic chromatography/capillary electrochromatography, CILs have been so far underexploited in chiral electrochemistry /electroanalysis meant as enantiodiscrimination based on electrode processes.

A number of recent studies concerns CIL application for modification of electrode surfaces with chiral layers, either as ingredients of hybrid materials or as polymeric CILs (PCILs) [48-51]:

(i) CIL-graphene oxide sheets obtained by electrolysis with graphite rod electrodes in a dicationic CIL electrolyte were used to modify a glassy carbon (GC) electrode. Enantiodiscrimination in terms of current (in some cases, also potential differences) was observed for chiral probes tryptophan, mandelic acid, malic acid, and tyrosine. In particular, in the tryptophan case, a peak potential separation of ~ 70 mV was achieved [48] Figure 12a.

(ii) A PCIL copper complex was used to modify a GC electrode tested for the same chiral probe series with similar results, including a peak potential difference of ~ 88 mV for the enantiomers of malic acid [49] Figure 12b.

(iii) An electroactive rotaxane consisting of a crown ether sliding along a PCIL was used to modify a GC electrode; tests with tryptophan, tyrosine, and cysteine mostly resulted in current differences and only small potential ones [50].

(iv) A nanosphere mesoporous functional material consisting of alternating achiral dicationic IL and (1*S*,2*S*)-1,2-diaminocyclohexane building blocks linked by organosilica units was tested as a GC modifier for discrimination of the enantiomers of various amino acids, mostly resulting in current differences; a peak potential difference of ~ 70 mV was observed for L- and D-cysteine [51] Figure 12c. Notably, however, in such cases, the CIL role at the interphase was not that of the medium or medium additive. Moreover, they only involved chirality originating from localized stereocenters.

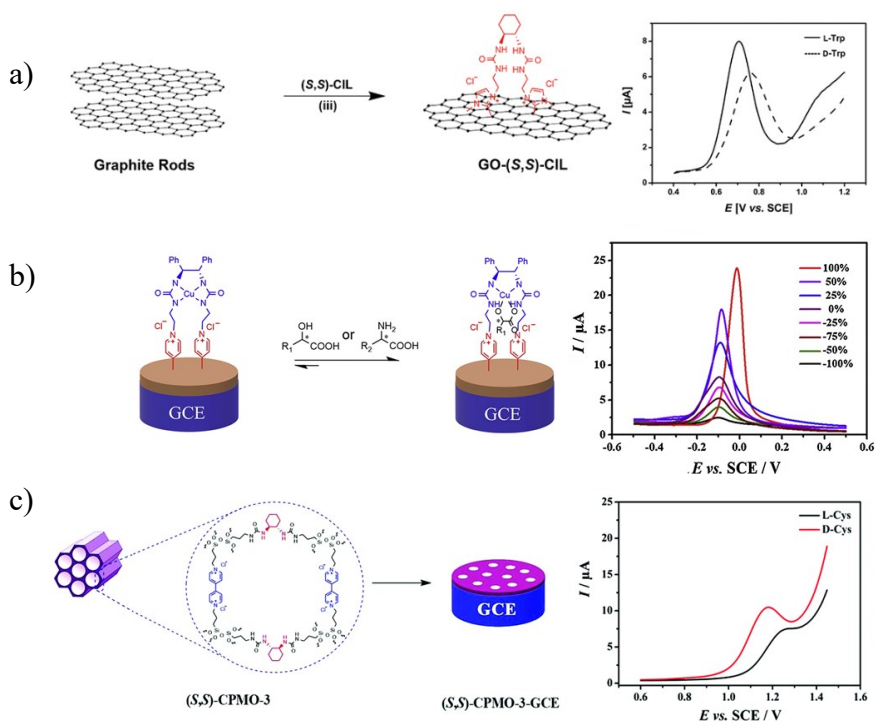


Figure 12. Selected examples of CIL performances in electroanalytical enantiodiscrimination experiments. Differential pulse voltammetry (DPV) curves (a) for 0.5 mM L and D-Trp at the electrode modified with functional graphene sheets GO-(*S,S*)-CIL [48]; (b) for racemic mandelic acid with different *ee* values, with chiral poly(ionic liquid)-metal complex (*S,S*)-PCIL-5-Cu(II)-GCE [49]; (c) for 0.5 mM L and D-Cys, with mesoporous organosilica spheres with the chiral group (*S,S*)-CPMO-3-GCE [51].

Chiral LCs (CLCs) and chiral ionic LCs (CILCs)

LCs (which can be neutral organic or inorganic compounds) present characteristics between the solid crystalline and the isotropic liquid states. They are anisotropic compounds with refractive index, electric permittivity, magnetic susceptibility, and mechanical properties that depend on the direction in which the measure is carried out. LC mesophases originate from different types of interactions between anisometric molecules and chiral LCs can form helical ‘cholesteric’ or ‘chiral nematic’ mesophases [52]. Mesophases can be modulated by temperature or by the presence of additives; for example, chiral additives in achiral LCs can induce a structural transition from achiral to chiral mesophase, which has been exploited for electrosynthesis of helical polymer films [53].

Polymer-stabilized cholesteric LCs, with peculiar electromechanical and electro-optical features, can be obtained from LC monomer polymerization within a cholesteric LC [53]. Being neutral, LCs are hardly suitable media for electrochemistry unless a suitable electrolyte is added, but this problem is overcome with ionic liquid crystals (ILCs) [54], containing anions and cations and characterized by a high ion conductivity in a specific direction.

ILCs can be considered as materials that combine the properties of LCs with those of ILs, and the principal features are: orientability, miscibility, phase stability, packing tunability, polar nanochannels [54].

From the electrochemical point of view, (C)ILCs are more advantageous media with respect to LCs because the latter require the addition of a supporting electrolyte owing to their low ion conductivity. CILCs were used in electrochemical polymerization processes affording helical conjugated systems useful for chiral extraction or for molecule detection [55].

However, applications of (C)ILCs in the electrochemical field are still at the beginning; in fact, the studies so far presented in literature principally focus on

the electrochromic behaviour or the mere electrochemical characterization of the ICIL as such [56,57].

Thus, investigating CILCs for analytical applications represents a quite promising but still overdue target.

Chiral deep eutectic solvents (DESs)

Deep eutectic solvents (DESs) are mixtures of two components, for example, Lewis or Brønsted acids and bases, whose reciprocal interactions result in an eutectic melting point significantly lower than the predicted one for an ideal liquid mixture [58-61]; many DESs are liquid at room temperature. Importantly, it is not required for the mixture to have the eutectic composition to be considered a DES, but only to be liquid below the ideal eutectic point; therefore, for any binary mixture, it is possible to modulate properties by tuning the component ratio.

In the last years, DESs have rapidly grown in popularity as chemical and electrochemical media, since they can be easily prepared in reasonable quantities by mixing two components that can be chosen in a wide range (so they can be considered as designer solvents, because their components can be chosen on account of useful additional functional properties), possibly cheap and widely available, low cost, biocompatible, and biodegradable (particularly when of natural origin, natural DESs (NADES) [62]; NADES are even assumed to occur in nature, for example, as a liquid phase in cells [62]).

Like ILs, also DESs look highly attractive for electrochemistry applications, such as electrodepositions (of nanomaterials, polymers, coatings), batteries [63], and modification of electrode surfaces for sensor applications [64,65], besides capillary electrochromatography [66]. Actually, DESs share with ILs good transport properties, wide potential windows, and compatibility with water traces. However, a key issue to explore for DES use in electrochemistry is

whether they also feature high structural order at the electrochemical interphase, such as ILs. Actually, while in the IL case, only involving ionic species, the interphase structure is prevalingly determined by coulombic forces, in the DES case, an important contribution should also come from other interactions between DES components, such as hydrogen bonding, acid/base, and van der Waals interactions. Unfortunately, unlike the IL case, only a few studies are so far available on this subject based on capacitance [67], atomic force microscopy (AFM) [68], density functional theory (DFT) [69], molecular dynamics (MD) [70] contact angle [71], CV, and laser-induced temperature jump technique [72]. Although the problem is more complex than in the IL case [72], the studies point to DES featuring multilayer structures, although less compact and extending less far away from the electrode surface [71,73] with modulation from the electrode potential [71,74], the water content [68,69] (DES features being retained up to 50% volume of water [68], water being involved in hydrogen-bonding interactions), and the alkyl chain length [73]. Sometimes a micellar structure is observed [74]. On the whole, DES interphases look more structured than classical solvent + supporting electrolyte systems. Such orders could be advantageously exploited for enantiodiscrimination purposes when working in chiral DESs. The latter ones are easily available by simply choosing a chiral component for the binary mixture (a study is also reported of DESs consisting of both chiral components [75]; however, this is not necessary, and having a single chiral selector is simpler for rationalization purposes) either from the wide natural pool or synthetic. Actually, many biobased DESs do have a chiral component (saccharides, amino acids, chiral acids, or bases [76]); but this property is surprisingly so far underexploited, and only a few applications have been so far reported, for example, as chiral media in synthesis and biosynthesis [75], for extractions [77], for induced circularly polarized luminescence [78], and as additives in electrokinetic enantioselective chromatography [79].

1.3 Advanced applications of chiral molecular selectors: sensing electrochemical devices

1.3.1 Bipolar electrochemistry with chiral conducting polymers

Chiral conducting polymers have been extensively studied due to their potential applications, as reported in chapter 1.1, including very interesting electrochemical features. Particularly in the last years some unconventional, fascinating applications are reported in literature, such as wireless light-emitting devices and actuators [83].

In particular, the wireless and asymmetric features of bipolar electrochemistry can be attractively combined with the electroactivity, tunability and easy processability of conducting polymers. In fact, bipolar electrochemistry is an interesting approach to generate asymmetric electroactivity on a conducting object: in the presence of an external electric field (ϵ), a polarization potential difference (ΔV) is generated at the extremities of a conducting object positioned anywhere in the solution. Thus, as long as the ΔV exceeds the thermodynamic threshold potential required to trigger both reactions (ΔV_{\min}), the conducting object behaves as a bipolar electrode.

In most examples of wireless actuation of conducting polymers, one extremity of the asymmetrically polarized film serves as a reaction site for a given molecule of interest, whereas the opposite end acts as a transducer by generating motion. Recently, the bipolar electrochemistry approach has also been explored for the transduction of chirality across different length scales, from the molecular to the macroscopic level and some examples will be presented below:

- the first wireless enantioselective actuator was realized coupling chirality with the electromechanical properties of a Ppy film, using an imprinted hybrid platinum-Ppy surface [84]; the mechanical deformation of the Ppy strip is directly related to the difference in oxidation kinetics of the two enantiomers of mandelic acid. However, the enantioselectivity is based on

the relative difference in conversion efficiency, making it intrinsically impossible to detect both enantiomers if they are simultaneously present in the same mixture (Figure 13).

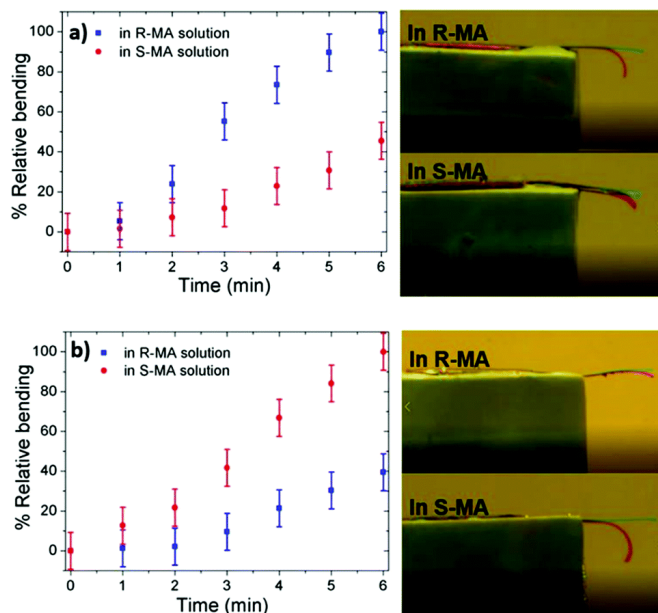


Figure 13. Bipolar electrochemical actuation of hybrid chiral Pt-PPy in 50 mM *R*-MA (blue) and *S*-MA (red). The pictures on the right have been taken after 6 min of applied potential. The green line indicates the initial position of the actuator, whereas red corresponds to its final position [84].

- The use of inherently chiral oligomers allows the discrimination of the enantiomers of chiral electroactive analytes based on thermodynamic differences in oxidation potential. In particular, a hybrid Ppy film modified with oligo-BT₂T₄, was used as bipolar electrode for the absolute enantiomeric discrimination of L- or D-DOPA [85]. Moreover, the induced redox reactions lead to well-pronounced wireless actuation when DOPA with the appropriate chirality is present in solution, whereas absolutely no electromechanical response is measured for the wrong enantiomer (Figure 14). In addition, a linear response for the degree of bending as function of the analyte concentration was obtained.

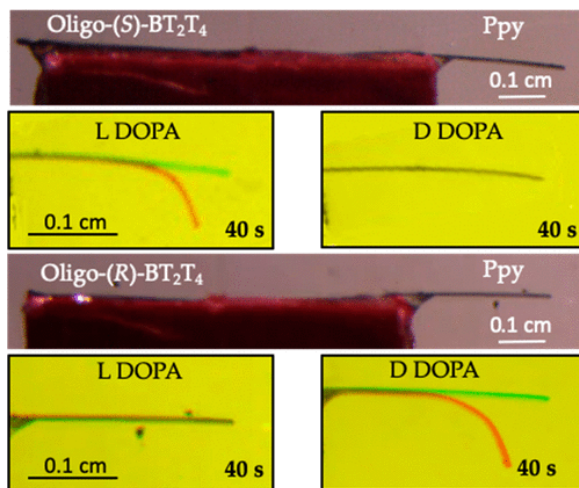


Figure 14. Bipolar enantioselective electrooxidation of L- and D-DOPA (5 mM) on the surface of oligo-(*S*)- and oligo-(*R*)-BT₂T₄ deposited on Ppy [85].

- The enantiomeric excess of unbalanced mixtures of L- and D-DOPA can be determined by using a couple of hybrid Ppy films modified with (*S*)- and (*R*)-oligo-BT₂T₄, as bipolar electrodes (Figure 15) [86]. A correlation between the degree of actuation and the concentration of the corresponding analyte in solution was obtained.

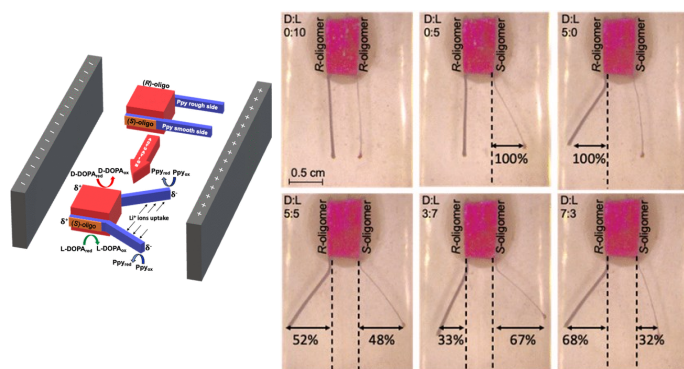


Figure 15. Schematic Illustration of the setup (left side) and bipolar electrochemical experiments for the enantiomeric excess determination of D- and L-DOPA solutions with different molar ratios (right side) [86].

- The propagation of chiral information to the macroscopic scale was also achieved, using a hybrid sandwich bipolar electrode, based on Ppy and (*S*)- and (*R*)-oligo-BT₂T₄, which was exposed to either L- or D-DOPA in solution [87]. In the presence of an electric field, macroscopic enantiomorphs are formed through chiro-specific curling, thus transducing the presence of chirality at the molecular scale (Figure 16).

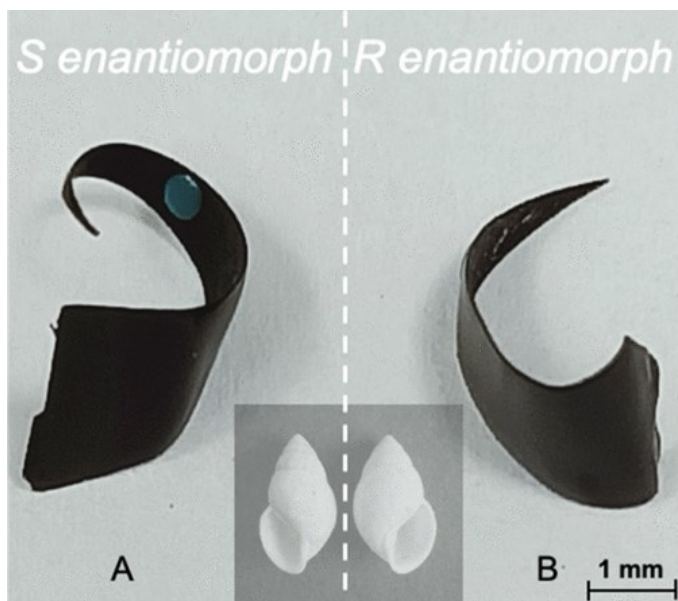


Figure 16. Picture of the two (*R*)- and (*S*)-enantiomorphs recovered at the end of the bipolar experiments [87].

- Finally, a very interesting and recent work [88] presents an innovative strategy, which allows the conversion of molecular information into macroscopic motion, based on bioinspired machines able to transfer chiral concepts from nature to hand-made structure. The authors describe the design and dynamic behaviour of hybrid bioelectrochemical swimmers that move spontaneously at the air–water interface. The motion is governed by the diastereomeric interactions between immobilized enantiopure oligomers, and the enantiomers of a chiral probe molecule present in solution. These dynamic bipolar systems are able to convert

chiral information present at the molecular level into enantiospecific macroscopic trajectories. Depending on the enantiomer in solution, the swimmers will move clockwise or counterclockwise; the concept can also be used for the direct visualization of the degree of enantiomeric excess by analysing the curvature of the trajectories (Figure 17).

Deciphering in such a straightforward way the enantiomeric ratio could be useful for biomedical applications, for the read-out of food quality or as a more general analogue of polarimetric measurements.

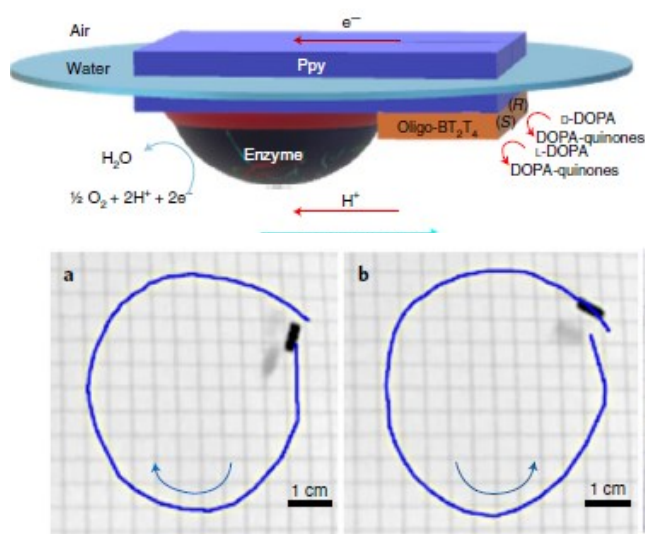


Figure 17. Illustration of the swimmer at the air–water interface (top) and macroscopic enantiospecific motion of swimmers (bottom) [88].

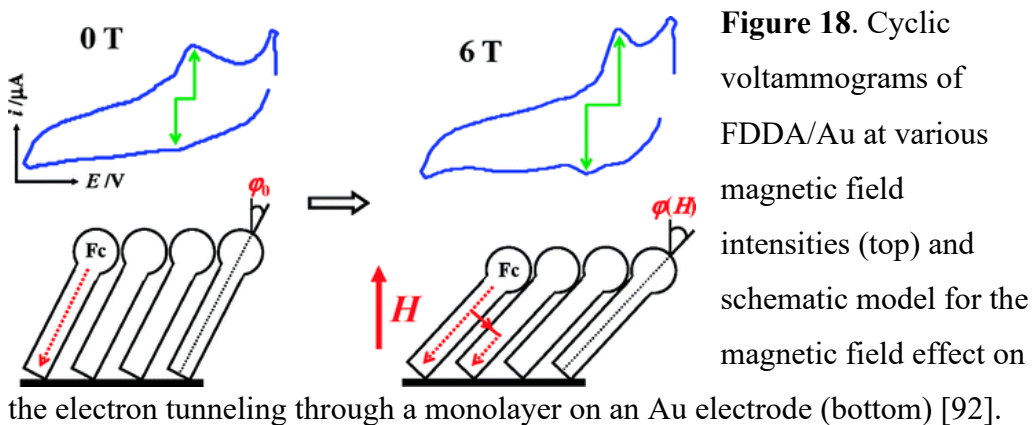
1.3.2 Magnetochemistry experiments with chiral molecules

The study of the mutual influence between chirality, magnetism and the electron spin is a well-documented field of research and in the past two decades, moreover, it has been demonstrated that chiral molecules possess unique electronic properties [89].

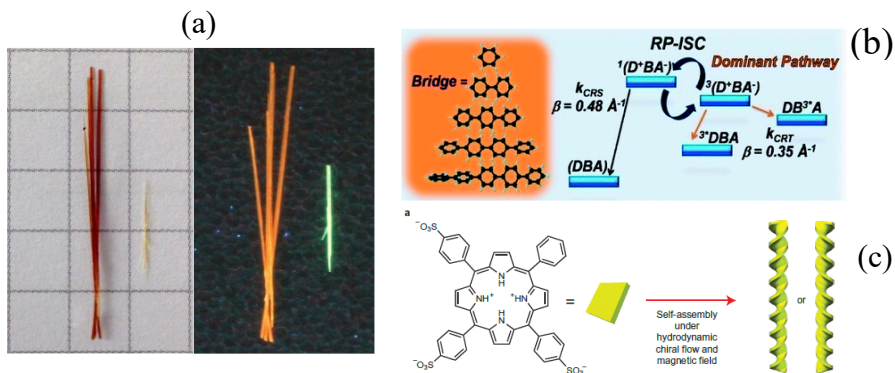
In this context, the interrelated disciplines of magnetochemistry, spintronics and Spin Dependent Electrochemistry (SDE) play a crucial role.

Actually, magnetic effects in electrochemical systems have been investigated focusing on Lorentz and Kelvin force effects [90,91] and the large majority of the available magnetochemistry studies deals with achiral systems.

An example is provided by the application of an external magnetic field able to induce conformational variations in self-assembled monolayers (SAMs) [92], as shown in Figure 18.



A magnetic field can also influence the morphology of molecular crystals [93] (Figure 19a), the reaction path in electrochemical redox mechanisms involving open-shell intermediate species [94-96] (Figure 19b) and crystallization processes [97,98] (Figure 19c).



Dealing with magnetic fields, it is important to distinguish between “true” and “false” chirality [99-105]. This problem was rationalized by Barron [99-102] (Figure 20), in fact he stated that several time-dependent mirror physical systems are not truly chiral since they are interconverted by combined space and time reversal; while true chirality is when successive space and time inversion leads to two systems which are not superimposable [99-103].

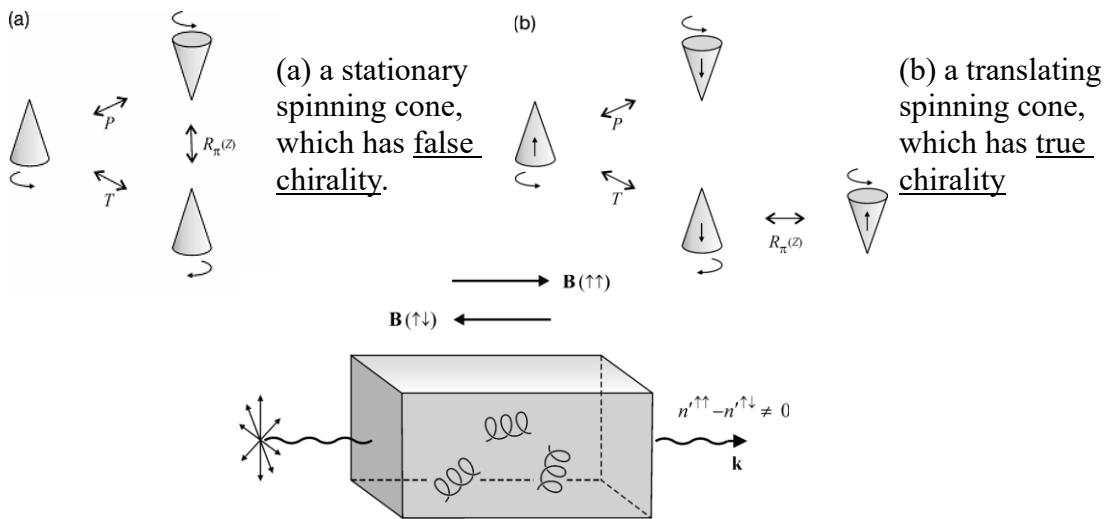


Figure 20. Schematic representation of true and false chirality.

Consistently, a magnetic field alone cannot produce true chirality; instead, according to Barron's approach, an electron in helical roto-translational motion can be regarded as chiral, existing as two possible enantiomers, corresponding to the α or β spin configurations, that do not coincide upon space and time inversion. Such peculiar "chiral actor" is the object of spintronics, the fascinating field of modern physics which deals with the active manipulation of spin degrees of freedom of charge carriers [106].

In fact, a general spintronics device is based on generation of carrier spin polarization (SP) in a suitable active material and spin polarized detection at the

output [107]. Important practical implications for the everyday life regard the magnetic information storage technology based on the giant magnetoresistance effect [108], resulting in a magnetic-oriented modulation of electric resistance of the device. So far spintronics has been mainly developed exploiting metal, oxide or inorganic semiconductor materials; however, molecular spintronics is regarded as an attractive target on account of the wide range, flexibility, processability and low cost, typical of molecular materials [109].

The combination of spintronics with magnetoelectrochemistry, particularly involving truly chiral molecular spin selectors, was promoted by the discovery of the Chiral Induced Spin Selectivity (CISS) effect by Ron Naaman and co-workers, observing SP in photo-ejected electrons transmitted through a thin layer of enantiopure material adsorbed on gold, acting as an electron spin filter [89, 110].

Such CISS effect was subsequently exploited in electrochemical experiments [89], giving raise to spin dependent electrochemistry SDE, in which electrons are generated, rather than by X-ray photoemission, by a low electric potential difference in electrochemical cells including a ferromagnetic electrode and a chiral molecular layer [89,105,111-116]. The process thus involves interaction/transfer of a truly chiral probe, the electron with spin-orbit coupling, with/through a truly chiral phase, the chiral molecular film acting as spin filter. In this frame, a key issue is the availability of molecular layers of high electroactivity and enantioselectivity providing top level spin filters.

1.4 The power of inherently chiral molecular selectors

In the field of chiral electroanalysis, extensively described and introduced in the previous chapters, a powerful tool is provided by chiral molecular selectors endowed with “inherent” chirality [17,117].

In inherently chiral molecules the stereogenic element responsible for chirality coincides with the functional group responsible for the specific property of the material, in this case the electroactivity, on account of the presence of atropisomeric (*i.e.* with hindered rotation) or helicoidal elements in the main conjugated backbone, resulting in a regular torsion with an energy barrier too high not to be overcome at room temperature, in the working operating conditions.

Such approach to electroactive oligomers and polymers of “robust” chirality had been already exploited, for example with binaphthyl elements [118] (for applications in chiral catalysis), or helical elements [119], often with conjugation partially impaired by ring connectivity, but hardly for application to electrochemical enantiodiscrimination. An exception was provided by chiral phenylethylamines behaviour on films obtained from thiophene-based monomers including a binol or a binaphthyl crown-ether atropisomeric scaffold [120].

The peculiar features of inherently chiral selectors endow them with outstanding chirality manifestations, much more powerful respect to more common chiral selectors having localized stereocentres as stereogenic elements.

In fact, outstanding discrimination ability, in terms of large peak potential differences between chiral probe enantiomers, has been observed when “inherently chiral” selectors were employed both as chiral selectors to modify the electrode surface and chiral media (with a very high local order).

The inherently chiral concept has been implemented in different structures:

1. 2,2'-[2-(5,2-bithienyl)]-3,3'-thianaphthene (**BT₂T₄**), which can be discussed as a model, being endowed with a bundle of interrelated important properties for the electrochemical enantioselection task [121-123]. It consists of two identical moieties with an atropisomeric bibenzothiophene core, corresponding to a $\sim 70^\circ$ torsional angle and a torsional energy barrier far too high to be overcome in the operating condition range. As a consequence, it exists in two stable enantiomers that can be separated by chiral HPLC. Moreover, a certain conjugation degree is maintained between the two moieties of the main backbone, which is the source of both molecular chirality and electroactivity, strictly reciprocally related. The monomer has good charge transfer and charge transport properties as well as very high oligomerization ability on account of its intrinsic 3D character. Racemic BT₂T₄ had been exploited as an outstanding comonomer to obtain fast and regular formation of MIPs for piezogravimetric sensors in the case of functional monomers with lower oligomerization ability [124-126], resulting in materials with excellent mechanical properties and retaining the functional properties of the less reactive comonomer.

Moreover, importantly, such oligomerization is intrinsically regioselective, on account of the molecule C_2 symmetry (only two homotopic thiophene terminals are available). This enables to fully transfer chirality from the monomer to the corresponding electroactive film obtained by chemical or electrochemical oxidation, which fully retains the monomer (*R*) or (*S*) configuration. Antipode films exhibit neat and specular CD signals, reversibly modulated by charge/discharge cycles [121,127], pointing to powerful and stable “macromolecular” chirality.

A further valuable feature is that oligo-BT₂T₄ films include a significant amount of cyclic oligomers besides linear terms [128], that is, a collection

of potentially coordinating heteroatom-rich cavities of different dimensions (in particular, cyclic dimers, trimers, tetramers were isolated and studied). Obviously, oligo-BT₂T₄ films showed remarkable enantioselection ability, testing different chiral probes, also of pharmaceutical interest [121,129,130].

The same enantioselection experiments were extended to other inherently chiral electroactive films, with different atropisomeric cores, such as:

2. **3,3'-bithiophene** [122], structure is reported in Figure 21 (left side).
3. **2,2'-biindole** (Figure 21, left side) [131], which offers peculiar advantages, such as very easy modulation of functional properties through easy design tuning. In particular, besides the possibility of modulating the synthesis of the monomer terminals, the *N* atoms in the core can be easily functionalized with alkyl chains of different lengths (an effective tool to tune, for instance, solubility and processability), or even more complex substituents with specific properties.
4. **1,1'-binaphthyl** [132] (the structure is reported in Figure 21, right side),

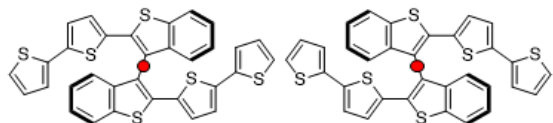
or with other stereogenic element, such as helix instead of a stereogenic axis:

5. **tetrathia[7]helicene** [133] (the structure is reported in Figure 21, right side).

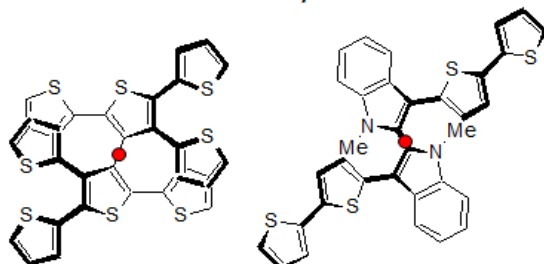
In all the cases, significant peak potential separation was achieved with chiral probes which present different chemical nature/bulkiness and electrochemical activity.

“Inherent chirality”

Biheteroaromatic
atropisomeric core

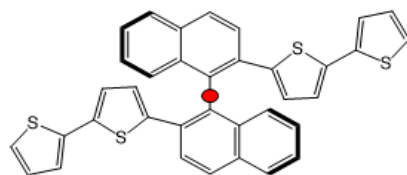


bibenzothiophene



3,3'-bitiophene

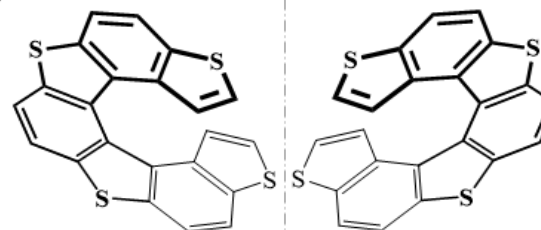
2,2'-biindole



1,1'-binaphthyl

achievable
through

Helix of fused
(hetero)aromatic rings



Tetra-thiahelicene

*Inherently Chiral
monomers used as chiral
selectors to modify the
electrode surface as chiral
oligomer films.*

Figure 21. Structures of the inherently chiral monomers with atropisomeric scaffold (left side) and helix as stereogenic element (right side).

Inherent chirality can be also implemented in advanced molecular media [134]. Some first examples have been proposed of ‘inherently chiral’ ionic liquids (ICILs) [134-137], in which chirality does not originate from localized stereocenters, but the same element, the whole cation backbone, being atropisomeric or helical, is responsible for both chirality and key functional properties; such property usually results in outstanding enantiodiscrimination performances [137].

- (i) The proof-of-concept case was based on a family of 3,3'-bicollidinium salts (Figure 22 left side) with inherently chiral dications on account of their atropisomeric biheteroaromatic system (of axial stereogenicity) [134]. Depending on alkyl substituent length and counterion nature, the family included both solid terms and liquid ones (ICILs). Their enantiodiscrimination ability was very successfully tested as additives in achiral commercial ILs on unmodified SPEs, with different chiral probes, that is, (*R*)- and (*S*)-Fc, L- and D-DOPA (also as racemate) and the inherently chiral monomer (*R*)- or (*S*)-BT₂T₄. The observed enantiomer potential differences regularly increase with the increasing amount of the inherently chiral salt in the IL medium [134].
- (ii) The high effectiveness of the inherent chirality strategy was also confirmed successfully testing as additives in achiral ILs a term of a salt family with inherently chiral 1,1'-bibenzimidazolium dications, of axial stereogenicity, resulting again in neat discrimination of (*R*)- and (*S*)-Fc (Figure 22 right side) [135]. The same additive was also tested for the enantioselective electrodeposition of the enantiomers of a chiral monomer [136].
- (iii) More recently, successful enantiodiscrimination was also obtained using the ICIL *N*-octyl-5-aza[6]helicenium bistriflimidate, including

an inherently chiral azahelicenium cation of helical stereogenicity, as chiral additive in achiral IL [137] (Figure 22 bottom).

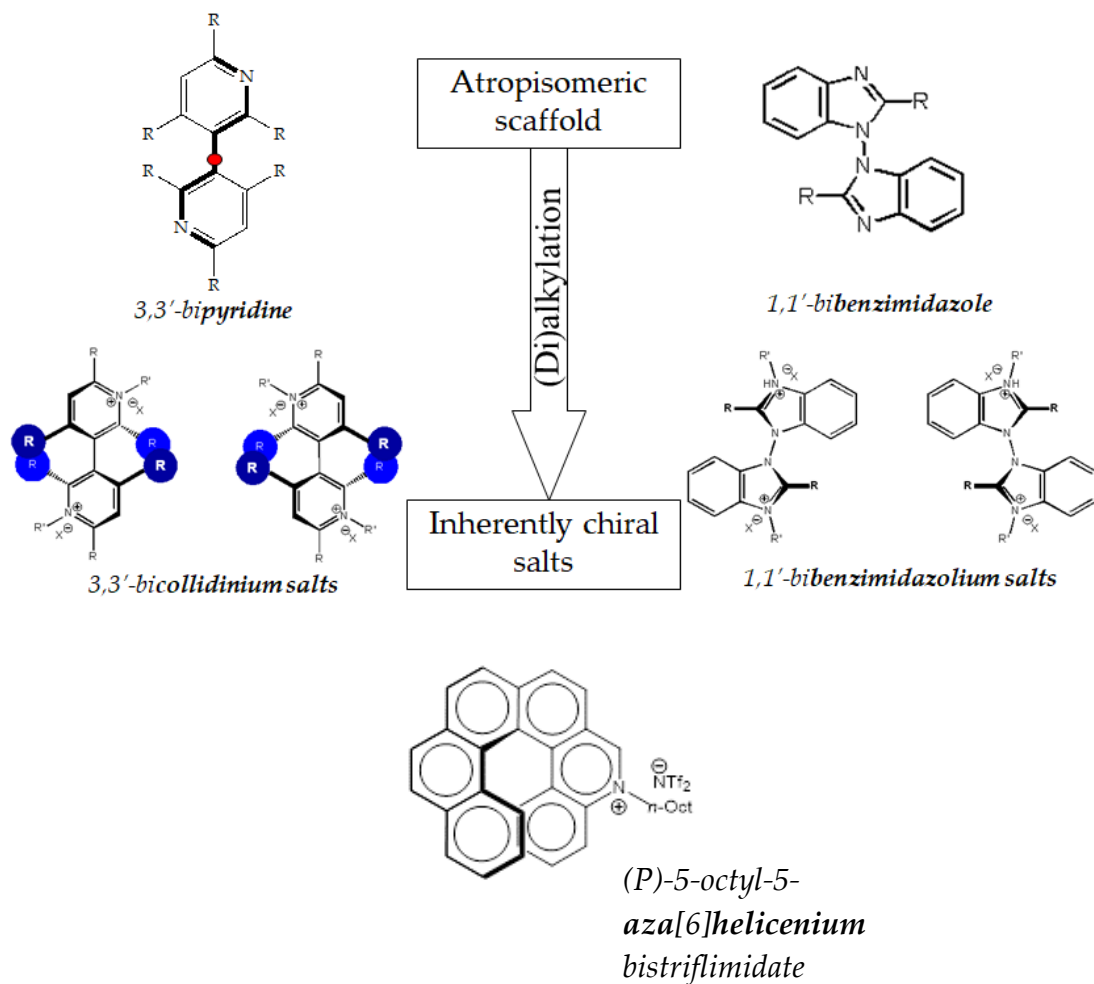


Figure 22. Structures of the inherently chiral salts: 3,3'-bicollidinium salts, 1,1'-bibenzimidazolium salts and *N*-octyl-5-aza[6]helicenium bistriflimidate.

1.5 Targets and guidelines of the present three-year thesis research work

This three-year thesis project is aimed to deeply investigate the innovative field of chiral electrochemistry and electroanalysis, obtained using chiral, and especially inherently chiral, selectors, which has been widely described in paragraph 1.4.

A particular focus was on the potentialities of the inherently chiral strategy, not only in the chiral voltammetry field, but also in circular dichroism and magnetoelectrochemistry ones.

Although the “inherent chirality” definition does not imply restrictions on the chemical nature of the stereogenic element, the concept was actually implemented by inserting atropisomeric or helical-type elements. Moreover, the strategy could be applied to both surfaces and media.

Concerning the modification of electrodes with inherently chiral oligomer films, several new inherently chiral monomers will be presented, in order to amplify the range of monomer structures studied and the combination of chiral selector/probe investigated (in fact, many new chiral probes, also of pharmaceutical interest will be used in enantioselection tests, with different nature, chemical structures, bulkiness and reactivity).

The characterization of the inherently chiral monomers (and of the corresponding oligomer films, enantiopure and/or racemic) will be shown, using different techniques, such as Cyclic Voltammetry (CV), Atomic Force Microscopy (AFM), high resolution Laser Desorption/Ionization (HR LDI) spectroscopy, Circular Dichroism (CD), *etc.* in order to study the electroactivity, the redox features, the electrooligomerization ability, the morphology, the composition and the spectroscopy properties of these molecules.

Moreover, the importance of the electrooligomerization will be highlighted, strongly supporting the assumption of an amplification effect of the chirality manifestations from the monomer to the oligomer films.

In order to try to explain the enantioselection mechanism and rationalize the probe-selector interactions, particular attention will be focused on the examination of systematic series of selectors and chiral probes.

Enantioselection tests will be discussed as a function of the experimental conditions, such as the supporting electrolyte and the number of electrodeposition cycle; discussion of experiments with a systematic series of planar stereogenicity ferrocenes will provide key clues concerning the probe-selector interactions in the process, while experiments on a systematic new family of inherently chiral monomers with different substituents on the *N* atoms in the biindole core will enable to study the effect of H bonds in the enantioselection process.

Moreover, the preparation, characterization and implementation of inherently chiral films as self-standing membranes in an ISE-like setup will be described.

Finally, the inherently chiral oligomer films will be discussed in advanced application for magnetoelectrochemistry experiments, employing an innovative experimental setup and resulting in impressive spin-related effects.

Also concerning the chiral media approach, several new chiral selectors will be presented, employing them as low concentration chiral additives in achiral commercial ionic liquids or as bulk media, testing their performances in enantioselection experiments.

First of all, a new family of CILs (with bile acid building blocks, with chirality arising from the presence of one or more stereocenters) of natural origin will be used, showing that the enantiodiscrimination ability appears to be significantly

modulated by the CIL molecular structure (and, in the case of IL+chiral additive systems, by the IL molecular structure as well as by the chiral additive molecular structure and concentration).

Subsequently, the performances of bio-based and synthetic chiral selectors will be compared, studying different artificial inherently chiral media: an inherently chiral molecular salt, based on a 3,3'-bipyridine scaffold (tested as both low concentration chiral additive and as bulk medium); a family of diazahelicenes, neutral, mono- and di-alkylated (with ethyl chains), which are still inherently chiral but with a different stereogenic element respect to the ICIL with the bipyridine scaffold; and finally, a family of chiral QUINAPs, employed as low concentration chiral additives.

Moreover, an inherently chiral monomer (*N*-Hex-Ind)₂Ph₂T₄ (unsuitable for electrooligomerization) will be tested as low concentration chiral additive in an achiral commercial ionic liquid.

The application of another kind of advanced chiral media will be exploited, studying the enantioselection ability and properties of chiral Deep Eutectic Solvents (DESs) of natural origin. The DESs employed in this research project are composed of a mixture of at least two components, a hydrogen bond acceptor (HBA) and a hydrogen bond donor (HBD), which are able to self-associate to form a new eutectic phase characterized by a melting point (< 100°C) lower than that of each individual component and significantly lower than the predicted one for an ideal case.

Chapter 2

Details on the techniques employed

2.1 Voltammetry

Voltammetry is a powerful tool for the study of molecules and their reactivity, providing qualitative, quantitative and mechanistic information on all the electroactive species present in the working solution and/or on the electrode surface.

The general experimental (Figure 23) setup necessary is:

- a cell with three electrodes (working WE, reference RE and counter CE electrodes);
- a potentiostat which varies the voltage of the cell (E_{cell}) and detects the current flowing between WE and CE (I_{cell}), as a function of the potential of the WE measured against the RE;
- the solvent containing the supporting electrolyte (to ensure sufficient conductivity and that the transport of the species studied occurs by diffusion) and analyte;
- a recorder for data acquisition (in this case, the software GPES[®] 4.9 was employed for the elaboration of the experimental data).

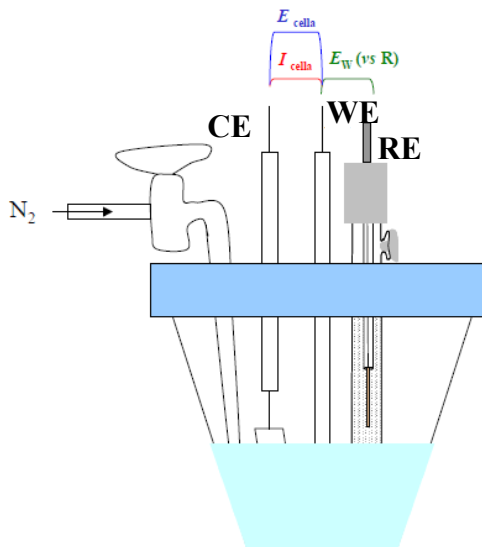


Figure 23. Schematic illustration of the general experimental setup for voltammetry experiments.

Voltammetry includes many different techniques which differ in:

- mode of potential variation with time: linear (simple or cyclic), baseline or staircase with overlapping pulses, series of square pulses..., even combined with controlled potential steps for accumulation purposes. The current can be detected either directly or by differential processing.
- Rate of potential variation with time: signals can be obtained either by a slow variation of the potential, in "steady conditions", or very quickly, under "non-stationary conditions" ($20\text{-}50000\text{ mV}\cdot\text{s}^{-1}$ and above).
- Type of working electrodes employed: commonly electrodes present surface areas of a few square millimeters (for peculiar studies ultramicroelectrodes can be employed, offering exceptional performances). In general, WE are solid (metals, graphite, oxides, *etc.*) with two exceptions: rotating disk electrodes, employed for kinetics studies, and mercury electrodes (stationary or dropping) particularly suitable for reduction studies in aqueous medium. The processes are

associated with very low current values and take place in very short periods of time; therefore, the technique can be considered non-destructive on a macroscopic scale.

2.1.1 Cyclic Voltammetry (CV)

Signal recording is performed by the measurement of the current (which is proportional to the rate of the electron transfer process) that flows between the working electrode (WE) and the counter electrode (CE) as a function of the potential applied to the WE with respect to a reference electrode (RE), with a regular modulation over time.

Let us consider the reaction: $O + ne^- \leftrightarrow R$, and assume to start scanning to a potential much more positive than the formal potential of the electrode (E°), initially only small currents, such as capacitive ones (corresponding to the charging process of the double layer) are detected.

For values of potential approaching E° a faradic current begins to be registered, corresponding to the redox reaction taking place at the electrode surface. The associated $I-E$ signal is a peak; this particular shape is determined by the fact that cyclic voltammetry never reaches a stationary regime due to the high scanning speed. In particular, unlike voltammetry experiments performed in stationary conditions (*i.e.* at slow potential rate), which imply linear concentration gradients in a "diffusion layer" of constant δ thickness at the electrode surface, such gradients increasing to a maximum in correspondence of zero concentration on the electrode surface, and thus resulting in increasing current signals with a limiting current corresponding to the maximum concentration gradient, when the experiment is performed at high scan rate convective motions fail to re-integrate the reagent concentration from the bulk (C°_b) to a constant distance from the electrode; therefore δ increases and the current, which is proportional to the concentration gradient, after reaching a maximum, decreases (Figure 24).

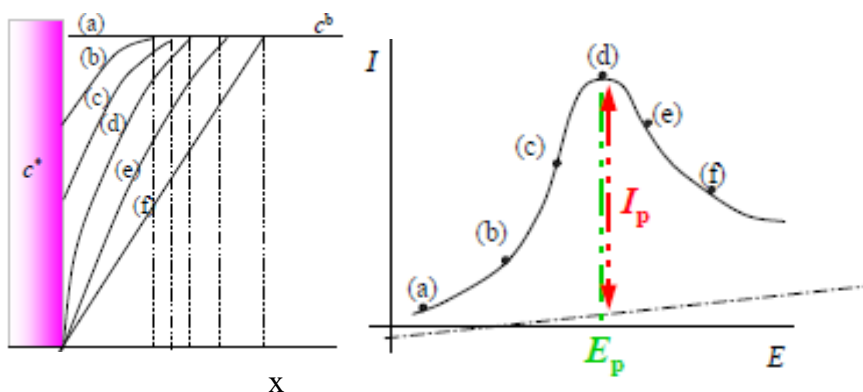
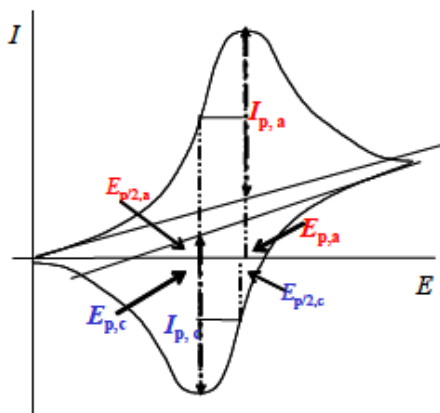


Figure 24. Increase in the width of the diffusion layer (boundary moving towards the bulk of the solution) and associated peak signal.

A simple electron transfer not coupled with chemical reactions can be of two types:

- Electrochemically reversible, if its activation barrier is negligible, so, as soon as the reagent reaches the electrode it undergoes charge transfer and it is instantly transformed into the product. In this case, the current, which represents the speed of the process, is controlled only by diffusion within the diffusion layer δ . The form of the signal is that of a reversible wave, in the electrochemical meaning, *i.e.* only controlled by the mass transfer (Figure 25). In the case of an electrochemically reversible signal, the peak potential E_p and the peak amplitude at half height $|E_p - E_{p/2}|$ are constant for different scan rates (in particular, $|E_p - E_{p/2}|$ is 0.057 V at 25°C for a monoelectronic peak). In the case of a chemically reversible process a return peak is observed, too, because electron transfer leads to a chemically stable product; the distance between the direct and return peak is constant for different scan rates, and equal to 0.057 V at 25 °C.

Figure 25. CV pattern for a chemically and electrochemically reversible electron transfer process.



- Electrochemically irreversible, if the electron transfer activation barrier is not negligible, and the charge transfer becomes kinetically important in the determination of the rate of the whole process. In this case, an additional energy, corresponding to an "overpotential", is required to obtain the same current with respect to the former case. As consequence, the signals are more stretched and widened, they are increasingly shifted at more extreme potentials with increasing scan rates, the peak amplitudes at half height $|E_p - E_{p/2}|$ are > 0.057 V at 25°C for a monoelectronic peak and increase with the scan rate. This broadening also applies to the return peak in the case of a chemically reversible process; in this case, the distance between the direct and return peak is greater than 0.057 V at 25°C , and increases as the scan rate increases, as well as the activation barrier increases (Figure 26).

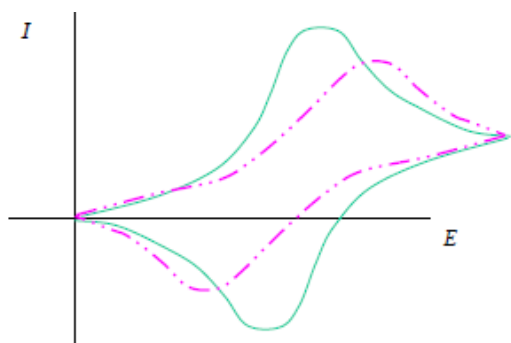


Figure 26. Blue line: example of a chemically and electrochemically reversible CV signal. Pink dotted line: example of a chemically reversible but electrochemically irreversible voltammetric signals.

Electrooligomerization of conductive polymers

Electrochemical techniques are effective tools for both the preparation and the characterization of conjugated systems such as oligo- and polythiophenes, with anodic oxidation as the most common approach. In particular, Cyclic Voltammetry (CV) is an extremely suitable technique in order to follow the electrooligomerization process, which is performed by repeatedly scanning the working electrode potential up to the oxidation potential of the monomer and back to the reduction potential of the generated polymer. The anodic electropolymerization of the monomer offers several advantages over the chemical oxidation, such as absence of catalyst, direct grafting of the polymer onto the electrode surface, easy control of the film thickness by the deposition charge, and possibility to perform *in situ* characterization of the growing process or of the polymer by electrochemical and/or spectroscopic techniques.

From a mechanistic point of view, potentiostatic, potentiodynamic, or galvanostatic techniques lead to the electrochemical formation of conducting polymers.

The process involves an oxidation step which generates a radical cation, it is followed by coupling and a deprotonation/rearomatization step generating the dimer, and proceeds via nucleation and a phase-growth mechanism [80-82]. The mechanism is summarized in Figure 27.

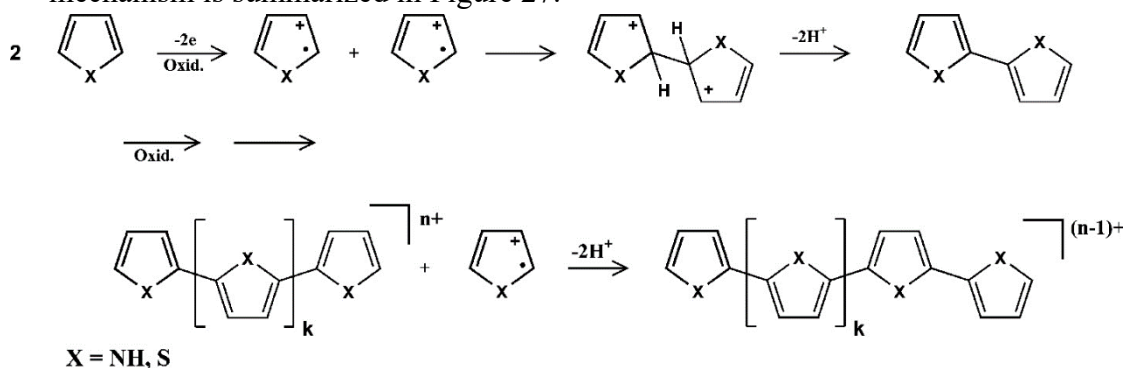


Figure 27. Classical mechanism for the growth of conducting polymers.

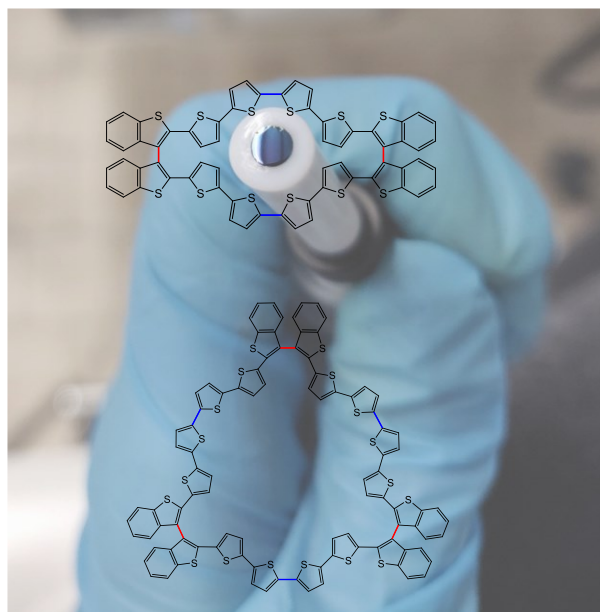
The polymerization starts with the formation of oligomers in solution; the next general step is the deposition, which includes nucleation, growth, and additional chemical steps under solid-state conditions. In the electrodeposition of CPs, different models for layer formation have been discussed. They all refer to the deposition of metals. There are two kinds of nucleation, namely instantaneous and progressive, and three types of growth involving one- (1D), two- (2D), and three-dimensional (3D) processes. In the case of instantaneous nucleation, the number of nuclei is constant, and they grow without the formation of further nuclei. In the case of progressive nucleation, nuclei are generated at all times. 1D growth occurs only in one direction, *e.g.* perpendicular to the electrode. In the 2D growth, the nuclei preferably grow parallel to the electrode, and in the 3D growth, the rates for these processes perpendicular and parallel to the electrode are very similar. In this thesis work we only focused on the potentiodynamic deposition technique, which gives information about the growth rate of CPs, but, unfortunately, no direct information on the nucleation and growth mechanism can be obtained [81]. An important feature of electropolymerization is its strong dependence on experimental variables such as the nature of the solvent, monomer concentration, temperature, type and geometry of the working electrodes and the applied electrical conditions.

2.1.2 Differential Pulse Voltammetry (DPV)

In order to reduce the detection limit, it is possible to use pulsed voltammetry. In fact, the voltametric signal is composed of capacitive (due to the charge of the double layer, independently of the analyte concentration) and faradic (TE of the studied process) current, therefore with decreasing concentration of the electroactive molecule the capacitive current tends to overwhelm the faradic one (resulting in a bad signal/background ratio in CV). Minimizing the capacitive current allows to lower the detection limit of the faradic signal.

Chapter 3

Inherently chiral monomers and oligomer films



In this three-year thesis project several new inherently chiral monomers (with different atropisomeric scaffolds, number/connectivity of the thiophene rings, alkyl substituents modulating the core properties *etc.*) have been studied and fully characterized by Cyclic Voltammetry (CV), Atomic Force Microscopy (AFM), high resolution Laser Desorption/Ionization (HR LDI) spectroscopy, Circular Dichroism (CD), *etc.*

The electrooligomerization ability of the chiral surfaces has been also tested and the stability of the films verified by repeated potential cycling in a monomer free solution. Finally, the inherently chiral films have been used in enantioselection experiments, employing different chiral probes, which have been electrochemically characterized.

In particular:

1. A family of molecules based on bi-naphthyl systems, which had already been fully studied by CV, were implemented as chiral selectors (testing L- and D-DOPA as chiral probes), modifying the electrode surface either by drop-casting or as chiral oligomer films, easy obtainable by the electrooligomerization of the corresponding enantiopure monomer.
2. A new family of inherently chiral monomers (fully characterized by CV and CD experiments), based on a 2,2'-biindole atropisomeric scaffold with phenyl spacer and *N* atoms functionalized with alkyl chains of different length (methyl, *n*-propyl and *n*-hexyl group), were tested in enantioselection experiments with chiral probes of pharmaceutical interest (Terazosin, Lansoprazole, Ramosetron and (*S*)-Clopidogrel).
3. An helmet cobalt phthalocyanine was electrochemically characterized and the helmet CoPc enantiomers were tested in two somehow specular kinds of voltammetry enantiodiscrimination experiments: as chiral modifiers of the working electrode surface by drop-casting and as chiral probes.
4. The growth of our benchmark monomer BT₂T₄ was studied in detail with different techniques (AFM and HR LDI), for example by changing the supporting electrolyte used in electrooligomerization process. Atomic Force Microscopy (AFM) and High Resolution Laser Desorption Ionization (HR LDI) were exploited for characterizing film morphology and film chemical composition, respectively. The importance of the first electrodeposition cycle was also analysed in detail (using ultra-flat ITO as working electrode, with a roughness value of a few Ångström). Finally, enantioselection ability was tested as a function of the electrodeposition cycles and of the different working protocols (with TBAPF₆ vs LiClO₄ supporting electrolytes).

In order to try to explain the enantioselection mechanism and rationalize the probe-selector interactions, attention was particularly focused on the examination of systematic series of selectors and chiral probes. Such study provided a fundamental background for the optimization of the chiral selector design as well as for the development of effective protocols with high performances in qualitative and quantitative electroanalysis of several probes.

In particular:

5. A systematic series of planar stereogenicity ferrocenes (characterized in terms of relationship between structure and electronic properties) has been tested in enantioselection experiments, providing key clues concerning the probe-selector interactions in the process.
6. Another systematic new family of inherently chiral monomers, based on a 2,2'-biindole atropisomeric scaffold (fully characterized by CV), has been tested as chiral selectors. In this case the *N* atoms in the biindole core were functionalized with $\text{CH}_2\text{CH}_2\text{-OH}$, $\text{CH}_2\text{CH}_2\text{-OCH}_3$ and $\text{-CH}_2\text{CH}_3$. This enabled to study the effect of H bonds in the enantioselection process, using as chiral probes different molecules of applicative interest, featuring many OH groups, like (+)-Catechin and (-)-Epicatechin, (-)-Epigallocatechin gallate (EGCG), (*S*)-Naproxen and (*S*)-Ketoprofen.

Finally,

7. Self-standing chiral electroactive synthetic membranes were realized and implemented in an ISE-like setup. Reliable transmembrane potential readings are obtained in preliminary tests, consistent with those predicted considering the membrane features, offering a first step towards extension of the protocol to chiral experiments.

3.1 General experimental setup for the electrochemical measurements: characterization and electrooligomerization of the monomers.

Cyclic Voltammetry (CV) and Differential Pulse Voltammetry (DPV) experiments were performed using an Autolab PGSTAT potentiostat (Eco-Chemie, Utrecht, The Netherlands), controlled by a PC with the GPES software provided by the same manufacturer.

The electrochemical characterization of the molecules was carried out in a V-shape three-electrode minicell ($V=3\text{ cm}^3$), including a glass-embedded glassy carbon disk (GC, Metrohm, $S = 0.031\text{ cm}^2$) as working electrode, a Pt disk as counter electrode, and an aqueous saturated calomel (SCE) as reference electrode, inserted in a compartment filled with the working medium and ending with a porous frit, to avoid KCl leakage into the working solution (Figure 28).

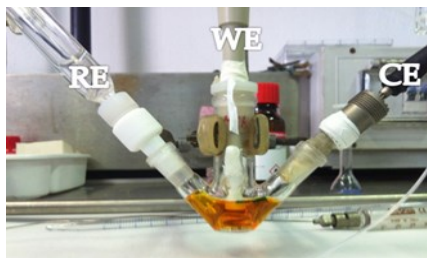


Figure 28. Example of a V-shape three-electrode minicell (RE=Reference electrode, WE= Working electrode and CE=Counter electrode).

The optimized preliminary polishing procedure for the GC disk electrode consisted in treatment with a diamond powder of $1\text{ }\mu\text{m}$ diameter (Aldrich) on a wet DP-Nap cloth (Struers[®]). The characterizations were performed at scan rates in the $0.05\text{-}2\text{ V/s}$ range, containing the analyte at a fixed concentration, dissolved in dichloromethane DCM (anhydrous, $\geq 99.8\%$, Aldrich) or acetonitrile ACN (Aldrich, HPLC grade), with 0.1 M tetrabutylammonium hexafluorophosphate TBAPF₆ (Fluka $\geq 98\%$) as supporting electrolyte, applying ohmic drop compensation by the positive feedback method and referring the potentials to the

$\text{Fc}^+|\text{Fc}$ (ferrocenium|ferrocene) redox couple (the intersolvental standard recommended by IUPAC [138]) measured in the same conditions (~ 0.39 V vs SCE in ACN and ~ 0.49 V vs SCE in DCM).

The electrooligomerization of the monomers was performed on GC (or Indium Tin Oxide, ITO) working electrode, starting from a solution of the corresponding monomer, by repeated different CV cycles around the potential corresponding to the activation of the α homotopic positions of the thiophene wings, involved in the electrooligomerization process. The stability of the films was then verified by subsequent potential cycling in a monomer free solution, a treatment performed in order to eliminate monomer residuals and to check the film stability in repeated doping/undoping cycles.

3.2 Result and discussion for the inherently chiral monomers exploited

3.2.1 “Inherently chiral” bi-naphthyl systems with different wings: modulating functional properties and performance as chiral selectors

A family of molecules based on bi-naphthyl systems (Figure 29: precursor **(1)** 2-Naphtol, **(2)** 1,1'-Bi-2-naphthol (BINOL), **(3)** SP26 and **(4)** Naph₂T₄ [132]), has been characterized by CV. Enantiopure **(3)** and **(4)** were used as chiral selectors to modify the electrode surface (by drop casting in the case of **(3)** and **(4)** and also as inherently chiral oligomer films in the case of **(4)**, while **(3)** was unsuitable to electrooligomerization), testing the enantiomers of 3,4-dihydroxyphenylalanine (L- or D-DOPA) as chiral probes, in enantioselection experiments. The three compounds employed in the enantioselection tests allowed to verify the importance of the improved conjugation in enantiorecognition process (for the presence of the thiophene wings in **(3)** and **(4)** cases) and/or of extended terminals with possible additional coordination points. Moreover, results obtained with the electrooligomerized **(4)** suggest an amplification effect of the chirality manifestations from the monomer to the oligomer films, promoted by the regioregular monomer structure.

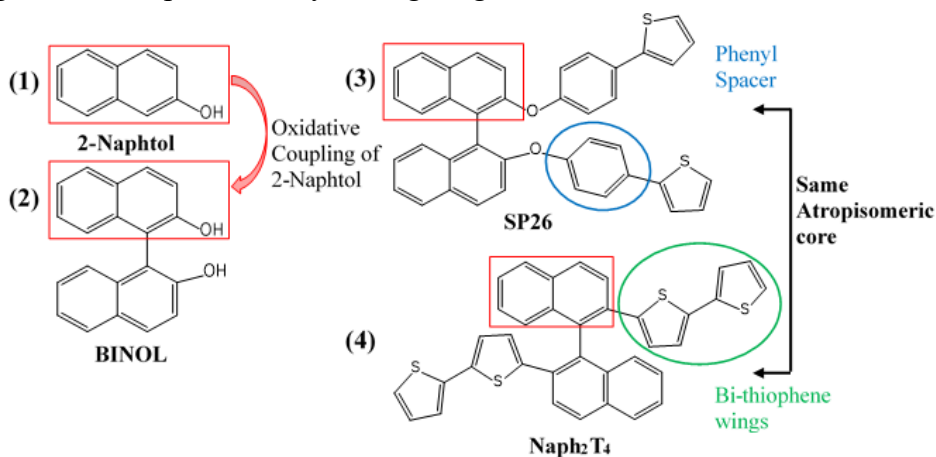


Figure 29. Molecular structures of 2-Naphtol **(1)**, 1,1'-Bi-2-naphthol (BINOL) **(2)**, SP26 **(3)** and Naph₂T₄ **(4)** [132].

a) Experimental conditions for CV measurements: electrochemical characterization and enantio-recognition experiments

The electrochemical characterizations of the bi-naphthyl systems were performed at scan rates in the 0.02-2 V/s range with solutions containing ~0.001 M **(1)**, ~0.0009 M **(2)**, ~0.00075 M **(3)** and ~0.00075 M **(4)**, dissolved in DCM or ACN, with 0.1 M TBAPF₆ as supporting electrolyte.

The enantiodiscrimination experiments were carried out with enantiopure L- or D- 3,4-Dihydroxy -phenylalanine DOPA (an α amino acid used in the treatment of Parkinson's disease) 0.005 M in pH 4 buffer solution, in different operating conditions:

- i)* on thin layers of **(R)**-**(3)**, **(R)**-**(4)** and **(R)**-**(2)** (for sake of comparison): the monomers were deposited by drop casting on commercial GC electrode, from 2 μ L of solution.
- ii)* **(R)**-**(4)** (0.00075 M in DCM + TBAPF₆ 0.1 M) was also tested as inherently chiral oligomer film, in order to verify the improved efficiency in the enantioselection ability. The films were obtained by performing 36 CV cycles in the presence of the corresponding enantiopure (*R*)-monomer, at 0.05 V/s scan rate on GC electrode.

Reproducibility tests were performed by repeatedly recording the CV patterns of chiral probes on freshly deposited chiral surfaces.

b) CV electrochemical characterizations of the bi-naphthyl systems

The complete CV patterns of **(1)**, **(2)**, **(3)** and **(4)** together with the key voltammetric parameters in both ACN (Figure 30a) and DCM (Figure 30b) are reported below in Table 1 (for more details see Gallery Section 1). Oxidative and reductive half cycles were analysed separately to avoid electrode conditioning by electron transfer products.

The simplest molecule in the series **(1)** presents a single broad peak corresponding to the formation of a radical on the oxygen atom with the concurrent loss of a hydrogen atom, and chemical follow ups (consistent with the signal irreversibility) including possible polymerization [139].

(2) can be considered as the combination of two equivalent and reciprocally interacting 2-naphthol redox sites. Indeed, the CV pattern of the molecule presents two nearly merging first oxidation peaks (which should again be correlated to radical formation on the oxygen atoms), with a smaller reciprocal interaction (possibly related to high torsional barrier). Comparing the DCM solvent with the more polar ACN, the peak potential splitting decreases, since the higher polarity results in a higher screening effect on the redox centres. The slightly improved conjugation between the two molecule moieties can justify the shift of the first oxidation peak to less positive potential value, respect to the reference **(1)** molecule. The further two oxidation peaks observed in ACN might be related to the oxidation of the naphthyl rings. The **(3)** CV pattern also shows a first twin oxidation peak system related to the oxidation of the atropisomeric core, at approximately the same potential of **(2)**, consistently with the lack of conjugation with the phenylthiophene terminals. The shoulder at a much more positive potential could correspond to the oxidation of the thiophenes, with negligible enhancement by conjugation with the phenyl group, acting more as a spacer (an alternative explanation could involve the presence of positive charges on the core, which is not conjugated with the thiophene wings), since a single thiophene should have a first oxidation peak potential at about 1.33 V vs $\text{Fc}^+|\text{Fc}$ in DCM. However, in this case the activation of the thiophene terminals does not lead to film deposition, since there could be an overoxidation of the core, resulting in molecule modification. Enantioselection tests were therefore performed modifying the electrode surface by drop casting.

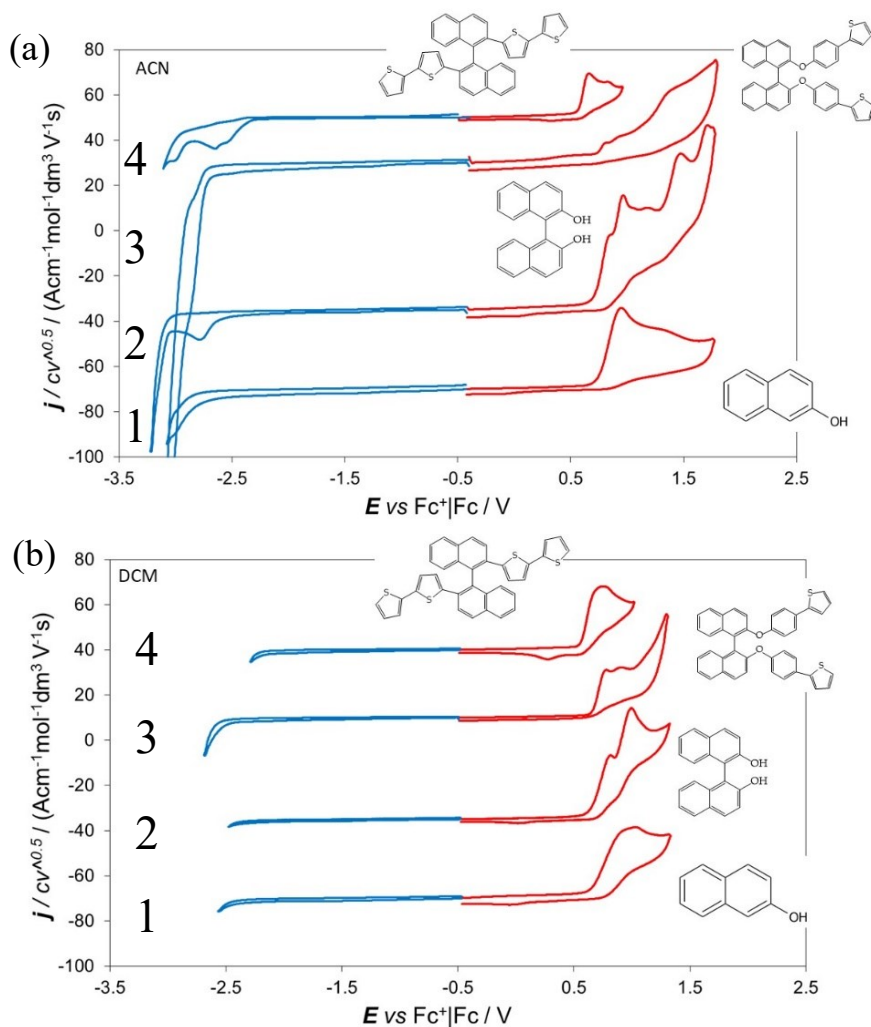


Figure 30. Normalized CV patterns for (1), (2), (3) and (4) on GC electrode in both ACN (a) and DCM (b) at 0.2 V s^{-1} potential scan rate, with 0.1 M TBAPF_6 as supporting electrolyte.

(4) oxidation is localized on the electron richer oligothiophene system, with only partial delocalization on the bi-naphthyl moieties [132]. In this case, because of the higher torsion angle, the two moieties cannot interact, and the pattern shows a complete (ACN) or nearly complete (DCM) merging of the oxidation peaks.

(4) is the only molecule that presents a twin peak system also in the reduction side, probably related to the radical anion formation on the thiophene wings that are partially interacting (in 3D space by a partial π -stacking interaction).

Table 1. Key CV parameters of molecules (1), (2), (3) and (4) on GC electrode in DCM and ACN at 0.2 V s⁻¹ potential scan rate, with 0.1 M TBAPF₆ supporting electrolyte.

		E_{Ipa} vs Fc ⁺ Fc / V	E_{Ipc} vs Fc ⁺ Fc / V	E_{HOMO} / eV ^[a]	E_{LUMO} / eV ^[b]	H-L Gap / eV
(1)	DCM	1.02	n.d.	-5.82	-	-
	ACN	0.88	n.d.	-5.68	-2.12	3.57
(2)	DCM	0.76	n.d.	-5.56	-	-
	ACN	0.89	-2.78	-5.69	-2.02	3.67
(3)	DCM	0.79	n.d.	-5.98	-	-
	ACN	0.84	n.d.	-5.64	-	-
(4)	DCM	0.73	n.d.	-5.53	-	-
	ACN	0.66	-2.55	-5.46	-2.25	3.21

^[a] $-1e \times [(E_{Ipa} / V (Fc^+|Fc) + 4.8 V (Fc^+|Fc \text{ vs zero})]$

^[b] $-1e \times [(E_{Ipc} / V (Fc^+|Fc) + 4.8 V (Fc^+|Fc \text{ vs zero})]$.

c) Enantioselection tests towards the enantiomers of DOPA

As preliminary experiments, L- and D-DOPA have been tested on bare electrode (Figure 31), and as expected, the two enantiomers present the same potential value (~ 0.54 V vs SCE), in fact, the enantiomers have the same electrochemical behaviour on an achiral surface. The oxidative mechanism of a DOPA-like catecholamine is a complex multistep process, with the first oxidation involving the catecholic site.

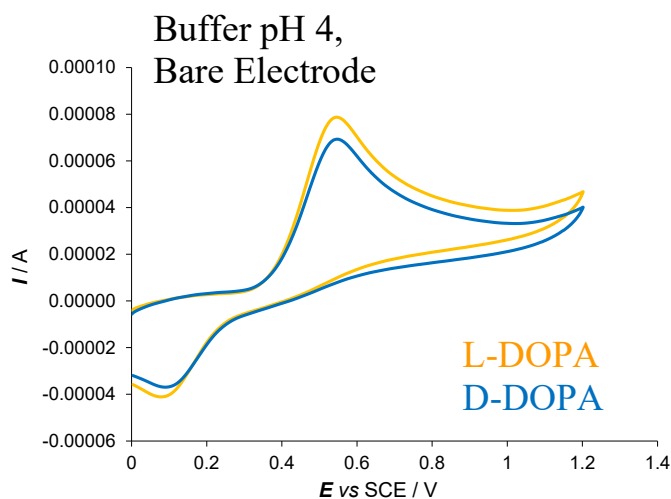
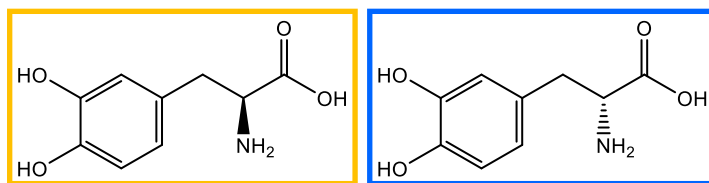


Figure 31. CV pattern of L- and D-DOPA (orange and blue respectively) on bare GC electrode, in buffer pH 4 aqueous solution, at 0.05 V s^{-1} potential scan rate.

Results obtained in the presence of the different chiral selectors **(R)-(2)**, **(R)-(3)** and **(R)-(4)** are reported in Figure 32 and 34. In particular: **(R)-(2)**, **(R)-(3)** were deposited by drop casting (Figure 32), and **(R)-(4)** both by drop casting in Figure 32 and as chiral oligomer film in Figure 34.

The enantiodiscrimination tests carried out with drop-casted **(R)-(2)** show nearly no potential difference for the antipodes of the DOPA (L-DOPA at $\sim 0.55 \text{ V vs SCE}$ and D-DOPA at $\sim 0.62 \text{ V vs SCE}$). Instead, with drop-casted **(R)-(3)** and **(R)-(4)** monomers large peak potential difference of $\sim 160 \text{ mV}$ was observed with the same enantiomeric peak sequence (D- before L-), consistently with enantioselectivity arising from the same monomer configuration (the *R*) and with both monomers having much more coordination elements than **(2)** on account of their wings featuring heteroatoms and heteroaromatic rings.

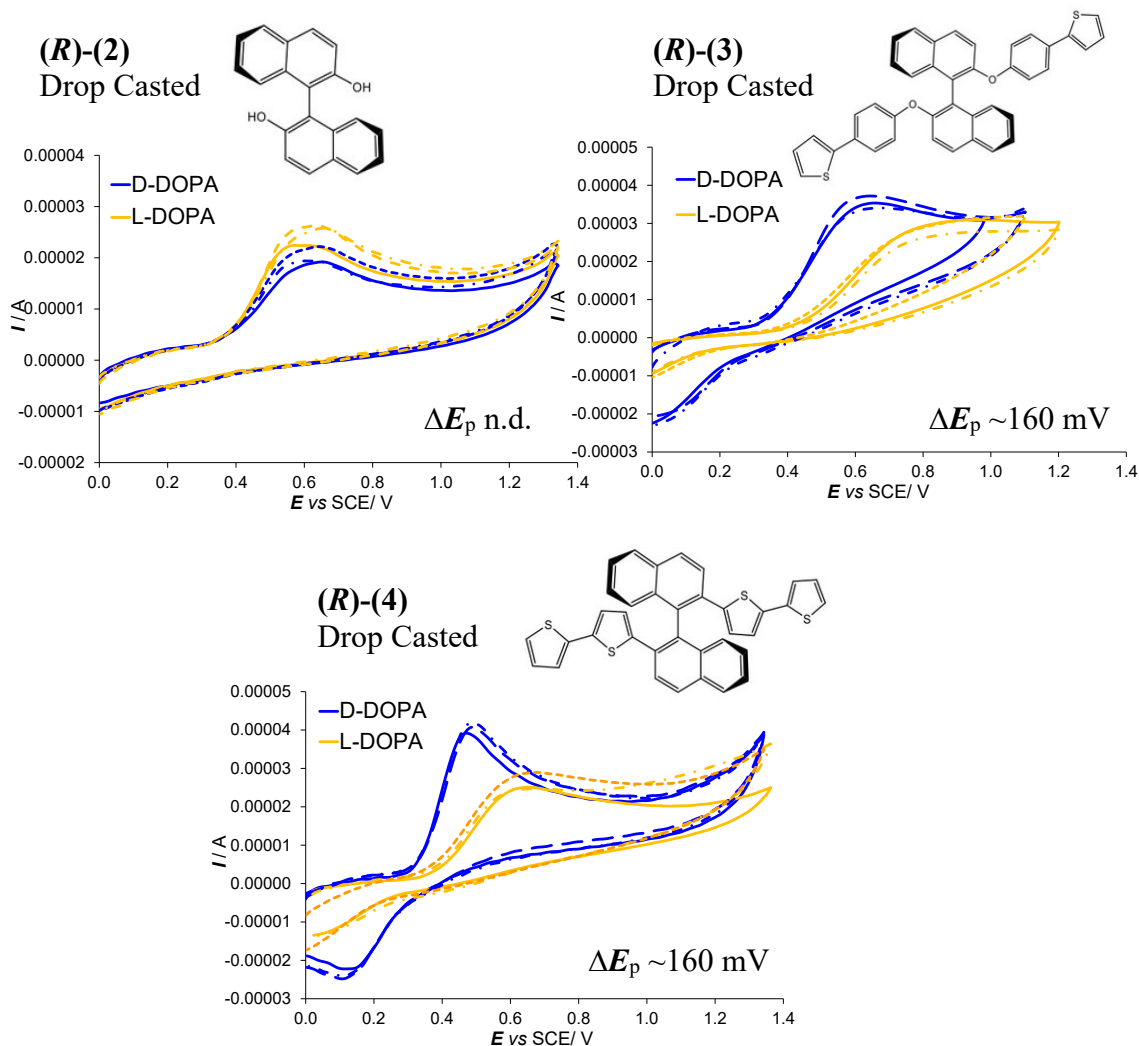


Figure 32. Enantioselection tests towards the enantiomers of DOPA (L- orange lines and D- blue lines) carried out with drop-casted **(R)-(2)**, **(R)-(3)** and **(R)-(4)**. Dotted lines represent the reproducibility test.

However, the best results were obtained with inherently chiral oligomer films, obtained from the corresponding enantiopure monomer **(R)-(4)** deposited for 36 CV cycles at 0.05 V s^{-1} (Figure 33a). The films grown in DCM show also good stability upon subsequent potential cycling in a monomer free solution (Figure 33b) [132].

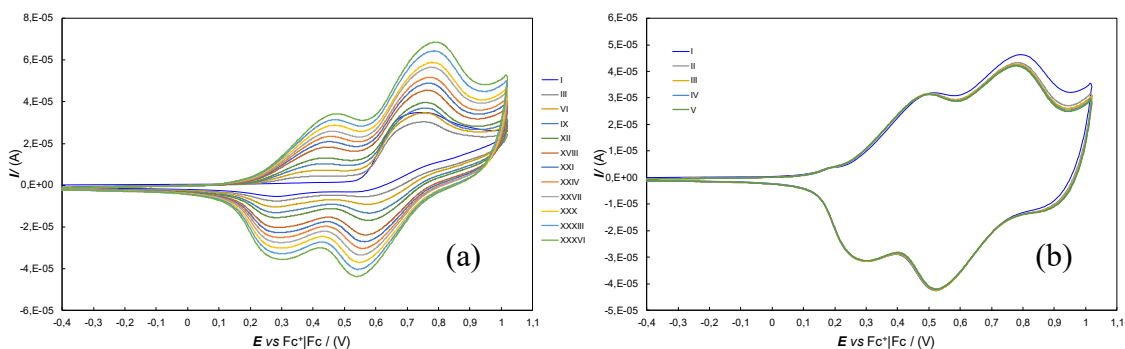


Figure 33. Electrooligomerization of **(R)-(4)** in DCM + TBAPF₆ 0.1 M on GC electrode, performing 36 CV cycles at 0.05 V s⁻¹ (a) and stability cycles in a monomer free solution (b).

The peak potential difference between the two antipodes of DOPA was about 410 mV (Figure 34). Such a huge difference in the film performance strongly supports the assumption of an amplification effect of the chirality manifestations from the monomer to oligomer films.

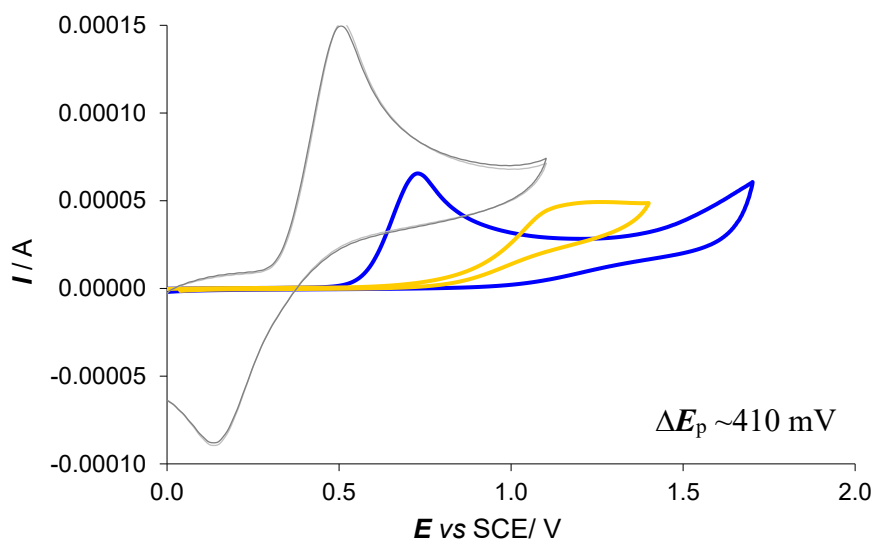


Figure 34. Enantioselection test on the enantiopure films **oligo-(R)-(4)** towards L- and D-DOPA (orange and blue lines respectively). For sake of comparison in grey are also reported the CV patterns of L- and D-DOPA on bare electrode.

3.2.2 “Inherently chiral” monomers and oligomer films based on a 2,2’-biindole core with phenyl spacer

A new family of inherently chiral electroactive selectors based on the 2,2’-biindole atropisomeric scaffold with phenyl spacer (obtainable in enantiopure form by HPLC), of easy synthesis and modulable functional properties, was studied and fully characterized by CV and CD experiments [140].

In particular, the series (*N*-alkyl-IND)₂-Ph₂T₄ (Figure 35 with R=methyl, *n*-propyl or *n*-hexyl) presents a systematic variation of the *N* alkyl substituents of the pyrrolic rings in the core, which results in a modulation of both the redox features and the enantioselection ability.

The enantiomers, showing remarkable chiroptical features (optical rotation and circular dichroism), were successfully exploited as chiral selectors for discrimination of different chiral electroactive probes of pharmaceutical interest, either by conversion into enantiopure electroactive electrode surfaces by electrooligomerization on GC electrode (the two monomers with shorter alkyl chains), or as chiral additive in achiral ionic liquid (the monomer with longest alkyl chains, see chapter 4.2.7).

Discrimination in terms of potential differences between the two probe enantiomers was achieved, specularly inverting the probe or the selector configuration. In one case the discrimination was also observed with the two probe enantiomers concurrently present in solution, both as racemate or in different concentration ratios.

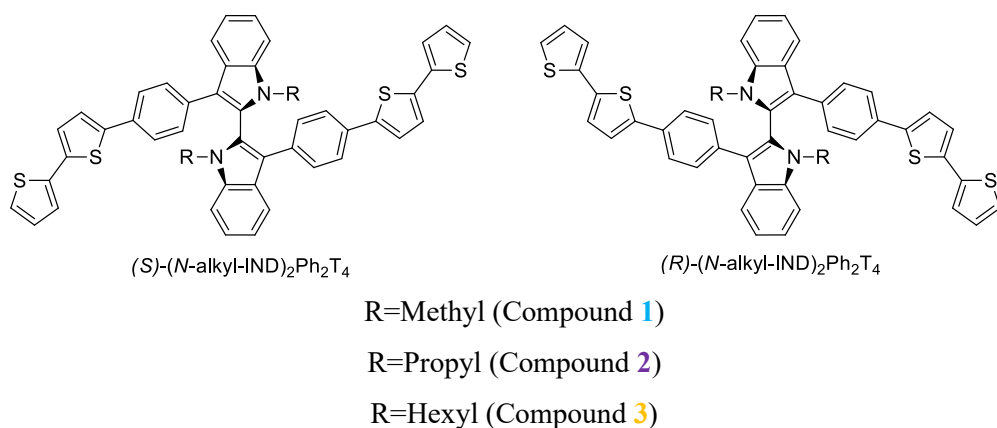


Figure 35. Molecular structures of the series **(N-alkyl-IND)₂-Ph₂T₄** based on the 2,2'-biindole atropisomeric scaffold.

a) Experimental conditions for CV electrochemical characterization, electrodeposition and DPV or CV enantioselection tests

*The CV characterizations of **1**, **2** and **3** monomers were performed at scan rates in the 0.05-2 Vs⁻¹ range, on 0.00075 M probe solutions in both ACN and DCM with 0.1 M TBAPF₆ as supporting electrolyte.*

*The electrodeposition of **oligo-1** and **oligo-2** were performed on GC disk electrode from enantiopure **1** and **2** monomers (0.00075 M), by cycling around the potential corresponding to the third oxidation peak (the first involving thiophene terminals), at 0.05 Vs⁻¹ scan rate, in DCM as solvent with 0.1 M TBAPF₆ supporting electrolyte.*

Enantiodiscrimination experiments were carried out in different operating conditions:

*i) by DPV (step potential 4 mV, modulation amplitude 50 mV) using the enantiomers of *N,N'*-dimethyl-1-ferrocenylethylamine as chiral probes, at 0.05 Vs⁻¹ scan rate in 0.002 M solutions of the probe in DCM+TBAPF₆ 0.1 M as*

supporting electrolyte. Reproducibility tests were performed by repeatedly recording the DPV patterns of model probes on freshly deposited chiral surfaces.

ii) by CV or DPV with the enantiomers of 0.003 M Terazosin in commercial pH 4 buffer solution (Fluka, prepared with citric acid, NaOH, and NaCl), Lansoprazole (NaOH 0.1 M + Buffer pH 4, ratio 3:2) and Ramosetron (pH 4 commercial buffer). In this case the optimized conditions for electrooligomerization were 20 CV cycles at 0.2 V s^{-1} . Reproducibility tests were performed by repeatedly recording the CV patterns of the probes on freshly deposited chiral surfaces.

iii) by DPV using (*S*)-Clopidogrel as active pharmaceutical ingredients (API) and as the main component of DuoPlavin[®] (pH 4 commercial buffer). In this case the optimized conditions for electrooligomerization were 10 CV cycles at 0.2 V s^{-1} .

b) Circular Dichroism spectra of 1, 2 and 3

The CD spectra of the **1**, **2** and **3** enantiomers in chloroform solution between 500 and 230 nm were recorded, as reported in Figure 36 [140].

As expected, the CD curves of the enantiomers were perfectly specular with high optical activity values, coherently with the presence of inherently dissymmetric chromophores. In all cases, the first eluted enantiomer (green curves), has shown a positive Cotton effect being dextrorotatory in chloroform solution. The chiroptical features were dominated by the “exciton coupling chirality” typical feature of the atropisomeric scaffold, *i.e.* a remarkable Davidov splitting effect resulting from the chiral molecule moieties behaving as two equivalent and reciprocally interacting chromophores with very little modulation from variations in either terminals or *N* alkyl substituents.

	(S)-(N-Hex)	(R)-(N-Hex)	(S)-(N-Pr)	(R)-(N-Pr)	(S)-(N-Me)	(R)-(N-Me)
$[\alpha]_{58}^{20}$	1101	-1096	993	-990	970	-968

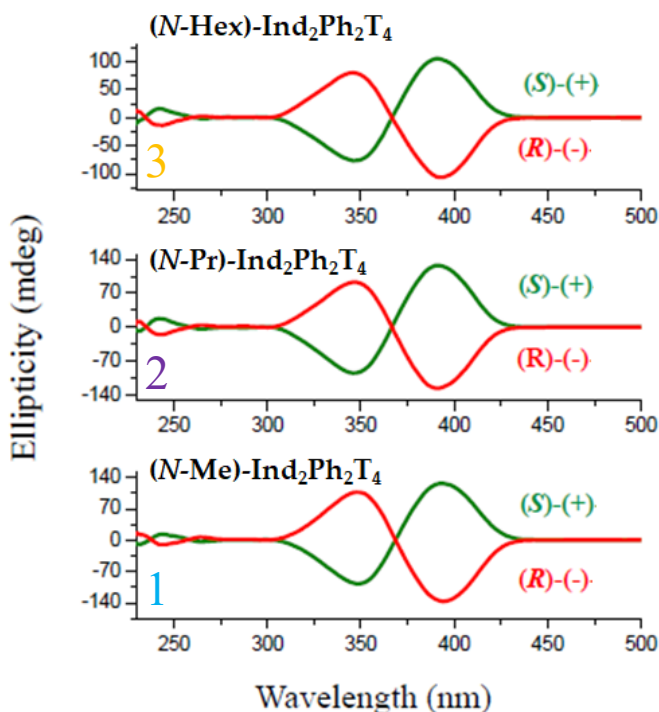


Figure 36. Specific rotations of **1**, **2** and **3** (concentration about 0.2 g/100 cm³) in chloroform solution (top), and CD spectra of the antipodes of **1**, **2** and **3** (bottom).

c) CV electrochemical characterizations of 1, 2 and 3 monomers

The monomers redox features were studied by CV measurements. The 2,2'-biindole monomers, unlike other atropisomeric families (for example, in papers [121,122,129,130]), present first oxidation peaks typically localized on the more electron rich indole core, with the pyrrolic units behaving as two equivalent reciprocally interacting redox centres.

As a consequence, a twin first oxidation peak system of reversible character is observed in voltammetry, since the radical cations resulting from oxidation are stable being too far from the monomer terminals to give coupling. For this reason, oligomerization can only be achieved by a further oxidation process occurring at more positive potentials and localized on the thiophene terminals. The phenyl spacers have been reported to scarcely contribute to, or even hamper, global effective conjugation in heteroaromatic-based conjugated systems. Thus a phenyl spacer could better define localization of the “internal” first oxidation and “peripheral” second oxidation processes of the inherently chiral monomer.

Normalized CV patterns recorded at 0.2 V/s scan rate in DCM and ACN for the three monomers **1**, **2** and **3** are collected in Figure 37 [140]:

- The series shows the typical first oxidation twin reversible peak system in DCM, resulting in no chemical follow up, consistent with localization of first oxidations on the two pyrrolic moieties of the molecule core;
- the same twin processes tend to merge in ACN, since the polar solvent hampers reciprocal interactions between the interacting redox centres; moreover, they tend to become chemically irreversible at low scan rates, pointing to a chemical follow up (as reported in Gallery, Section 2);
- in ACN, enabling observation of reduction processes, too (unlike in DCM where the reduction window is too narrow), the potentials for first reduction onset are similar to the parent case (*N*-Me-Ind)₂T₄ (without phenyl spacer) [131];
- the phenyl group probably act more as a spacer than as a linker (*i.e.* a contributor to the conjugation of the adjacent oligoheteroaromatic systems);
- It is also interesting to note that in the present series, and especially in the **2** and **3** terms, the twin peak potential difference is significantly lower

with respect to parent case without phenyl linker [131]. This feature could point to lower interaction between equivalent redox sites on account of less convenient reciprocal positions of the two moieties in space.

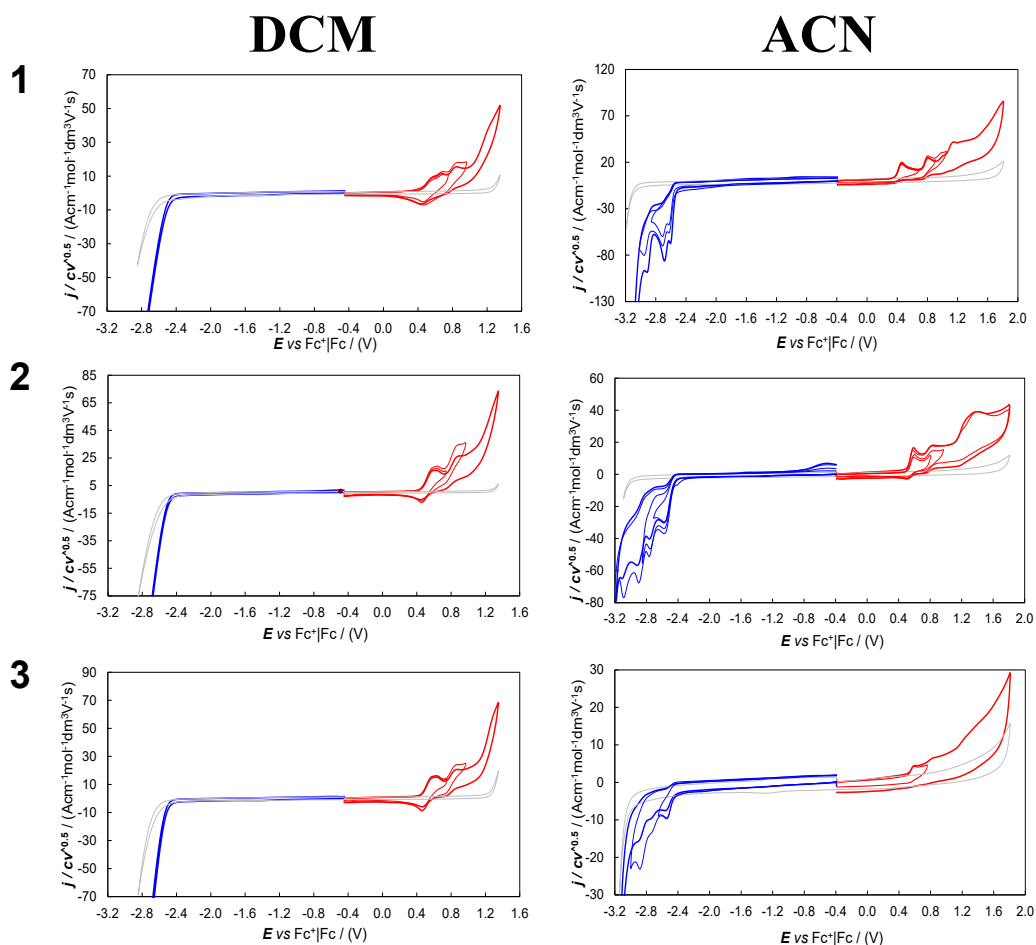


Figure 37. Normalized CV patterns obtained for 0.00075 M **1**, **2** and **3** in ACN (right side) and DCM (left side) with 0.1 M TBAPF₆ supporting electrolyte, on GC electrode, at 0.2 V s⁻¹. Background patterns are also reported in grey, for sake of comparison [140].

d) Electrooligomerization ability of 1, 2 and 3 monomers

Electrooligomerization of **1** and **2**, following the usual thiophene electrooligomerization scheme [81], proceeds fast (Figure 38, left side) and the

grown oligomer films (**oligo-1** and **oligo-2**) show good stability upon subsequent potential cycling in monomer-free solution (Figure 38, right side). Instead, no significant film formation can be achieved by applying the same protocol to monomer **3** (Figure 38 last line), probably due to the higher solubility of the oligomers, originating from the very long alkyl chains on the *N* atoms. For this reason, monomer **3**, unlike **1** and **2**, was tested as chiral additive in achiral ionic liquid (see Chapter 4.2.7).

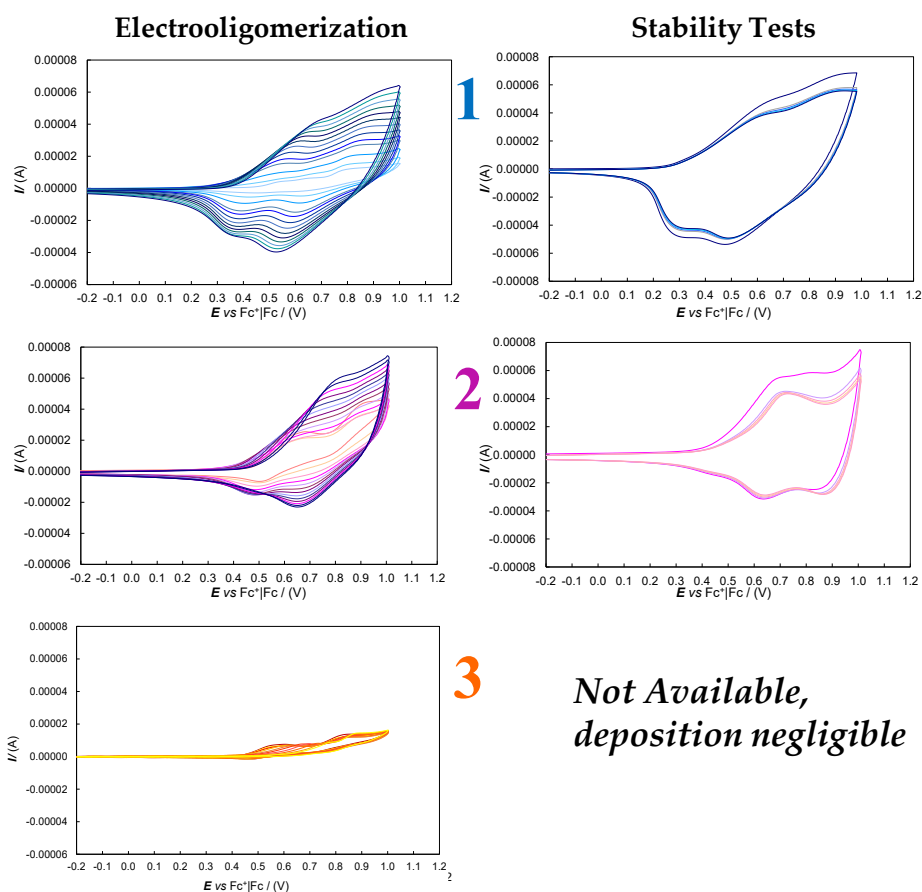


Figure 38. Comparison between the electrooligomerization CV patterns of monomers **1**, **2** and **3** (0.00075 M in DCM + 0.1 M TBAPF₆) on GC electrode by oxidative potential cycling at 0.05 V s⁻¹ (left side) and stability cycles in monomer-free solution (right side). Electrodeposition and stability cycles are reported with the same scale to allow comparison.

e) Enantioselection tests on different chiral electroactive probes, also of pharmaceutical interest

Voltammetry experiments were carried out on GC electrodes modified with enantiopure (*S*)- or (*R*)-electrodeposited oligomer films, testing different chiral probes, also of pharmaceutical interest.

The first chiral probe was the *N,N'*-dimethyl-1-ferrocenylethylamine (namely, (*S*)-Fc and (*R*)-Fc, Figure 39), which is our model chiral probe (commercially available), due to its chemically and electrochemically reversible first CV oxidation peak in a potential range close to 0 V vs $\text{Fc}^+|\text{Fc}$, at which the chiral oligomer film is still uncharged.

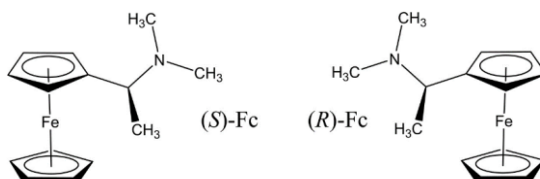


Figure 39. Chemical structures of enantiopure (*S*)- and (*R*)- *N,N'*-dimethyl-1-ferrocenylethylamine, namely (*S*)-Fc and (*R*)-Fc.

Very good enantiodiscrimination in terms of DPV peak potential differences was obtained for the (*S*)-Fc and (*R*)-Fc enantiomers on **oligo-1** enantiopure films (~160 mV). On **oligo-2** the difference is smaller, ~ 80 mV, pointing to a less effective enantioselection, but still significant and reproducible [140]. Notably, the same probe/selector enantiomer combination order was observed in both cases, *i.e.* with the *S,R* (or specularly *R,S*) combination preceding the *S,S* (or specularly *R,R*) one (Figure 40). This is indeed consistent with enantioselectivity arising from the same atropisomeric bisindole scaffold.

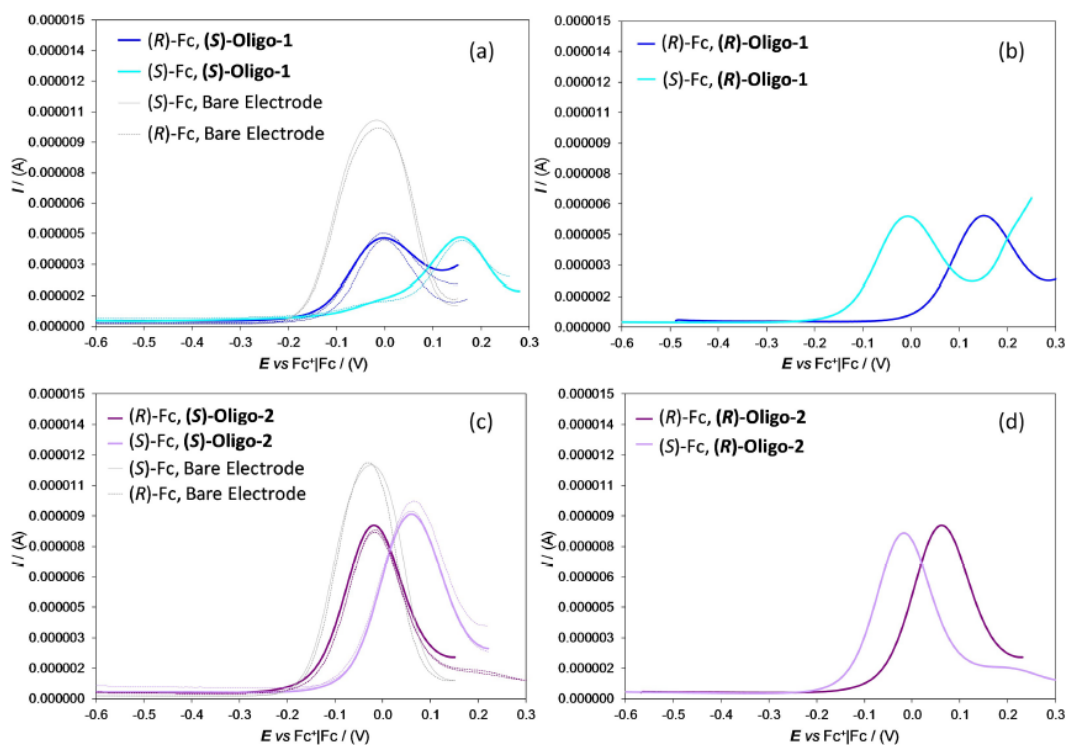


Figure 40. Enantiodiscrimination performance of enantiopure (a) **(S)-oligo-1** and (b) **(R)-oligo-1** and of (c) **(S)-oligo-2** and (d) **(R)-oligo-2** electrode surfaces towards 0.002 M (S)- and (R)-Fc probes in DCM + 0.1 M TBAPF₆. Patterns recorded for the two probe enantiomers on bare GC are also reported in grey.

Such potential differences between probe enantiomers, concerning a chemically and electrochemically reversible electron transfer process, should correspond to the thermodynamic energy difference for the diastereomeric probe/selector combinations obtained testing the two enantiomers with the same selector configuration (or *vice versa*). In fact, some coordination could be assumed between probe and selector, at least moderate/transient, and rather wide-scope than specific, hinging on the many involved π systems and heteroatoms; and such coordination could be significantly more effective for one combination with respect to the other one. Actually, consistently with the well-known treatment by

Kolthoff and Lingane for electroactive species undergoing reversible electron transfer [141], coordination results in a formal potential shift (in negative or positive direction depending on the process being a reduction or oxidation, and on the species most stabilized by coordination being the reagent or product one) of $(k/n)\log K$, where K is the coordination equilibrium constant.

Thus, even mild coordination with $K \sim 10/10^2/10^3$, or a $\sim 10/10^2/10^3$ coordination constant ratio for diastereomeric situations, would justify a shift/difference of 60/120/180 mV in peak potential for a species undergoing monoelectronic reversible process. In this light the smaller peak potential difference in the **oligo-2** case should point to less effective coordination and/or smaller differentiation in coordination ability, linked to the perturbing presence of the long aliphatic chains, more likely than to the chiral film being possibly thinner. Concerning peak currents, they are notably lower than on the bare electrode; this looks consistent with the neutral state of the oligomer film, implying that the probe can only react diffusing inside the film [142].

This could be easier in the case of **oligo-2** (in the same conditions the film was thinner) and could justify the higher currents with respect to the **oligo-1** case.

The two chiral probe enantiomers were also successfully discriminated when simultaneously present, either in 1 :1 ratio (racemate (\pm)-Fc) or in asymmetric ratios (Figure 41 (a) and (b), respectively) [140] on electrodes modified with **oligo-1**. In all cases two neatly separated peaks, located at potentials close to the single enantiomer are observed. Moreover, the peak current ratios for the two enantiomers appear to be consistent with their concentrations, pointing to the possibility of direct evaluation of enantiomeric excesses from the CV pattern analysis.

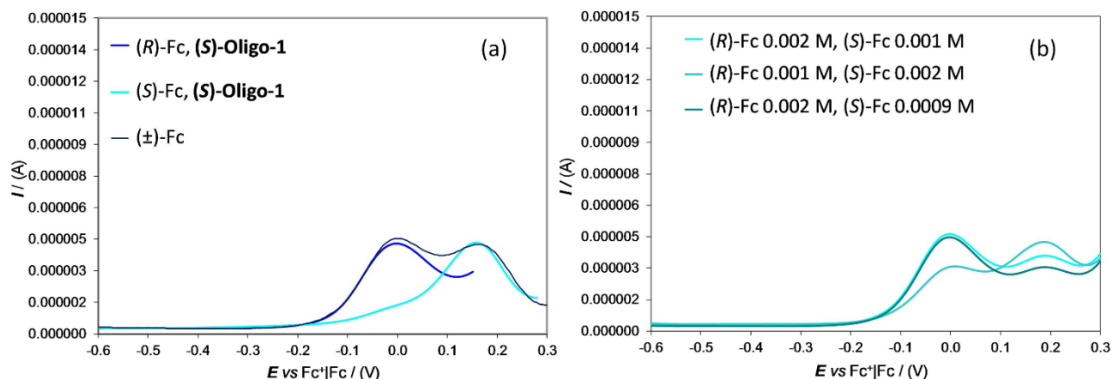


Figure 41. Enantiodiscrimination performance of enantiopure **(S)-oligo-1** towards the ferrocenyl probe enantiomers simultaneously present (a) in 1 :1 ratio (racemate, (\pm)-Fc); (b) in different ratios.

CV tests with the enantiomers of chiral probe terazosin, (*S*)-Tz, (*R*)-Tz (Figure 42), were performed in aqueous buffer pH 4 solution (Figure 43).

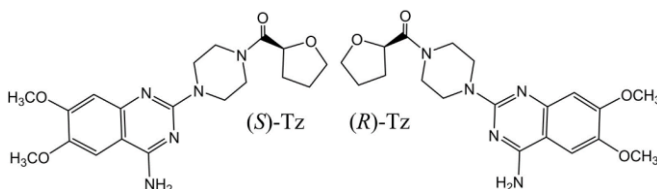


Figure 42. Chemical structures of enantiopure (*S*)- and (*R*)- Tz.

Tz is an API used to treat high blood pressure and prostatic hyperplasia, featuring (on bare electrode) a chemically and electrochemically irreversible first CV oxidation peak ($E_{p,a}$ about 0.96 V vs SCE, Gallery Section 3), possibly corresponding to the oxidation of the methylated catecholic ring, and falling in a potential range at which the chiral oligomer film is positively charged [140].

In all the cases reported in Figure 43, the peak potential separation is smaller but still significant and reproducible (80 mV vs SCE on **oligo-1** and 40 mV on **oligo-2**) inverting selector or probe configuration. Notably, the enantiodiscrimination is less effective for the selector with longer alkyl chain (propyl). Comparing current intensity values vs probe concentrations, recorded on the electrode

covered by the oligomer film, with the previous ferrocenylic case, they appear higher respect to those on bare electrode. This feature looks consistent with the whole film having become conductive during the enantioselection tests considering that Tz enantiomers fall in a potential range at which the chiral oligomer film is positively charged.

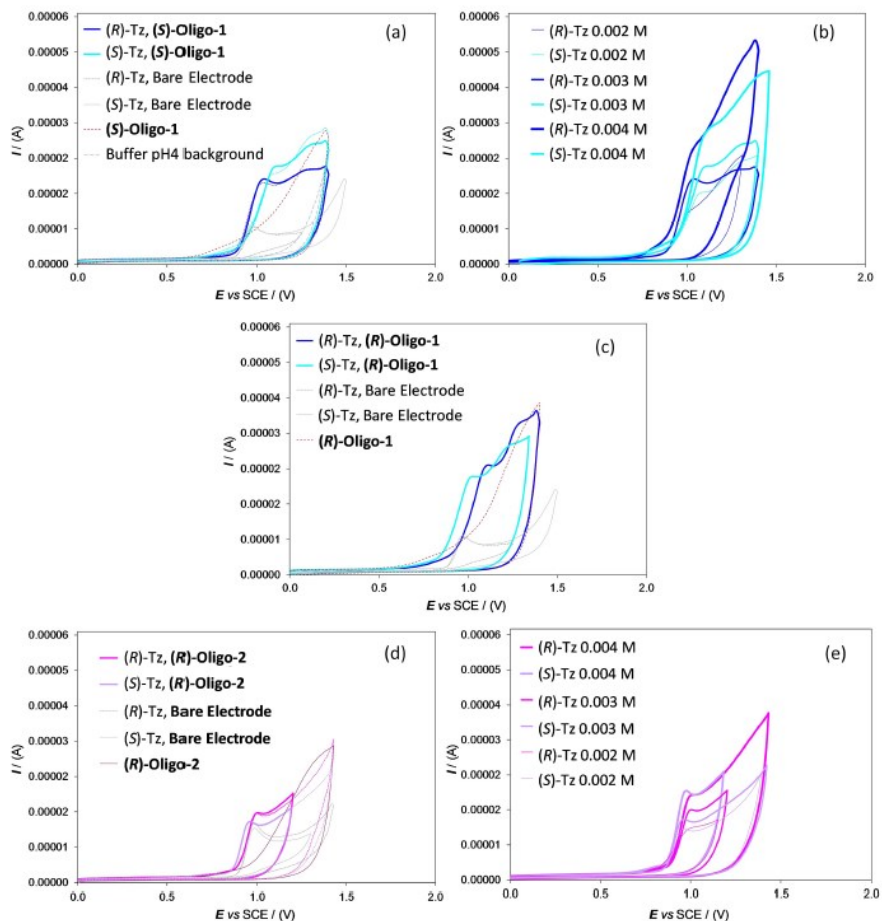


Figure 43. Enantiodiscrimination performance: a) and b) on enantiopure (S)-oligo-1; c) on (R)-oligo-1; d) and e) on (R)-oligo-2 electrode surfaces towards (S)- and (R)-Tz probes (0.002 M in a,c,d) in aqueous pH 4 buffer. In b) and e) enantioselection tests at different probe concentrations. For sake of comparison, patterns of the film oxidation in the absence of the probe (red dotted thin lines) and for the two enantiomers on bare GC (grey lines) are also reported.

Since in the case shown above the best performances were obtained with the **oligo-1** film, the other chiral APIs (Lansoprazole, Ramosetron and Clopidogrel) were tested only on enantiopure **oligo-1** films.

The enantiomers of Lansoprazole, Lans-1 and Lans-2 reported in Figure 44 (which present different bulkiness, chemical nature and electrochemical activity respect to Tz) have been tested as chiral analyte. Also in this case, on bare electrode Lans-1 and Lans-2 have shown an oxidative peak at the same potential value (~ 1.06 V vs SCE, Gallery Section 4), which could correspond to the oxidation of the amine function of benzimidazole moiety (the easiest oxidizable group in the drug molecule) [143]. Enantio-recognition tests were performed on (**R**)-**oligo-1** films (electrodeposited by performing 20 CV cycles in DCM + TBAPF₆ 0.1 M as supporting electrolyte).

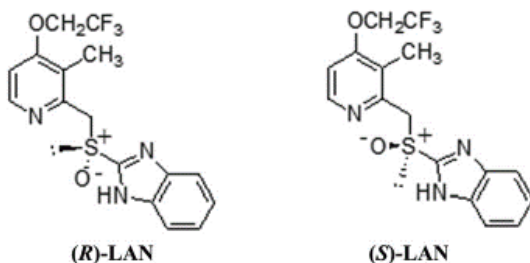


Figure 44. Chemical structures of enantiopure (*S*)- and (*R*)- Lans.

A large and reproducible peak potential difference (about 250 mV) was observed (Figure 45). Also in this case a good linear dynamic range with peak currents was obtained (Figure 45, inset).

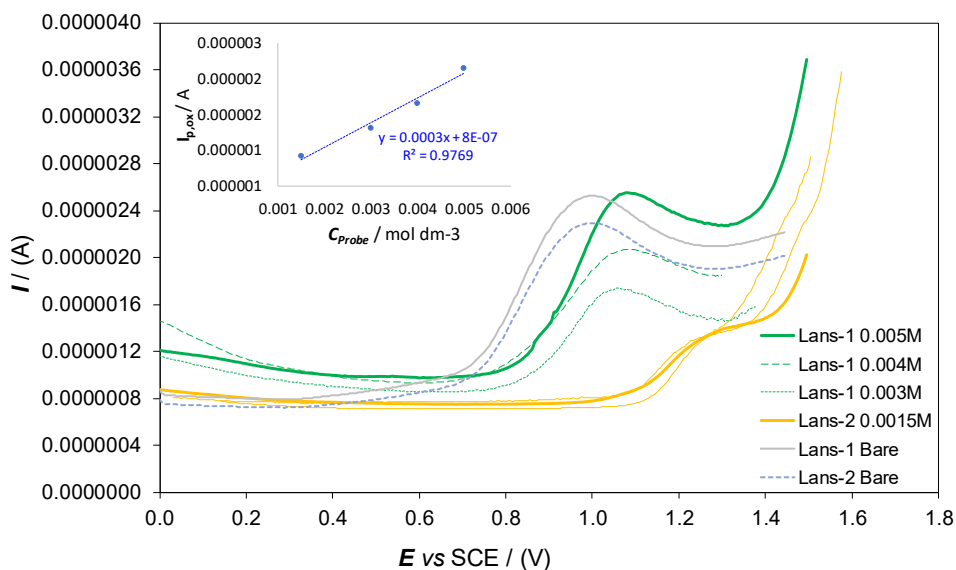


Figure 45. Enantiodiscrimination performance of enantiopure (*R*)-oligo-1 electrode surfaces towards the enantiomers of Lansoprazole (Lans-1 in green and Lans-2 in orange) in the 0.0015-005 M range in NaOH + buffer pH 4 (ratio 3:2). (Inset: concentration calibration plots). In grey are also reported the DPV patterns of the enantiomers of Lansoprazole on bare electrode.

(*S*)-Clopidogrel ((*S*)-CLOP, Figure 46), an antiplatelet drug used to reduce the risk of heart disease was also tested.

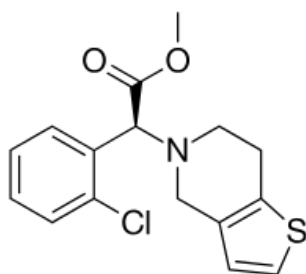


Figure 46. Chemical structure of enantiopure (*S*)-Clop.

The electrochemical characterization of (*S*)-CLOP on bare GC electrode results in a first oxidation peak at ~ 1 V vs SCE (Gallery Section 5), possibly corresponding to the oxidation of the tertiary amine group in the molecule [144].

An enantioselective sensor for the molecular discrimination of the enantiomers of Clopidogrel has already been proposed in literature, employing chiral carbon paste electrode modified with β -cyclodextrin complexes and platinum nanoparticle, resulting in a peak potential separation of about 102 mV [145].

Enantiorecognition tests were performed on (**R**)- and (**S**)-**oligo-1** films (electrodeposited by performing 10 CV cycles in DCM + TBAPF₆ 0.1 M as supporting electrolyte). A large and reproducible peak potential difference (about 150 mV) was observed (Figure 47). It should be noted that, since only one antipode of the pharmaceutical probe was available, the discrimination was verified only by inverting the configuration of the inherently chiral selector (*i.e.* the film). Concentration calibration plots have also been obtained on both the enantiomers of the modified chiral electrode surfaces, and peak currents exhibit good linear dynamic ranges (Figure 47, Inset).

The (*S*)-CLOP has been also tested in a real matrix (Figure 48), as the main component of DuoPlavin[®] (composed by 75 mg of (*S*)-CLOP and 100 mg of acetylsalicylic acid). Results, obtained by testing the drug, like in the case of the Clopidogrel as API, on either the enantiomers of the **oligo-1** film, are reported in Figure 48, where the same enantiomer peak sequence and peak potential separation could be observed, as in the aforementioned (*S*)-CLOP case.

Reproducibility tests were performed by repeatedly recording the CV patterns of chiral probes on freshly deposited chiral surfaces.

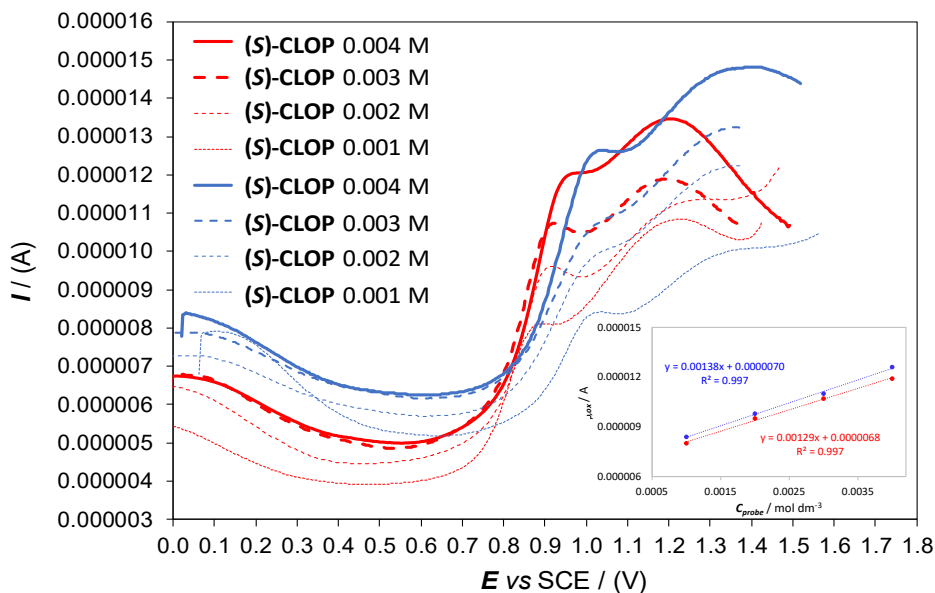


Figure 47. Enantiodiscrimination performances of enantiopure (*R*)- and (*S*)-**oligo-1** (blue and red lines respectively) electrode surfaces towards (*S*)-CLOP in the 0.001-004 M range in buffer pH 4. (Inset: concentration calibration plots).

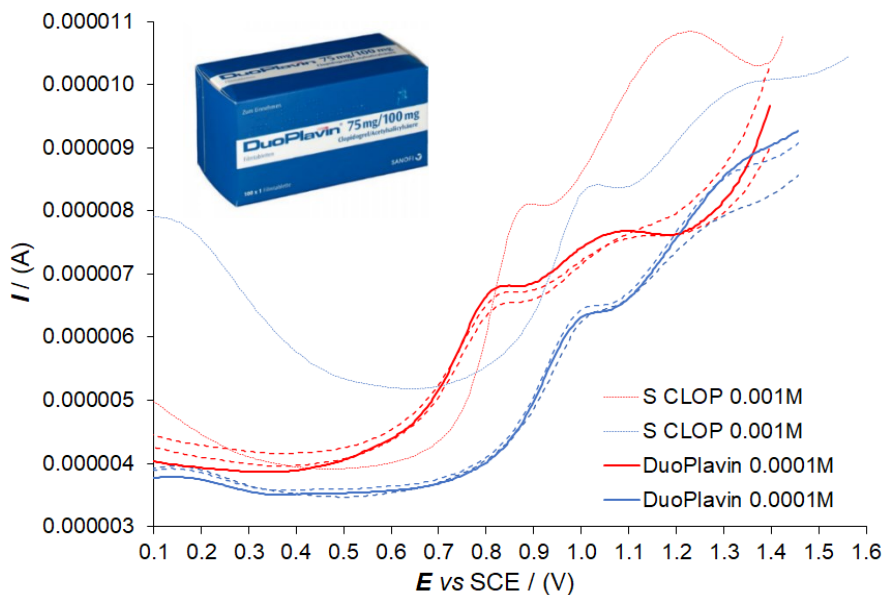


Figure 48. Enantiodiscrimination performance of enantiopure (*R*)- and (*S*)-**oligo-1** (blue and red respectively) electrode surfaces towards DuoPlavin® in buffer pH 4.

The last chiral probe analysed in chiral voltammetry experiments was Ramosetron (1-methylindol-3-yl)-[(5*R*)-4,5,6,7-tetrahydro-3*H*-benzimidazol-5-yl]methanone), namely Ram (Figure 49), which is a serotonin 5-HT₃ receptor antagonist, for the treatment of nausea, also indicated for "irritable bowel syndrome". In India it is marketed under the Ibset brand and is licensed only for use in Japan (under the trade name Irribow) and some Southeast Asian countries.

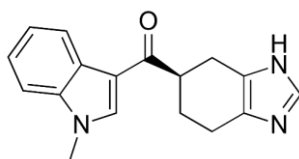


Figure 49. Chemical structure of Ram.

Ram shows on bare electrode a twin oxidation peak system, chemically and electrochemically irreversible (E_{Ip} , at ~ 1.1 V vs SCE and E_{IIp} , at ~ 1.3 V vs SCE, Gallery Section 6), probably related to the oxidation localized on the benzimidazole and on the indole system, respectively.

The enantioselection measurements (Figure 50) on the Ram enantiomers (*R* Ram and *S* Ram) were carried out in buffer pH 4. As expected, also in this case, *R* Ram and *S* Ram, on bare GC electrode, show practically overlapping and coincident DPV peaks. Instead, by depositing on the electrode surface the (***R***)-oligo-1, a separation in terms of peak potential values of ~ 40 mV between the antipodes of the chiral probe was obtained. The peak potential separation is smaller than in the previous cases, but still significant and reproducible.

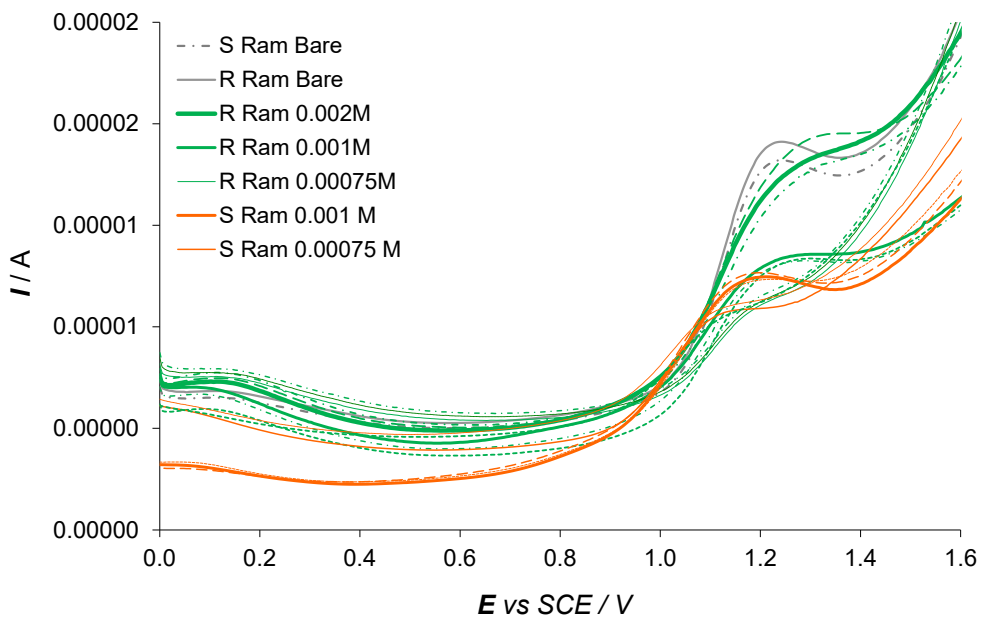


Figure 50. Enantiodiscrimination performance of enantiopure **(R)-oligo-1** electrode surfaces towards *R* Ram and *S* Ram (green and orange respectively) in the 0.00075-002 M range in buffer pH 4.

3.2.3 Cobalt(III)-containing penta-dentate “Helmet”-type phthalogens

The family of porphyrinoid systems, phthalocyanines (Pcs, Figure 51) (which adopt a planar and conjugated structure, as well as high thermal and chemical stability) present many peculiar properties, for example in the electronic/magnetic and catalysis fields [146,147]. Such compounds find applications in different fields, including nonlinear optics [147], semiconductors [149] chemical sensors [150] and catalysis [151]. Phthalogens are another member in porphyrinoids family, which can be used, for example, as precursors for metallophthalocyanines (MPcs) synthesis by thermal or photochemical treatment or by electrochemical reduction [152]. Phthalogens are not a true dye but a special intermediate product which permits the production of the metallophthalocyanine as a pigment in the fibre [153]. However, MPcs represent the pendants of phthalogens since both share in their core at least a chemical connective building block. Nevertheless, phthalogens have different chemical and physical properties in comparison with MPcs, mainly due to skeletal modification that result in the loss of the aromaticity of their pendants.

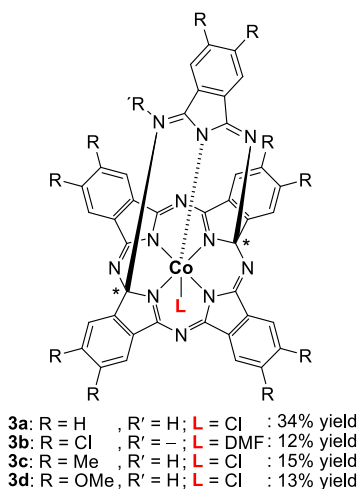


Figure 51. Structure of the helmet CoPc.

a) Experimental protocols for CV characterizations and enantioselection tests

The helmet cobalt phthalocyanine was *electrochemically characterized* by CV as a function of the potential scan rate on GC disk electrode, both

- in ACN (the solvent to be employed for the enantioselectivity test with the GC electrode modified with the electrodeposited oligo-BT₂T₄ inherently chiral film), and
 - in DMF (for comparison with the reference compound cobalt (II) phthalocyanine, which is hardly soluble in acetonitrile)
- in both cases with 0.1 M TBAPF₆ supporting electrolyte.

The helmet CoPc enantiomers were tested in two somehow specular kinds of voltammetry *enantiodiscrimination experiments*:

- a) as chiral modifiers of the working electrode surface by drop-casting, using a drop of 2 μ L (considering that unhelmeted CoPc is a popular reagent for easy electrode surface activation as redox mediator and easily adsorbs onto the electrode surface), to discriminate the enantiomers of chiral DOPA (0.005 M) in aqueous buffer solution (pH 4);
- b) and as chiral probes (0.001 M) in ACN solution, to be discriminated by working electrodes modified with enantiopure inherently chiral oligomer films.

b) CV electrochemical characterization

Figure 52 reports the CV features of cobalt (II) phthalocyanine, with potentials normalized against the Fc⁺|Fc redox reference couple, and currents normalized against geometrical surface, concentration, and square root of scan rate. A partial DPV scan in ACN is also reported.

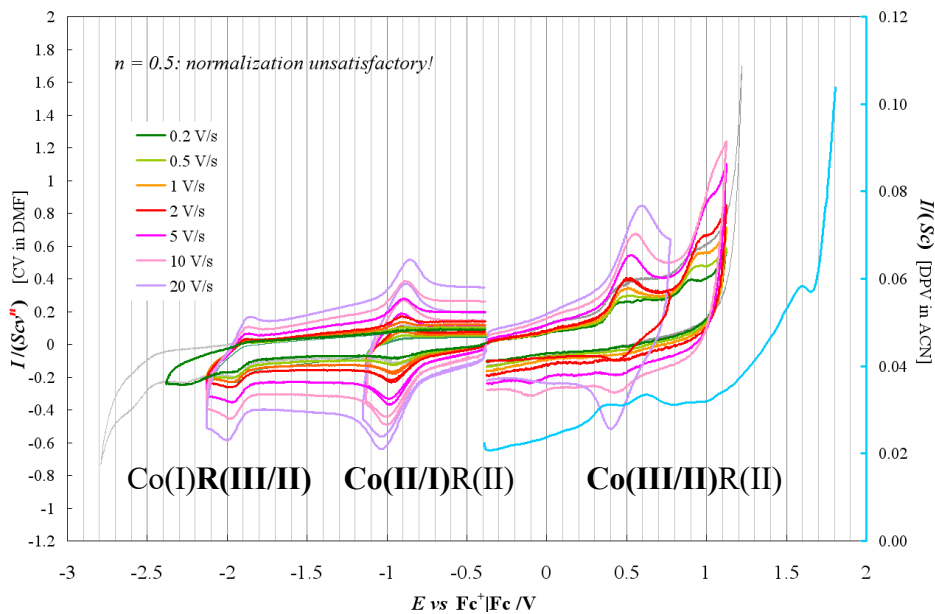


Figure 52. CoPc features in DMF (normalized with $n = 0.5$).

According to Compton *et al.* [154], in a polar coordinating solvent like DMSO (or in the present case DMF) the three chemically reversible CV peaks can be assigned to the redox processes reported in the figure; moreover, respect to DMSO [154] further redox processes can be seen in DMF at more extreme potentials on the positive and negative side. Remarkably, peak current normalization against $v^{0.5}$ (typical of canonical diffusive processes) looks here quite unsatisfactory. Instead, looking for the n value in $I/(Scv^n)$ resulting in the best peak current normalization gave $n \approx 0.9$ (Figure 53). This looks consistent with a mixed behaviour between diffusive ($n=0.5$) and (prevalingly) pseudocapacitive ($n=1$) as for a layer of the redox active molecule on the electrode surface. Actually, electrodes modified with CoPC, a popular tool, can be prepared by simple immersion in CoPc solution followed by washing with pure solvent and water. Features consistent with pseudocapacitive behaviour were also observed by Compton in DMSO for the Co(III/II)R(II) process, while in that case the remaining two had diffusive character [154].

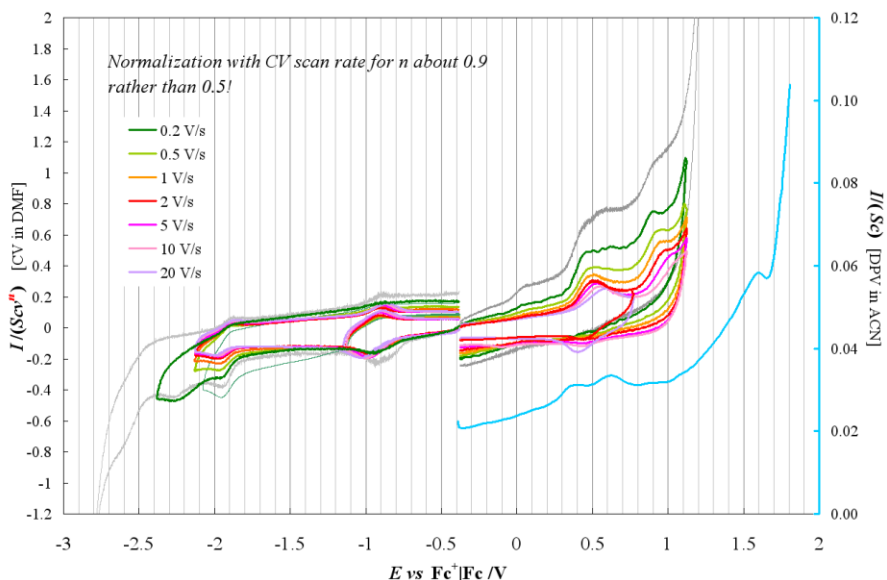


Figure 53. CoPc features in DMF (normalized with $n = 0.9$).

Moreover, the Co(III/II)R(II) process corresponds to a single peak at high scan rates, but becomes a more complex peak system at low scan rates and a double peak in the DPV scan in ACN solvent.

In the cited DMSO literature example [154] the same process had a shoulder for which a solid-state reorganization was assumed.

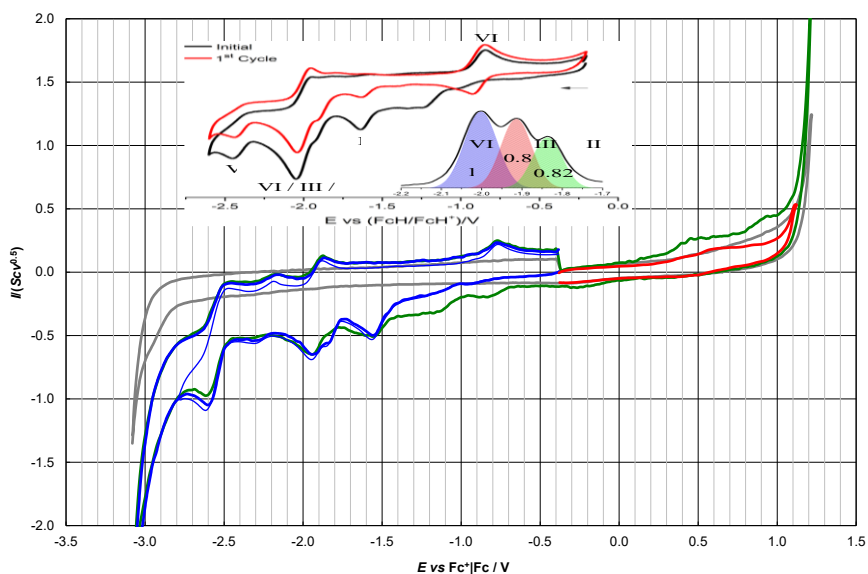


Figure 54. Helmet CoPc features in DMF, 0.2 V/s (normalized with $n = 0.5$).

The Co(III)/Co(II) system is missing scanning the potential from 0 vs SCE in positive direction (red half curve) consistently with the nature of helmet Co(III)Pc respect to Co(II)Pc). On the other hand, scans started from the same potential in negative direction result in a much more complex pattern than CoPc, which is consistent with the additional ligand and loss of symmetry.

As in the paper draft, performing subsequent redox cycles it is also observed the formation of an interesting additional reduction peak marked with * in Figure 55, combined with a decrease in intensity of the following features.

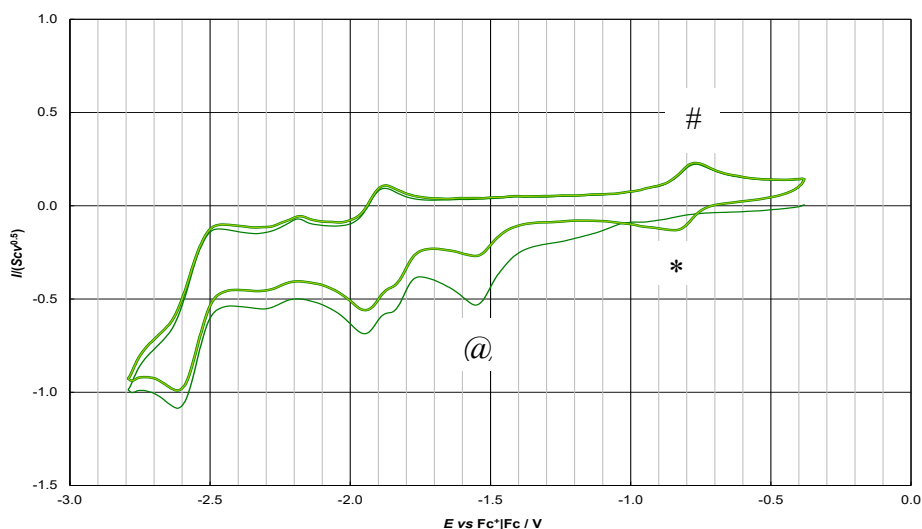


Figure 55. Helmet CoPc in DMF, first and second scan from 0 (SCE) in negative direction. Third scan practically coincides with the second one.

Such a peak looks related to the oxidative peak # at about -0.8 V ($\text{Fc}^+|\text{Fc}$), which in turn appears including in the negative potential scan at least the reduction peak @ at -1.5 V ($\text{Fc}^+|\text{Fc}$) (Figure 56), although a more canonical shape is only obtained by further widening the potential scan.

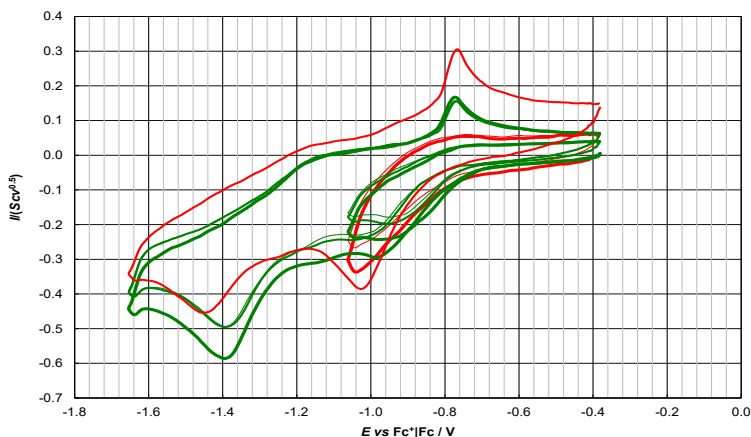


Figure 56. Helmet CoPc in DMF, normalized short scans from 0 (SCE) in negative direction, at 0.2 V/s and 2 V/s (respectively green and red lines of increasing thickness for I,II,III cycle).

Increasing the scan rate, the II and III cycles remarkably tend to a simpler pattern (Figure 57a and b).

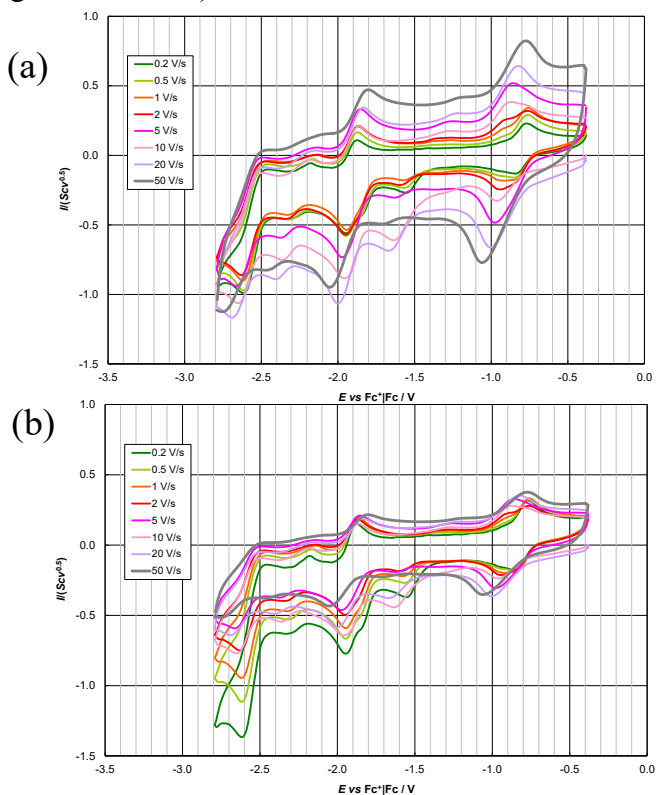


Figure 57. Helmet CoPc in DMF, normalized (with $n = 0.5$ (a), or with $n = 0.7$ (b)) II scans from 0 (SCE) in negative direction, at increasing scan rates from 0.2 V/s to 50 V/s.

Such a pattern remarkably coincides with the one of unhelmeted CoPc in the same conditions (Figure 58).

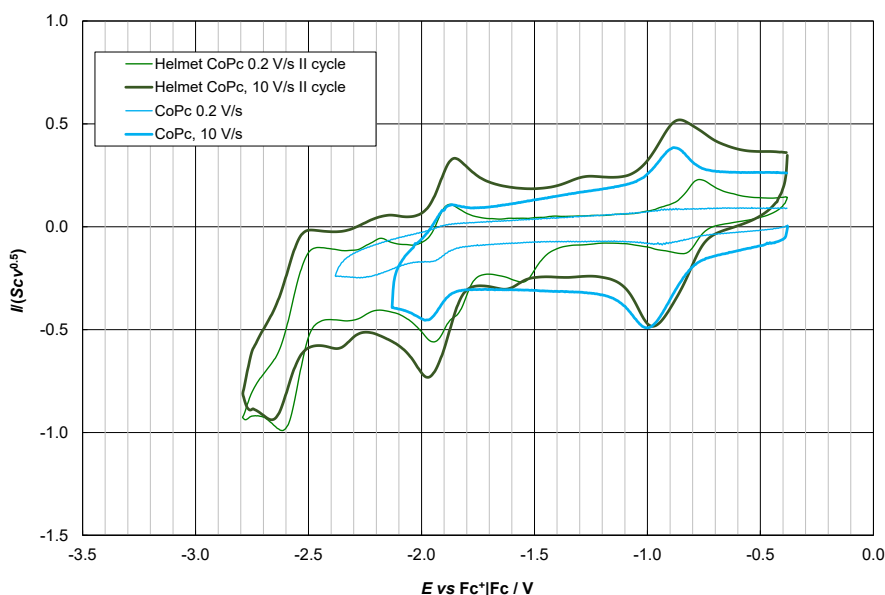


Figure 58. Helmet CoPc in DMF, normalized (with $n = 0.5$) II scans from 0 (SCE) in negative direction, at 0.2 V/s and 10 V/s, compared to CoPc.

Accordingly, maybe the CoIII/CoII reduction process corresponding to peak @ could lead to “helmet loss” (the helmet compound being actually formed from Co(II) and phthalazine precursor with concurrent Co(II/III) oxidation), which could also result in lower solubility and more regular solid state packing at the electrode surface, so that oxidation peak # and new reduction peak * might correspond to the unhelmeted CoPc Co(II/III) reversible redox process; this would be more evident at high scan rate, while at lower ones the larger time scale could allow to involve new helmet CoPc, too.

In acetonitrile (Figure 59 a, b and c) the pattern of the helmet CoPc is very similar, but process * is evident also in the first cycle together with the @ one and return peak # is obtained even in the first cycle around * only, at high scan rate.

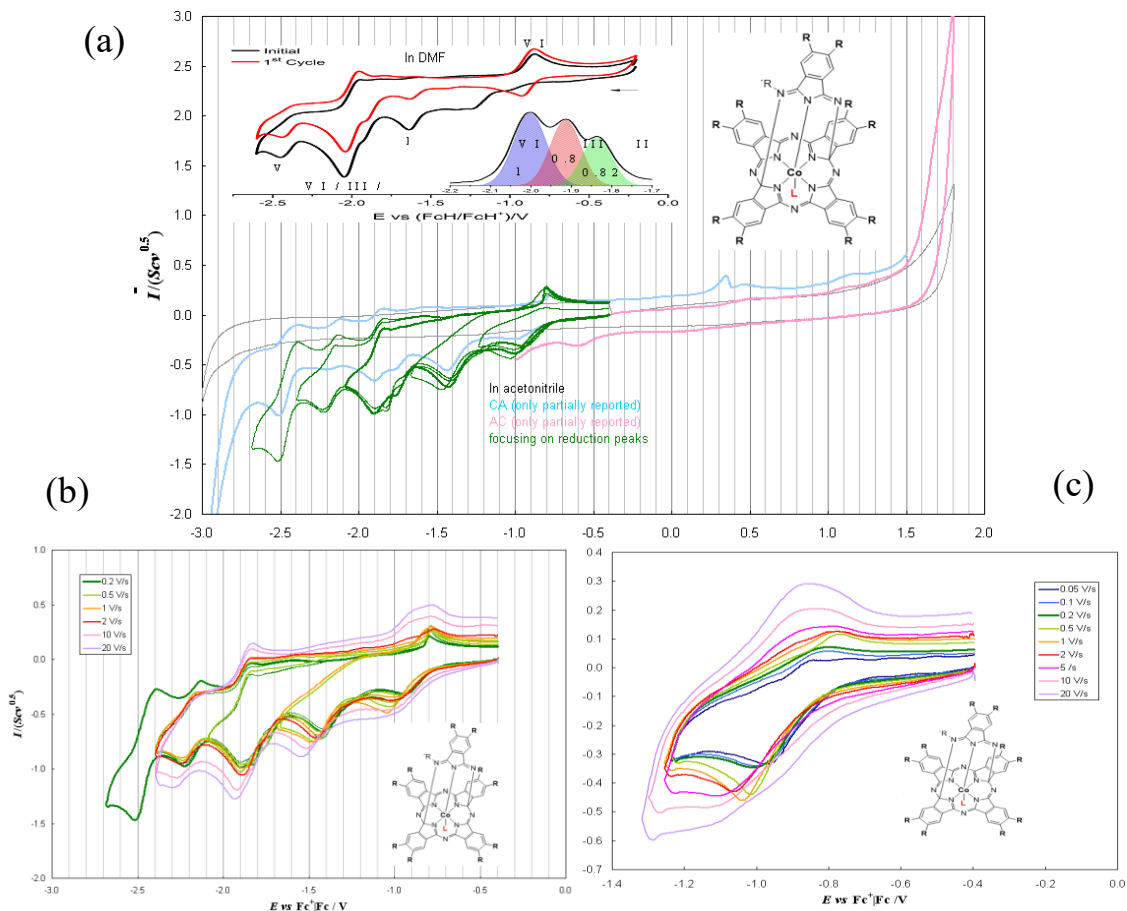


Figure 59. CV pattern of racemate helmet PC in ACN: general features at 0.2 V/s (a), normalized first cycles at different scan rates and different inversion potentials (b) normalized first cycles at different scan rates around the first reduction process (c).

Interestingly, the CV pattern of enantiopure helmet CoPc (Figure 60) looks similar, but not coincident with the racemate one. Actually, a difference between racemate and enantiomers could not be expected for diffusive ET processes, but, as observed before, in the present cases CV features are of mixed diffusive/ solid state character. And, remarkably, the differences mainly concern the “critical” above Co(III/II) processes (as evidenced in the superimposition of racemate and enantiopure patterns in Figures 61 and 62).

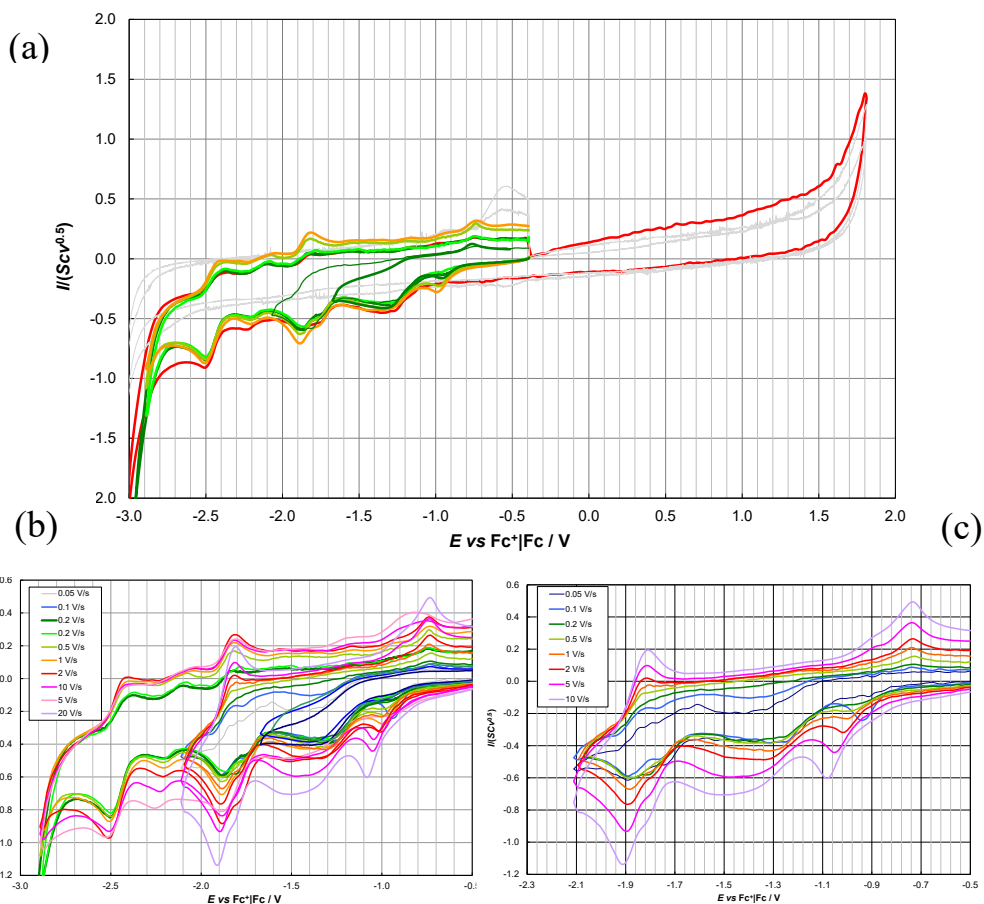


Figure 60. CV pattern of enantiopure helmet PC in ACN: general features at 0.2 V/s (a), normalized first cycles at different scan rates and different inversion potentials (b) normalized first cycles at different scan rates around the first reduction process. (c) normalized second cycles at different scan rates.

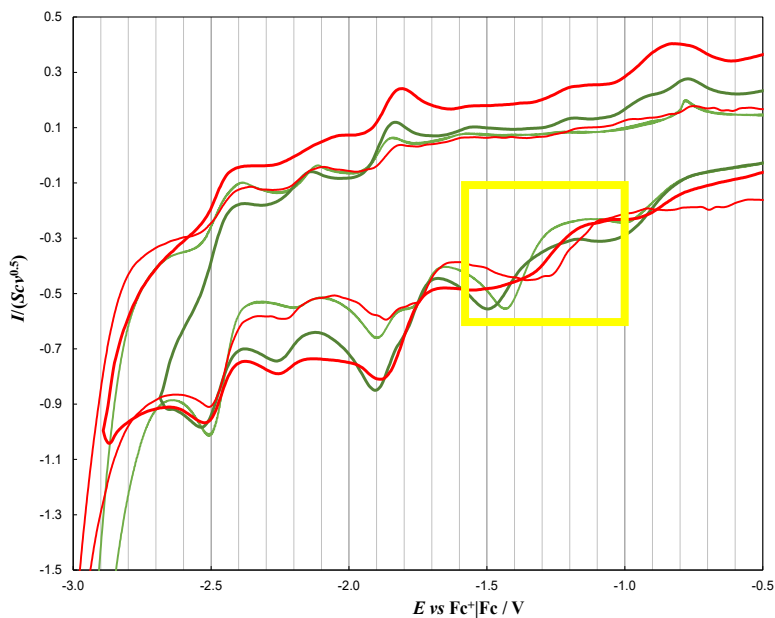


Figure 61. Normalized CV patterns in ACN at 0.2 V/s (thin lines) or 10 V/s (thick lines) for enantiopure helmet PCo (red) compared with racemate helmet PCo (green).

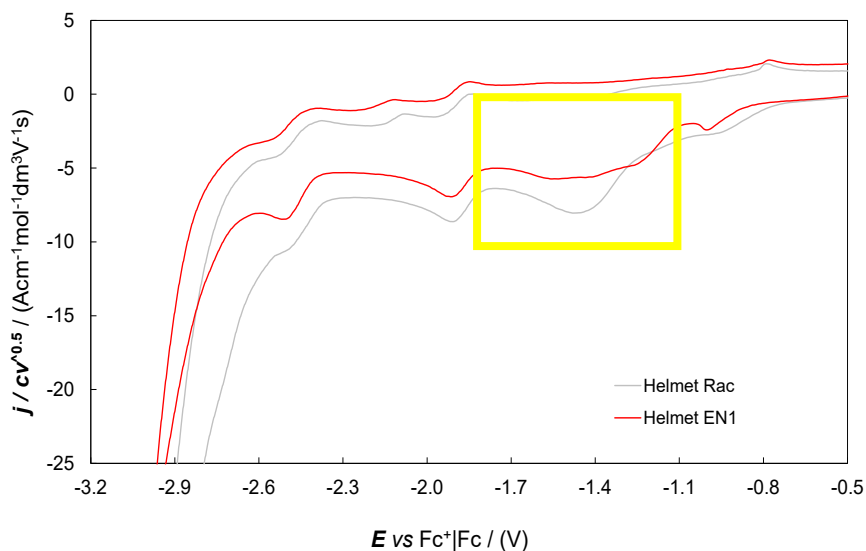


Figure 62. Normalized CV patterns in ACN at 0.2 V/s for enantiopure helmet PCo (red) compared with racemate helmet PCo (grey). Experiment performed to test reproducibility, about two months after the one in Figure 61.

c) *Enantioselection tests, using enantiopure Helmet CoPc both as chiral selector to modify the WE and as chiral probe*

DOPA enantiomers in water discriminated on WE drop casted with helmet enantiomers.

In the first case a GC disk electrode was drop casted with a very thin layer of either enantiopure helmet CoPc and employed to test by DPV aqueous solutions of either DOPA enantiomer.

A small but statistically significant and reproducible peak potential difference was observed for the two DOPA enantiomers (Figure 63 a and b, Table 2), specularly inverting either helmet CoPc or DOPA configuration.

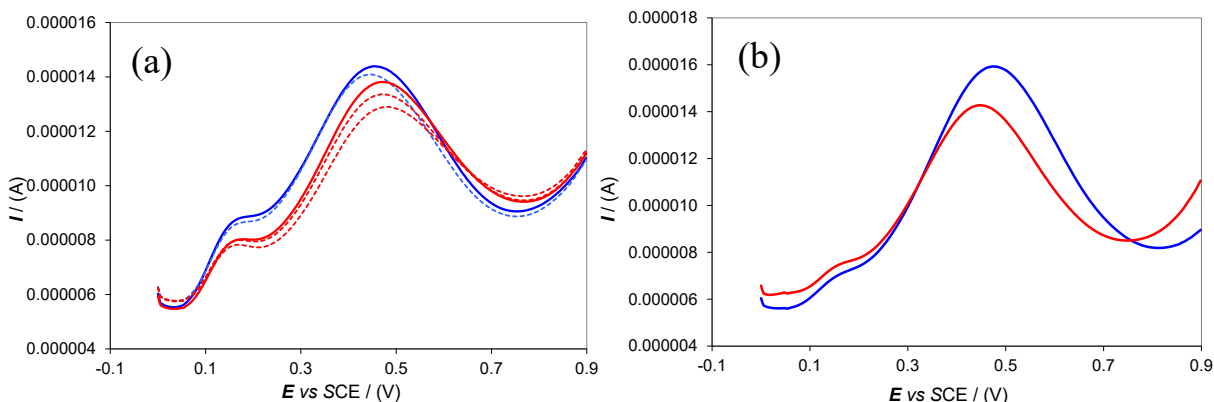


Figure 63. DPV tests on D- and L- DOPA (blue and red respectively) enantiopure aqueous solutions performed on GC working electrode drop casted with a) Helmet EN1 (with reproducibility tests) and b) Helmet EN2.

Table 2

Dropcasted helmet EN1		Dropcasted helmet EN2	
D-Dopa	L-Dopa	D-Dopa	L-Dopa
0.454	0.478	0.454	0.483
0.449	0.478		
	0.483		
0.4515	0.480	0.454	0.483
0.004	0.003		

0.001 M Helmet CoPc enantiomers in ACN, discriminated on WE modified with a very thin oligo BT₂T₄ film, electrodeposited (1 cycle, 50 mV/s) from 0.00075 M (*R*)- or (*S*)- inherently chiral BT₂T₄ enantiomer.

In the second case a GC disk electrode was modified by electrodeposition in acetonitrile of a very thin layer of enantiopure BT₂T₄ inherently chiral oligomers of either configuration, and employed to test by CV acetonitrile solutions of either helmet CoPc enantiomer. A significant difference (consistently with the presence of an inherently chiral actor) in potentials and shapes particularly of the first reduction peak potentials (corresponding to Co(III)|Co(II) reduction in the molecule core, close to the two stereocentres) was observed for the helmet CoPc enantiomers (Figure 64 a,b and c), specular inverting either helmet CoPc or oligo-BT₂T₄ configuration.

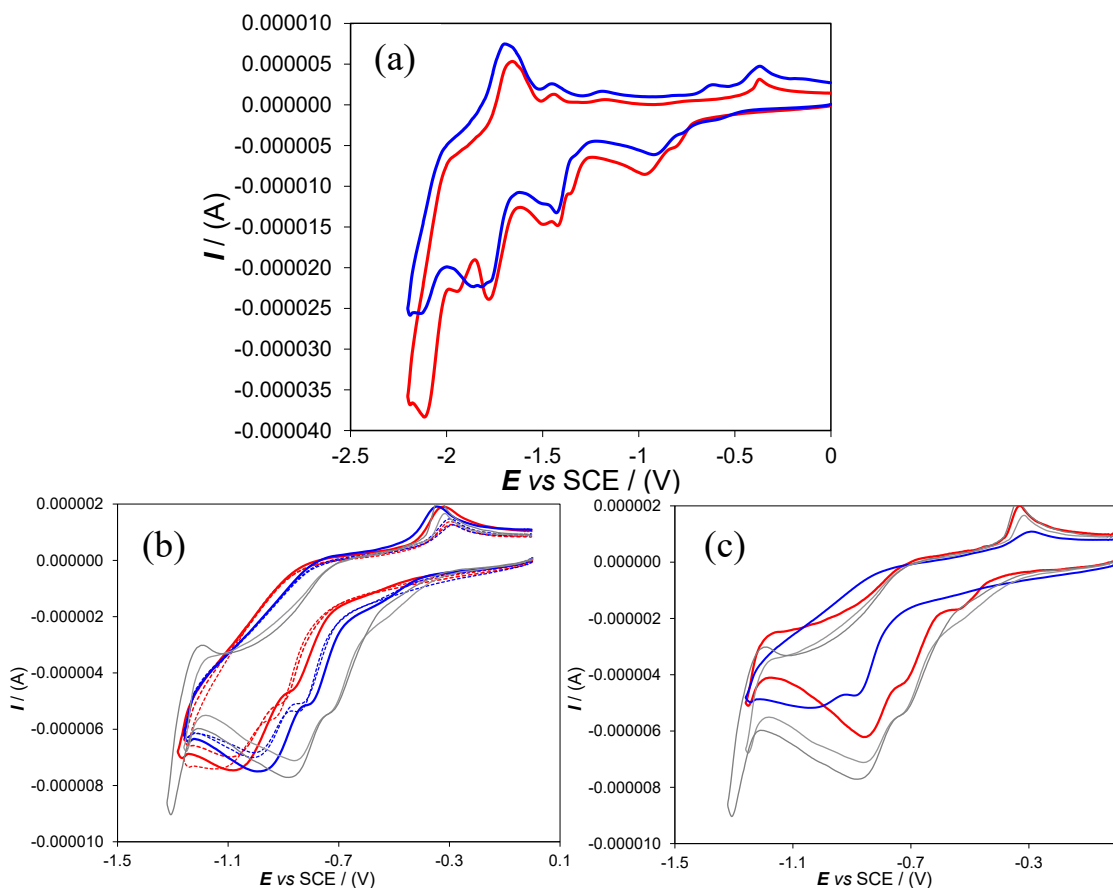


Figure 64. CV tests on enantiopure helmet CoPc (EN1 in red and EN2 in blue) in acetonitrile solutions performed on GC working electrode modified with (b) (*R*)- and (c) (*S*)-oligo-BT₂T₄ films. (a) Whole reduction half cycle (0.2 V/s) with the two helmet enantiomers on oligo-(*R*)-BT₂T₄ enantiopure film (b) First reduction peak system of the two helmet enantiomers on the two oligo-BT₂T₄ enantiopure films. In one case reproducibility cycles are also reported. In grey are also reported the CV signals of Helmet EN1 and EN2 on bare electrode.

3.2.4 Electrodeposition of inherently chiral films: morphological and functional properties as a function of the operating conditions

From previous works, reported in literature, it has been shown that the efficiency of the electrodeposition and the chemical composition of the films depend on the experimental parameters [155,156]. For this reason, first of all, the electrooligomerization process of our benchmark monomer BT₂T₄ was studied changing the supporting electrolyte (TBAPF₆, TBAClO₄, TBABF₄, LiClO₄, NaClO₄, TEAPF₆, TEABF₄, TEAClO₄); in fact, the nature of the electrolyte strongly influenced the morphology and roughness of the films [155], the percentage of dimers, trimers and tetramers, the ratio between open and closed oligomers [156], as well as the enantioselection ability.

Then, a systematic study was also developed by comparing the BT₂T₄ molecule with other two inherently chiral monomers (*vs* BT₂T₆ and BT₂(T₃)₂, all the structures are reported in Figure 65), which present the same bibenzothiophene atropisomeric core, but different ring number and/or connectivity of the thiophene terminals.

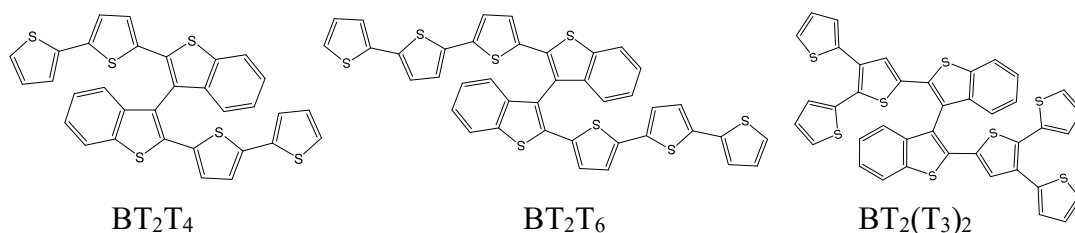


Figure 65. The three inherently chiral monomers based on a 3,3'-bibenzothiophene atropisomeric core.

The inherently chiral oligomer films obtained at fixed monomer concentration and potential scan rate on ultra-flat ITO as working electrode, varying the electrodeposition cycles (1-5-10-108), were studied in different conditions, in particular:

- racemic and enantiopure oligomer films of BT₂T₄ in ACN and two different supporting electrolytes (TBAPF₆ and LiClO₄);
- racemic oligomer films of BT₂(T₃)₂ in ACN + TBAPF₆;
- enantiopure oligomer films of BT₂T₆ in ACN + TBAPF₆.

The monomers were fully characterized by CV experiments, and the films studied with different techniques: AFM (in order to obtain information on the film morphology at nanometer level and to quantitatively evaluate their surface roughness) and HR LDI (for the chemical composition of the films).

Finally, the enantiopure inherently chiral films were tested in enantioselection experiments, as a function of different working protocols (with TBAPF₆ vs LiClO₄ supporting electrolytes) and electrodeposition cycles (1,5 and 10).

a) Experimental set-up and conditions for: CV electrochemical characterization, electrodeposition protocol, enantioselection tests, AFM and HR LDI measurements

The electrochemical characterizations were carried out in ACN (or DCM) solutions containing BT₂T₄, BT₂(T₃)₂ or BT₂T₆ ~0.00075 M and TBAPF₆ 0.1 M as supporting electrolyte. The experiments were performed on GC as working electrode (using a V-shape three-electrode minicell, Figure 28).

The electrodepositions (Figure 66) of the oligomer films were performed starting from the corresponding monomer (~0.00075 M) dissolved in ACN + TBAPF₆ 0.1 M (in the case of BT₂T₄ the oligomerization was also carried out using LiClO₄ 0.1 M as supporting electrolyte), performing different CV cycles (1, 5, 10 or 108). In fact, by varying the electrodeposition conditions it was possible to obtain further information on the chemical composition and morphology of the film. For the *enantioselection tests* (Figure 66), the enantiomers of the ferrocenyl probes (~ 0.004 M) were tested in a ACN + TBAPF₆/LiClO₄ 0.1 M solution on

ITO electrode, modified with the chiral (or racemic) oligomer film (oligo-BT₂T₄ and oligo-BT₂T₆). The films were obtained by varying the number of deposition cycles (1-5-10-108 cycles), in an appropriate potential range (0-1.35 V vs SCE, in order to activate the α homotopic positions of the thiophenes) at 0.05 V/s potential scan rate.



Figure 66. Experimental setup for the electrodeposition and enantioselection tests with ITO as working electrode (W), an aqueous saturated calomel electrode SCE as reference electrode (R) and Pt wire as counter electrode (C).

The AFM measurements were performed in air using a Nanoscope Multimode IIIId system (Bruker, Santa Barbara, CA, USA) operating in tapping mode. Rectangular silicon probes with nominal spring constant around 2.5 N/m (NT-MDT, Russia) and cantilever length of 120 μm were used. The cantilever resonance frequency was about 130 kHz. Images were recorded at ~ 1 Hz line rate and a resolution of 512x512 pixels per image was chosen. AFM images were subject to a line-by-line subtraction of linear background to eliminate sample tilt from the images and correct for step-wise changes between individual scan lines. The rms surface roughness has been calculated according to the following equation (equation (1)):

$$\text{rms}_{xy} = \sqrt{\sum_{x,y=1}^N \frac{(Z_{x,y} - Z_{\text{average}})^2}{N^2}} \quad (1)$$

where Z_{average} is the average Z value within the examined area, $Z_{x,y}$ is the local Z value, and N indicates the number of points within the area.

For all samples the rms surface roughness has been measured on $250 \times 250 \text{ nm}^2$ areas. Rms data have been reported as: mean \pm SD; $n = 30$.

High-resolution LDI spectra have been obtained by a MALDI ToF-ToF Autoflex III Spectrometer at UNITECH COSPECT.

b) CV electrochemical characterizations of the inherently chiral BT₂T₄, BT₂(T₃)₂ and BT₂T₆ monomers

DCM

Figure 67 shows the complete CV patterns of the monomers BT₂T₄ (a), BT₂(T₃)₂ (b) and BT₂T₆ (c), recorded at 0.2 V/s, in DCM + TBAPF₆ 0.1 M. Since the DCM solvent has a narrower potential window (on account of the solvent bulk reduction at a rather early potential), the reduction peaks are difficult to observe and fall on the background discharge.

(a) BT₂T₄ shows a similar reactivity to linear double terthiophene [157] and exhibits a first oxidation peak at a slightly higher potential, probably due to the partially hampered conjugation along the main backbone. It is possible to observe two oxidation peaks ($\sim 0.62 \text{ V}$ and $\sim 0.76 \text{ V}$ vs Fc⁺|Fc) which correspond to the oxidation of the two terthiophene systems (equivalent and partially interacting redox sites) to radical cations, with possible coupling. The distance between the two peaks accounts for the reciprocal interactions between redox centres: the higher the energy barrier the more independent the two sites are (instead, the two peaks can completely merge if the sites are completely independent).

(b) $\text{BT}_2(\text{T}_3)_2$ presents the same core of the BT_2T_4 monomer, but a different number (3 vs 2 for each half) and connectivity of thiophenes (the first thiophene is linked to other two thiophenes: one in α and one in β position; in the first case the conjugation is more effective). The monomer shows two oxidation peaks at similar potential values to the BT_2T_4 , corresponding again to the equivalent interacting redox sites; however, in this case, there is a clear splitting of the two signals, because of the presence of a third thiophene which modifies the delocalization of the charge on the molecule; a larger difference was found in the first reduction peak, which is less negative for the $\text{BT}_2(\text{T}_3)_2$ and therefore resulting in a narrower HOMO-LUMO gap (Table 3).

(c) BT_2T_6 is a structural isomer of $\text{BT}_2(\text{T}_3)_2$, with the third thiophene linked in α position instead of β . Therefore, it exhibits a reactivity similar to a couple of equivalent interacting tetrathiophenes, with a higher conjugation than the other monomers. This is also evident from the less positive value of the first oxidation peak ($E_{1,\text{pa}} \sim 0.57 \text{ V vs Fc}^+|\text{Fc}$ in the BT_2T_4 case, compared to $\sim 0.62 \text{ V vs Fc}^+|\text{Fc}$ in the $\text{BT}_2(\text{T}_3)_2$ case), resulting in a lower HOMO-LUMO gap (Table 3). The longer thiophene chains allow a better delocalization of the charge.

Table 3. Key CV parameters for BT_2T_4 , $\text{BT}_2(\text{T}_3)_2$ and BT_2T_6 monomers in DCM + TBAPF₆ 0.1 M.

	$E_{\text{Ipa}} \text{ vs Fc}^+ \text{Fc}/\text{V}$	$E_{\text{IIpa}} \text{ vs Fc}^+ \text{Fc}/\text{V}$	$E_{\text{Ipc}} \text{ vs Fc}^+ \text{Fc}/\text{V}$	$E_{\text{HOMO}} / \text{eV}^{[\text{a}]}$	$E_{\text{LUMO}} / \text{eV}^{[\text{b}]}$	H-L Gap / eV
BT₂T₄	0.62	0.76	-2.64	-5.42	-2.16	3.26
BT₂(T₃)₂	0.63	0.75	-2.57	-5.43	-2.23	3.22
BT₂T₆	0.57		-2.46	-5.37	-2.34	3.03

^[a] $-1\text{e} \times [(E_{\text{Ipa}} / \text{V} (\text{Fc}^+|\text{Fc}) + 4.8 \text{ V} (\text{Fc}^+|\text{Fc} \text{ vs zero})]$

^[b] $-1\text{e} \times [(E_{\text{Ipc}} / \text{V} (\text{Fc}^+|\text{Fc}) + 4.8 \text{ V} (\text{Fc}^+|\text{Fc} \text{ vs zero})]$.

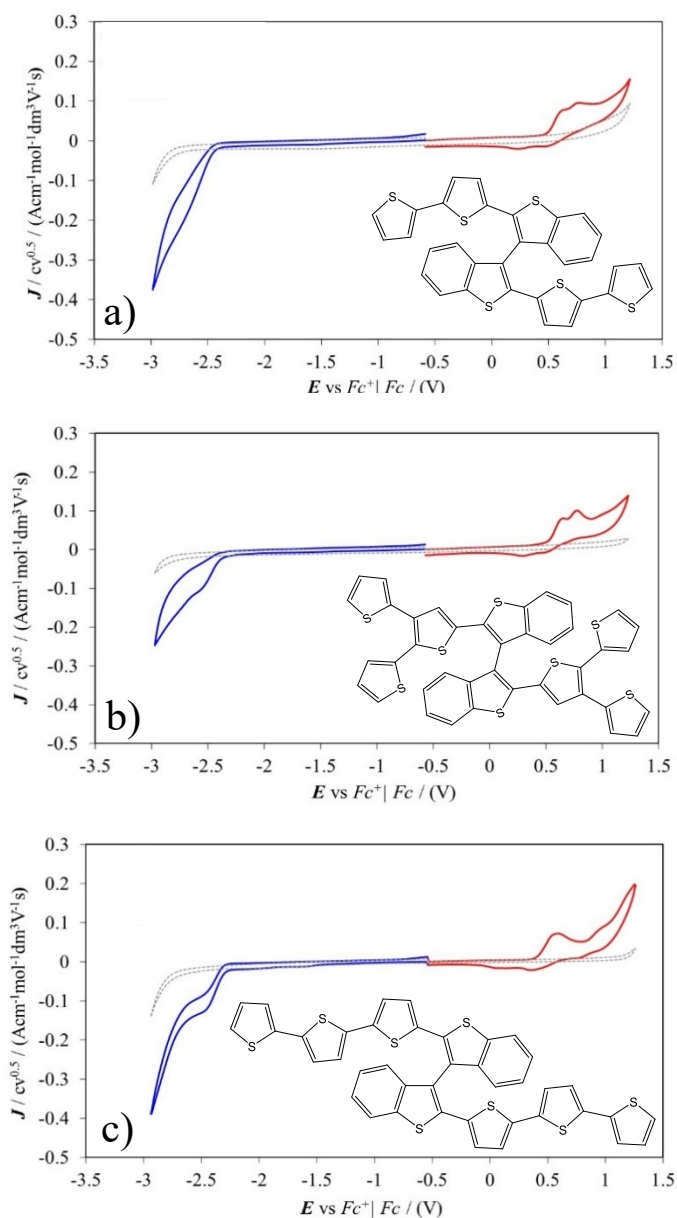


Figure 67. Complete CV patterns of BT_2T_4 (a), $\text{BT}_2(\text{T}_3)_2$ (b) and BT_2T_6 (c) monomers, on GC electrode in DCM + TBAPF₆ 0.1 M at 0.2 V/s potential scan rate. Background patterns are also reported in grey, for sake of comparison.

ACN

Figure 68 shows the complete CV patterns of the monomers BT_2T_4 (a), $\text{BT}_2(\text{T}_3)_2$ (b) and BT_2T_6 (c), recorded at 0.2 V/s, in ACN + TBAPF₆ 0.1 M. A polar solvent, like ACN, tends to screen the radical cations obtained during the electrooxidation process, hampering the interaction between the two redox sites.

(a) The CV pattern (Figure 68a) of the BT_2T_4 monomer shows a first peak (of canonical shape), corresponding to the oxidation of the two α homotopic positions and a second anodic peak (probably related to adsorption phenomena, with specific interactions with the electrode surface), which could correspond to a subsequent chemical reaction, or a further oxidation process of an electroactive product formed by chemical follow up, as evident from its disappearance upon increasing the potential scan rate (see Gallery Section 8). However, differences can be observed respect to a previously work reported in literature [121], in fact in this case two anodic peaks instead of one are clearly visible (Figure 68a). For this reason, the monomer was studied also at higher potential scan rates (5, 10, 20 and 50 V/s, in Gallery Section 8): the non-canonical peak tends to disappear increasing the potential scan rate, while the canonical one tends to split (probably the second anodic peak could be the sum of two peaks, one related to the adsorption process and the other related to the oxidation of one of the two redox sites of the molecule; the latter process appears to be in competition with the oxidation on the α homotopic position).

(b) and **(c)** This phenomenon can also be observed in the $\text{BT}_2(\text{T}_3)_2$ and BT_2T_6 cases, although in a lesser marked way (Figure 68 b and c), but without the splitting of the signal.

Moreover, the CV patterns of the three monomers show a peak at higher potential value, probably due to an oxidation process which involves the product formed in the previously mentioned chemical step. The first reduction peaks of the three monomers (Figure 68 a, b and c) are chemically and electrochemically reversible.

Furthermore, the cathodic signal in the case of BT₂(T₃)₂ and BT₂T₆ cases tend to split into two consecutive peaks, consistently with the C₂ symmetry of the molecule.

Instead, the BT₂T₄ shows, in the same potential range, a single reduction peak (even at high potential scan rate) probably due to the lower interaction between the two redox sites.

Furthermore, as observed in DCM solvent, BT₂T₄ and BT₂(T₃)₂ monomers are very similar, while the BT₂T₆ peaks are at less positive potentials, due to the greater conjugation of the molecule. Consistently, the HOMO-LUMO gap is almost identical for BT₂T₄ and BT₂(T₃)₂ and smaller for BT₂T₆ (Table 4).

Table 4. Key CV parameters for BT₂T₄, BT₂(T₃)₂ and BT₂T₆ monomers in ACN + TBAPF₆ 0.1 M.

	E_{Ipa} vs Fc ⁺ Fc / V	E_{Ipc} vs Fc ⁺ Fc / V	E_{HOMO} / eV ^[a]	E_{LUMO} / eV ^[b]	H-L Gap / eV
BT₂T₄	0.69	-2.29	-5.49	-2.51	2.98
BT₂(T₃)₂	0.71	-2.28	-5.51	-2.52	2.99
BT₂T₆	0.57	-2.22	-5.37	-2.58	2.79

^[a] $-1e \times [(E_{Ipa} / V (Fc^+|Fc) + 4.8V (Fc^+|Fc \text{ vs zero})]$

^[b] $-1e \times [(E_{Ipc} / V (Fc^+|Fc) + 4.8V (Fc^+|Fc \text{ vs zero})]$.

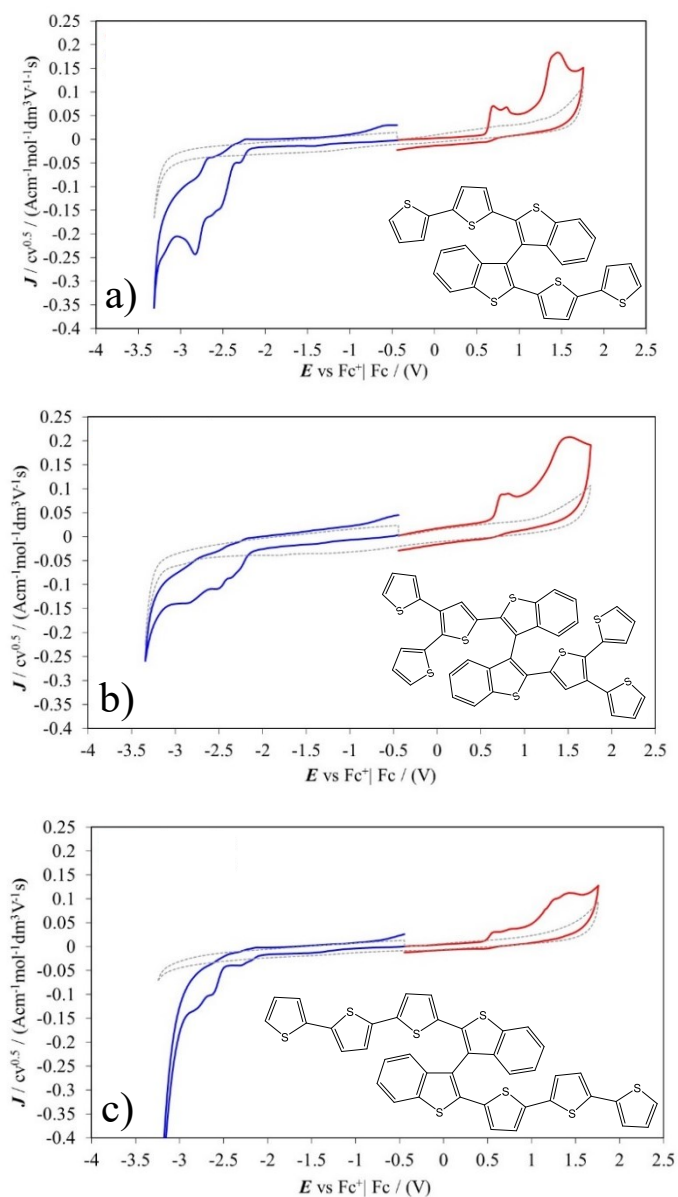


Figure 68. Complete CV patterns of BT_2T_4 (a), $\text{BT}_2(\text{T}_3)_2$ (b) and BT_2T_6 (c) monomers, on GC electrode in ACN + TBAPF₆ 0.1 M at 0.2 V/s potential scan rate. Background patterns are also reported in grey, for sake of comparison.

c) Electrooligomerization ability of BT_2T_4 , $BT_2(T_3)_2$ and BT_2T_6 in ACN on GC working electrode

The electrooligomerization ability of BT_2T_4 , $BT_2(T_3)_2$ and BT_2T_6 monomers was tested and, unlike the case of the DCM solvent (where only BT_2T_6 has shown significant film formation), the oligomerization for all the monomers proceeds fast, with the current intensity regularly increasing with increasing the deposition cycles (Figure 69), and the films grown show good stability in a monomer free solution. However, the BT_2T_4 films formation is faster than in the other two cases. This could be justified with the presence of longer thiophene chains in the $BT_2(T_3)_2$ and BT_2T_6 , which make the formation of the oligomers more difficult, and enhance solubility in ACN of the oligomers produced.

Moreover, in Figure 69 a variation in the onset value ($BT_2T_4 \sim 0.78$ V, $BT_2(T_3)_2 \sim 0.88$ V and $BT_2T_6 \sim 0.64$ V) of the signal can be observed; in the case of the BT_2T_6 the onset shifts to less positive potential, due to the greater conjugation of the molecule, and of the corresponding film (comparable to the conjugation of an octathiophene).

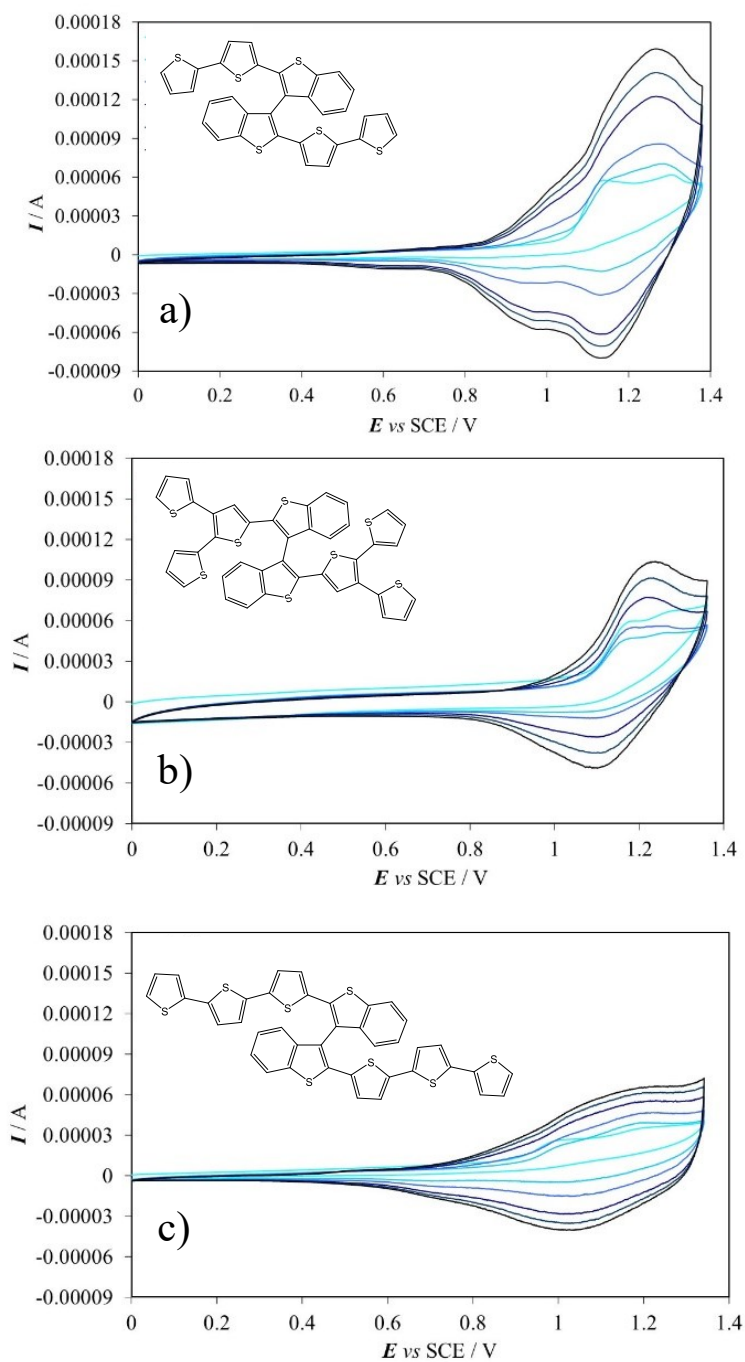
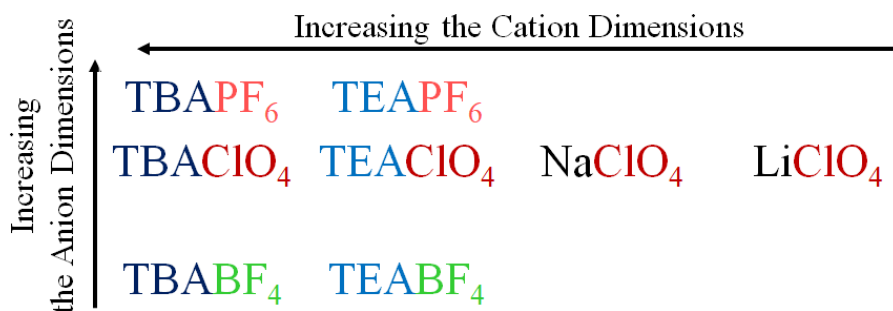


Figure 69. Electrooligomerization of BT₂T₄ (a), BT₂(T₃)₂ (b) and BT₂T₆ (c), obtained performing 36 CV cycles at 0.2 V/s, on GC electrode in ACN + TBAPF₆ 0.1M.

d) Studying the influence of the supporting electrolyte, changing the dimension of both the cation and the anion

In order to analyze in detail the growth of the BT₂T₄ monomer (performed on non-flat ITO as working electrode, in this case), a systematic study was carried out, by varying the size of the cation and/or the anion of the supporting electrolyte, in particular using the 8 electrolytes reported below, in the oligomerization process.



After the electrodeposition, the detached inherently chiral oligomer films were submitted to high resolution LDI, in order to analyze the chemical composition of the films, changing the supporting electrolyte involved in the electrooligomerization process. The results are summarized in the Table 5.

Indeed, it has been observed (Table 5) that the inherently chiral films based on BT₂T₄ are mainly constituted by dimers (closed and open), as prevailing species detected by HR LDI technique, but in smaller amounts (and in some cases hardly detectable) there are also trimers and tetramers, as well as, in traces, pentamers, hexamers, heptamers and octamers.

Having expanded the series of electrolytes tested (reported in Table 5), it was possible to study the influence of the type and size of the cation / anion used on the chemical composition of the film.

As already mentioned, dimers are the main components of films, but the ratio of closed / open dimers varies according to the deposition conditions. In fact, in the presence of small cations, and in particular with LiClO₄, closed dimers prevail over the open ones; moreover, the smaller the cation, the smaller the number of higher weight terms of oligomers obtainable.

Table 5. Comparison of the observed/estimated relative intensities of the main HR LDI peaks for the main components of the films, referred to closed dimers, as a function of the nature of the supporting electrolyte.

	TEAPF ₆	TBAPF ₆	TEABF ₄	TBABF ₄	LiClO ₄	NaClO ₄	TEAClO ₄	TBAClO ₄
Closed Dimers	1	1						
Open Dimers	0.31	0.56	0.30	0.34	0.26	0.29	0.32	0.34
CT/CD	0.07	0.05	0.22	0.03	0.04	0.04	0.02	0.04
OT/OD	0.12	0.16	0.10	0.10	0.13	0.16	0.08	0.11
T/D	0.08	0.09	0.19	0.05	0.06	0.06	0.04	0.05
Closed Trimers	1	1						
Open Trimers	0.56	1.63	0.13	1.03	0.84	2.05	1.27	1.02
CTt/CD	0.02	0.02	0.01	0.02	0.02	0.02	0.01	0.02
OTt/OD	0.08	0.11	0.04	0.09	0.04	0.16	0.02	0.07
Tt/D	0.04	0.06	0.02	0.04	0.02	0.05	0.01	0.04
Closed Tetramers	1	1						
Open Tetramers	1.10	2.53	0.96	1.93	0.61	2.08	0.49	0.97
Pentamers	Yes	Yes	Yes	<i>perc.</i>	<i>perc.</i>	Yes	Yes	Yes
Hexamers	Yes	Yes	<i>perc.</i>	<i>perc.</i>	<i>perc.</i>	Yes	<i>perc.</i>	Yes
Eptamers	<i>perc.</i>	<i>perc.</i>			<i>perc.</i>	Yes		<i>perc.</i>
Octamers	<i>perc.</i>					Yes		<i>perc.</i>

[CD: Closed Dimers, OD: Open Dimers,

CT: Closed Trimers, OT: Open Trimers]

It was therefore possible to identify two significantly different conditions for electrooligomerization:

- supporting electrolyte LiClO₄, promoting the formation of closed oligomers (in particular closed dimers);
- supporting electrolyte TBAPF₆, resulting in balanced mixture of open and closed oligomers.

e) The importance of the working electrode surface: ultra-flat vs no-flat ITO

The morphology of the working electrode plays a crucial role in the electrodeposition process; in fact, too high roughness values could affect the growth of the film and the morphology properties of the corresponding films. For this reason, ultra-flat ITO electrodes were used (Kuramoto Co., LTD), having a roughness value in the order of a few Ångström (RMS < 0.3 nm), instead of "classic" no-flat ITO (Sigma Aldrich, RMS ≈ 1.5 nm).

A comparison of the AFM images for ultra-flat and no-flat ITO is reported in Figure 70.

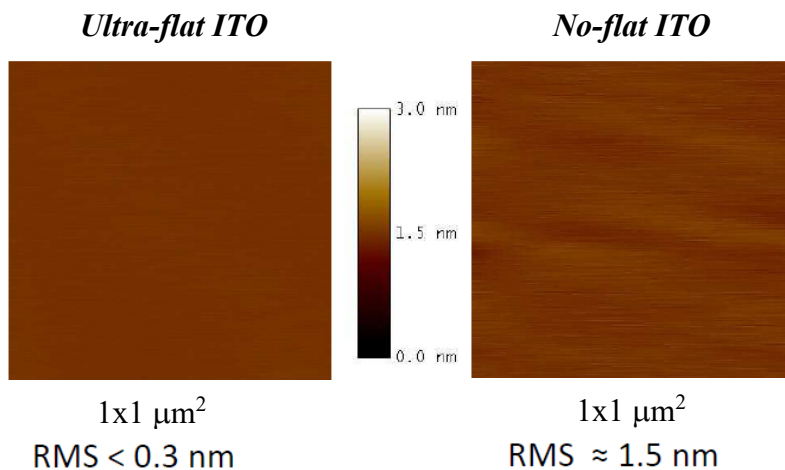


Figure 70. AFM images for ultra-flat and no-flat ITO (left side and right side respectively).

In a preliminary study case, the BT_2T_4 films were obtained performing 1 or 108 CV cycles, on both ultra-flat and no-flat ITO, in order to verify the influence of the substrate on their growth and morphology.

The AFM images are reported in Figure 71 and even after 1 CV cycle there is significant film deposition on the electrode with remarkable formation of nanometric agglomerates (especially in the case of the no-flat ITO support in Figure 71(a), where the whole surface seems to be covered by the film and the oligomers present many globular structures of different dimensions, joined together, which seem to be randomly arranged on the surface, indicating that the nucleation process is irregular, heterogeneous and without a preferential direction). On the other hand, in the case of the ultra-flat ITO support (Figure 71 (b)), some areas of the electrode seem to be bare, but the film tends to grow with preferential directions resulting in branched and well-defined patterns.

A further difference is the roughness of the films (1 CV cycle: $\text{RMS} = 1.5 \pm 0.4$ nm for ultra-flat ITO and $\text{RMS} = 2.6 \pm 0.8$ nm for no-flat ITO; 108 CV cycles: $\text{RMS} = 3.7 \pm 1.2$ nm for ultra-flat ITO and $\text{RMS} = 4.0 \pm 1.2$ nm for no-flat ITO). Therefore, on no-flat ITO, even after 1 deposition cycle, there seems to be a strong interaction between oligomer and substrate, which greatly influences the growth of the film. In fact, rough substrates have specific adsorption sites on which the material tends to adsorb and grow more easily, while on the smoother ones the deposition is more homogeneous. The interaction with the support tends, however, to decrease increasing the deposition cycles; in fact, after 108 cycles, in both cases, the films are composed by globular structures with similar size (only the thickness changes) and with comparable surface roughness values.

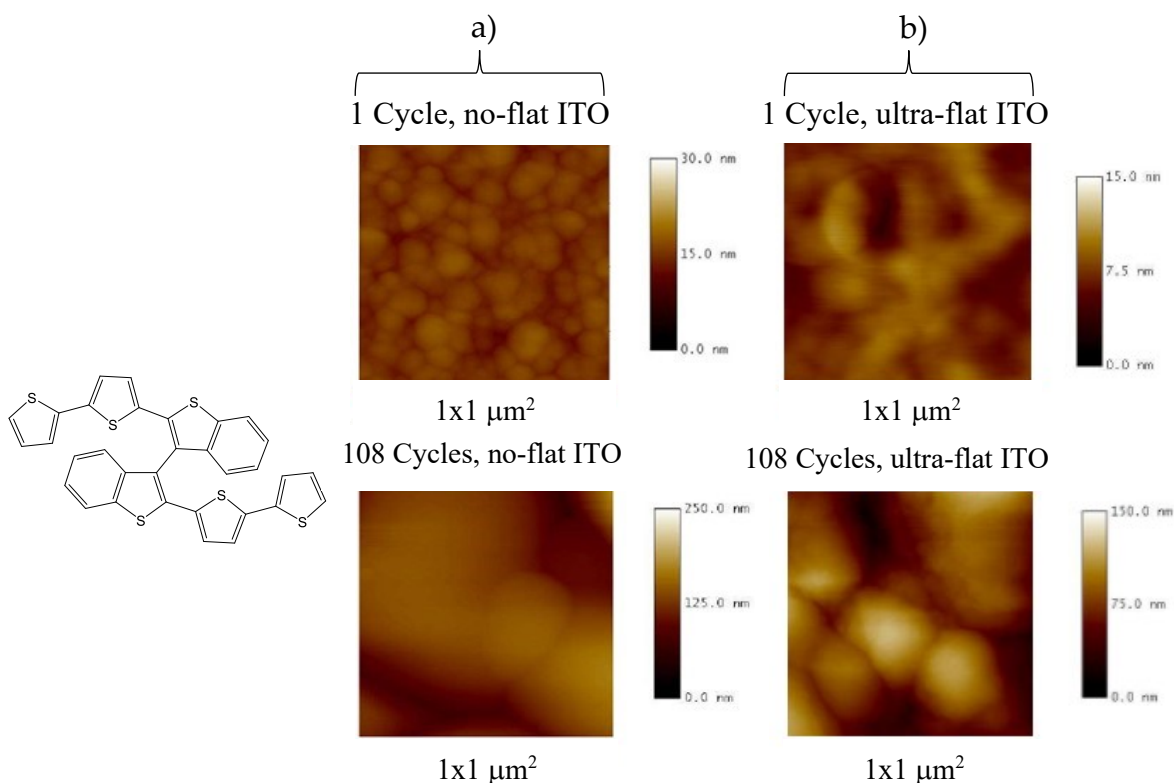


Figure 71. AFM images of the BT₂T₄ films obtained after 1 and 108 CV cycles, in ACN + TBAPF₆ 0.1 M, at 0.05 V / s, on no-flat ITO (a) and ultra-flat ITO (b). Scan area: 1x1 μm².

Therefore, having identified the two above specific operating conditions, modulating the film composition (LiClO₄ and TBAPF₆) and selected a suitable working electrode with low roughness, ultra-flat ITO (in order not to affect the morphology and structure of the film during its growth), it was decided to study in detail the first deposition cycles of the benchmark monomer BT₂T₄. In particular: HR LDI analysis and AFM measurements were carried out on films based on oligo-BT₂T₄, obtained at different CV electrodeposition cycles (1 vs 5 vs 10 vs 108, Figure 72) and in two different supporting electrolytes (LiClO₄ and

TBAPF₆), at fixed concentration monomer and potential scan rate, but comparing the racemic BT₂T₄ with the two enantiomers of the films.

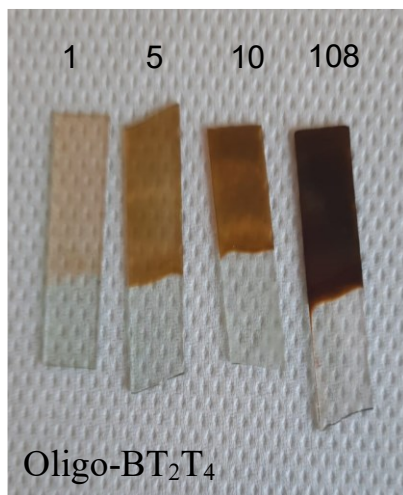


Figure 72. The electrooligomerized inherently chiral BT₂T₄ monomer on ultra-flat ITO electrode at different electrodeposition cycles.

The same study was also carried out on oligo-BT₂T₆ (at different electrodeposition cycles, in ACN + TBAPF₆ as supporting electrolyte), enabling to study also the influence of the length of the thiophene chains on the morphology of the films.

Moreover, the enantioselection ability was then tested as a function of the electrodeposition cycles (1, 5 and 10) and the supporting electrolyte.

f) LDI analysis of the films composition obtained at different electrodeposition cycles on ultra-flat ITO electrode

From HR LDI spectra obtained on the detached films electrooligomerized in ACN + TBAPF₆ (Table 6), it is possible to observe the presence of peaks relative to higher terms (dimers, trimers), even from the first deposition cycles. Instead, in the case of LiClO₄ these oligomers only appeared after 108 cycles. However, in all cases, the dimers are the prevailing species, as well as trimers, but in smaller amount. The data obtained were collected in Table 6 and in **TBAPF₆**:

- the racemic oligo-BT₂T₄, after 108 cycles, show a clear prevalence of closed dimers compared to open ones, while for the enantiomers there is a greater balance of the two components. This is probably due to the higher number of freedom degrees in the racemate;
- the ratio of closed dimers increases increasing the number of deposition cycles;
- closed trimers appear more abundant than open trimers regardless the number of electrodeposition cycles; however, due to their lesser abundance, it was not possible to identify a trend.

Instead, HR LDI data relating to films electrodeposited in LiClO₄ show that:

- in the racemate, closed dimers clearly prevail over the open ones;
- in the enantiomers there is a greater balance between open and closed dimers (only in the (*S*) enantiomer case there was a prevalence of the open observed).

Finally, both in TBAPF₆ and in LiClO₄ it was possible to observe the presence of the tetramers only in one case ((*S*)-oligo-BT₂T₄ in LiClO₄, after 108 cycles); this is probably due to a low volatility of the fragments analysed in the HR LDI measurements or to an inefficiency and difficult formation of these films on ultra-flat ITO supports.

A similar systematic analysis on the chemical composition of the films based on BT₂(T₃)₂ and BT₂T₆ was also carried out, using TBAPF₆ as a supporting electrolyte, in order to study the influence of the thiophene chains (different for the number and/or connectivity of the thiophene rings) on the oligomers obtained. However, due to the lower ability of these monomers to electrooligomerize it was possible to carry out the HR LDI measurements only after 10 and 108 deposition cycles, and in most cases, it was not possible to identify any peak related to higher terms in the LDI spectra (both after 10 and 108 deposition cycles), but only signals of monomer fragments.

Table 6. Comparison of the observed/estimated relative intensities of the main HR LDI peaks for the main components of the racemic and enantiopure films, as a function of the nature of the two supporting electrolytes and the number of electrodeposition cycles.

	TBAPF ₆					LiClO ₄				
	Cycle Nr	CD/OD	CT/OT	CT/CD	OT/OD	n° cycles	CD/OD	CT/OT	CT/CD	OT/OD
rac BT₂T₄	1	n.d.	n.d.	n.d.	n.d.	1	n.d.	n.d.	n.d.	n.d.
	5	1.6	n.d.	0.046	n.d.	5	n.d.	n.d.	n.d.	n.d.
	10	1.9	150	0.045	0.001	10	n.d.	n.d.	n.d.	n.d.
	108	4.2	44	0.040	0.004	108	14.7	n.d.	n.d.	n.d.
en1 BT₂T₄	1	0.4	n.d.	0.093	n.d.	1	n.d.	n.d.	n.d.	n.d.
	5	0.8	3.9	0.102	0.022	5	n.d.	n.d.	n.d.	n.d.
	10	0.9	1.2	0.109	0.079	10	n.d.	n.d.	n.d.	n.d.
	108	1.4	n.d.	0.089	0.028	108	0.4	0.2	0.062	0.013
en2 BT₂T₄	1	0.5	2.8	0.090	0.017	1	n.d.	n.d.	n.d.	n.d.
	5	1	n.d.	0.139	n.d.	5	n.d.	n.d.	n.d.	n.d.
	10	1.4	2.2	0.075	0.049	10	n.d.	n.d.	n.d.	n.d.
	108	0.9	3	0.039	n.d.	108	1.1	5.2	0.060	0.156

[CD: Closed Dimers, OD: Open Dimers,

CT: Closed Trimers, OT: Open Trimers]

The only suitable sample was the racemic BT₂(T₃)₂, obtained after 108 cycles and despite the steric hindrance of the molecule, it is mainly composed of closed dimers, in a 8.7 ratio with respect to the open ones. However, trimers are apparently absent.

g) AFM measurements: a comparison of the film morphology obtained at different cycle numbers on ultra-flat ITO electrode

BT₂T₄ in ACN + TBAPF₆

Racemic and enantiopure films of BT₂T₄ (in ACN + TBAPF₆) were analyzed by AFM at different electrodeposition cycles, using ultra-flat ITO as working electrode (Figure 73). The AFM images of the racemic BT₂T₄ show a very similar morphology (with a pattern of branched structures) for both the films obtained after 1 and 5 CV cycles, but in this latter case the thickness is obviously higher. This suggests that the film grows in a homogeneous and regular way.

However, after 10 CV cycles, the morphology of the film strongly changes (growing mainly, in some areas, along the Z axis than along the plane) and seems to be constituted by many small islands of high thickness, but between them there are considerable differences in height, which can even reach 100 nm. This type of growth is also observed on the sample deposited after 108 cycles, where the film is composed of very large islands, partially overlapped and partially separated by deep differences in height. The AFM images obtained on both (*R*) and (*S*) enantiopure BT₂T₄ samples (even after only 1 CV cycle) show a different morphology respect to the racemic films. In fact, instead of small, branched nanostructures, the film seems to be constituted by a single well-defined nanostructure. These differences with the racemic BT₂T₄ are also found after 5, 10 and 108 deposition cycles, where many macrostructures superimposed on each other are observed, with uniform thickness, although after 108 cycles, differences in level height seem to be present between the macrostructures. The high values on the vertical scales indicate that more material has been deposited.

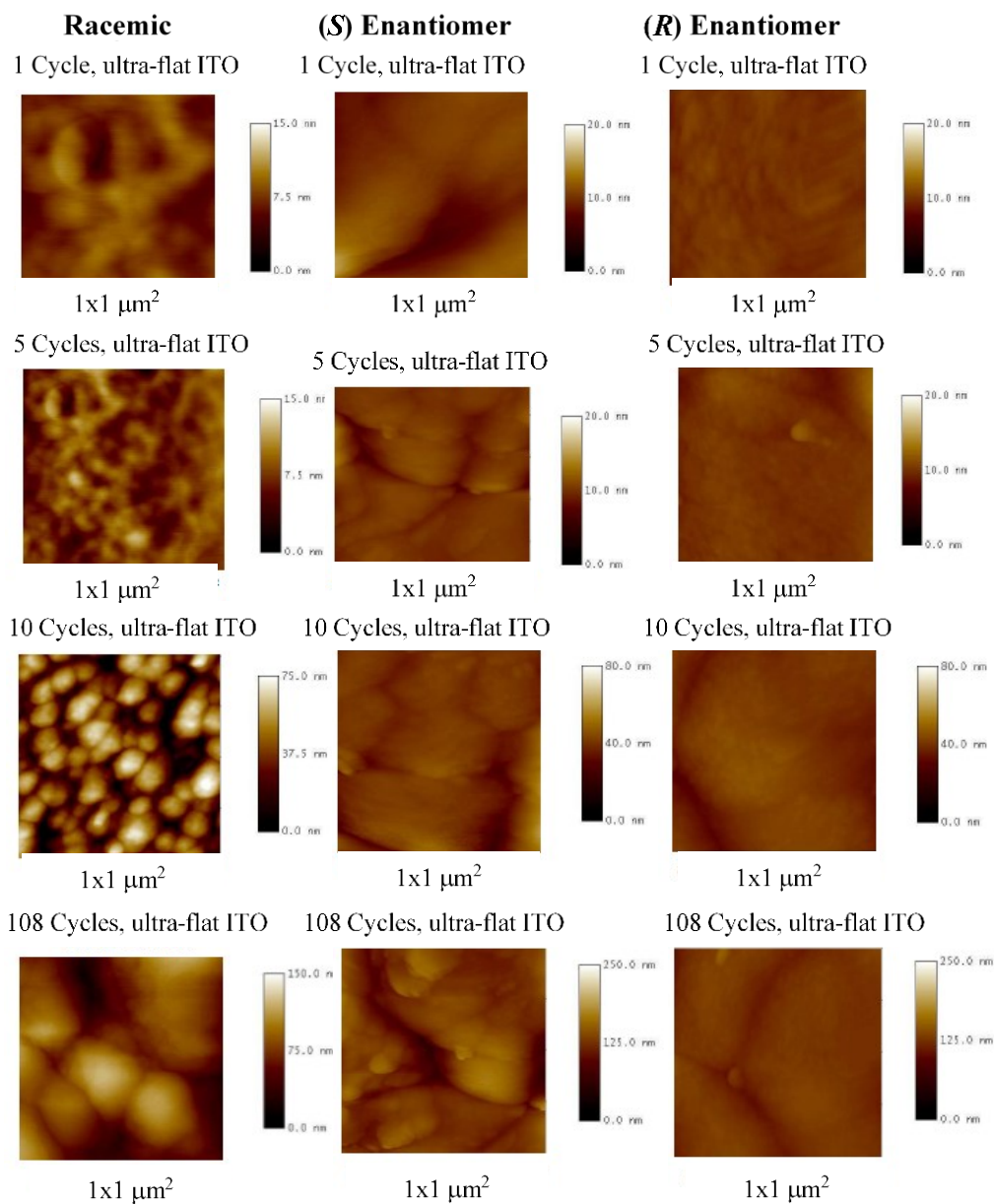


Figure 73. AFM topography images of the racemic oligo-BT₂T₄, oligo-(S)-(+)- and (R)-(-)-BT₂T₄ obtained at different CV cycles (1,5,10,108, grown in ACN + TBAPF₆ 0.1 M). For all images: $1 \times 1 \mu\text{m}^2$.

A comparison between the roughness values of the three types of BT₂T₄ (both as racemate and enantiopure films) is reported in Table 7:

- the roughness of the enantiopure BT₂T₄ is always double (at 108 cycles triple) respect to the racemic;
- the greatest variation in the roughness values (from 5 to 10 deposition cycles) confirms what is observed by the images and indicates how the main changes in the film occur during the very early stages of growth.

Table 7. Comparison between the roughness values of racemic and enantiopure oligo-BT₂T₄, electrooligomerized in ACN + TBAPF₆ 0.1 M, at 0.05 V/s, on ultra-flat ITO, as a function of the CV deposition cycles.

	Rac BT ₂ T ₄	(<i>S</i>)-BT ₂ T ₄	(<i>R</i>)-BT ₂ T ₄
1 cycle	RMS = 1.5 ± 0.4 nm	RMS = 3.9 ± 1.3 nm	RMS = 2.9 ± 1.0 nm
5 cycles	RMS = 1.8 ± 0.5 nm	RMS = 4.9 ± 1.4 nm	RMS = 3.5 ± 1.2 nm
10 cycles	RMS = 3.1 ± 1.1 nm	RMS = 7.4 ± 1.7 nm	RMS = 5.7 ± 1.5 nm
108 cycles	RMS = 3.7 ± 1.2 nm	RMS = 12.1 ± 1.9 nm	RMS = 10.6 ± 2.3 nm

In order to observe the nanostructures more in detail, the AFM images were collected on the same samples, but on smaller scan areas (500x500 and 250x250 nm²) (Figure 74).

The images confirm that, contrary to what happens in the enantiopure film case, there are some grooves in the racemic samples (no material has been deposited). Moreover, both the film types are composed of spherical substructures of nanometric dimensions; in the racemic case the nanostructures appear irregular (probably due to the greater freedom degrees), both in shape and in size. In the enantiomer cases, instead, the structures are much more similar to each other and tend to maintain the same shape even during growth.

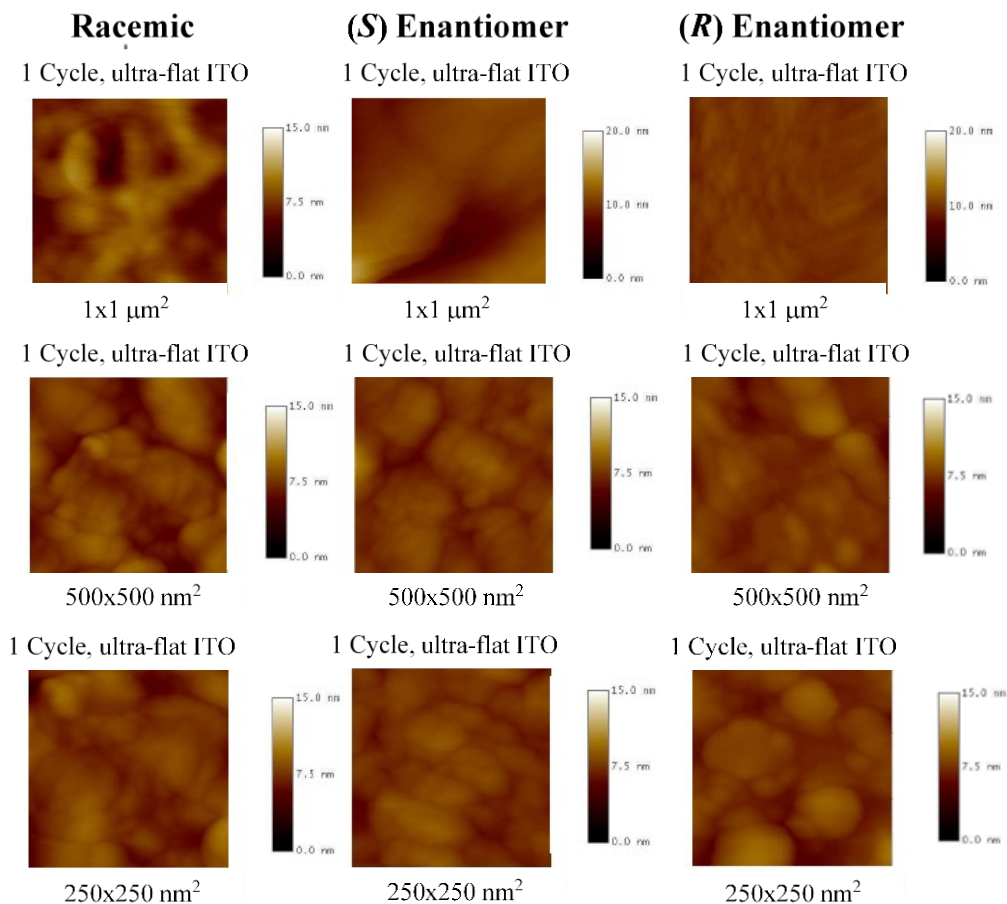


Figure 74. AFM topography images of the inherently chiral oligomer films (racemic and enantiopure, grown in ACN + TBAPF₆ 0.1 M) obtained performing 1 CV cycle with different scan areas: $1 \times 1 \mu\text{m}^2$, $500 \times 500 \text{ nm}^2$ and $250 \times 250 \text{ nm}^2$.

BT₂T₄ in ACN + LiClO₄

The BT₂T₄ films electrodeposited in ACN + LiClO₄ at 4 different deposition cycles (1-5-10-108) were then analyzed by AFM, again on ultra-flat ITO as working electrode.

In this way, it was possible to study the influence of the supporting electrolyte on the morphology of the film. However, AFM characterizations could only be performed on samples obtained after 1 and 108 deposition cycles (Figure 75).

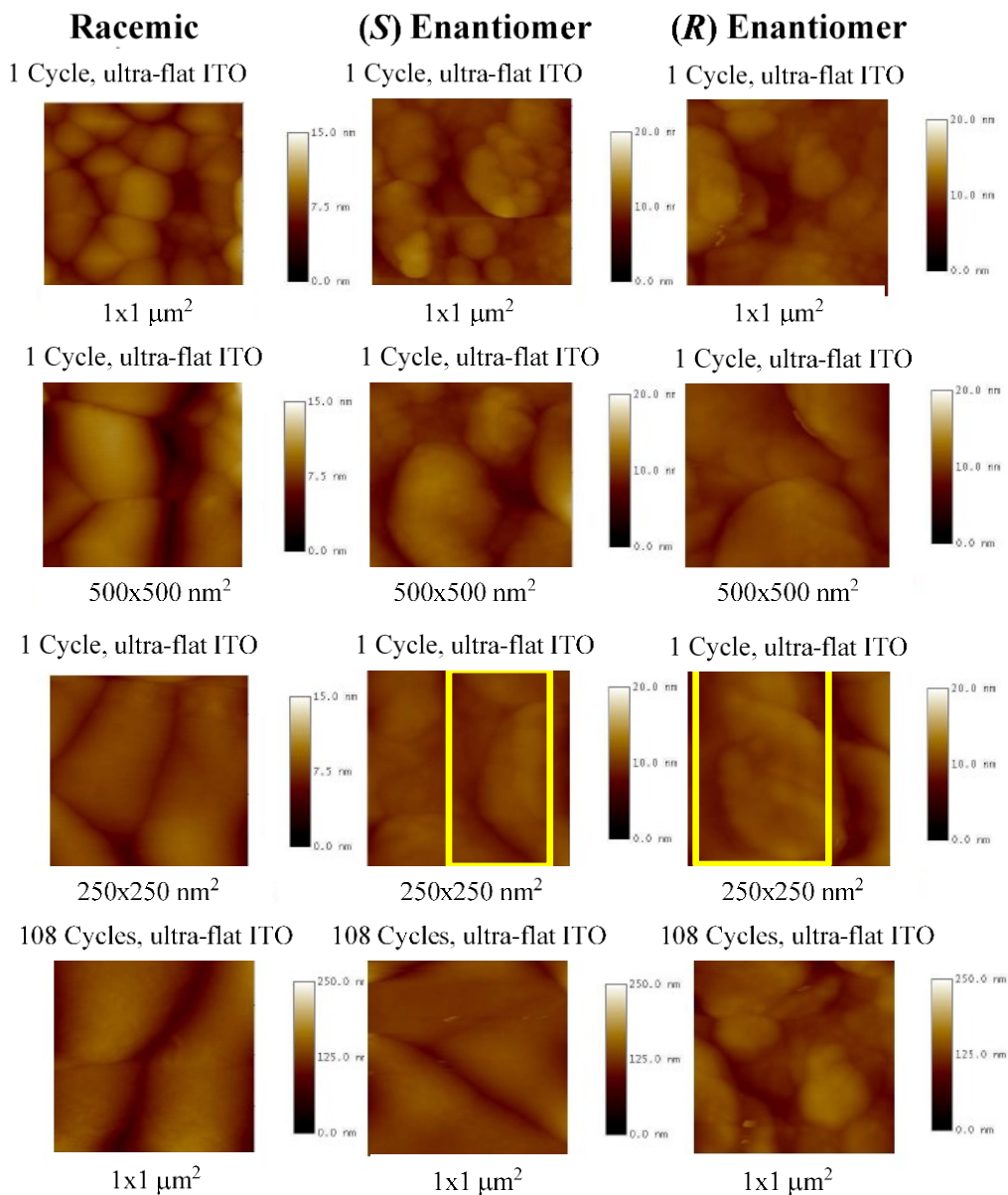


Figure 75. AFM topography images of the inherently chiral oligomer films (racemic and enantiopure grown in ACN + LiClO₄ 0.1 M) obtained performing 1 CV cycle with different scan areas: $1 \times 1 \mu\text{m}^2$ (for 1 and 108 CV cycles), $500 \times 500 \text{ nm}^2$ and $250 \times 250 \text{ nm}^2$ (for 1 CV cycle).

Comparing the AFM images, reported in Figure 75, with the previous cases, the film obtained after 1 CV cycle shows a different morphology; in fact, it is not composed of branched or spherical structures, but of large rectangular structures, similar to slabs, superimposed on each other. They are present both in the racemic and enantiopure films. This type of morphology is also observed for the samples obtained after 108 CV cycles. The film roughness values (Table 8) show no evident differences between 1 and 108 deposition cycles; actually, the film grows very wrinkled even from the very first deposition cycle and also in a uniform, orderly and compact way.

This suggests that the type of supporting electrolyte, used in the electrooligomerization process, can affect the morphology of the film. Also in this case, AFM images were collected on smaller scan areas, 500x500 and 250x250 nm², for the sample obtained after 1 deposition cycle. From the images of the enantiomers, and in particular from those on areas of 250x250 nm², it seems to be composed by large helical nanostructures (about 100x250 nm²) and with opposite direction of rotation, which would suggest that the configuration of the enantiomers might orient the two helices in opposite directions.

Table 8. Comparison between the roughness values of racemic and enantiopure oligo-BT₂T₄, electrooligomerized in ACN + LiClO₄ 0.1 M, at 0.05 V/s, on ultra-flat ITO, as a function of the CV deposition cycles.

	Rac BT ₂ T ₄	(<i>S</i>)-BT ₂ T ₄	(<i>R</i>)-BT ₂ T ₄
1 cycle	RMS = 7.2 ± 1.4 nm	RMS = 8.4 ± 1.5 nm	RMS = 8.8 ± 1.6 nm
108 cycles	RMS = 11.7 ± 2.1 nm	RMS = 12.2 ± 1.9 nm	RMS = 12.5 ± 2.3 nm

BT₂T₆ in ACN + TBAPF₆

In order to study how the different length of the thiophene wings affects the morphology of the film, enantiopure samples of BT₂T₆ were analyzed by AFM; the films were electrooligomerized in TBAPF₆ on ultra-flat ITO, performing 4 different CV cycles (1,5,10 and 108). The AFM images are collected in Figure 76, comparing the results on (*R*)- and (*S*)-BT₂T₆ with (*S*)-BT₂T₄.

It is evident that both the morphology and the growth of the BT₂T₆ films are very different from BT₂T₄. In fact, the films are composed by many small nanostructures and, moreover, there are several dark areas, which indicate the presence of grooves in the film. Only after 10 and 108 cycles larger and well-defined structures are observed. The surface roughness values (Table 9) show that at 1 and 5 CV cycles the roughness is very low. In fact the films, from the AFM images, seem to be quite uniform, while after 10 and 108 cycles the roughness increases with comparable values to those measured for the BT₂T₄ samples. These differences are probably due to the less effective oligomerization of the BT₂T₆ monomer; in fact, as seen from the voltammetric curves, BT₂T₆ oligomers tend to grow very slowly with a very low nucleation rate and aggregation rate of the macrostructures.

Table 9. Comparison of the roughness values between the antipodes of the BT₂T₆ films and (*S*)-BT₂T₄, electrooligomerized in ACN + TBAPF₆ 0.1 M, at 0.05 V/s, on ultra-flat ITO, as a function of the CV deposition cycles.

	(<i>S</i>)-BT ₂ T ₆	(<i>R</i>)-BT ₂ T ₆	(<i>S</i>)-BT ₂ T ₄
1 cycle	RMS = 2.1 ± 0.4 nm	RMS = 1.7 ± 0.5 nm	RMS = 3.9 ± 1.3 nm
5 cycles	RMS = 3.5 ± 1.0 nm	RMS = 2.8 ± 0.9 nm	RMS = 4.9 ± 1.4 nm
10 cycles	RMS = 7.7 ± 1.8 nm	RMS = 6.2 ± 1.6 nm	RMS = 7.4 ± 1.7 nm
108 cycles	RMS = 13.4 ± 2.4 nm	RMS = 12.1 ± 2.2 nm	RMS = 12.1 ± 1.9 nm

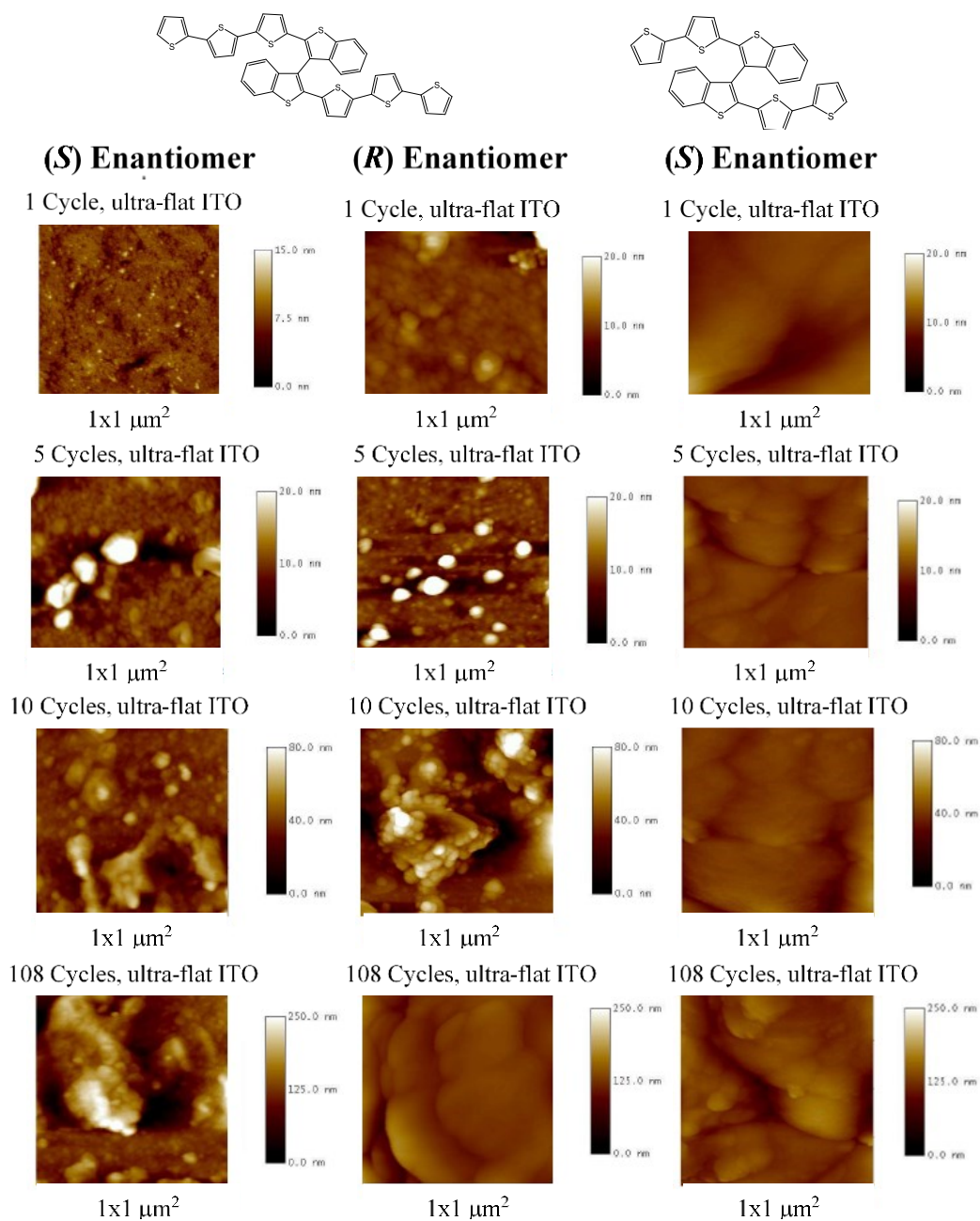


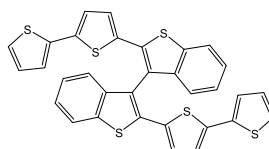
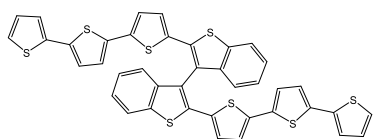
Figure 76. AFM images of the *(R)* and *(S)*-oligo-BT₂T₆ obtained performing 1, 5, 10 or 108 CV cycles in ACN + TBAPF₆ 0.1 M. Comparison with oligo-*(S)*-BT₂T₄ is also reported. Scan areas: 1x1 μm².

Also in this case, AFM images were also recorded on smaller scan areas (500x500 and 250x250 nm²) (Figure 77), giving more information about the small structures observed previously.

In fact, the AFM images, especially those relating to the (*S*)-enantiomer, show ring / half ring nanostructures with a diameter of the dimension of about 10-15 nm, which tend to bind to each other, and cover the surface of the support. This confirms how the film struggles to nucleate and therefore forms these very small structures, at the expense of the macroscopic ones seen previously.

Furthermore, the enantiomer (*S*) and the enantiomer (*R*) present very different morphologies. In fact, it seems that (*R*)-BT₂T₆ grows faster yet still resulting in very small nanostructures.

We are planning in the future to perform all the AFM analysis on the same samples, but with a higher resolution, in order to appreciate a greater difference in the morphology of the inherently chiral oligomer films.



(S) Enantiomer

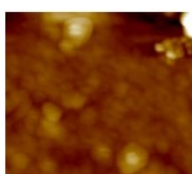
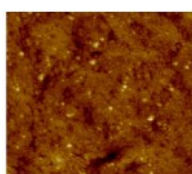
(R) Enantiomer

(S) Enantiomer

1 Cycle, ultra-flat ITO

1 Cycle, ultra-flat ITO

1 Cycle, ultra-flat ITO



1x1 μm²

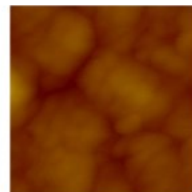
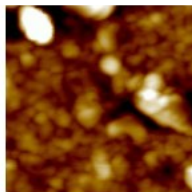
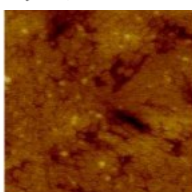
1x1 μm²

1x1 μm²

1 Cycle, ultra-flat ITO

1 Cycle, ultra-flat ITO

1 Cycle, ultra-flat ITO



500x500 nm²

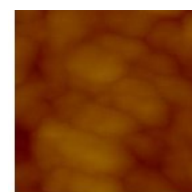
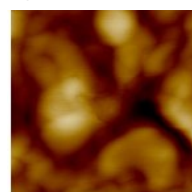
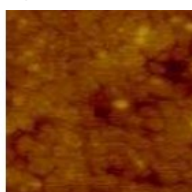
500x500 nm²

500x500 nm²

1 Cycle, ultra-flat ITO

1 Cycle, ultra-flat ITO

1 Cycle, ultra-flat ITO



250x250 nm²

250x250 nm²

250x250 nm²

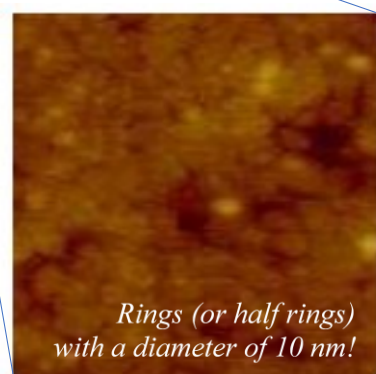


Figure 77. AFM topography images of (S)- and (R)-oligo-BT₂T₆ (grown in ACN + TBAPF₆ 0.1 M) obtained performing 1 CV cycle with different scan areas: 1x1 μm², 500x500 nm² and 250x250 nm². Comparison with oligo-(S)-BT₂T₄ is also reported.

h) Enantioselection tests on electrodes modified with oligo-BT₂T₄ as a function of both the number of deposition cycles and the supporting electrolyte

The enantiodiscrimination experiments were performed as a function of both the supporting electrolyte and the electrodeposition cycles, in order to study the enantioselection ability of inherently chiral oligo-BT₂T₄ (comparing the results with those obtained on electrode modified with oligo-BT₂T₆, to verify the effect of the length of the thiophene wings) as very thin layer.

In particular, the enantioselection tests were carried out with the enantiomers of the ferrocenyl probe (dissolved in solution with the same supporting electrolyte used in the electrooligomerization process) on ultra-flat ITO electrodes modified with (*S*) - or (*R*) -oligo- BT₂T₄, varying the number of electrodeposition cycles (1, 5 and 10).

Reproducibility tests were also performed by freshly depositing a new inherently chiral film, with the same working protocol.

TBAPF₆

The enantioselection ability of enantiopure (*S*) - and (*R*) -oligo-BT₂T₄ were tested as a function of the deposition cycles and the most significant results are collected in Figure 78.

The two enantiomers of the chiral ferrocenyl probe were preliminarily tested on bare electrode (Figure 78 grey lines) and as expected, the two CV signals for both the configurations (Fc R and Fc S) are practically overlapped at the same potential (~ 0.49 V vs SCE) and with canonical reversible shape, typical of the oxidation of the ferrocenyl core.

Subsequently, for sake of comparison, Fc R and Fc S were tested on electrodes modified with racemic oligo-BT₂T₄ (performing different CV cycles, 1 vs 5 vs 10), as shown in Figure 79 (dashed blue line Fc R, dashed red line Fc S). Also in this case, the CV signal for the enantiomers of the chiral probe is overlapped at

the same potential (respectively ~ 0.51 V *vs* SCE for 1 cycle, ~ 0.78 V *vs* SCE for 5 cycles and ~ 0.8 V *vs* SCE for 10 cycles), with the same shape and current intensity.

These two situations are consistent with the fact that diastereoisomeric conditions have not yet been generated (the only ones to be energetically different).

However, it is already possible to observe some peculiarities, which demonstrate how important is the film thickness, in fact:

- by carrying out a single deposition cycle, Fc R and Fc S fall at the same potential value of the two enantiomers tested on the bare electrode (also maintaining their reversibility character);
- on the other hand, with films obtained after 5 and 10 deposition cycles, the signals of Fc R and Fc S are at more positive potentials than those obtained on bare electrode (more difficult process to take place).

Finally, enantiopure films of (*S*) - and (*R*) - oligo-BT₂T₄ were prepared, testing the enantiomers of the chiral probe; in all cases an excellent separation was observed, in terms of peak potential difference (Figure 78 and 79), but with a strong dependence on the number of deposition cycles;

- the separation decreases increasing the film thickness (~ 600 mV *vs* SCE for 1 cycle *vs* ~ 270 mV *vs* SCE for 5 cycles *vs* ~ 190 mV *vs* SCE for 10 cycles);
- at 1 deposition cycle the greatest separation is obtained (~ 600 mV) (Figure 78 and 80); moreover, it is possible to observe that the voltammetric signal of the enantiomer, which falls at more positive potentials shows a non-canonical shape, probably due to a strong specific interaction with the film;
- in the case of 1 and 5 deposition cycles, the enantiomer signal of the chiral probe at lower potentials has the same potential value and a similar shape to the signals of the enantiomers tested on an electrode modified with racemic BT₂T₄ film. Instead, at 10 cycles, this signal tends to move towards more positive potentials

(probably the thickness of the film at 10 cycles affects the interaction with the probe).

- At 5 and 10 cycles, it is also possible to observe how the ferrocene enantiomer signal at more positive potentials is close to the onset of the film (which is reflected in the non-canonical form of the signal).

Reproducibility tests were carried out, each time depositing a new film on a new electrode support, using the same working protocol. Furthermore, it is very important to underline that by inverting the configuration of the deposited oligomer film, perfectly specular results are obtained (Figure 80).

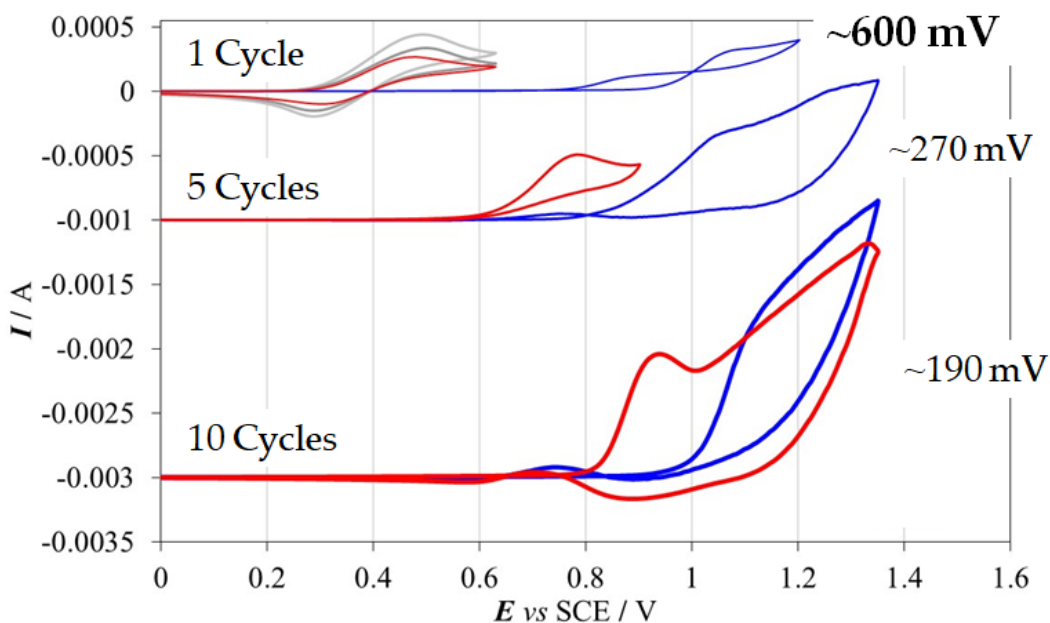


Figure 78. Synopsis of the enantioselection tests towards FcR (in blue) and FcS (in red) on oligo-(*S*)-BT₂T₄ at different CV cycles (1, 5 and 10).

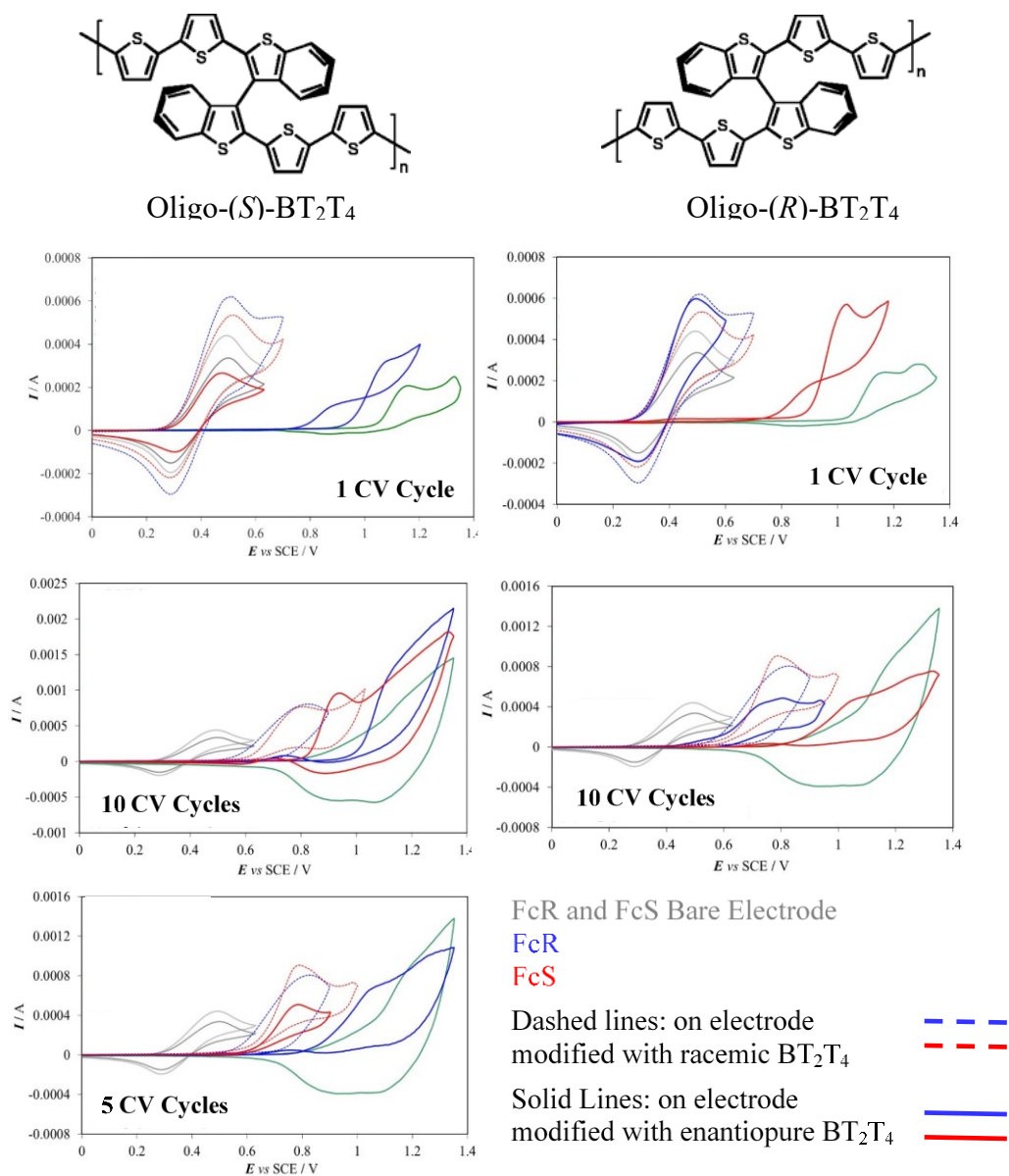


Figure 79. Enantioselection tests towards the enantiomers of chiral ferrocene, FcR (in blue) and FcS (in red) on electrodes modified with racemic BT₂T₄ (dashed lines) or enantiopure BT₂T₄ (solid lines), electrooligomerized on ultra-flat ITO as working electrode, in ACN+TBAPF₆ 0.1 M (0.05 V s⁻¹ potential scan rate). In green is also reported the CV signal of the BT₂T₄ films at different CV cycles and in grey the CV signal of FcR and FcS on bare electrode.

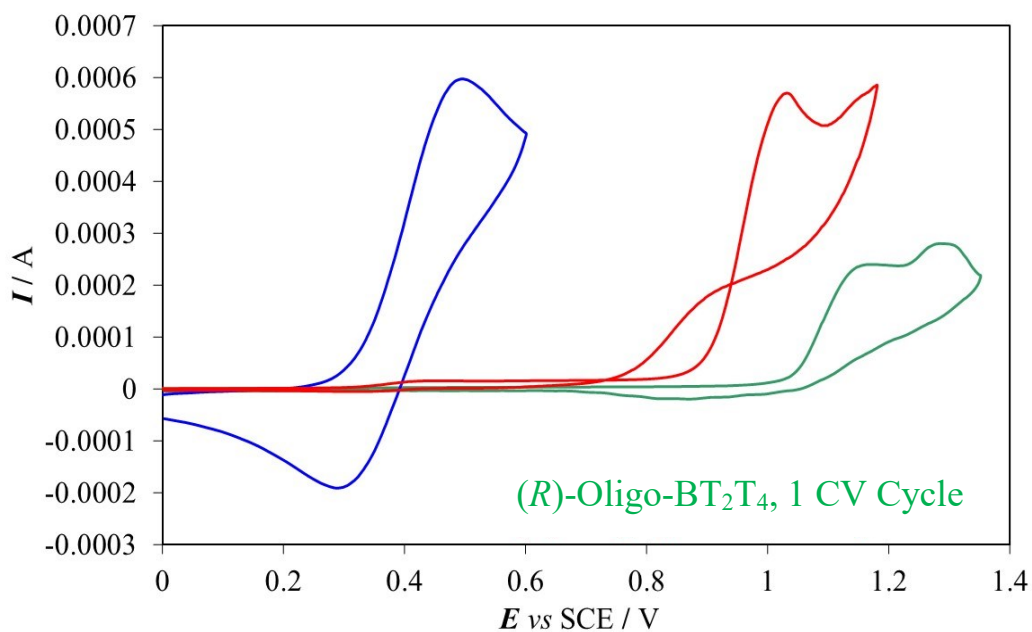
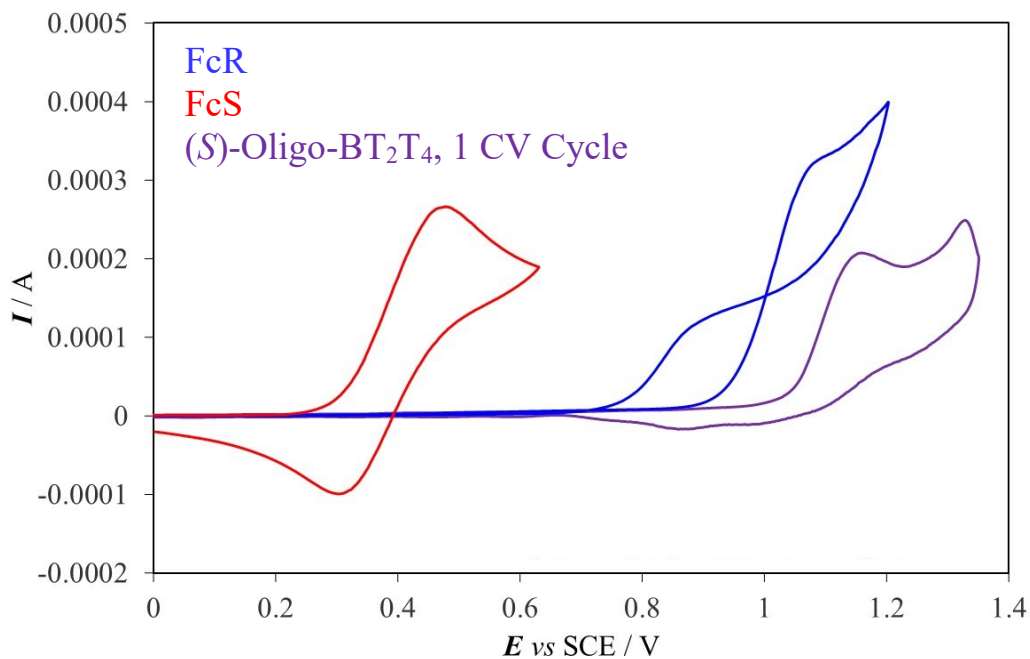


Figure 80. Enantioselection tests on (S)-oligo-BT₂T₄ (top, in purple) and (R)-oligo-BT₂T₄ (bottom, in green), electrooligomerized performing 1 CV cycle in ACN+TBAPF₆ 0.1 M.

LiClO₄

The enantioselection ability of (*S*) - and (*R*) -oligo-BT₂T₄ were tested, at different deposition cycles (1, 5 and 10, *i.e.* the same used in the measurements carried out in TBAPF₆) in LiClO₄, in order to observe the influence of the supporting electrolyte (the most significant results are shown in Figure 81).

Also in this case, the two enantiomers of the chiral ferrocene were preliminarily tested on bare electrode (Figure 81 and 82 grey lines) and the CV signals for both the configurations (Fc R and Fc S) have the same potential value (~ 0.49 V *vs* SCE), the same current intensity and the same canonical and reversible shape.

Subsequently, Fc R and Fc S were tested on electrodes modified with racemic oligomer (at different deposition cycles, 1 *vs* 5 *vs* 10), as shown in Figure 81 (dashed blue line Fc R, dashed red line Fc S). Also in this case, the signal obtained, for the two enantiomers of the electroactive chiral probe, have the same potential value (respectively ~ 0.68 V *vs* SCE for 1 cycle, ~ 0.80 V *vs* SCE for 5 cycles and ~ 0.85 V *vs* SCE for 10 cycles), shape and current intensity.

However, in this case, it is possible to observe some differences with respect to TBAPF₆:

- after 1 CV cycle of racemic BT₂T₄, the voltammetric signals of Fc R and Fc S are not at the same potential value of the two enantiomers tested on bare electrode (as in the TBAPF₆ case) and they become irreversible;
- after 5 CV cycles of racemic BT₂T₄, the CV signals of Fc R and Fc S are at more positive potentials than those obtained on the film after 1 CV cycle;
- finally, after 10 CV cycles of racemic BT₂T₄, the Fc R and Fc S signals move further to more positive potentials.

Therefore, there seems to be an influence of the racemic film on the probe, even after 1 deposition cycle (unlike what happened by depositing only one cycle of the racemic BT₂T₄ in TBAPF₆); moreover, the effect of the film thickness is in this case much more pronounced.

Finally, (*S*) - and (*R*) - oligo-BT₂T₄ enantiopure films were prepared, testing the enantiomers of the chiral probe; in all cases, a separation was observed, in terms of peak potential differences (Figure 81), with a strong dependence on the number of deposition cycles.

However, it is important to underline some fundamental differences in the behaviour of the two supporting electrolytes employed: the peak potential separations were found to be much lower, in the case of LiClO₄. Furthermore, considering the same configuration of the enantiopure oligomer film (for example, (*S*)-oligo-BT₂T₄), the enantiomer peak sequence for the chiral probe is the opposite (for TBAPF₆ FcS before FcR, while for LiClO₄ FcR before FcS).

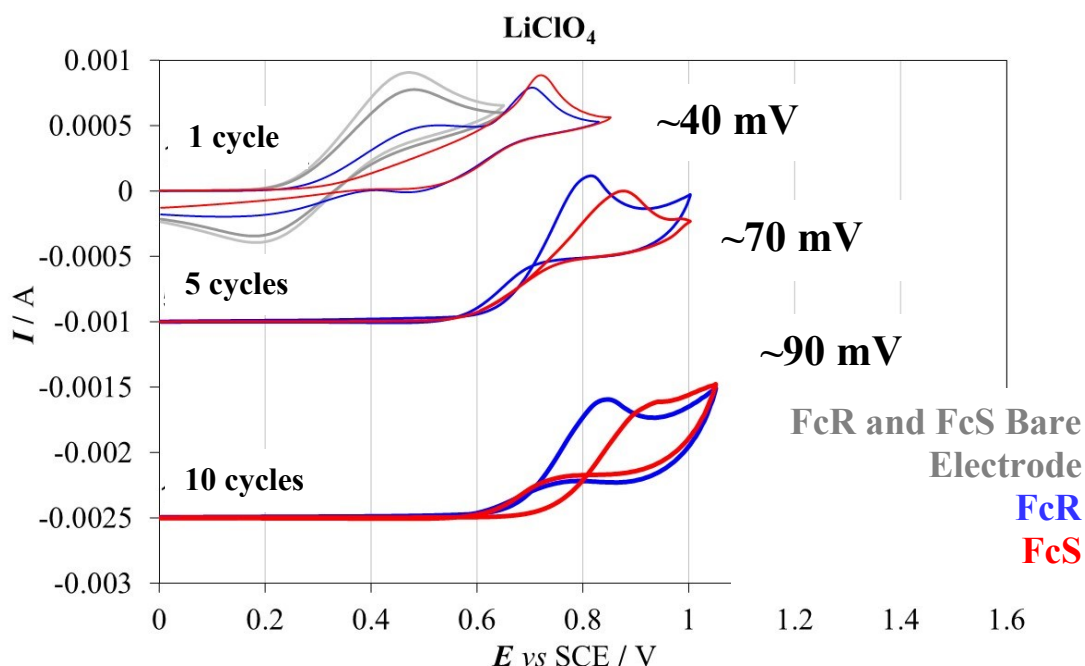
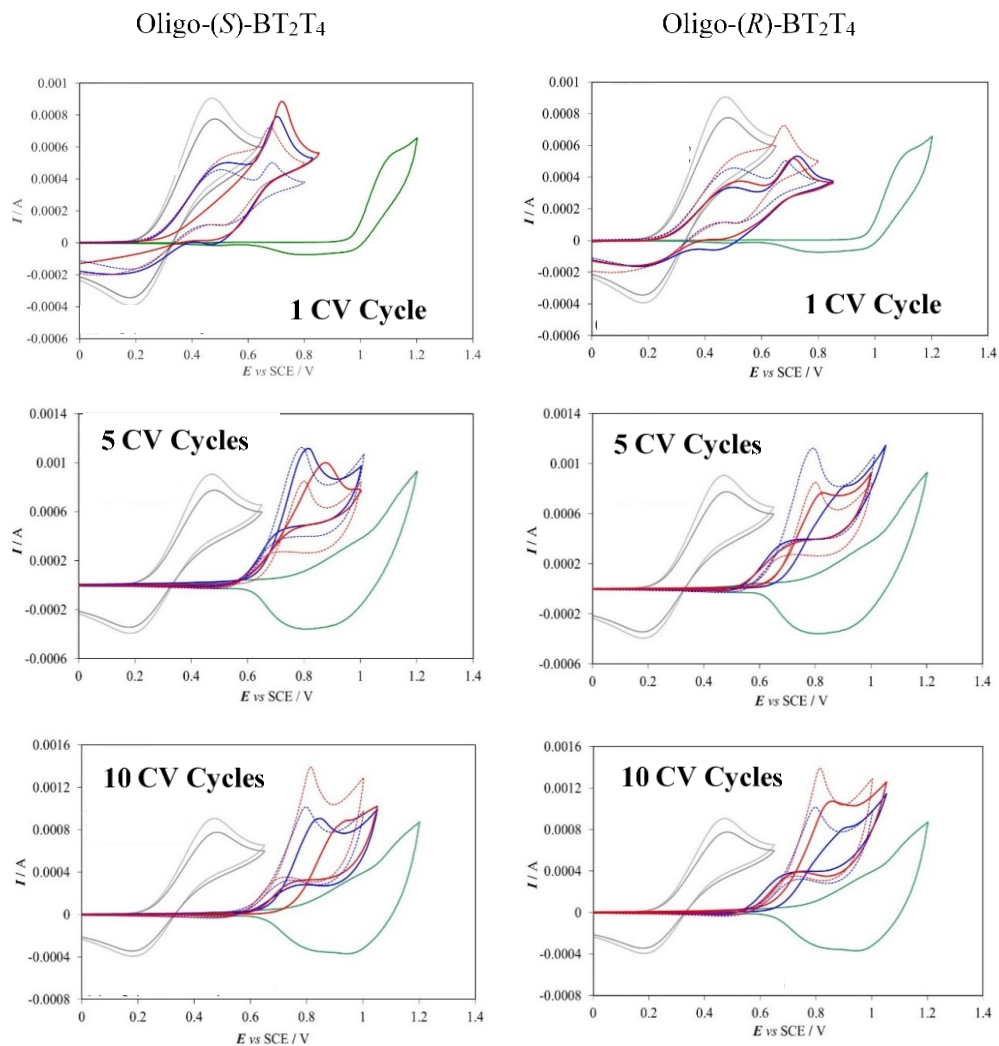


Figure 81. Synopsis of the enantioselection tests towards FcR (in blue) and FcS (in red) on oligo-(*S*)-BT₂T₄ grown with LiClO₄ as supporting electrolyte, at different CV cycles (1, 5 and 10).

In particular:

- the peak potential separation increases increasing the film thickness (~ 40 mV vs SCE for 1 cycle vs ~ 70 mV vs SCE for 5 cycles vs ~ 90 mV vs SCE for 10 cycles), as reported in the synopsis in Figure 81 and 82; this behaviour is exactly the opposite of the TBAPF₆ case;
- the lower separation (~ 40 mV) is obtained with 1 CV cycle; moreover, it is possible to observe that the signals of both the enantiomers of the chiral probe fall at potentials very similar to those obtained for Fc R and Fc S on an electrode modified with racemic BT₂T₄;
- After 5 CV cycles, the enantiomer signal of the chiral probe that falls at lower potentials, has the same potential value and a similar shape to the signals of the enantiomers tested on an electrode modified with racemic BT₂T₄; the signal of the second enantiomer, on the other hand, is shifted to more positive potentials and falls close to the onset of the film;
- after 10 CV cycles, both the signals of the enantiomers of the chiral probe are shifted to more positive potentials than those of the enantiomers tested on an electrode modified with racemic BT₂T₄.

This behaviour suggests that both enantiomers of the chiral probe interact with the film in a similar way. As observed from the AFM images discussed above, the films of BT₂T₄ obtained in LiClO₄ are thicker and rougher than those obtained in TBAPF₆. The different morphology of the film could change the interaction mechanism between the probe and the selectors. Reproducibility tests were also carried out in this case, each time depositing a freshly (*S*) - or (*R*) -oligo-BT₂T₄ on a new electrode support, using the same operating protocol.



FcR and FcS Bare Electrode

FcR

FcS

Dashed lines: on electrode
modified with racemic BT₂T₄

Solid Lines: on electrode
modified with enantiopure BT₂T₄

—

Figure 82. Enantioselection tests with the enantiomers of chiral ferrocene, FcR (in blue) and FcS (in red) on electrodes modified with racemic BT₂T₄ (dashed lines) or enantiopure BT₂T₄ (solid lines), electrooligomerized on ultra-flat ITO as working electrode, in ACN+LiClO₄ 0.1 M.

i) Enantioselection tests on electrodes modified with oligo-BT₂T₆ as a function of the number of deposition cycles in TBAPF₆

To verify the influence of the length of the thiophene wings on the enantioselection ability, the enantioselection tests were also carried out on enantiopure (*S*) - and (*R*) -oligo-BT₂T₆ towards the enantiomers of chiral ferrocene (Figure 83).

Also in this case, the two enantiomers of the chiral probe were tested on bare electrode (Figure 83 grey lines), and the CV signals for both the configurations (Fc R and Fc S) have the same potential value (~ 0.49 V vs SCE), the same current intensity and the same canonical and reversible shape.

However, in this case on account of a very small quantity of available BT₂T₆ sample, the results obtained for the chiral ferrocenes on electrodes modified with enantiopure BT₂T₆ were not compared with those obtained on racemic BT₂T₆ films.

Therefore, enantiopure (*S*) - and (*R*) - oligo-BT₂T₆ were tested with the enantiomers of chiral ferrocene; in all cases a small, but reproducible peak potential separation was observed (Figure 83 and 84) with a mild dependence on the number of deposition cycles.

In particular:

- the peak potential separation decreases increasing the film thickness (~ 40 mV vs SCE for 1 cycle vs ~ 30 mV vs SCE for 5 cycles vs ~ 25 mV vs SCE for 10 cycles), as reported in synopsis in Figure 83;
- after 1 CV cycle the greatest separation (~ 40 mV) is obtained, which is, however, 10 times lower than in the BT₂T₄ case;
- After 5 and 10 CV cycles, both the signals of the enantiomers of the chiral probe are shifted to more positive potentials than the respective signals on the bare electrode and lose their electrochemical reversibility; however, compared to the previous cases, this shift is not very high.

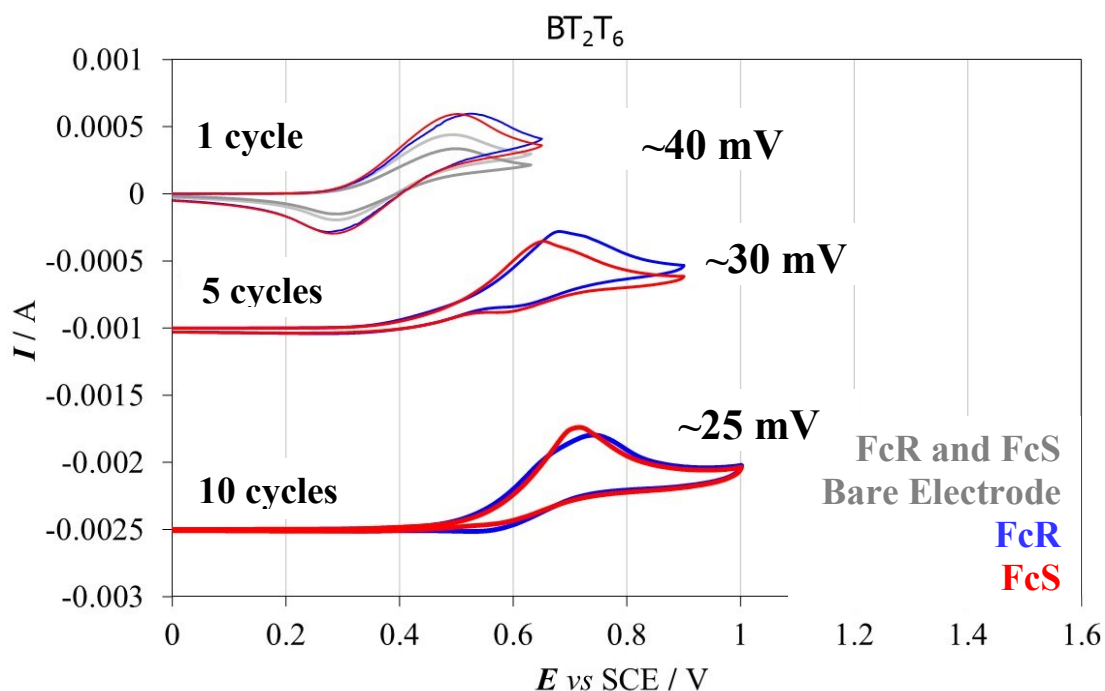


Figure 83. Synopsis of the enantioselection tests towards FcR (in blue) and FcS (in red) on oligo-(*S*)- BT_2T_6 at different CV cycles (1, 5 and 10).

The behaviour of the BT_2T_6 is very similar to the BT_2T_4 ; in fact, the separation decreases increasing the number of electrodeposition cycles and the enantiomer peak sequence is the same. This is consistent with the fact that the structures of the two monomers are very similar (in fact they differ only for one thiophene term in the terminal chains), and they have also been tested under the same conditions (ACN + $TBAPF_6$). Reproducibility tests were also carried out, by freshly depositing a new oligomer film on a new electrode support, using the same working protocol. Furthermore, by inverting the configuration of the electrodeposited oligomer film, perfectly specular results are obtained (Figure 84).

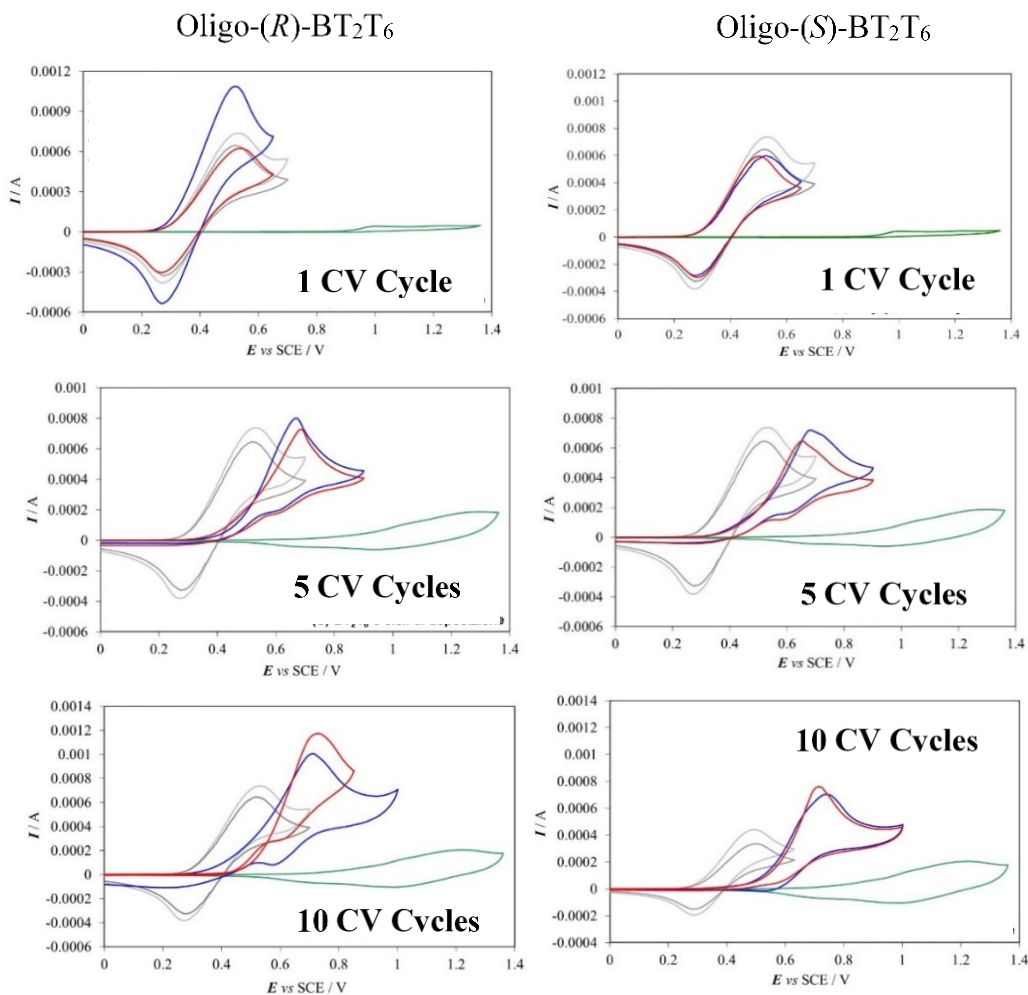


Figure 84. Enantioselection tests towards the enantiomers of chiral ferrocene, FcR (in blue) and FcS (in red) on electrodes modified with (*R*)- and (*S*)-oligo-BT₂T₆ in ACN+TBAPF₆ 0.1 M.

3.2.5 A family of “inherently chiral” bisindole systems with *N,N'* functionalization: modulating functional properties and performances as chiral selectors

Another new inherently chiral monomer family, synthesized in enantiopure form without HPLC separation steps and based on 2,2'-biindole atropisomeric scaffold, namely **EN-OH**, **EN-OCH₃**, **EN-Et** was investigated (Figure 85).

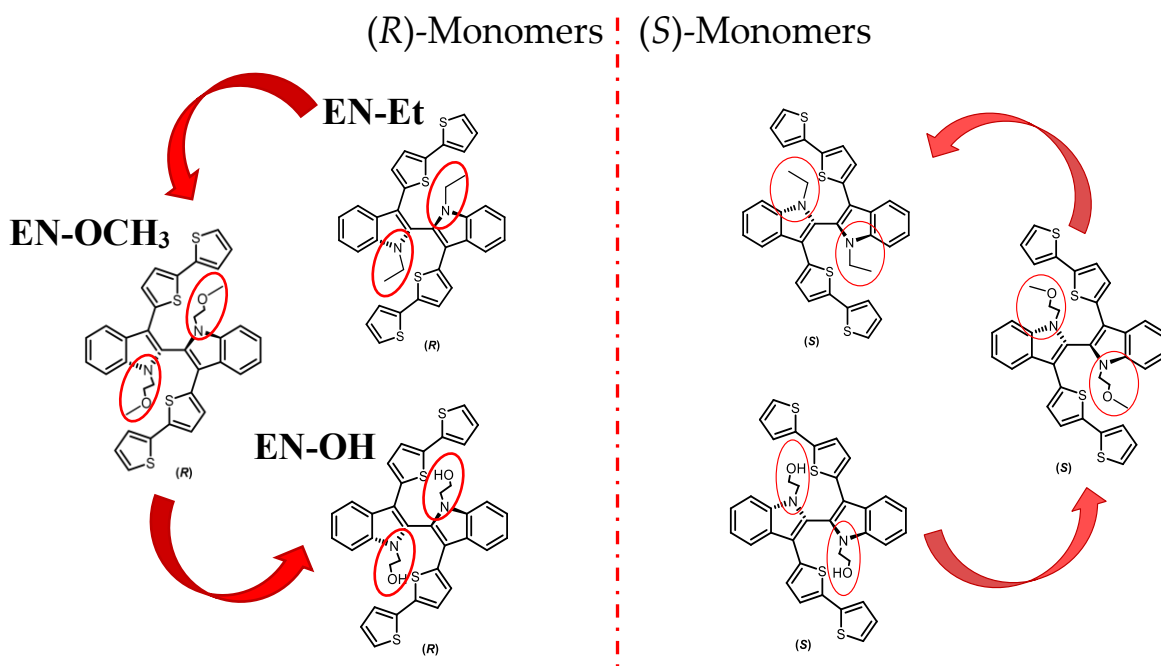


Figure 85. Chemical structures of the three inherently chiral monomers: **EN-OH**, **EN-OCH₃** and **EN-Et**.

The 2,2'-biindole monomers were considered very interesting candidates, because the *N* atoms can be functionalized with different substituents, in order to modulate many properties (such as the solubility). In particular, the three inherently chiral monomers present the following different substituents on the nitrogen atom: **-CH₂CH₃**, **-CH₂CH₂OH** and **CH₂CH₂OCH₃**.

The electrochemical properties of the monomers, the electrooligomerization ability, and the stability of the films were studied. Finally, the inherently chiral oligomer films were implemented in enantioselection experiments, for the discrimination of the enantiomers of different chiral probes, also of pharmaceutical interest (such as Naproxen and Ketoprofen), which present many OH groups, in order to study the role of the hydrogen bonds in the enantioselection mechanism.

a) Experimental section

The electrochemical characterization of the monomers was carried out in a three-electrode minicell filled with 3 cm³ of solution containing ~0.00075 M of the sample dissolved in DCM or ACN with 0.1 M TBAPF₆ as supporting electrolyte. Two NSAIDs were electrochemically characterized by CV, in particular: (*S*)-Ketoprofen (~0.00075 M) in DCM + 0.1 M TBAPF₆ as supporting electrolyte and (*S*)-Naproxen (~0.00075 M) in aqueous pH 7 buffer solution.

Electrodepositions were performed in potentiodynamic mode of conducting chiral **oligo-(R)-** and **(S)-EN-OH**, **oligo-(R)-** and **(S)-EN-OCH₃**, **oligo-(R)-** and **(S)-EN-CH₂CH₃** and **oligo-(R)-** and **(S)-EN-CH₃** films on the GC electrode with 0.00075 M solutions of the corresponding enantiopure (*R*)- or (*S*)- monomer, in DCM with 0.1 M TBAPF₆ supporting electrolyte.

In particular, 36 (or 20) consecutive oxidative potential cycles at 0.05 V s⁻¹ (or at 0.2 V s⁻¹) were performed around the first peak involving the oxidation of the thiophene wings. After the electrodeposition of the film, a stability test was performed, by repeated potential cycling in a monomer-free solution.

The enantioselection experiments were performed in different conditions:

i) on **oligo-(S)-EN-OH**, **oligo-(S)-EN-CH₂CH₃** or **oligo-(R)-EN-OCH₃**, deposited by performing 36 CV cycles at 0.05 V/s (in the case of **EN-OH**) and 0.2 V/s (in the case of **EN-OCH₃**) on GC from ~0.00075 M solutions of the

corresponding enantiopure (*R*)- or (*S*)- monomer, in DCM + 0.1 M TBAPF₆, testing **FcR** and **FcS** (~0.002 M) in DCM + 0.1 M TBAPF₆.

ii) on both **oligo-(*S*)-** and **oligo-(*R*)-EN-OH**, **EN-CH₂CH₃** and **EN-OCH₃**, deposited by performing 20 CV cycles at 0.2 V/s on GC from ~0.00075 M solutions of the corresponding enantiopure (*R*)- or (*S*)- monomer, in DCM + 0.1 M TBAPF₆, testing **(+)-Catechin** and **(-)-Epicatechin** (~0.003 M) in pH 4 buffer solution.

iii) on both **oligo-(*S*)-** and **oligo-(*R*)- EN-OH** and **EN-CH₂CH₃** deposited by performing 20 CV cycles at 0.2 V/s on GC from ~0.00075 M solutions of the corresponding enantiopure (*R*)- or (*S*)- monomer, in DCM + 0.1 M TBAPF₆, testing **(-)-Epigallocatechin gallate (EGCG)** (~0.003 M) in pH 4/pH 7 buffer solution.

iv) on both **oligo-(*S*)-** and **oligo-(*R*)-EN-OH**, **EN-CH₂CH₃** and **EN-OCH₃**, deposited by performing 20 CV cycles at 0.2 V/s on GC from ~0.00075 M solutions of the corresponding enantiopure (*R*)- or (*S*)- monomer, in DCM + 0.1 M TBAPF₆, testing **(*S*)-Naproxen** (~0.003 M) in pH 7 buffer solution and **(*S*)-Ketoprofen** (~0.003 M) in DCM + 0.1 M TBAPF₆.

b) Redox features of the three inherently chiral monomers

The complete CV patterns in both ACN (Figure 86, left side) and DCM (Figure 86, right side) of the **EN-OH**, **EN-CH₂CH₃** and **EN-OCH₃** monomers are reported in Figure 86 (more details are collected in Gallery section 9).

For all four molecules the oxidative cyclic voltammetry (CV) patterns are characterized by multiple peaks. The first couple of peaks (A, B in Figure 87) is localized on the more electron-rich indole core moieties with only partial delocalization on the oligothiophene terminals. This is consistent with the results reported in previous studies [131,134]. Moreover, no oligomerization is observed cycling around A and/or B.

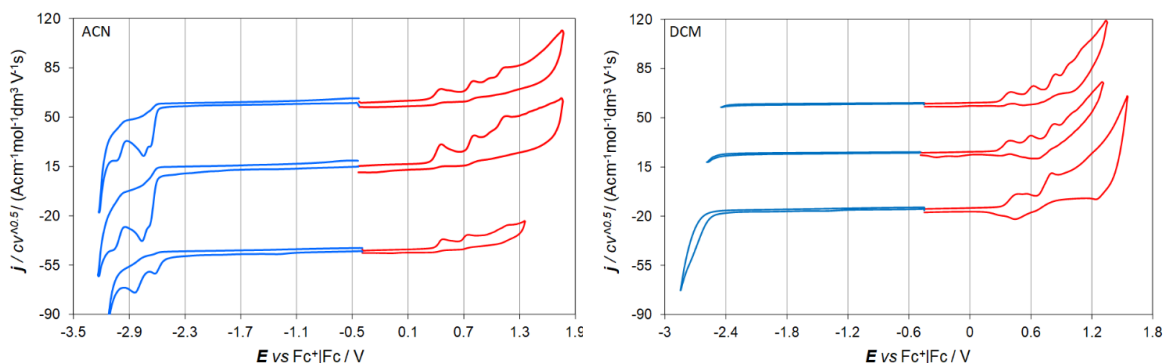


Figure 86. Normalized CV patterns of monomers **EN-OH**, **EN-CH₂CH₃** and **EN-OCH₃** on GC electrode in ACN (left side) DCM (right side) at 0.2 V s⁻¹ potential scan rate.

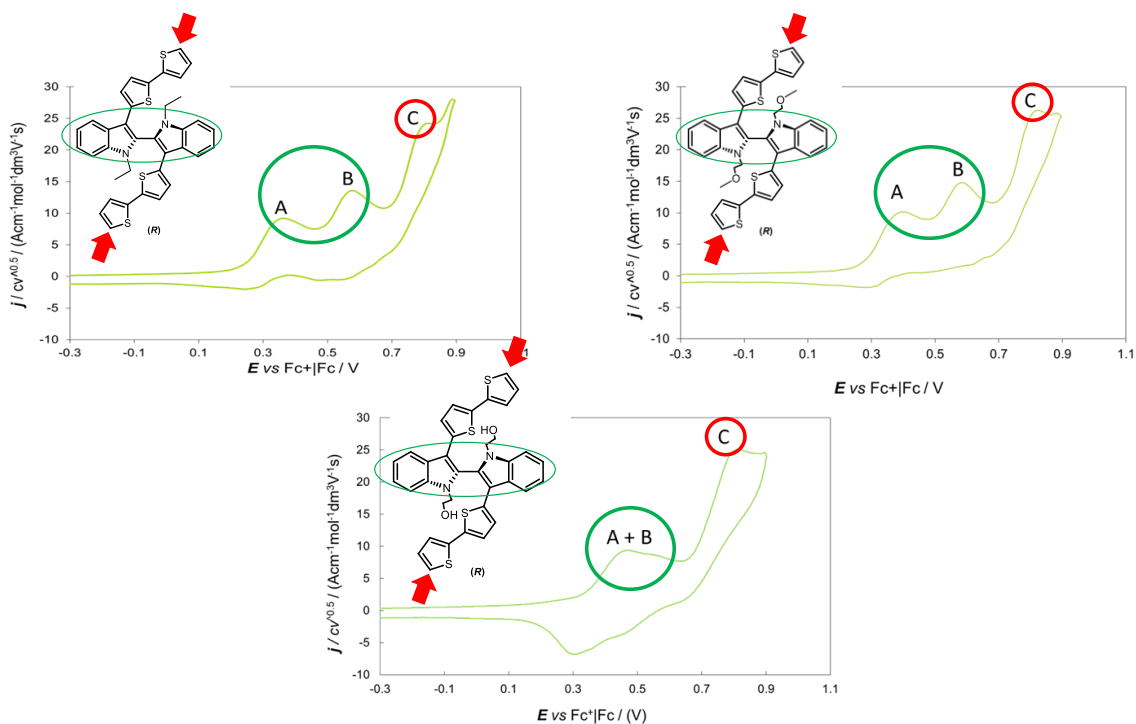


Figure 87. Anodic part of the monomers in DCM+TBAPF₆ 0.1 M at 0.2 V s⁻¹ including first (A) second (B) and third (C) oxidation peaks.

A two-peak first oxidation system was often observed for bisindole systems, with the two equal molecule moieties behaving as equivalent and partially interacting redox centres. The twin peak potential difference increased with increasing reciprocal interaction. In a previous work, it was found that peak splitting is strongly dependent on solvent polarity. In a polar solvent, like acetonitrile (with a higher dipolar moment than DCM and higher charge screening ability) a tendency is observed to twin peak merging, a pattern similar for all molecules. Furthermore, no electrodeposition was observed in ACN [131,134]. In spite of the difference in the nitrogen substituent, **N-Et** and **N-CH₂CH₂OCH₃** feature similar peak-to-peak potential differences, which suggests a similar degree of interaction between the two symmetric moieties in accordance with their similar structures (Figure 86 and 87).

An outlier in the studied series is instead represented by the **-CH₂CH₂OH** case (**EN-OH** monomer), which presents a significantly smaller separation between A and B peaks (ΔE_{pB-pA} around 13 mV, with $E_{pA} \sim 0.44$ V and $E_{pB} \sim 0.57$ V).

It seems that the presence of the oxygen alone does not influence the twin peak separation. In fact, the pattern of **EN-OCH₃** monomer presents a splitting between A and B oxidation peaks similar to **EN-Et**. Thus, the proton is determining in the peculiar behaviour of **EN-OH**.

Actually, the **-CH₂CH₂OH** branch is free to move and therefore there could be a hydrogen bond formation between the oxygen and the sp^3 nitrogen. The coordination can result in a lower interaction between the two moieties, which can explain the peak merging.

Moreover, the first oxidation peak for **EN-OH** monomer (Figure 87), is localized at a significantly more positive potential respect to all the other monomers, in both DCM ($E_{p,ox} \sim 0.44$ V vs Fc^+/Fc) and ACN (~ 0.47 V vs Fc^+/Fc) and this could be another indication of this interaction, probably due to the presence of hydrogen bond in **EN-OH** monomer; indeed redox processes involving a reactant species

coordinated (and therefore stabilized) by a ligand require more energy (and thus are found at more extreme potentials respect to the free species alone).

In all the cases, the peak separation between A and B is lost in ACN, since the polar solvent hampers reciprocal interactions between the interacting redox centres, as mentioned above (Figure 87).

The third peak C is localized on the α homotopic positions of the thiophene wings, involved in the electrooligomerization process.

c) Inherently chiral oligomer films formation

By cycling around the peaks associated with the activation of the thiophene alpha terminals of the molecules (peaks C in Figure 87) a film formation is achieved (Figure 88). The inherently chiral oligomer films are obtained for all the monomers, however in the case of **EN-OCH₃** and **EN-Et** the films appear thinner, probably due to the higher solubility of the oligomers obtained.

However, all the films show good stability in a monomer-free solution, a necessary condition to use these films as chiral selectors.

d) Enantioselection experiments

• N,N-dimethyl-1-ferrocenyl-ethylamine (FcR and FcS)

The first enantiodiscrimination experiment was carried out with enantiopure chiral probe (*R*)- or (*S*)-*N,N'*-dimethyl-1-ferrocenyl-ethylamine (as enantiopure antipodes FcR and FcS, structure reported below in Figure 89), which is our usual choice as model probe when testing chiral electrode surfaces and media, due to its chemical and electrochemical reversibility as well as commercial availability. The chosen probe has a chemical and electrochemical reversible peak corresponding to the oxidation process in the region where the film is uncharged.

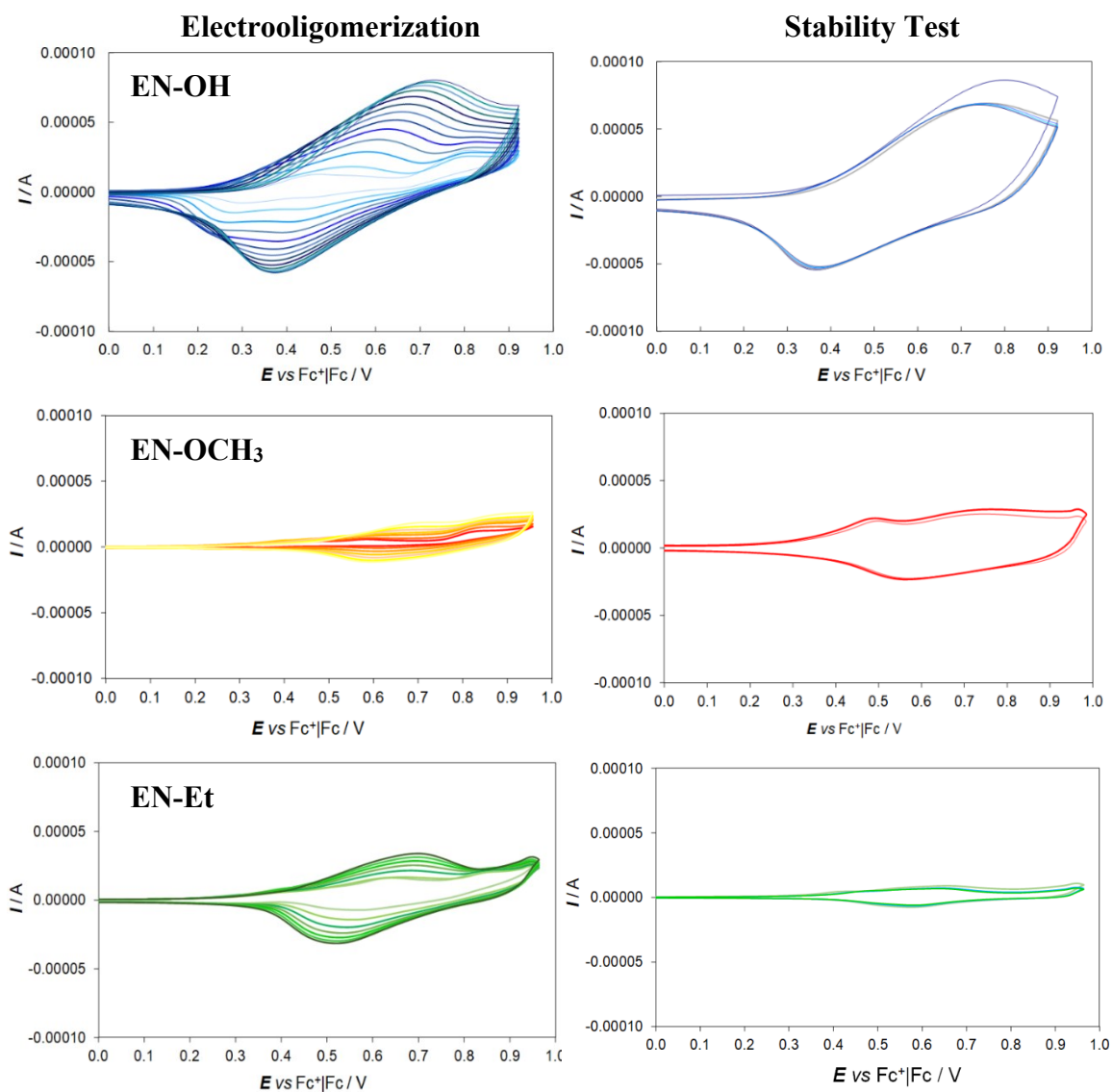


Figure 88. Electrooligomerization of 0.00075 M EN-OH, EN-OCH₃ and EN-Et monomers on a GC tip electrode in DCM with 0.1 M TBAPF₆ performing 36 CV cycles at 0.05 V s⁻¹ (left side). Stability tests in monomer-free solution (right side).

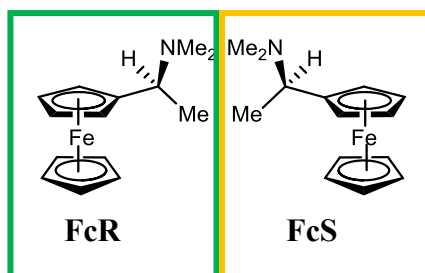


Figure 89. Chemical structures of FcR (in green) and FcS (in yellow).

The tests were carried out on **oligo-(S)-EN-OH** and **oligo-(S)-EN-CH₂CH₃** or **oligo-(R)-EN-OCH₃** films, deposited by 36 CV cycles at 0.05 V/s (in the case of **EN-OH**) and 0.2 V/s (in the case of **EN-OCH₃**) on the GC disk electrode from 0.00075 M solutions of the corresponding enantiopure (*R*)- or (*S*)- monomer, in DCM + 0.1 M TBAPF₆ as supporting electrolyte.

The enantiodiscrimination tests were performed in 0.002 M solutions of the probe in DCM + 0.1 M TBAPF₆ at 0.05 V/s scan rate. Reproducibility tests were performed by repeatedly recording the CV patterns of model probes on freshly deposited chiral surfaces.

The results of the experiments are reported in Figure 90. Enantiodiscrimination tests carried out with **EN-OH** show a peak potential separation of 250 mV for the two antipodes of the chiral probe while enantiodiscrimination tests carried out with **EN-OCH₃** and **EN-Et** show a separation of 200 mV and 100 mV, respectively. Such trend can be justified with the decrease of coordinating elements in the selector. Another observation is that the larger the separation, the more irreversible is the signal. It seems that if further chemical reactions are present (*i.e.*, reactions between probe and film) the separation is higher with the concurrent loss of canonical shape of the signal.

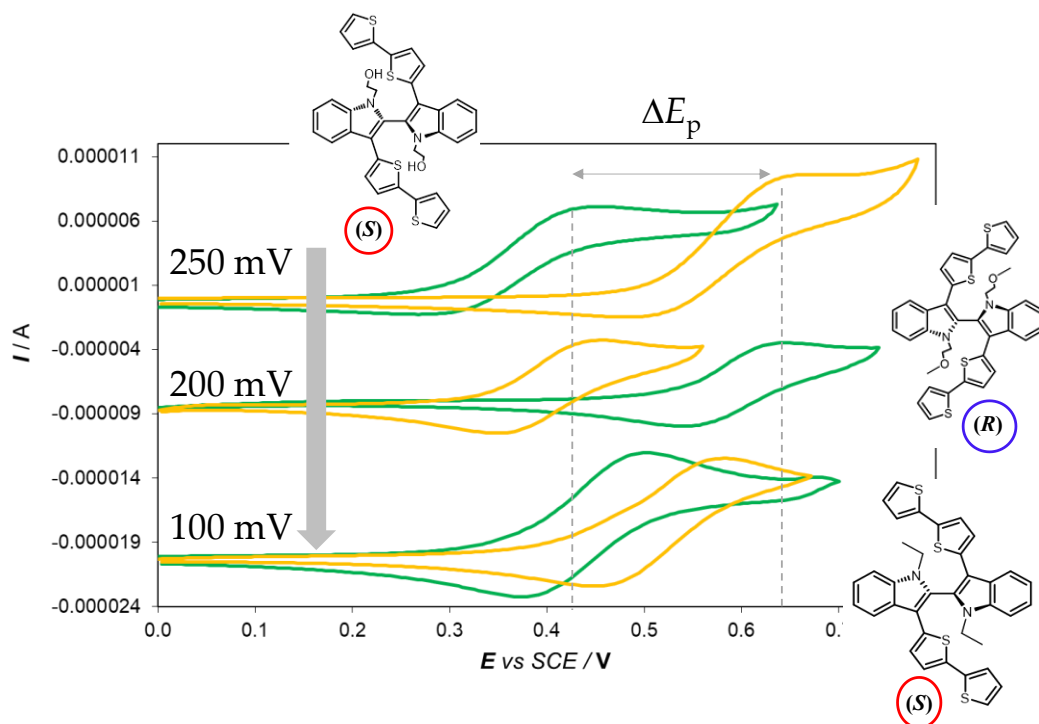


Figure 90. Enantioselection tests of FcR and FcS (red and orange respectively).

• *(+)-Catechin and (-)-Epicatechin*

A further enantiodiscrimination experiment series was carried out with enantiopure chiral probes (+)-Catechin and (-)-Epicatechin, the structures of which are reported below (Figure 91).

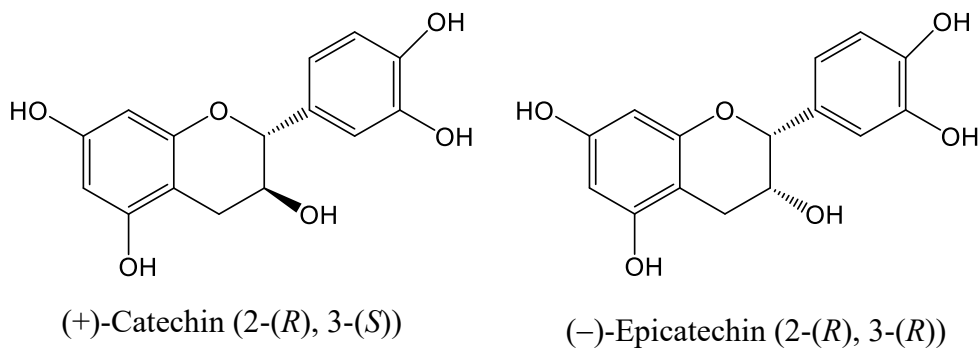


Figure 91. Chemical structures of (+)-Catechin (left side) and (-)-Epicatechin (right side).

These probes belong to the polyphenol class (flavanol subclass); they are present in many plants and natural beverages and foods (for example, they are major components in tea) and can form polymers that are called protoantocyanidine or condensed tannins. They are particularly interesting for their antioxidant properties *e.g.* in view of preventing cardiovascular and neurodegenerative diseases [158] or for up-to-date antiviral applications. As evident from the above structures, the two probes are in a reciprocal diastereoisomeric relationship (featuring two stereocentres on the central ring, the relative configurations of which define two enantiomer couples) and therefore, differing only for the configuration of an hydroxy substituent on the central ring, they can be in principle electrochemically discriminated even in the absence of chiral selectors. Actually on bare GC electrode we observed a remarkable difference for the CV patterns of the two molecules, with first oxidation peak potentials at 0.51 V vs SCE for (-)-Epicatechin and 0.71 V vs SCE for (+)-Catechin, as reported in Figure 92.

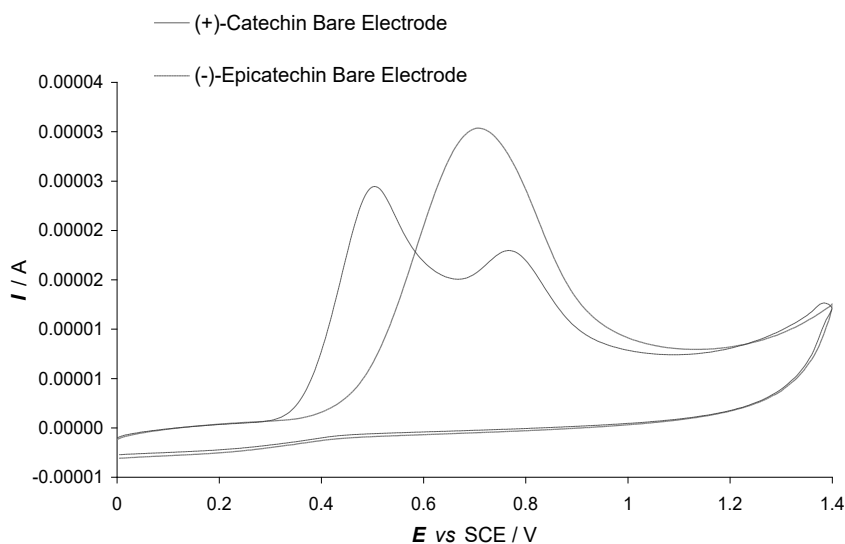


Figure 92. CV patterns of (-)-Epicatechin (grey line) e (+)-Catechin (dotted dark grey line) at 50 mV s^{-1} on bare GC electrode, in pH 4 buffer solution.

Both (+)-Catechin and (-)-Epicatechin have a specular enantiomer ((-)-Catechin (2-(*S*), 3-(*R*)) and (+)-Epicatechin (2-(*R*), 3-(*R*), respectively), less common in nature. The enantiomers of each couple cannot of course be discriminated in the absence of a chiral selector. Thus the catechin or epicatechin enantiomer couples would be good candidates for our standing research on chiral voltammetry.

Unfortunately, we only had available the more common enantiomer in each couple. However, in such a case, a “specular” experiment can be performed to confirm the possibility of enantiodiscrimination, provided that both the enantiomers of the chiral selector be available. In fact, testing a given probe enantiomer with both the enantiomers of a chiral selector must give exactly the same results as testing both probe enantiomers with a given enantiomer of the chiral selector (Figure 93 and 94).

Accordingly, we performed enantiodiscrimination tests working on (*S*)/(*R*)- **EN-OH** and (*S*)/(*R*)- **EN-OCH₃** and (*S*)/(*R*)-**EN-Et** films, deposited by repeated 20 CV cycles at 0.2 V/s scan rate on the GC disk electrode with 0.00075 M solutions of the corresponding enantiopure (*R*)- or (*S*)- monomer, in DCM + 0.1 M TBAPF₆ as supporting electrolyte.

The tests were performed in 0.003 M solutions of the probe in pH 4 buffer solution at 0.05 V/s scan rate.

Reproducibility tests were performed by repeatedly recording the CV patterns of model probe on freshly deposited chiral surfaces.

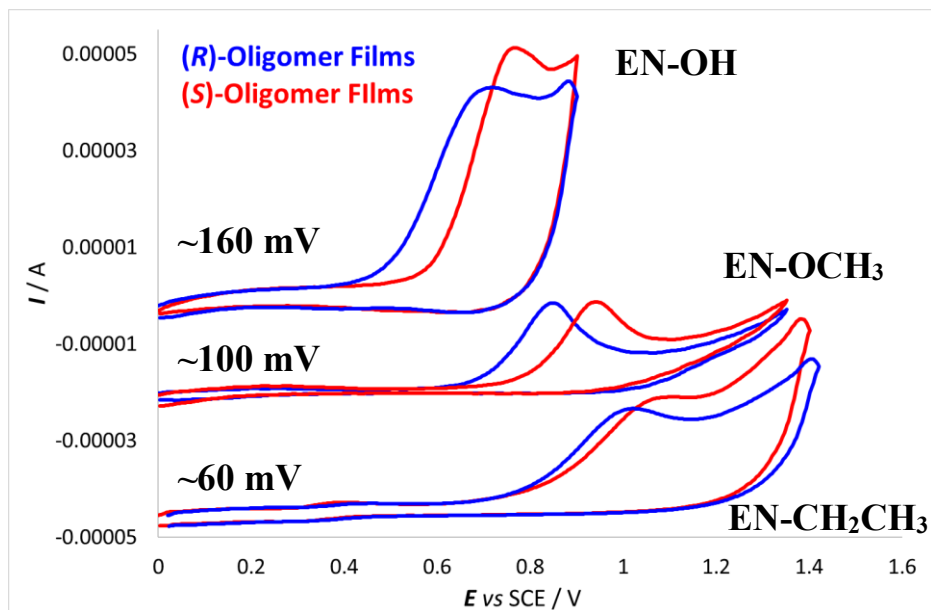


Figure 93. Enantiodiscrimination tests with (+)-Catechin on both (*S*)- and (*R*)-enantiomers of the three inherently chiral oligomer films, in pH 4 buffer solution.

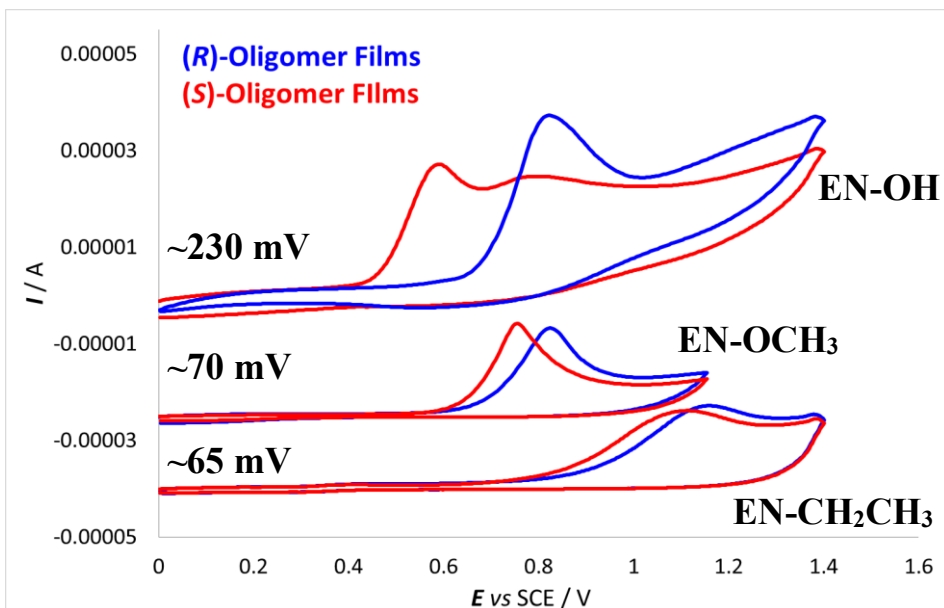


Figure 94. Enantiodiscrimination tests with (-)-Epicatechin on both (*S*)- and (*R*)-enantiomers of the three inherently chiral oligomer films, in pH 4 buffer solution.

The results of the experiments are reported in Figure 93 and 94. Enantiodiscrimination tests carried out with **(S)/(R)-EN-OH** show a peak potential separation of 230 mV for (-)-Epicatechin and 160 mV for (+)-Catechin; enantiodiscrimination tests carried out with **(S)/(R)-EN-OCH₃** show a separation of 70__mV for (-)-Epicatechin and 100 mV for (+)-Catechin; enantiodiscrimination tests carried out with **(S)/(R)-EN-Et** show a separation of 65 mV for (-)-Epicatechin and 60 mV for (+)-Catechin. In general, it can be said that separations for epicatechin are larger than the ones for catechin. This feature as well as the above mentioned easier oxidizability should be related to the configuration of the OH group on the central ring, for which it can be remarked that it is located on the same side as the catechol group (*i.e.* the redox centre corresponding to the first oxidation process).

- *(-)-Epigallocatechin Gallate (EGCG)*

EGCG is a derivative of (-)-Epicatechin (Figure 95), and they present the same configuration for both the stereocentres (in this way it has been possible to verify the enantiomers peak sequence in the enantioselection experiments), with no other added ones. EGCG is another probe of applicative interest being a popular molecule, also used in many dietary supplements (with much increased bulkiness with respect to the other ones).

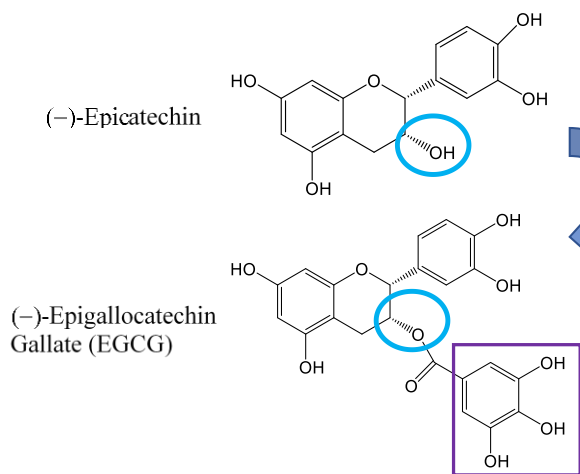


Figure 95. Chemical structure of (-)-Epigallocatechin Gallate (EGCG).

Figure 96 summarizes the enantioselection tests. The electrodes were modified with the enantiopure inherently chiral oligomer films; in particular we have tested **oligo-(R)-** and **(S)- EN-OH** (testing EGCG as chiral probe in buffer pH 7 solution) and **oligo-(R)-** and **(S)- EN-Et** (testing EGCG in both pH 4 and pH 7 buffer solutions).

A remarkable potential difference of about 265 mV is observed working with (S)- or (R)- surfaces electrodeposited from the monomer **EN-OH** (Figure 96, left side, top). The enantiomer order is, as expected, the same as for the parent compound (–)-Epicatechin. Interestingly, however, unlike the parent case, huge shifts are observed towards more positive potentials on both enantiopure surfaces, pointing to a much stronger selector/probe interaction in the EGCG case (probably linked to the many heteroatoms present and to the increasing bulkiness of the molecule).

A very good performance is also observed with the selector **EN-Et**, but the potential difference is this time smaller (~ 200 mV), consistently with the above mentioned results.

In this last case we were also able to investigate the pH effect on the enantioselection ability, performing the experiment both at pH 7 and pH 4. Apparently, as shown in Figure 96, the enantiodiscrimination ability decreases with increasing pH. This is somehow intriguing, at least at a first glance, since considering the EGCG speciation diagram both at pH 7 and pH 4 the molecule should be nearly completely in the same form, that is, the entirely protonated one.

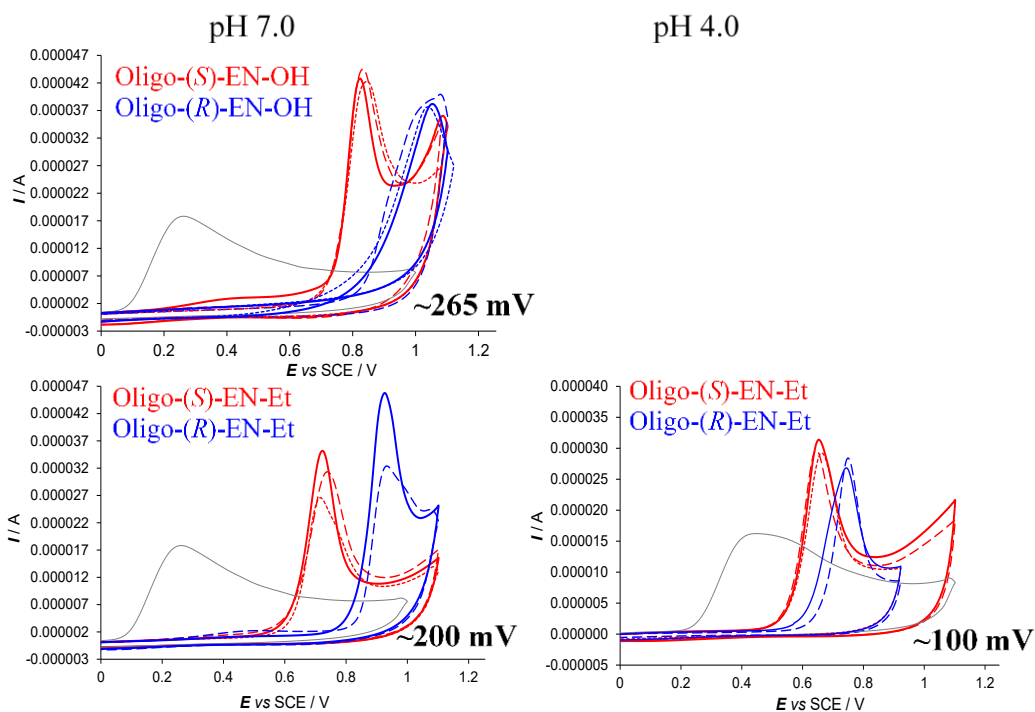


Figure 96. Enantiodiscrimination tests with (–)-EGCG performed in aqueous buffer solutions (left side pH 7 and right side pH 4), employing as chiral selector a GC electrode modified with (*S*)- or (*R*)- enantiomer (red and blue respectively) of EN-OH (top) or EN-Et (bottom).

- *Non-Steroidal Anti-Inflammatory Drugs (NSAIDs)*

Most NSAIDs are chiral molecules that are prepared as a racemic mixture but typically only a single enantiomer is pharmacologically active. For some drugs (typically profens), an isomerase enzyme exists *in vivo* which converts the inactive enantiomer into the active form. Ibuprofen and Ketoprofen are now available in single active enantiomer preparations while naproxen has always been marketed as single active enantiomer.

(S)-Naproxen (Figure 97)

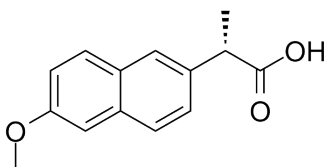


Figure 97. Chemical structure of (S)-Naproxen.

The enantiodiscrimination experiment (Figure 98) was carried out with enantiopure chiral probe (S)-Naproxen, working on (S)/(R)- **EN-OH** and (S)/(R)- **EN-OCH₃** and (S)/(R)-**EN-Et** films, deposited by 20 CV cycles at 0.2 V/s scan rate on the GC disk electrode from 0.00075 M solutions of the corresponding enantiopure (R)- or (S)- monomers, in DCM + 0.1 M TBAPF₆ as supporting electrolyte. Enantiodiscrimination tests were performed in ~0.003 M solution of the chiral probe, working in all cases in pH 7 buffer solution at 0.05 V/s scan rate. Reproducibility tests were performed by repeatedly recording the CV patterns of the (S)-Naproxen probe on freshly deposited chiral surfaces.

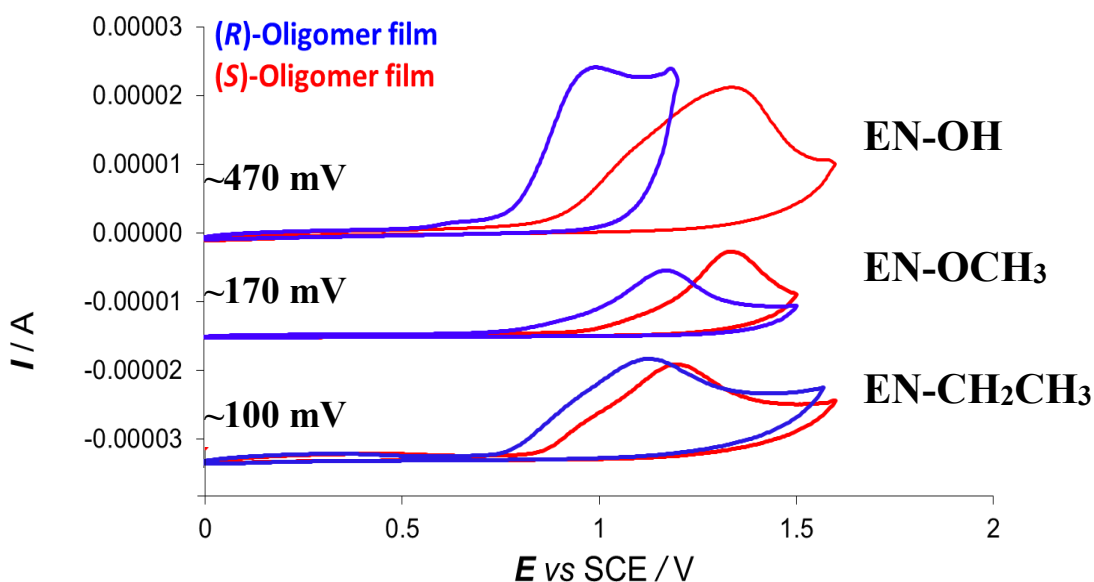


Figure 98. Enantiodiscrimination tests with (S)-Naproxen on both (S)- and (R)- enantiomers of the three inherently chiral oligomer films, in pH 7 buffer solution.

The results of the experiments are reported in Figure 98. Enantiodiscrimination tests carried out with (*S*) and (*R*)-**EN-OH** show a stunning separation of 470 mV while enantiodiscrimination tests carried out with (*S*) and (*R*)-**EN-OCH₃** show a separation of 170 mV, and 100 mV with **EN-Et**. As above mentioned, the medium used for the enantiodiscrimination was the pH 7 buffer, on account of it corresponding to higher currents respect to the pH 4 case and we related this feature to the speciation diagram showing that at pH 7 Naproxen is almost present only as anionic form. Considering that at 1.09 V *vs* SCE the film is positively charge, such feature also suggests that there could be an electrostatic interaction between the film and the probe, enhancing the chiral probe coordination by the chiral film selector.

(*S*)-Ketoprofen (Figure 99)

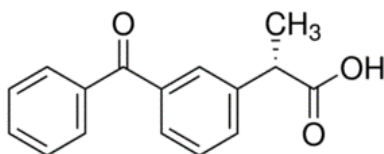


Figure 99. Chemical structure of (*S*)-Ketoprofen.

In this case, the enantiodiscrimination (Figure 100) experiment was carried out with enantiopure chiral probe (*S*)-Ketoprofen, working on **oligo-(*S*)/(*R*)- EN-OH** and **oligo-(*S*)/(*R*)- EN-OCH₃** films, deposited by 20 CV cycles at 0.2 V/s scan rate on the GC disk electrode from 0.00075 M solutions of the corresponding enantiopure (*R*)- or (*S*)- monomer, in DCM + 0.1 M TBAPF₆ as supporting electrolyte. In both cases, enantiodiscrimination tests were performed in 0.0025 M probe solutions in DCM + 0.1 M TBAPF₆ at 0.05 V/s scan rate. Reproducibility tests were performed by repeatedly recording the CV patterns of (*S*)-Ketoprofen on freshly deposited chiral surfaces.

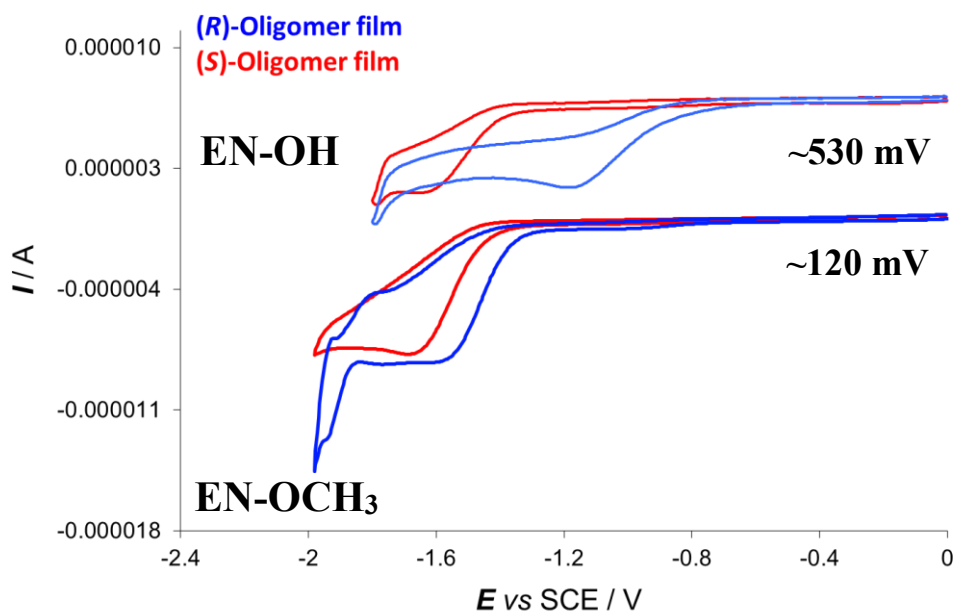


Figure 100. Enantiodiscrimination tests with (*S*)-Ketoprofen on both (*S*)- and (*R*)- enantiomers of two inherently chiral oligomer films, in DCM + TBAPF₆ 0.1 M.

The results of the experiments are reported in Figure 100. Enantiodiscrimination tests carried out with (*S*) and (*R*)-**EN-OH** show a stunning separation of 530 mV while enantiodiscrimination tests carried out with (*S*) and (*R*)-**EN-OCH₃** show a separation of 120 mV.

This case study is very interesting, because it provides an example of enantiodiscrimination based on a reduction process, respect to the formerly reported oxidation cases. Moreover, in this case we were able to the test to the same active pharmaceutical ingredient in a commercial drug, as detailed at the following paragraph.

Enantyum®: (S)-Ketoprofen Drug

The enantiodiscrimination experiment was carried out with enantiopure commercial drug Enantyum® (Figure 101) (having (S)-Ketoprofen as active pharmaceutical ingredient), working on **oligo-(S)/(R)- EN-OH** films, deposited by 20 CV cycles at 0.2 V/s scan rate on the GC disk electrode from 0.00075 M solutions of the enantiopure (R)- or (S)- monomer, in DCM + 0.1 M TBAPF₆. Enantiodiscrimination tests (Figure 101) were performed at 0.05 V/s scan rate in a solution obtained dissolving one sachet of Enantyum® in DCM + 0.1 M TBAPF₆. Reproducibility tests were performed by repeatedly recording CV patterns of the probe on freshly deposited chiral surfaces.

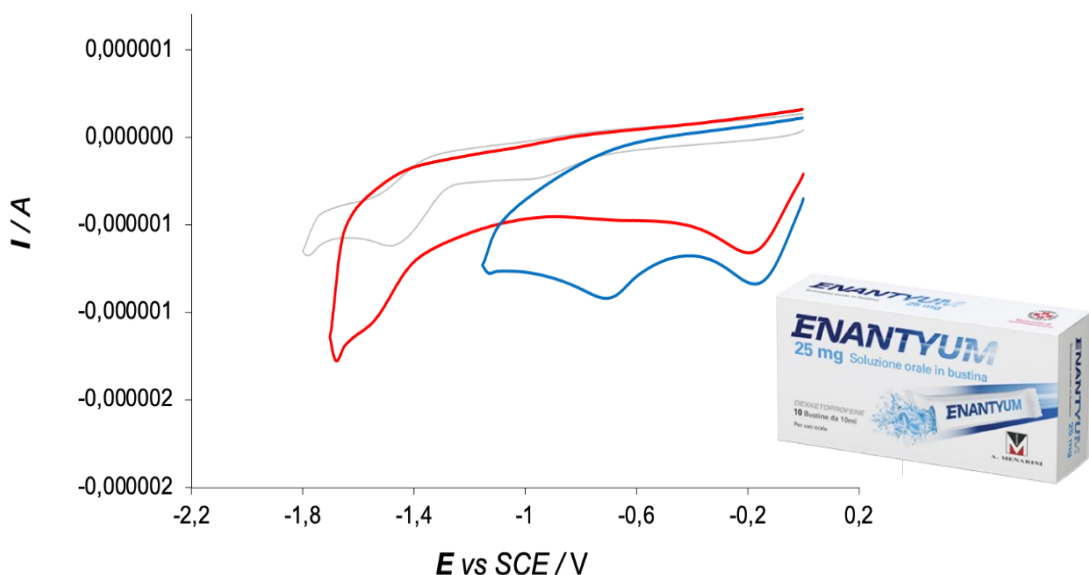


Figure 101. Enantioselection tests with a solution of the Enantyum® commercial drug on enantiopure electrode surfaces of **oligo-(S)-EN-OH** (red line) and **oligo-(R)-EN-OH** (blue line), at 0.05 V/s. For sake of comparison the CV pattern of the same Enantyum® solution recorded on the bare electrode (in grey) is also reported.

The results of the experiments are reported in Figure 101. A stunning peak potential difference is observed with the two oligomer film enantiomers of more than 800 mV! In justifying such surprising enantiodiscrimination enhancement in the real drug case, the possible presence might be taken into consideration of some chiral molecule as excipient/additive in the drug formulation.

The electron transfer process must take place at the enantiopure interface between the electrode and the probe within the chiral oligomer film or even on the surface of the oligomer film. The combination between the enantiomers of a given chiral probe and the enantiopure chiral film results in a diastereomeric interaction, which is energetically different (potential difference) from the electrochemical point of view. Consistently with this consideration, significant potential differences would require significant differences in selector/probe (as reagent and/or product) coordination. In this frame the nature of the terminal alkyl substituent on the nitrogen atom must play a crucial role in providing possible additional coordination points.

Therefore, the observed increasing enantiodiscrimination ability in the series Et < OCH₃ << OH look consistent with the availability of an additional oxygen heteroatom in the OCH₃ case, and of an oxygen heteroatom plus a proton to be involved in Lewis acid/base interactions in the OH case.

The assumption of the presence of a hydrogen bond involved, is supported by ATR measurements performed at the J. Heyrovský Institute of Physical Chemistry, Prague, Czech Republic.

e) Attenuated Total Reflectance (ATR)

ATR spectra are similar to IR spectra, but one of the advantages of ATR spectroscopy is that polymers/films can be studied just by pressing the sample on the crystal.

The absorbance varies with the incidence angle independently from the thickness; the radiation can penetrate for just few μm . The intensity of the ATR band is usually proportional to the concentration. The ATR technique was used to study both the monomer powder and the film deposited on ITO electrode (the setup is reported in Figure 102). Importantly, these measurements enabled to compare the differences in bond stretching between the monomer powder and the conductive film, and above all supported the assumption of possible intramolecular interactions involving the hydroxyl proton in the **EN-OH** monomer.

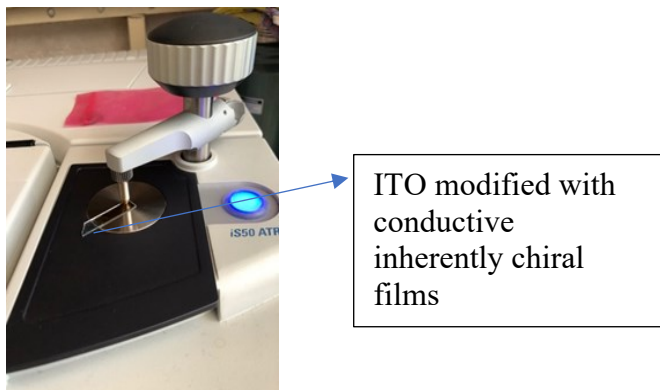


Figure 102. ATR setup.

ATR spectra of **EN-OH** monomer and film are reported in Figure 103 and 104 respectively. The spectra (both for the monomer and the film) do not show the typical sharp absorption band at $3700\text{-}3650\text{ cm}^{-1}$ corresponding to the stretching of O-H bond in alcohol. This can provide a further proof of the mechanism proposed above.

Since the **-CH₂CH₂OH** substituent is free to move, there could be a hydrogen bond interaction involving both the oxygen and the sp³ nitrogen atoms. Actually, the monomer spectra present a weak broad band at 3550-3000 cm⁻¹ that is comparable with literature values for O-H bond stretching in alcohols with intramolecular bonds. As expected, the films, constituted by a series of oligomers with the same maximum conjugation length, present an intermolecular bond interaction consistent with this type of structure. The film spectra also present, unlike the monomer, some strong signals at 1800-1600 cm⁻¹ in the double bond region. It is worthwhile underlining that ATR spectra were collected without sample solution preparation and for this reason we are sure that no solvent interactions are present. Differences in intensity of the absorption band are probably due to the thickness (different spots were analyzed). Deposition can be affected by the position of the electrode and current line geometry in the small setup.

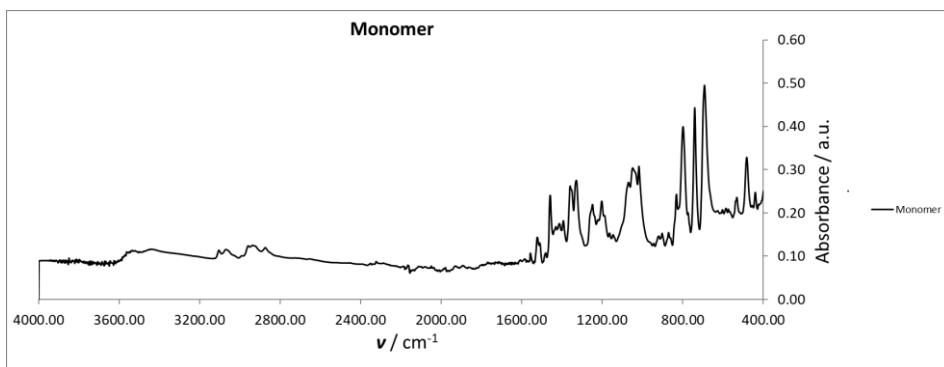


Figure 103. ATR spectra of EN-OH monomer.

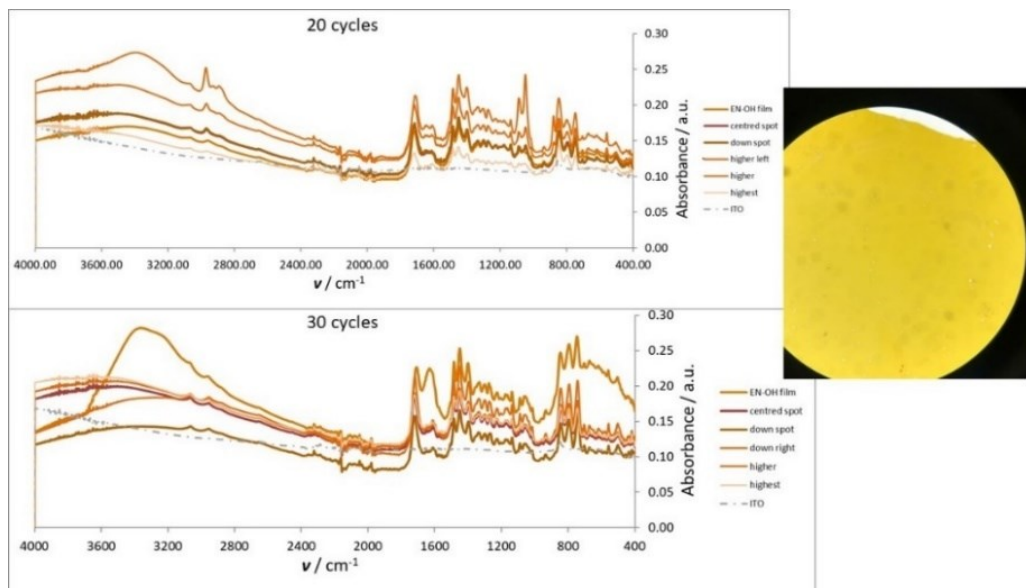
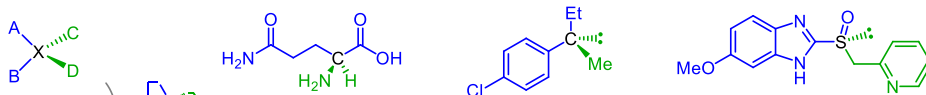


Figure 104. ATR spectra of **EN-OH** film electrodeposited on ITO with 20 (top) and 30 (bottom) cycles, respectively, analyzing different spots.

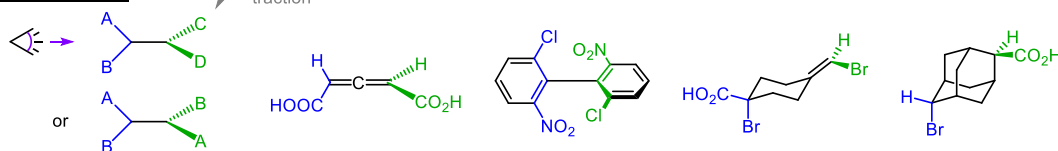
3.2.6 Widening the scope of “inherently chiral” electrodes: enantiodiscrimination of chiral electroactive probes with planar stereogenicity

A series of planar-stereogenicity ferrocenes [159], important as chiral promoters in enantioselective catalysis, has been characterized in terms of relationships between structure and electronic properties. Then, the enantiomers of six selected model cases were successfully discriminated in voltammetry experiments on electrodes modified with electrodeposited inherently chiral oligomer films, in terms of significant potential differences, specular inverting probe or selector configuration.

A: stereogenic center



B: axial chirality



C: planar chirality (reported herein)



D: helical chirality

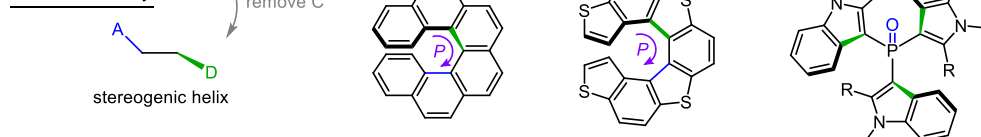


Figure 105. The four stereogenic elements, highlighting their logical sequence, and with some examples: (a) central stereogenicity; (b) axial stereogenicity; (c) planar stereogenicity; (d) helical stereogenicity.

Small substituent changes in the series of ferrocene do not alter the enantiomer peak sequence, but result in significant modulation of peak potential differences,

looking consistent with the availability of chiral/selector matching elements. The present stereogenic plane case, combined with former ones involving stereogenic centres, axes and/or helices, shows that the inherent chirality strategy in electroanalysis can be effective with all four rigid stereogenic elements (Figure 105): stereocentres, stereogenic axes, helices, and stereogenic plane [159].

a) Experimental section

The characterizations of the ferrocene derivatives as racemates were performed at scan rates in the 0.02-2 V/s range, on 0.001-0.0005 M probe solutions in ACN with 0.1 M TBAPF₆ as supporting electrolyte.

Electrodepositions of conducting chiral (*R*)-oligo-BT₂T₄ and (*S*)-oligo-BT₂T₄ films were performed by repeated 36 CV cycles at 0.05V/s scan rate on the GC disk electrode with 0.00075 M solutions of the corresponding enantiopure (*R*)- or (*S*)-BT₂T₄ monomer, in ACN with 0.1 M TBAPF₆ supporting electrolyte.

The enantiodiscrimination experiments were performed with enantiopure chiral probes **1,5,7,14,15,16** (Table 10) at 0.05 V/s scan rate in 0.001 M solutions of the probe in ACN + TBAPF₆ 0.1 M as supporting electrolyte.

Reproducibility tests were performed by repeatedly recording the CV patterns of model probes on freshly deposited chiral surfaces.

b) Electrochemical investigation of the redox features of the planar ferrocenyl family as racemates

The series of chiral ferrocene racemates shown in Table 10 was investigated electrochemically, including both oxidative and reductive features. The chosen measurement conditions were 0.1 M TBAPF₆ in ACN, which is an appropriate medium for the subsequent enantiodiscrimination experiments on electrodes modified with oligo-(*S*)-BT₂T₄ films. In contrast, DCM, while resulting in easier ferrocene compound solubility, would be less convenient for operating the oligo-(*S*)-BT₂T₄ films on account of lower stability of the latter [133]. Moreover, it

would prevent observation of the reductive features, on account of DCM reduction at relatively mild potentials.

Key parameters of the CV patterns (Gallery Section 11) are summarized in Table 10. For comparison, data are also provided for a series of first oxidation formal potentials formerly observed in DCM for compounds **1–6** [160], as well as for triphenylphosphane sulphide (**I**) and diphenylferrocenylphosphane sulphide (**II**) [161] together with its parent P^{III}-derivative **III** [161,162], in ACN and/or DCM [160]. Relevant values of Hammett's constants [163] are also included.

Oxidation

In most cases, except for aldehyde **11**, the first oxidation process appears electrochemically reversible or quasi reversible, since peak potentials are nearly constant with increasing scan rate (Gallery Section 11) pointing to facile electron transfer. Moreover, such peaks correspond to single electron processes (considering half-peak widths) and are chemically reversible. Accordingly, Table 10 provides both peak potentials (E_{IA}) and formal potentials (E°_{Fc}), the latter calculated as the average of forward and backward peaks. The peak features and the small slopes of the linear trends in systematic series of formal potentials with Hammett's σ parameters (Figure 106), pointing to a significant distance between substituent and redox site, are consistent with the first oxidation involving the ferrocene site. Instead, switching to DCM as working medium (orange series, in Figure 106) results in a linear fit similar to one for ACN, but with higher slope, consistently with the lower solvent shielding effect. The peak potential values of 0.22–0.32 V vs unsubstituted $Fc^+|Fc$ are quite justified by the presence of the highly electron withdrawing P^V group S=PPh₂ ($\sigma_p=0.47$) compared to P^{III} in PPh₂ ($\sigma_p = 0.19$), whereby the weakly electron donating styrene group is less determining ($\sigma_p = -0.07$). The only exception is observed for aldehyde **11**, displaying an electrochemically irreversible behaviour.

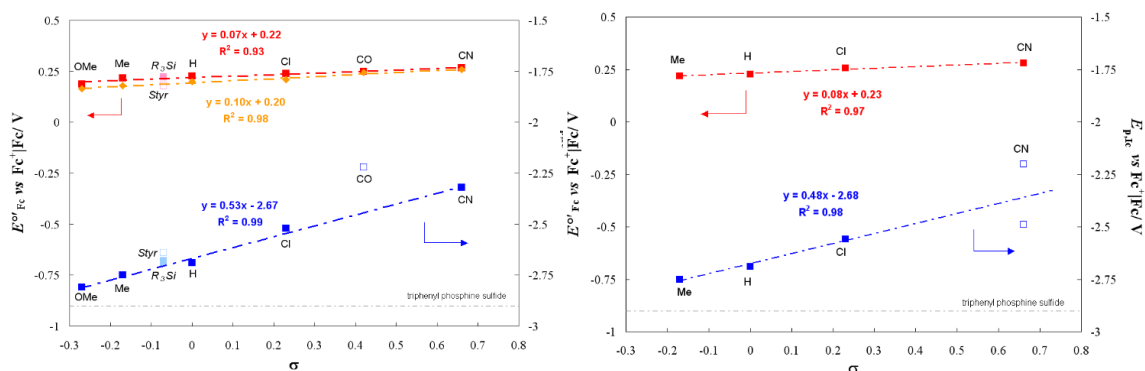


Figure 106. Hammett relationships for the formal first (ferrocenyl-based) oxidation potentials $E^{\text{ox}}_{\text{Fc}}$ (red) and the first reduction peak potentials E_{IC} (blue) of a series of planar stereogenicity chiral ferrocenes. Left: altering the substituents on the phenyl ring of the styrene system (**1**, **2–6**, upright characters) and 1'-substituted ferrocenyl derivatives (**7–9**, italic characters). Right: altering the substituents of the phenyl groups in the phosphinyl moiety (**1**, **12–14**).

The first oxidation process is anodically shifted to 0.49 V vs $\text{Fc}^+|\text{Fc}$, due to the strong electron-withdrawing character of the formyl functionality ($\sigma_{\text{p}} = 0.42$). Moreover, the peak appears nearly chemically irreversible, pointing to a chemical follow up reaction, the only case in the series, which could be justified by the much more positive potential and/or by some involvement of the aldehyde group besides the ferrocene one (although oxidation of the formyl group could correspond to the second oxidation peak at 0.79 V). Anisyl derivative **2** also exhibits a further redox process, observed at 0.87 V, most likely occurring at the methoxyphenyl group. The 1'-functionalized ferrocene **7**, bearing two phenyl vinyl functionalities, shows a process at 0.91 V, for which an intramolecular π -stacking might be involved.

All compounds exhibit a further process at ~ 1.2 V vs $\text{Fc}^+|\text{Fc}$ which closely matches the oxidation peak potential of $\text{S}=\text{P}(\text{Ph})_3$ itself (Table 10 and Gallery Section 11).

Reduction

Unlike the first oxidation peaks, first reduction events appear chemically irreversible and, in most cases, also electrochemically irreversible. However, they also can be correlated in systematic sequences in terms of potential vs σ linear regressions (Figure 106). For instance, for the series with different substituents on the styryl group (parent **1** plus **2–6**) a linear Hammett plot is observed (Figure 106 left side). Compared with the correlation of the first oxidation peaks, the slope is much higher, pointing to first reductions taking place in proximity of, or directly at, the respective phenyl substituent. This assumption is also supported by the peculiar two-peak reduction patterns observed for specific cases like **4** (chlorophenyl substituent) and **6** (acyl substituent). In particular, in the first case first reduction must correspond to the carbon-chloride reductive cleavage [164], while in the second case it should be mostly centred on the formyl group, a feature that would justify why the acyl derivative **6** does not correlate with the Hammett plot of the related compounds **2–5** (Figure 106 left side).

It is worthwhile noticing that the reduction potentials appear by far less negative than the corresponding simple substituted benzenes (for example, benzonitrile reduction takes place at about 2.8 V vs Fc^+/Fc on GC in ACN + 0.1 M $[\text{NEt}_4][\text{BF}_4]$ [165]), which is reasonable considering that in this case the benzene ring is part of an extended conjugated system, including the double bond and the ferrocene ring itself, bearing the highly electron attracting P=S group. Concerning reduction of the phosphane sulphide group, it might correspond to the second reduction peak system, falling in the range between -2.88 V and -3.10 V (Table 10), which is similar to triphenyl phosphane sulphide itself (-2.9 V vs Fc^+/Fc). Figure 106 (left side) also includes the three cases of functionalization on the second cyclopentadienyl ring. While the presence of trialkylsilyl groups in 1' position (**8,9**) is practically unperceivable in respect to the parent case, consistent

with a Hammett constant close to zero, a styrene group (**7**) results in a more positive reduction peak and a more negative oxidation peak (*i.e.* both easier oxidation and reduction), which can be justified in terms of a mesomeric effect as a result of extended conjugation, possibly also via π stacking.

This might also explain the double peak system (Gallery Section 11), which might account for two near-equivalent redox centres (*i.e.* the two styrene-cyclopentadienyl moieties) reciprocally interacting, although the presence of the electron attracting phosphane sulphide on one of the conjugated systems may also contribute to the potential difference.

Similarly, changing the substituents on the phenyl groups on the phosphane sulphide site (parent **1** plus **12–14**, Figure 106 right side), predominantly impacts the reduction potentials (higher slope in the Hammett correlation), whereas the ferrocenyl-based oxidation process is far less affected. This suggests that in this sub-series, the first reduction process moves on the thiophosphinyl groups, in particular the aryl substituents. Notably, the reduction potentials are very similar to the former series. In this case, the positive shifts of the reduction potentials, with respect to simple substituted benzenes, can be justified by the adjacent electron attracting phosphane sulphide group. Again, the expected complex pattern starting with C–Cl bond cleavage is observed for chlorophenyl group reduction in **13**. The two reversible one-electron peak systems observed in the cyanophenyl case **14** might point to a couple of equivalent interacting redox sites, namely the two *gem*-*p*-CN-C₆H₄ substituents of the phosphane sulphide. This hypothesis could also explain why the Hammett correlation is intermediate between the two first reduction peak potentials.

In case of non-substituted phenyl rings (**1**), the challenge is to understand the reduction sequence between, on one side, the phosphane sulphide site, and on the other side the phenyl terminal of the opposite styryl conjugated system. Taking triphenyl phosphane sulphide (**I**) as benchmark for the electrochemical activity

of the P=S group ($E_{p1c} = -2.90$ V vs $Fc^+|Fc$, Table 10), and considering that addition of the weakly electron donating ferrocenyl substituent could result in a negative shift of the signal, we assume the first reduction peak of the ferrocene derivatives (more positive than -2.82 V vs $Fc^+|Fc$ for all styryl-bearing compounds, Table 10) to correspond to an aromatic group rather than to P=S reduction. *Vice versa*, phenyl group reduction, usually located at more negative potentials, as above mentioned, could be promoted in the present compounds, either, on one molecule side, by the strongly electron attracting character of the phosphane sulphide group or, on the other side, by extended π conjugation (also evident in the case of an analogous compound with a ferrocenyl group replacing the phenyl one in the styryl system [160]). Actually, the parent compound **1** appears to fit on both Hammett correlations together with substituted relatives (**12–14** in one case, **2–6** in the other case).

Thus, first reduction could indeed involve a phenyl ring; to decide which one, it is interesting to note that:

- i*) replacement of phenyl by furyl substituents (compare **1** to **16**) only results in slight changes in the CV pattern on both sides;
- ii*) changing from aromatic to aliphatic phosphane sulphide substituents (compare **1** with **15**), the second reduction system at -2.93 V disappears. Thus it should correspond to the reduction of the phenyl groups on the phosphane sulphide site, while the first reduction peak at -2.82 V, still consistent with the Hammett straight line, should correspond to the reduction of the phenyl group of the styrene moiety. Thus, the second reduction of **15** at -3.57 V should correspond to the reduction of the alkyl phosphane sulphide group, which could be significantly less favoured with respect to the aryl case consistently with the well-known higher oxidability of alkyl phosphanes compared to aryl ones.
- iii*) Replacing the styryl moiety with an hydroxymethyl one (compound **10**), locates the first reduction peak at -3.04 V, very close to prototypical

triphenylphosphane sulphide -2.90 V. *Vice versa*, a formyl group in the same position (compound **11**) results in a remarkable positive shift of the first reduction (-2.44 V), since the process specifically concerns the aldehyde group.

In conclusion, the above clues point to consider the phenyl unit of the styrene moiety as the most easily reducible site (-2.7 V vs $\text{Fc}^+|\text{Fc}$) in the prototype **1**.

Concerning interpretation of the phenyl sulphide group reduction, a puzzling feature is the splitting observed in many cases for the second reduction peak, which might even account for interacting redox centers (the aryl substituents), but is hard to analyze, being so close to the background. Among the investigated racemic ferrocenes, we have carefully selected six terms to be separated by preparative chiral HPLC and employed as model probes for the enantioselection voltammetry tests: **1**, the parent compound; **5** and **14**, enabling to evaluate the effect of the same substituent in the styrene vs the phosphane sulphide moiety (notably $-\text{CN}$, also potentially acting as valuable coordination site in stereoselective analysis and catalysis); **16**, enabling to compare heteroaromatic vs aromatic phosphane sulphide substituents; **15**, to compare aliphatic vs aromatic phosphane sulphide substituents; and **7**, a case in which the styrene units could be reciprocally engaged in π -stacking.

Table 10. Electrochemical characterization of planar stereogenic ferrocenes as racemates key CV features in ACN + 0.1 M TBAPF₆. Formal first oxidation potentials (related to the ferrocene site) $E^{\text{ox}}_{\text{Fc}}$, first oxidation and reduction peak potentials, E_{Ia} and E_{Ic} respectively, oxidation and reduction peak potentials for the subsequent redox processes, $E_{\text{IIa,IIIa}}$ and $E_{\text{IIc,IIIc}}$. All potentials are referred to the formal potential of the Fc^+/Fc .

Compound	σ ^[51]	$E^{\text{ox}}_{\text{Fc}}$	$E_{\text{IIc,IIIc}}$	E_{Ic}	E_{Ia}	$E_{\text{IIa,IIIa}}$
	I			-2.90	1.18	1.42
	II	S=PPh ₂ : σ_p =0.47	0.248 ^a			
	III	PPh ₂ : σ_p = 0.19 Fc: σ_p =-0.18/-0.15	0.064 ^a 0.080 ^b 0.101 ^c 0.097 ^d			
	1	Styr: σ_p = -0.07	0.227 (0.200 ^e)	-2.93 -3.07	-2.69	0.26 1.17
	2	OMe: σ_p = -0.27	0.188 (0.165 ^e)	-3.10	-2.81	0.22 0.87, 1.20
	3	Me: σ_p = -0.17	0.216 (0.180 ^e)	-3.07	-2.75	0.26 1.22
	4	Cl: σ_p = 0.23	0.240 (0.210 ^e)	-3.08	-2.52 -2.71	0.28 1.16
	5	CN: σ_p = 0.66	0.267 (0.260 ^e)	-2.88 -3.03	-2.32 -2.49	0.30 1.25, 1.52
	6	CHO: σ_p = 0.42	0.250 (0.245 ^e)	-3.08	-2.22 -2.51 (-2.41st)	0.28 1.32
	7	Styr: σ_p = -0.07	0.180	-3.12	-2.64 -2.79	0.22 0.91, 1.23
	8	SiMe ₃ : σ_p = -0.07	0.223	-2.91 -3.02	-2.69	0.26 1.27
	9	SiEt ₃ : σ_p = -0.07	0.226	-2.88	-2.68	0.26 1.27
	10	CH ₂ OH: σ_p = 0	0.169	-3.21	-3.04	0.20 1.37
	11	CHO: σ_p = 0.35	0.494	-3.39	-2.44	0.55 0.79, 1.20
	12	Me: σ_p = -0.17	0.219	-3.48	-2.75	0.25 1.24
	13	Cl: σ_m = 0.37	0.257	-3.45	-2.56 -2.72	0.29 1.24
	14	CN: σ_p = 0.66	0.281	-2.86 -3.12	-2.20 -2.48	0.32 1.29
	15	Cyclohexyl: σ_p = -0.15	0.185	-3.57	-2.82	0.23 1.23
	16	Furyl: σ_p = 0.02/0.06	0.231	-2.98 -3.14	-2.74	0.27 1.26

c) Separation of the ferrocenyl chiral probes into pure enantiomers by chiral HPLC and CD spectra

The chromatographic enantioseparations of the chiral ferrocenes (Figure 107) were carried out using the polysaccharide-based Chiralpak IG-3 CSP in combination with normal-phase eluents. In the Chiralpak IG-3 CSP the chiral selector amylose tris(3-chloro-5-methylphenylcarbamate) is immobilized onto 3 μm particles of silica. Two types of binary mixtures were used as mobile phases, namely n-hexane/2-propanol 60:40 for the compounds **1**, **7**, **15**, **16**, and n-hexane/2-propanol 40:60 for **5** and **14**. As shown in Figure 107 (left column) an excellent enantiomer separation was achieved in all cases, significantly modulated by the ferrocenyl substituents. Indeed the compound family can provide an attractive model case for a fundamental HPLC study concerning planar stereogenicity compounds, a topic so far surprisingly underexplored. The described process was scaled-up to a semipreparative level, where both enantiomers could be collected in multi-milligram quantities, by performing injections of about 10–20 mg of racemic samples on a 10-mm I.D. Chiralpak IG column. All enantioseparations were achieved in non-overlapping band conditions, and the analytical control of the collected fractions results in an *ee* of >99% for both enantiomers and excellent recovery rates between 90% and 95%. In order to determine the enantiomer elution order, DCM solutions of the collected enantiomers were submitted to circular dichroism (CD) analysis.

As reported in Figure 107 (right column) the shape and the absorption maxima of the CD spectra of the first eluting enantiomers of chiral compounds are strictly correlated with those of the less retained (*S_p*)-enantiomer of **1** and **16**. For both, enantiopure samples could be used for comparison, synthesized according to a previously reported procedure [166]. Therefore, the empirical CD correlation method indicates that all ferrocene analogues studied exhibit the same sense of

chiral recognition, and consequently the same enantiomer elution order on the Chiralpak IG CSP with preferential retention of the (R_p)-enantiomer.

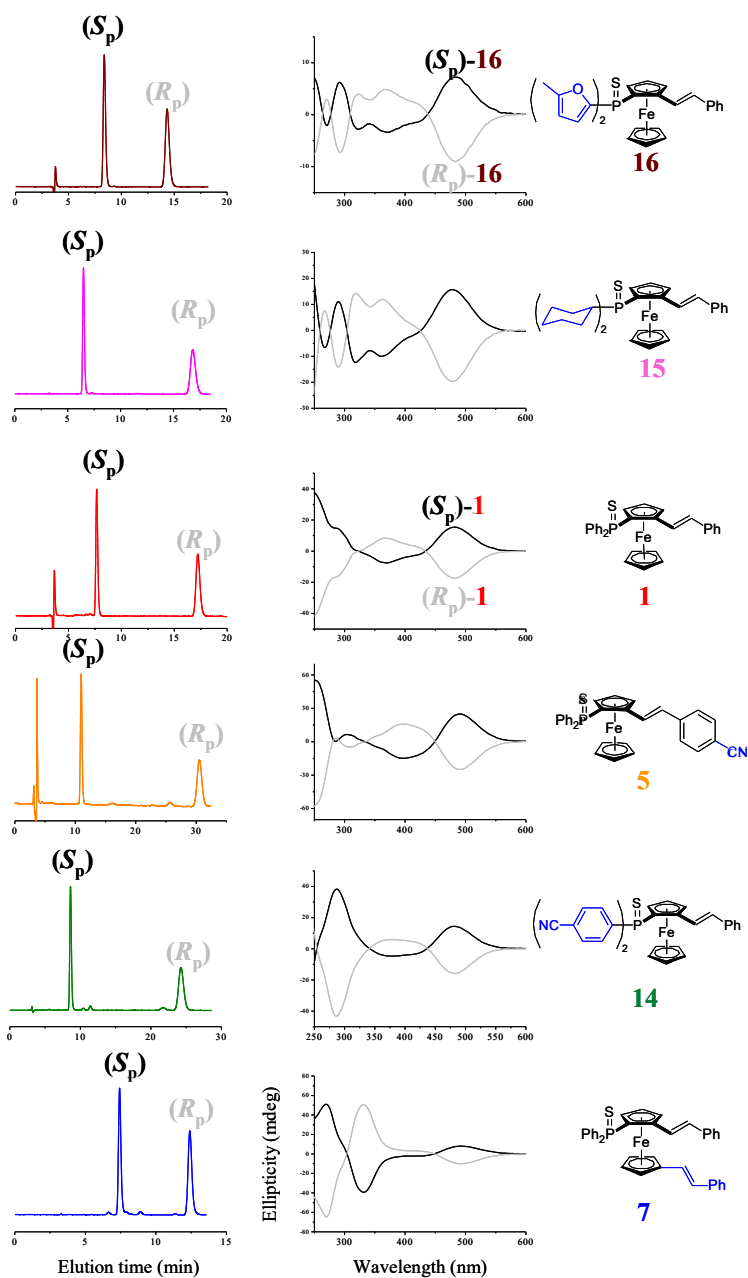


Figure 107. Chiral HPLC separation of the selected probes and circular dichroism spectra of the isolated fractions.

d) *Enantiorecognition in CV experiments*

The enantiopure antipodes of the six selected planar-stereogenicity model cases of the ferrocenes series have been studied in CV experiments on a GC electrode modified with inherently chiral electroactive oligo-(BT₂T₄) films (Figure 108), potentiodynamically electrodeposited in ACN solutions containing 0.1 M TBAPF₆ as supporting electrolyte along the protocol described in the experimental section (a).

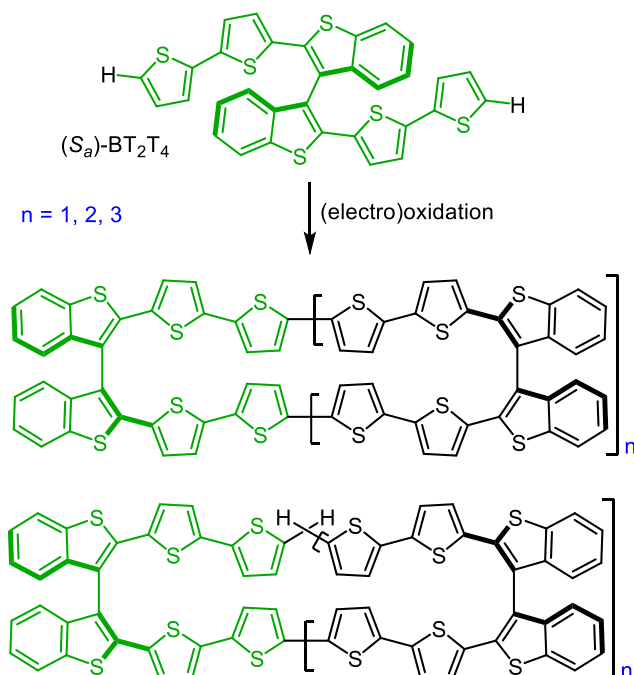


Figure 108. The inherently chiral BT₂T₄ starting monomer in (S_a) configuration (top) together with general formulas of its cyclic (middle) and open oligomers (bottom) constituting the electrodeposited chiral electrode surface [128, 156].

Figure 109 provides a synopsis of the first oxidation CV peaks observed for the (S_p) and the (R_p) enantiomers (red and blue, respectively) of ferrocenes **1,5,7,14,15,16** selected as probes on oligo-(R_a)-(BT₂T₄) and oligo-(S_a)-(BT₂T₄) surfaces.

Contrary to (*S*)-(-)- and (*R*)-(+)-*N,N'*-dimethyl-1-ferrocenylethylamine, a standard chiral ferrocenyl probe with central stereogenicity, which undergoes first oxidation well before the film oxidation, and usually results in (quasi) canonical, reversible peaks on oligo-(BT₂T₄) films [121,128,156], the first oxidation process of the planar-stereogenicity probes is shifted to the onset of the film oxidation, on account of the highly electron attracting phosphane sulphide substituent, as discussed earlier. This can justify the irreversible, non-canonical first oxidation peak shape, quite different from the bare electrode case. Actually, the ferrocenyl-based oxidation process also appears to have some effect on the film oxidation onset, which is usually very reproducible, while it shows significant differences in the considered cases. Nevertheless, a significant peak potential difference is observed for the two enantiomers in all the six probe cases, neatly specular upon inverting either probe or surface configuration. In particular, specular (*i.e.*, energetically equivalent) combinations A (*S_p*)-probe+(*R_a*)-selector and (*R_p*)-probe+(*S_a*)-selector, respectively, have their first oxidation at a less positive potential with respect to specular combinations B (*R_p*)-probe+(*R_a*)-selector and (*S_p*)-probe+(*S_a*)-selector. Actually, the A and B combination couples are reciprocally in a diastereomeric relationship, which implies an energy difference, which is affected by the probe substituents. Notably, the same sequence of configuration combinations applies to all the six selected cases; thus, the considered structural and electronic modifications in respect to the parent molecule **1** do not basically alter the probe-selector configurational matching. However, they appear to remarkably modulate the energy difference between the A and B diastereomeric couples. In particular, taking as benchmark the CV patterns of the parent probe **1** enantiomers (couples A at ~0.27 V; couples B at ~0.33 V; ~50 mV separation),

- in the furyl case **16** the peak difference is only slightly higher (couples A at ~0.32 V; couples B at ~0.38 V; ~60 mV separation)
- the peak difference is significantly narrower in the cyclohexyl derivative **15** (couples A at ~0.30 V; couples B at ~0.33 V; ~30 mV separation) and in the double styrene case **7** (couples A at ~0.30/31 V; couples B at ~0.33 V; ~20/30 mV separation);
- conversely, the peak difference is remarkably larger in both nitrile cases. Compound **14**: couples A at ~0.35/0.36 V; couples B at ~0.43/0.44 V; ~70/90 mV separation. Compound **5**: couples A at ~0.18 V; couples B at ~0.28/0.30 V; ~100/120 mV separation.

Actually, assuming probe-selector matching elements to consist of *i*) in the conjugated systems (with related π conjugation/stacking effects), and *ii*) in the heteroatoms (with related lone pair availability), both largely present in our model cases, and strictly related to the stereogenic elements, the above listed peak differences could be justified as follow:

- the number of available matching elements decreases changing the phenyl substituents (parent compound **1**) into alkyl ones (compound **15**);
- according to the above assumed engagement of both styrene groups in reciprocal π interaction in compound **7**, the availability of these groups for chiral matching should be much lower in **7** respect to **1**;
- conversely the nitrile substituents in **5** and **14** provide powerful additional matching elements (particularly effective in **5**, maybe on account of higher availability). Also the slight improvement observed with furyl blades (in **16**) might be related to the additional heteroatoms.

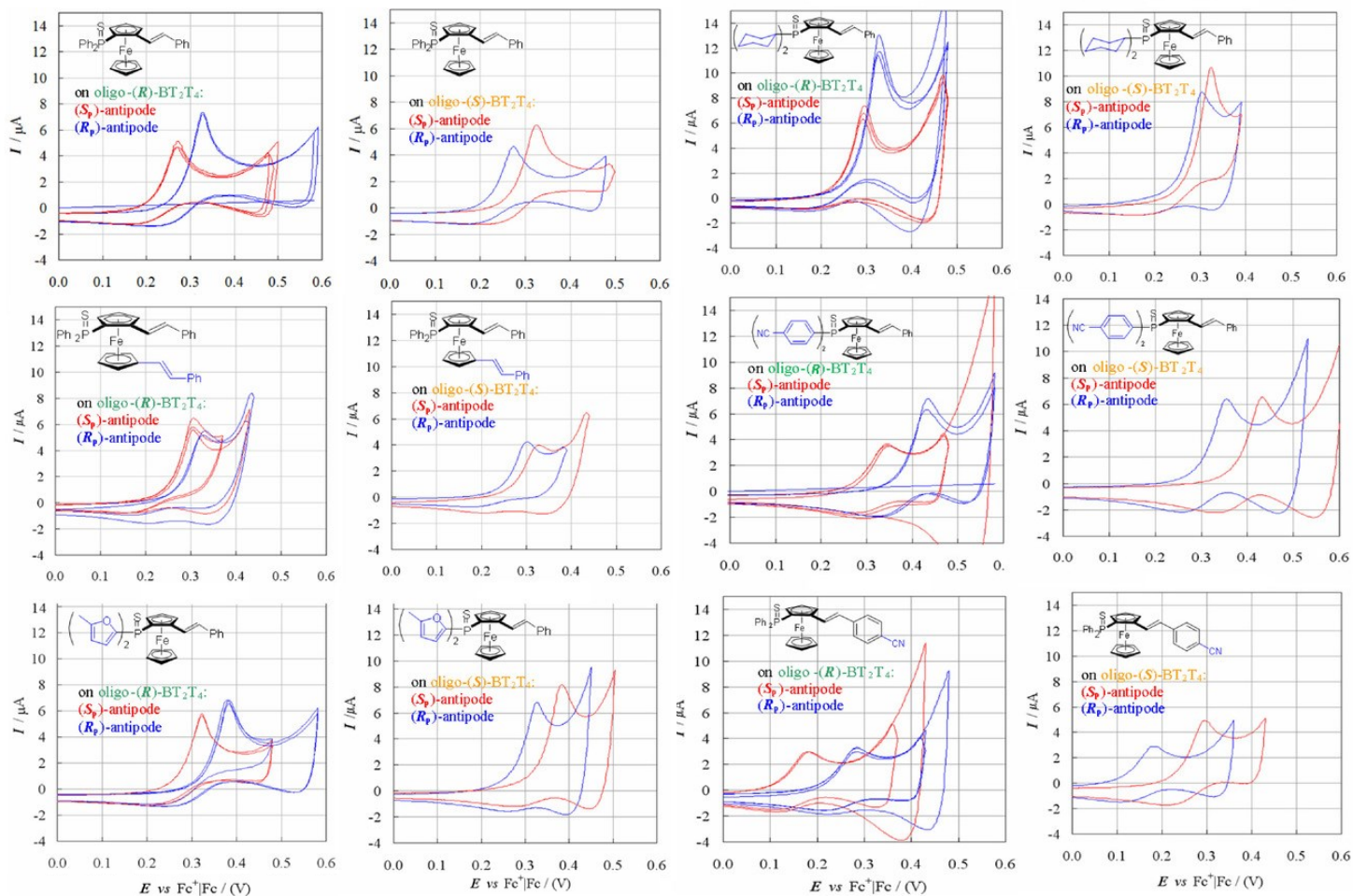


Figure 109. Enantiodiscrimination experiments with planar stereogenicity probes as enantiopure (S_p , red lines) and (R_p , blue lines) antipodes. CV patterns on a GC electrode modified with oligo- (R) -BT₂T₄ films (in green, also providing reproducibility tests as superimposed CV curves) and oligo- (S) -BT₂T₄ films (in orange).

3.2.7 Self-standing inherently chiral membranes: potentiometric tests in an ISE-like setup

Chiral membranes are important tools for enantiomer discrimination or/and separation in a broad range of applications, particularly concerning preparative separations in the pharmaceutical field [167,168]. Many chiral membranes are of natural origin (*e.g.* polysaccharides, polyaminoacid derivatives), or based on natural chiral components (like proteins, amino acids, nucleic acids, enzymes...) while less common so far are membranes based on synthetic chiral components (*e.g.* calixarenes or crown ethers) [167]. However, synthetic chiral membranes have interesting intrinsic features, like wide range of molecular designs and functional properties, equal availability of both enantiomers, and easy synthesis scalability. Among analytical applications of chiral membranes, a potentially interesting one concerns implementation as key components in chiral potentiometric sensors. Furthermore, conducting oligo- or polymer films, enabling charge carrier transduction on account of their combining ion transport and electron transfer, look excellent materials for all-solid-state ISEs. A necessary condition for developing chiral potentiometric sensors is that the chiral probe should be either a charged species, or, if neutral in itself, either ionizable (*e.g.* through an acid-base equilibrium) [169-171], or converted in a salt through alkylation (*e.g.* of suitable nitrogen positions) or functionalization with a convenient charged substituent [172]; as an alternative, a MIP-based sensor can first capture a neutral chiral probe and then exchange it with uncharged mimic species [173,174].

Self-standing chiral electroactive synthetic membranes have been investigated, prepared by oxidative electrooligomerization of a thiophene-based “inherently chiral” electroactive monomer on indium tin oxide (ITO) or fluorine-doped tin oxide (FTO) electrodes, followed by detachment of the electrodeposited thin films in aqueous solution. The membranes, possibly mesoporous, consist of a

mixture of open and cyclic “inherently chiral” oligomers and the electrosynthesis conditions significantly modulate the oligomer distribution. Circular dichroism confirms that (*R*)- or (*S*)- enantiopure films are obtained, starting from the corresponding (*R*)- or (*S*)- enantiopure monomers. Reliable transmembrane potential readings are obtained in preliminary tests in ion selective electrode (ISE)-like setups, consistent with those predicted considering the membrane features, offering a first step towards extension of the protocol to chiral experiments.

a) Electrosynthesis and peeling-off of the inherently chiral membrane and implementation in an ISE-like setup

The inherently chiral membranes were prepared by electrooligomerization of the BT₂T₄ monomer (racemate or enantiopure) ~0.0025–0.001 M in ACN +0.1 M TBAPF₆ (or, in a single case, in CD₃CN+0.1M LiClO₄) in a glass minicell (working volume ~2 cm³) including an indium tin oxide ITO (Kintech Company 10 Ω/sq) or in some cases a fluorine doped tin oxide FTO (Sigma Aldrich 10 Ω/sq) working electrode, a Pt counter electrode and an aqueous saturated calomel electrode SCE as reference electrode. The membrane preparation (Figure 110) was carried out by repeated potential cycling around the BT₂T₄ monomer (enantiopure or racemate) first oxidation peak (in the 0-1.35 V vs SCE range), at 0.05 V/s scan rate. In particular, 72 or 108 deposition cycles were performed, in order to achieve sufficient film thickness yielding a detachable self-standing membrane: membranes grown with 108 cycles were easier implemented in the ISE setup, while membranes grown with 72 cycles were more convenient for the chiroptical characterization by electronic circular dichroism in transmission mode, requiring a certain degree of membrane transparency. Transferring the thus modified ITO electrode into deionized water, the thin film could be

detached, forming a self-supported membrane, which could be managed using a glass pipette.

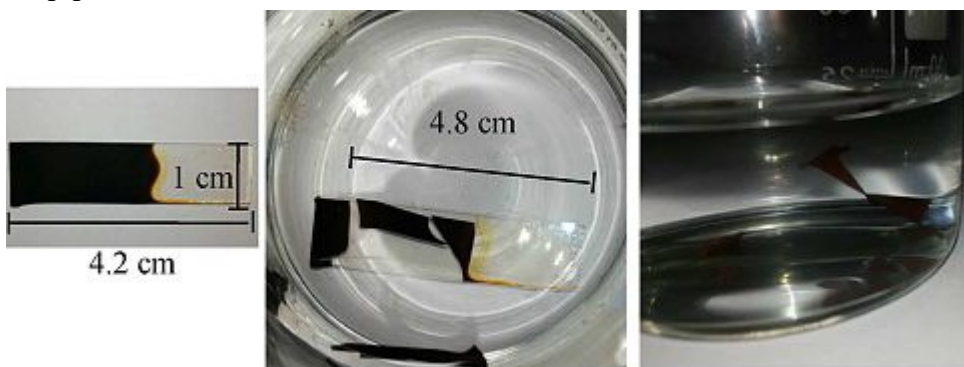


Figure 110. From left to right: electro-synthesized membrane on the ITO electrode support, while being detached, and stored in water.

The membranes were then implemented in a commercial Electrode body for ISE with Lemo connector for mounting of ion-selective membranes (Figure 111), with coaxial cable and connector (Fluka, now corresponding to Sigma Aldrich/Merck 45137). Such ISE body includes an Ag|AgCl electrode, acting as ion/electron transducer through the Nernstian half-reaction $\text{AgCl} + e^- \rightarrow \text{Ag} + \text{Cl}^-$ with electrode potential $E = E^\circ_{\text{AgCl}} - k \log a_{\text{Cl}^-}$. It also acts as internal fixed potential reference electrode, a fixed a_{Cl^-} being provided by the internal solution, based on a chloride binary electrolyte, according to the experiment, 0.01 m KCl, 0.01 m CaCl_2 ; 0.01 M HCl and 0.01 M L-tyrosine hydrochloride.



Figure 111. Assembling an electro-synthesized membrane in the commercial ISE body.

b) Electrosynthesis, HR LDI and ECD spectra of membranes

The electrooligomerization of BT₂T₄ monomer results in electroactive films consisting of an oligomer mixture (from LDI [121]; in particular, open and closed dimers were detected in films deposited on ITO [128]) that could include both open and closed terms, which have been obtained separately by chemical route to be electrochemically and chiroptically characterized [128,175]. Their formation can be explained in terms of the typical thiophene radical cation coupling mechanism [81], with the monomer configuration playing a significant role, too. For example, it has been pointed out that the configuration of (*R,R*)- or (*S,S*)- open dimers promotes cyclization by coupling of the free terminals, unlike the case of (*R,S*)- open dimers, usually resulting in further monomer addition, promoting cyclic trimer formation [175]. The films also exhibited high growth rate and regularity even after many deposition cycles, which can be related to the high three-dimensional character of the starting monomer (on account of the high torsional angle) and to its offering only two homotopic terminals available for the radical cation coupling.

The detached films were submitted to high resolution LDI analysis, pointing to a mixture of open and closed oligomers, including (Figure 112) dimers as prevailing species, as well as trimers, in smaller amounts, and tetramers, in even smaller amounts (in some cases hardly detectable). In particular, by comparison with model LDI spectra for pure cyclic oligomers [128]:

i) in all cases in which 0.1 M TBAPF₆ was adopted as supporting electrolyte both open and closed dimers were present in significant amounts. In fact, the approximately estimated closed to open dimer ratio ranges from 2.6–1.6 for films grown on FTO (respectively, from racemate or enantiopure monomer) to 1.13/0.95–0.74 for films grown on ITO (respectively, from racemate, with/without contact with water, or enantiopure monomer), to 0.48 for the film

undergoing treatment with isopropanol, resulting in a remarkable colour change from orange to vivid red.

ii) in the same cases, the closed to open estimated ratios for trimers are much lower than the corresponding dimer ones at constant conditions; however, again, significantly higher values are obtained on FTO (1.0–0.7 from racemate or enantiopure monomer) respect to ITO (0.11–0.36 from racemate or enantiopure monomer).

iii) in the same cases, a quantitative estimation is difficult for the tetramer ratio on account of the low peaks and background noise; however, as for the trimer case, closed ones appear to neatly prevail on open ones.

iv) a peak system is also observed in the m/z range=1217.8–1223.8, *i. e.* slightly above the dimer one, for which we are considering the possibility of sulfur overoxidation (*e. g.* to sulfoxide), particularly involving the terminal positions in the open dimers.

v) Incidentally, it is worthwhile noticing that, as expected considering the increasing probability of finding isotopes in a molecule with increasing number of atoms constituting it, the most intense LDI peak in each peak system shifts from the first one for dimers to the third one for trimers, to the fourth one for tetramers.

vi) racemic BT₂T₄ film was electrodeposited from LiClO₄ as supporting electrolyte (rather than TBAPF₆) in combination with CD₃CN as solvent. Strikingly, in this case the film appeared being mostly constituted by closed species, chiefly closed dimers.

Conditions	Closed dimer	Open dimer	Closed trimer	Open trimer
Racem., CH ₃ CN, TBAPF ₆ , on ITO, scratched off	1	1.1	0.006	0.055
Racem., CH ₃ CN, TBAPF ₆ , on ITO, detached in W	1	0.89	0.008	0.069
Racem., CH ₃ CN, TBAPF ₆ , on FTO, detached in W	1	0.39	0.024	0.018
Racem., CD ₃ CN, LiClO ₄ , on ITO, scratched off	1	0.05	0.005	n.q.

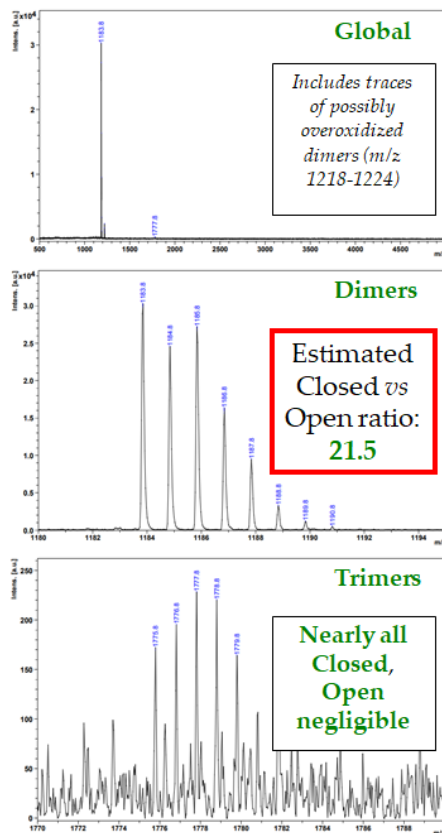


Figure 112. Comparison of relative observed/estimated intensities of main HR LDI peaks for the four main film components, referred to the closed dimer one, as a function of film preparation

Starting from (*R*)- or (*S*)-enantiopure BT₂T₄ films, the corresponding (*R*)- or (*S*)-enantiopure membranes are obtained. We confirmed it by electronic circular dichroism ECD, applied to both (*i*) films still attached to the ITO or FTO electrode supports or (*ii*) detached and sandwiched between two quartz slides (Figure 113). Reproducibility of the ECD signal while changing the probe orientation and/or side proves that it is genuine ECD without important contributions from linear dichroism and circular birefringence. Care must be taken to avoid distortions due to absorption flattening effects, as reported in references [176,177]; in this case good results were obtained with a standard CD

setup because of the high quality of films, macroscopically regular and intact also after detachment. Neatly specular (particularly in the FTO case) bisignated signals were obtained for films obtained from BT_2T_4 enantiomers (Figure 113), confirming that chirality and its CD sign are fully transferred from monomers to oligomer films; ellipticity maxima are red shifted respect to the monomer ones [121], consistently with the improved conjugation of the oligomers. It can be also noticed that a larger useful wavelength range is available in the case of the detached membranes, due to the absence of the absorbing oxide support, extension below 250 nm was not possible due to film thickness.

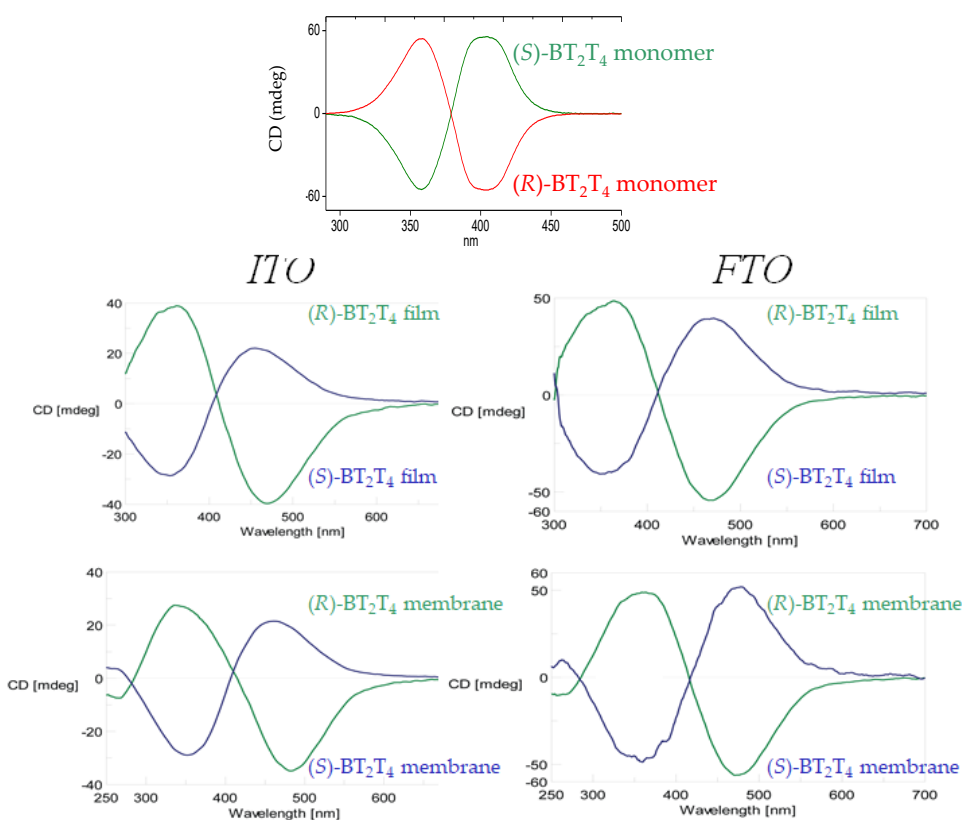


Figure 113. Top: ECD spectra for $(R)\text{-}$ or $(S)\text{-BT}_2\text{T}_4$ monomers (red and green respectively). Bottom: ECD spectra for $(R)\text{-}$ or $(S)\text{-BT}_2\text{T}_4$ films (green and blue lines, respectively) grown on ITO (left) and FTO (right), both as such and as detached membranes.

c) Potentiometric membrane tests in a classical ISE-like setup

The electrosynthesized membranes were assembled in an ISE-like setup placing them on a Teflon[®] nozzle and filling with the latter the hole in the ISE body cap (Figure 114). They could thus be tested in a potentiometric cell consisting of a sensing membrane electrode and an external reference electrode with in-built salt bridge immersed in a chloride solution (with Pt terminals as conventional notation for a regularly open galvanic cell, and with “commercial” polarities, implying the membrane sensing electrode with shielded cable to be connected to the + shielded input of the high-resistance electrometer, no matter what would be the true cell polarity, *i. e.* resulting in a positive reversible potential difference).

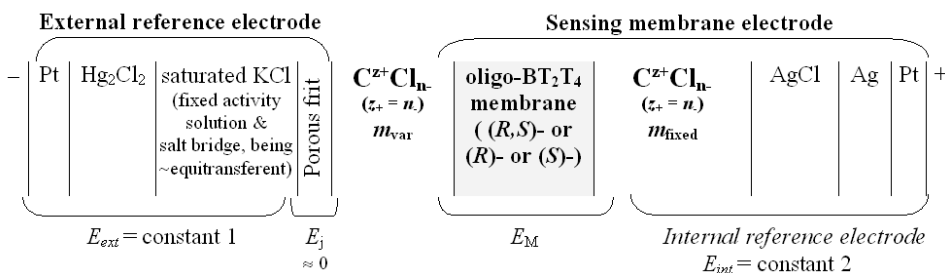


Figure 114. Detailed galvanic chain of the whole cell assembly.

The reversible potential difference of the cell can be expressed as equation (2)

$$E_{\text{cell}} = E_{\text{int}} - E_{\text{ext}} + E_M + E_j \quad (2)$$

Where, E_{ext} is the (constant) potential of the external reference electrode, E_{int} is the (constant) potential of the internal reference electrode, E_M is the membrane potential and E_j is the liquid junction potential, assumed to be minimized by the salt bridge [Eqs. (3) and (4)].

$$E_{\text{ext}} = E^{\circ}_{\text{Hg}_2\text{Cl}_2|\text{Hg}} - k \log a_{\text{Cl}} \text{ in saturated KCl (constant 1)} \quad (3)$$

$$E_{\text{int}} = E^{\circ}_{\text{AgCl}|\text{Ag}} - k \log a_{\text{Cl}} \text{ in CCl}_n \text{ at fixed } m \text{ (constant 2)} \quad (4)$$

Thus, the $(E_{\text{int}} - E_{\text{ext}})$ difference is a constant which can be calculated, although with some approximation as a consequence of the conventional nature of single

ion activities. As an alternative, it can be experimentally estimated, by measuring the E_{cell} with identical solutions on the two membrane sides (see further on).

Moreover, $E_j \approx 0$, since the liquid junction potential between external reference electrode and variable solution should be minimized by the saturated KCl salt bridge (especially considering the moderate concentration range of the variable solutions).

Thus we can study the transmembrane potential E_M as

$$E_M \approx E_{\text{cell}} - (E_{\text{int}} - E_{\text{ext}}) \quad (5)$$

To discuss the dependency of the transmembrane potential E_M on the nature and activity of the two adjacent solutions, it is useful to remember that

(i) at a non-selective junction between two different solutions in the same solvent, like *e.g.* through a non-selective diaphragm like a porous frit, a potential difference arises, usually termed "liquid junction potential", proportional to the ion activity gradients, and modulated by the differences in cation and anion diffusion coefficients D_i , and implicitly in mobilities u_i (the two quantities being interrelated through the Nernst Einstein equation) in the solvent considered. This can be expressed as

$$dE_{\text{non ion-selective junction}} = \sum \tau_j k d \log a_j = \sum (t_j/z_j) k d \log a_j \quad (6)$$

in terms of transference numbers in the considered medium, either t_i (classical transference numbers) or τ_j ("signed" transference numbers introduced by Scatchard):

$$t_j = q_j / (\sum q_j) = z_j u_j M_j / (\sum z_j u_j M_j); \quad \tau_j = t_j / z_j \quad \sum t_j = \sum \tau_j z_j = 1 \quad (7)$$

(ii) however, ion transference numbers can be modified by specific interactions with "non-innocent" diaphragms; in particular, in the case of an ion-selective membrane, $t_i \rightarrow 1$ for the so called "primary" ion i and $t_j \rightarrow 0$ for the remaining ones; thus equation (5) modifies into

$$dE_{\text{ion-selective junction}} = \tau_i k d \log a_i + \sum \tau_j k d \log a_j = (t_i/z_i) k d \log a_i + \sum (t_j/z_j) k d \log a_j$$

$$\text{with } t_i \rightarrow 1, \text{ all } t_j \rightarrow 0; t_i + \sum t_j = \tau_i z_i + \sum \tau_j z_j = 1 \quad (8)$$

Thus, for an ideal ion-selective membrane

$$dE_{\text{ion-selective junction}} \approx (t_i/z_i)k d \log a_i \rightarrow k/z_i d \log a_i \quad (9)$$

Actually the potential response of an ion-selective electrode is based on the pseudo-Nernstian relationship (9), integrated between the "primary" ion activity in the internal and external solution, and with the addition of the constant potential of the internal reference electrode, expressed as follows (with "commercial" polarity convention):

$$E_{\text{ISE}} \approx E_{\text{int ref}} + k/z_i \log(a_{i,\text{var}}''/a_{i,\text{fixed}}') \approx E_{\text{int ref}} + k/z_j \log(a_{i,\text{var}}''/a_{i,\text{fixed}}') \approx U + k/z_j \log(a_{i,\text{var}})$$

$$\text{(or } U + Q \log(a_{i,\text{var}}) \text{ with a non-ideal membrane)} \quad (10)$$

Different approaches can be adopted to develop an ion-selective membrane [178-180]; in any case, a fundamental issue concerns preventing the counter ion ingress in the membrane concurrently with the primary one to preserve the necessary electroneutrality condition. For the present discussion it is useful to consider the popular, well known case of the so called "liquid" ion-selective membranes, in which an inert polymer like PVC supports a hydrophobic, very viscous solvent/plastifier in which a ionophore is dissolved, selective to the desired primary ion i . Particularly when such ionophore is neutral, it is necessary to add a fourth component in the "membrane cocktail", *i.e.* an electrolyte additive ("ion exchanger") in which the ion with the same sign as primary ion i must have high affinity for the external solvent phase while the ion with opposite sign must have high affinity for the membrane phase. Thus electroneutrality is maintained by exchange of same sign ions rather than concurrent ingress of cation and anion. Now, the present chiral membranes include most of the functionalities of the above described ISE components, namely (*i*) the support (oligomeric rather than polymeric), (*ii*) the selector (through the heteroatoms and aromatic systems,

particularly cyclic ones) and (iii) the ion-to-electron transducer (when implemented in solid-ISE setups). On the other hand, in the present form it lacks the ion exchanger functionality, although we are developing a starting monomer modified with fixed charge groups. Moreover, the membrane appears mesoporous (as above discussed), with pore sizes of the order of tens of nanometers, which could be modified by changes in the deposition protocol.

For these reasons, we discuss the transmembrane potentials starting from an assumption of non-selective junctions between solutions of a single binary electrolyte $C^{z^+} A^{z^-}$; thus equation (5) becomes

$$dE = (t_C/z_C)kd\log a_C + (t_A/z_A)kd\log a_A = (t_C/z_C)kd\log a_C - (t_A/z_A)kd\log a_A \quad (11)$$

with $a_C = m_C\gamma_C$ (or $c_C\gamma_C$) $a_A = m_A\gamma_A$ (or $c_A\gamma_A$)

According to the Debye-Hückel convention concerning single ion coefficients:

$$\gamma_C = \gamma_{\pm CA} z_C / |z_A| \quad \gamma_A = \gamma_{\pm CA} |z_A| / z_C \quad (12)$$

Moreover,

$$m_C = n_C m_{CA} \text{ and } m_A = n_A m_{CA} \quad (13)$$

$$\text{and } a_{CA} = n_C^{n_C} n_A^{n_A} (m_{CA} \gamma_{\pm CA})^{(n_C+n_A)} \quad (14)$$

Therefore

$$dE = (t_C/z_C)kd\log n_C m_{CA} \gamma_{\pm CA}^{z_C/|z_A|} - (t_A/z_A)kd\log n_A m_{CA} \gamma_{\pm CA}^{|z_A|/z_C} = (t_C/z_C)kd\log n_C + (t_C/z_C)kd\log m_{CA} + (t_C/|z_A|)kd\log \gamma_{\pm CA} - (t_A/z_A)kd\log n_A - (t_A/|z_A|)kd\log m_{CA} - (t_A/z_C)kd\log \gamma_{\pm CA} = t_C/z_C - (t_A/|z_A|)kd\log m_{CA} + (t_C/|z_A| - t_A/z_C)kd\log \gamma_{\pm CA} \quad (15)$$

yielding for a 1:1 electrolyte like HCl or KCl:

$$dE = (t_C - t_A)kd\log m_{CA} + (t_C - t_A)kd\log \gamma_{\pm CA} = (t_C - t_A)kd\log m_{CA} \gamma_{\pm CA} = (t_C - t_A)kd\log a_{CA}^{1/2} = (t_C - t_A)kd\log a_{C=A} \quad (16)$$

and for a 2:1 electrolyte like $CaCl_2$:

$$dE = (t_C/2 - t_A)kd\log m_{CA} + (t_C - t_A/2)kd\log \gamma_{\pm CA} = (t_C/2 - t_A)kd\log m_C + (t_C - t_A/2)k/2d\log \gamma_C \text{ or } (t_C/2 - t_A)kd\log m_A + (t_C - t_A/2)2kd\log \gamma_A \quad (17)$$

Since

$$t_i = z_i u_i M_i / \sum z_i u_i M_i \quad (18)$$

and for a binary electrolyte

$$t_+ = n_+ \lambda_+ / (n_+ \lambda_+ + n_- \lambda_-) \quad t_- = n_- \lambda_- / (n_+ \lambda_+ + n_- \lambda_-) \quad (19)$$

with λ = ion molar conductances, approximating λ values with tabulated λ° ones, we get for KCl:

$$dE \approx (t_{C^-} - t_A) k d \log a_{C=A} \approx -0.0017 d \log a_{C=A} \quad (20)$$

for HCl:

$$dE \approx (t_{C^-} - t_A) k d \log a_{C=A} \approx 0.037 d \log a_{C=A} \quad (21)$$

for CaCl₂:

$$dE \approx (t_{C/2} - t_A) k d \log m_C + (t_{C^-} - t_A/2) k/2 d \log \gamma_C \approx -0.0207 d \log m_C + 0.0044 d \log \gamma_C \quad (22)$$

The experimental membrane potential data observed for the galvanic cell with a racemate membrane and KCl, or HCl, or CaCl₂ as the binary electrolyte at fixed concentration in the internal ISE solution and at variable concentration in the external solution are reported in Table 11 and plotted as a function of $\log a_{C^+}$ in Figure 115. They show excellent consistency with the predicted values of both E_m vs $\log m_C$ slopes and of $(E_{int} - E_{ext})$ biases, confirming that reliable potentials readings can be made across the new membranes in electrochemical setups, as well as confirming the assumption that the membranes in their present state (mesoporosity, absence of fixed negative charges) must behave as non-selective junctions, particularly towards the small ions of the electrolytes chosen as models. Finally, we also report a preliminary test (Table 11 last row, Figure 115), carried out with a (*R*)-enantiopure membrane and L-tyrosine hydrochloride, *i.e.* a chloride probe with a chiral cation, significantly larger than the former achiral ones.

Table 11. Potentiometric tests of transmembrane potential readings with different chloride electrolytes at constant m_{fixed} and different m_{var} : overall cell potential differences $E_{\text{rev,cell}}$; estimated and experimental values of potential difference between internal and external reference electrodes ($E_{\text{int}}-E_{\text{ext}}$); membrane potentials E_{membrane} estimated subtracting ($E_{\text{int}}-E_{\text{ext}}$) from $E_{\text{rev,cell}}$; estimated and experimental values of E_{membrane} vs $\log a_{\text{C}^+}$ slopes.

	m_{var} / (mol kg ⁻¹)	γ_{\pm}	$\log a_{\text{C}^+}$, var	$E_{\text{rev, cell}}$ /V	E_{membrane} /V	
KCl <i>racemic</i> membrane, 108 cycles	0.000295				-0.0008	E_{membrane} vs $\log a_{\text{K}^+}$ slope -0.0017 V (est.)
	0.000992	0.980	-3.54	0.0978	-0.0014	
	0.00327	0.965	-3.02	0.0972	0.0001	0.0003±0.0004 V (exp.)
	0.0109	0.939	-2.51	0.0987	0.0018	
	0.0331	0.897	-2.01	0.1004	0.0008	$(E_{\text{int}} - E_{\text{ext}})$ 0.099 V (est.) 0.097 V (exp.)
	0.112	0.841	-1.56	0.0994	-0.0002	
	0.411	0.760	-1.07	0.0984	-0.0006	
m_{fixed} 0.00986	0.902	-2.05	0.0980			
HCl <i>racemic</i> membrane, 108 cycles	0.000295					E_{membrane} vs $\log a_{\text{H}^+}$ slope -0.037 V (est.)
	0.000983	0.981	-3.54	0.0381	-0.0559	
	0.00298	0.966	-3.02	0.0596	-0.0344	0.0386±0.0007 V (exp.)
	0.00996	0.943	-2.55	0.0780	-0.016	
	0.0301	0.905	-2.05	0.0940	0	$(E_{\text{int}} - E_{\text{est}})$ 0.099 V (est.) 0.094 V (exp.)
	0.100	0.857	-1.59	0.1136	0.0196	
	0.00990	0.797	-1.10	0.134	0.04	
CaCl₂ <i>racemic</i> membrane, 72 cycles	0.000364				0.0239	E_{membrane} vs $\log a_{\text{Ca}^{2+}}$ slope [-0.0207 V est. neglecting activity coefficient]
	0.00102	0.929	-3.50	0.1094	0.0172	
	0.00330	0.887	-3.09	0.1027	0.0107	-0.0213±0.0016V (exp.)
	0.0110	0.818	-2.66	0.0962	0.0017	
	0.0327	0.720	-2.24	0.0872	-0.0076	$(E_{\text{int}} - E_{\text{ext}})$ 0.083 V (est.) 0.087 V (exp.)
	0.110	0.617	-1.90	0.0779	-0.0186	
	0.00991	0.509	-1.54	0.0669		
CaCl₂ <i>racemic</i> membrane, 108 cycles	0.000286				0.0240	E_{membrane} vs $\log a_{\text{Ca}^{2+}}$ slope [-0.0207 V est. neglecting activity coefficient]
	0.00107	0.936	-3.60	0.1103	0.0176	
	0.00312	0.885	-3.08	0.1039	0.0112	-0.0207±0.0047V (exp.)
	0.0110	0.822	-2.68	0.0975	0.0019	
	0.0334	0.720	-2.24	0.0882	-0.0079	$(E_{\text{int}} - E_{\text{ext}})$ 0.083 V (est.) 0.088 V (exp.)
	0.111	0.615	-1.90	0.0784	-0.0186	
	0.0099	0.509	-1.54	0.0677		
CaCl₂ <i>racemic</i> membrane, 108 cycles	0.000378				0.0244	E_{membrane} vs $\log a_{\text{Ca}^{2+}}$ slope [-0.0207 V est. neglecting activity coefficient]
	0.00104	0.928	-3.49	0.1106	0.0180	
	0.00270	0.886	-3.09	0.1039	0.0116	-0.0220±0.001V (exp.)
	0.0104	0.832	-2.73	0.0975	0.0023	
	0.0296	0.725	-2.26	0.0882	-0.0075	$(E_{\text{int}} - E_{\text{ext}})$ 0.083 V (est.) 0.088 V (exp.)
	0.103	0.627	-1.93	0.0784	-0.0182	
	0.0099	0.514	-1.56	0.0677		
L-tyrosine hydrochloride (<i>R</i>)- membrane, 108 cycles	0.000302				0.0341	E_{membrane} vs $\log m_{\text{HTyr}^+}$ slope -0.0226±0.0002 V (exp.) →est. transference numbers $t_{\text{HTyr}^+} = 0.308$ $t_{\text{Cl}^-} = 0.692$ $(E_{\text{int}} - E_{\text{est}})$ 0.101 V (exp.)
	0.00110		-3.52	0.1348	0.0218	
	0.00327		-2.96	0.1225	0.0110	
	0.0115		-2.49	0.1117	-0.0012	
	0.0332		-1.94	0.0995	-0.0122	
	0.00988		-1.48	0.0885		

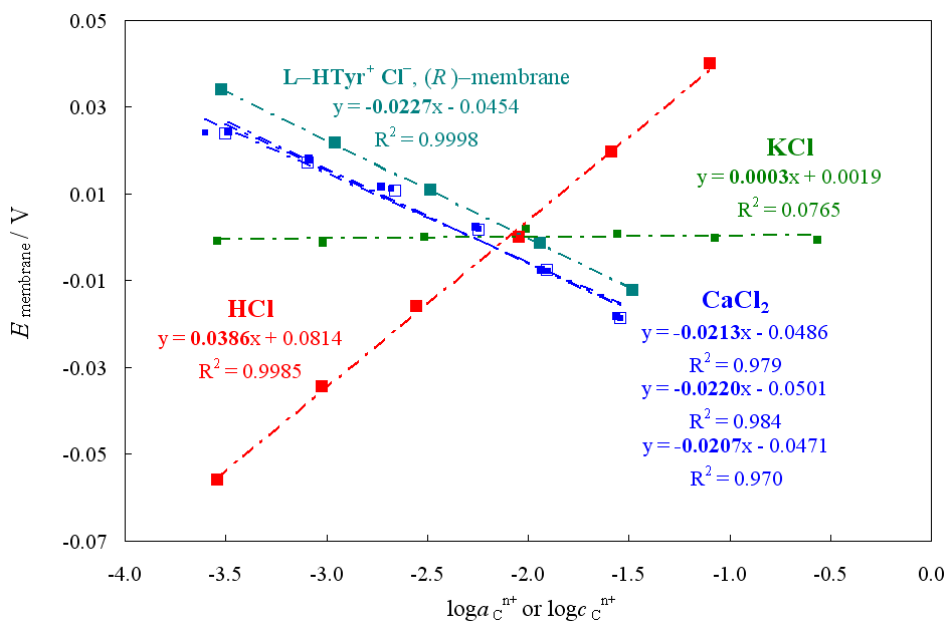


Figure 115. Transmembrane potential readings with racemate or enantiopure membranes in ISE-like setups with different chloride solutions, as a logarithmic function of the cation activity in the external variable solution.

The transmembrane potential readings, plotted in this case vs the logarithm of the cation concentration as an acceptable approximation for the cation activity, show, again, a good linear trend, as well as a -0.0226 slope, implying $t_{\text{HTyr}^+} = 0.308$ and $t_{\text{Cl}^-} = 0.692$, in consistency with the significant bulkiness difference between the two ions.

Actually reliable transmembrane potential readings are obtained in preliminary tests in ISE-like setups, in excellent consistency with those predicted considering the membrane features.

Such verification of the protocol soundness is an important first step towards its extension to a systematic program of chiral potentiometric tests performed on all

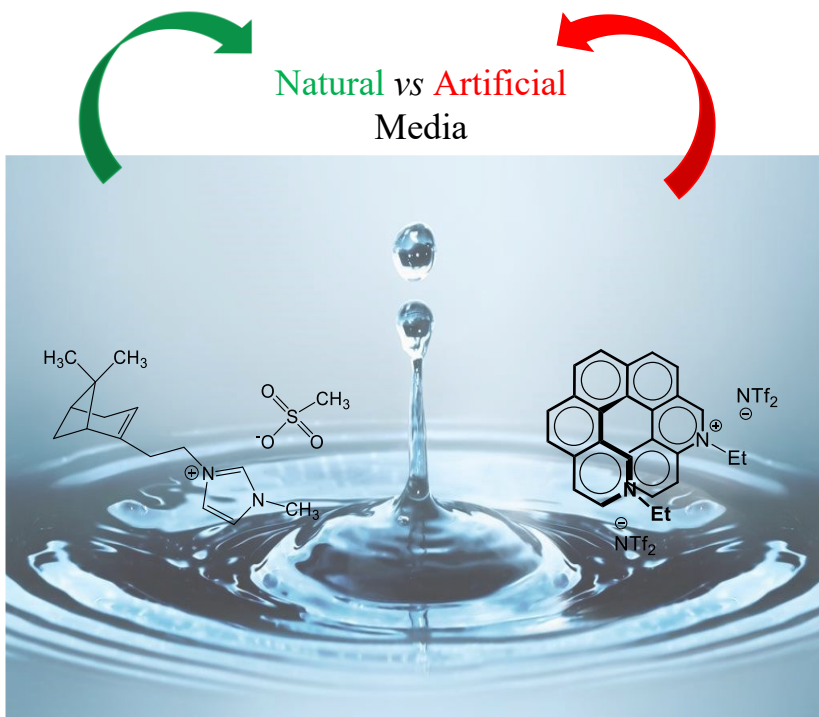
combinations of chiral membrane configurations and of chiral ion concentrations and configurations on each membrane side.

Although these membranes are not ion-selective in their present form for the above discussed reasons, the slopes of their linear E vs $\log a$ characteristics reliably account for the mobility difference between cation and anion in the electrolyte solutions on the membrane sides. Such a difference might be modulated not only by the ion nature, as in these first tests, but also, operating with enantiopure membranes and enantiopure ions, by different combinations of membrane and ion configurations.

We are also looking forward to modulating porosity and/or adding an in-built ion exchanger functionality (thus possibly endowing the membrane with ion-selectivity properties), as well as to comparing the membrane performance in classical ISE setups with solid-state ISE ones.

Chapter 4

Chiral media



Following my former research during my master thesis, in this three-year PhD project, several new chiral selectors were studied and employed as low concentration chiral additives in achiral commercial ionic liquid or as bulk media, testing their performances in enantioselection experiments.

As it could be expected, the enantiodiscrimination ability appears to be significantly modulated by the ICIL molecular structure (and, in the case of IL+chiral additive systems, by the IL molecular structure as well as by the chiral additive molecular structure and concentration).

Large peak potential differences have been observed in Ionic Liquids (ILs) with the addition of molecular salts with “inherently chiral” cations of axial or helical

stereogenicity [134,135,137,181,182], either solid or liquid at room temperature, and better performances could be obtained employing the latter ones, inherently chiral ionic liquids (ICILs), as bulk media.

However, the less conspicuous but significant potential differences observed in ionic liquid media with chirality arising from the presence of one or more stereocenters [182] should be regarded with high interest, too.

Chiral selectors can be either of natural or artificial origin. Although many natural chiral selectors are currently employed in electroanalysis, the second alternative looks particularly advantageous for many reasons, including the virtually unlimited range of tailored structures, the possibility to have both enantiomers of a given selector equally available, the possibility to optimize production to reduce costs. Thus, efforts are increasingly being devoted to achieve chiral electroanalysis based on artificial selectors, in fact I have studied, during this three-year thesis project, different artificial inherently chiral media:

In particular, the performances of natural based and artificial media were compared, studying:

- a new family of CILs (with bile acid building blocks) [183], after the terpenoid-based CIL family studied in this paper [182], for a first systematic investigation of features and enantiodiscrimination ability in electrochemistry and electroanalysis; the family included a group of six CILs with the chiral building block implemented in the cation and two different achiral anions: bistriflimide (NTf₂) and tosylate (OTs) and a second group of four CILs with the chiral building block implemented in the carboxylate anion, combined with four different cations, *i.e.* 1-butyl-3-methylimidazolium, trioctyl methyl ammonium, trioctyl methyl phosphonium, tributyl methyl phosphonium.

- A further attractive CIL family with chiral “tweezer” dications consisting of a biobased isomannide or isosorbide chiral core with two cation arms including heteroatoms and aromatic systems providing coordination elements for selector/probe interactions.
- An inherently chiral salt, based on a 3,3'-bipyridine scaffold (tested as both low concentration chiral additive and as bulk media, in enantioselection experiments, using the enantiomers of chiral ferrocene, also coexistent in the same solution, as well as (+)-catechin and (-)-epicatechin).
- A family of diazahelicenes [181], neutral, mono- and di-alkylated (with ethyl chains), which are inherently chiral but with a different stereogenic element respect to the ICILs reported above, *i.e.* a helix instead of an axis. Their selectivity was investigated using as chiral probes a chiral ferrocene as well as tryptophan.
- A family of chiral QUINAPs, employed as low concentration chiral additives in enantioselection tests.
- Moreover, an inherently chiral monomer (*N*-Hex-Ind)₂Ph₂T₄ (unsuitable for electrooligomerization, as reported in 3.2.2) [140] was tested as low concentration chiral additive in an achiral commercial ionic liquid, because no significant film formation was achieved performing different CV cycles around the potential corresponding to the activation of the α homotopic positions on the thiophene wings (such behaviour was probably due to the high solubility of the oligomers, originating from the long alkyl chains).

Finally, the application of another advanced chiral media was exploited, studying the enantioselection ability and properties of chiral Deep Eutectic Solvents (DESS) of natural origin [184]. The DESS employed in this research project

consist of a mixture of at least two components, a hydrogen bond acceptor (HBA) and a hydrogen bond donor (HBD), which are able to self-associate to form a new eutectic phase characterized by a melting point ($< 100^{\circ}\text{C}$) lower than that of each individual component and significantly lower than the predicted one for an ideal case.

4.1 General Experimental setup for the electrochemical measurements: characterization of the chiral selectors and enantioselection tests

Cyclic Voltammetry (CV) and Differential Pulse Voltammetry (DPV) experiments were performed using an Autolab PGSTAT potentiostat (Eco-Chemie, Utrecht, The Netherlands), controlled by a PC with the GPES software provided by the same manufacturer.

The electrochemical characterization of the (inherently) chiral salts/media was carried out by cyclic voltammetry CV at scan rates ranging 0.05–2 V s⁻¹ using an AutoLab PGStat potentiostat and a classical three-electrode glass minicell (working volume about 3 cm³). The latter included as working electrode a glassy carbon GC disk (Metrohm, S=0.072 cm²) polished by diamond powder (1 μm Aldrich) on a wet cloth (Struers DP-NAP), as counter electrode a platinum disk, and as reference electrode a saturated aqueous calomel one (SCE) inserted in a compartment with the working medium ending in a porous frit, to avoid contamination of the working solution by water and KCl traces. Experiments were run on solutions at a fixed concentration value in ACN (and DCM) + 0.1 mol dm⁻³ TBAPF₆ as the supporting electrolyte, previously deaerated by nitrogen bubbling. Positive and negative half cycles have been separately recorded to avoid reciprocal contamination by electron transfer products. The reported potentials have been normalized vs the formal potential of the intersolvental ferricenium|ferrocene (Fc⁺|Fc) reference redox couple, recorded in the same conditions [138].

The CV or DPV enantioselection tests were performed at 0.05 V/s scan rate using different screen-printed electrode cells (SPE) constituted of working, counter, and Ag/AgCl pseudo-reference electrodes. The SPEs (provided by Università Tor Vergata, Rome, Italy) were home-produced in foils of 48 with a 245 DEK

(High performance multi-purpose precision screen printer, Weymouth-UK) screen-printing machine and flexible polyester film (Autostat HT5) as support obtained from Autotype Italia (Milan, Italy).

Three kinds of screen-printed electrode cells were considered for the electrochemical studies:

- "C SPE" (Figure 116 top): graphite-based ink (Elettrodag 421) from Acheson (Milan, Italy) was used to print the working and the counter electrode. The SPE support was a folding polyester film (Autostat HT5) obtained from Autotype Italia (Milan, Italy). The electrodes were produced in foils of 48. The diameter of the SPE working electrode was 0.3 cm resulting in an apparent geometric area of 0.07 cm². A silver ink was used to print the reference electrode (Acheson Elettrodag 4038 SS). The application of an insulating print (Argon Carbonflex 25.101S) defines the actual surface area. The diameter of the SPE working electrode was 0.4 cm resulting in an apparent geometric area of 0.126 cm².
- "Au SPE" (Figure 116 bottom): first, a silver/silver chloride conductive ink (Electrodag 477 SS, Acheson, Italy) was printed onto a flexible poly-ester substrate (Autostat HT5, Autotype, Italy), to print the contacts and the reference electrode. These layers were then cured in an oven at 100 °C for 10 min. After, gold-based conductive ink (BQ331, DuPont, Italy) was printed to fabricate working electrodes.
- "Commercial Au SPE": commercial Dropsens DRP-X-C220AT-ND screen-printed electrodes (SPE) cells, including gold working electrodes and counter electrodes and Ag pseudoreference, without insulating layer.



Figure 116. Sheets containing C (top) and Au (bottom) screen-printed electrodes (SPE).

The experiments were performed using (inherently) chiral selectors as low-concentration chiral additives in achiral commercial IL 1-butyl-3-methylimidazolium bis (trifluoromethanesulfonyl)imide BMIMNTf₂ (CAS 174899-83-3; Aldrich ≥98%) or as bulk media.

Statistical tests for peak potentials were performed by repeatedly recording the CV or DPV pattern of each enantiopure probe, at constant working protocol. In all cases a small volume (6 μL) of aqueous KCl solution 0.1 mol dm⁻³ was added to the chiral medium, to stabilize the potential of the pseudo-reference electrode, besides advantageously resulting in lower viscosity.

4.2 Result and discussion for the (inherently) chiral media

4.2.1 Chiral biobased ionic liquids with cations or anions including bile acid building blocks as chiral selectors in voltammetry

Central stereogenicity, which is the most common case, often corresponds to chiral selectors easily affordable and available in large quantities, including many natural compounds that can be advantageously exploited as enantiomerically pure building blocks for CILs preparation. For example, the CILs considered in this paper [185] consisted in cations with biobased chiral building blocks from natural terpenoids (*1R*)-myrtenol, (*S*)-perillyl alcohol, (*1R*)-nopol, and (*S*)-citronellol, combined with bistriflimide as counter anion, to lower melting points below room temperature.

In this frame, it is quite interesting to comparatively test as media for electroanalysis and electrochemistry CILs that exploit different kinds of chiral biobased building blocks. Of course, the chiral natural compounds used for the synthesis of CILs must possess functional groups that allow for the introduction of suitable moieties both for enantiodiscrimination of interactions and for conversion into salts. Deoxycholic acid, one of the most common and commercially available bile acids, fulfils these criteria: it is characterized by a concave structure endowed with several stereogenic centers of established absolute configuration, two hydroxyl groups, which have different reactivity due to the different steric environment, and a carboxylic acid group in the lateral chain, which can be used for conversion into salt.

By virtue of these peculiarities, deoxycholic acid has been successfully used as scaffold for the preparation of different chiral auxiliaries, whose properties not only depend on the introduced moieties, but also on the position of these moieties on the cholestanic backbone. Their use span from the enantioselective chromatography [186-189] to asymmetric catalysis [189-194] and

enantioselective synthesis [195-197]. Despite these interesting characteristics, CILs obtained from deoxycholic acid, and also from other bile acids, are to the best of our knowledge not reported in the literature. Thus, the longstanding experience of some of us in the field of the ionic liquids [198-202] and in the use of bile acids in chemical enantiodiscrimination processes [203-210] suggested the synthesis of new CILs starting from deoxycholic acid (Figure 117).

To this aim, the carboxylic group was converted in a good leaving group for the nucleophilic displacement with 1-methylimidazole to obtain CILs having the chiral steroidal cation or underwent a neutralization reaction to obtain CILs having the steroidal anion. To lower the melting point of the ionic compounds one or two long alkyl chains were introduced, by derivatization of the hydroxyl groups as esters. In addition, an aromatic group was introduced at the two different functionalized positions, which could provide an additional coordination element for chiral recognition. Thus, respect to the terpenoid-based CIL family formerly tested for chiral electroanalysis [182], the present one features extremely bulkier chiral building blocks, with no less than ten stereocenters. It also offers a convenient molecular structure series for a first systematic investigation of features and enantiodiscrimination ability in electrochemistry and electroanalysis, including:

(i) a group of six CILs with the chiral building block implemented in the cation; it includes all combinations of three systematically different chiral imidazolium cations (having the same chiral steroid block, with either two long chain esters or one long chain ester and one naphthyl ester substituents) with two different achiral anions: tosylate (OTs) and bistriflimide (NTf₂) (**1a-c** and **2a-c** in Figure 117);

(ii) a group of four CILs with the chiral building block implemented in the carboxylate anion (having in all cases the same chiral steroid block with two decanoyl ester substituents, as in cases **1a** and **2a**) combined with four different

cations, *i.e.* 1-butyl-3-methylimidazolium, trioctyl methyl ammonium, trioctyl methyl phosphonium, tributyl methyl phosphonium (**3a–d** in Figure 117).

The novel CIL family has been thus characterized concerning key physico-chemical and electrochemical properties and tested as media for enantioselective voltammetry experiments with the enantiomers of a model electroactive chiral probe.

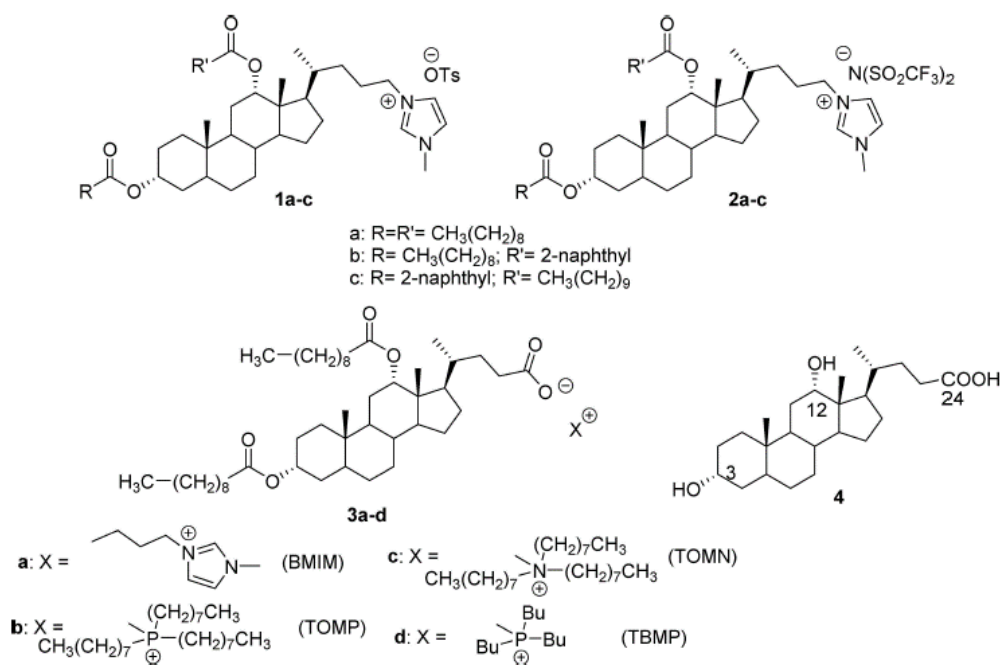


Figure 117. Structure of the synthesized CILs (**1-3**) and deoxycholic acid (**4**).

a) Thermal analysis: TGA and DSC features

The thermal degradation of the CBILs was investigated by thermogravimetric analysis (TA Instruments Q500 TGA). The instrument was calibrated using weight standards (1 g and 100 mg) and the temperature calibration was performed using a Curie temperature of nickel standard. All the standards were supplied by TA Instruments Inc. The sample (10–15 mg) was heated at 40°C in a platinum crucible for the drying procedure and maintained in N_2 flow (90 mL min^{-1}) for

30 min. Then, CBIL was heated from 40°C to 700°C with a heating rate of 10°C min⁻¹ under nitrogen (90 mL min⁻¹) and maintained at 700°C for 3 min. Mass change was recorded as a function of temperature and time. TGA experiments were carried out in duplicate.

DSC analyses have been performed by a DSC 3500 STARe system from Mettler-Toledo® equipped with a HUBER TC100-MTcooler, on a few mg of CILs (weighed on a high-precision balance) in pinholed standard aluminum crucibles (No. 00026763, 40 mm³). Weight constancy between room temperature and 200 °C has been verified by a combined TGA/DSC 3 STARe system from Mettler-Toledo®, in standard alumina crucibles (No. 00024123, 70 mm³), under the same nitrogen flux. DSC thermograms were acquired at 10°C min⁻¹ scan rate, in nitrogen flow (50 cm³ min⁻¹), according to the following temperature program: cooling from 25°C to -85°C; heating from -85°C to 200°C; cooling from 200 °C to -85°C; heating from -85°C to 25°C; cooling from 25°C to -85°C; heating from -85°C to 200°C. The thermal stability of the new CILs has been studied by thermogravimetric (TGA) analysis. The TGA features of all CILs are compared in Figure 118.

The two series of CILs with chiral cations correspond to the blue curves (**1a–c** with tosylate counter anion) and red curves (**2a–c** with bistriflimide counter anion). Cases **1a** and **2a**, featuring both aliphatic (decanoyl) ester groups, have simple patterns consisting in two neat subsequent steps, both of which are significantly shifted to higher temperatures in the case of bistriflimide anions; thus the bistriflimide salt combines in this case its typical advantage of a lower melting point with better thermal stability. Less straightforward is the comparative discussion of cases **1b** and **2b** or **1c** and **2c** involving a naphthoyl-substituent in two different positions, 12 (axial) in the first case and 3 (equatorial) in the second case, and a long alkyl chain (decanoyl or undecanoyl) in the

complementary position. In particular, it seems that the axial ester structure in combination with the anion type plays a great effect.

Considering the first degradation event, **1b** which is characterized by the naphthoyl ester in position 12 results as the most stable IL. However, when the same cationic moiety is paired with the less nucleophilic NTf₂ anion, the corresponding IL **2b** is the least stable IL of the series. Conversely, the more flexible aliphatic ester in the same axial position as well as the naphthoyl group in the usually more stable equatorial position seem to have less impact on the thermal stability, with **1c** and **2c** showing thermal degradation profiles more similar to **1a** and **2a**. Therefore, subtle effects of the structure of the axial substituent and of the type (size and nucleophilicity) of the anion can be envisaged in triggering the thermal degradation process.

The TGA features of the four CILs **3a–d** with chiral anions are reported as green curves in Figure 118. They look remarkably modulated by the achiral counterion, in this case a cation, with a clear ammonium<imidazolium<phosphonium stability sequence. In fact, a first step is observed at ~160 °C with trioctyl methylammonium (**3c**), at ~220 °C with butyl methylimidazolium cations (**3a**), and at ~290°C with tributyl methyl- or trioctyl methylphosphonium cations (**3b** and **3d**). Instead a second step, corresponding to the sharper maximum in the first derivative, is nearly coincident in all cases, and can be therefore linked to the common chiral anion moiety. Solid/liquid phase transitions of the new CILs have been studied by differential scanning calorimetry DSC. The DSC features of the six CILs with chiral cations are reported in Gallery Section 12.

In all cases, weak but significant features pointing to liquid/solid and solid/liquid reversible glassy transitions can be observed, becoming reproducible from the second cycle, while in the first one they can be significantly different. Such transitions (particularly considering the stationary cycles) appear systematically shifted to lower temperatures with the bistriflimide anion, a well-known tool

promoting melting point lowering in IL design. Moreover, notably, changing a long-chain alkyl ester substituent with a naphthyl one results in a remarkable increase of the liquid/solid transition temperature, even becoming border line respect to room temperature.

The DSC features of the four CILs with chiral anions are reported in Gallery Section 13. The glass transitions are in these cases even more difficult to perceive but located at temperatures even lower than former cases **1a** and **2a** (which feature the same chiral building block with two decanoyl esters).

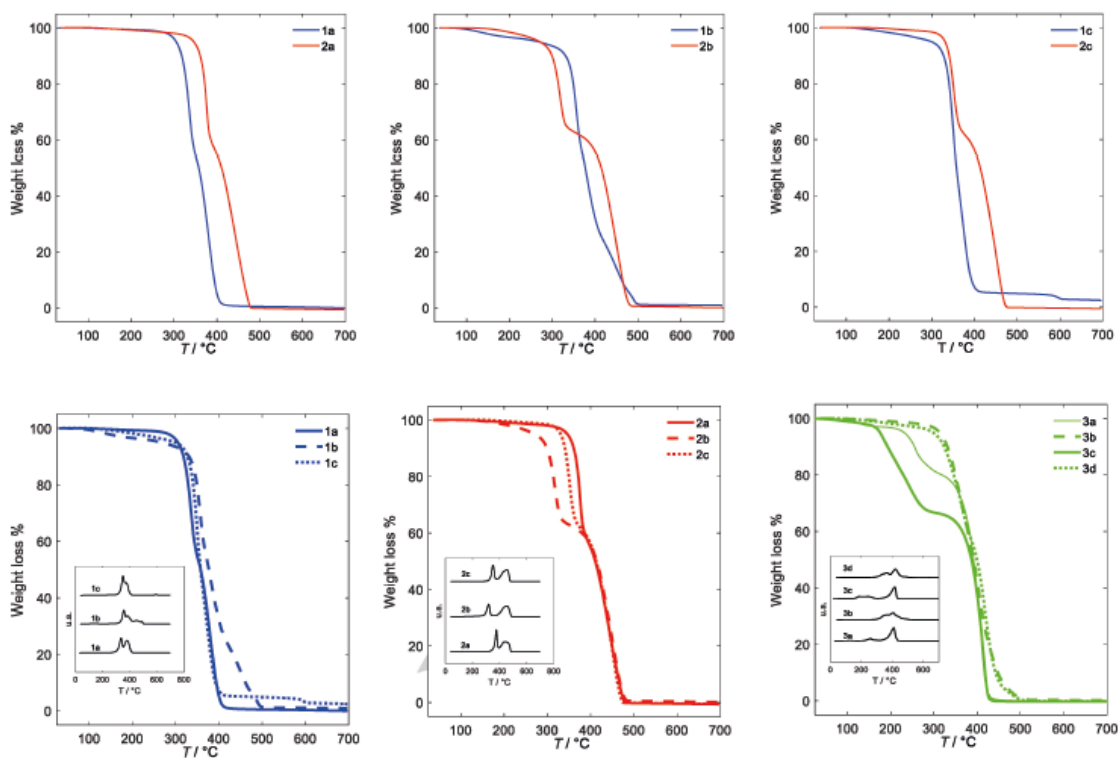


Figure 118. Comparing TGA features of CILs with chiral cations **1a–c** (blue curves) and **2a–c** (red curves), as well as of CILs with chiral anions **3a–d** (green curves); insets provide a comparison of the curve derivatives.

b) Electrochemical properties of the CIL family

The electrochemical properties of the new CIL family were investigated by cyclic voltammetry CV in the 0.05–2 V s⁻¹ potential scan rate range on 0.00075 mol dm⁻³ solutions in ACN + 0.1 M TBAPF₆ as the supporting electrolyte.

A synopsis of CV patterns for the six CILs with chiral cations is reported in Figure 119 (top). The first reduction peak at ~ -2.5 V vs Fc⁺|Fc as well as the oxidation peak at $\sim +1.6$ V vs Fc⁺|Fc, which are only featured by couples **1b/2b** and **1c/2c**, should be ascribed to reduction (approaching chemical reversibility with increasing scan rate, see Gallery Section 14) and oxidation of the aromatic naphthyl system, respectively. Instead, the second reduction peak at ~ -3 V, also featured by the **1a/2a** couple, should be assigned to the reduction of the imidazolium cation (chemically irreversible in the scan rate range considered).

Overall, these CILs offer large potential windows for electroanalysis and electrochemistry, both on the oxidation and reduction sides, particularly in the **1a/2a** cases (~ 4.6 V), but even in the **1b/2b** and **1c/2c** ones (~ 3.7 V). A synopsis of CV patterns for the four CILs with chiral anions is reported at Figure 119 (bottom) (while Gallery Section 15 shows the effect of scan rate on selected CV peaks). A reduction peak at ~ -3 V, analogous to those observed in the former cases, is perceivable for **3a** only, consistently with it being the only CIL in the **3a–3d** group including an imidazolium cation. Instead, the oxidation peak at ~ 0.8 V vs Fc⁺|Fc can be ascribed to the oxidation of the carboxylate anion. In fact, its potential is consistent with that observed in ACN for the oxidation of tetrabutylammonium acetate on glassy carbon GC in acetonitrile in non-catalytic conditions [211].

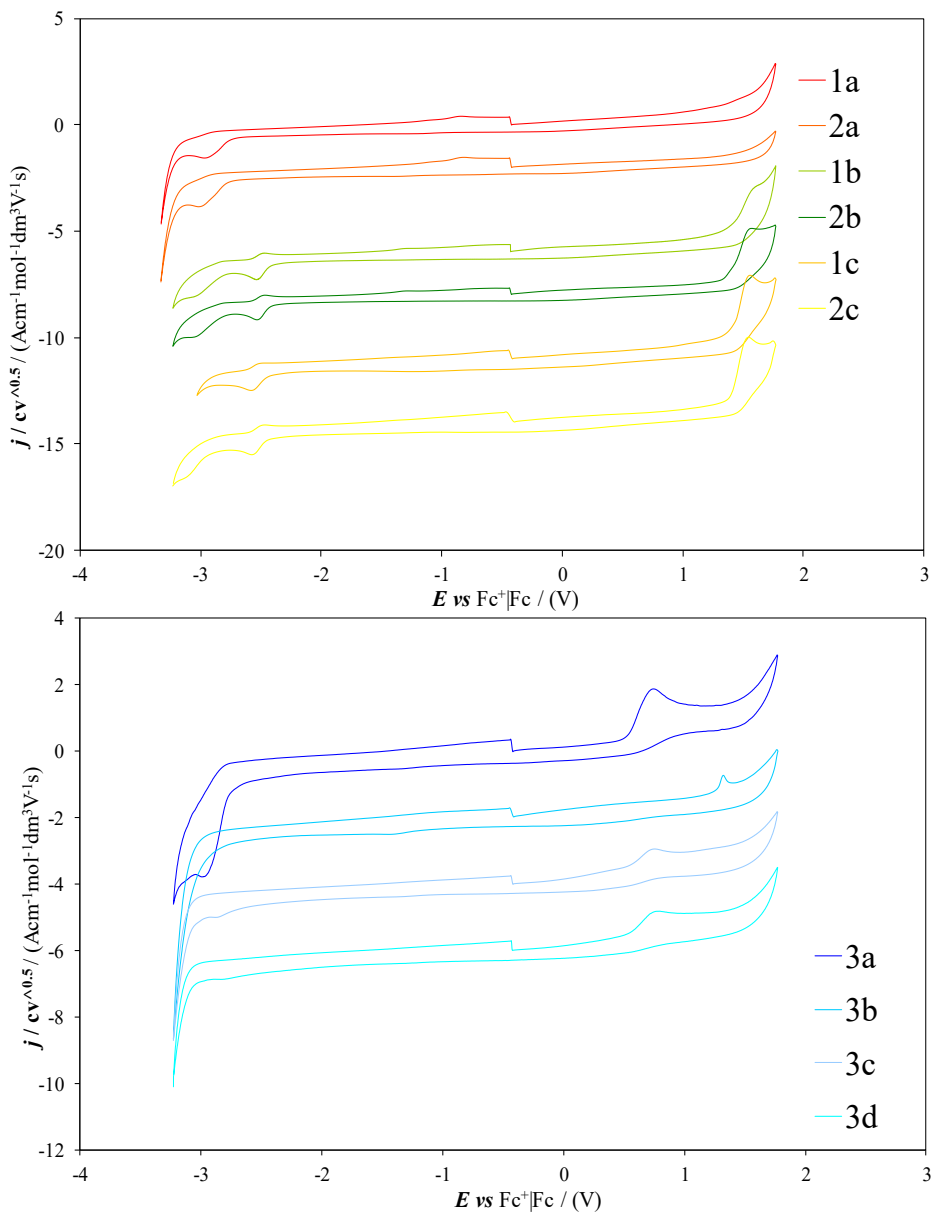


Figure 119. A synopsis of CV features of the six CILs with chiral cations (top) and of four CILs with chiral anions (bottom), recorded at 0.2 V s^{-1} scan rate, in 0.00075 M solutions in $\text{ACN} + \text{TBAPF}_6 \text{ 0.1 M}$.

c) Enantiodiscrimination tests

The CIL enantiodiscrimination ability has been tested in CV experiments with (*R*)-(+)- or (*S*)-(–)-*N,N'*-dimethyl-1-ferrocenylethylamine (*R*)-Fc and (*S*)-Fc, the enantiomers of our benchmark chiral electroactive model probe, commercially available and resulting in chemically and electrochemically reversible canonical CV peaks at mild potentials, well within the potential windows of the current tested media. The chiral salts were tested as 0.05 mol dm⁻³ chiral additives in bulk BMIMNTf₂, recording in the resulting media the CV patterns of (*R*)-Fc and (*S*)-Fc at 0.05 V s⁻¹ scan rate in open air on laboratory screen printed electrode (SPE) cells on plastic sheet, including graphite working and counter electrodes and Ag pseudo-reference electrode, resulting in good reproducibility at constant conditions with the present working protocol. Addition of a small volume of 0.1 mol dm⁻³ KCl aqueous solution to the chiral medium enabled to stabilize the potential of the pseudo-reference electrode, besides advantageously resulting in lower viscosity. Repetitions on new SPE supports were performed in order to check the result repeatability.

As shown in Figure 120a (salts with chiral cations) and Figure 120b (salts with chiral anion), statistically significant differences, of the order of several tens of mV, are observed in all cases for the formal potentials of the ferrocenyl probe enantiomers. In the case of the additives with chiral cations:

- i)* The signals of the ferrocenyl probes maintain canonical reversibility features.
- ii)* The sequence of activation of the chiral probes is (*R*)- before (*S*)- in all cases; this is consistent with chirality originating from the same chiral steroid building block in all the chiral salts considered.

iii) However, at constant sequence of probe enantiomer CV peaks, the achiral anions appear to modulate enantiodiscrimination; in particular, peak potential differences look systematically larger with NTf₂ anion respect to the OTs one.

iv) In the case **2c** a test about additive concentration effect is also provided, resulting in increasing enantiomer potential differences at increasing additive concentrations.

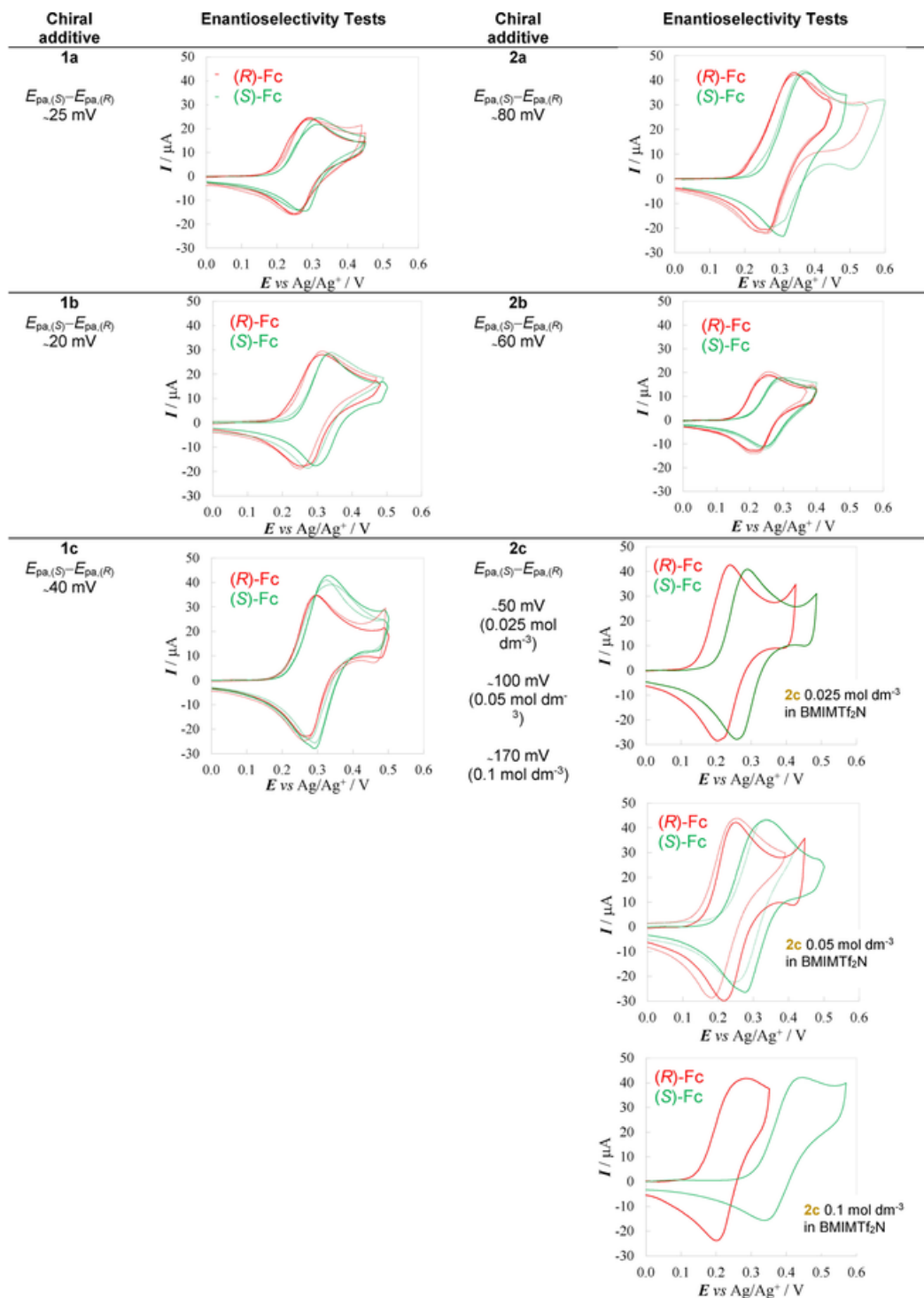
Significant peak potential differences were also observed with the additives with chiral anions, again with the same enantiomer peak order (consistently with the anion chirality originating from the same steroid building block) slightly modulated by the achiral cation.

Notably, working in the concurrent presence of carboxylate and ferrocene groups, complications could be expected. In fact, it has been shown that ferrocene can act as a mediator for carboxylate oxidation, which thus shifts to a much lower potential, namely that of ferrocene oxidation; this is evidenced by the ferrocene oxidation peak increasing in current and becoming chemically irreversible [212]. However, very conveniently, in this case the ferrocene oxidation CV peaks remain canonical, pointing to the above process not taking place (at least significantly).

Actually it should be considered that the cited literature study (a) has been performed in acetonitrile, and the mechanism proposed for the follow up of the charge transfer process involves addition of ACN; (b) consider acetate or benzoate salts, which form methyl or benzyl radicals and then carbocations, which are likely to be much more reactive than in our case.

We also verified that performing the same protocol in achiral BMIMNTf₂ in the absence of the chiral additive, the (*R*)- and (*S*)- probe enantiomers give practically coincident peak potentials (Gallery Section 16).

(a)



(b)

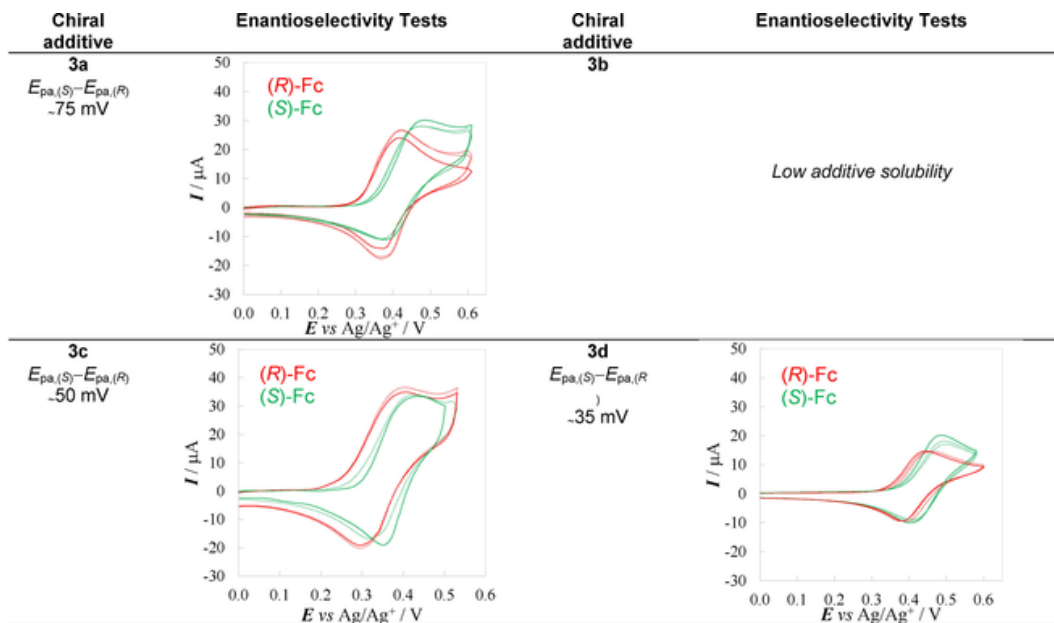


Figure 120. Enantiodiscrimination tests with (*S*)- or (*R*)-Fc (green and red respectively), using the CBILs with chiral cation (a) or anion (b) as low concentration chiral additives (0.05 M) in commercial IL. For compound **2c** a series of enantioselection tests is also provided at increasing CBIL concentration in the 0.025–0.1 M range. Repetition tests are also reported (thin lines)

4.2.2 Enantioselective electrooligomerization of an inherently chiral monomer

In order to try to realize an enantioselective electrooligomerization, an imidazolium based CIL with chiral cation and methansulphonate as the anion (the structure is reported in Figure 121, chiral bio-based component [NopolMIm]Mes (3-{2-[(1*R*,5*S*) -6,6- dimethylbicyclo[3.1.1]hept-2-enyl]ethyl} -1-methyl-1*H*-imidazol-3-ium methanesulfonate)) [182] was synthesized and employed as low concentration chiral additive during the electrodeposition of the BT₂T₄ inherently chiral monomer.

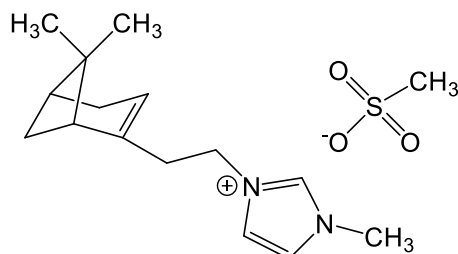


Figure 121. Structure of the chiral salt [NopolMIm]Mes.

This chiral salt (precursor of the bistriflimide CIL, used as bulk medium and liquid at room temperature [182]) has recently been used in voltammetry enantiodiscrimination experiments as chiral additive with promising features and results, testing the enantiomers of chiral ferrocene [182].

a) Experimental conditions for the electrooligomerization of the BT₂T₄ monomer

The CV electrooligomerization experiments were performed on C SPEs (obtained as described in 4.1) using different solutions:

1. enantiopure (*R*)- or (*S*)-BT₂T₄ (0.01 M) in achiral BMIMNTf₂;
2. racemic BT₂T₄ (0.01 M) in achiral BMIMNTf₂;
3. enantiopure (*R*)- or (*S*)-BT₂T₄ (0.01 M) in a solution consisting of 0.05 M [NopolMIm]Mes (low concentration chiral additive) in achiral commercial BMIMNTf₂;

4. racemic BT_2T_4 (0.01 M) in a solution consisting of 0.05 M $[\text{NopolMIm}]\text{Mes}$ (low concentration chiral additive) in achiral commercial BMIMNTf_2 .

CVs were recorded in open air conditions at 0.05 V s^{-1} , depositing on the working electrode a drop of one of the above solutions and performing 36 CV cycles.

b) Enantioselective electrodeposition of enantiopure or racemic BT_2T_4 in achiral BMIMNTf_2

The CV patterns reported in Figure 122 show the first and the 36 cycles of each oligomerization carried out with the solutions 1 and 2 previously described in point a). The signals of the (*R*) and (*S*) enantiopure monomers are almost equivalent, in terms of signal morphology, potential and current values; this is consistent with the solutions having the same concentration and oligomerization being carried out in an achiral and therefore non-discriminating medium. The growth of the oligomers proceeds in an equivalent way for both the monomers as can be seen from the last scan cycle. However, the electrooligomerization of the racemic BT_2T_4 appears to proceed faster than the two enantiomers; this could be justified for the higher number of freedom degrees.

c) Enantioselective electrodeposition of enantiopure or racemic BT_2T_4 in $\text{BMIMNTf}_2 + [\text{NopolMIm}]\text{Mes}$

The CV patterns reported in Figure 123 show for each oligomerization the first and 36 cycles obtained with the solutions 3 and 4 previously described in point a). In this case, with the addition of the chiral additive $[\text{NopolMIm}]\text{Mes}$ (0.05 M), the first oxidation peaks of the starting monomers (*R*) and (*S*)- BT_2T_4 present two different potential values, with a separation of about 115 mV. Furthermore, observing the last deposition cycles of the two enantiomers, it can be seen that the growth of the two monomers is different in terms of morphology and that the racemic signal appears to be an average of the signal of the two enantiomers.

By comparing the 36 oligomerization cycles of the three experiments, significant differences are observed:

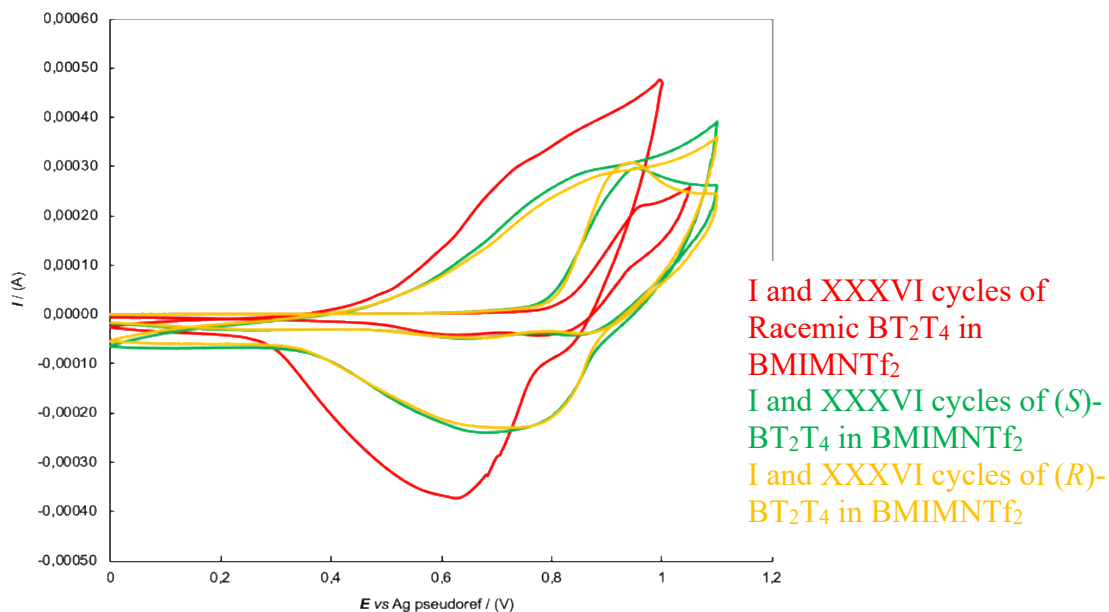


Figure 122. I and XXXVI CV cycle for racemic BT_2T_4 (in red), (*S*)- and (*R*)- BT_2T_4 (green and yellow respectively) 0.01 M, in achiral commercial IL BMIMNTf_2 , at 0.05 V s^{-1} on C SPEs.

- in the peak potential: the three films present significantly different oxidative potentials, although in all the cases with a similar sequence of two main peaks; in particular, the most easily oxidizable film is the one obtained from the enantiopure (*S*) monomer; the less easily oxidizable one is that obtained from the enantiopure (*R*) monomer; with the racemic BT_2T_4 the behaviour is intermediate between the two enantiomers.
- in size: the film that grows faster is the one obtained from the (*S*) monomer; instead, the electrodeposition of the (*R*) monomer proceeds slowly and again, the racemic seems to have a behaviour which is intermediate between the two enantiomers.

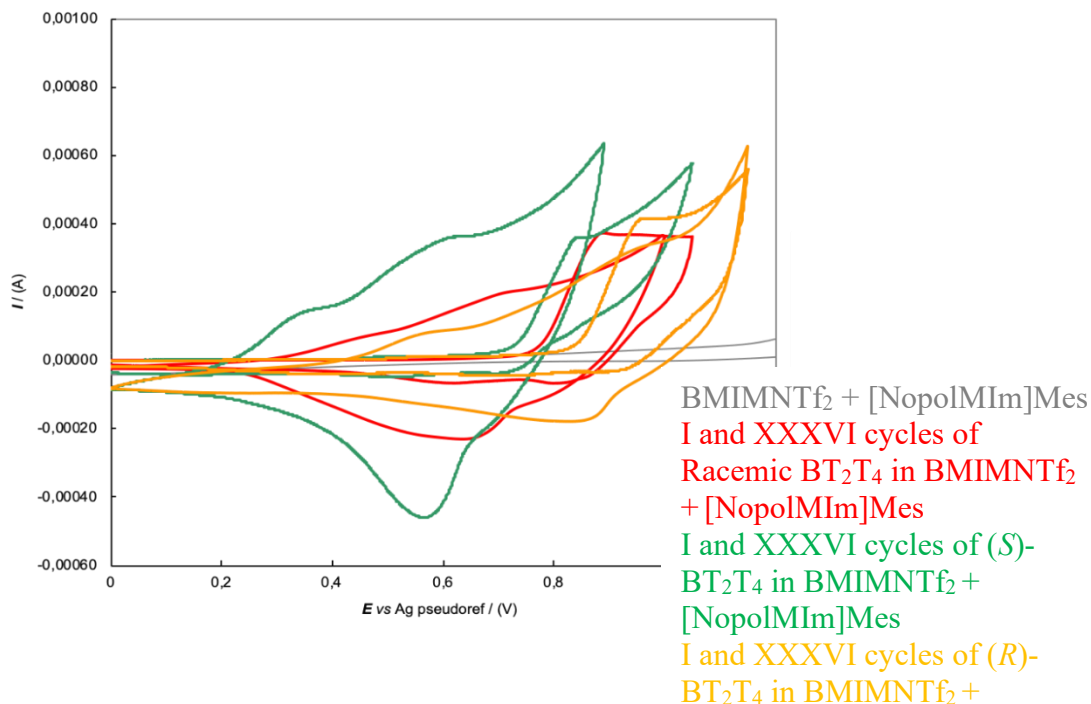


Figure 123. I and XXXVI CV cycle for racemic BT₂T₄ (in red), (*S*)- and (*R*)-BT₂T₄ (green and yellow respectively) 0.01 M, in BMIMNTf₂ + [NopolMIm]Mes (0.05 M) at 0.05 V s⁻¹ on C SPEs.

Therefore, considering the experiments with and without the chiral additive, we can suppose that the chiral [NopolMIm]Mes significantly influences the growth of the enantiopure monomers, the energy and the kinetics of the process. The chiral additive [NopolMIm]Mes is therefore able to discriminate the two enantiomers in the electrodeposition.

4.2.3 Chiral Tweezers and chiral moieties

An attractive CIL family with chiral “tweezer” dications, consisting of a biobased isomannide or isosorbide chiral core with two cation arms including heteroatoms and aromatic systems [213] providing coordination elements for selector/probe interactions, were explored as chiral selector candidates in enantioselection experiments. This family is based on chiral building blocks from the natural “chiral pool” already successfully employed in enantiodiscrimination processes in other contexts, which should be suitable for enantioselective electrochemistry, is based on isomannide **I** and isosorbide **II** (Figure 124) as chiral cores [213].



Figure 124. Isomannide **I** ($3R,3aR,6R,6aR$)-hexahydrofuro[3,2-*b*]furan-3,6-diol and isosorbide **II** ($3R,3aR,6S,6aR$)-hexahydrofuro[3,2-*b*]furan-3,6-diol, the two biobased building blocks exploited as chiral cores for the tweezer selectors.

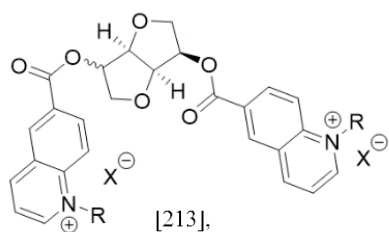
These natural compounds, respectively known as ($3R,3aR,6R,6aR$)-hexahydrofuro[3,2-*b*]furan-3,6-diol and ($3R,3aR,6S,6aR$)-hexahydrofuro[3,2-*b*]furan-3,6-diol, are two by-products of the starch industry obtained from dehydration of D-mannitol and D-sorbitol, characterized by a vaulted structure arising from the *cis* junction between the two tetrahydrofuran rings. It is worthwhile noticing that, involving four stereocentres, only one of which has different *R* or *S* configuration, they are diastereoisomers, and the two hydroxy groups are *syn* in isomannide and *anti* in isosorbide.

An easy derivatization of the hydroxyl groups as quinoline esters can give rise to a “chiral pocket” able to establish π - π interactions through the aromatic groups and dipole-dipole or hydrogen bond interactions through the ester groups, thus

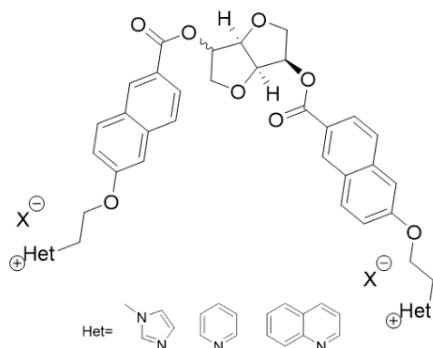
enantiodiscriminating substrates endowed with an electronically complementary (electron-rich) aromatic ring [213]. The eight thus achieved chiral selectors (Figure 125 top), five of which ionic liquids according to thermal analysis (*i.e.*, with melting point or glass transition below 100 °C according to the usual definition), exhibited neat circular dichroism patterns [213], pointing to possible significant chirality manifestations, which was also supported by theoretical modeling and confirmed by a preliminary NMR enantiodiscrimination experiment [213]. They are therefore worthy to be also investigated as possible chiral selectors in electrochemistry experiments, too.

Moreover, to expand the applicability of this kind of selectors, also electron-rich aromatic ester derivatives could be interesting. New CILs were synthesized, employing 6-hydroxynaphthoic acid as derivatizing group, characterized by an electron-donating phenolic group that could be further derivatized with an methylimidazolium MeIm, or pyridinium Py, or quinolinium Qu group to introduce ionic moieties (Figure 125 bottom); we were also confident that the introduction of such flexible chains could be useful to lower the melting point of the final salts, leading to the formation of ionic liquids instead of “simple” organic salts.

The structures of related molecules also investigated for sake of comparison are also reported in Figure 126.

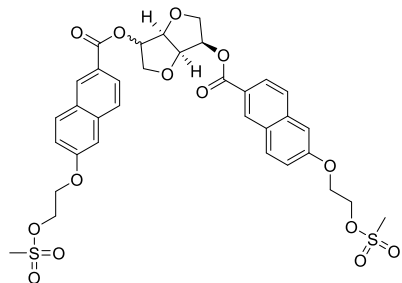


- 1mI** R = Me, isomannide core, I⁻
- 1mT** R = Me, isomannide core, Tf₂⁻
- 1sI** R = Me, isosorbide core, I⁻
- 1sT** R = Me, isosorbide core, Tf₂⁻
- 2mI** R = Bu, isomannide core, I⁻
- 2mT** R = Bu, isomannide core, Tf₂⁻
- 2sI** R = Bu, isosorbide core, I⁻
- 2sT** R = Bu, isosorbide core, Tf₂⁻

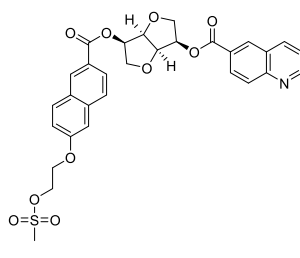


- 3mM** Het=Melm, isomannide core, CH₃SO₃⁻
- 3mT** Het=Melm, isomannide core, Tf₂⁻
- 3sM** Het=Melm, isosorbide core, CH₃SO₃⁻
- 3sT** Het=Melm, isosorbide core, Tf₂⁻
- 4mM** Het=Pyr, isomannide core, CH₃SO₃⁻
- 4mT** Het=Pyr, isomannide core, Tf₂⁻
- 4sM** Het=Pyr, isosorbide core, CH₃SO₃⁻
- 4sT** Het=Pyr, isosorbide core, Tf₂⁻
- 5mM** Het=Quin, isomannide core, CH₃SO₃⁻
- 5mT** Het=Quin, isomannide core, Tf₂⁻

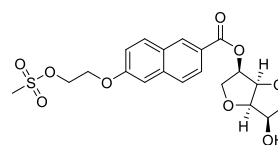
Figure 125. Synopsis of the chiral tweezers electrochemically investigated, either formerly synthesized ([213], top), or newly synthesized (bottom).



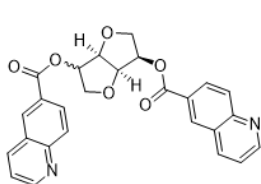
- 6m** isomannide core
- 6s** isosorbide core



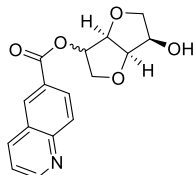
- 7m** isomannide core



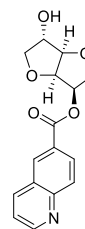
- 8m** isomannide core



- 9m** isomannide core
- 9s** isosorbide core



- 10m** isomannide core
- 10s** isosorbide core



- 11s** isosorbide core

Figure 126. Related molecules also investigated for sake of comparison.

a) Thermal analysis of the new tweezers: assessing CIL nature and stability

As for the formerly introduced quinoline based CILs [213], the thermal behaviour of the naphthalene containing ionic derivatives was investigated by differential scanning calorimetry (DSC) at 10 °C min⁻¹ under nitrogen atmosphere in the range spanning from -90 °C to 220 °C for 4sM, to 240°C for 3mM, 3sM, 3mT, 4mM, 4mT and 5mM, to 250°C for 3sT and 4sT and to 280°C for 5mT (Table 12).

The stereochemistry of the central scaffold showed a deep influence on the thermal properties. Methanesulfonates with isomannide core 3mM, 4mM and 5mM were solid at room temperature and showed a melting during the first heating cycle, while isomannide derived compounds 3sM and 4sM were obtained as glassy solids. However, even when present, the melting was observed only initially, since in the second heating cycle all the ionic derivatives showed a glass transition. While during the first heating cycle compounds 3mM and 4mM behaved as crystalline solids, once their “thermal history” had been deleted they assumed the typical thermodynamic and kinetic behaviour that they show when employed as ionic liquids. For the same methanesulfonates 3mM, 3sM, 4mM, 4sM and 5mM the stereochemistry of the central scaffold had a lower influence on the glass transition in the second heating cycle, with T_g being lower for 1-methylimidazolium containing derivatives (3mM and 3sM) and higher for pyridinium salts of the same chiral scaffolds (4mM and 4sM). The cationic heterocyclic moiety affected the thermal behaviour, with the transition temperature lowering on moving from quinolinium > 1-methylimidazolium > pyridinium (5mM>3mM>4mM) in the first heating cycle. The trend changed when considering the second heating cycle, with the glass transition lowering on moving from quinolinium > pyridinium > 1-methylimidazolium (5mM>4mM>3mM) (Figure 127). To sum up, only derivatives 3mM, 3sM and 4mM,4sM could be correctly classified as ionic liquids.

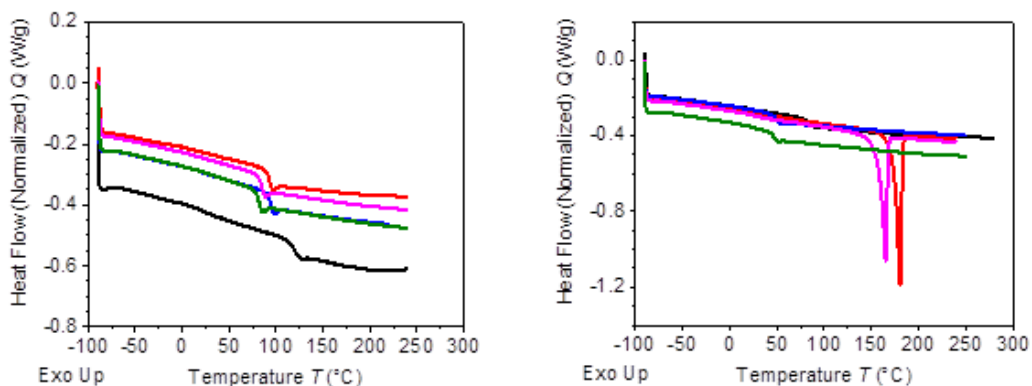


Figure 127. Second heating cycle (10 °C/min) of DSC analysis. Left side: compounds 3mM (magenta line), 3sM (green line), 4mM (red line), 4sM (blue line) and 5mM (black line). Right side: compounds 3mT (magenta line), 3sT (green line), 4mT (red line), 4sT (blue line) and 5mT (black line).

It is to note that the first heating cycle is not particularly significant when determining the thermal properties of a compound, since it is influenced by the whole history of the sample. In particular, different events could occur during this cycle due to limited crystallization of the sample or humidity-loss. This latter phenomenon causes for instance the low glass transition recorded for derivative 3sM, as it could be observed from the thermogram (Figure 128). Once the water was removed during the first heating cycle, the glass transition was observed at a higher temperature (Figure 128). A similar trend was observed even for compound 4sM (Gallery section 17). A water loss could be clearly observed for compound 5mM, where a large endothermic peak was recorded below 100 °C (Gallery section 17). The water content in the sample was probably due to its hygroscopicity, since it was dried at 80 °C at low pressure for 24 h before the measurement. Compound 3mM showed a glass transition before the melting during the first heating cycle: while the melting was not present in the second heating cycle, the glass transition could still be observed at a similar temperature

(Table 12 and Gallery section 17). Compound 4mM was characterized by more than one process during the first heating cycle, as showed by the non-symmetrical endothermic peak (Gallery section 17).

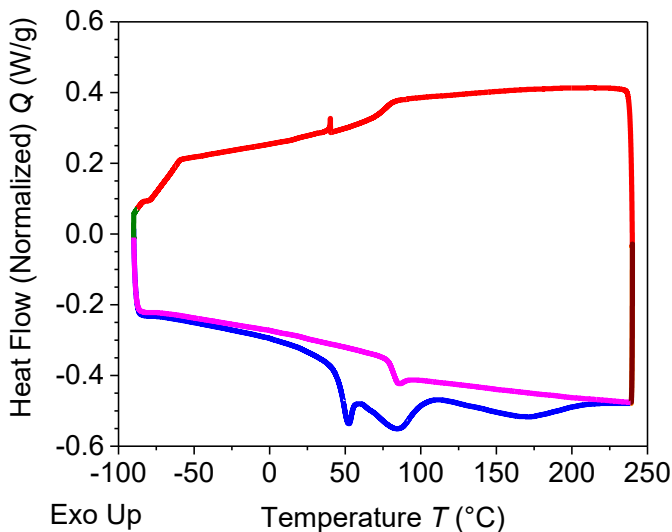


Figure 128. DSC of compound 3sM (first heating ramp at 10°C/min (blue line); cooling ramp at 10°C/min (red line); second heating ramp at 10°C/min (magenta line)).

Compounds 3mT, 3sT, 4mT, 4sT and 5mT possessing Tf_2N as the anion showed a more peculiar behaviour. Isomannide containing derivatives 3mT and 4mT were solids at room temperature and they were characterized by a melting temperature higher than 100 °C (157.8 °C for 3mT and 174.1 °C for 4mT) in all heating cycles (Table 12). These compounds crystallized on cooling, as showed by the thermograms (Gallery section 17). A particular behaviour could be observed for 4mT during the first heating cycle, since two crystallizations were observed while heating (Gallery section 17). Compound 3mT was characterized by an exothermic peak due to a structural rearrangement before melting in the first heating cycle.

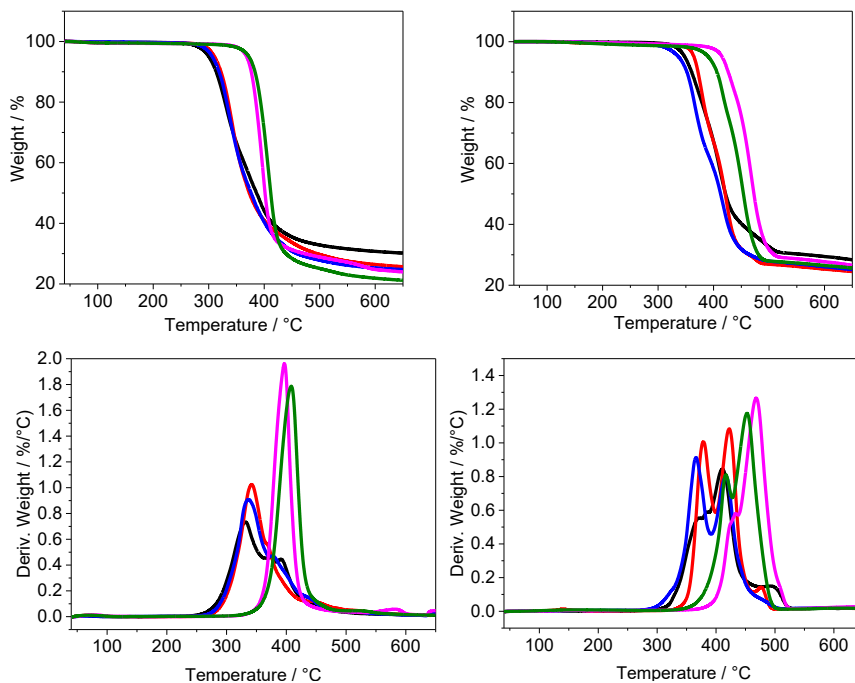


Figure 129. Top left: TGA of compounds 3mM (magenta line), 3sM (green line), 4mM (red line), 4sM (blue line) and 5mM (black line). Top right: TGA of compounds 3mT (magenta line), 3sT (green line), 4mT (red line), 4sT (blue line) and 5mT (black line). Bottom left: DTG of compounds 3mM (magenta line), 3sM (green line), 4mM (red line), 4sM (blue line) and 5mM (black line). Bottom right: DTG of compounds 3mT (magenta line), 3sT (green line), 4mT (red line), 4sT (blue line) and 5mT (black line).

A slightly different behaviour was found for derivative 5mT: while a melting temperature could be observed in the first heating cycle, the product did not crystallize on cooling and displayed only a glass transition in the second heating cycle. Similarly to 5mM, a water loss due to adsorbed humidity was observed for compound 5mT (Gallery section 17). Again, the ionic heterocyclic moiety affected the thermal behaviour, with the transition temperature varying in the order 4mT > 3mT > 5mT.

Table 12. Selected DSC data. T_g , T_c , T_m values ($^{\circ}\text{C}$) and ΔH_m , ΔH_c (kJ/mol) for compounds 3mM, 3sM, 3mT, 3sT, 4mM, 4sM, 4mT, 4sT and 5mM, 5mT at a heating or cooling rate of $10^{\circ}\text{C}/\text{min}$. The value on brackets indicates the cycle in which the transition was observed: (I) the first heating cycle from -90°C to T_{max} , (II) the cooling cycle from T_{max} to -90°C and (III) the second heating cycle from -90°C to T_{max} .

	<i>Core</i>	<i>Terminal</i>	<i>Anion</i>	T_m	ΔH_m	T_c	ΔH_c	T_g
3mM	Isomannide	MeIm	OMs	138(I)	38(I)			86 (I) 84(III)
3sM	Isosorbide	MeIm	OMs					47(I) 81(III)
3mT	Isomannide	MeIm	Tf ₂ N	159(I) 158(III)	40(I) 42(III)	123(II)	38(II)	
3sT	Isosorbide	MeIm	Tf ₂ N					33 (I) 46 (III)
4mM	Isomannide	Pyr	OMs	94(I)	38.(I)			92 (III)
4sM	Isosorbide	Pyr	OMs					70 (I) 94 (III)
4mT	Isomannide	Pyr	Tf ₂ N	177(I) 174(III)	44 (I) 43 (III)	125, 133 (I) 137(II)	15(I) ¹ 38(II)	
4sT	Isosorbide	Pyr	Tf ₂ N					48 (I) 48(III)
5mM	Isomannide	Quin	OMs	142 (I)	20 (I)			120 (III)
5mT	Isomannide	Quin	Tf ₂ N	125(I)	20(I)			84(III)

¹The value was measured considering both crystallizations together.

Considering the stereochemistry of the isohexide scaffold, a dramatic effect was noticed. Isosorbide derived compounds 3sT and 4sT did not show a melting neither in the first nor in the second heating cycle (Gallery section 17), but only glass transitions at a very similar temperature (slightly lower for pyridinium containing derivatives, 46.2°C for 3sT and 48.5°C for 4sT) (Figure 127).

Therefore, according to the usual classification, only isosorbide containing compounds 3sT, 4sT and isomannide derivative 5mT could be defined ionic liquids with full rights [214]. The short thermal stability of the prepared ionic derivatives was investigated by thermal gravimetric analysis which was performed with a heating rate of 10 °C min⁻¹ under a nitrogen atmosphere. The data are collected in Table 13. All compounds, with the only exception of 3mM and 3sM, showed more than one degradation event. Within the methanesulfonate derivatives, a clear influence of the ionic heterocyclic moiety on the thermal stability could be observed, with *N*-methyl imidazolium containing derivatives 3mM and 3sM possessing a higher stability than their analogues 4mM and 4sM endowed with pyridinium, and derivative 5mM containing quinolinium being the less stable. The stereochemistry of the central scaffold had a little influence on the final T_{onset} , with isosorbide containing derivatives being slightly less stable than their isomannide analogues.

Compounds 3mT, 3sT, 4mT, 4sT and 5mT containing Tf₂N as the anion were characterized by a higher thermal stability, a trend already well-reported for ILs [215,216] and related to the lower nucleophilicity of the latter anion. The same trend on the thermal stability could still be observed even on changing the anion, with increasing stability in the order 1-methylimidazolium > pyridinium > quinolinium (3mT,3sT > 4mT,4sT > 5mT) and isomannide derivatives being still more stable than the isosorbide analogues (3mT > 3sT and 4mT > 4sT). It is to note that a significant difference in the thermal stability could be observed only for compounds 4mT and 4sT, with 4mT having a higher T_{onset} . The data here reported suggest that derivatives 3mM, 3sM, 3sT and 5mT are the most stable isohexide-based chiral ionic liquids, possessing a stability even higher than the previously synthesized quinoline CILs 1mT, 1sT [213]. Considering the classification reported by Mu and Cao [217], which divides ILs into five stability levels on the basis of their T_{onset} values, the prepared CILs clearly belong to two well-defined

categories: moderate in the case of 4mM, 4sM and 4sT ($300\text{ }^{\circ}\text{C} < T_{\text{onset}} < 350\text{ }^{\circ}\text{C}$) and more stable in the case of 3mM, 3sM, 3sT and 5mT ($350\text{ }^{\circ}\text{C} < T_{\text{onset}} < 400\text{ }^{\circ}\text{C}$). Compound 3sT is borderline with the most stable category ($400\text{ }^{\circ}\text{C} < T_{\text{onset}} < 450\text{ }^{\circ}\text{C}$), possessing a $T_{\text{onset}} \approx 400\text{ }^{\circ}\text{C}$ ($399.7\text{ }^{\circ}\text{C}$).

Table 13. Selected TGA data. $T_{\text{start}5\%}$, $T_{\text{start}10\%}$, T_{onset} and T_{peak} values ($^{\circ}\text{C}$) for compounds 3mM, 3sM, 3mT, 3sT, 4mM, 4sM, 4mT, 4sT, 5mM, 5mT at a heating rate of $10\text{ }^{\circ}\text{C}/\text{min}$.

	<i>Core</i>	<i>Terminal</i>	<i>Anion</i>	$T_{\text{start } 5\%}$	$T_{\text{start } 10\%}$	T_{onset}	T_{peak}
3mM	Isomannide	MeIm	OMs	368	376	376	396
3sM	Isosorbide	MeIm	OMs	361	372	374	397
3mT	Isomannide	MeIm	Tf ₂ N	401	412	398 439	419 454
3sT	Isosorbide	MeIm	Tf ₂ N	392	407	400 442	417 454
4mM	Isomannide	Pyr	OMs	304	316	310 361 422	336 363 423
4sM	Isosorbide	Pyr	OMs	306	319	312 372 431	336 382 442
4mT	Isomannide	Pyr	Tf ₂ N	362	369	360 408 469	374 420 476
4sT	Isosorbide	Pyr	Tf ₂ N	338	353	347 407	367 419
5mM	Isomannide	Quin	OMs	300	313	304 371 389	332 374 393
5mT	Isomannide	Quin	Tf ₂ N	348	360	369 383 411 500	344 381 400 497

b) Voltammetry study of the whole chiral tweezer family and of some related molecules

In view of testing the tweezers as chiral selector additives for enantiodiscrimination in voltammetry, analogously to former examples of advanced chiral media and/or additives successfully, based on chiral ionic liquids [182,183] and chiral deep eutectic solvents [184], a preliminary investigation has been performed on the electrochemical properties of the tweezers together with some tweezer moieties as well as two electroactive chiral probe candidates. The study has been carried out by CV at different potential scan rates (and in some cases also by differential pulse voltammetry DPV) in ACN with 0.1 M TBAPF₆ as supporting electrolyte (while the tweezers were usually at ~0.0007-0.001 M concentration), using an Autolab PGStat potentiostat (managed by a PC with GPES software) also enabling to correct ohmic drop by the positive feedback technique. The 3-electrode glass minicell (working solution volume: 3 cm³) included an AMEL glassy carbon working electrode (diameter 1.5 mm, mechanically polished when necessary with Aldrich synthetic diamond powder on a wet Struers DP-nap cloth), a Pt wire counter electrode, as well as a saturated calomel electrode (SCE) as reference electrode; to avoid water and KCl contamination of the working solution, the reference electrode was inserted in a compartment filled with the solvent + supporting electrolyte medium, communicating with the working compartment through a porous frit. The potentials of the recorded voltammograms were afterwards referred to the formal potential of the ferricinium|ferrocene Fc⁺|Fc intersolvental reference redox couple, measured in the same conditions. A selection of the CV features of the tweezers and tweezer moieties is shown in Figures 130 to 136, and key parameters are collected and compared in Table 14, with colours evidencing proposed assignments of the observed electron transfers to different redox sites in the tweezers.

I. Tweezers with N^+ alkyl salt terminals

In the cases of tweezers with quinolinium or pyridinium salt terminals and naphthyl ester linkers (the 4m, 4s and 5m series, Figures 130 and 131), the first reduction peak should correspond to the reduction of the quinolinium or pyridinium cations to the corresponding radicals, a process which appears kinetically rather easy, considering the small variation of peak potentials with increasing scan rates. It takes place much before in the quinolinium case (5m tweezers, -1.23/-1.24 V) respect to the pyridinium one (4m and 4s tweezers, -1.63/-1.65 V) consistently with the improved heteroaromatic system conjugation promoting the process. Remarkably, instead, neither the counteranion nature (methanesulfonate “M” vs bistriflimidate “T” compounds) nor the configuration of the stereocentre (isomannide “m” vs isosorbide “s” compounds) differentiating between isomannide and isosorbide core appear to have significant effects (a consideration which, as will be shown later on, holds also for other systematic series tested).

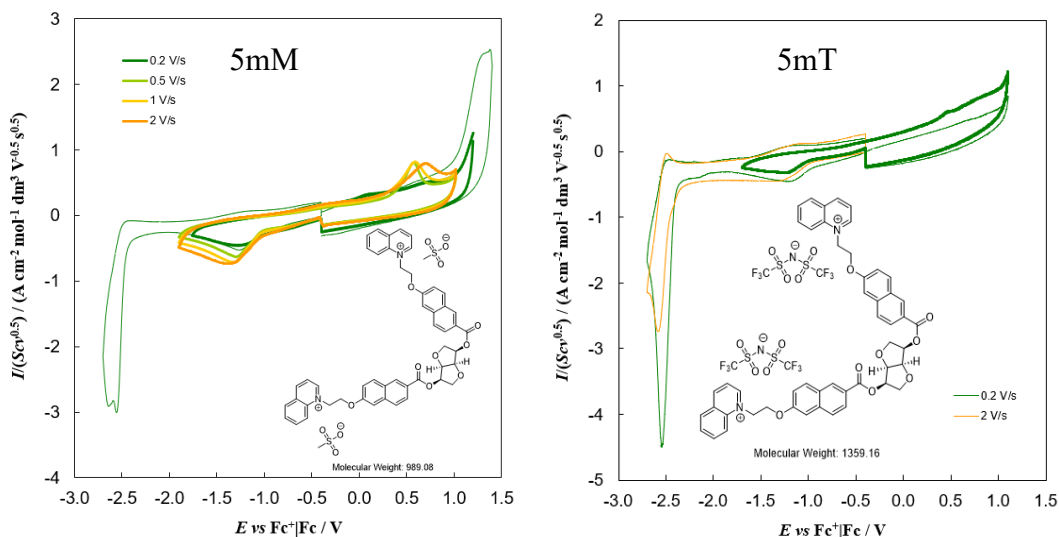


Figure 130. Normalized CV patterns of tweezers with **quinolinium** terminals in ACN + 0.1 M TBAPF₆.

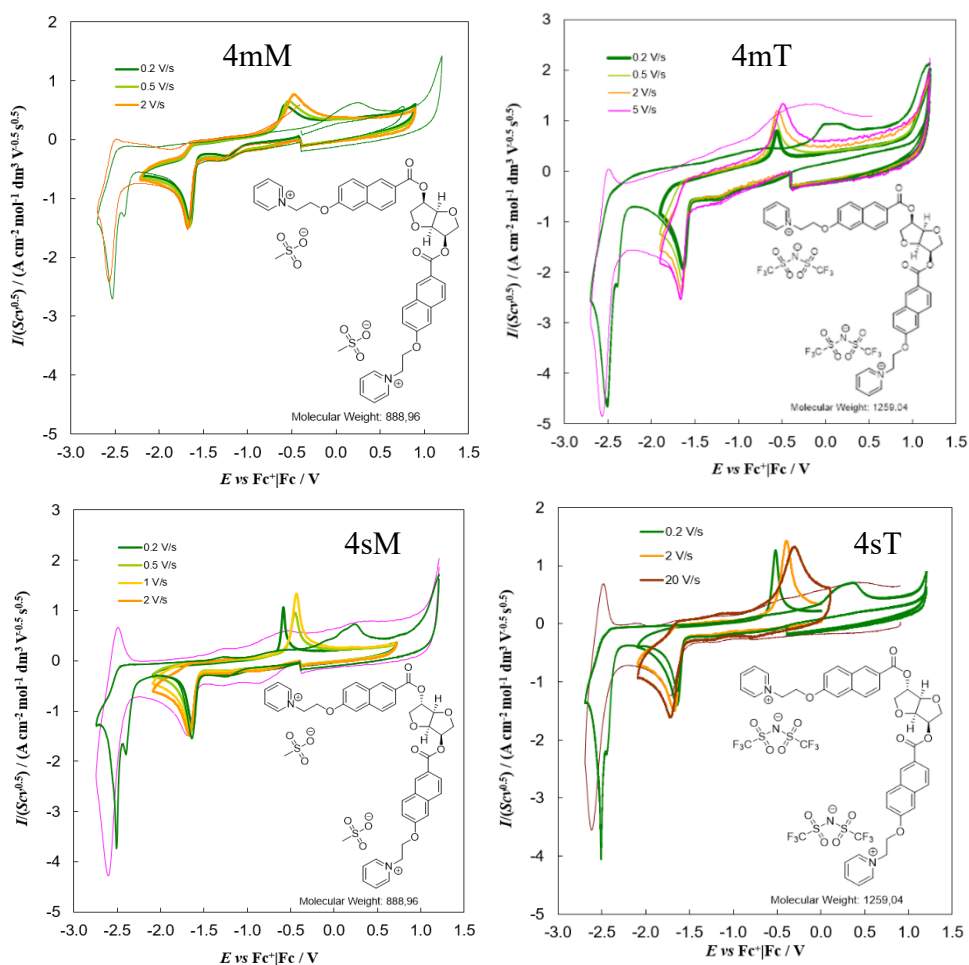


Figure 131. Normalized CV patterns of tweezers with **pyridinium** terminals in ACN + 0.1 M TBAPF₆.

A second reduction peak at more negative potentials (about -2.5 V), tending to chemical reversibility with increasing scan rate, and absent in tweezers with no naphthyl ester linker unit (see later on), should be ascribed instead to reduction of the naphthalene system in the naphthyl ester, resulting in quasi reversible radical anion formation.

Interestingly, upon reverting the potential scan after the first reduction peak, a neat oxidation peak appears, at much more positive potentials than the forward

process (at 0.5/0.6 in the 5m quinolinium case, at -0.5/-0.6 in the 4m and 4s pyridinium cases), but regularly and reproducibly even in subsequent potential cycles, of area comparable with, or approaching, the area of the reduction peak, and strictly related to such reduction process, since it cannot be observed without performing the first reduction process first. By analogy with similar cases involving reduction of pyridinium sites in aza and diazahelicenes, a tentative assumption might be in terms of radical reversible dimerization, a sort of redox-driven switch [137,218].

In the case of imidazolium salts (3m and 3s compounds, Figure 132) the first reduction process is even less favoured, and the first reduction process is only observed at about -2.45 V; in this case it is doubtful whether it should correspond to reduction of the naphthyl ester redox sites, or of the imidazolium cations, or both (but it looks too small for this last assumption); in any case, a linked reoxidation peak at much more positive potentials (-0.8/-1 V) is observed also in this case.

Upon exploring the oxidation side of the potential window, no independent peak can be found before a signal at about 1.3 V close to the positive background reaction, which should correspond to the naphthyl ester redox site.

The tweezers with methylquinolinium or butylquinolinium terminals and no naphthyl ester linker (1m and 2m compound subseries, Figures 133 and 134), share practically the same CV features, consistently with them differing only for the alkyl chain length. They undergo reduction very early, at about -1.13 V (with associated reoxidation peak at -0.2/-0.3 V), that is, even more easily than the above 5m quinolinium ones, which is clearly related to the electron-withdrawing nature of the ester group which is in this case present on the quinoline system only in cases 1m and 2m. No oxidation peaks are perceivable besides the above

ones related to first reduction; an exception is represented by the tweezers with iodide counterions, that is 1mI, 1sI, 2mI and 2sI, featuring additional peaks strictly linked to the anion oxidation (as confirmed by performing a CV test in the same conditions on a tetraalkylammonium iodide salt), which prevents use of such additives in a large portion of the potential window.

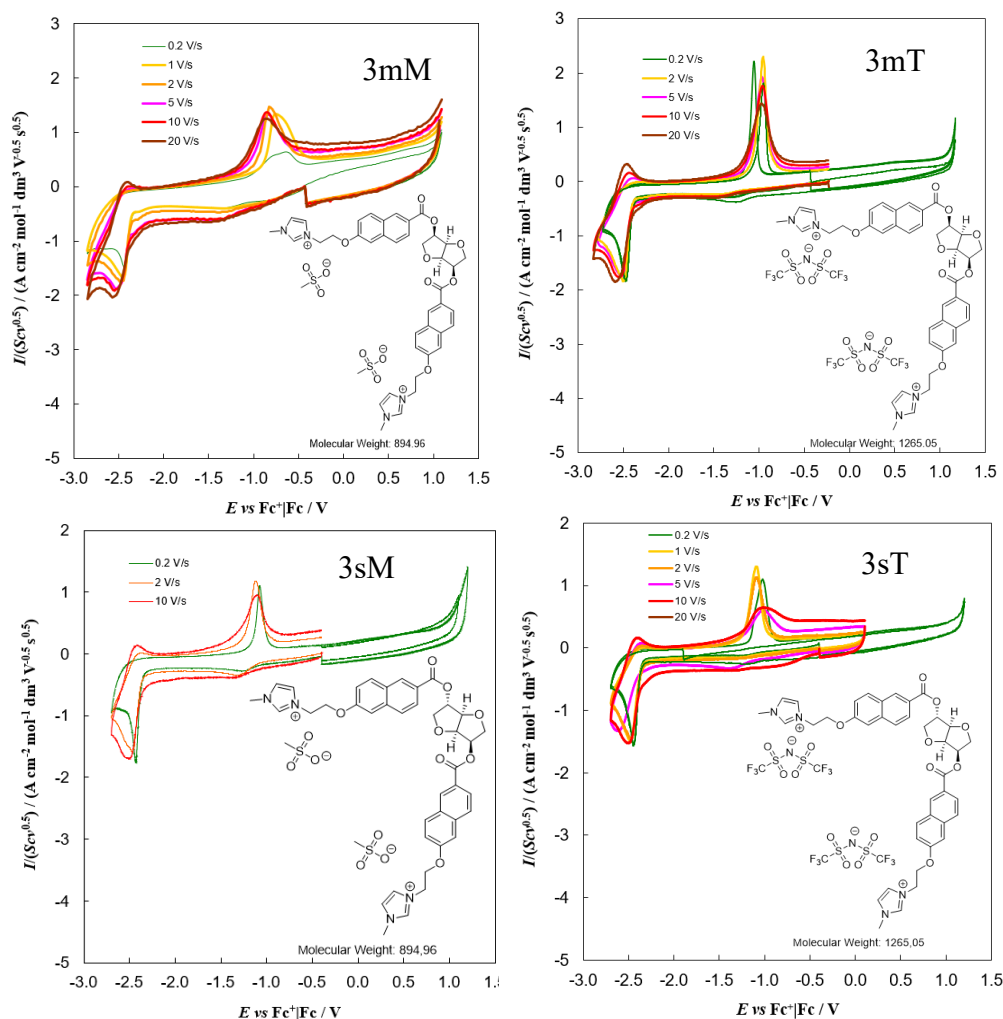


Figure 132. Normalized CV patterns of tweezers with **imidazolium** terminals in ACN + 0.1 M TBAPF₆.

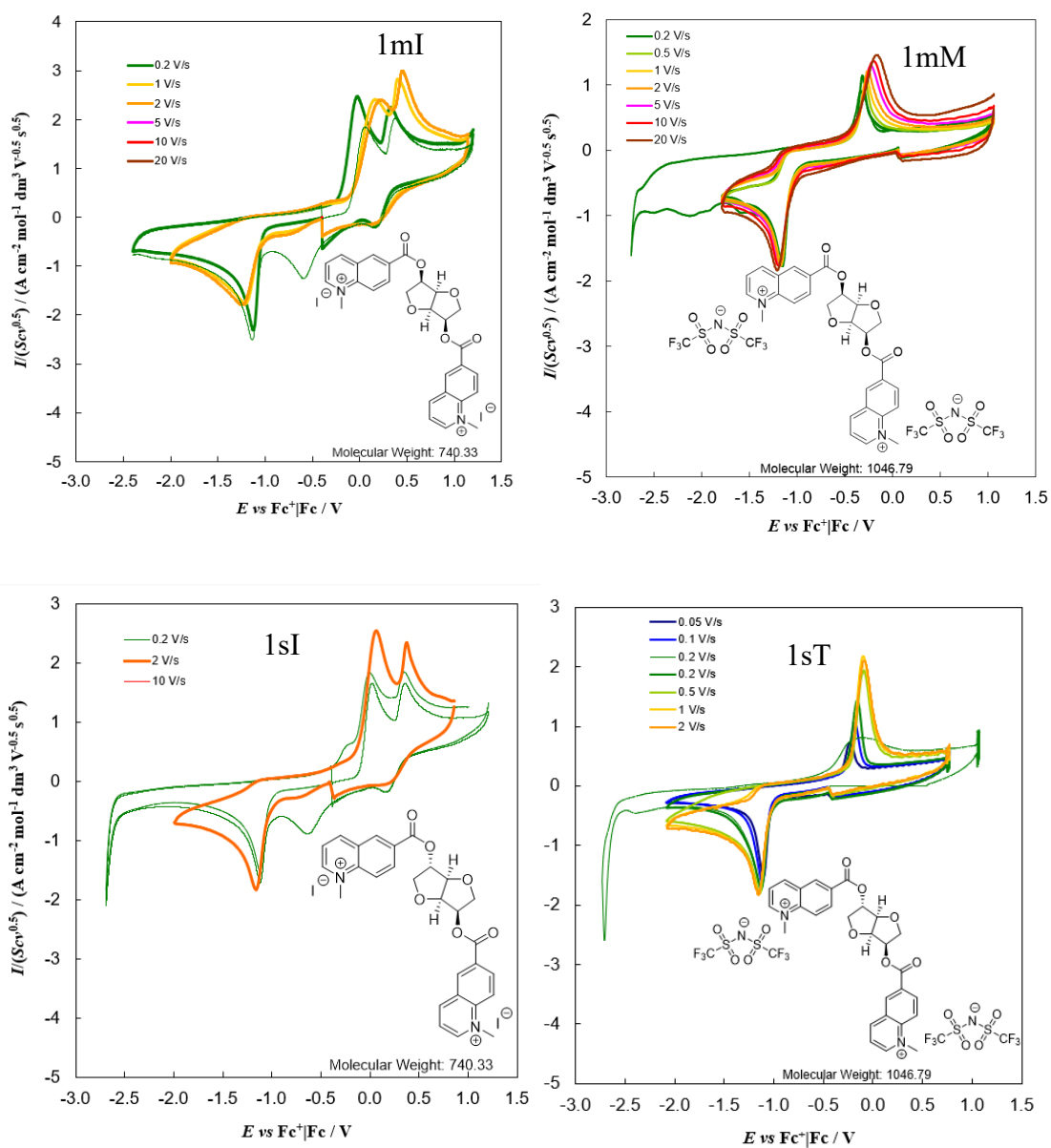


Figure 133. Normalized CV patterns of tweezers with **methylquinolinium** terminals and **no naphthyl ester spacers** in ACN + 0.1 M TBAPF₆.

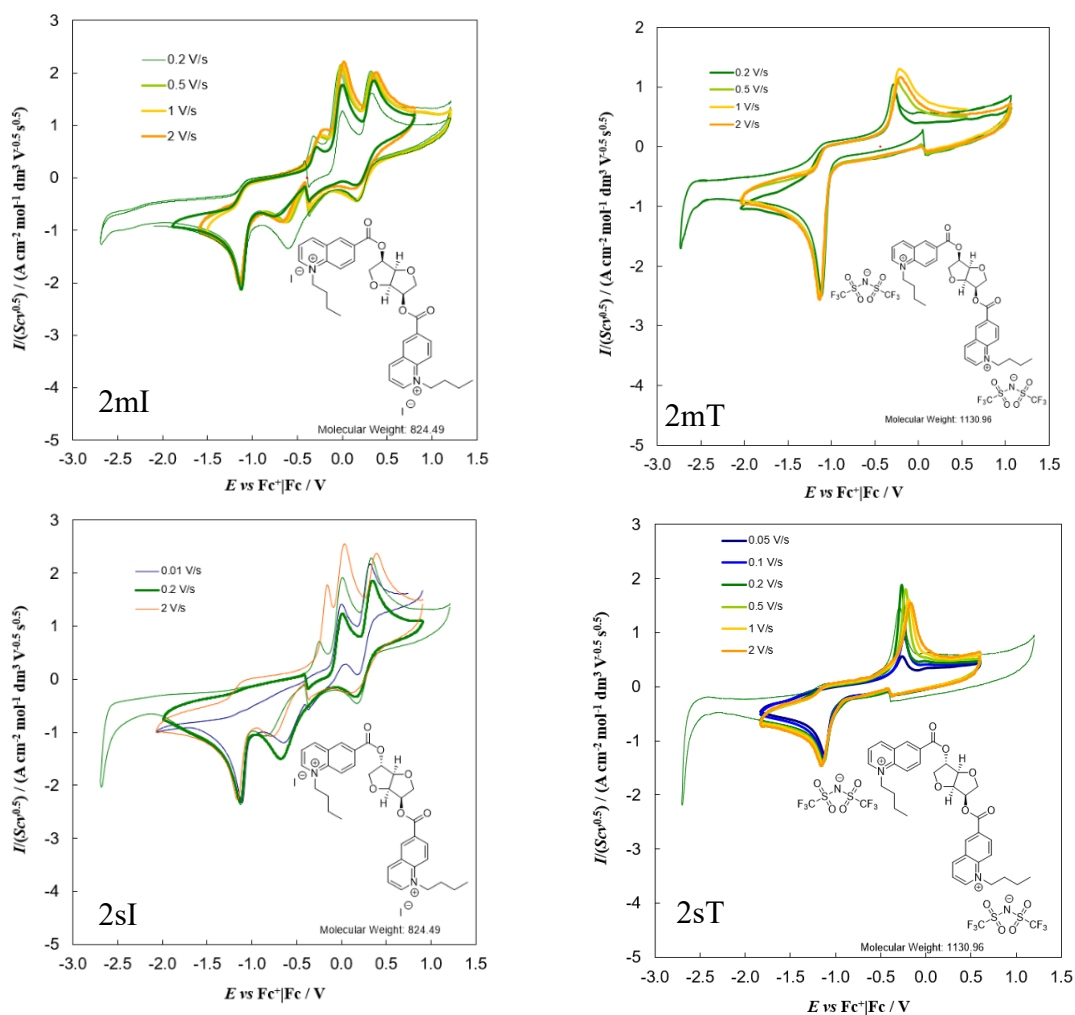


Figure 134. Normalized CV patterns of tweezers with **butylquinolinium** terminals and **no naphthyl ester spacers** in ACN + 0.1 M TBAPF₆.

On the whole, the methylimidazolium tweezers of subseries 3m and 3s look the most convenient option in terms of potential window width for use as additives in electrochemical experiments, although of course not necessarily in terms of coordination ability.

II. Neutral tweezers and tweezer moieties

With pyridine terminals

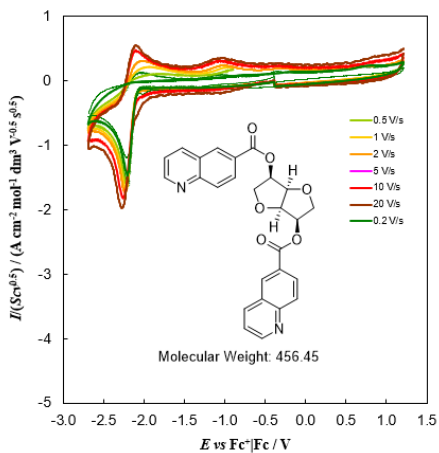
Comparing the neutral tweezers 9m, 9s with quinoline terminals (Figure 135) with their analogues with quinolinium salt terminals (Figure 130) the first reduction potentials are shifted to remarkably more negative potentials (from -1.2 V to -2.2 V), consistently with the free *N* redox site being significantly electron richer.

Moreover, unlike the former case, the process now tends to chemical reversibility, which can be justified by its consisting in radical anion rather than radical formation. No further reduction peak is observed, consistently with the lack of the naphthyl ester linkers.

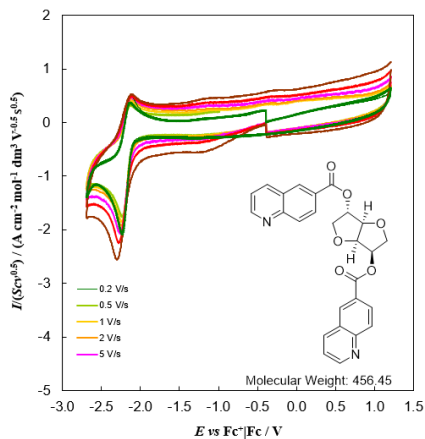
The three tweezer 10m, 10s, 11s (Figure 135) have features similar to the tweezer ones, but, reasonably, the tweezer reduction peak currents are double respect to the tweezer moiety ones, consistently with both quinoline terminals reacting at the same potential in a totally independent way.

With methanesulphonate terminals

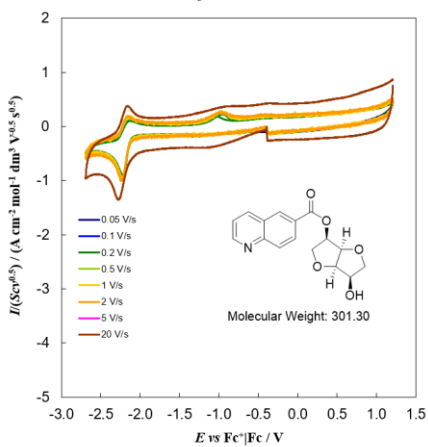
The electrochemical reactivity of the neutral tweezers 6m, 6s with methane sulfonate ester terminals, as well as of related moieties 7m, 8m, (Figure 136) looks dominated by their naphthyl ester linkers and, in the last asymmetric case 8m, also by the quinoline group; in this case the two reduction peaks corresponding to naphthyl ester and quinoline look to be simply added in the voltammogram with no reciprocal interaction, which once more is quite reasonable considering the molecular structure.



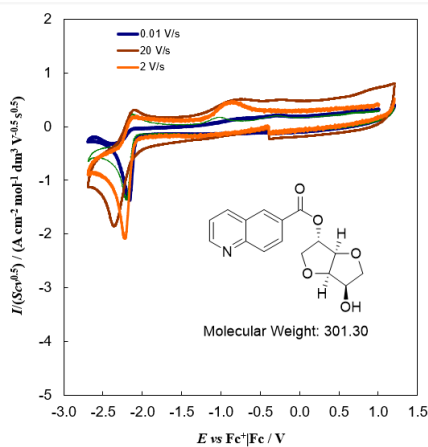
9m



9s

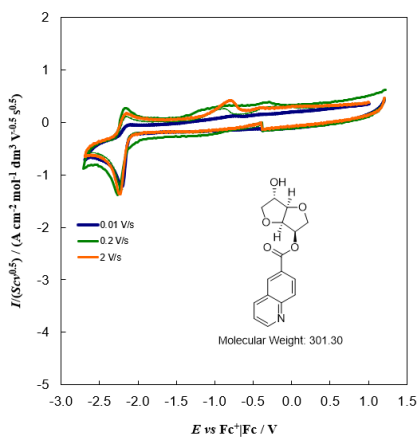


10m



10s

Figure 135. Normalized CV patterns of neutral tweezers and tweezer moieties with **quinoline** terminals and **no naphthyl ester spacers**, in ACN + 0.1 M TBAPF₆



11s

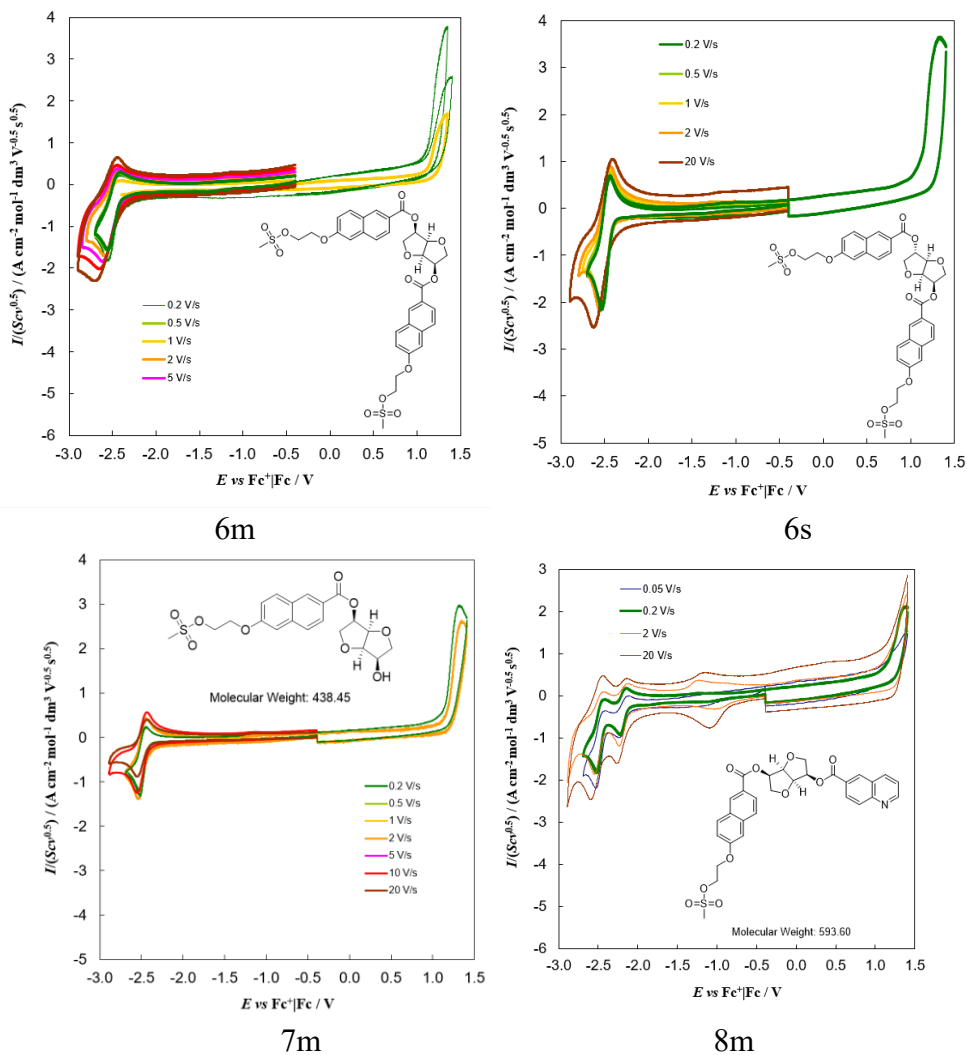


Figure 136. Normalized CV patterns of neutral tweezers 6m, 6s with methanesulfonate ester terminals and naphthyl ester spacers, as well as of relate tweezer moieties 7m and 8m, in ACN + 0.1 M TBAPF₆.

Table 14. Key CV features of the chiral tweezers as well as of some tweezer moieties in ACN + 0.1 M TBAPF₆: reduction and oxidation peak potentials recorded on GC at 0.2 V/s potential scan rate, referred to the Fc⁺|Fc intersolvental reference redox couple. Colours show proposed assignments of the CV peaks to tweezers building blocks/redox sites.

	core	linker	terminal	anion	$E_{p,c}/V$	$E_{p,ra}/V$ (rel. to $E_{p,c}$)	$E_{p,la}/V$
1mI	isomannide		methylquinolinium	I ⁻	-1.13	-0.3 ^{small}	-0.03
1mT	isomannide		methylquinolinium	Tf ₂ N ⁻	-1.16	-0.32	
1sI	isosorbide		methylquinolinium	I ⁻	-1.12	-0.22 ^{small}	-0.03
1sT	isosorbide		methylquinolinium	Tf ₂ N ⁻	-1.13	-0.16	
2mI	isomannide		butylquinolinium	I ⁻	-1.13	-0.28 ^{small}	-0.03
2mT	isomannide		butylquinolinium	Tf ₂ N ⁻	-1.12	-0.27	
2sI	isosorbide		butylquinolinium	I ⁻	-1.13 -0.84 ^{broad}	-0.24 ^{small}	-0.02
2sT	isosorbide		butylquinolinium	Tf ₂ N ⁻	-1.13	-0.265	
3mM	isomannide	naphthyl ester	imidazolium	MsO ⁻	-2.45 (→rev)	-0.77	[1.3]
3mT	isomannide	naphthyl ester	imidazolium	Tf ₂ N ⁻	-2.48 (→rev)	-1.06/-0.96	[1.3]
3sM	isosorbide	naphthyl ester	imidazolium	MsO ⁻	-2.43 (→rev)	-1.07	[1.3]
3sT	isosorbide	naphthyl ester	imidazolium	Tf ₂ N ⁻	-2.45 (→rev)	-1.02/-1.09	[1.3]
4mM	isomannide	naphthyl ester	pyridinium	MsO ⁻	-2.39 ^{pre} , -2.54 ^{→rev} - 1.65	-0.58	>1.2
4mT	isomannide	naphthyl ester	pyridinium	Tf ₂ N ⁻	-2.54 ^{→rev} - 1.63	-0.56	≥ 1.2
4sM	isosorbide	naphthyl ester	pyridinium	MsO ⁻	2.40 ^{pre} -2.51 ^{→rev} - 1.63	-0.58	>1.2
4sT	isosorbide	naphthyl ester	pyridinium	Tf ₂ N ⁻	2.45 ^{pre} 2.51 ^{→rev} - 1.64	-0.52	>1.2
5mM	isomannide	naphthyl ester	quinolinium	MsO ⁻	-2.56 ^{→rev?} , -2.65 - 1.24	0.61 ^{0.5}	1.31
5mT	isomannide	naphthyl ester	quinolinium	Tf ₂ N ⁻	-2.55 ^{→rev} - 1.23	0.47	[1.3]
6m	isomannide		Methanesulfonate ester		-2.55 ^{→rev@}		1.40
6s	isosorbide		Methanesulfonate ester		-2.53 ^{→rev@}		1.33
7m	isomannide		Methanesulfonate ester / Quinoline		-2.52 ^{→rev} -2.22 ^{→rev}		1.39
8m	isomannide		Methanesulfonate ester		-2.54 ^{→rev}		1.32
9m	isomannide		quinoline		-2.21 ^{→rev @}		
9s	isosorbide		quinoline		-2.24 ^{→rev @}		
10m	isomannide		quinoline		-2.22 ^{→rev}		
10s	isosorbide		quinoline		-2.20 ^{→rev}		
11s	isosorbide		quinoline		-2.22 ^{→rev}		

→rev tending to chemical reversibility^{0.5} at 0.5 V/s

@ Double current intensity respect to tweezer moiety

c) Highlighting chirality properties with electronic circular dichroism

Electronic circular dichroism ECD enables to highlight how powerful are chirality manifestations of molecules which include both stereogenic elements and UV-Vis chromophores (the latter often corresponding to redox sites), in terms of difference in the ϵ_L and ϵ_R molar extinction coefficients for absorption of the left-handed and right-handed circularly polarized light components [219,220]. The enantiomers of a chiral probe give of course specular ECD signals. Sharper signals are usually observed with “inherently chiral” probes respect to probes with localized stereocentres, as well as with macromolecules displaying high order in their secondary structure respect to random coil ones [219,220]. The presence in a given probe of two equivalent, reciprocally interacting chromophores results in loss of degeneracy in the excited energy level (“exciton coupling”, analogous to the coupling of two interacting equivalent redox centres in electrochemistry), usually unperceived in the UV-Vis spectrum, but revealed by a typical sigmoidal signal in the ECD one (Davydov splitting) [219,220]. The tweezer subseries 3, 4, 5 and 6 were characterized in terms of UV-Vis and electronic circular dichroism ECD spectra, recorded in acetonitrile as the solvent with a concentration of $\approx 10^{-4}$ M. The ECD results are compared in Figure 137.

Neutral tweezers 6m and 6s, in spite of being diastereoisomers (on account of the presence of three stereocentres of constant *R*- configuration besides the key one the *R*- or *S*- configuration of which determines the isomannide or isosorbide nature of the tweezer core) are characterized by quasi enantiomeric ECD spectra, showing the same bands at the same wavelengths and with almost the same intensity but opposite in sign (Figure 137 top). This behaviour had been already observed for the 1m, 1s, 2m, 2s quinolinecarboxylate series [213], as well as for bis(*p*-bromobenzoate) derivatives of isomannide and isosorbide [221].

Like for such derivatives, the most conspicuous feature in the ECD spectra of 6m and 6s is an exciton couplet in the region between 270 and 220 nm, which is likely due to the coupling of the electrically allowed 1B_b transitions of the naphthalene chromophores on the two tweezer arms, polarized along the long axis of the aromatic ring and perturbed by the alkoxy and carboxyl substituents leading to a red shift of the corresponding band [222]. Unlike common occurrences only resulting in widening of UV-Vis peaks [219,220], this exciton coupling is also perceivable in the UV-Vis spectra as a splitting of the more intense absorption band, which presents two maxima at the same wavelengths of the two bands of the couplet. The couplet is positive for 6m ($\Delta\epsilon = +118$ at 254 nm, $\Delta\epsilon = -86$ at 233 nm) and negative for 6s ($\Delta\epsilon = -126$ at 254 nm, $\Delta\epsilon = +86$ at 233nm) as observed for the other derivatives of isomannide and isosorbide, but appears more symmetric than in the case of the analogous quinolincarboxylate derivatives [213]. The ECD spectra also feature a further signal at 304 nm, its simple shape consistent with no exciton coupling; it is attributable to the 1L_a transition polarized along the short axis of the chromophores [223], positive for 6m ($\Delta\epsilon = +9$) and negative for 6s ($\Delta\epsilon = -10$).

The same trend is found for ionic tweezer subseries 3,4 and 5, which show excitonic ECD spectra, quasi enantiomeric in passing from isomannide to isosorbide derivatives (Figure 137 bottom). The amplitude of the couplet depends both on the cation and on the anion, suggesting that their nature can affect the reciprocal orientation of the chromophores [222]. Anyway, no drastic change can be supposed, since the spectra are very similar among themselves. In the isomannide group, considering the same cation, the exciton couplet is more intense for the bistriflimide derivatives and, considering the same anion, the pyridinium salts show more intense couplets than the quinolinium ones, which, in turn, show more intense couplets than imidazolium ones. The trend is different in the isosorbide group, where the two pyridinium salts show very similar spectra

that present a less intense couplet than that in the spectra of the corresponding imidazolium salts.

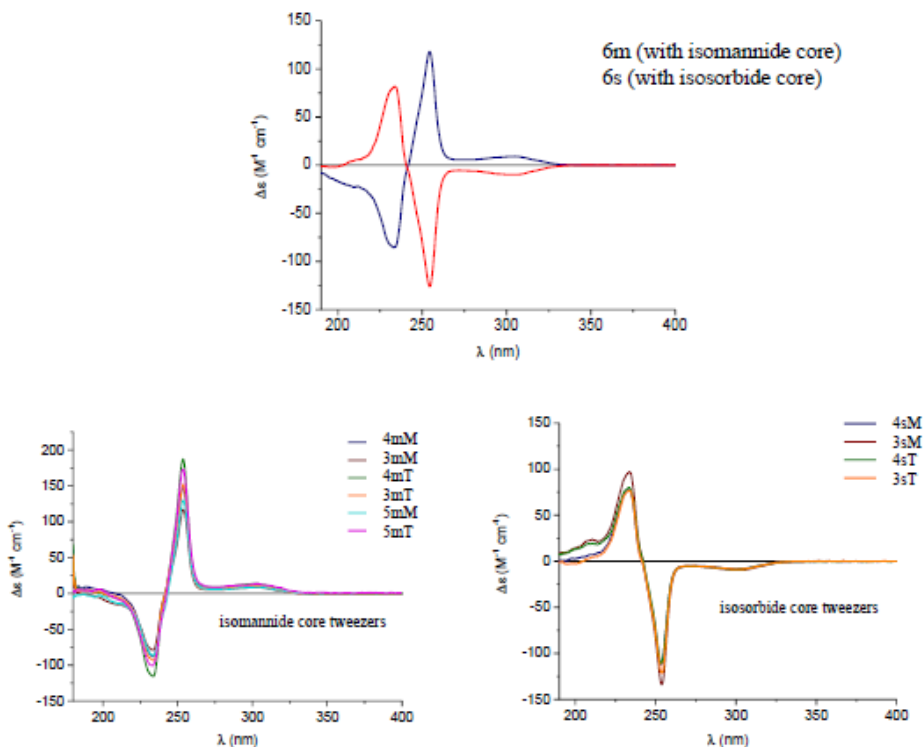


Figure 137. Top: superimposition of ECD spectra of 6m (blue line, $3.2 \cdot 10^{-4}$ M) and 6s (red line, $3.4 \cdot 10^{-4}$ M) (ACN, 0.02 and 0.1 cm path length). Bottom: Left side: superimposition of ECD spectra of 3mM (dark red line, $2.8 \cdot 10^{-4}$ M), 4mM (blue line, $2.1 \cdot 10^{-4}$ M), 3mT (orange line, $1.9 \cdot 10^{-4}$ M), 4mT (dark red line, $2.0 \cdot 10^{-4}$ M), 5mM (light blue line, $2.9 \cdot 10^{-4}$ M) and 5mT (light magenta line, $4.6 \cdot 10^{-4}$ M). Right side: superimposition of ECD spectra of 3sM (dark red line, $1.8 \cdot 10^{-4}$ M), 4sM (blue line, $4.6 \cdot 10^{-4}$ M), 3sT (orange line, $1.9 \cdot 10^{-4}$ M) and 4sT (dark red line, $2.0 \cdot 10^{-4}$ M). (ACN, 0.01, 0.02, 0.05 and 0.1 cm path length).

d) Features of two chiral probe candidates

The CV features of chiral probe candidates (Figure 138) for enantiodiscrimination experiments 2,5-dinitrobenzoyl phenyl glycine methyl ester (DNB-PhGly in Figure 138 left side, a molecule related to popular stationary phases in chiral HPLC) and 2,2,2-trifluoro-1-(9-anthryl)ethanol (TFAE in Figure 138 right side, a popular reagent to resolve ^1H NMR spectra of enantiomers, which resolution was also recently achieved in the case of member of the tweezer subseries introduced in [213]) were also recorded in the same conditions.

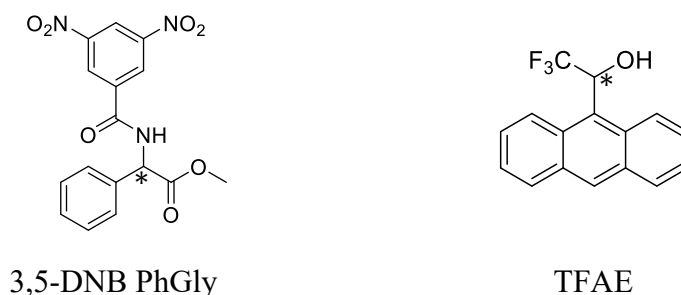


Figure 138. The two chiral electroactive probes *N*-3,5-dinitrobenzoyl phenylglycine methylester (3,5-DNBPhGlyCOOMe, 3,5-DNB PhGly) and 1-(9-Anthryl)-2,2,2-trifluoroethanol (TFAE) employed in the enantiodiscrimination tests.

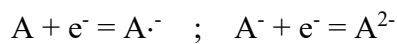
Selected CV patterns are shown in Figure 139 and Figure 140, respectively; the same Figures also report the remarkable changes observed in CV and DPV patterns upon addition of tweezer 4mT (from green lines to pink lines), which can only partially be ascribed to the tweezer CV features, and thus might point to significant probe/selector interactions.

The two probes had also been investigated together for mutual interactions by theoretical computations [224]. Instead, to our knowledge, electrochemical characterizations/applications are still lacking, excepting electrochemical studies

in aqueous medium of monomers consisting of DNB-PhGly conjugated to pyrrole, and related electrochromic polymeric films on ITO [225].

TFAE exhibits a first oxidation peak at about 0.95 V vs Fc⁺/Fc and a first reduction peak at about -2.3 V vs Fc⁺/Fc, closely followed by other ones. Both electron transfer processes look fast (potential nearly constant with scan rate); at 0.2 V/s scan rate they appear to have chemical follow ups (possibly coupling processes considering the aprotic medium), but tend to chemical reversibility with increasing scan rate (return peak of increasing height) [226].

DNB-PhGly exhibits three subsequent reduction processes with associated return peaks, at about -1.25, -1.6 and -1.8 V vs Fc⁺/Fc. In particular, the first one (chemically and electrochemically reversible) and second one (quasi reversible), could be ascribed to two subsequent monoelectronic reduction steps, to radical anion and dianion (stable in the aprotic medium) [227]



(unlike in water media, in which dinitroaryl systems have irreversible CV patterns, since proton availability results in nitroso/hydroxylamino/amino derivative formation [227]).

The potential difference for such two processes in dinitroaromatics has been shown to depend on the distance and conjugation of the nitro groups [227]; in particular, for *m*-dinitrobenzene $E^{\circ}_I = -1.31$ V and $E^{\circ}_{II} = -1.75$ V are reported in DMF [227], quite consistent to the first and second reduction peak potential here observed for DNB-PhGly in acetonitrile.

Unlike TFAE, DNB-PhGly does not show oxidation peaks in the potential window here considered, although irregular oxidation peaks related to products from reduction processes are observed upon cycling.

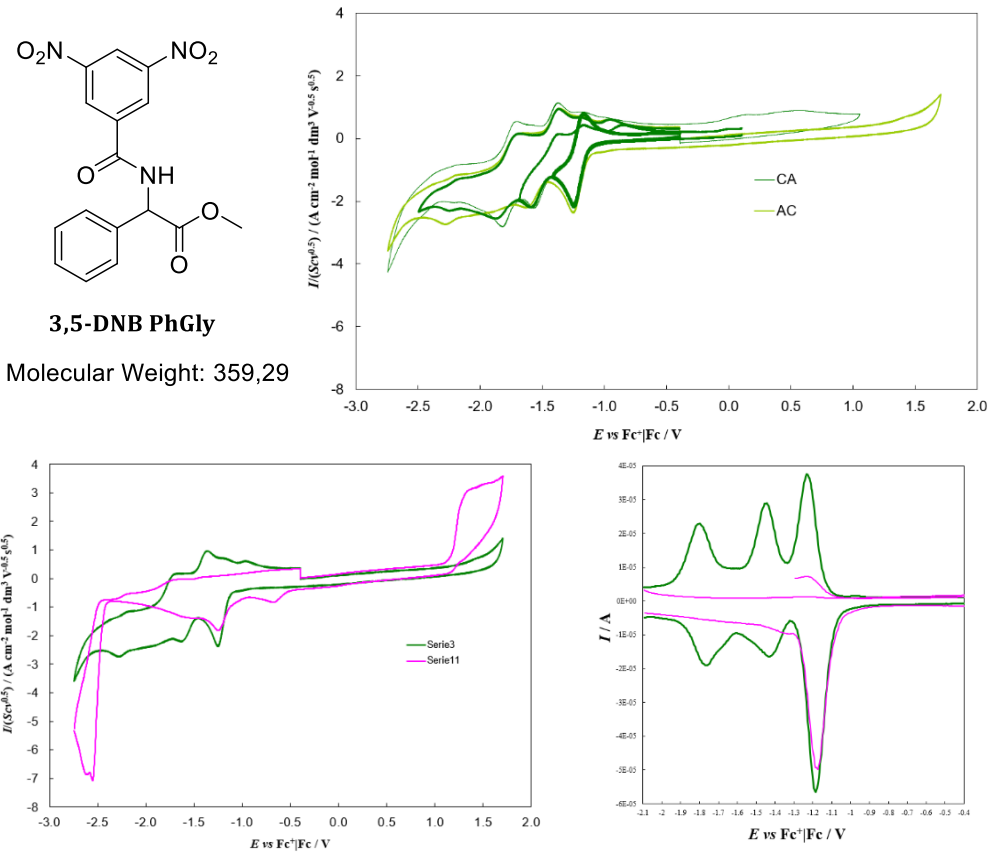
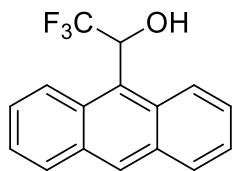


Figure 139. Normalized CV patterns of chiral probe candidate 2,5-dinitrobenzoyl phenyl glycine methyl ester (DNB-PhGly), in ACN + 0.1 M TBAPF₆.



TFAE (T)

Molecular Weight: 276,26

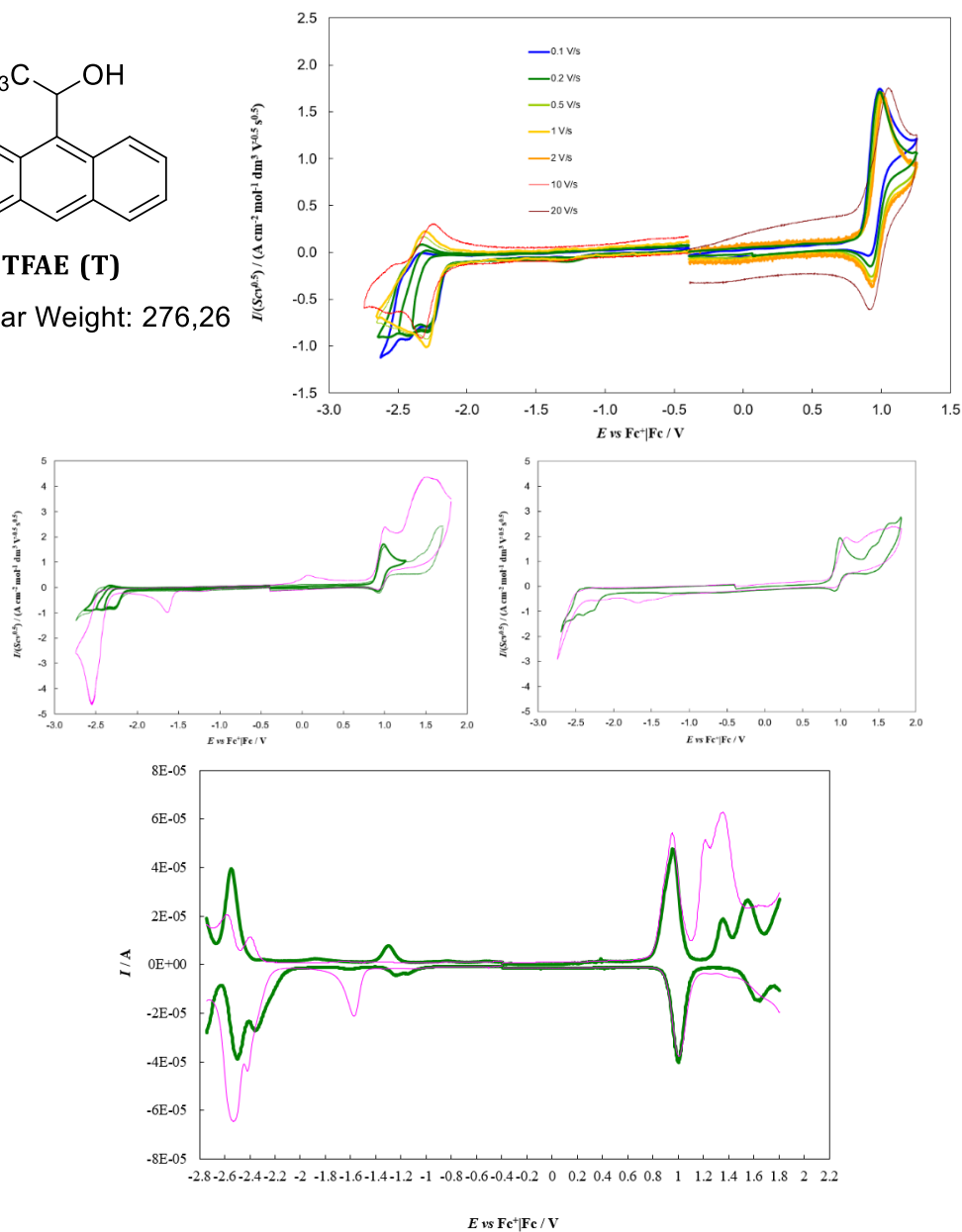


Figure 140. Normalized CV patterns of chiral probe candidate 2,2,2-trifluoro-1-(9-anthryl)ethanol, in ACN + 0.1 M TBAPF₆.

e) Enantiodiscrimination experiments

First enantiodiscrimination tests were carried out using:

- (+) or (-)-DNB-PhGly as enantiopure chiral probes (0.005 M) in BMIMTFSI with the addition of 3mT as low concentration chiral additive (0.01 M), in Figure 141;
- (S)-(+)-TFAE in BMIMTFSI (0.005 M) with the addition of chiral tweezers 2mT or 2sT (0.01 M) as low concentration chiral additives, in Figure 142.

The CV patterns have been recorded working in a drop of BMIMTFSI achiral ionic liquid with addition of chiral tweezers 3mT, 2mT or 2sT (having the same bistriflimide counteranion as the achiral ionic liquid) in 0.01 M concentration. The working solution drop was deposited on minicells with C working and counter electrodes and Ag pseudoreference electrodes, screen printed on flexible plastic supports.

Concerning the results reported in Figure 141, the first observed oxidation peaks for the probe/selector systems (which might be attributed to oxidation of the naphthyl linker in the selector) are located at significantly different potentials in the cases of the (+) and (-) enantiomers (~ 1.35 V and ~ 1.59 V vs $\text{Ag}^+|\text{Ag}$), pointing to significantly different interactions of 3mT with the two DNB-PhGly probe enantiomers and resulting in a peak potential separation of ~ 240 mV.

Reproducibility tests were performed by repeatedly recording the CV patterns of the chiral probes on new SPE (Figure 141 dotted lines).

Instead, concerning the results reported in Figure 142, the enantiopure (S)-(+)-TFAE chiral probe in solutions containing the chiral tweezers 2mT and 2sT show a peak potential separation of ~ 100 mV, consistently with the two chiral tweezers being diastereoisomers.

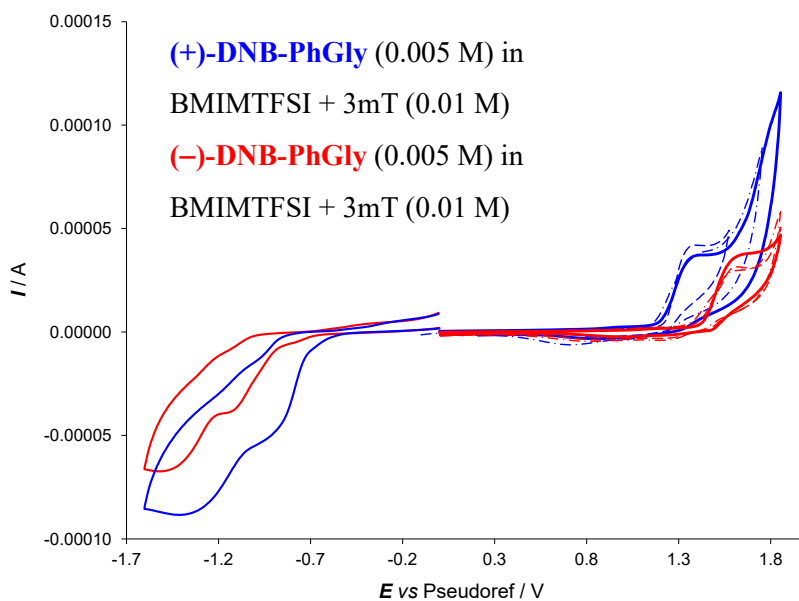


Figure 141. Enantioselection tests with (+) and (-) enantiomers of probe DNB-PhGly in a drop of BMIMTFSI achiral ionic liquid with addition of chiral tweezers 3mT in 0.01 M concentration.

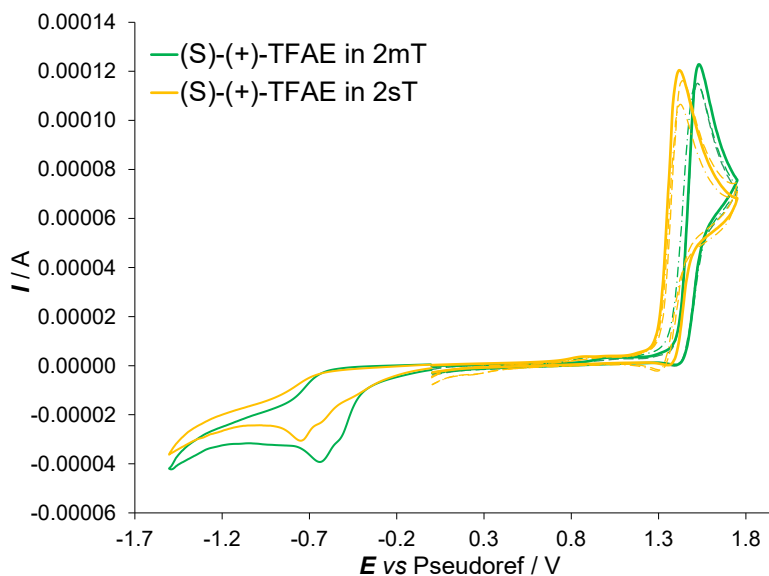


Figure 142. Enantioselection tests with (S)-(+)-TFAE in a drop of BMIMTFSI achiral ionic liquid with addition of chiral tweezers 2mT or 2sT (green and orange respectively) in 0.01 M concentration.

4.2.4 *Natural or artificial selector? Looking for an ideal chiral selector*

A summary of desirable features for an ideal chiral selector is the following one:

- Above all, it should be able to discriminate probe enantiomers in terms of the largest possible peak potential differences, to (analytically) recognize or (preparatively) manage either antipode at its own activation potential. In this respect discrimination in terms of current differences appear less useful.
- It should be available in both enantiomer configurations, so that the first activable electron transfer can correspond to the preferred target enantiomer (particularly for preparative purposes).
- It should exhibit a linear dynamic range for currents, possibly with low limit of detection, to complement enantiodiscrimination with quantitative analysis and enantiomeric excess estimation (particularly for analytical purposes).
- It should be of general applicability to many probes and operating protocols/conditions.
- It should have reproducibility in preparation and recognition as well as stability and robustness.
- It should be of easy, fast and low-cost preparation, and/or be required in low quantity, and/or recyclable.

Either natural or artificial chiral selectors can be considered. Actually, many natural ones are currently employed in electroanalysis (*e.g.*, enzymes, antibiotics ...); however, the second alternative looks particularly attractive for many reasons, including the virtually unlimited range of tailored structures possible as well as the possibility to have both enantiomers of a given selector equally available, thus enabling to freely choose the probe enantiomer to be activated first and, finally the possibility to optimize production to reduce costs.

Thus, efforts are increasingly being devoted to achieve chiral electroanalysis based on artificial selectors either chiral electrode surfaces or chiral media. For these reasons, the following paragraphs are focused on the study and exploitation of different artificial chiral selectors, using them as chiral additive or as bulk media, and tested in enantioselection experiments.

Particularly attention will be devoted to inherently chiral ionic liquids (which present a C_2 stereogenic axis or an helix as stereogenic element).

4.2.5 Inherently chiral ionic liquid based on a 3,3'-bipyridine scaffold

Bi-*N*-heteroaromatic cations with a rotational barrier arising from sterical hindrance between alkyl substituents could yield inherently chiral ionic liquids (ICILs). In this frame, artificial inherently chiral (*R*)- and (*S*)-1,1'-Dioctyl-2,2',4,4',6,6'-hexamethyl-3,3'-bipyridine-1,1'-diiumbis(trifluoromethane sulfonyl)imidate, (*R*)- and (*S*)-3mO₂NTf₂ [134] (Figure 143), liquid at room temperature, were synthesized. They are based on a 3,3'-bipyridine scaffold with the *N* atoms functionalized with octyl alkyl chains and bistriflimide (NTf₂) as counteranion (in order to decrease the melting point, widely used in IL design for its relatively high stability and low toxicity) and were tested as selector media in voltammetry enantiodiscrimination experiments.

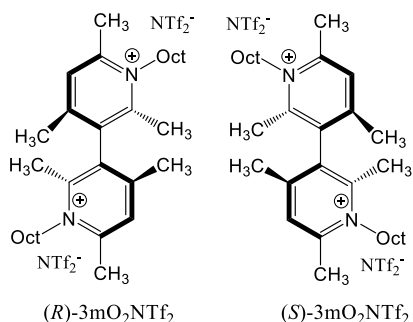


Figure 143. Structures of the enantiomers of the inherently chiral ionic liquid *N,N'*-dialkyl-3,3'-bicylidinium salts.

As in previous cases, reported in the chapter dedicated to inherently chiral monomers, the CD spectra of (*R*)- and (*S*)-3mO₂NTf₂ enantiomers in MeOH solution were recorded, as reported in Figure 144 [134] and as expected they are perfectly specular.

The enantioselection tests were performed with the enantiomer probes (*R*)-(+)- or (*S*)-(-)-*N,N'*-dimethyl-1-ferrocenylethylamine (namely FcR and FcS), using (*R*)- and (*S*)-3mO₂NTf₂ as both (a) low concentration chiral additive (0.01 M) in achiral BMIMNTf₂ and (b) as bulk media.

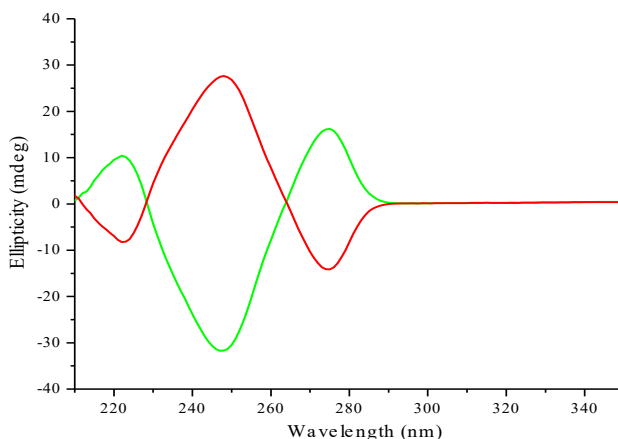


Figure 144. CD spectra (MeOH, $c = 0.2 \text{ mg/cm}^3$) of (*R*)- and (*S*)-3mO₂NTf₂ (green and red respectively).

(a) The results obtained in the first case, *i.e.* using (*S*)-3mO₂NTf₂ as chiral additive (0.01 M) in BMIMNTf₂ are reported in Figure 145, achieving a peak potential separation of about 170 mV between the two antipodes of the chiral probe.

(b) FcS and FcR were studied by CV (0.05 V s⁻¹ potential scan rate), both alone (Figure 146 and 147) and in mixtures (Figure 148 and details in Gallery Section 18), in small solution volumes at concentrations in the 0.004-0.001 M range, on two different kinds of SPE cells:

- i)* A commercial one with gold as working and counter electrodes and silver as pseudoreference electrode (DropSens, DRP-X-C220AT-ND, 3.4 x 1.0 x 0.05 cm) (Figure 146).
- ii)* A laboratory screen printed electrode one on plastic sheet (details in 4.1), including graphite working and counter electrodes and Ag pseudoreference electrode (Figure 147 and 148).

Reproducibility tests were performed by repeatedly recording the CV patterns of model probes on new SPE (Figure 146) and concentration calibration plots have also been obtained for all enantiomer combinations, by recording CV

patterns at increasing substrate concentration in the 0.001–0.004 M range (Figure 147, peak currents exhibit linear dynamic ranges).

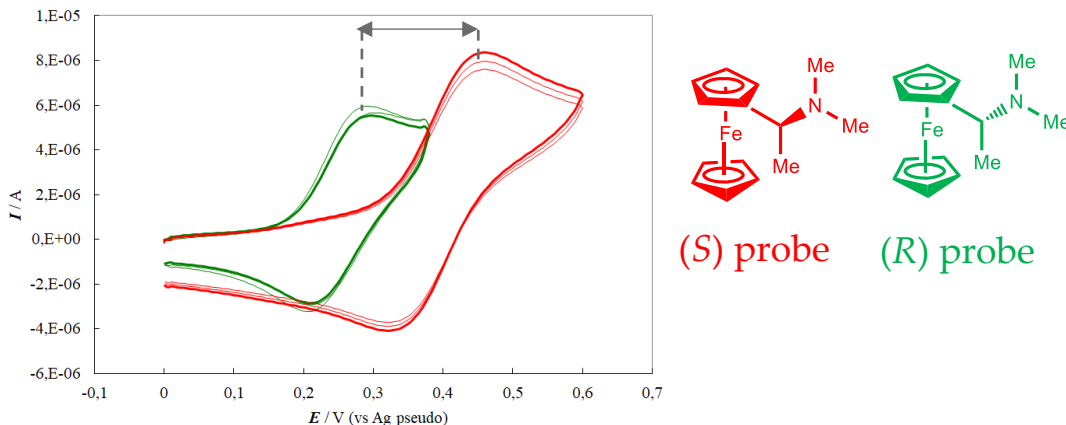


Figure 145. CV enantioselection tests of FcR (green) and FcS (red) solutions on gold SPE (Dropsens) in (*S*)-3mO₂NTf₂ inherently chiral media. Reproducibility tests are also reported.

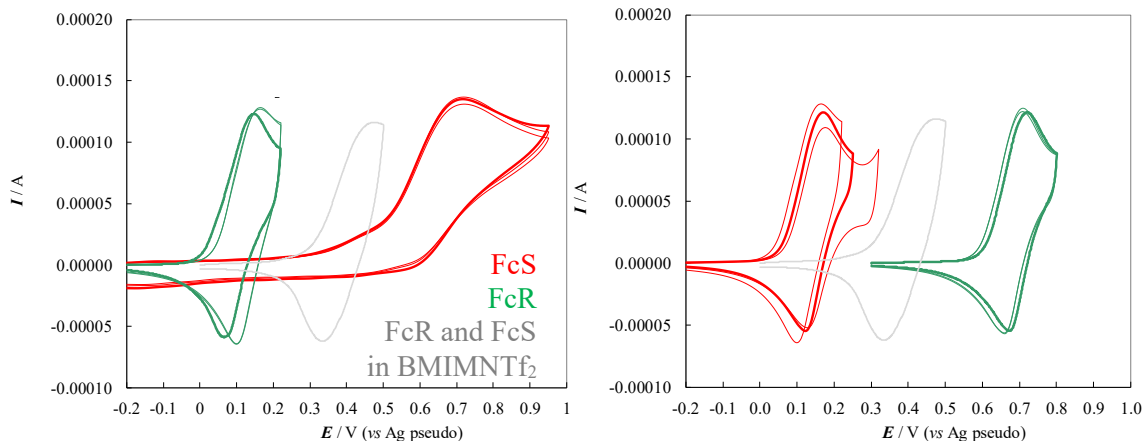


Figure 146. CV enantioselection tests of FcR and FcRS solutions on gold SPE (Dropsens) in (*R*)- and (*S*)-3mO₂NTf₂ (left side and right side respectively) inherently chiral media. Reproducibility tests and the CV pattern of Fc in achiral BMIMNTf₂ (grey line) are also reported.

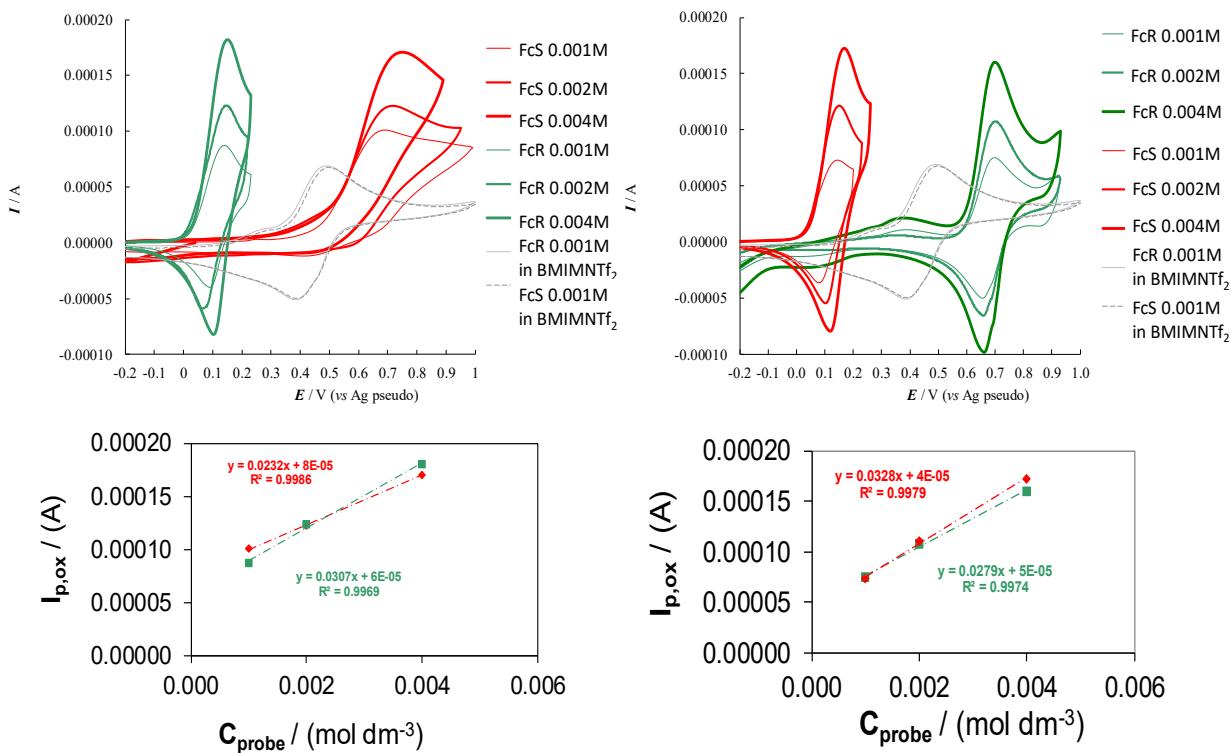


Figure 147. CV enantioselection tests (row above) and linear dynamic range (row below) of FcR and FcRS solutions (increasing the substrate concentration in the 0.001-0.004 M range) on graphite SPE cells in (R) - and (S) -3mO₂NTf₂ (left side and right side respectively) inherently chiral media.

Enantiodiscrimination in terms of significant potential difference is observed in all cases (about 540 mV) and with specular results by changing the probe or the selector configurations. This important feature can be justified in terms of significantly different energy conditions for the electron transfer for the two enantiomers, resulting from diastereoisomeric interactions with the enantiopure environment.

However, it is possible to observe not perfectly specular results in the shape of the CV signal for FcS in (R) -3mO₂NTf₂ as bulk medium (Figure 146 and 147); in fact, only in this case the signals lose their canonical reversibility features,

probably due to the viscosity of the medium as well as for the presence of some impurities in the ICIL.

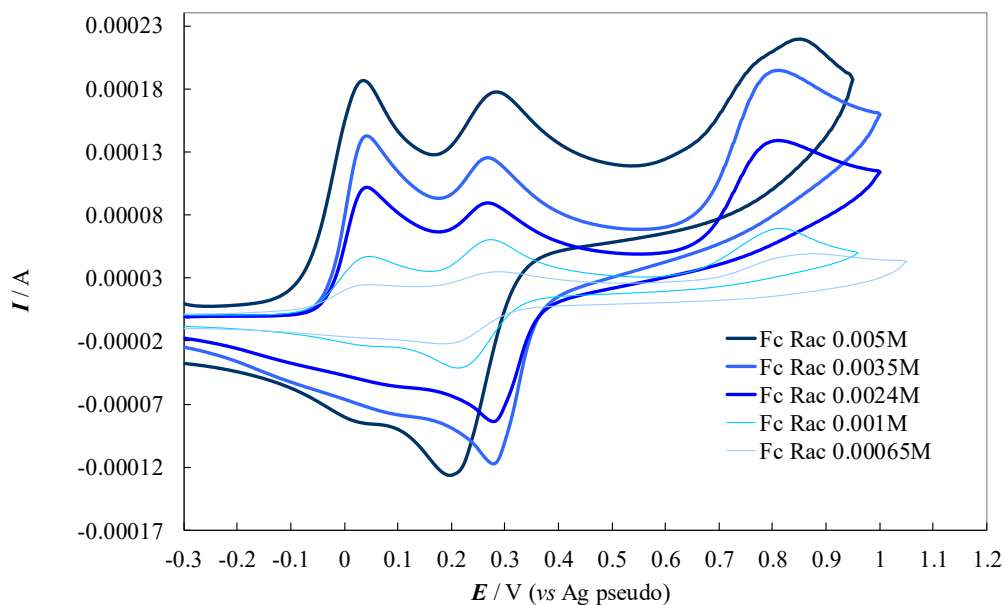


Figure 148. CV patterns of racemic Fc at different concentrations on graphite SPE in (R) - $3mO_2NTf_2$.

To verify the general ability in enantioselection experiments of the inherently chiral $3mO_2NTf_2$, the tests were also carried out using the inherently chiral ionic liquid (R) - $3mO_2NTf_2$ as low concentration chiral additive (0.01 mol dm^{-3}) in $BMIMNTf_2$ and as chiral probe the enantiomers of an inherently chiral monomer based on a 2,2'-biindole atropisomeric scaffold $Ind_2(N-Me)T_4$ (Figure 149). A peak potential separation of about 150 mV is observed.

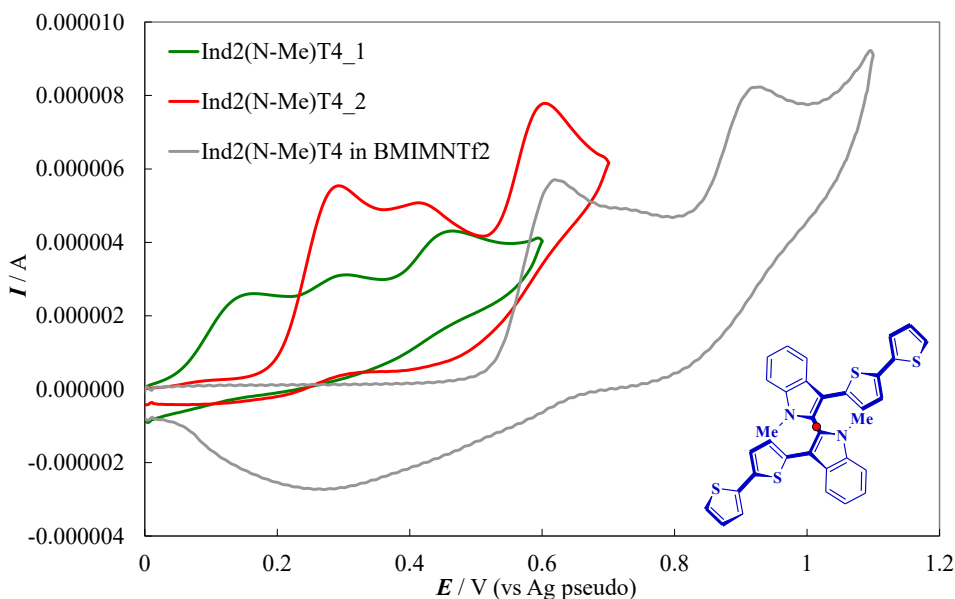


Figure 149. CV enantioselection tests of inherently chiral Ind₂(N-Me)T₄_1 (green line) and Ind₂(N-Me)T₄_2 (red line) solutions on gold SPE (Dropsens) at 0.05 V s⁻¹ potential scan rate, in BMIMNTf₂ + (*R*)-3mO₂NTf₂ as low concentration chiral additive (0.01 M). CV pattern of Ind₂(N-Me)T₄ in achiral BMIMNTf₂ (grey line) is also reported.

Then, another series of experiments have been carried out, using (+)-catechin and (-)-epicatechin as chiral probes (0.002 M). In particular, the most abundant natural isomers, (+)-catechin and (-)-epicatechin, are reciprocally diastereoisomers, and therefore, as already pointed out in the former chapter 3.2.5, they can be electrochemically discriminated in terms of potential difference on achiral electrodes. Instead, (+) and (-)-catechin or (+) and (-)-epicatechin are enantiomer couples and thus cannot be discriminated in terms of potential difference on any achiral electrode. However, as previously shown in chapter 3.2.5 such enantiodiscrimination is successfully possible by implementing powerful inherently chiral films at the electrochemical interphase.

Instead, in this case, the enantioselection tests were performed using bulk inherently chiral ionic liquid medium (Figure 150).

Actually, since we did not own both catechin and epicatechin enantiomers to be tested with the chiral selector in a given configuration, we performed a specular kind of tests, that is, testing a single probe enantiomer with both selector configurations (*i.e.* (*R*)- and (*S*)-3mO₂NTf₂), which, however, must yield exactly the same result as when testing both probe enantiomers with a single selector configuration.

Figure 150 shows excellent enantiodiscrimination ability (ΔE_p for (+)-catechin of ~ 300 mV and for (–)-epicatechin of ~ 400 mV) in terms of potential differences (related to the energetically different probe + selector situations), although in the chiral medium cases the chiral probe signal appears shifted at less positive potentials with respect to the achiral case, while quite the opposite happens with the electrode surface modified with inherently chiral oligomer films (chapter 3.2.5), a feature which our research group is looking forward to investigate in more detail since it could provide important clues concerning the probe/selector recognition mechanism.

The enantioselection tests were performed on screen-printed electrode SPE cells (with graphite as working and counter electrodes and Ag as pseudo reference electrode). In all cases a small volume (6 μ L) of aqueous KCl solution was added to the chiral medium, to stabilize the potential of the pseudoreference electrode, besides advantageously resulting in lower viscosity.

Reproducibility tests were performed by repeatedly recording the CV patterns of chiral probes on new SPEs as reported in Figure 150 (dotted lines).

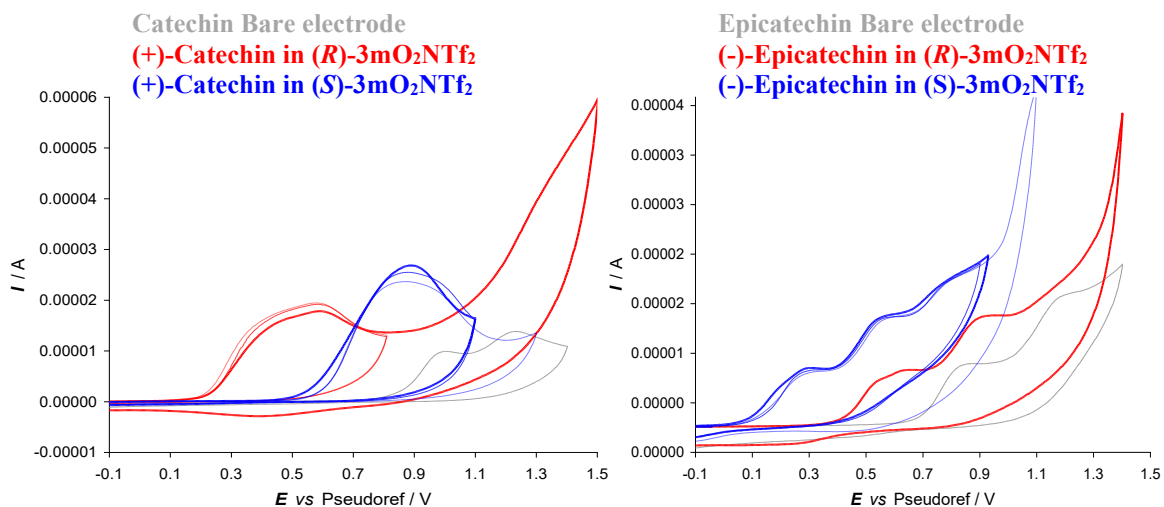
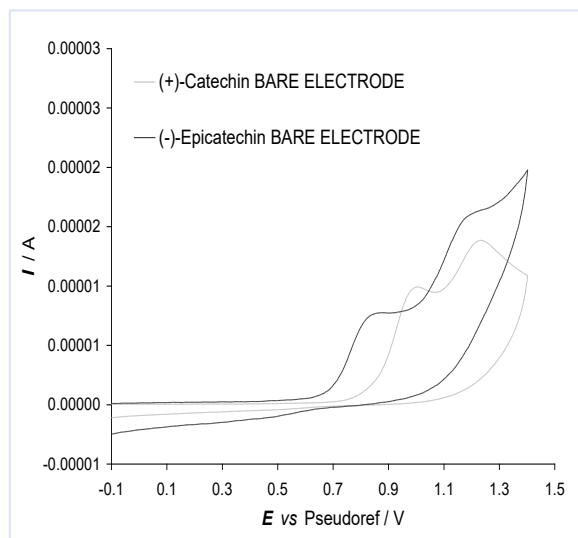


Figure 150. Top: (+)- catechin and (–)-epicatechin in achiral BMIMTFSI. Bottom: (+)- catechin (left side) and (–)-epicatechin (right side) in enantiopure (*R*)- and (*S*)-3mO₂NTf₂ (red and blue respectively) as bulk media.

4.2.6 2,12-Diaza[6]helicene: an efficient non-conventional stereogenic scaffold for enantioselective electrochemical interphases

The investigation of inherently chiral selectors, employed in enantioselective electroanalysis, was extended from the ICIL presented in the above paragraph 4.2.5 and characterized by a stereogenic axis, to helical compounds, prompted by the consideration that aza[*n*]helicenes are a class of chiral molecules possessing peculiar electronic and chiroptical properties [228] and display high configurational stability when constituted by at least six fused 6-membered rings [229].

Thus, the 5-octyl-5-aza[6]helicenium bistriflimidate was synthesized, and exhibited very good enantiodiscrimination ability for the antipodes of benchmark ferrocenyl ethyl amine as well as tyrosine methyl ester [137]. The aim was to check the possibility of increasing the enantioselection ability of the aza-helicenium compound [137] by introducing a further quaternary ammonium function on the helical scaffold. In this light, the synthesis of the enantiomerically pure antipodes of new 2,12-diaza[6]helicene was planned (Figure 151).

Moreover, the investigations carried out on bi-benzimidazolium salts in previous work [135] clearly demonstrated a remarkably progressive stereoselectivity enhancement from plain bicollidine to the corresponding mono-alkylated compounds and then to the di-alkylated salts [135]. Mono- and dialkylation could afford a platform of salts to be tested as chirality inducers for achiral ILs in chiral voltammetry experiments, according to a well-established paradigm. The investigation could also give a further proof of the parallel increase of enantiorecognition ability vs the number of quaternarized nitrogen atoms.

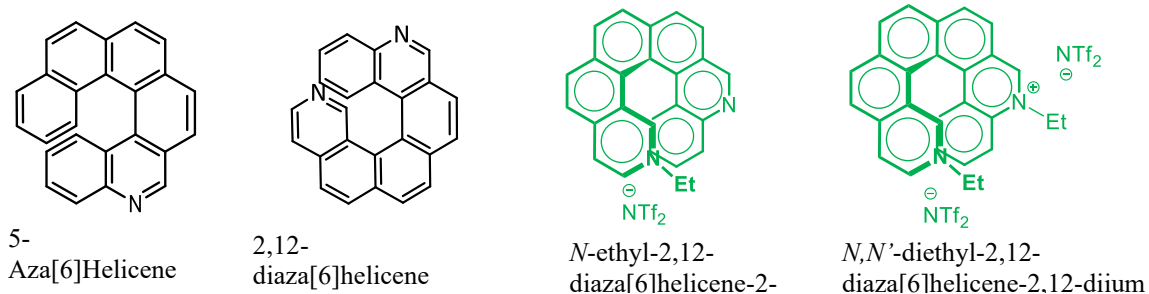


Figure 151. From left to right: structures of 5-aza[6]Helicene, 2,12-diaza[6]helicene, *N*-ethyl-2,12-diaza[6]helicene-2-ium and *N,N'*-diethyl-2,12-diaza[6]helicene-2,12-dium salts.

a) Resolution of the enantiomers by HPLC and CD spectra

The direct resolution of racemic 2,12-diaza[6]helicene was successfully carried out by HPLC on the polysaccharide based Chiralpak IA chiral stationary phase (CSP). Optimized chromatographic conditions were achieved by using the mixture *n*-hexane-acetone-2-propanol-diethylamine 50:50:0.2:0.2 (*v/v/v/v*) as a mobile phase and setting the column temperature at 5°C (Figure 152a). The use of the immobilized-type Chiralpak IA CSP in combination with a mobile phase containing a non-standard solvent such as acetone allowed a good chiral recognition in terms of enantioselectivity and resolution degree. Furthermore, this condition was extremely attractive for mg-scale enantioseparations due to the high solvating power of acetone and the relative simplicity of the evaporation of the mobile phase. The analytical separations were easily scaled up to the milligram range using a 250 mm × 10 mm Chiralpak IA column (Figure 152b). Iterative chromatography of 3.3 mg of racemic sample, followed by fraction collection and pooling, allowed to collect multimilligram quantities of individual enantiomers with *ee* >99.9%. The assignment of the absolute configuration of 2,12-diaza[6]helicene was carried out by comparing the circular dichroism (CD) properties of the enantiomers isolated on a semipreparative scale with those of

the enantiomers of the structurally related 5-aza-[6]-helicene, whose stereochemistry was established in a previous work [230]. The first eluted enantiomer exhibited a clear bisignate CD spectrum in the 450-220 nm spectral range with a maximum and a minimum of ellipticity located at 324 and 243 nm, respectively.

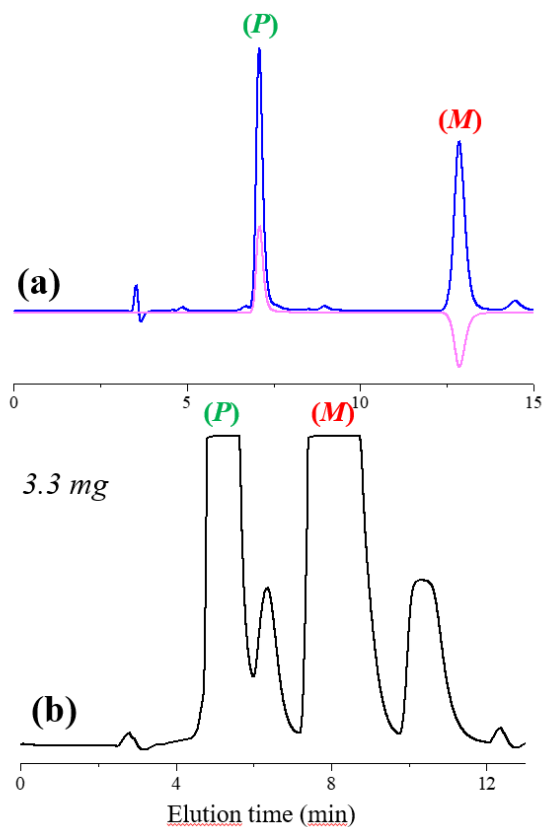
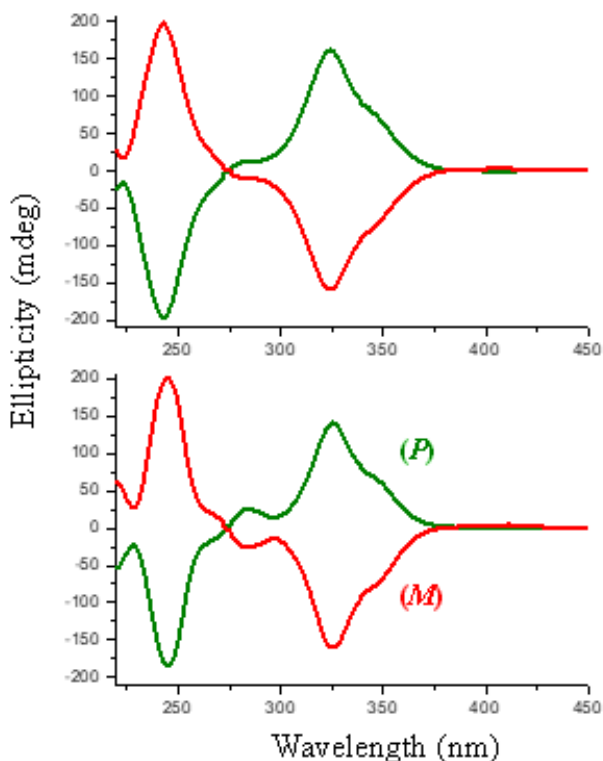


Figure 152. Chromatograms illustrating the (a) analytical and (b) semipreparative enantioseparation of 2,12-diaza[6]helicene. Detector, UV/CD at 330 nm (a) and UV at 330 nm (b).

As shown in Figure 153, the CD profile of the less eluted enantiomer of 2,12-diaza[6]helicene was in strict agreement, both in sign and magnitude, with the CD spectrum of the (*P*)-enantiomer of the parent helicene. Furthermore, as expected, the shape of the CD spectrum of the second eluted enantiomer (*M*)-2,12-diaza[6]helicene was perfectly specular to that of the (*P*)-enantiomer.

Figure 153. CD spectra of the enantiomers of 2,12-diaza[6]helicene (top) and 5-aza-[6]-helicene (bottom) in dichloromethane.



b) Electrochemical characterizations of 2,12-diaza[6]helicene, N-ethyl-2,12-diaza[6]helicene-2-ium and N,N'-diethyl-2,12-diaza[6]helicene-2,12-dium salts

Cyclic voltammetry experiments were performed on compound 2,12-diaza[6]helicene, *N*-ethyl-2,12-diaza[6]helicene-2-ium and *N,N'*-diethyl-2,12-diaza[6]helicene-2,12-dium salts on a glassy carbon GC electrode. Positive and negative half cycles have been separately recorded to avoid reciprocal contamination by electron transfer products. The reported potentials have been normalized vs the formal potential of the intersolvental ferricinium|ferrocene ($\text{Fc}^+|\text{Fc}$) reference redox couple, recorded in the same conditions, whereas currents are normalized against surface, concentration and square root of scan rate, assuming the diffusive character of the electron transfer processes.

A synopsis of the normalized CV patterns is provided in Figure 154, and the corresponding CV peak potentials are collected in Table 15 and compared with

those formerly observed for two monoazahelicene compounds, *i.e.* 5-aza-6-helicene and its *N*-octyl-5-aza-6-helicenium bistriflimidate salt [137].

By comparing the parent diazahelicene with its mono- and dialkylated salts, the most evident feature is the inversion in redox activity already observed in the mono case [137], since conversion of the nitrogen sites into alkylated cations turns them from electron rich to electron poor. In particular:

i) only diazahelicene undergoes oxidation within the available electrochemical window. Only one irreversible oxidation peak, followed by a shoulder, is perceivable before the background. It should correspond to oxidation of one of the nitrogen sites, according to the similar value measured for monoazahelicene [137] and significantly less positive than that of carbahelicenes. Given the above-mentioned conjugation between nitrogen sites, the second oxidation should take place at more positive potentials.

Instead no oxidation peak at all is observed either for *N,N'*-diethyl-2,12-diaza[6]helicene-2,12-dium, in which both *N* positions are alkylated, and for *N*-ethyl-2,12-diaza[6]helicene-2-ium, featuring a free *N* position besides an alkylated one. This observation might be justified by considering the above-mentioned conjugation between the two nitrogen sites, which reduces the electron density on both of them compared to the parent diazahelicene 2,12-diaza[6]helicene.

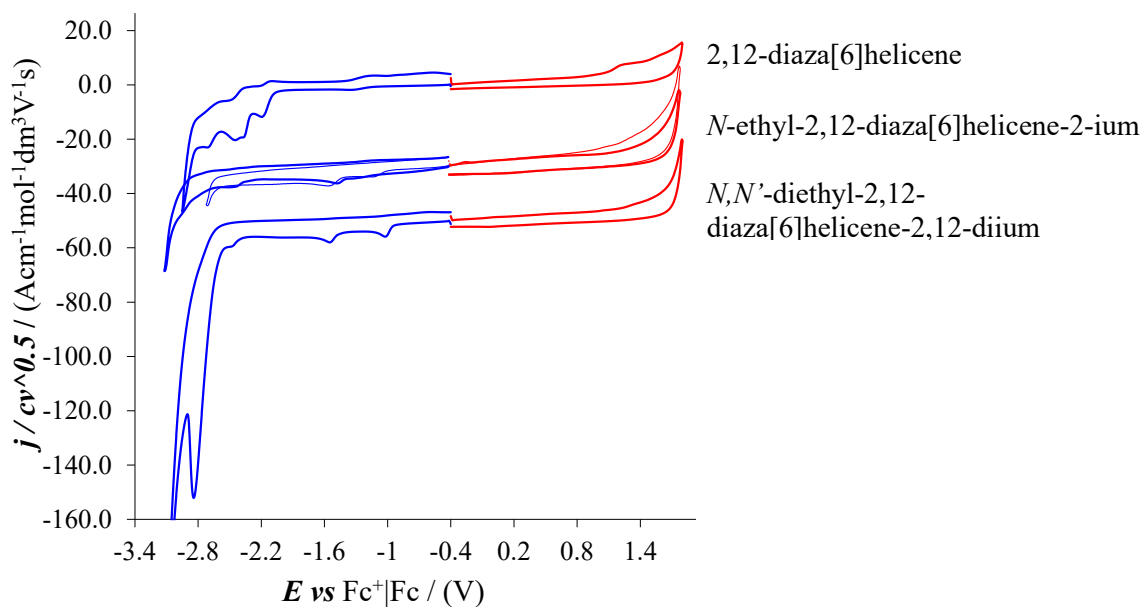


Figure 154. CV patterns for compound 2,12-diaza[6]helicene and for the bis-triflimidates *N*-ethyl-2,12-diaza[6]helicene-2-ium and *N,N'*-diethyl-2,12-diaza[6]helicene-2,12-diium salts, 0.00075 M solutions in ACN + 0.1 M TBAPF₆ on GC electrode at 0.2 V/s scan rate.

Table 15. CV peak potentials, normalized vs the Fc⁺|Fc couple, for oxidative and reductive electron transfer processes of diazahelicene compounds 2,12-diaza[6]helicene and for the bis-triflimidates *N*-ethyl-2,12-diaza[6]helicene-2-ium and *N,N'*-diethyl-2,12-diaza[6]helicene-2,12-diium salts and of two monoazahelicene compounds [137], for comparison

	$E_{p, 1a} / V$	$E_{p, 1c} / V$
5-aza-6-helicene [137]	1.07, 1.47	-2.25, -2.52, -2.66
<i>N</i> -octyl-5-aza-6-helicenium bistriflimidate [137]	1.46	-1.19 (nearly splitting), -2.58
2,12-diaza[6]helicene	1.26	-2.16, 2.41, -2.48, -2.73
<i>N</i>-ethyl-2,12-diaza[6]helicene-2-ium	no peaks	-1.52 (with prepeak); -2.47
<i>N,N'</i>-diethyl-2,12-diaza[6]helicene-2,12-diium	no peaks	-1.00, -1.52, -2.45, -2.83

ii) huge positive shift of reduction peak potentials with strong reciprocal interaction between *N* sites for cations. Parent diazahelicene 2,12-diaza[6]helicene features a complex reduction peak system, although starting with a monoelectronic chemically and electrochemically reversible peak. This can be assumed to account for reductions on both helicene sides, in the -2.2/-2.8 V range, similar to that formerly observed for the monoazahelicene case. There are, however, differences in peak potentials and multiplicity, consistently with the change in the nature of the two terminals. Instead in the case of *N*-ethyl-2,12-diaza[6]helicene-2-ium a reduction peak is observed at -1.52 V, *i.e.* much more positive respect to 2,12-diaza[6]helicene, as the nitrogen site, becoming cationic, now provides a preferential site for the first reduction. However, such potential is significantly less positive than the one observed in the case of the monoaza analogue. Since in monoazahelicene salts it has been observed that the first reduction potential is nearly constant, regardless of the position of the nitrogen atom, such a large potential difference could be ascribed, again, to the interaction in space between the aza cation and the free aza terminal, making the first reduction site less electron poor. At the same time, the reduction peak system in the -2.2/-2.8 V range looks much simpler compared to 5-aza[6]helicinium, and should correspond to reduction of the non-alkylated aza site. The azahelicinium double salt *N,N'*-diethyl-2,12-diaza[6]helicene-2,12-diiium features a neat couple of first reduction peaks (spaced about 0.5 V) that, considering again the above remarks about the first reduction potential of an aza cation, should be likely described as the response of two nearly equivalent redox sites, with significant reciprocal interaction along the carbohelicene chain as well as across space. This was also observed in a similar literature case [218], for which two reversible monoelectronic twin peaks are reported at -1.32 and -1.59 V. However, compared with ref. [218], in the case of *N,N'*-diethyl-2,12-diaza[6]helicene-2,12-diiium both reductions occur at less negative potentials, consistently with the overall

more efficient conjugation. In our case, the distance between the peaks is higher, which could be ascribed to stronger reciprocal interactions. It is also worth mentioning that in cases *N*-ethyl-2,12-diaza[6]helicene-2-ium and *N,N'*-diethyl-2,12-diaza[6]helicene-2,12-diiium, where cation reduction results in radical formation, a possible follow-up is dimerization [218].

c) Chiral discrimination experiments

The three diazahelicene compounds have been investigated as inherently chiral selectors by adding them in low concentration to the achiral IL 1-butyl-3-methylimidazolium bis-triflimidate BMIMNTf₂ and testing the resulting three chiral media:

(i) for enantioselective CV experiments with the benchmark electroactive enantiomer probes (*R*)-(+)- or (*S*)-(-)- *N,N'*-dimethyl-1-ferrocenylethylamine ((*R*)-Fc and (*S*)-Fc, Figure 155),

(ii) for enantioselective differential pulse voltammetry (DPV) experiments with the enantiomers of an electroactive probe of biological interest, *i.e.* L- or D-tryptophan (Trp), an α -amino acid (Figure 156 and 157).

Both of the above enantioselection tests were performed on disposable screen-printed electrode (SPE) cells on plastic polyester sheet with graphite working electrodes.

A synopsis of CV features of (*R*)-Fc and (*S*)-Fc solutions in the three tested chiral media is reported in Figure 155 (reproducibility tests are reported in Gallery Section 19).

Enantiodiscrimination in terms of significant potential differences is observed in all cases, with the same probe enantiomer sequence (*i.e.* with (*R*)- undergoing easier oxidation than (*S*-), consistently with the inherently chiral selectors having the same configuration.

However, the peak potential differences significantly increase from 2,12-diaza[6]helicene to *N,N'*-diethyl-2,12-diaza[6]helicene-2,12-dium, that is, with increasing number of alkylated, positively charged nitrogen atoms (2,12-diaza[6]helicene ~65 mV < *N*-ethyl-2,12-diaza[6]helicene-2-ium ~90 mV < *N,N'*-diethyl-2,12-diaza[6]helicene-2,12-dium ~113 mV).

The same effect with the same probes had been observed employing as additives in achiral ionic liquids a series of compounds (non-alkylated, monoalkylated, dialkylated) based on an atropisomeric bipyridinium scaffold (*i.e.* also inherently chiral, but of axial instead of helical stereogenicity) [135].

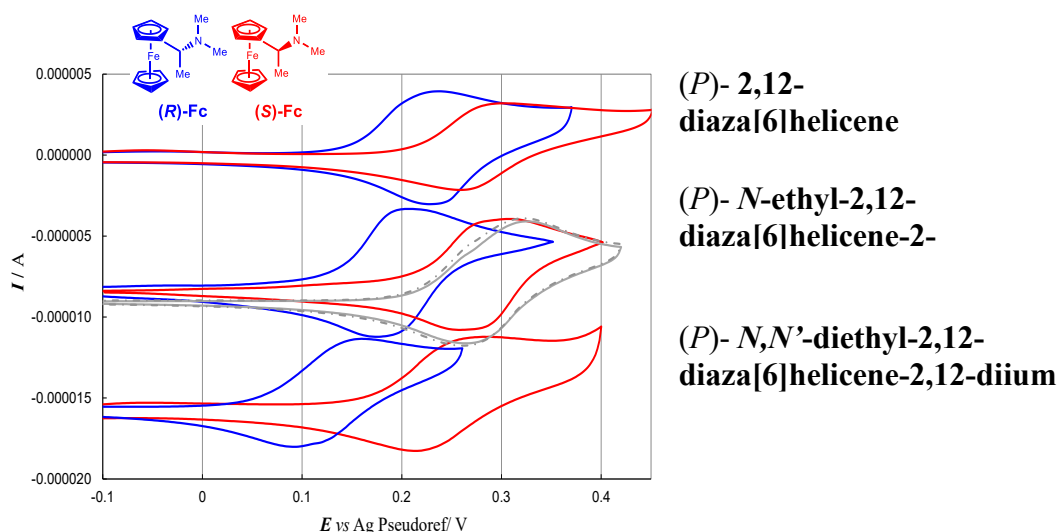


Figure 155. A synopsis of the CV features of (*R*)-Fc (blue line) and (*S*)-Fc (red line) solutions on graphite SPE in BMIMNTf₂ with (*P*)-2,12-diaza[6]helicene, (*P*)-*N*-ethyl-2,12-diaza[6]helicene-2-ium and (*P*)-*N,N'*-diethyl-2,12-diaza[6]helicene-2,12-dium as low concentration chiral additives (0.02 M). In grey the voltammograms referred to experiments in absence of inherently chiral salts are also reported.

Figures 156 and 157 account for the DPV enantioselection tests on the enantiomers of tryptophan. In particular,

i) Figures 156(a), 156 (b) and 156 (c) provide a comparison of the enantiodiscrimination ability of 2,12-diaza[6]helicene, *N*-ethyl-2,12-diaza[6]helicene-2-ium and *N,N'*-diethyl-2,12-diaza[6]helicene-2,12-diium as 0.02 M chiral additives in achiral commercial BMIMNTf₂ with L- and D-Trp (0.03 M). As in the former study case, once more the same probe enantiomer sequence (in this case, L- before D-) is obtained with all the inherently chiral additives, but the peak potential differences significantly increase from 2,12-diaza[6]helicene to *N,N'*-diethyl-2,12-diaza[6]helicene-2,12-diium (~60 mV < ~100 mV < ~180 mV) that is, with increasing number of alkylated nitrogen sites.

ii) Figure 156(c') highlights the selector concentration effect in the case of inherently chiral salt *N,N'*-diethyl-2,12-diaza[6]helicene-2,12-diium, the most effective selector in the series. In particular, the observed peak potential difference for the probe enantiomers is significantly larger when working with *N,N'*-diethyl-2,12-diaza[6]helicene-2,12-diium at 0.02 M concentration (solid lines) with respect to 0.01 M concentration (dashed lines). A similar beneficial concentration effect was already been observed by employing as additives in achiral ionic liquids an inherently chiral molecular salt based on either an atropisomeric bipyridinium scaffold [135] or on a chiral bile acid scaffold with many stereocentres as stereogenic elements [182]. Altogether, by considering such three cases, we can assume the above concentration effect to be general.

iii) Testing *N*-ethyl-2,12-diaza[6]helicene-2-ium and *N,N'*-diethyl-2,12-diaza[6]helicene-2,12-diium with L- and D-Trp in the 0.005-0.03 M concentration range, a linear dynamic range with very good correlation coefficients is observed for the peak currents as a function of the concentration for both enantiomers (Figure 157). Thus, quantification through peak current analysis can be added to configuration assignment based on the peak potential.

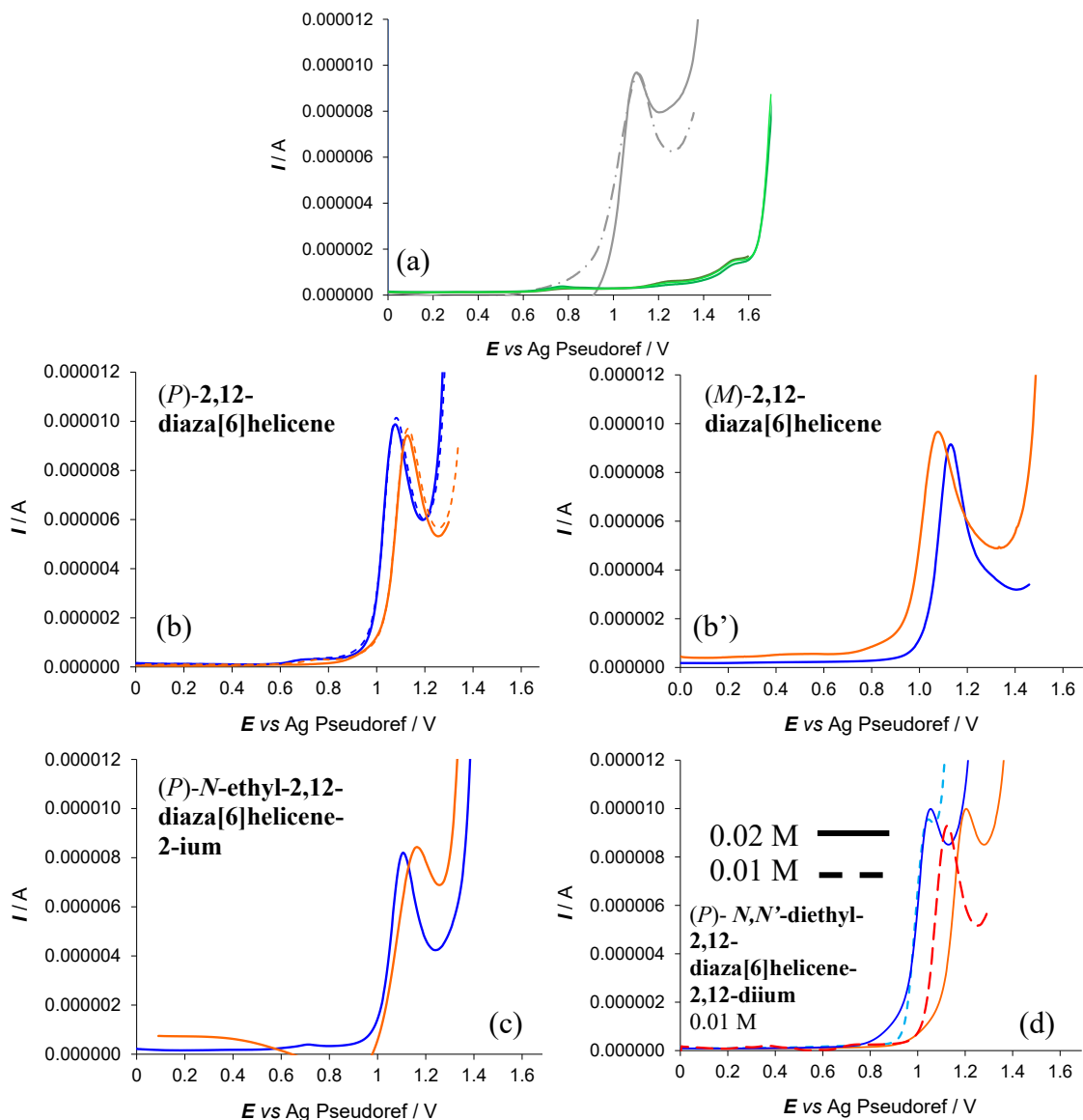


Figure 156. (a) DPV features of L- and D- Trp in absence of inherently chiral salts (grey dashed and straight lines respectively) and the three diazahelicenes in BMIMNTf₂ (in green). Enantioselection tests with L- and D-Trp (blue and orange, respectively) in BMIMNTf₂ with (b) (*P*)- 2,12-diaza[6]helicene 0.02M, (b') (*M*)- 2,12-diaza[6]helicene 0.02M, (c) (*P*)-*N*-ethyl-2,12-diaza[6]helicene-2-ium 0.02M and (d) (*P*)- *N,N'*-diethyl-2,12-diaza[6]helicene-2,12-diium 0.002M (straight lines) or 0.01M (dashed lines).

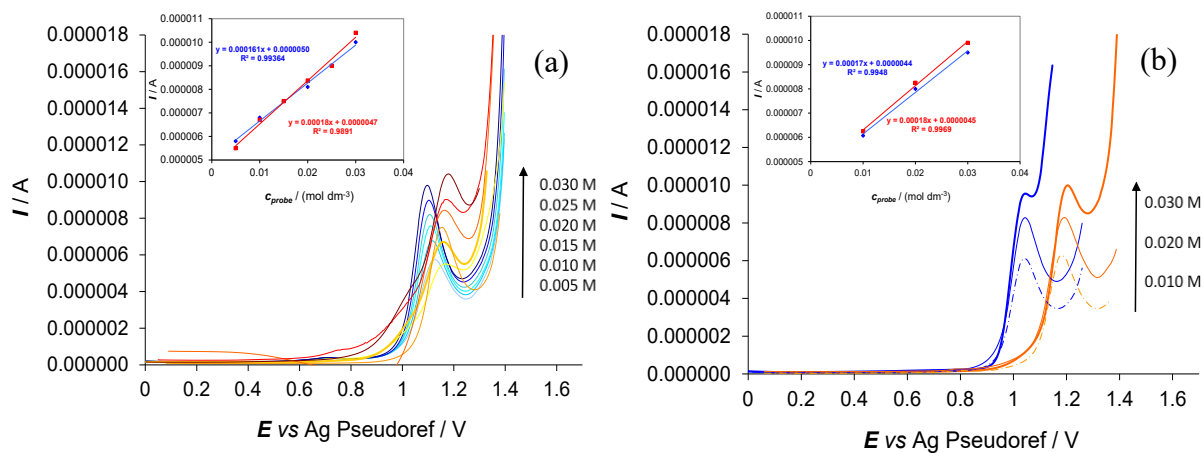


Figure 157. Verification of peak current vs concentration linearity for each enantiomer. (a) L- and D-Trp (blue and orange, respectively) in the 0.005-0.03 M concentration range with *N*-ethyl-2,12-diaza[6]helicene-2-ium (0.03M) in BMIMNTf₂. (b) L- and D-Trp (blue and orange, respectively) in the 0.01-0.03 M concentration range with *N,N'*-diethyl-2,12-diaza[6]helicene-2,12-dium (0.03M) in BMIMNTf₂.

4.2.7 (*N*-Hex-Ind)₂Ph₂T₄ as low concentration chiral additive

The inherently chiral monomer (*N*-Hex-Ind)₂Ph₂T₄ (Figure 158) discussed in paragraph 3.2.2, which was unsuitable for the electrooligomerization, as a consequence of the high solubility originating from the very long alkyl chains, was tested as chiral additive in achiral ionic liquid.

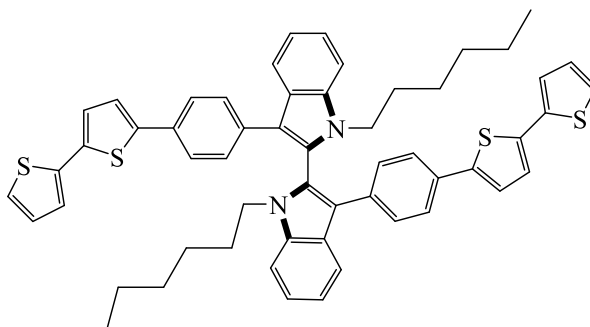


Figure 158. Chemical structure of the inherently chiral monomer (*N*-Hex-Ind)₂Ph₂T₄.

a) Experimental conditions for enantiodiscrimination tests

CV tests with ferrocenyl probes were carried out in a drop of achiral ionic liquid BMIMNTf₂ with (*N*-Hex-Ind)₂Ph₂T₄ as chiral additive (0.01 M), using screen-printed electrode cells constituted of working, counter, and Ag/AgCl pseudoreference electrodes. The electrodes were produced in foils of 48 using screen-printing machine DEK 245 (Weymouth, UK) and flexible polyester film (Autostat HT5) as support, obtained from Autotype Italia (Milan, Italy). Graphite-based ink (Elettrodag 421) from Acheson (Milan, Italy) was used to print the working and the counter electrode while silver/silver chloride ink was used to print the reference electrode (Acheson Elettrodag 4038 SS). The diameter of the SPE working electrode was 0.4 cm resulting in an apparent geometric area of 0.126 cm².

b) Enantiodiscrimination tests: selector implemented as inherently chiral additive in ionic liquid

The enantiodiscrimination ability of inherently chiral monomer (*N*-Hex-Ind)₂Ph₂T₄ was tested employing it as chiral additive in achiral ionic liquid BMIMNTf₂.

In this case CV tests were performed with (*R*)-Fc and (*S*)-Fc probes in very thin solution layers on screen printed graphite working electrodes, resulting in a potential difference for the two enantiomers even larger (about 230 mV, Figure 159) than that obtained for the same probes on **oligo-1** films in DCM + 0.1 M TBAPF₆ (paragraph 3.2.2 in chapter 3, Figure 40).

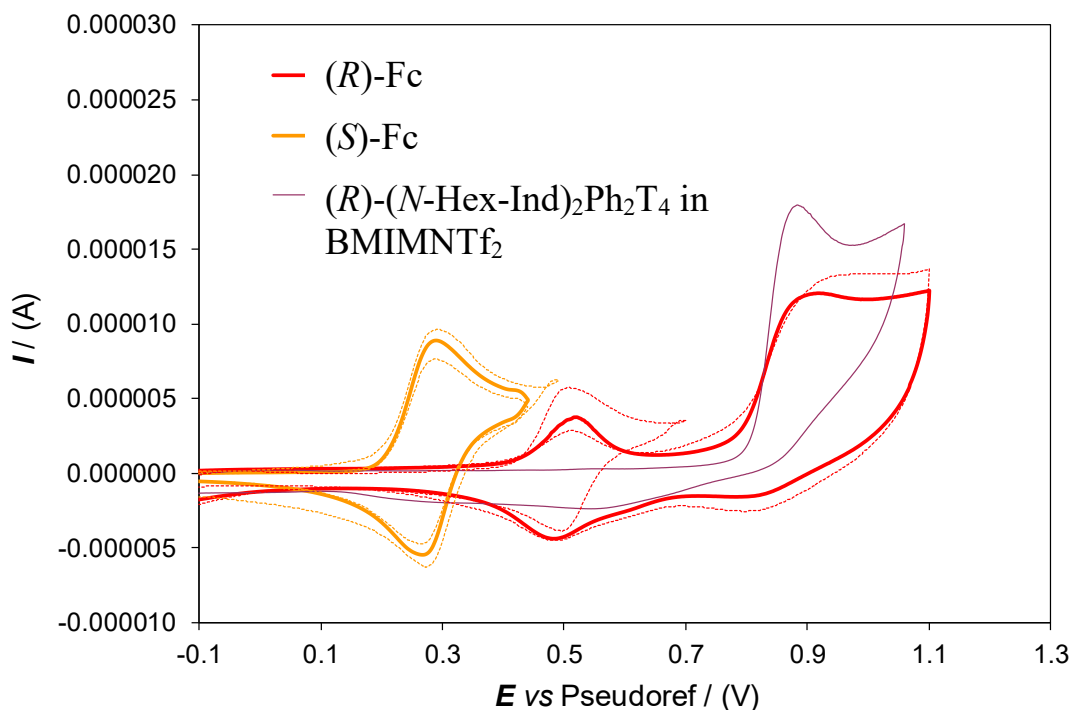


Figure 159. Enantiodiscrimination performances of enantiopure (*R*)- (*N*-Hex-Ind)₂Ph₂T₄ (employed as chiral additive in BMIMNTf₂, at 0.01 M) towards (*S*)- and (*R*)-Fc probes (0.002 M). For sake of comparison, the CV pattern is also reported for the monomer oxidation in the absence of the probe (purple thin lines).

4.2.8 A family of inherently chiral QUINAP derivatives

A family of chiral QUINAPs (Figure 160), which present different numbers of alkylated positions on the *N* and *P* site, have been also tested as low concentration chiral additives (0.01 M) in achiral commercial BMIMNTf₂, testing the enantiomers of chiral ferrocene. The DPV enantioselective experiments were carried out on C SPEs.

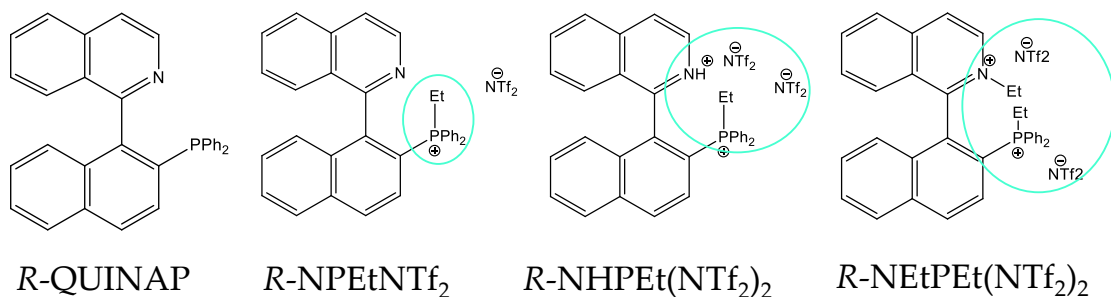


Figure 160. Structures of the chiral QUINAPs family.

The chiral selectors have shown a similar behaviour to 2,12-[6]diazahelicene family, presented in the paragraph 4.2.6. In fact, again, the peak potential separation increases with increasing number of alkylated, positively charged nitrogen atoms (Figure 161).

The peak potential separation, as shown in Figure 161, systematically increases with the number of alkylated positively charged atoms: *R*-QUINAP ~110 mV < *R*-NPEtNTf₂ ~200 mV < *R*-NHPEtNTf₂ ~300 mV < *R*-NEtPEt(NTf₂)₂ ~360 mV. Moreover, the enantiomer peak sequence is the same in all the cases (in particular, *R* before *S*), consistently with the chiral selectors having the same chiral configuration (in particular, the *R* one). Unfortunately, the *S* configuration of the chiral QUINAP selectors was not available and it has not been possible to perform the “double inversion” check measurements.

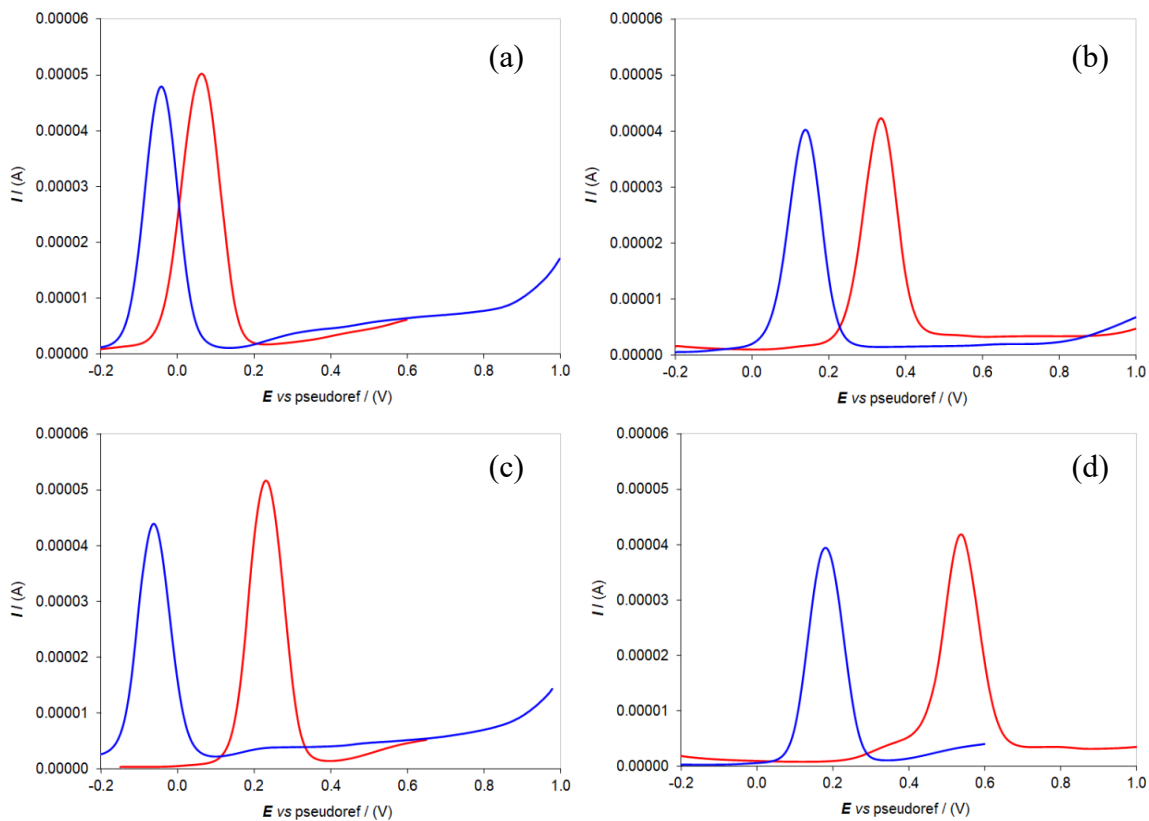


Figure 161. DPV Patterns of FcR (in blue) and FcS (in red) on C SPE with (a) *R*-QUINAP (b) *R*-NPEtNTf₂ (c) *R*-NHPeTNTf₂ and (d) *R*-NEtPEt(NTf₂)₂ as chiral additive (0.01M) in BMIMNTf₂.

4.2.9 Chiral Deep Eutectic Solvents (DES): a novel, effective tool for enantiodiscrimination in electroanalysis

Deep Eutectic Solvents (DESs) offer advantages similar to ionic liquid (IL) ones, with easier and more sustainable synthesis; moreover, bio-based DESs often include chiral components, surprisingly underexploited. A proof of concept is offered of the impressive potential of enantiopure chiral DESs as chiral media for enantioselective electroanalysis.

- a) Three chiral DESs, consisting of a molecular salt with bio-based chiral cation [NopolMIm]⁺ (presented in paragraph 4.2.2) combined with three natural and/or low-cost partners (levulinic acid, glycerol and urea), are investigated as chiral voltammetry media. Significant potential differences are observed for the enantiomers of a model chiral probe, with a dramatic tuning depending on the achiral DES component, reaching an impressive ~0.5 V in the levulinic acid case (while less efficient appears [NopolMIm]⁺ as chiral additive in IL).

With the same medium good enantiodiscrimination is also observed for amino acid tryptophan, a quite different probe and of applicative interest. These findings can be considered as a remarkable step further in chiral electroanalysis as well as in the development of task-specific enantioselective media.

- b) Such results also suggest many interesting developments, including a deeper investigation of the molecular interactions within the three-actor (probe and DES components: HBD and HBA) system, as such and at the interphase with the charged electrode surface, and a further analysis of the role of acid/base interactions. For this reason, in order to explore more in detail the performances of chiral DESs (always of natural origin) for application in chiral electroanalysis, many different DESs (with different HBD and HBA, also in different ratios) were studied.

a) Natural-based chiral task-specific deep eutectic solvents: DES A, DES G and DES U

A new family of chiral biobased salts was studied and also tested as CILs and/or CIL additives in bulk ILs for voltammetry enantiodiscrimination experiments, with promising features that could be assumed to apply to the whole family [182]. The salt family includes 3-{2-[(1*R*,5*S*)-6,6-dimethylbicyclo[3.1.1]hept-2-enyl]ethyl}-1-methyl-1*H*-imidazol-3-iummethanesulfonate ([NopolMIm] Mes, precursor of the corresponding bistriflimide CIL [182], Figure 121 in section 4.2.2), which appears to be a good candidate as DES component in conjunction with appropriate HBD partners on account of its methanesulfonate anion of strong HBA character. Other family members with bistriflimide anions look less convenient not only because of the additional required metathesis step and of their being expensive and environmentally unfriendly, but also because of their lower HBA character compared with methanesulfonate homologues.

Counteranion methanesulfonate is also quite preferable from the electrochemical perspective with respect to halide ones, which are often featured in DES [231], because halide anions are quite electrochemically active, resulting in a much narrower potential window on the oxidation side as well as in specific adsorption phenomena under suitable conditions.

Thus an original series of electroanalytical enantiodiscrimination experiments were performed with model electroactive chiral probes in three chiral DESs prepared combining chiral [NopolMIm] Mes with convenient HBA partners. Moreover, for comparison's sake, the same protocol is also investigated using the same chiral selector as 0.05 M additive in achiral IL BMIMNTf₂.

Chiral [NopolMIm] Mes [182] was combined with three natural and/or low-cost HBDs, often employed in the preparation of DESs, including

- a weak ketoacid, levulinic acid (4-oxopentanoic acid);
- a polyalcohol, glycerol;

- a NH donor, urea.

The DES character of the three resulting binary systems was evaluated by differential scanning calorimetry (DSC), comparing experimental temperature data for melting (or solid/liquid glass transition) with "ideal" phase diagrams, calculated assuming no specific interactions between components in the liquid phase [231, 232]. Such diagrams (solid lines in Figure 162) were obtained in terms of melting T vs x_i curves for the binary mixture components A and B, their intersection providing the eutectic point. Such curves were calculated from the thermodynamic equations accounting for the activity in the liquid phase of the binary mixture components A and B as a function of temperature [232],

$$\ln(x_A\gamma_A) = \left(\frac{\Delta H_{m,A}}{R}\right) \left(\frac{1}{T_{m,A}} - \frac{1}{T}\right) + \left(\frac{\Delta C_{p,m,A}}{R}\right) \left(\frac{T_{m,A}}{T} - \ln\left(\frac{T_{m,A}}{T}\right) - 1\right)$$

(1)

$$\ln(x_B\gamma_B) = \left(\frac{\Delta H_{m,B}}{R}\right) \left(\frac{1}{T_{m,B}} - \frac{1}{T}\right) + \left(\frac{\Delta C_{p,m,B}}{R}\right) \left(\frac{T_{m,B}}{T} - \ln\left(\frac{T_{m,B}}{T}\right) - 1\right)$$

(2)

assuming $\gamma_A, \gamma_B = 1$ as in ideal liquid mixture [233], and employing experimental data of melting temperatures $T_{m,A}$ and $T_{m,B}$, molar melting enthalpies $\Delta H_{m,A}$ and $\Delta H_{m,B}$, and variations of molar heat capacities from the solid to the liquid state $\Delta C_{p,m,A}$ and $\Delta C_{p,m,B}$, for the two pure components A and B.

Comparing the three cases in order of decreasing melting temperature of the HBD component, that is, urea ($T_m \sim 136$ °C, Figure 162a), levulinic acid ($T_m \sim 33$ °C, Figure 162b) and glycerol ($T_m \sim 17$ °C, Figure 162c), the "ideal" eutectic mole fraction in the chiral HBA component [NopolMIm] Mes (having $T_m \sim 119$ °C; a detailed DSC study is reported at Gallery section 20) remarkably decreases from

slightly above 0.4 to very low values (~ 0.1 and ~ 0.05), as for rather low molar ratios of the HBA salt in the HBD component.

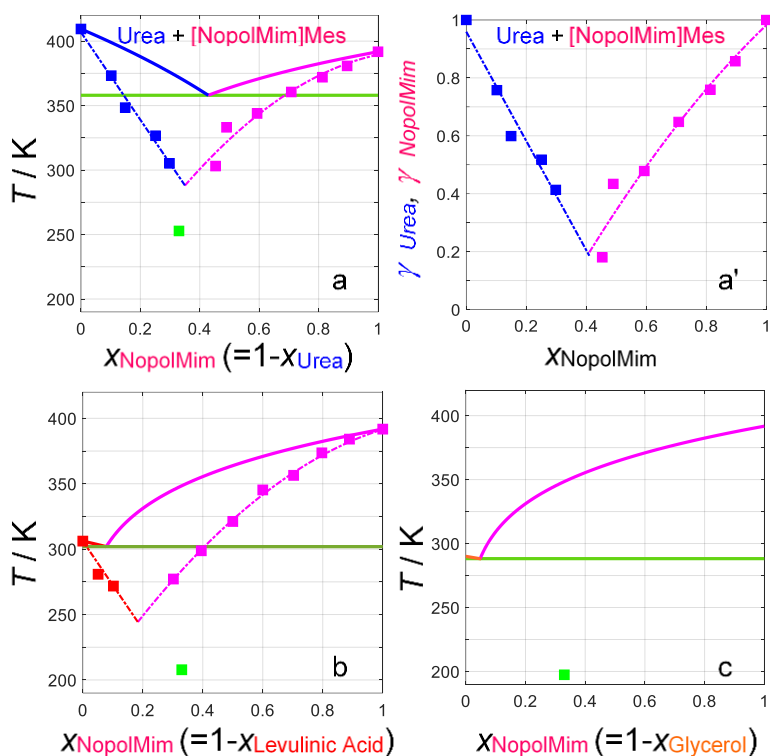


Figure 162. Estimated "ideal" eutectic diagrams (solid lines) and experimental onset temperatures for melting (blue and pink squares) or glass transitions (green squares) at different system compositions. For DES U also experimental activity coefficients are provided.

At the same time the "ideal" eutectic temperature decreases from significantly above room temperature (~ 75 °C) to just above room temperature (~ 30 °C), to slightly below room temperature (~ 10 °C); in the last two cases the melting point lowering respect to the pure HBD component is very small. However, quite different are the trends of the experimental onset temperatures for melting, obtained across the whole composition range of the binary systems with HBD urea and levulinic acid. They are reported in Figures 162a and 162b as squares,

interpolated by dash-and-dot lines; the latter ones should converge in the eutectic melting point; however, it should only be considered a virtual one, since, in agreement with literature cases [234,235], close to the eutectic composition only glass transitions, located quite below the above extrapolated melting point, are observed, rather than melting points possibly followed by glass transitions.

Thus, real phase equilibria show strong deviations respect to the corresponding ideal ones (also highlighted in terms of dramatic decrease of the activity coefficients calculated from the above equations with experimental x/T data, Figure 162a').

In particular:

(i) in both cases a shift is observed in the eutectic point composition, particularly remarkable in the levulinic acid case, towards a higher content of the higher melting component (urea in the first case, [NopolMIm]Mes in the second case);

(ii) at the same time, a dramatic lowering is observed for the melting temperatures respect to ideal ones on both converging curves, pointing to a huge decrease of the eutectic temperature. Thus, for both binary systems, the DES requirement of having a eutectic point at a temperature quite below the one predicted for an ideal mixture, is surely satisfied. Moreover, as mentioned above, any component mixture in the liquid state at a working temperature below the ideal eutectic point can be considered as a DES. In this perspective, a large interval of DES media looks available in both cases, although the composition range shrinks, especially in the urea case, if we only consider temperatures below 25 °C and aim to use the mixtures as liquid media at room temperature.

A good choice in both cases looks selecting $x[\text{NopolMIm}]\text{Mes} \sim 0.33$, implying a 1:2 [NopolMIm]Mes: HBD partner ratio; the resulting media will be hence referred as DES A in the case of levulinic acid and DES U in the case of urea.

The same composition was also adopted for the case of glycerol, verifying that the corresponding mixture (DES G) has a much lower glass transition point than the theoretical eutectic temperature (Figure 162c), and therefore can be considered as a DES, too. DSC curves for [NopolMIm]Mes and for DES A, DES U and DES G are reported in Gallery Section 20.

The electrochemical windows of bulk DES A and DES G (DES U, the highest melting DES in the series, is very viscous and requires addition of a small water quantity to be applied for electrochemical experiments at room temperature, a quite acceptable modulation according to the above cited literature [236,237], resulting all the same in a DES interphase) were explored with cyclic voltammetry in thin layers on screen printed electrode cells with graphite working electrodes and Ag|Ag⁺ pseudoreference electrodes. As shown in Figure 163, the new chiral media have convenient potential windows for electrochemical experiments, about 3 V wide, with reasonable extension on both the oxidation and reduction side.

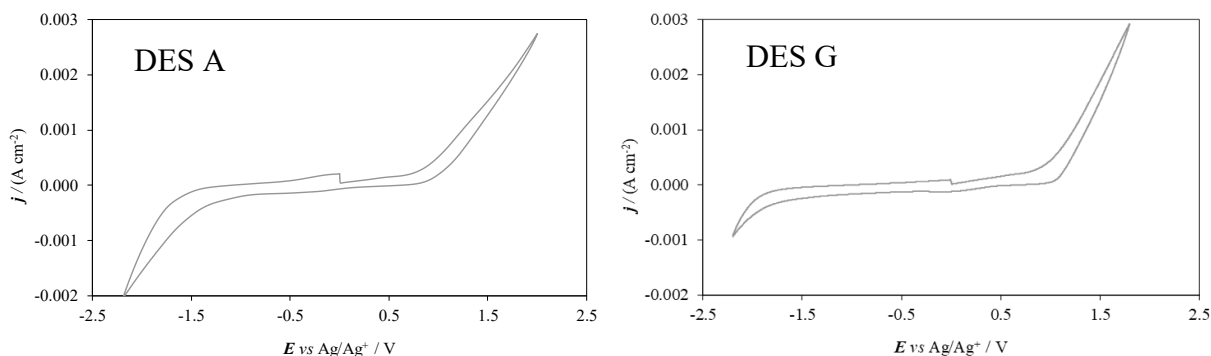


Figure 163. CV potential windows (at 0.2 V/s scan rate) of bulk DES A and DES G, as thin films spread on screen printed electrode cells with graphite working and counter electrodes and Ag|Ag⁺ pseudoreference electrodes.

The same two DESs were also studied by electrochemical impedance spectroscopy EIS as thin films on a flat cell with concentric graphite electrodes.

The recorded EIS features (Figure 164) are numerically well fitted by a $(RC)Q_1Q_2$ equivalent circuit, with R and C accounting for the bulk electrolyte resistance and capacitance (dominating at high frequencies, with $\tau_{RC} = RC$) and constant phase elements Q_i , associated to reactance $Z_{Q_i} = 1/(i\omega M_i^{n_i})$, dominating at medium low (Q_1) and low (Q_2) frequencies.

Numerical fitting of experimental data gives values for all the above parameters (details in Gallery Section 21), including

(i) $n_1 = 0.40/0.41$, *i.e.* approaching the 0.5 value typical of a Warburg element accounting for diffusive control; actually, considering the nice rationalization provided in [238], this frequency domain should account for ion diffusion (with $\tau_D = L^2/D$) limiting the charging process;

(ii) $n_2 = 0.98/1.0$, *i.e.* approaching the ideal capacitance behaviour, clearly accounting for the double layer capacitance at the two interphases.

The electrolyte resistance R is also perceivable as semicircle diameter in the Nyquist diagram and as horizontal plateau in the Bode modulus plot. Specific conductance (or conductivity) κ can be estimated from $R = 1/\kappa \cdot \text{cell constant}$ (cm^{-1}) by comparison with 0.1 m KCl (a IUPAC standard [239]), resulting in the 0.1–0.3 mS/cm range, significantly lower than that of bulk ionic liquid BMIMNTf₂, as such or with 0.05 M [NopolMIm]Mes as chiral additive, but still acceptable for electrochemical experiments.

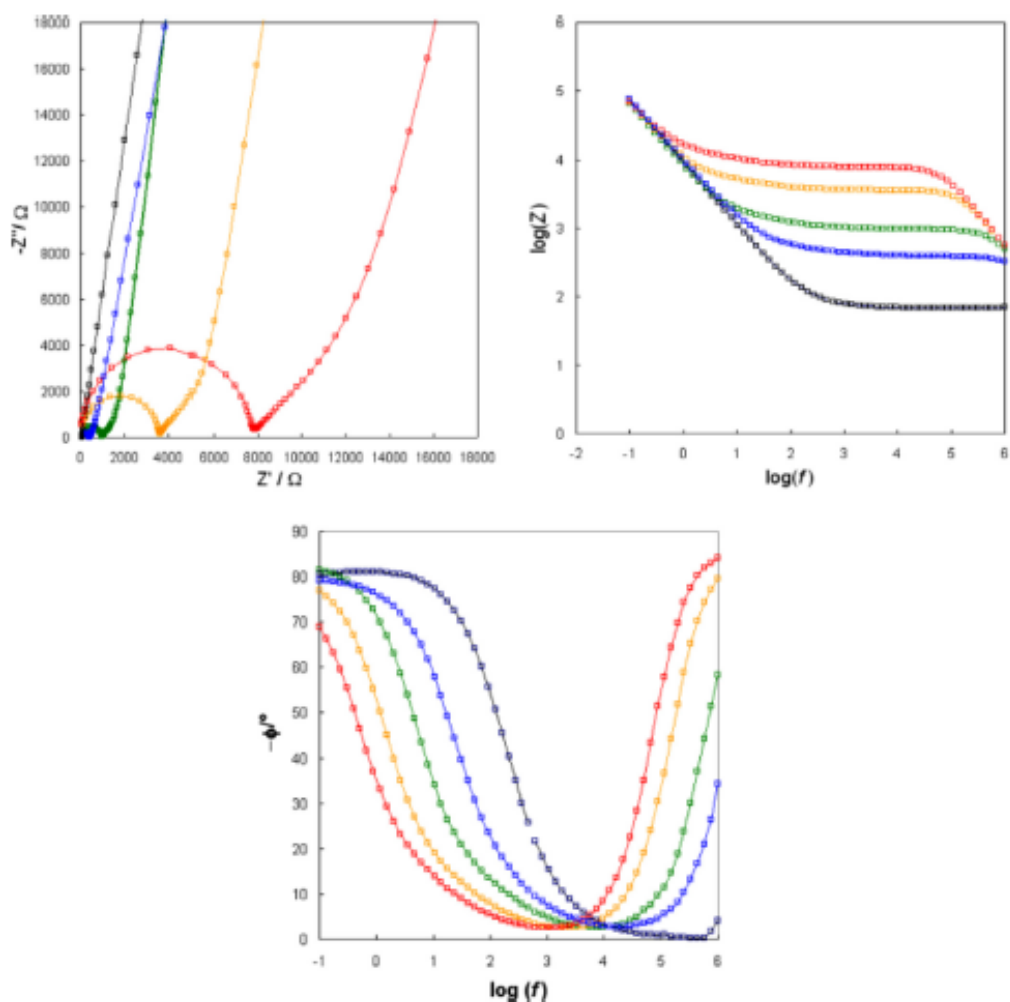


Figure 164. EIS features (as Nyquist, Bode modulus and Bode phase diagrams) of DES A and DES G (red and orange, respectively) as films on a flat conductivity cell with concentric graphite electrodes. The features are also reported of standard 0.1 m KCl (black) and of ionic liquid BMIMNTf₂, as such (blue) and with 0.05 M [NopolMIm]Mes as chiral additive (green).

The three chiral DESs, DES A, DES G and DES U, were tested as selector media in voltammetry enantiodiscrimination experiments, to our knowledge the first example so far of such an application. The study also included ionic liquid

BMIMNTf₂ with 0.05 M [NopolMIm]Mes as chiral additive, for comparison's sake.

Comparative voltammetry tests in the above media were performed with enantiomer probes (*R*)-Fc and (*S*)-Fc. It is also interesting to note that in the present case such probes, including a tertiary amino group as one of the stereocentre substituents, can have acid/base interactions with the levulinic acid component in DES A.

(*R*)-Fc and (*S*)-Fc were studied by differential pulse voltammetry DPV, both alone and in mixtures, in small solution volumes at concentrations in the 0.05-0.0075 M range, on screen-printed electrode SPE cells. In all cases a small volume of aqueous KCl solution (0.003 cm³ per 0.1 cm³ DES A and DES G, 0.006 cm³ per 0.1 cm³ in the case of more viscous DES U) was added to the chiral medium, to stabilize the potential of the pseudoreference electrode, besides advantageously resulting in lower viscosity (an important issue, especially in the DES U case); again, such addition should be regarded as fully compatible with a DES-like interphase considering the above cited literature [236,237].

Three models of SPE cells were considered, one with graphite working electrodes and two with gold working electrodes (details in section 4.1), verifying that enantiodiscrimination could be achieved on all of them, although gold electrodes resulted in better performance.

A synopsis of DPV features of single (*R*)-Fc and (*S*)-Fc solutions in the four tested media on Au SPE is reported in Figure 165. Enantiodiscrimination in terms of significant potential differences is observed in all cases.

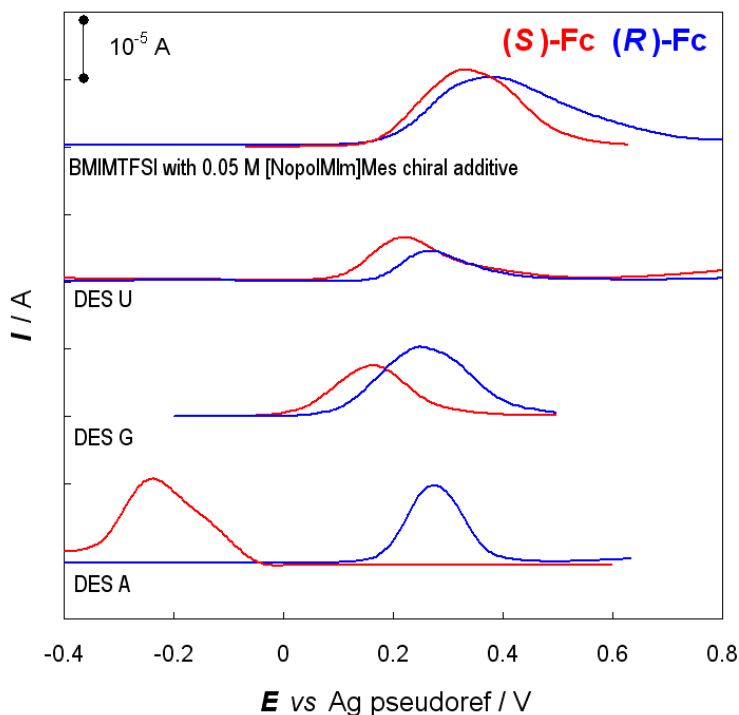


Figure 165. A synopsis of DPV features of (*R*)-Fc and (*S*)-Fc solutions on Au SPE in different chiral media based on [NopolMIm]Mes as chiral selector.

This important feature can be justified in terms of significantly different energy conditions for the electron transfer for the two enantiomers, resulting from diastereoisomeric interactions with the enantiopure environment, which could rely:

- on one hand, on a (supramolecular) peculiar chiral DES order at the interphase at the charged electrode, probably less tight than in the ILs case, and with stronger contribution of packing/clustering respect to ion layering effects, but still effective at least close to the electrode surface, according to the above discussed literature [236,237,240-245];
- on the other hand, on (molecular) specific interactions between chiral DES cations and chiral probe molecules; in fact, even mild coordination (here

supported *e.g.* by the presence of heteroatoms and aromatic systems) is known to result in significant potential shift for an electroactive probe undergoing electrochemically reversible electron transfer. In particular [141], the potential is known to shift by $(k/n)\log K$ (*i.e.*, considering a monoelectronic process, by about 60 mV per decade in coordination constant K) plus an additional $(k/n)\log c_L$ contribution linked to the ligand concentration; the shift direction depends on coordination stabilizing the electron transfer reactant or product.

Of course, both the above effects should increase with increasing concentration of the chiral selector component in the medium, and, indeed, the selector concentration has been pointed to as an important factor, resulting in a regular increase of the enantiomer peak potential difference in the case of bipyridine-based inherently chiral additives in achiral ionic liquids [134], reaching a maximum of about 0.5 V in bulk inherently chiral ionic liquid (as discussed in section 4.2.5). In the case of the family of biobased chiral molecular salts which includes [NopolMIm]Mes, tests on salts liquid at room temperature consisting of cations very similar to [NopolMIm]⁺ in combination with anion bistriflimide, only showed limited improvements when using the chiral selector as bulk chiral ionic liquid rather than as additive in achiral ionic liquid, although such observations only refer to cases with bistriflimide anions, resulting in low melting points and therefore in room temperature CILs [134]].

According to the present comparative experiments the chiral [NopolMIm]⁺ selector looks more powerful when employed as DES component rather than as IL additive, with a dramatic modulation depending from the nature of the HBD component. In fact, the enantiomer peak potential difference remarkably increases in the order DES U < DES G <<< DES A, reaching an impressive ~0.5 V difference in the levulinic acid case. The enantiomer sequence is the same in all cases, as reasonable considering that the chiral selector is kept the same, *i.e.*

[NopolMIm]⁺. The improved chiral selector performance of [NopolMIm]⁺ as DES component respect to when used as IL additive in the DES cases could be at least partially justified with its higher concentration. However, the impressive difference in the three performances observed in the present case with the chiral selector at the same mole fraction in the three DESs, points to a fundamental role of the nature of the DES achiral partner, with the real huge improvement being observed in the case of DES A. The latter case, on account of the above considerations, could be considered a peculiar case, maybe even a task-specific chiral DES for amino compounds, hinging on specific acid/base interactions beyond general-scope interactions based on the available heteroatoms and aromatic rings.

Given the availability of a single enantiomer of the chiral selector [NopolMIm]Mes, corresponding to the configuration of its natural building block, it was not possible in this case to perform our usual "double inversion" enantioselection check, consisting in verifying that a specular response is obtained inverting either probe or selector configuration. However, the chosen probe molecule, undergoing a reversible electrode process resulting in none or little electrode filming, enabled an even stronger verification experiment, *i.e.* racemate resolution.

In fact, as shown in Figure 166, working in DES A with a 1:1 solution of (*R*)-Fc and (*S*)-Fc results in two neatly separated peaks, located at potentials close to the single enantiomer ones. Experiments carried out with mixed enantiomer solutions in different ratios, varying one enantiomer while keeping the other constant (Figures 166 last row), show a good dynamic range with concentrations and confirm that the two peaks correspond to the same enantiomers as in the single experiments, *i.e.* the (*S*) enantiomer at about -0.2 V preceding the (*R*) one

at about 0.3 V. The first peak looks sharper and better reproducible/with a better dynamic range than the second one, which might be ascribed to the first process partially conditioning the interphase and affecting the result of the following one. Notably, although the peak separation looks narrower on C than on Au (Gallery section 22), a large enantiomer resolution is obtained on all the SPE cells tested; this feature is also important, since it can be regarded as an indicator of the robustness of the proposed approach to enantioselective voltammetry based on chiral DES.

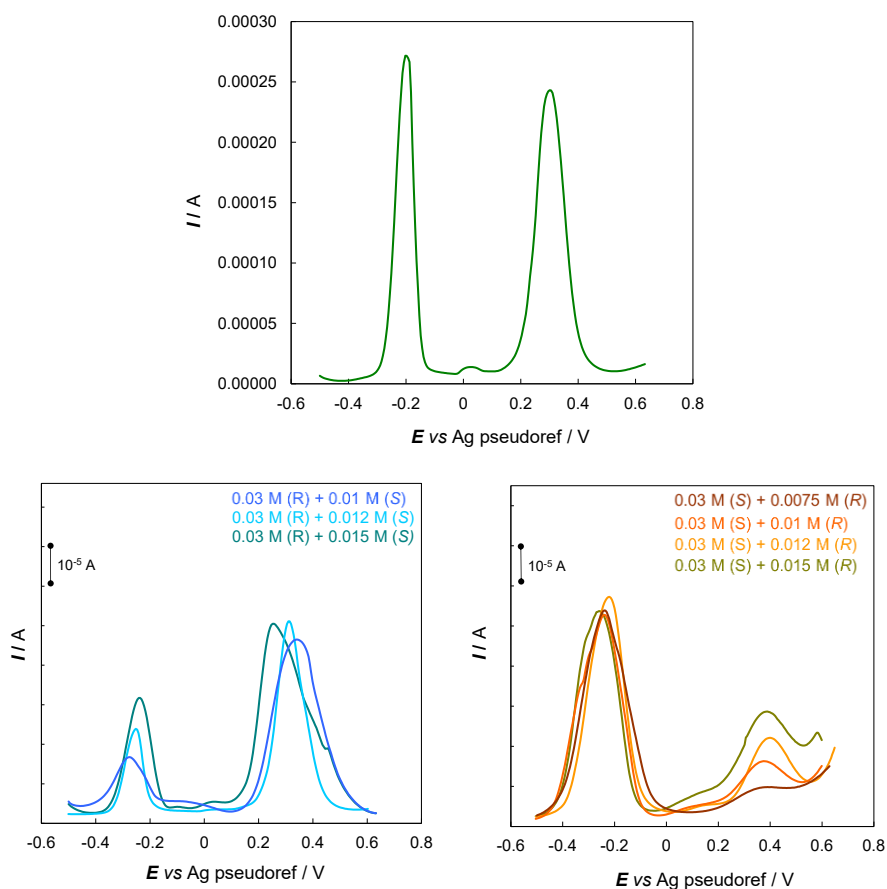


Figure 166. DPV patterns of (*R*)-Fc and (*S*)-Fc mixed solutions on Au SPE in DES A.

The enantiodiscrimination ability of DES A was also tested with the L- and D-antipodes of aminoacid tryptophan, an example of chiral probe of applicative interest, undergoing a chemically irreversible first oxidation. Notably, it includes two *N* sites, both of which however have the *N* doublet by far less available than the one in the above model Fc probes. In fact, the amino group is involved in highly favoured zwitterion formation by intramolecular neutralization equilibrium with the carboxylic group; on the other hand, the doublet of the indolic *N* is involved in the conjugation of the heteroaromatic system, so that the indole basicity is very weak, and with protonation taking place in C₃ position rather than on the *N* atom [246,247], so that tryptophan is usually reported with two p*K*_as only (referred to COOH and NH₃⁺ as in the simplest amino acid cases [248]).

The tests were performed at different enantiomer concentrations, by DPV in a drop of DES A (with a small addition of aqueous KCl as in the former case) on C SPEs, *i.e.* on graphite working electrodes. For sake of comparison, the tryptophan antipodes were also tested with the same protocol in achiral BMIMNTf₂ ionic liquid. The results are summarized in Figure 167.

Clear enantiodiscrimination is observed also in this case, with a peak potential difference of ~0.23 V for the two enantiomers in DES A (while the peak potentials are practically coincident in the achiral medium, Figure 167 top); a remarkable one, although not so outstanding as in the Fc case, which might be justified by the above comparison of *N* group availability. Moreover, also in this case a linear dynamic range with very good correlation coefficients is observed for peak currents as a function of concentration for both enantiomers (Figure 167 bottom).

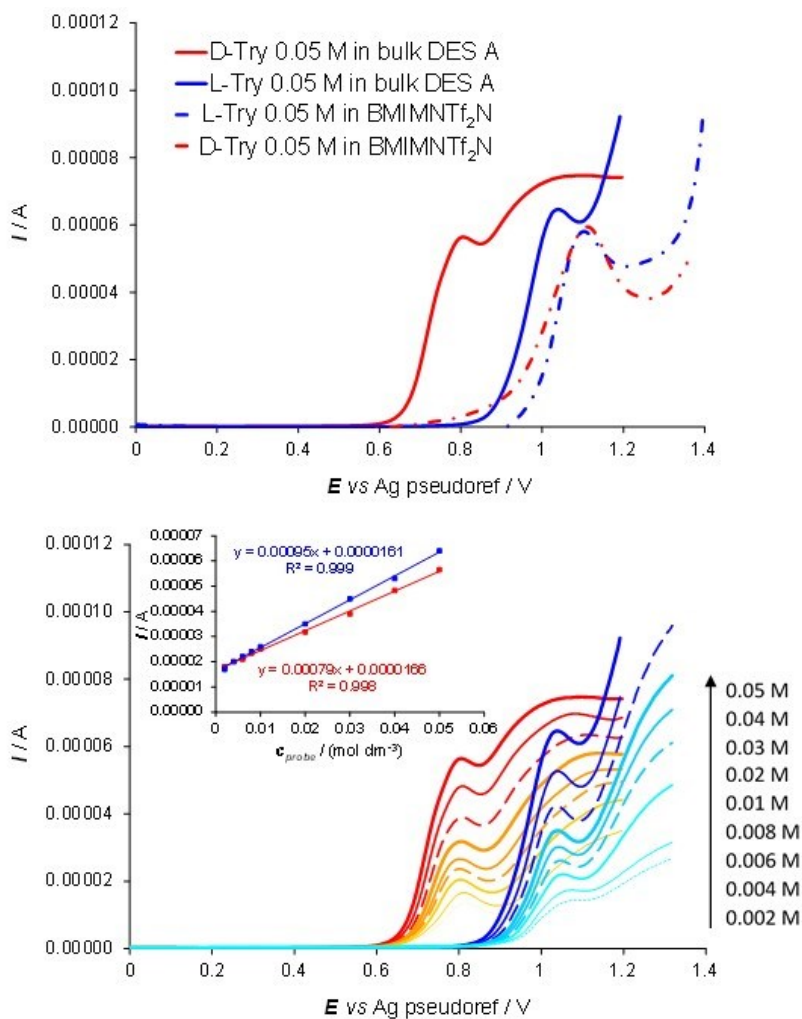


Figure 167. A synopsis of DPV features of D- and L- tryptophan (red and blue, respectively) in chiral DES A on C SPEs. Top: comparison with the same protocol in achiral BMIMNTf₂ at 0.05 M concentration. Bottom: verification of peak current vs concentration linearity for each enantiomer.

This second experiment confirms that working in a suitable chiral DES large enantiomer peak potential differences can be obtained also with significantly different chiral probes, and with good linear dynamic ranges for peak currents. This combination provides a most desirable background for the development of

effective protocols for qualitative and quantitative electroanalysis of chiral electroactive probes in chiral DESs.

The results presented constitute the first proof of concept of the remarkable potentialities of enantiopure chiral DESs as selector media for enantioselective electrochemistry and electroanalysis. DES interphases, although less defined and expanded than IL ones, and involving a higher amount of packing/clustering vs ion layering effects according to the first available studies [236,237,240-245], definitely look able to provide effective enantiodiscrimination in electron transfers involving chiral electroactive probes. Even more, the performances as chiral selector of our investigated molecular salt with biobased cation appear enhanced when it is employed as DES component rather than as IL additive.

In the case of DES A, the results are particularly impressive, since a selector with stereocentre-based stereogenicity results in a striking outcome, similar to performances obtained with very powerful inherently chiral selectors. In particular, large to huge DPV potential differences as well as good linear dynamic ranges for currents, a most desirable combination for development of quali/quantitative electroanalysis protocols, are obtained for the enantiomers of two quite different electroactive chiral probes, a model ferrocenyl amine one, and tryptophan, an amino acid of applicative interest.

Such results also suggest many interesting developments, including a deeper investigation of the molecular interactions within the three-component (probe and DES components) system, as such and at the interphase with the charged electrode surface, and a further analysis of the role of acid/base interactions. These studies should be regarded as an important step further in the frontier field of enantioselective electroanalysis and, more generally, can positively impact the development of task-specific enantioselective media and also promote development of DESs with more powerful stereogenicity elements in the chiral component.

b) New natural DESs with different HBA and HBD, also in different ratios

The results reported in 4.2.9 (point a) also suggest many interesting developments, including a deeper investigation of the molecular interactions within the three-actor (probe and DES components: HBD and HBA) system, as such and at the interphase with the charged electrode surface, and a further analysis of the role of acid/base interactions.

For this reason, in order to explore more in detail the performances of chiral DESs (always of natural origin) for application in chiral electroanalysis, many different DESs (with different HBD and HBA, also in different ratios) were studied (Table 16).

Table 16. DESs used as chiral media in enantioselection experiments, with chiral cations or anions and different HBA and HBD.

DES	HBA	HBD	HBA (g)	HBD (g)	X HBD	Tot	X H ₂ O
1	L-proline	LevA	250	756.4361	3	1006.436	
1.1	L-proline	LevA	350	706.007	2	1056.007	
1.2	L-proline	LevA	200	806.8652	4	1006.865	
1.3	L-proline	LevA	180	907.7233	5	1087.723	
2	L-proline	Gly	300	719.8781	3	1019.878	
2.1	L-proline	Gly	400	639.8916	2	1039.892	
2.2	L-proline	Gly	250	799.8645	4	1049.865	
2.2	L-proline	Gly	210	839.8577	5	1049.858	
3	D-proline	LevA	250	756.4361	3	1006.436	
4	D-proline	Gly	300	719.8781	3	1019.878	
5	L-carnetine	LevA	320	691.5335	3	1011.533	
6	L-carnetine	Gly	370	634.1185	3	1004.118	
7	ChCl	L-TarA	600	322.4968	0.5	922.4968	0.25
8	ChCl	S-MandA	480	784.6154	1.5	1264.615	
9	ChCl	R-MandA	480	784.6154	1.5	1264.615	
10	L-proline	EG	400	646.9444	3	1046.944	
11	L-proline	GlyA	350	693.5735	3	1043.573	

The electrochemical windows of bulk DESs **1**, **2**, **3**, **4**, **5**, **6**, **7**, **8** and **9** were explored with cyclic voltammetry in thin layers on screen printed electrode cells with graphite working electrodes and Ag|Ag⁺ pseudoreference electrodes. As shown in Figure 168, the new chiral media have convenient potential windows for electrochemical experiments, about 2.4-2.6 V wide, with reasonable extension on both the oxidation and reduction side.

However, the DESs **7**, **8** and **9** which present ChCl as HBA show a narrower potential window (about 1.7-1.9 V), probably due to the decomposition of the ChCl component [249].

The enantioselection tests were performed using the enantiomers of chiral ferrocene (0.003 M) dissolved in bulk DESs as chiral media, on screen printed electrodes (SPEs), printed on a plastic support, with graphite as working and counter electrodes, and Ag as pseudo-reference electrode (as described in 4.1). All the experiments were carried out with the addition of a small volume of aqueous KCl solution 0.1 M (in particular 30% of aqueous solution was added to the chiral medium), to stabilize the potential of the pseudoreference electrode, besides advantageously resulting in lower viscosity.

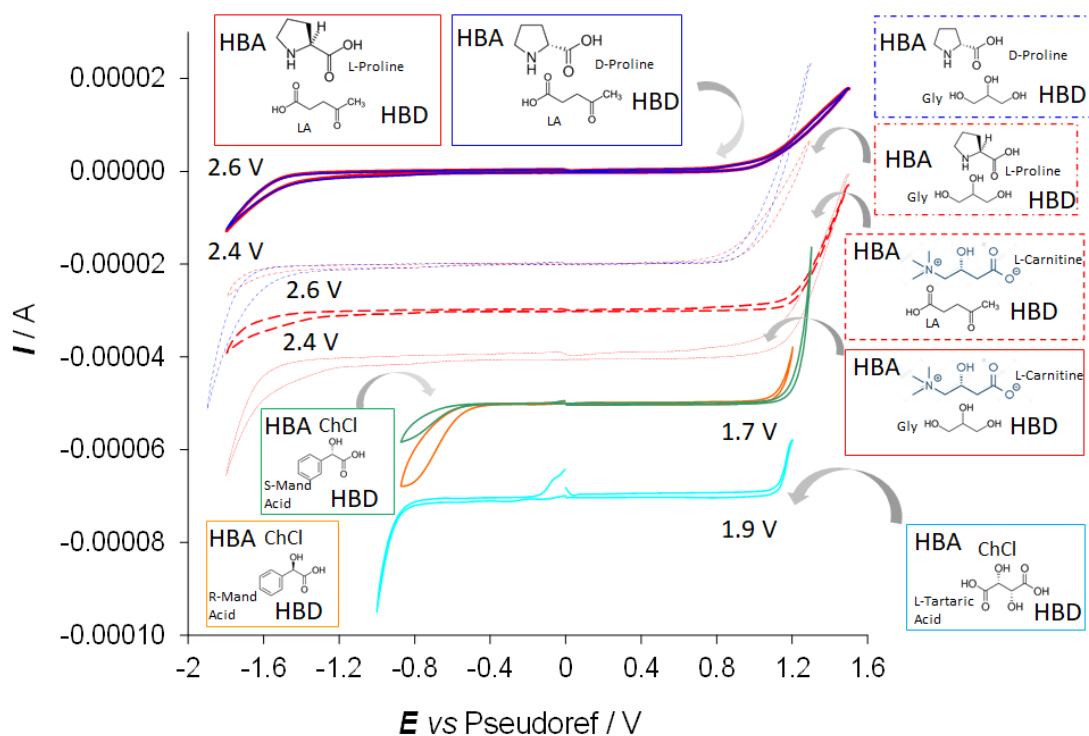


Figure 168. CV potential windows (at 0.2 V/s scan rate) of bulk DESs **1, 2, 3, 4, 5, 6, 7, 8** and **9** as thin films spread on screen printed electrode cells with graphite working and counter electrodes and Ag|Ag⁺ pseudoreference electrodes.

Moreover, unlike the previous cases (reported in section 4.2.9 point a)) where only one enantiomer of the chiral DESs was available ([NopolMIm]Mes corresponding to the configuration of its natural building block), in this case it was possible in the DESs cases **1** and **3** (L- and D-Proline as HBA, Figure 169), **2** and **4** (L- and D-Proline as HBA, Figure 170), **8** and **9** (*S*- and *R*-Mandelic Acid as HBD, Figure 171) to perform our usual "double inversion" enantioselection check, consisting in verifying that a specular response is obtained inverting either probe or selector configuration.

Enantiodiscrimination in terms of significant potential differences is observed in all cases with:

- Solutions of single FcR and FcS enantiomers
- in DES case **1**, also solutions of probe racemate.

The results are collected in Figures 169-173.

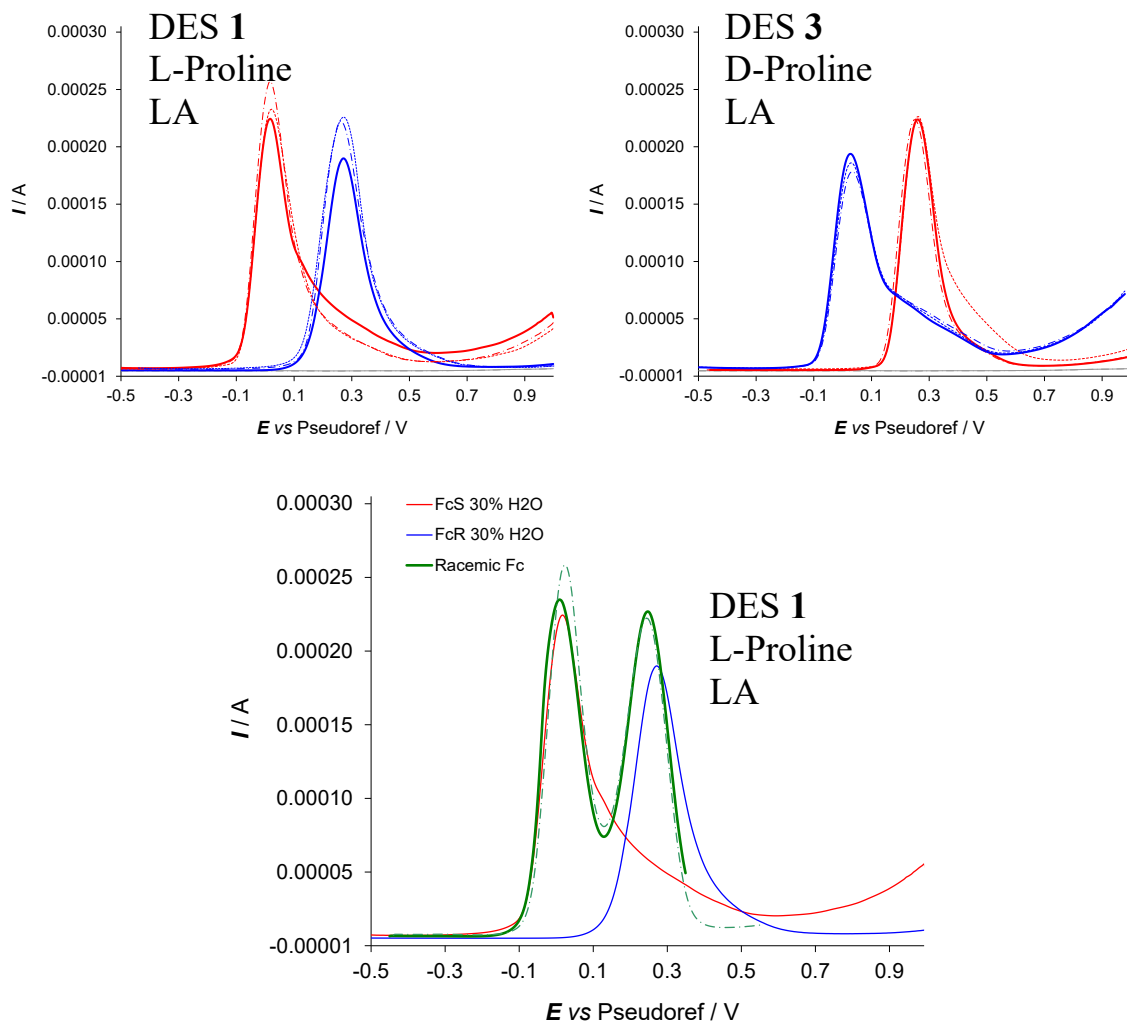


Figure 169. DPV patterns of FcS (in red), FcR (in blue) in DESs **1** and **3** and racemic Fc (in green) in DESs **1**, on C SPE.

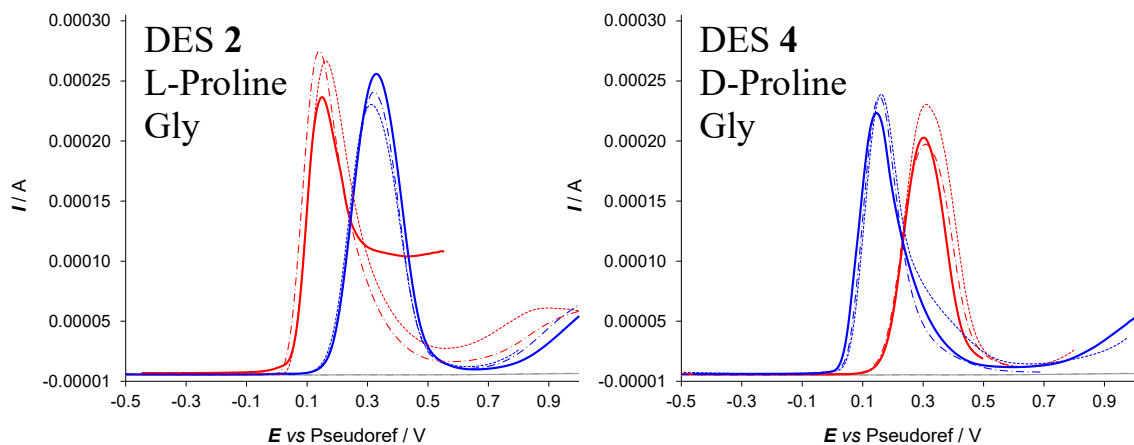


Figure 170. DPV patterns of FcS (in red) and FcR (in blue) on C SPE in DESs **2** and **4**.

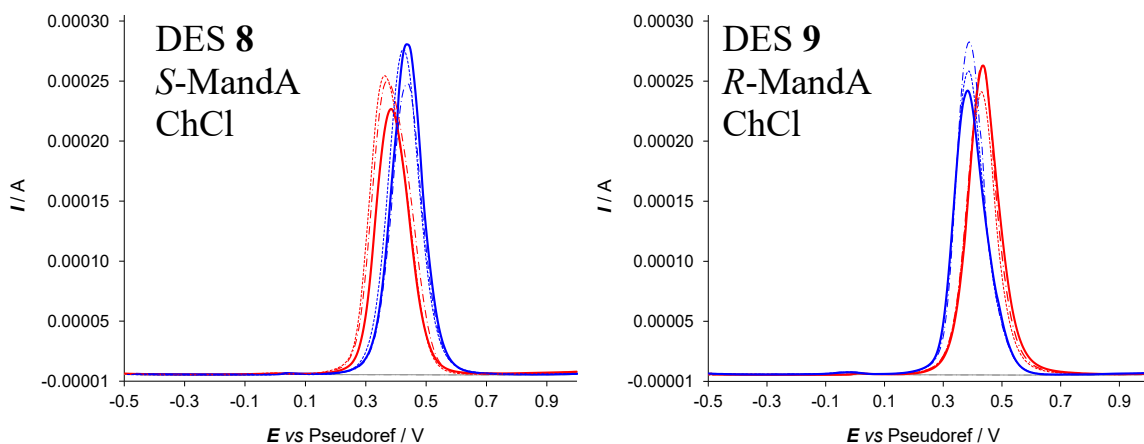


Figure 171. DPV patterns of FcS (in red) and FcR (in blue) on C SPE in DESs **8** and **9**.

The enantiomer peak potential difference remarkably increases in the order **8,9** (~ 70 mV) < **2,4** (~ 180 mV) < **1,3** (~ 260 mV), confirming the above considerations (in section 4.2.9 point a) on the acid/base interactions at least concerning the comparison of **1,3** vs **2,4**, with specular results changing the

configuration of the chiral HBA (L- or D-proline, in Figure 169 and 170) or HBD (*R*- or *S*-Mandelic Acid, in Figure 171).

Moreover, the same probe/selector enantiomer combination order is observed in the DESs cases **1,3** and **2,4**, as reasonable considering that the chiral HBA (L- or D-proline) is kept the same, *i.e.* with the L,*S* (or specularly D,*R*) combination preceding the L,*R* (or specularly D,*S*) one.

The improved performances in DES cases which present levulinic acid as HBA are confirmed again with the enantiodiscrimination experiments carried out on FcR and FcS probe solutions in bulk DESs **5** and **6** (Figure 172). In fact, the peak potential separation value is:

- ~240 mV in the DES **5** case
- ~140 mV in the DES **6** case

Furthermore, a linear dynamic range with very good correlation coefficients is observed for peak currents as a function of concentration for both enantiomers.

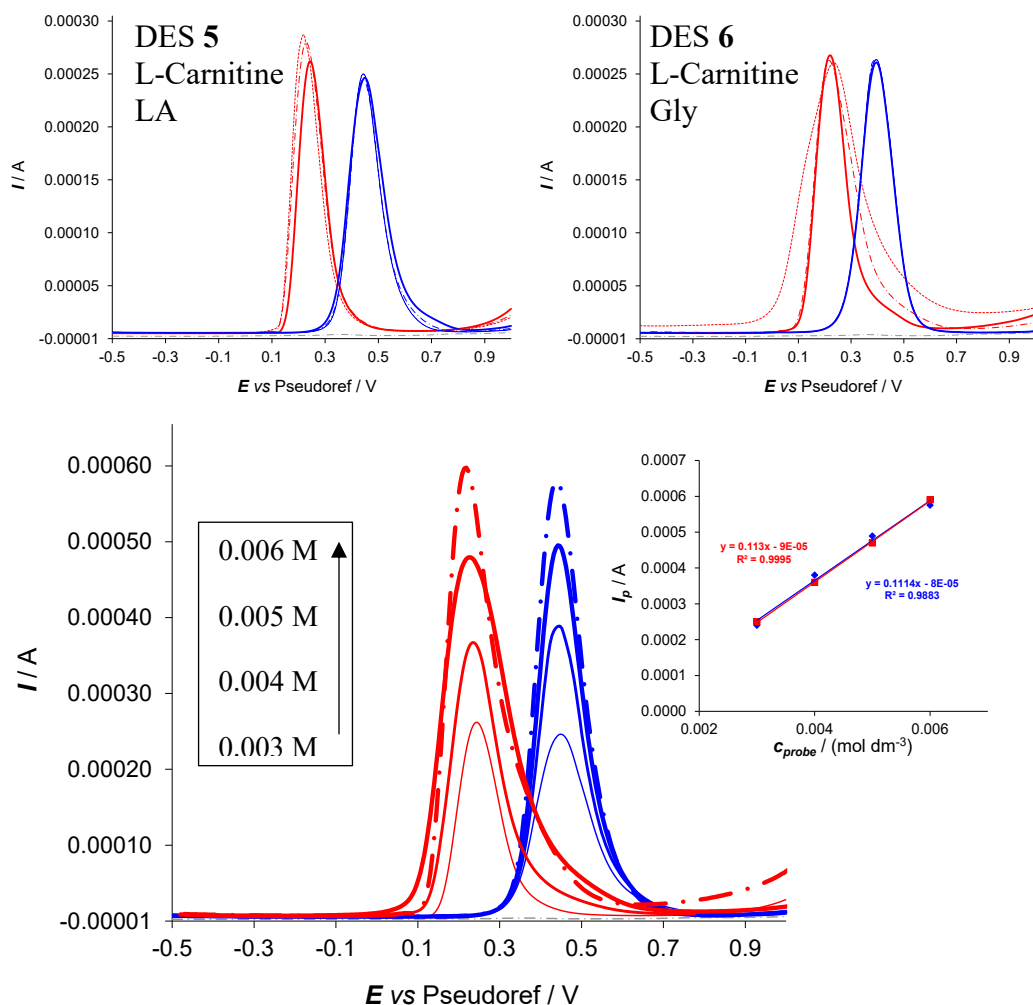


Figure 172. DPV patterns of FcS (in red) and FcR (in blue) on C SPE in DESs **5** and **6**. Bottom: verification of peak current vs concentration linearity for each enantiomer of chiral Fc in DES **5**.

Finally, DES **7** was also tested obtaining a peak potential separation of about 100 mV (Figure 173), with the same enantiomer peak sequence (*i.e.* FcS before FcR) of the other cases which present the L- enantiomer as chiral component (L-proline and L-carnitine). Also in this case a linear dynamic range with very

good correlation coefficients is observed for peak currents as a function of concentration for both enantiomers.

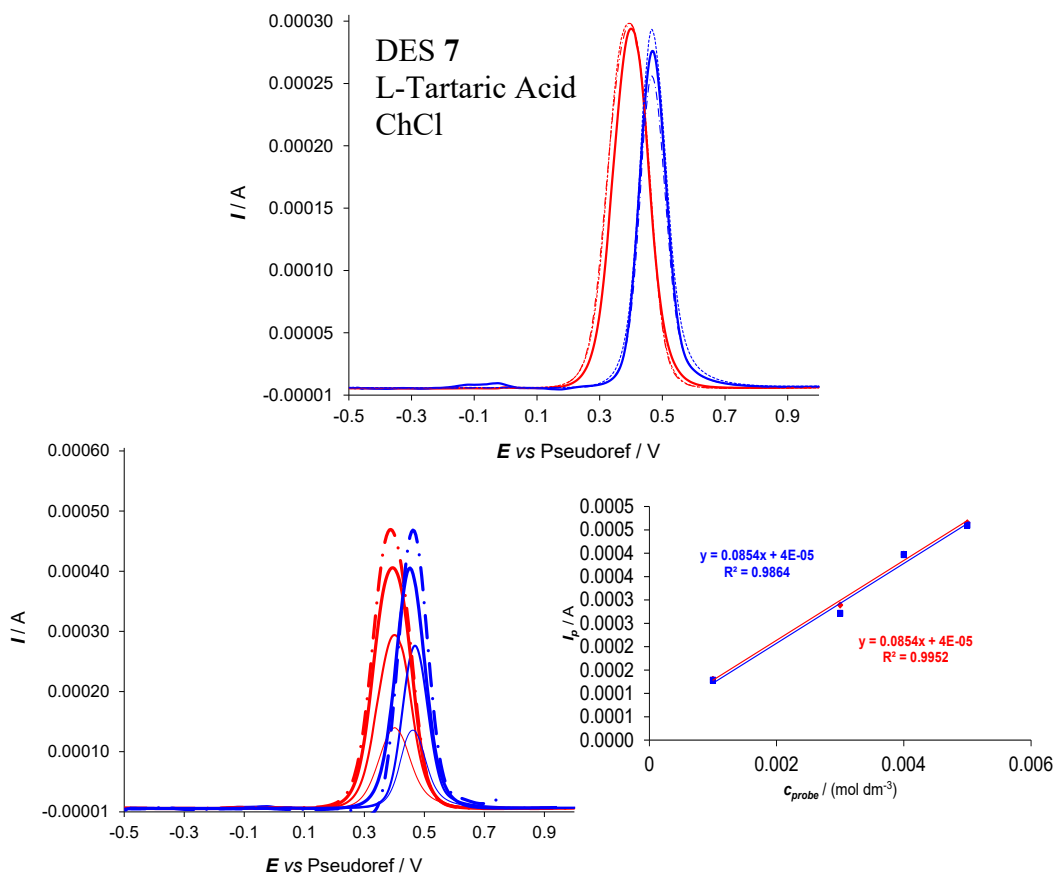


Figure 173. DPV patterns of FcS (in red) and FcR (in blue) on C SPE in DES 7. Bottom: verification of peak current vs concentration linearity for each enantiomer.

Since the best results were obtained in the case of DES 1 (*i.e.* with L-Proline as HBA and levulinic acid as HBD), other experiments were carried out with DESs:

- **1.1** (HBA:HBD 1:2)
- **1.2** (HBA:HBD 1:4)
- and **1.3** (HBA:HBD 1:5)

increasing the X HBD, *i.e.* levulinic acid.

All the experiments were performed with the addition of 30% H₂O.

The peak potential separation increases **1.1** (~100 mV) < **1** (~260 mV in Figure 169) < **1.2** (~390 mV) < **1.3** (~490 mV), as reported in Figure 174.

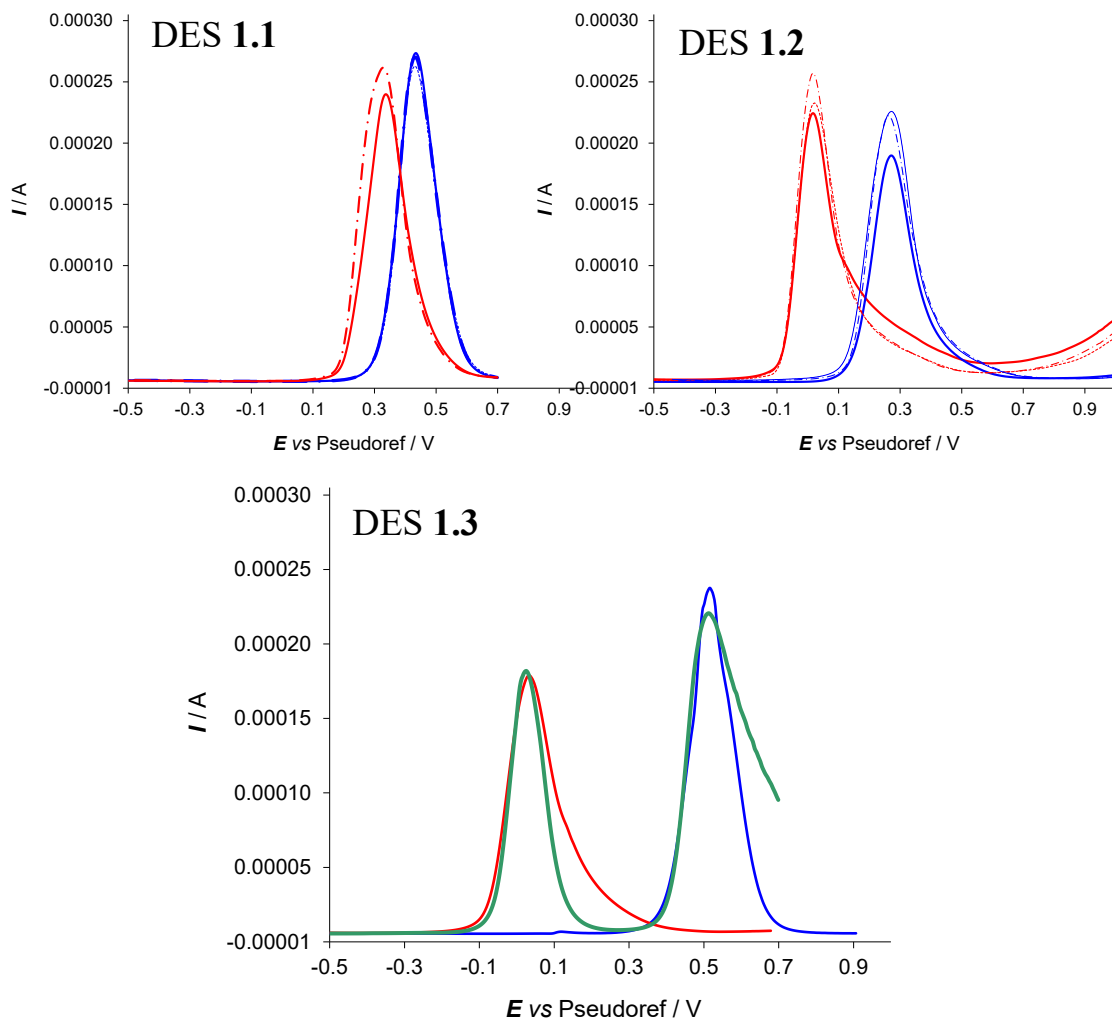


Figure 174. DPV patterns of FcS (in red), FcR (in blue) in DESs **1.1**, **1.2** and **1.3** and racemic Fc (in green) in DES **1.3**, on C SPE.

The same experiments were also carried out with DES **2** in different ratios for the HBD component (*i.e.* glycerol):

- **2.2** (HBA:HBD 1:2)
- **2.3** (HBA:HBD 1:4)

All the experiments were performed with the addition of 30% H₂O (Figure 175).

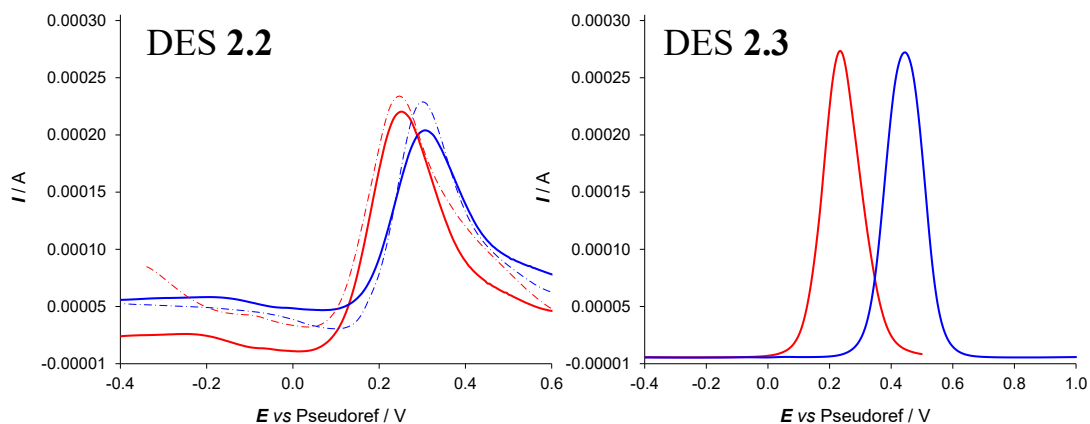


Figure 175. DPV patterns of FcS (in red) and FcR (in blue) on C SPE in DESs **2.2** and **2.3**.

Also in this case the peak potential separation increases **2.2** (~60 mV) < **2** (~180 mV in Figure 170) < **2.3** (~240 mV), as reported in Figure 175.

The effect of the H₂O percentage on the enantioselection ability was studied in the DES case **1**: L- Proline (HBA) and LA (HBD) (Figure 176). In fact, it has been demonstrated that even small, simple ionic liquids with no liquid crystal features, have a high supramolecular order at the interphase with a charged surface; unlike the electrode|solution with its double layer, the electrode|IL interface resembles a quasi-solid crystal, extending for about 200 nm [250], even in the presence of significant amounts of water [185]. DESs can be considered to have an interphase order intermediate between ionic liquid and double layer. Surprisingly, such DES interphase structure holds up to 30–50 wt% of water, with water even incorporated/cooperating in the structural order [236,245] (the same also holds for bulk DES order, although within a lower reported threshold

of 0.4/0.5 mole fraction water, corresponding to several wt% only [251]). This is a great advantage for electrochemical applications, enabling to simplify the operating conditions and to widely modulate the medium properties [236,251] (for example, to lower resistance and viscosity) while maintaining DES interphacial properties [236,245].

In particular, the enantioselection ability increases with decreasing water percentage, reaching a peak potential separation of about 640 mV with 10% of H₂O (Figure 176).

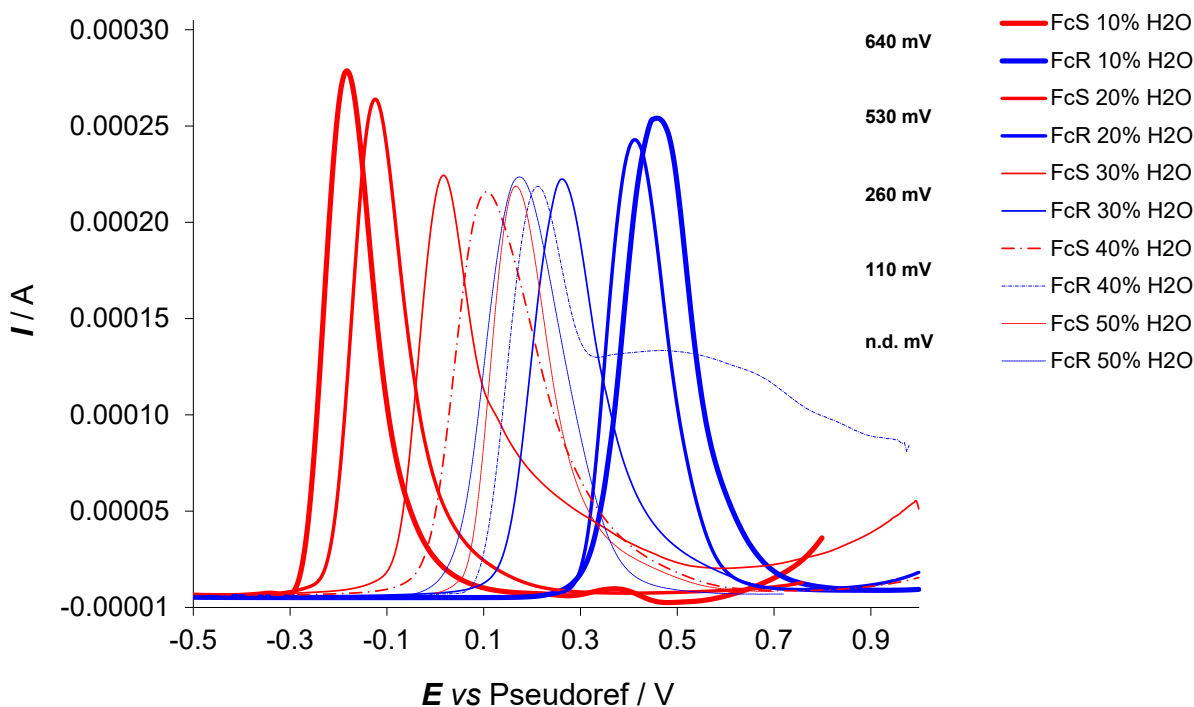


Figure 176. Enantioselection tests in DES **1** with LA as HBD and L-Proline as HBA towards the enantiomers of chiral ferrocene (FcS in red and FcR in blue) as a function of the water weight percentage.

Finally, other two DESs (**10** and **11**, in Table 16) were employed as chiral media to test the enantiomers of chiral ferrocene, with a good peak potential separation in both the cases: DES **10** of about 190 mV and DES **11** of about 200 mV (Figure 177).

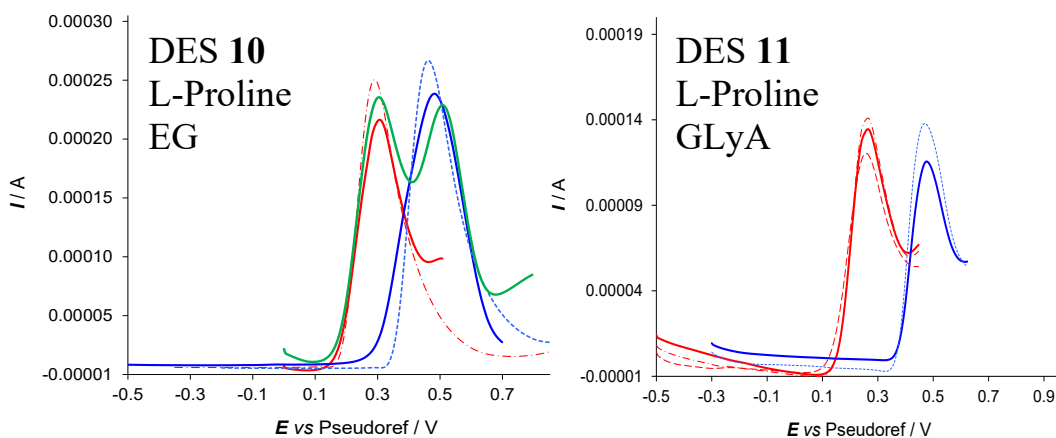
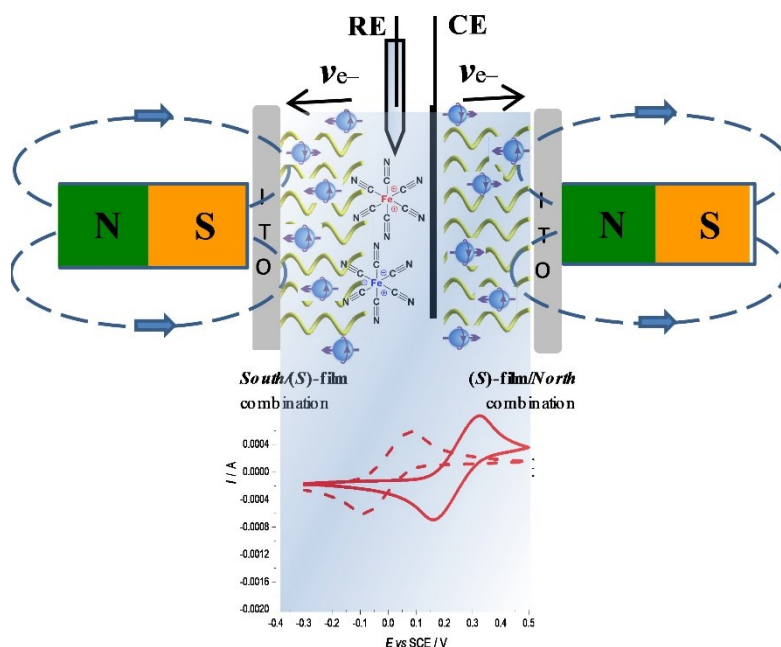


Figure 177. DPV patterns of FcS (in red), FcR (in blue) in DESs **10** and **11** and racemic Fc (in green) in DES **10**, on C SPE.

Chapter 5

Advanced application in magnetochemistry experiments



Impressive spin-related effects are observed in cyclic voltammetry (CV) experiments performed under applied magnetic field on a non-ferromagnetic electrode modified with a thin electroactive oligothiophene film, either "inherently chiral" or featuring chiral pendants with stereogenic centres. By flipping the magnet north/south orientation, the CV peaks of two achiral, chemically reversible Fe(III)/Fe(II) redox couples in aqueous or organic solution undergo impressive potential shifts (up to nearly 0.5 V depending on protocol conditions), specularly by changing the film (*R*)- or (*S*)-configuration. The magnitude of the potential shift decreases both increasing the polymer film

thickness and the distance between the permanent magnet from the electrode surface. Such unprecedented spin-related redox potential modulation, obtained in the absence of a magnetic electrode acting as spin injector, provides a striking evidence (as well as an attractive evaluation criterion) of the spin selectivity properties of chiral thin films [252].

Chiral films obtained by electrooligomerization of (*R*)- or (*S*)- BT₂T₄ monomers, successfully tested as chiral selectors (as also reported in the experiments presented in chapter 3) for electroactive chiral molecular probes in former experiments were evaluated as spin selectors. Their performance was also compared with that of chiral thiophene-based enantiopure films (c-PEDOT) obtained from electropolymerization of (*2R,3R*)-2,3-dimethyl-2,3-dihydrothieno[3,4-*b*][1,4]dioxine (c-EDOT) monomer, including two stereocentres localized outside the main conjugated backbone. To rule out any false positive results, achiral PEDOT (electrodeposited from commercially available 2,3-dihydrothieno[3,4-*b*][1,4]dioxine monomer), was tested with the same protocol [252].

a) Experimental procedures

Electrodeposition of thiophene-based thin films.

Magneto-electrochemistry measurements were carried out employing as working electrode (WE) a slice (0.8×4.5) cm² of ITO coated glass where a chiral enantiopure organic thin film or an achiral one was electrodeposited on an area of about 1 cm². Films were electrodeposited by potentiodynamic oxidation of the corresponding monomer at 0.2 V s⁻¹ in acetonitrile (ACN) + 0.1 M tetrabutylammonium hexafluorophosphate (TBAPF₆) supporting electrolyte by cycling the potential in a proper electrochemical window including the oxidation

peak of the corresponding monomer. The three types of thiophene-based thin films were prepared according to the following protocols:

- Enantiopure oligo-(*R*) and oligo-(*S*)-BT₂T₄ films: (*R*)- or (*S*)-BT₂T₄ monomer $5 \cdot 10^{-4}$ M, by cycling from 1 to 10 times the potential in the 0-1.35 V vs SCE window;
- Enantiopure c-PEDOT films: c-EDOT monomer $5 \cdot 10^{-4}$ M, by cycling 1 time (1 CV cycle) the potential in the -0.2-1.1 V vs SCE window;
- Achiral PEDOT films: EDOT monomer $5 \cdot 10^{-4}$ M, by cycling 1 time (1 CV cycle) the potential in the -0.2-1.1 V vs SCE window.

It is important to underline that during the deposition step no external magnetic field was applied.

Experimental magnetoelectrochemistry set-up.

Magnetoelectrochemistry study was carried using a cuvette as working cell where the hybrid ITO| film WE, a Pt wire as counter electrode and an aqueous saturated calomel electrode (SCE) as reference one were immersed in a solution containing the achiral redox couple (Figure 178), made by:

- i*) an equimolar aqueous solution of K₃[Fe(CN)₆] and K₄[Fe(CN)₆] (indicated as Fe(III)/Fe(II)), each of them at 2.5 mM concentration, with 400 mM KCl as supporting electrolyte;
- ii*) a 2 mM solution of ferrocene in ACN with 0.1 M TBAPF₆ as supporting electrolyte.

A magnetic field perpendicular to the electrode surface was applied by placing a permanent magnet (nickel-coated NdFeB B88X0 Grade N42 K&J Magnet, Inc.) close to the WE, at a distance of around 2.6 mm (considering that the thickness of ITO-coated glass electrode and cuvette were ca. 1 mm and ca. 1.6 mm, respectively). The nominal magnetic field strength at the surface of the magnet is 6353 Gauss. Change in the orientation of the magnetic field was obtained by mechanically flipping the magnet around its magnetic axis (north vs south orientation).

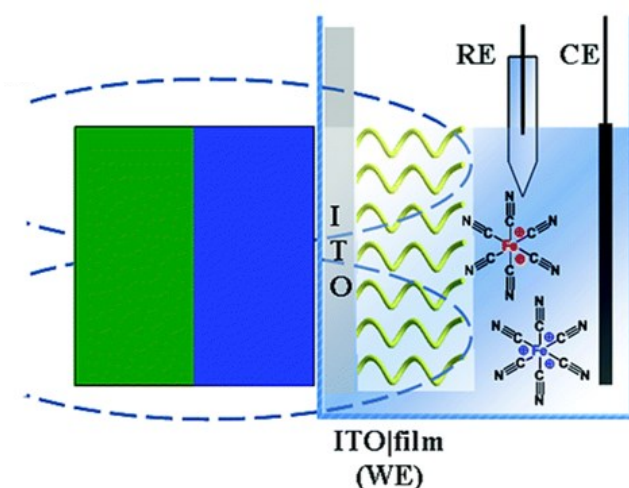


Figure 178. Schematic representation of the magnetoelectrochemistry experimental setup.

Measurements changing the strength of the magnetic field were carried out by placing rigid plastic foils of different thickness (0.1 mm, 0.3 mm, 0.8 mm, 1 mm, 2 mm, 3 mm) between the cuvette and the permanent magnet and by recording CV signals of the achiral redox couples mechanically flipping the magnet. These additional tests were performed on enantiopure oligo-(*S*)-BT₂T₄ film that was electrodeposited on ITO electrode at constant protocol as described above.

Measurements changing the thickness of the inherently chiral films were obtained by electrodepositing enantiopure (*S*)-BT₂T₄ monomer by varying the

number of deposition cycles (10, 4, 2, 1) and then recording CV signals of the achiral Fe(III)/Fe(II) couple mechanically flipping the magnet.

b) Magnetochemistry experiments

The proposed strategy is a variation of the Spin Dependent Electrochemistry (SDE) protocols presented in literature, where, in general, a permanent magnet is placed in close contact to a ferromagnetic Ni electrode that acts as electron spin injector for the adjacent chiral interface obtained by a proper functionalization of the metal surface [216,253-255].

Instead, the setup adopted in this case involves a non-ferromagnetic material as electron collector (source/drain) for the working electrode (indium tin oxide coated glass, ITO).

The magnetic field is applied by an external magnet, placed at a distance of ca. 2.6 mm from the ITO|film interface, considering that the thickness of the bare ITO electrode and cuvette were ca. 1.0 mm and ca. 1.6 mm, respectively (Figure 179); this implies no direct spin injection into the film by the electrode substrate, resembling recently proposed solid-state architectures [256].

As schematically depicted in Figure 178, the hybrid ITO|chiral film WE, as well as a Pt wire and an aqueous saturated calomel electrode (SCE) used as counter (CE) and reference (RE) respectively, were immersed in

- i)* an equimolar aqueous solution of $K_3[Fe(CN)_6]$ and $K_4[Fe(CN)_6]$ (reversible achiral redox couple, in the following indicated as Fe(III)/Fe(II)), each of them at 2.5 mM concentration, with 400 mM KCl as supporting electrolyte
- ii)* or in a 2 mM solution of ferrocene in ACN with 0.1 M TBAPF₆ as supporting electrolyte.

During CV tests (reported in Figure 179) with the achiral redox couple a magnetic field was applied, perpendicular to the electrode surface, by placing a permanent

magnet. Change in the orientation of the magnetic field was obtained by mechanically flipping the magnet along its magnetic axis (north versus south magnet pole). CV curves for the achiral Fe(III)/Fe(II) redox probe on the bare ITO surface do not show any change as a function of the magnetic field orientation (Figure 179a) with a half-wave potential ($E_{1/2}$) of 0.22 V vs SCE, being $E_{1/2}$ defined as the average between peak potentials of forward and backward scan; such chemically reversible signal is virtually identical to that obtained in the absence of the magnetic field (not shown).

No difference is also observed when recording CV curves for the same achiral probe on the ITO electrode modified with an enantiopure oligo-BT₂T₄ film of either (*R*)- or (*S*)- configuration, in the absence of an applied magnetic field (Figure 179b).

Perturbing the last setup by the external magnetic field perpendicular to the WE surface, working *e.g.* on the enantiopure oligo-(*S*)-BT₂T₄ film (Figure 179c), an impressive ~0.47 V splitting is observed for the $E_{1/2}$ of the achiral Fe(III)/Fe(II) couple upon flipping the magnetic field orientation, north vs south and *vice versa* (Table 17). Specular results are obtained working on the enantiomeric oligo-(*R*)-BT₂T₄ electrode (Figure 179d, Table 17) [252].

In order to give more generality to the above results, we performed the same experiments at constant protocol with the chiral thin film c-PEDOT, obtained by electrodeposition of c-EDOT. The latter monomer is still characterized by a C_2 symmetry axis but it presents two identical homotopic stereocentres instead of a stereogenic axis. Figure 179e shows the relevant CV patterns as a function of the magnetic field orientation. Also in this case a splitting was found for $E_{1/2}$ of the achiral Fe(III)/Fe(II) probe, although smaller than in the previous case (about 0.15 V, Table 17). This is in line with the fact that on one hand inherently chiral materials exhibit more prominent chirality manifestations; on the other hand it has been shown that monomers with chirality originating from localized

stereocentres, but C_2 -symmetric and undergoing regioregular polymerization, can result in helical packing of predominantly planar chains, with high, although labile, chirality manifestations [257].

Table 17. Key CV parameters (related patterns are shown in Figure 179) obtained for Fe(III)/Fe(II) redox couple recorded at 0.2 V s^{-1} potential scan rate on: bare ITO electrode (without magnet), on hybrid ITO/oligo-(*S*)- and oligo-(*R*)-BT₂T₄ electrodes (with and without magnet), and on hybrid ITO/c-PEDOT interface (with magnet).

^a Half-wave potential, $E_{1/2}$, is calculated according to $E_{1/2} = (E_{p,an} + E_{p,cat})/2$.

^b $\Delta E_{1/2}$ corresponds to the difference between the $E_{1/2}$ related to the two specular cases: $E_{1/2}^{(S) \text{ film-}}$

	$E_{p, an} /$ V vs. SCE	$E_{p, cat} /$ V vs. SCE	$E_{1/2}^a /$ V vs. SCE	$\Delta E_{1/2}^b /$ V
<i>Bare ITO</i>	0.25	0.13	0.19	
oligo-(<i>S</i>)-BT ₂ T ₄	0.29	0.08	0.18	
oligo-(<i>R</i>)-BT ₂ T ₄	0.29	0.08	0.18	
oligo-(<i>S</i>)-BT ₂ T ₄ - <i>South</i>	0.07	-0.06	-0.00	-0.47
oligo-(<i>S</i>)-BT ₂ T ₄ - <i>North</i>	0.52	0.42	0.47	
oligo-(<i>R</i>)-BT ₂ T ₄ - <i>South</i>	0.53	0.43	0.48	0.51
oligo-(<i>R</i>)-BT ₂ T ₄ - <i>North</i>	0.00	-0.07	-0.03	
c-PEDOT- <i>South</i>	0.10	-0.10	0.00	-0.15
c-PEDOT- <i>North</i>	0.25	0.05	0.15	

South – $E_{1/2}^{(S) \text{ film-North}}$ and/or $E_{1/2}^{(R) \text{ film-South}} - E_{1/2}^{(R) \text{ film-North}}$ obtained by flipping magnet orientation (South or North) and changing film configuration ((*R*) or (*S*)).

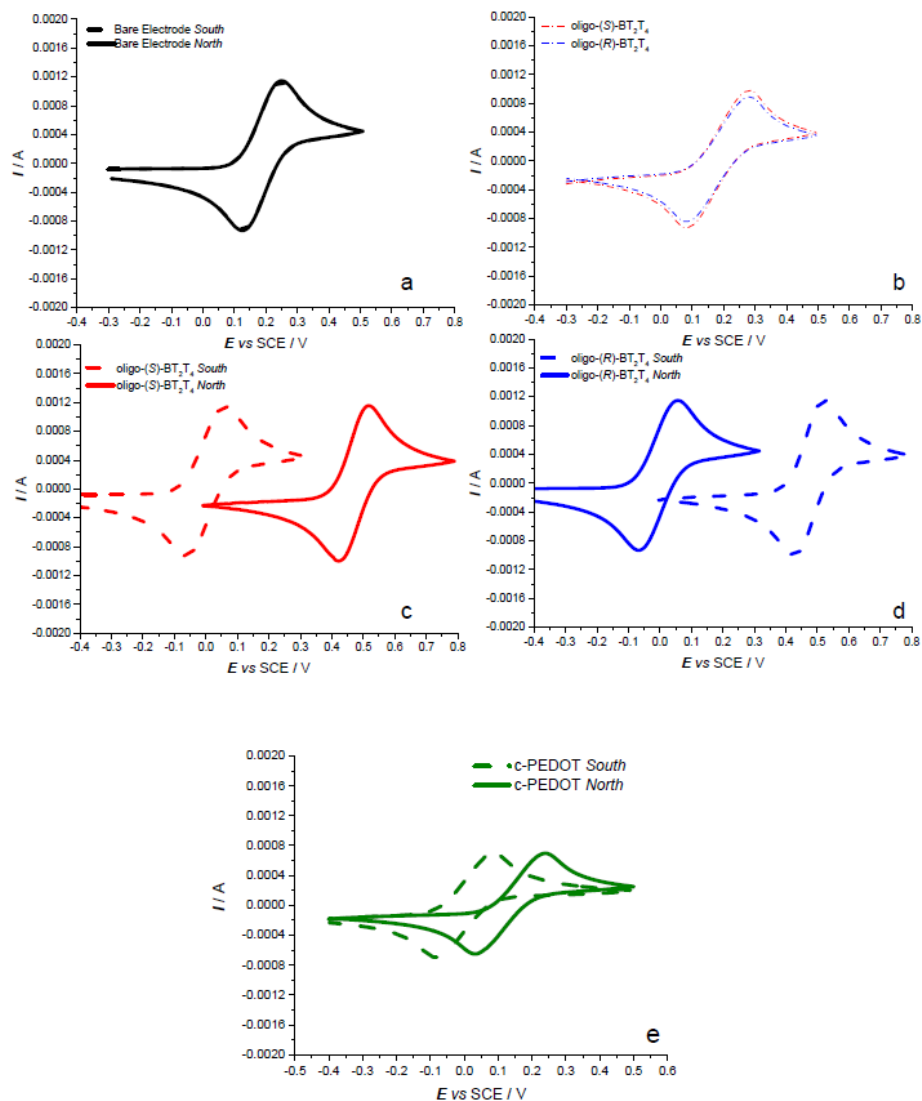


Figure 179. CV patterns recorded at 0.05 V s^{-1} for the Fe(III)/Fe(II) achiral couple: (a) on bare ITO electrode, as a function of the magnetic field orientation (solid line for north pole towards electrode, dashed line for south pole); (b) on hybrid ITO|oligo-BT₂T₄ electrodes (blue line for (R)-configuration, red for (S)-) without the external magnet; (c) e (d) at hybrid ITO|oligo-BT₂T₄ interface, as a function of the applied magnetic field orientation (solid vs dashed lines, same colour legend as before for the film configuration); (e) at hybrid ITO|c-PEDOT interface (same legend for magnetic field orientation).

c) Effect of the chiral film thickness on the shift of the Fe(III)/Fe(II) peak potential in magnetochemistry experiments

Consistently with former studies about spin coherence conservation [258], increasing the film thickness (by a higher number of electrodeposition cycles) the shift in the Fe(III)/Fe(II) peak potential upon magnet flipping decreases, becoming negligible for thickness around 50 nm (Figure 180) [252].

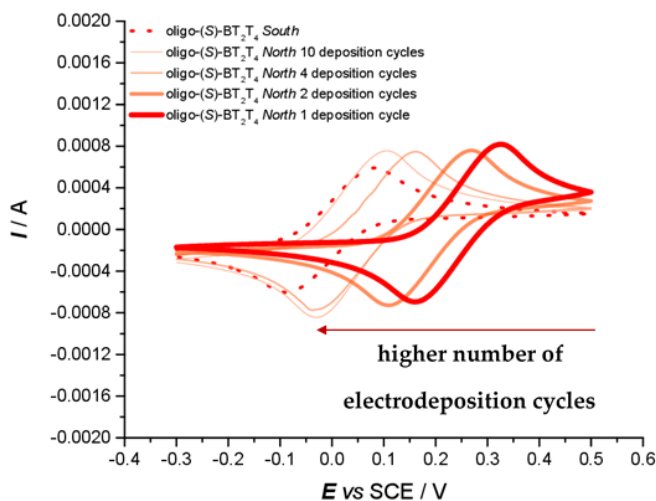


Figure 180. CV patterns recorded at 0.2 V s^{-1} for the Fe(III)/Fe(II) achiral redox couple on hybrid ITO|oligo-(S)-BT₂T₄ electrode as a function of the applied magnetic field orientation respect to the WE (solid lines North vs dashed line South) by increasing from 1 to 10 the electrodeposition cycles. For South orientation only one curve (1 cycle) has been reported, because all the CV patterns recorded by varying the deposition cycles are practically superimposed.

d) Effect of the magnet distance on the shift of Fe(III)/Fe(II) peak potentials in magnetochemistry experiments

To further confirm the role of the magnetic field on the observed phenomenon as well as evaluate the impact of its strength on the observed potential shift, a systematic series of CV experiments was carried out placing different sheet spacers of increasing thickness between the cuvette and the permanent magnet.

As expected, the potential difference observed by flipping the permanent magnet exhibited a sharp, regular decrease with increasing distance of the magnet from the ITO|oligo-(S)-BT₂T₄ interface (Figure 181 with inset, Table 18) [252].

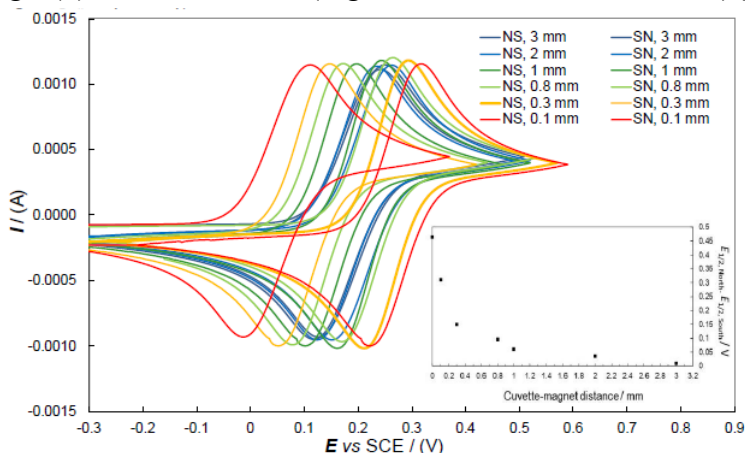


Figure 181. CV patterns recorded at 0.05 V s⁻¹ for the Fe(III)/Fe(II) achiral couple in aqueous solution at hybrid ITO|oligo-(S)-BT₂T₄ interface, as a function of the applied magnetic field orientation (north-south vs south-north) and of the magnetic field strength.

Table 18. Relevant data observed for the Fe(III)/Fe(II) achiral couple (Figure 181) by varying cuvette-magnet distance and the magnet orientation, using oligo-(S)-BT₂T₄ film. All peaks and half-wave potential values are referred to SCE electrode.

Cuvette-magnet distance / mm	South orientation			North orientation			$E_{1/2, \text{North}} - E_{1/2, \text{South}} / \text{V}$
	$E_{p, \text{an}} / \text{V}$	$E_{p, \text{cat}} / \text{V}$	$E_{1/2, \text{South}} / \text{V}$	$E_{p, \text{an}} / \text{V}$	$E_{p, \text{cat}} / \text{V}$	$E_{1/2, \text{North}} / \text{V}$	
3	0.24	0.11	0.18	0.25	0.12	0.19	0.01
2	0.23	0.12	0.18	0.27	0.15	0.21	0.03
1	0.20	0.09	0.15	0.25	0.16	0.21	0.06
0.8	0.18	0.07	0.13	0.27	0.17	0.22	0.09
0.3	0.15	0.05	0.10	0.30	0.20	0.25	0.15
0.1	0.11	-0.19	-0.04	0.32	0.22	0.27	0.31

^a Half-wave potential, $E_{1/2}$, is calculated according to $E_{1/2} = (E_{p, \text{an}} + E_{p, \text{cat}}) / 2$.

This is coherent with the complex, non-linear dependence of the strength of the magnetic field with the distance. The same behaviour was observed when a

different achiral probe, the ferrocinium|ferrocene redox couple, was employed with the same set-up previously described, working in acetonitrile solvent. (Figure 182, 183 and Table 19) [252].

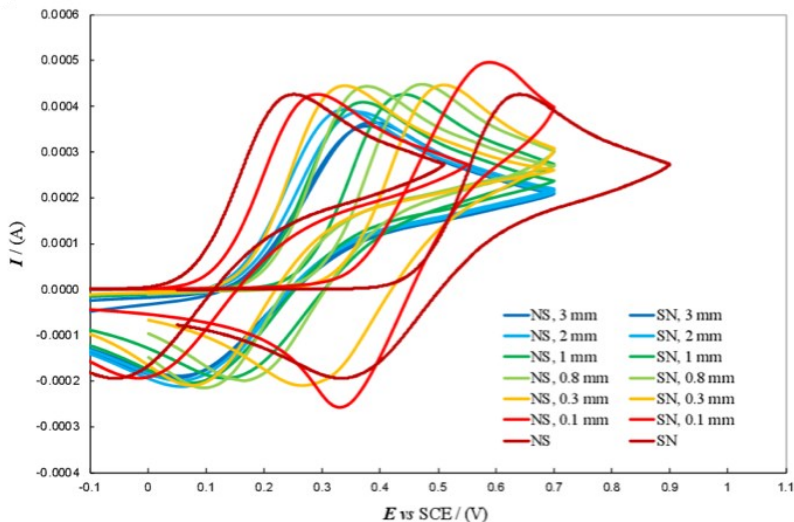


Figure 182. CV patterns recorded at 0.05 V s^{-1} for the $\text{Fc}^+|\text{Fc}$ achiral couple in ACN + TBAPF₆ 0.1 M at hybrid ITO|oligo-(S)-BT₂T₄ interface, as a function of the applied magnetic field orientation (north vs south) and of the magnetic field strength (*i.e.*, modulated varying the magnet-cuvette distance).

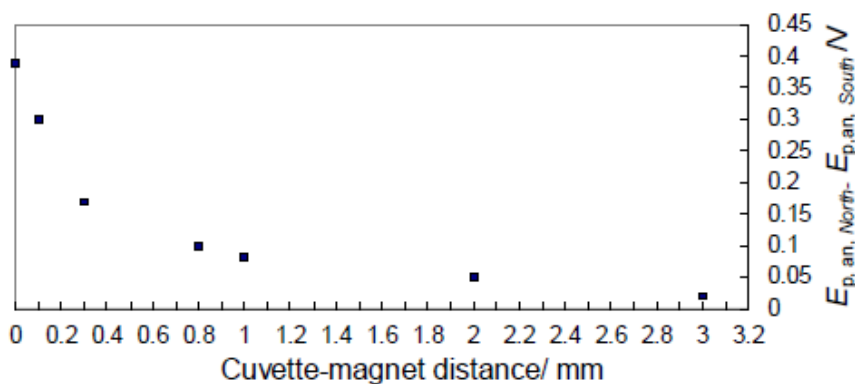


Figure 183. Relationship between cuvette-magnet distance and potential difference between the two voltammetric signals of $\text{Fc}^+|\text{Fc}$ redox couple related to north vs south orientations.

Table 19. Relevant data observed for the $\text{Fc}^+|\text{Fc}$ achiral couple by varying cuvette-magnet distance and the magnet orientation, depicted in Figure 182.

Cuvette-magnet distance / mm	$E_{p, \text{an, South}} / \text{V vs SCE}$	$E_{p, \text{an, North}} / \text{V vs SCE}$	$E_{p, \text{an, North}} - E_{p, \text{an, South}} / \text{V vs SCE}$
3	0.37	0.39	0.02
2	0.33	0.38	0.05
1	0.36	0.44	0.08
0.8	0.37	0.47	0.10
0.3	0.34	0.51	0.17
0.1	0.29	0.59	0.30

^a Half-wave potential, $E_{1/2}$, is calculated according to $E_{1/2} = (E_{p, \text{an}} + E_{p, \text{cat}}) / 2$.

e) "Control" magnetochemistry experiments with achiral PEDOT as thin film on ITO electrode

In order to verify that the observed huge potential shift of the redox couple is actually determined by the combination of the effects described above, measurements with achiral PEDOT, under the same conditions, at constant protocol, were performed. In this case no peak shift for the Fe(III)/Fe(II) couple was observed by flipping magnet orientation (Figure 184) [252].

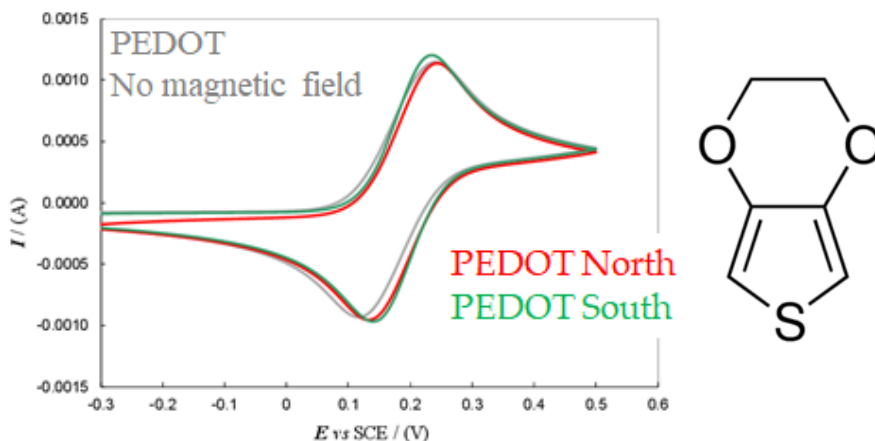


Figure 184. CV patterns recorded at 0.05 V s^{-1} for the Fe(III)/Fe(II) redox couple on hybrid ITO|achiral PEDOT electrode, without the external magnet (grey line) and as a function of the applied magnetic field orientation (red line: north orientation and green line: south orientation).

f) Tentative explanation of the observed phenomenon

To rationalize such observations, first of all it could be noted that the probe reversible CV peaks barely undergo a potential shift, their morphology appearing practically unaffected by the magnet orientation, suggesting an effect of thermodynamic nature. Moreover, considering that no systematic variations in peak intensities were obtained, unlike previous SDE experiments [254,259], the present phenomenon cannot be explained in terms of a different resistance, ΔR , for the transport of α and β electrons within the chiral film [254,259].

In fact, a potential shift originating from an ohmic drop implies, according to $E=I \cdot R$, a distortion in the I vs E voltammetric signal (the potential drop linearly increasing with the current); moreover, in the case of a chemically reversible signal, forward and backward peaks would be distorted and shifted in opposite directions, with $E_{1/2}$ remaining practically constant. On the contrary, the observed rigid shifts, resulting in neatly different $E_{1/2}$, could be described as $I_{\text{config,north}}(E) = I_{\text{config,south}}(E + \text{constant})$ (with "config" standing for the (*R*)- or (*S*)-configuration of the chiral film; "north" or "south" standing for the pole close to the electrode surface; and $\text{const} = 0.15$ or 0.46 V, accounting for the constant potential shift observed for c-PEDOT and oligo-BT₂T₄, respectively).

Such considerations suggest to look for a rationalization of the experimental observations in terms of spin-resolved electron energy levels (or, from the electrochemical perspective, of spin-resolved electrochemical potentials [260]) as a function of the orientation of the external achiral magnetic field as well as of the configuration of the built-in chiral one of the enantiopure film, as follows (by steps of increasing complexity referring to the cases reported in Figure 179).

a) Magnetic field only (Figure 179a). Application of an external magnetic field should result in a Zeeman splitting of the electron energy levels corresponding to

the two possible α or β spin configurations (consistently to their being parallel or antiparallel to the magnetic field), with a small excess of electron population on the lower level, increasing with increasing energy gap and decreasing with temperature. A 180° rotation in the orientation of the magnetic field vector should result in a specular situation (*e.g.* lower β , higher α instead of lower α , higher β), energetically identical to the initial one in terms of energy levels and gap, as well as population ratio (Scheme 1, top right);

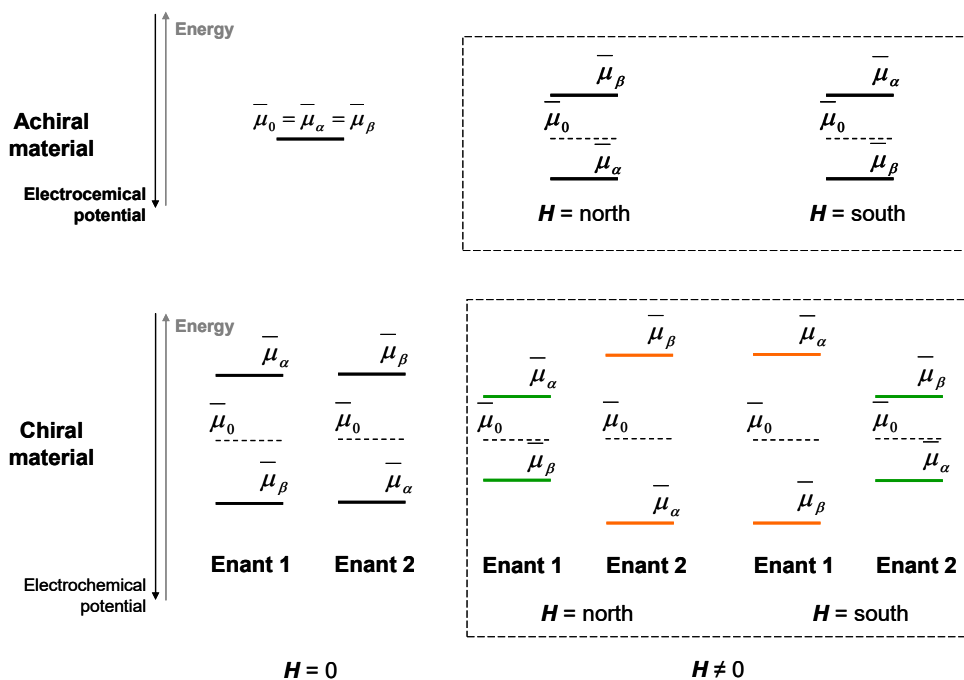
b) Chiral film only (Figure 179b). A splitting of α and β electron energy levels should also occur within a chiral film phase, consistently with its molecular electrostatic potential [261,262] (Scheme 1 bottom left); in this case specular and energetically identical situation must be obtained depending on the (*R*)- or (*S*)-film configuration. Incidentally, the splitting should be particularly remarkable in the case of inherently chiral selectors with high macro-/supramolecular order;

c) Chiral film plus magnetic field (Figure 179c,d, Scheme 1 bottom right). Combining the two above effects, two couples of situations can arise (orange or green in the scheme), depending on the film configuration and magnet orientation (north-south NS or south-north SN): (*i*) (*R*)-film/NS magnet and (*S*)-film/SN magnet and (*ii*) (*R*)-film/SN magnet and (*S*)- film/NS magnet. Importantly, one couple of situations (the orange cases) must correspond to external applied magnetic field and internal “chiral field” [261] in synergy, *i.e.* favouring the same α or β spin configuration while unfavouring the opposite β or α one. Instead, the other couple (the green cases) must correspond to external applied magnetic field and internal “chiral field” in opposition, *i.e.* favouring/unfavouring opposite spin configurations (*i.e.* with film favouring α and magnet favouring β , or *vice versa*). The two “synergistic” situations are reciprocally specular and energetically equivalent (the only difference being the favoured spin configuration). However,

they are energetically different from the two (reciprocally specular and equivalent) “opponent” situations. In particular the “synergistic” cases must correspond to a lower energy for the preferred spin and a higher energy for the unfavoured one, resulting in a higher energy gap between the two levels, and therefore a higher population ratio for the lower level respect to the higher one. Such a situation can justify the observed halfwave potential shift.

Notably, similar outstanding potential differences had been formerly observed on oligo-BT₂T₄ surfaces “recognizing” the (*R*)- or (*S*)-enantiomer of redox probes in solution (as widely described in chapter 3), without applied magnetic field. Indeed, by analogy with the present case, one might now consider to explain such results in terms not only of probe-film molecular interactions, but also of spin-related electron energy level splitting, resulting in that case from the chiral film field being modulated by the presence of the (*R*)- or (*S*)- probe enantiomer. In any case, comparing the cited experiments with the present ones, the achiral redox probes combined with the external magnetic field appear as mimic of chiral redox probes in the absence of magnetic field.

We are looking forward to explain this effect from a quantitative point of view.



Scheme 1.

This statement is strongly supported by the observation that exactly the same feature has been found for circular dichroism CD spectra, which result from different absorption of the L- and D- circularly polarized light components by a chiral molecular probe, are specular according to the sample (*R*)- or (*S*)-configuration, and very sharp for inherently chiral chromophores [219,220]. Although achiral chromophores are of course CD inactive, some of them yield increasingly sharp CD spectra under increasing magnetic field strength, specularly inverting the magnetic field orientation [263].

Notably, both ferrocyanide and ferrocene, involved in the redox couples considered, have been long known to exhibit magnetic dichroism [264,265]. Also a very preliminary test about the temperature dependence of the spin-related potential splitting effect might be compared with magnetic CD features. Indeed optical and electronic dichroism are strictly connected, as recently pointed out [262] (Figure 185). In fact, performing at low temperature (-35°C , in dry ice/methanol bath) the magneto-electrochemistry experiment with the achiral $\text{Fc}^+|\text{Fc}$ probe on oligo-(*R*)- BT_2T_4 films under application of the external magnetic field resulted in a significant increase of the half-wave potential splitting $\Delta E_{1/2}$, from ~ 0.39 V (room temperature) to ~ 0.50 V (-35°C) [252].

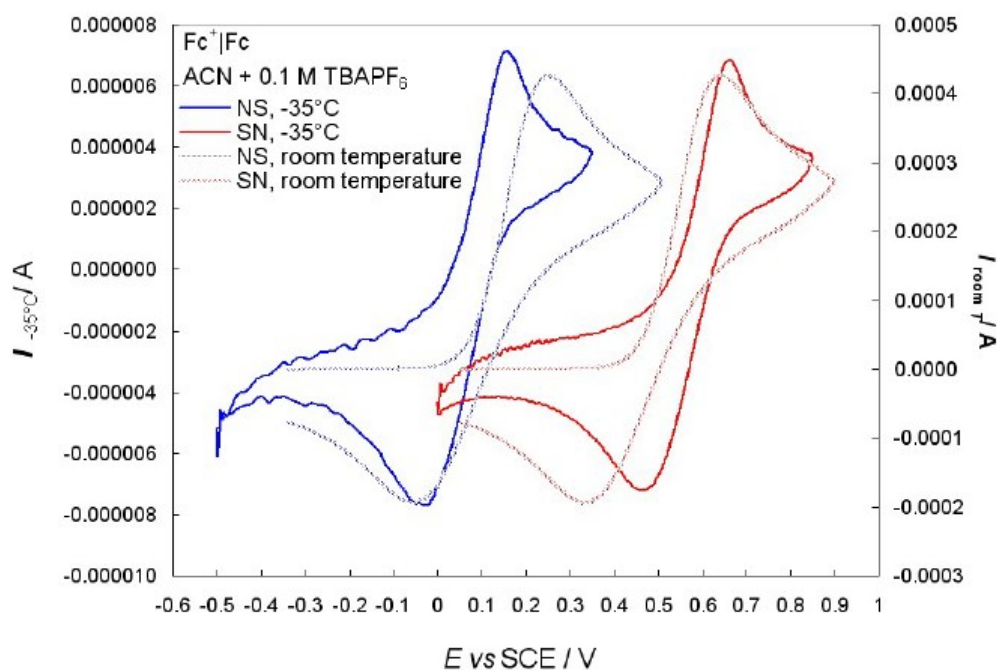


Figure 185. CV patterns recorded at 0.05 V s^{-1} for the $\text{Fc}^+|\text{Fc}$ achiral couple in $\text{ACN} + \text{TBAPF}_6$ 0.1 M at hybrid $\text{ITO}|\text{oligo-}(R)\text{-BT}_2\text{T}_4$ interface, as a function of the applied magnetic field orientation (north-south or south-north), at room temperature (shadowed lines, righthand y axis) and at -35°C (solid lines, left-hand axis).

Interestingly, a similar effect can also be observed in magnetic CD, which, as mentioned in the main paper, shows striking analogies with the magnetochemistry experiments, presented in this PhD thesis.

The magnetic CD effect requires the achiral molecule to comply with at least one of three A, B, or C “Faraday terms”, each one representing a kind of interaction between ground states/excited states and external magnetic field [263]. In particular, the C term is typical of paramagnetic molecules, like ferricinium Fc^+ and ferricyanide (III), the oxidized members of the reversible redox couples, which are low-spin paramagnetic complexes with an unpaired electron spin. It has been demonstrated that the C term originates from a Zeeman loss of degeneration for the α or β spin configurations in the electron ground level energy under magnetic field. This results in a small excess for a spin configuration over the other one, remarkably increasing with decreasing temperature, with the CD spectrum becoming sharper and sharper at constant magnetic field. Actually, such temperature dependence is considered a diagnostic criterion for this effect [263].

In summary, an achiral redox couple combined with an external magnetic field enables to highlight the spin filter properties of the chiral film. In particular, at constant protocol, the magnitude of the potential shift could be exploited as analytical signal to highlight/compare spin filter properties of chiral thin layers, with the shift sign accounting for film configuration. In this sense the here reported protocol looks as a solution-based equivalent of magnetoresistance determination in all-solid devices (except for the distinction between electron transfer and electron transport, respectively).

An intriguing issue concerns classification of the observed phenomenon within the frame of "true/false chirality" mentioned in the introduction (chapter 1).

Notwithstanding the nonstationary character of the CV experiment, the observation of very large rigid shifts in reversible peak potentials at constant peak morphology, for different redox probes and different films, points to a thermodynamic effect, which would imply true chirality. Actually, the electron translating in a ballistic (*i.e.* rototranslational) motion from probe to electrode (oxidation) or from electrode to probe (reduction), with its spin projection parallel or antiparallel to the direction of propagation through the truly chiral spin filtering interface, looks as a truly chiral system, with a loss of degeneration for the α and β electron energies (consistently with Naaman's CISS effect [264]). However, the resulting imbalance of the normal 50:50 α : β spin ratio in the chiral film phase is not perceivable from the CV signal, which is the same for the two possible film configurations since they correspond to specular, energetically equivalent situations (although one film configuration should correspond to the electron transfer process involving an excess of α electrons and the other an excess of β electrons). In this context the addition of a magnetic field, although in itself not producing true chirality, cooperates in evidencing the above spin filter effect by modifying the couple of energetically equivalent combinations into two couples of energetically different ones, according to its orientation once the chirality of the interphase is fixed. Such "double splitting" effect by the magnetic field could gradually decrease with increasing magnet distance or film thickness, consistently with the above reported observations.

It is worthwhile also noticing that the experimental outcome here reported is in general agreement with the "electrical magnetochirality anisotropy" results reported by Rikken, Avarvari and coworkers [265] concerning single crystal of a bulk molecular conductor, as well as of impressive spin-polarization values observed in charge transmission through single chiral molecules by Mujica et coworkers [262]. Moreover, the present enantioselective experimental results

obtained in the absence of any ferromagnetic material are definitively consistent with the similar outcome obtained by electrochemically driving, and spin-filtering, the charge transmission through a chiral interface, when using a magnetless non-ferromagnetic (GaN) system [266].

g) Other experiments changing the inherently chiral monomer and the support

The thiahelicene-based enantiopure films

We consider interesting and useful to compare the outstanding features and performance of the C_2 -symmetric bibenzothiophene BT_2T_4 and its electrodeposited films with the helicene selectors [133] (Figure 186). In fact (i) both monomers 7-TH and BT_2T_4 are endowed with inherent chirality, but on account of different stereogenic elements, *i.e.* helicity vs stereogenic axis; (ii) both monomers have electroactivity based on thiophene conjugated systems: in the case of 7-TH, a system of four thiophene rings alternated to condensed benzene ones with an helicoidal torsion; in the case of BT_2T_4 , two weakly interacting linear terthiophene systems; (iii) both monomers have two free homotopic thiophene.

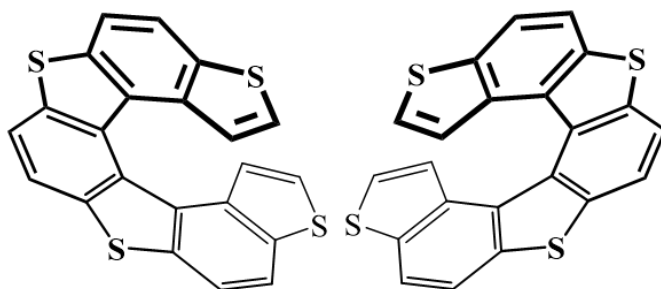


Figure 186. Inherently chiral thiahelicene (7-TH).

The inherently chiral 7-TH monomers have just been employed in chiral electrochemistry experiments, resulting in a huge peak potential separation of chiral electroactive probes [133]. Such enantiodiscrimination performances could be justified considering the electrochemical process to take place in diastereomeric and thus energetically different situations, resulting from

intermolecular interactions between enantiopure selector and enantiopure probe, particularly hinging on the many available aromatic rings and heteroatoms. Moreover, diastereomeric conditions could also originate from modulation of the internal magnetic field of the chiral film in the presence of the (*R*)- or (*S*)- probe, as already pointed out in the above-described experiments with axial stereogenicity films (chapter 3).

In this context, the new selector films based on helical elements were also preliminarily tested concerning interactions with electron spin moments under applied magnetic field, following the approach presented in the former study, already described [131,252]. CV patterns were recorded for the achiral, reversible ferrocyanide/ferricyanide couple in aqueous solution, both on ITO and on screen-printed single-walled carbon nanotube (SWNT SPE) working electrode, modified with a very thin enantiopure oligo-(*P*)-7-TH film electrodeposited in a single CV cycle.

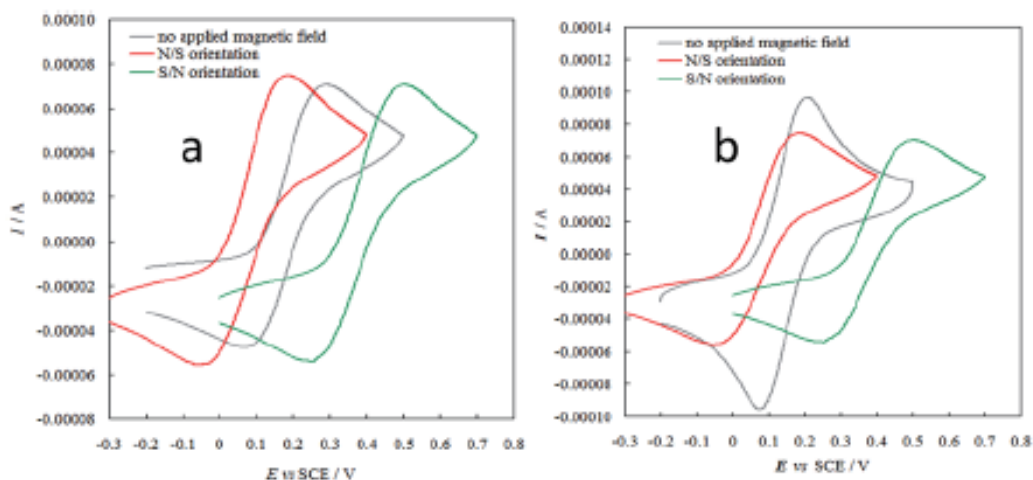


Figure 187. CV patterns for the achiral $\text{Fe}(\text{CN})_6^{3-}|\text{Fe}(\text{CN})_6^{4-}$ redox couple, recorded at 0.05 V s^{-1} in aqueous solution on ITO electrodes (a) or SWCN SPEs (b) modified by a thin layer of (*P*)-enantiopure oligo-7-TH thin film, as such and under application of an external magnet with N/S or S/N orientation (red or green lines respectively).

Application of an external magnetic field resulted in both cases in remarkable formal potential shifts according to the N/S or S/N magnet orientation (Figure 187), the impressive effect observed also on inherently chiral films based on atropisomeric units (oligo-BT₂T₄ films [252] and on 2,2'-biindole-based films [131], see later), besides a chiral C₂-symmetry PEDOT.

Again, the phenomenon can be tentatively justified considering the combined effects of the internal magnetic field intrinsic of the chiral layer (particularly effective for an inherently chiral one) and of the external applied magnetic field on the electron energy levels, as a function of the α or β spin magnetic moment.

The biindole-based enantiopure films

Enantiopure electrodeposited oligo-(*N*-Me)Ind₂T₄ (Figure 188) films also gave outstanding performances when tested in magneto-electrochemistry experiments as molecular spin filters, of potential interest in spintronics [131].

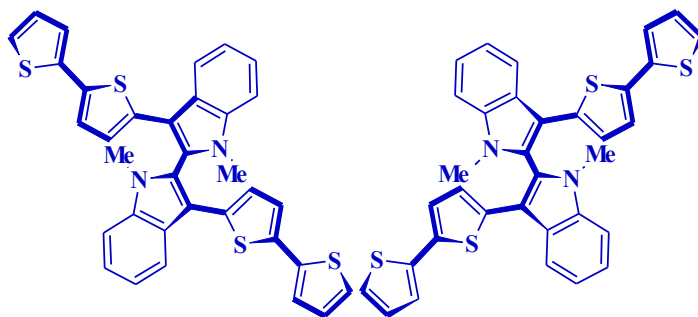


Figure 188. Inherently chiral (*R*)- and (*S*)-(*N*-Me)Ind₂T₄

In particular, CV patterns were recorded for an achiral, reversible Fe(III)/Fe(II) couple in aqueous solution, on ITO electrode modified with a very thin oligo-(*N*-Me)Ind₂T₄ film, under application of an external magnetic field. A wide shift in the couple redox potential was observed upon flipping the north/south magnet orientation or changing the (*R*)- or (*S*)- enantiopure film configuration (Figure

189) [131], the same striking behaviour observed in the previous cases reported above.

Recording CV patterns for the achiral redox probe on bare ITO under external magnetic field, or on ITO modified with an inherently chiral film, implying a local "internal" magnetic field, but without applying an external one, results in no potential difference upon changing the N vs S magnet orientation in the first case, or the (*R*)- vs (*S*)- film configuration in the second case [252].

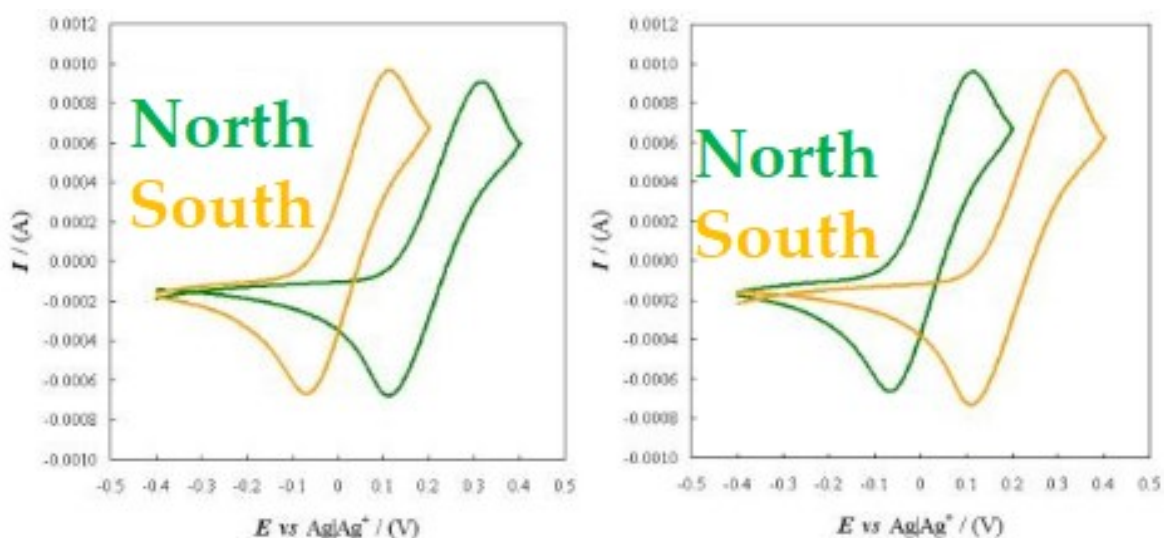


Figure 189. CV patterns for the achiral $\text{Fe}(\text{CN})_6^{3-}/\text{Fe}(\text{CN})_6^{4-}$ redox couple, recorded at 0.05 V/s in aqueous solution on ITO electrodes modified by a thin layer of (*S*)- or (*R*)- enantiopure oligo-(*N*-Me)Ind₂T₄ thin film (right and left box, respectively), applying an external magnet with NS or SN orientation (green or orange lines respectively).

Chapter 6

Conclusion and Perspective

6.1 A comparison between the two approaches proposed in this thesis project: advantages and disadvantages of using chiral media or modified electrode surfaces

A wide variety of chiral surfaces and chiral media, reported in literature, have been developed and tested to achieve enantioselective electrochemistry, with different degrees of enantioselectivity and transduction modes in analytical experiments, including, *e.g.*, enantiomer differences in currents (the most common occurrence), potentiometric response, conductance and/or EIS patterns, mass variations, photocurrents... as well as significant enantiomeric excesses in preparative experiments. High to full specificity for a single enantiomer can be reached using very specifically tailored selectors, like, *e.g.*, in several MIP or enzyme sensor cases. However, in nearly all cases the kind of response is unsuitable to enable recognition of the (*R*)- or (*S*)-probe enantiomer configuration (alone or in mixture) by a single selector.

In this frame, a valuable asset appears to be provided by inherently chiral selectors, as confirmed by this three-year thesis project, resulting in the observation of significant potential differences between probe enantiomers, working either on inherently chiral electrodes or on achiral electrodes in (inherently) chiral media. Importantly, this feature appears to be of general character (testing different kinds of probes and selectors) and requires in most cases only small amounts of inherently chiral selectors (thin chiral films, low-concentration chiral additives). Moreover, the newly available attractive palette of inherently chiral tools must be supported by detailed studies about the discrimination mechanism, as well as fully exploited by exploring a wider range

of selector/probe combinations, as well as applications of preparative character and in advanced electrochemistry devices.

However, after this detailed study, the question is: when is it better to use the modified chiral electrode surface approach rather than the chiral media one?

Therefore, the advantages and disadvantages of both the approaches have been reported below, in order to focus on the potential and real applications in chiral electrochemistry (collected in Figure 190).

Chiral media

Advantages

- little selector quantity required (as low concentration chiral additive, few mg);
- little quantity of solution, using them as bulk media (few μL);
- possibility to work on disposable SPEs, useful for possible *in situ*/ in field miniaturized application;
- laboratory SPEs printed on a plastic support, made by convenient material for WE, RE and CE;
- in general, on account of the above points, reduced costs;
- easy synthesis or preparation (especially in the case of chiral DESs, obtainable by mixing the two components with moderate heating);
- easy availability from relatively inexpensive and non-toxic components;
- low production cost with respect to conventional ILs;
- in some cases (particularly with DESs) possibility of large scale application;
- possibility to modulate the selector design, obtaining virtually unlimited range of tailored structures;
- ionic liquids and particularly Deep Eutectic Solvents (especially NADES) are considered “green solvent”;

- good linear dynamic range for currents and evaluation in some cases of the enantiomeric excess.

Disadvantages

- Concerning ICILs, necessity to separate the two enantiomers of the chiral selectors by HPLC;
- the solution containing the chiral probe is not recoverable and/or recyclable;
- in the case of CILs of natural origin only one enantiomer is available (corresponding to the configuration of its natural building block), and for this reason it is not possible to perform the usual "double inversion" enantioselection check, consisting in verifying that a specular response is obtained inverting either probe or selector configuration.

Modified chiral electrode surfaces

Advantages

- The electrode surfaces modified with chiral films could be recyclable;
- also the solution containing the probe could be recoverable and/or recyclable, because the chiral selector is not mixed in the same solution with the chiral analyte;
- as mentioned in this thesis work, some of our inherently chiral monomers could be synthesized in enantiopure form, without HPLC separation steps;
- little quantity of monomer necessary;
- equal availability of the selector in both enantiomer configurations, so that the first ET can correspond to the preferred target enantiomer (especially for preparative purposes);
- possibility to analyze different probes in different working media (aqueous and organic solvents);

- with chiral probes which present a chemically and electrochemically reversible CV (or DPV) pattern, it is possible to discriminate the two enantiomers when simultaneously present, either in 1:1 ratio or in asymmetric ratios, pointing to the possibility of direct evaluation of enantiomeric excesses.

Disadvantages

- Stability and robustness of the inherently chiral films;
- there are many parameters to consider, as reported and studied in this thesis project (*i.e.* deposition scan rate, concentration of the inherently chiral monomer, number of deposition cycles, morphology and chemical composition of the chiral films, thickness and so on);
- this implies complex preparation protocols;
- in the case of chiral analytes with a more complex and irreversible CV pattern, it is hard to evaluate the enantiomeric excess, probably due to the first process, which can heavily condition the film|solution interphase, affecting the process involving the second enantiomer.

Therefore, due to the considerations on the advantages and disadvantages of the two approaches reported above, the final conclusions suggest that:

It is better to use the chiral media approach if you want to do fast *in situ* analysis, with small quantities of the chiral selector and if you do not want to recover the chiral probe solution. Instead, it is better to use the other approach (*i.e.* modified chiral electrode surfaces) if you do not want to contaminate the solution of the enantiopure probe (in fact, in this case the chiral selector is electrodeposited on the working electrode, even recyclable, and not mixed in solution with the chiral analyte) or if it is necessary to analyze a probe in a specific solvent (for example organic or aqueous, in fact many drugs are stable in specific pH conditions).

Modified Chiral Electrode Surfaces

- The modified electrode surfaces and the probe solution could be **recyclable** 
- Some of our inherently chiral monomers could be **synthesized in enantiopure form**, without HPLC separation steps
- **Little quantity** of monomer necessary
- equal availability of the selector in **both enantiomer configurations** (*R*) and (*S*)
- possibility to analyze different probes in **different working media** (aqueous and organic solvents)



(Inherently) Chiral Media

- **little** selector/solution **quantity** required
- **disposable SPEs**, useful for possible in situ/ in field application; 
- **easy synthesis** and preparation
- **easy availability** from relatively  Especially in the DES case
- inexpensive and non-toxic components
- For artificial ICILs, possible **modulation of the selector design**.
- CILs and especially DESs are considered **“green solvent”**. 

- **Stability and robustness** of the inherently chiral films;
- there are **many parameters to consider** (*i.e.* deposition scan rate, concentration, number of deposition cycles, thickness);
- in the case of chiral analytes with a **more complex and irreversible** pattern it is usually impossible to **evaluate the enantiomeric excess**, probably due to the first process, which can heavily condition the film|solution interphase, affecting the process involving the second enantiomer

- Concerning ICILs, **separation of the two enantiomers by HPLC**;
- The **solution** containing the chiral probe is usually **neither** recoverable nor **recyclable**;
- In the case of CILs of natural origin **only one enantiomer is available** (corresponding to the configuration of its natural building block), and for this reason it is not possible to perform our usual "double inversion" enantioselection check, consisting in verifying specular response.

Figure 190. Scheme for the advantages and disadvantages of both the approaches proposed.

6.2 A Global critical insight: towards common guidelines

The systematic series of chiral probes/selector studied in this thesis project have revealed important correlations on the interaction of the two actors involved (chiral analyte and chiral selector), on the enantioselection mechanism, on the structural properties of both probe and selector, on the interactions involved in the enantiorecognition process, which can provide fundamental suggestions on the optimization of the experimental conditions for chiral voltammetry measurements as well as to achieve rational criteria for optimization of inherently chiral selector design and management in order to obtain the best results.

In particular, concerning the inherently chiral films, first of all the importance of the oligomerization step and relevant details emerges.

In fact, by using the monomer as such (by drop casting) good performances are obtained consistently with its inherent chirality; however, much more impressive results are obtained by monomer electrooligomerization; in other words, the powerful chirality manifestations of inherently chiral selectors can be further amplified by converting the latter into oligomer films.

It has also been demonstrated how the electrodeposition conditions deeply influence the morphology and composition of the film, which in turn affect the enantioselection ability. A systematic study with our chiral ferrocenyl model probe pointed to TBAPF₆ as electrolyte, ACN as solvent, 50 mV s⁻¹ potential scan rate as outstanding conditions for electrodeposition of our benchmark oligo-BT₂T₄ chiral selector film, enabling to achieve an impressive enantioseparation in terms of potential of about 600 mV (never observed before with this monomer and this probe), with specular results inverting probe or selector configurations. Moreover, strikingly, the thinner the film, the better the performance of the modified chiral electrode surface (this result seems to be in connection with the results obtained in the molecular spintronics measurements).

Furthermore, the availability of systematic series to investigate enabled to achieve clues concerning probe-selector interactions.

From the study performed on a systematic family of planar stereogenicity ferrocenes, it was possible to highlight groups that can provide matching elements, such as CN groups or heteroatoms, while the alkyl groups seem to have less prominence and less impact.

From the study performed on systematic biindole family, hydrogen bonds also emerged as highly influential.

Concerning chiral media, several chiral molecular salts with bio-based building blocks (some of them liquid at room temperature and therefore CILs) resulted in moderate but significant enantiodiscrimination performances, although only one configuration was available (the natural one).

Obviously, as in the case of inherently chiral oligomer films, the best results have been obtained with inherent chirality media, because, as mentioned before, they give more prominent chirality manifestations. Different inherently chiral ionic liquids or additives were tested, showing that the enantioselection ability is influenced by the concentration of the chiral additive (just as in films, thickness control is essential).

Moreover, the increased number of protonated positions favours a larger separation in terms of peak potential, as observed in two different cases (diazahelicenes and QUINAP, as well as others already reported in the literature). In the DES case the acid-base interaction seems to be fundamental (just as hydrogen bonding was important in the film case) enabling to achieve outstanding ability in chiral voltammetry, even in the absence of inherent chirality.

Managing these media required viscosity modulation, through the addition of water. This led to a systematic study of the effect of the percentage of water on the enantioselection ability, showing a remarkable and impressive correlation.

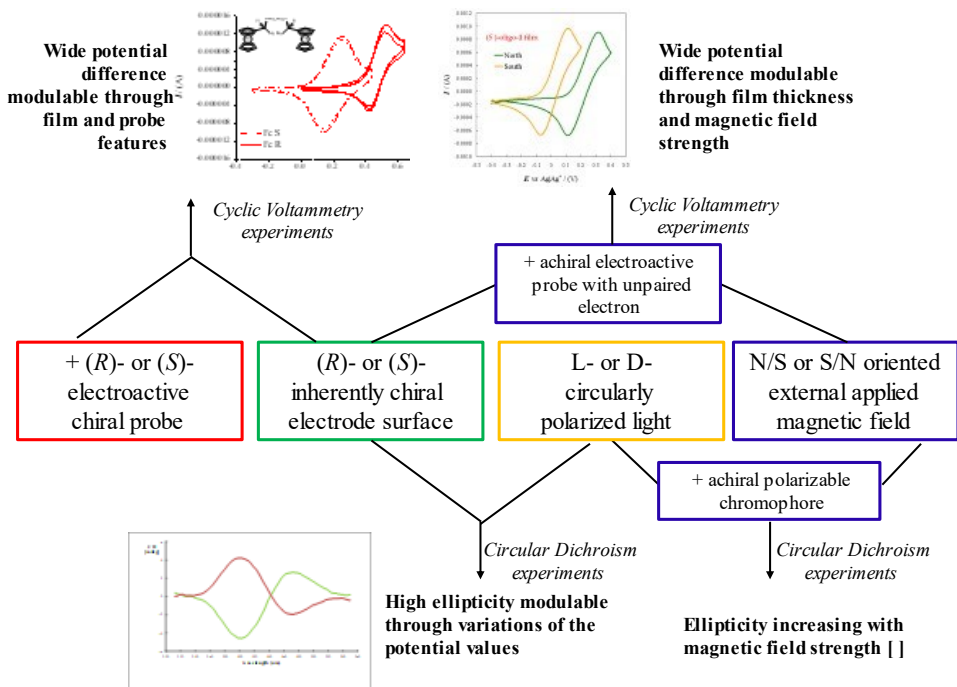
In conclusion, the results obtained in this thesis project have to be consolidated by:

- (i) extending the electrodeposition studies to outline the film features on other inherently chiral films (with different atropisomeric core, for example the 2,2'-biindole one, and different stereogenic elements), to achieve clues for mechanism rationalization and to optimize performance and reproducibility.
- (ii) EIS measurements to investigate in detail the mechanism of enantiorecognition on these surfaces in solution.
- (iii) Scanning Electrochemical Microscopy (SECM) analysis can be obtained by using smaller microelectrode tips (*e.g.*, at sub-micrometer levels). However, this would also require the use of smoother oligomer films, which in principle can be obtained by decreasing the number of CV cycles during the electrodeposition step and smoother surfaces of the underlying electrode material.
- (iv) Theoretical calculations in order to understand the enantioselection mechanisms, supporting the assumptions arising from this PhD thesis.
- (v) Extending the study to inherently chiral oligomer/polymer films with different stereogenic elements.
- (vi) A deeper investigation of the probe-selector interactions extending the combination of chiral probes and selectors, in the case of both chiral surfaces and media (in particular, concerning the molecular interactions within the three-actor in the DES case: probe and DES components).
- (vii) A detailed study on the enantioselection mechanism (also by theoretical calculations and complementary electrochemical and non-electrochemical techniques).

Moreover, further developments of the three research lines (enantioselective electroanalysis, circular dichroism and magnetochemistry experiments) exploited during this PhD thesis, will be devoted to other studies and applications of these advanced (inherently) chiral molecular selectors.

For example,

- it could be very interesting to evaluate also chiral ionic liquids (especially inherently chiral and chiral DESs) for applications in magnetochemistry experiments, due to their properties which are very similar to semisolid liquid crystals.
- The CV experiments performed on our inherently chiral electrodes under applied magnetic field, resulting in potential differences for achiral redox couples upon flipping the magnetic field orientation, show very nicely parallel with the long known "magnetic ECD" (MCD) experiments, in which an ECD response is obtained for achiral chromophores under an external applied magnetic field, with mirror image spectrum upon changing field orientation (Scheme 2). For this reason, our research group will thoroughly explore this fascinating parallelism.
- Testing the films in other electrochemical applications and devices, such as the development of a cargo-towing electro-pumps based on chiral conducting polymers for targeted drug-delivery applications.



Scheme 2.

References

- [1] P. T. T. Ha, A. Van Schepdael, T. Hauta-Aho, E. Roets, J. Hoogmartens, *Electrophoresis* **2002** 23(19), 3404–9.
- [2] D. M. Burley, W. Lenz, *Lancet* **1962**, 279, 271–272.
- [3] H. Hao, G. Wang, J. Sun, Z. Ding, X. Wu, M. Roberts, *Biol. Pharm. Bull.* **2005**, 28(4) 682–687.
- [4] S. Assavapanumat, M. Ketkaew, Al. Kuhn, C. Wattanakit, *J. Am. Chem. Soc.* **2019**, 141, 18870–18876.
- [5] C. Wattanakit, A. Kuhn, *Chem. Eur. J.* **2020**, 26, 2993 – 3003.
- [6] S. Butcha, S. Assavapanumat, S. Ittisanronnachai, V. Lapeyre, C. Wattanakit, A. Kuhn, *Nature Communications* **2021**, 12(1), 1314.
- [7] J. Zhao, L. Cong, Z. Ding, X. Zhu, Y. Zhang, S. Li, J. Liu, X. Chena, H. Houc, Z. Fana, M. Guoa, *Microchem. J.* **2020**, 159, 105469.
- [8] D. Wu, F. Pan, L. Gao, Y. Tao, Y. Kon, *Anal. Chem.* **2020**, 92, 13711-13717.
- [9] D. Kim, K.-D. Seo, D. Moon, Y.-B. Shim, S. Hak Lee, O.-S. Jung, *Inorg. Chem.* **2020**, 59, 5808-5812.
- [10] H. Lu, Z. Wang, X. Fan, H. Wang, Q. Zhang, M. Fu, G. Ning, Y. Zhang, H. Wang, *Anal. Methods* **2020**, 12, 3901-3908.
- [11] M. M. Moeina, *Talanta* **2021**, 224, 121794.
- [12] J. Chen, R.P. Liang, X.N. Wang, J.D. Qiu, *J. Chromatogr. A* **2015** 1409 268–276.
- [13] D. Duan, H. Yang, Y. Ding, *Elcetrochimica Acta* **2019**, 302, 137-144.
- [14] B. Liu, H. Lian, L. Chen, X. Wei, X. Sun, *Anal. Biochem.* **2019**, 574, 39-45.
- [15] L. Wenting, R. Yanqin, F. Lifang, D. Wenjuan, D. Qingchen, Y. Cheng, Z. Zhihui, D. Chuan, S. Shaomin, W. Wai-Yeung, *J. Mat. Chem. C* **2018**, 6, 12822-12829.
- [16] C. Pu, Y. Xu, Q. Liu, A. Zhu, G. Shi, *Anal. Chem.* **2019**, 91, 3015-3020.

- [17] S. Arnaboldi, M. Magni, P. R. Mussini, *Curr Opin Electrochem* **2018**, 8, 60–72.
- [18] Q. Lin, L. Li, S. Luo, *Chem Eur J* **2019**, 25, 10033–10044.
- [19] A. M. Faisca Phillips, A. J. L. Pombeiro, *Org Biomol Chem* **2020**, 18, 7026–7055.
- [20] X. Chang, Q. Zhang, C. Guo, *Angew Chem Int Ed* **2020**, 59, 12612–12622.
- [21] H. Li, Y-Fa Xue, Q. Ge, M. Liu, H. Cong, Z. Tao, *Mol Catal* **2021**, 499, 111296–111330.
- [22] M. J. Trujillo-Rodríguez, H. Nan, M. Varona, M. N. Emaus, I. D. Souza, J. L. Anderson, *Anal Chem.* **2019**, 91, 505–531.
- [23] P. Hapiot, C. Lagrost, *Chem Rev* **2008**, 108, 2238–2264.
- [24] C. Lagrost, D. Carrie, M. Vaultier, P. Hapiot, *J Phys Chem A* **2003**, 107, 745–752.
- [25] Q. Zhang, Q. Wang, S. Zhang, X. Lu, X. Zhang *Chem. Phys. Chem* **2016**, 17, 335–351.
- [26] R. Hayes, G. G. Warr, R. Atkin, *Chem Rev* **2015**, 115, 6357–6426.
- [27] A. Rehman, X. Zeng, *Curr Opin Electrochem* **2020**, 23, 47–56.
- [28] J. W. Yan, Z. Q. Tian, B. W. Mao, *Curr Opin Electrochem* **2017**, 4, 105–111.
- [29] Y. Fu, A. V. Rudnev, *Curr Opin Electrochem* **2017**, 1, 59–65.
- [30] K. Motobayashiand, M. Osawa, *Curr Opin Electrochem* **2018**, 8, 147–155.
- [31] C. Rodenbücher, K. Wippermann, C. Korte, *Appl Sci* **2019**, 9, 2207–2234.
- [32] R. Qiao, *Curr Opin Electrochem* **2019**, 13, 11–17.
- [33] K. Ma, R. Jarosova, G. M. Swain, G. J. Blanchard, *Langmuir* **2016**, 32, 9507–9512.
- [34] Y. Wang, R. Jarošová, G. M. Swain, G. J. Blanchard, *Langmuir* **2020**, 36, 3038–3045.

- [35] Y. Wang, F. Parvis, M. Iqbal Hossain, K. Ma, R. Jarošová, G. M. Swain, G. J. Blanchard, *Langmuir* **2021**, 37, 605–615.
- [36] Y. Zhong, J. Yan, M. Li, L. Chen, B. Mao, *ChemElectroChem* **2016**, 3, 1–7.
- [37] T. Cui, A. Lahiri, T. Carstens, N. Borisenko, G. Pulletikurthi, C. Kuhl, *J Phys Chem C* **2016**, 120, 9341–9349.
- [38] T. Payagala, D. W. Armstrong, *Chirality* **2012**, 24, 17–53.
- [39] G. K. E. Scriba, *Chromatographia* **2012**, 75, 815–838.
- [40] H. Xu, Y. Du, Z. Feng, X. Sun, J. Liu, *J Chromatogr A* **2020**, 1615, 460721–460728.
- [41] S. Xue, S. Ren, L. Wang, Q. Zhang, *J Chromatogr A* **2020**, 1611, 460579–460585.
- [42] S. Salido-Fortuna, M. Greño, M. Castro-Puyana, M. L. Marina, *J Chromatogr A* **2019**, 1607, 460375–460382.
- [43] Y. Zhang, Y. Du, T. Yu, Z. Feng, J. Chen, *J Pharmaceut Biomed Anal* **2019**, 164, 413–420.
- [44] X. Zhu, C. Chen, J. Chen, G. Xu, X. Ma, X. Sun, Z. Feng, Z. Huang, Y. Du, *J Pharmaceut Biomed Anal* **2020**, 180, 113030–113037.
- [45] R. B. Yu, J. P. Quirino, *Molecules* **2019**, 24, 1135–1152.
- [46] A. Hussain, M. F. Alajmi, I. Hussain, I. Ali, *Crit Rev Anal Chem* **2019**, 49, 289–305.
- [47] S. Ren, S. Xue, X. Sun, M. Rui, L. Wang, Q. Zhang, *J Chromatogr A* **2020**, 1609, 460519–460528.
- [48] D. Wu, W. Tan, Y. Yu, B. Yang, H. Li, Y. Kong, *Anal Chim Acta* **2018**, 1033, 58–64.
- [49] D. Wu, J. Yang, Y. Peng, Y. Yu, J. Zhang, L. Guo, Y. Kong, J. Jiang, *Sensor Actuator B Chem* **2019**, 282, 164–170.

- [50] D. Wu, F. Pan, G-C. Fan, Z. Zhu, L. Gao, Y. Tao, Y. Kong, *Analyst* **2019**, 144, 6415–6421.
- [51] D. Wu, W. Tan, H. Li, Z. Lei, L. Deng, Y. Kong, *Analyst* **2019**, 144, 543–549.
- [52] I. Dierking, *Symmetry* **2014**, 6, 444–472.
- [53] S. Natsushita, B. Yan, S. Yamamoto, Y. S. Jeong, K. Akagi, *Angew Chem Int Ed* **2014**, 53, 1659–1663.
- [54] K. Salikolimi, A. A. Sudhakar, Y. Ishida, *Langmuir* **2020**, 36, 11702–11731.
- [55] S. Yamakawa, K. Wada, M. Hidaka, T. Hanasaki, K. Akagi, *Adv Funct Mater* **2019**, 29, 1806592–1806607.
- [56] R-T. Wang, G-H. Lee, C.K Lai, *J Mater Chem C* **2018**, 6, 9430–9444.
- [57] S. Kirchhecker, D. W. Bruce *New J Chem* **2019**, 43, 2053–2056.
- [58] M. A. R. Martins, S. P. Pinho, J. A. P. Coutinho, *J Solut Chem* **2019**, 48, 962–982.
- [59] L. J. B. M. Kollau, M. Vis, A. van den Bruinhorst, A. C. C. Esteves, R. Tuinier, *Chem Commun* **2018**, 54, 13351–13354.
- [60] A. González de Castilla, J. P. Bittner, S. Müller, S. Jakobtorweihen, I. Smirnova, *J Chem Eng Data* **2020**, 65, 943–967.
- [61] A. Alhadid, L. Mokrushina, M. Minceva, *Molecules* **2019**, 24, 2334–2352.
- [62] H. Vanda, Y. Dai, E. G. Wilson, R. Verpoorte, Y. H. Choi, *C R Chimie* **2018**, 21, 628–638.
- [63] J. Wu, Q. Liang, X. Yu, Q-F. Lü, L. Ma, X. Qin, G. Chen, B. Li, *Adv Funct Mater* **2021**, 2011102–2011126.
- [64] C. M. A. Brett, *Curr Opin Electrochem* **2018**, 10, 143–148.
- [65] L. I. N. Tomé, V. Baião, W. da Silva, C. M. A. Brett, *Appl Mater Today* **2018**, 10, 30–50.
- [66] R. Wang, Z. Mao, Z. Chen, *J Chromatogr A* **2018**, 1577, 66–71.

- [67] R. Costa, M. Figueiredo, C.M. Pereira, F. Silva, *Electrochim Acta* **2010**, 55, 8916–8920.
- [68] O. S. Hammond, H. Li, C. Westermann, A. Y. M. Al-Murshedi, F. Endres, A. P. Abbott, G. G. Warr, K. J. Edler, R. Atkin, *Nanoscale Horiz* **2019**, 4, 158–168.
- [69] M. H. Mamme, S. L. C. Moors, E. A. Mernissi Cherigui, H. Terryn, J. Deconinck, J. Ustarroz, F. De Proft, *Nanoscale Adv* **2019**, 1, 2847–2856
- [70] N. Zec, G. Mangiapia, M. L. Zheludkevich, S. Busch, J-F. Moulin, *Phys Chem Chem Phys* **2020**, 22, 12104–12112.
- [71] Z. Chen, B. McLean, M. Ludwig, R. Stefanovic, G.G. Warr, G.B. Webber, A.J. Page, R. Atkin, *J Phys Chem C* **2016**, 120,2225–2233.
- [72] P. Sebastian, E. Gomez, V. Climent, J. M. Feliu, *Electrochim Acta* **2019**, 311, 30–40.
- [73] Z. Chen, M. Ludwig, G. G. Warr, R. Atkin, *J Colloid Interface Sci* **2017**, 494, 373–379.
- [74] K. Häckl, H. Li, I.M. Aldous, T. Tsui, W. Kunz, A.P. Abbott, G.G. Warr, R. Atkin, *J Phys Chem Lett* **2019**, 10, 5331–5337.
- [75] T. Palomba, G. Ciancaleoni, T. Del Giacco, R. Germani, F. Ianni, M. Tiecco, *J Mol Liq* **2018**, 262, 285–294.
- [76] N. Xia, L. Xiong, S. Bi, F. Qian, P. Wang, *Bioproc Biosyst Eng* **2020**, 43, 1987–1997.
- [77] S. Ma, F. Li, L. Liu, L. Liao, L. Chang, Z. Tan, *J Mol Liquids* **2020**, 319, 114106–114111.
- [78] L. VandenElzen, T. A. Hopkins, *ACS Sustain Chem Eng* **2019**, 7, 16690–16697.
- [79] S. Salido-Fortuna, N. Casado, M. Castro-Puyana, M. L. Marina, *Microchem J* **2021**, 160 (Part B), 105669–105675.
- [80] I. F. Perepichka, D. F. Perepichka, *John Wiley & Sons Ltd.* **2009**.

- [81] J. Heinze, B. A. Frontana, S. Ludwigs, *Chem. Rev.* **2010**, 110, 4724–4771.
- [82] T. A. Skotheim, J. R. Reynolds, *Taylor & Francis Group* **2007**.
- [83] G. Salinas, S. Arnaboldi, L. Bouffier, A. Kuhn, *ChemElectroChem* **2022**, 9, 202101234.
- [84] S. Assavapanumat, B. Gupta, G. Salinas, B. Goudeau, C. Wattanakit, A. Kuhn, *Chem. Commun.* **2019**, 55, 10956–10959.
- [85] S. Arnaboldi, B. Gupta, T. Benincori, G. Bonetti, R. Cirilli, A. Kuhn, *Anal. Chem.* **2020**, 92, 10042–10047.
- [86] S. Arnaboldi, G. Salinas, G. Bonetti, R. Cirilli, T. Benincori, A. Kuhn, *ACS Meas. Au* **2021**, 1, 3, 110–116.
- [87] S. Arnaboldi, B. Gupta, T. Benincori, G. Bonetti, R. Cirilli, A. Kuhn, *Chem. Mater.* **2020**, 32, 10663–10669.
- [88] S. Arnaboldi, G. Salinas, A. Karajić, P. Garrigue, T. Benincori, G. Bonetti, R. Cirilli, S. Bichon, S. Gounel, N. Mano, A. Kuhn, *Nature Chemistry* **2021**, 13, 1241–1247.
- [89] R. Naaman, Y. Paltiel, D. H. Waldeck *Annu. Rev. Biophys.* **2022**, 51, 99–114.
- [90] L. M. Monzon, J. M. D. Coey, *Electrochem. Commun.*, **2014**, 42, 38.
- [91] L. M. Monzon, J. M. D. Coey, *Electrochem. Commun.*, **2014**, 42, 42.
- [92] G. Saravanan, S. Ozeki, *J. Phys. Chem. B.*, **2008**, 112, 3.
- [93] J. Potticary, L. R. Terry, C. Bell, A. N. Papanikolopoulos, P. C. M. Christianen, H. Engelkamp, A. M. Collins, C. Fontanesi, G. Kociok-Köhn, S. Crampin, E. Da Como, S. R. Hall, *Nat. Commun.*, **2016**, 7, 11555.
- [94] M. R. Wasielewski, *J. Org. Chem.*, **2006**, 71, 5051.
- [95] J. Lee, H. Ye, S. Pan, A. Bard, *J. Anal. Chem.*, **2008**, 80, 7445.
- [96] A. M. Scott, T. Miura, A. Butler Ricks, Z. E. X. Dance, E. M. Giacobbe, M. T. Colvin, M. R. Wasielewski, *J. Am. Chem. Soc.*, **2009**, 131, 17655.

- [97] N. Micali, H. Engelkamp, P. G. van Rhee, P. C. M. Christianen, L. Monsù Scolaro, J. C. Maan, *Nat. Chem.*, **2012**, 4, 201.
- [98] A. Nakamura, J. Ohtsuka, K.-i. Miyazono, A. Yamamura, K. Kubota, R. Hirose, N. Hirota, M. Ataka, Y. Sawano, M. Tanokura, *Cryst. Growth Des.*, **2012**, 12, 1141.
- [99] L. D. Barron, *Chem. Phys. Lett.* **1986**, 123, 423.
- [100] L. D. Barron, *J. Am. Chem. Soc.* **1986**, 108, 5539.
- [101] L. D. Barron, *Rend. Fis. Acc. Lincei* **2013**, 24, 179.
- [102] L.D. Barron, *Molecular light scattering and optical activity*, 2nd ed., Cambridge University Press, Cambridge, **2004**, p.38.
- [103] B. L. Feringa, R. A. van Delden, *Angew. Chem. Int. Ed.* **1999**, 38, 3418.
- [104] P. Lazzeretti, *J. Phys.: Condens. Matter* **2017**, 29, 443001.
- [105] K. Banerjee-Ghosh, O. Ben Dor, F. Tassinari, E. Capua, S. Yochelis, A. Capua, S-H. Yang, S.S.P. Parkin, S. Sarkar, L. Kronik, L.T. Baczewski, R. Naaman, Y. Paltiel, *Science* **2018**, 360, 1331.
- [106] I. Žutić, J. Fabian, S. Das Sarma, *Rev. Mod. Phys.* **2004**, 76, 323.
- [107] V. Dediu, M. Murgia, F. C. Matacotta, C. Taliani, S. Barbanera, *Solid State Commun.* **2002**, 122, 181.
- [108] M. Baibich, J. M. Broto, A. Fert, F. Nguyen Van Dau, F. Petroff, P. Etienne, G. Creuzet, A. Friederich, J. Chazelas, *Phys. Rev. Lett.* **1988**, 61, 2472.
- [109] R. Naaman, D. H. Waldeck, *Annu. Rev. Phys. Chem.* **2015**, 66, 263.
- [110] K. Ray, S. P. Ananthavel, D. H. Waldeck, R. Naaman, *Science* **1999**, 283, 814.
- [111] D. Mishra, T. Z. Markus, R. Naaman, M. Kettner, B. Göhler, H. Zacharias, N. Friedman, M. Sheves, C. Fontanesi, *Proc. Natl. Acad. Sci.* **2013**, 110, 14872.
- [112] P. C. Mondal, N. Kantor-Uriel, S. P. Mathew, F. Tassinari, C. Fontanesi, R. Naaman, *Adv. Mater.* **2015**, 27, 1924.

- [113] P. C. Mondal, C. Fontanesi, D. H. Waldeck, R. Naaman, *Acc. Chem. Res.*, **2016**, 49, 2560.
- [114] A. Kumar, E. Capua, K. Vankayala, C. Fontanesi, R. Naaman, *Angew. Chem. Int. Ed.* **2017**, 56, 14587.
- [115] P. C. Mondal, W. Mtangi, C. Fontanesi, *Small Methods*. **2018**, 2, 1700313.
- [116] C. Fontanesi, *Curr. Opin. Electrochem.* **2018**, 7, 36.
- [117] S. Arnaboldi, S. Grecchi, M. Magni, P. R. Mussini, *Curr Opin Electrochem* **2018**, 7, 188–199.
- [118] L. Pu, *Macromol. Rapid Commun.* **2000**, 21, 795–809.
- [119] Y. Shen, C-F. Chen, *Chem. Rev.* **2012**, 112, 1463–1535.
- [120] S. Kang, I. Cha, J.G. Han, C. Song, *Mater. Express* **2013**, 3, 119–126.
- [121] F. Sannicolò, S. Arnaboldi, T. Benincori, V. Bonometti, R. Cirilli, L. Dunsch, W. Kutner, G. Longhi, P.R. Mussini, M. Panigati, M. Pierini, S. Rizzo, *Angew. Chem. Int. Ed.* **2014**, 53, 2623–2627.
- [122] F. Sannicolò, P.R. Mussini, T. Benincori, R. Martinazzo, S. Arnaboldi, G. Appoloni, M. Panigati, E. Quartapelle Procopio, V. Marino, R. Cirilli, S. Casolo, W. Kutner, K. Noworyta, A. Pietrzyk-Le, Z. Iskierko, K. Bartold, *Chem. Eur. J.* **2016**, 22, 10839–10847.
- [123] F. Sannicolò, S. Rizzo, T. Benincori, W. Kutner, K. Noworyta, J.W. Sobczak, V. Bonometti, L. Falcioia, P.R. Mussini, M. Pierini, *Electrochim. Acta* **2010**, 55, 8352–8364.
- [124] A. Pietrzyk, W. Kutner, R. Chitta, M.E. Zandler, F. D’Souza, F. Sannicolò, P.R. Mussini, *Anal. Chem.* **2009**, 81, 10061–10070.
- [125] T-P. Huynh, A. Wojnarowicz, A. Kelm, P. Woznicki, P. Borowicz, A. Majka, F. D’Souza, W. Kutner, *ACS Sensors* **2016**, 1, 636–639.
- [126]. T-P. Huynh, A. Wojnarowicz, M. Sosnowska, S. Srebnik, T. Benincori, F. Sannicolò, F. D’Souza, W. Kutner, *Biosens. Bioelectron.* **2015**, 70, 153–160.

- [127] G. Longhi, S. Abbate, G. Mazzeo, E. Castiglioni, P.R. Mussini, T. Benincori, R. Martinazzo, F. Sannicolò, *J. Phys. Chem. C* **2014**, 118, 16019–16027.
- [128] F. Sannicolò, P.R. Mussini, T. Benincori, R. Cirilli, S. Abbate, S. Arnaboldi, S. Casolo, E. Castiglioni, G. Longhi, R. Martinazzo, M. Panigati, M. Pappini, E. Quartapelle Procopio, S. Rizzo, *Chem. Eur. J.* **2014**, 20, 15261–15634.
- [129] S. Arnaboldi, T. Benincori, R. Cirilli, W. Kutner, M. Magni, P.R. Mussini, N. Krzysztow, F. Sannicolò, *Chem. Sci.* **2015**, 6, 1706–1711.
- [130] S. Arnaboldi, T. Benincori, R. Cirilli, S. Grecchi, L. Santagostini, F. Sannicolò, P.R. Mussini *Anal. Bioanal. Chem.* **2016**, 408, 7243–7254.
- [131] S. Arnaboldi, T. Benincori, A. Penoni, L. Vaghi, R. Cirilli, S. Abbate, G. Longhi, G. Mazzeo, S. Grecchi, M. Panigati, P. R. Mussini *Chem. Sci.* **2019**, 2708-2717.
- [132] G. Bonetti, S. Arnaboldi, S. Grecchi, G. Appoloni, E. Massolo, S. Rossi, R. Martinazzo, F. Orsini, P. R. Mussini, T. Benincori, *Molecules* **2020**, 25, 2175.
- [133] S. Arnaboldi, S. Cauteruccio, S. Grecchi, T. Benincori, M. Marcaccio, A. Orbelli Biroli, G. Longhi, E. Licandro, P.R. Mussini, *Chem.Sci.* **2019**, 6, 1706-1711.
- [134] S. Rizzo, S. Arnaboldi, V. Mihali, R. Cirilli, A. Forni, A. Gennaro, A. A. Isse, M. Pierini, P.R. Mussini, F. Sannicolò, *Angew. Chem. Int. Ed.* **2017**, 56, 2079–2082.
- [135] S. Rizzo, S. Arnaboldi, R. Cirilli, A. Gennaro, A. A. Isse, F. Sannicolò, P.R. Mussini, *Electrochem Commun* **2018**, 89, 57–61.
- [136] S. Arnaboldi, R. Cirilli, A. Forni, A. Gennaro, A.A. Isse, V. Mihali, P.R. Mussini, M. Pierini, S. Rizzo, F. Sannicolò, *Electrochim Acta* **2015**, 179, 250–262.

- [137] F. Fontana, G. Carminati, B. Bertolotti, P.R. Mussini, S. Arnaboldi, S. Grecchi, R. Cirilli, L. Micheli, S. Rizzo, *Molecules* **2021**, 26, 311–324.
- [138] G. Gritzner, J. Kuta, *Pure Appl. Chem.* **1982**, 54, 1527-1532.
- [139] M. Panizza, G. Cerisola, *Electrochim Acta* **2003**, 23, 3491-3497.
- [140] L. Scapinello, S. Grecchi, S. Rossi, F. Arduini S. Arnaboldi, F. Penoni, R. Cirilli, P.R. Mussini, T. Benincori, *Chemistry: a European Journal* **2021**, 27, 13190-13202.
- [141] I. M. Kolthoff, J. J. Lingane, *Polarography*, Vol. 1 (2nd Ed.), Interscience, New York, **1952**, 189–234.
- [142] M. Donnici, R. Toniolo, S. Arnaboldi, P. R. Mussini, T. Benincori, R. Cirilli, S. Daniele, *Molecules* **2020**, 25, 5368–5383.
- [143] Radi A., *Journal of Pharmaceutical and Biomedical Analysis* **2003**, 31, 1007-1012.
- [144] Oliveira Nascimento L., Scremin J., Junquetti Mattos G., Gomes A., Nobile Clausen D., Romão Sartori E., *Electroanalysis* **2020**, 32, 191 –197.
- [145] Sharad S. Upadhyay, Pramod K. Kalambate, Ashwini K. Srivastava, *Journal of Electroanalytical Chemistry* **2019**, 840, 305–312.
- [146] N. B. McKeown, Phthalocyanine materials: Synthesis, Structure and Function, ed., *Cambridge University Press* **1998**.
- [147] C. C. Leznoff, A. B. P. Lever, Phthalocyanines: Properties and Applications, ed., *Wiley-VCH*, New York, **1996**
- [148] D. Dini, M. Calvete, M. Hanack, *Chem. Rev.* **2016**, 116, 13043–13233.
- [149] M. L. Esqueda, M. E. S. Vergara, J. R. Á. Bada, R. Salcedo, *Materials* **2019**, 12, 434–451.
- [150] M. Bouvet, P. Gaudillat, J-M. Suisse, *J. Porphyrins Phthalocyanines* **2013**, 17, 913–919.
- [151] J. H. Zagal, S. Griveau, J. F. Silva, T. Nyokong, F. Bedioui, *Coord. Chem. Rev.* **2010**, 254, 2755–2791.

- [152] F. Baumann, B. Bienert, G. Rösch, H. Vollmann, W. Wolf, *Angew. Chem.* **1956**, 68, 133–150, and patents cited therein.
- [153] F. Gund, *J. Soc. Dyers Colour.* **1953**, 69, 671–682.
- [154] B.R. Kozub, R.G. Compton, *Sensors and Actuators B*, **2020**, 147, 350-358.
- [155] L. Pigani, R. Seeber, F. Terzi, O. Cerri, M. Innocenti, R. Udisti, G. Sanna, *Electrochimica Acta*, **2006**, 51, 2698–2705.
- [156] S. Arnaboldi, D. Vigo, M. Longhi, F. Orsini, S. Riva, S. Grecchi, E. Giacobelli, V. Guglielmi, R. Cirilli, G. Longhi, G. Mazzeo, T. Benincori, P. R. Mussini, *ChemElectroChem*, **2019**, 6, 4204–4214.
- [157] K. Meerholz, J. Heinze, *Electrochimica Acta*, **1996**, 41, 1839-1854.
- [158] Shaoping Feng, Shaoqin Hu, Xianlan Chen, Guowei Zhang, Guiyang Liu, Wei Liu, *Int. J. Electrochem. Sci.*, **2020**, 15, 6778 – 6789
- [159] S. Grecchi, S. Arnaboldi, M. Korb, R. Cirilli, S. Araneo, V. Guglielmi, G. Tomboni, M. Magni, T. Benincori, H. Lang, P.R. Mussini, *ChemElectroChem.*, **2019**, 7, 3429–3438.
- [160] D. Schaarschmidt, A. Hildebrandt, S. Bock, H. Lang, *J. Organomet. Chem.*, **2014**, 751,742-753
- [161] M. J. Verschoor-Kirss, O. Hendricks, C. M. Verschoor, R. Conry, R. U. Kirss, *Inorg. Chim. Acta*, **2016**, 450, 30–38.
- [162] M. A. Bennett, S. K. Bhargava, A. M. Bond, I. M. Burgar, Si-Xuan Guo, G. Kar, Steven H. Privér, J. Wagler, A. C. Willis, A. A. J. Torriero, *Dalton Trans.*, **2010**, 39, 9079–9090.
- [163] C. Hansch, A. Leo, R.W. Taft, *Chem. Rev.* **1991**, 91, 165-195.
- [164] A.A. Isse, L. Falciola, P.R. Mussini, A. Gennaro, *Chem. Comm.*, **2006**, 344-346.
- [165] A.A. Isse, P.R. Mussini, A. Gennaro, *J. Phys. Chem. C*, **2009**, 113, 14983-1499

- [166] P. Štěpnička, M. Lamac̣, I. Císařová, *J. Organomet.Chem.*, **2008**, 693, 446–456.
- [167] R. Xie, L. -Y.Chu, J.-G. Deng, *Chem. Soc. Rev.* **2008**, 37, 1243–1263, and references therein cited.
- [168] A. Higuchi, M. Tamai, Y.-A. Ko, Y.-I. Tagawa, Y.-H. Wu, B. N. Freeman, J.-T. Bing, Y. Chang, Q.-D. Ling, *Polym. Rev.* **2010**, 50, 113–143.
- [169] S. Kang, I. Cha, J. G. Han, C. Song, *Mater. Express* **2013**, 3, 119–126.
- [170] G. Radecki, H. Radecka 2013, *Intech* open access peer-reviewed chapter, DOI: 10.5772/52803.
- [171] R.-I. Stefan van Staden, J. F. Van Staden, *J. Electrochem. Soc.* **2013**, 160, B196-B200.
- [172] M. Shamsipur, A. A. M. Beigi, M. Teymouri, S. Rasoolipour, Z. Asfari, *Anal. Chem.* **2009**, 81, 6789–6796.
- [173] R. Liang, L. Chen, W. Qin, *Scient. Reports* **2015**, 5, 12462.
- [174] H. Zhang, R. Yao, N. Wang, R. Liang, W. Qin, *Anal. Chem.* **2018**, 90, 657–662.
- [175] E. Quartapelle, T. Benincori, G. Appoloni, P. R. Mussini, S. Arnaboldi, C. Carbonera, R. Cirilli, A. Cominetti, L. Longo, R. Martinazzo, M. Panigati, R. Po, *New J. Chem.* **2017**, 41, 10009–10019.
- [176] E. Castiglioni, S. Abbate, G. Longhi, R. Gangemi, *Chirality* **2007**, 19, 941–946.
- [177] E. Castiglioni, P. Biscarini, S. Abbate, *Chirality* **2009**, 21, E28–E36.
- [178] E. Bakker, P. Buhlmann, E. Pretsch, *Chem. Rev.* **1997**, 97, 3083–3132.
- [179] P. Buhlmann, E. Pretsch, E. Bakker, *Chem. Rev.* **1998**, 98, 1593–1687.
- [180] E. Zdrachek, E. Bakker, *Anal. Chem.* **2019**, 91, 2–26.
- [181] F. Fontana, B. Bertolotti, S. Grecchi, P. R. Mussini, L. Micheli, R. Cirilli, M. Tommasini, S. Rizzo, *Chemosensors* **2021**, 9, 216.

- [182] M. Longhi, S. Arnaboldi, E. Husanu, S. Grecchi, I. F. Buzzi, R. Cirilli, S. Rizzo, C. Chiappe, P. R. Mussini, L. Guazzelli, *Electrochim. Acta* **2019**, 298, 194–209.
- [183] S. Grecchi, C. Ferdeghini, M. Longhi, A. Mezzetta, L. Guazzelli, S. Khawthong, F. Arduini, C. Chiappe, A. Iuliano, P. R. Mussini, *ChemElectroChem* **2021**, 8, 1377–1387.
- [184] S. Arnaboldi, A. Mezzetta, S. Grecchi, M. Longhi, E. Emanuele, S. Rizzo, F. Arduini, L. Micheli, L. Guazzelli, P. R. Mussini, *Electrochimica Acta* **2021**, 380, 138189.
- [185] T. Cui, A. Lahiri, T. Carstens, N. Borisenko, G. Pulletikurthi, C. Kuhl, F. Endres, *J. Phys. Chem. C* **2016**, 120, 9341–9349.
- [186] L. Vaton-Chanvrier, V. Peulon, Y. Combret, C. J. Combret, *Chromatographia* **1997**, 46, 613.
- [187] T. Takeuchi, J. Chu, T. Miwa, *Chromatographia* **1998**, 47, 183.
- [188] L. Vaton-Chanvrier, H. Oulyadi, Y. Combret, G. Coquerel, J. Combret, *Chirality* **2001**, 13, 668–674.
- [189] A. Iuliano, G. Félix, *J. Chromatogr. A* **2004**, 1031, 187–195.
- [190] A. Iuliano, P. Scafato, *Tetrahedron: Asymmetry* **2003**, 14, 611–618.
- [191] A. Iuliano, P. Scafato, R. Torchia, *Tetrahedron: Asymmetry* **2004**, 15, 2533–2538.
- [192] G. L. Puleo, M. Masi, A. Iuliano, *Tetrahedron: Asymmetry* **2007**, 18, 1364–1375.
- [193] V. R. Jumde, A. Iuliano, *Adv. Synth. Catal.* **2013**, 355, 3475–3483.
- [194] V. Zullo, A. Iuliano, *Eur. J. Org. Chem.* **2019**, 1377–1384.
- [195] U. Maitra, P. Mathivanan, *J. Chem. Soc. Chem. Commun.* **1993**, 1469–1471.
- [196] P. Mathivanan, U. Maitra, *J. Org. Chem.* **1995**, 60, 364–369.

- [197] U. Maitra, A. K. Bandyopadhyaya, N. M. Sangeetha, *J. Org. Chem.* **2000**, 65, 8239–8244.
- [198] S. Caporali, C. Chiappe, T. Ghilardi, A. Iuliano, G. Longhi, P. Margari, C. S. Pomelli, *RSC Adv.* **2016**, 6, 8053–8060.
- [199] A. Mezzetta, J. Łuczak, J. Woch, C. Chiappe, J. Nowicki, L. Guazzelli, *J. Mol. Liq.* **2019**, 289, 111155.
- [200] C. Chiappe, P. Margari, A. Mezzetta, C. S. Pomelli, S. Koutsoumpos, M. Papamichael, P. Giannios, K. Moutzouris, *Phys. Chem. Chem. Phys.* **2017**, 19, 8201–8209.
- [201] S. Becherini, A. Mezzetta, C. Chiappe, L. Guazzelli, *New J. Chem.* **2019**, 43, 4554–4561.
- [202] A. Mezzetta, V. Perillo, L. Guazzelli, C. Chiappe, *J. Therm. Anal. Calorim.* **2019**, 138, 3335–3345.
- [203] A. Iuliano, P. Salvadori, G. Félix, *Tetrahedron: Asymmetry* **1999**, 10, 3353–3364.
- [204] A. Iuliano, G. Masini, P. Salvadori, G. Félix, *Tetrahedron: Asymmetry* **2001**, 12, 2811–2825.
- [205] A. Iuliano, D. Losi, S. Facchetti, *J. Org. Chem.* **2007**, 72, 8472–8477.
- [206] A. Iuliano, S. Facchetti, T. Funaioli, *Chem. Commun.* **2009**, 457–459.
- [207] S. Facchetti, I. Cavallini, T. Funaioli, F. Marchetti, A. Iuliano, *Organometallics* **2009**, 28, 4150–4158.
- [208] V. R. Jumde, S. Facchetti, A. Iuliano, *Tetrahedron: Asymmetry* **2010**, 21, 2775–2781.
- [209] G. Iannucci, A. Iuliano, *J. Organomet. Chem.* **2016**, 806, 88.
- [210] A. Passera, A. Iuliano, J. J. Pérez-Torrente, V. Passarelli, *Dalton Trans.* **2018**, 47, 2292–2305.
- [211] L. Guglielmero, A. Mezzetta, C. S. Pomelli, C. Chiappe, L. Guazzelli, *J. CO₂ Util.* **2019**, 34, 437–445.

- [212] L. S. Hernández-Muñoz, A. Galano, P. D. Astudillo-Sánchez, M. M. Abu-Omar, F. González, *Electrochim. Acta* **2014**, 136.
- [213] V. Zullo, M. Górecki, L. Guazzelli, A. Mezzetta, G. Pescitelli, A. Iuliano, *J. Mol. Liq.* **2021**, 322, 114528.
- [214] T. Welton, *Biophys. Rev.* **2018**, 10, 691–706.
- [215] C. Maton, N. De Vos, C. V. Stevens, *Chem. Soc. Rev.* **2013**, 42, 5963–5977.
- [216] Y. Chen, T. Mu, in *Encycl. Ion. Liq.* (Eds.: R. Fehrmann, C. Santini), Springer Singapore, Singapore, **2020**, pp. 1–13.
- [217] Y. Cao, T. Mu, *Ind. Eng. Chem. Res.* **2014**, 53, 8651–8664.
- [218] J.R. Brandt, L. Pospisil, L. Bednarova, R. Correa da Costa, A. J. P. White, T. Mori, F. Teply, M. J. Fuchter, *Chem. Commun.* **2017**, 53, 9059–9062.
- [219] N. Berova, L. Di Bari, G. Pescitelli, *Chem. Soc. Rev.* **2007**, 36,914.
- [220] J. T. Vázquez, *Tetrahedron: Asymmetry* **2017**,28, 1199.
- [221] N. Harada, K. Nakanishi, University Science Books, Mill Valley, CA, **1983**.
- [222] Y. Gao, W. Yao, J. Sun, H. Zhang, Z. Wang, L. Wang, D. Yang, L. Zhang, H. Yang, *J. Mater. Chem. A* **2015**, 3, 10738–10746.
- [223] H. H. Jaffe, M. Orchin, Wiley, New York, **1962**.
- [224] W. H. Pirkle, D. L. Sikkenga, M. S. Pavlin, *J. Org. Chem.* **1977**, 42, 384-387.
- [225] A. Santos Ribeiro, A. Urbano da Silva, M. Navarro, J. Tonholo, *Electrochim. Acta* **2006**, 51, 4892-4896.
- [226] R. E. Ramirez, C. García-Martínez, F. Méndez, *Molecules* **2013**, 18, 10254-10265.
- [227] N. A. Macías-Ruvalcaba, J. P. Telo, D. H. Evans, *J. Electroanal. Chem.* 600 (2007) 294-302.

- [228] C. Bazzini, S. Brovelli, T. Caronna, C. Gambarotti, M. Giannone, P. Macchi, P. Meinardi, A. Mele, W. Panzeri, F. Recupero, A. Sironi, R. Tubino, *Eur. J. Org. Chem.* **2005**, 1247–1257.
- [229] R.-H. Janke, G. Haufe, E.-U. Würthwein, J. H. Borkent, *J. Am. Chem.Soc.* **1996**, 118, 6031–6035.
- [230] S. Abbate, G. Longhi, F. Lebon, E. Castiglioni, S. Superchi, L. Pisani, F. Fontana, F. Torricelli, T. Caronna, C. Villani, R. Sabia, M. Tommasini, A. Lucotti, D. Mendola, A. Mele, D. A. Lightner, *J. Phys. Chem. C* **2014**, 118, 1682–1695.
- [231] M. Francisco, A. van den Bruinhorst, M.C. Kroon, *Angew. Chem. Int. Ed.* **2013**, 52, 3074–3085.
- [232] M. A. R. Martins, S. P. Pinho, J. A. P. Coutinho, *J. Solution Chem.* **2019**, 48, 962–982.
- [233] L.J.B.M. Kollau, M. Vis, A. van den Bruinhorst, G. de With, R. Tuinier, *Pure Appl. Chem.* **2019**, 91, 1341–1349.
- [234] D. O. Abranches, M. A. R. Martins, L. P. Silva, N. Schaeffer, S. P. Pinho, J. A. P. Coutinho, *Chem. Commun.* **2019**, 55, 10253
- [235] R. Craveiro, I. Aroso, V. Flammia T. Carvalho, M. T. Viciosa, M. Dionísio, S. Barreiros, R.L. Reis, *J. Mol. Liq.* **2016**, 215, 534–540.
- [236] O. S. Hammond, H. Li, C. Westermann, A.Y.M. Al-Murshedi, F. Endres, A. P. Abbott, G.G. Warr, K. J. Edler, R. Atkin, *Nanoscale Horiz.* **2019**, 4, 158–168.
- [237] M. H. Mamme, S. L. C. Moors, E.A. Mernissi Cherigui, H. Terry, J. Deconinck, J. Ustarroz, F. De Proft, *Nanoscale Adv.* **2019**, 1, 2847–2856.
- [238] B.-A. Mei, O. Munteshari, J. Lau, B. Dunn, L. Pilon, *J. Phys. Chem. C* **2018**, 122, 194–206.
- [239] K.W. Pratt, W. F. Koch, Y.C. Wu, P.A. Berezansky, *Pure Appl. Chem.* **2011**, 73, 1783–1793.

- [240] Z. Chen, B. McLean, M. Ludwig, R. Stefanovic, G.G. Warr, G.B. Webber, A. J. Page, R. Atkin, *J. Phys. Chem. C* **2016**, 120, 2225–2233.
- [241] M. Atilhan, S. Aparicio, *J. Phys. Chem. C* **2016**, 120, 10400–10409.
- [242] S. Kaur, S. Sharma, H. K. Kashyap, *J. Chem. Phys.* **2017**, 147, 194507-194510.
- [243] Z. Chen, M. Ludwig, G.G. Warr, R. Atkin, *J. Colloid Interf. Sci.* **2017**, 494, 373–379.
- [244] P. Sebastian, E. Gomez, V. Climent, J.M. Feliu, *Electrochim. Acta* **2019**, 311, 30-40.
- [245] K. Häckl, H. Li, I. M. Aldous, T. Tsui, W. Kunz, A. P. Abbott, G.G. Warr, R. Atkin, *J. Phys. Chem. Lett.* **2019**, 10, 5331–5337.
- [246] R. L. Hinman, E. B. Whipple, *J. Am. Chem. Soc.* **1962**, 84, 2534-2539.
- [247] R. L. Hinman, J. Lang, *J. Am. Chem. Soc.* **1964**, 86, 3796-3806.
- [248] L. A. Kochergina, W. W. Chernikov, O. V. Platonykeva, *Russian J. Phys. Chem. A* **2011**, 85, 938-943.
- [249] D. Yuea, Y. Jia, Y. Yao, J. Sun, Y. Jing, *Electrochimica Acta* **2012**, 65, 30– 36.
- [250] K. Ma, R. Jaronova, G. Swain, G. Blanchard, *Langmuir* **2016**, 32, 9507–9512
- [251] T. Zhekenov, N. Toksanbayev, Z. Kazakbayeva, D. Shah, F.S. Mjalli, *Fluid Ph. Equilib.* **2017**, 441, 43–48.
- [252] T. Benincori, S. Arnaboldi, M. Magni, S. Grecchi, R. Cirilli, C. Fontanesi, P. R. Mussini, *Chem. Sci.* **2019**, 10, 2750.
- [253] D. Mishra, T. Z. Markus, R. Naaman, M. Kettner, B. Göhler, H. Zacharias, N. Friedman, M. Sheves, C. Fontanesi, *Proc. Natl. Acad. Sci.* **2013**, 110, 14872.
- [254] P. C. Mondal, C. Fontanesi, D. H. Waldeck, R. Naaman, *Acc. Chem. Res.* **2016**, 49, 2560.
- [255] P. C. Mondal, W. Mtangi, C. Fontanesi, *Small Methods* **2018**, 2, 1700313.

- [256] O. B. Dor, S. Yochelis, S. P. Mathew, R. Naaman, Y. A. Paltiel, *Nat. Commun.* **2013**, 4, 2256.
- [257] B.M.W. Langeveld-Voss, R.A.J. Janssen, E.W. Meijer, *J. Mol. Struct.* **2000**, 521, 285.
- [258] V. Dediu, M. Murgia, F. C. Maticotta, C. Taliani, S. Barbanera, *Solid State Commun.* **2002**, 122, 181.
- [259] A. Kumar, E. Capua, K. Vankayala, C. Fontanesi, R. Naaman, *Angew. Chem. Int. Ed.* **2017**, 56, 14587.
- [260] I. Žutić, J. Fabian, S. D. Sarma, *Rev. Mod. Phys.* **2004**, 76,323.
- [261] V. V. Maslyuk, R.Gutierrez, A.Dianat, V. Mujica, G. Cuniberti, *J. Phys. Chem. Lett.* **2018**, 9, 5453.
- [262] A. C. Aragonès, E. Medina, M. Ferrer-Huerta, N. Gimeno, M. Teixidó, J. L. Palma, N. Tao, J.M. Ugalde, E. Giralt, I.Díez-V. Mujica, *Small* **2017**, 13, 1602519.
- [263] B. Han, X. Gao, J. Lv, Z. Tang, *Adv. Mater.* **2018**, 1801491
- [264] R. Naaman, D. H. Waldeck, *Annu. Rev. Phys. Chem.* **2015**, 66, 263.
- [265] F. Pop, P. Auban-Senzier, E. Canadell, G. L.J.A. Rikken, N. Avarvari, *Nature Comm.* **2014**, 5, Article number: 375.7
- [266] A. Kumar, E. Capua, C. Fontanesi, *ACS Nano* **2018**, 12, 3892.

List of Publications

1. M. Longhi, S. Arnaboldi, E. Husanu, S. Grecchi, I. F. Buzzi, R. Cirilli, S. Rizzo, C. Chiappe, P. R. Mussini, L. Guazzelli (2019). A family of chiral ionic liquids from the natural pool: Relationships between structure and functional properties and electrochemical enantiodiscrimination tests. *ELECTROCHIMICA ACTA*, 298, 194-209.
2. S. Arnaboldi, S. Cauteruccio, S. Grecchi, T. Benincori, M. Marcaccio, A. Orbelli Biroli, G. Longhi, E. Licandro, P. R. Mussini (2019). Thiahelicene-based inherently chiral films for enantioselective electroanalysis. *CHEMICAL SCIENCE*, 10, 1539-1548.
3. S. Arnaboldi, T. Benincori, A. Penoni, L. Vaghi, R. Cirilli, S. Abbate, G. Longhi, G. Mazzeo, S. Grecchi, M. Panigati, P. R. Mussini (2019). Highly enantioselective “inherently chiral” electroactive materials based on a 2,2'-biindole atropisomeric scaffold. *CHEMICAL SCIENCE*, 10, 2708-2717.
4. T. Benincori, S. Arnaboldi, M. Magni, S. Grecchi, R. Cirilli, C. Fontanesi, P. R. Mussini (2019). Highlighting spin selectivity properties of chiral electrode surfaces from redox potential modulation of an achiral probe under an applied magnetic field. *CHEMICAL SCIENCE*, 10, 2750.
5. S. Arnaboldi, D. Vigo, M. Longhi, F. Orsini, S. Riva, S. Grecchi, E. Giacovelli, V. Guglielmi, R. Cirilli, G. Longhi, G. Mazzeo, T. Benincori, P. R. Mussini (2019). Self-standing membranes consisting of inherently chiral electroactive oligomers: electrosynthesis, characterization and preliminary tests in potentiometric setups. *CHEMELECTROCHEM*, 6, 4204–4214.
6. G. Bonetti, S. Arnaboldi, S. Grecchi, G. Appoloni, E. Massolo, S. Rossi, R. Martinazzo, F. Orsini, P. R. Mussini, T. Benincori (2020). Effective Enantiodiscrimination in Electroanalysis Based on a New Inherently Chiral 1,1'-

Binaphthyl Selector Directly Synthesizable in Enantiopure Form. *MOLECULES*, 25(9), 2175.

7. S. Grecchi, S. Arnaboldi, M. Korb, R. Cirilli, S. Araneo, V. Guglielmi, G. Tomboni, M. Magni, T. Benincori, H. Lang, P.R. Mussini (2020). Widening the scope of “inherently chiral” electrodes: enantiodiscrimination of chiral electroactive probes with planar stereogenicity. *CHEMELECTROCHEM.*, 7, 3429–3438.

Back Cover 16/2020, DOI: 10.1002/celc.202000891.

8. V. Pelliccioli, G. Dilauro, S. Grecchi, S. Arnaboldi, C. Graiff, F. M. Perna, P. Vitale, E. Licandro, A. Aliprandi, S. Cauteruccio, V. Capriati (2020). Ligand-Free Suzuki-Miyaura Cross-Coupling Reactions in Deep Eutectic Solvents: Synthesis of Benzodithiophene Derivatives and Study of Their Optical and Electrochemical Performance. *EUR. J. ORG. CHEM.*, 45, 6981–6988.

9. F. Fontana, G. Carminati, B. Bertolotti, P.R. Mussini, S. Arnaboldi, S. Grecchi, R. Cirilli, L. Micheli, S. Rizzo (2021). Helicity: a non-conventional stereogenic element for designing inherently chiral ionic liquids for electrochemical enantiodifferentiation. *MOLECULES*, 26(2), 311.

10. S. Grecchi, C. Ferdeghini, M. Longhi, A. Mezzetta, L. Guazzelli, S. Khawthong, F. Arduini, C. Chiappe, A. Iuliano, P. R. Mussini (2021). Chiral biobased ionic liquids with cations or anions including bile acid building blocks as chiral selectors in voltammetry. *CHEMELECTROCHEM*, 8, 1377–1387.

11. S. Arnaboldi, A. Mezzetta, S. Grecchi, M. Longhi, E. Emanuele, S. Rizzo, F. Arduini, L. Micheli, L. Guazzelli, P. R. Mussini (2021). Natural-based chiral task-specific deep eutectic solvents: a novel, effective tool for enantiodiscrimination in electroanalysis. *ELECTROCHIMICA ACTA*, 380, 138189.

12. S. Grecchi, S. Arnaboldi, S. Rizzo, P. R. Mussini (2021). Advanced chiral molecular media for enantioselective electrochemistry and electroanalysis.

CURRENT OPINION IN ELECTROCHEMISTRY, DOI:
10.1016/j.coelec.2021.100810.

13. C. Malacrida, L. Scapinello, R. Cirilli, S. Grecchi, A. Penoni, T. Benincori, S. Ludwigs (2021). In-situ Electrochemical Investigations of Inherently Chiral 2,2'-Biindole Architectures with Oligothiophene Terminals. *CHEMELECTROCHEM*, 8, 3250 - 3261.

14. L. Scapinello, S. Grecchi, S. Rossi, F. Arduini, S. Arnaboldi, A. Penoni, R. Cirilli, P. R. Mussini, T. Benincori (2021). Modulating the Enantiodiscrimination Features of Inherently Chiral Selectors by Molecular Design: A HPLC and Voltammetry Study Case with Atropisomeric 2,2'-Biindole-Based Monomers and Oligomer Films. *CHEM. EUR. J.*, 27, 13190–13202.

15. F. Fontana, B. Bertolotti, S. Grecchi, P. R. Mussini, L. Micheli, R. Cirilli, M. Tommasini, S. Rizzo (2021). 2,12-Diaza[6]helicene: An Efficient Non-Conventional Stereogenic Scaffold for Enantioselective Electrochemical Interphases. *CHEMOSENSORS*, 9 (8), 216.

16. S. Arnaboldi, S. Grecchi, L. Vaghi, A. Penoni, L. Scapinello, I. F. Buzzi, R. Cirilli, M. Pierini, T. Benincori, P. R. Mussini (2021). Trópos and Átropos biindole chiral electroactive monomers: A voltammetry and HPLC comparative insight. *CHEMELECTROCHEM*, DOI: 10.1002/celc.202100903.

17. S. Grecchi, S. Arnaboldi, A. A. Isse, C. D'Aloi, A. Gennaro, P. R. Mussini (2021). Electrocatalytic Reduction of Bromothiophenes vs Bromobenzenes on Gold and Silver Electrodes: enhancement from S specific adsorption and modulation from substituent effects. *ELECTROCHIMICA ACTA*, DOI: 10.1016/j.electacta.2021.139563.

18. S. Grecchi (2021). Chiralità inerente e voltammetria enantioselettiva. *LA CHIMICA E L'INDUSTRIA*, 2, 50-52, ISSN 2283-544X.

List of attendant conferences and doctorate school.

1. 13th ECHEMS Meeting, 20-23 May 2019, Saint-Pierre-d'Oléron, France.

Oral Communication: Spin Selectivity Properties Displayed by Chiral Electrode Surfaces under an External Magnetic Field.

2. IX SMCBS2019, 8-12 November 2019, Zelechów, Poland.

Poster Presentation: Spin Filter Properties of Chiral Thin Film Highlighted by an External Magnetic Field.

I was awarded with the “First Poster Award” with this presentation

3. CHESS School 2019, 2-6 December 2019, Florence, Italy.

Conventional and High-Energy Spectroscopies for Inorganic, Organic and Biomolecular Surfaces and Interfaces.

I was awarded with the scholarship that fully covered the school registration fees.

4. NANO DAY IV, 11-14 December, Milan, Italy.

Poster Presentation: Innovative Chiral Materials and Media for Enantioselection in Chiral Electrochemistry and Advanced Applications in Spintronics.

5. Italian School on Magnetism, V Edition, 3-7 February 2020, Rome, Italy.

Poster Presentation: Highlighting spin selectivity properties of chiral thin film under an applied magnetic field.

6. ISE-2020 Meeting, 31 August-4 September 2020, online event.

Poster Presentation: Inherently Chiral Artificial Membranes as Key Components in Chiral Potentiometric Sensors.

Oral Presentation: New Families of Inherently Chiral Monomers with Different Atropisomeric Cores for Applications as Oligomeric Films in Chiral Electrochemistry

7. X SMCBS2021, 5-9 November 2021, online event.

Oral Presentation: Wide-scope Enantiodiscrimination at Chiral Electrochemical Interphases: Highlighting Structure Effects on Probe-Selector Interactions

8. XXVII Congresso Nazionale della Società Chimica Italiana. (I was awarded with the scholarship for young researcher), 14-23 September 2021, online event.

Poster Presentation: Enantioselective electroanalysis for different chiral active pharmaceutical ingredients and a real matrix, using inherently chiral 2,2'-biindole based oligomer films.

9. ISE, 72nd Annual Meeting, 29 August-3 September 2021, online event.

Poster Presentation: Inherently Chiral 2,2'-biindole Oligomer Films for the Enantioselection of Chiral Active Pharmaceutical Ingredients, including a Real Matrix.

I was awarded with the “Best Poster Award” with this presentation

Oral Presentation: Wide-scope Enantiodiscrimination at Chiral Electrochemical Interphases: Highlighting structure effects on Probe-Selector Interactions.

10. XVII IHSS, Italian-Hungarian Symposium on Spectrochemistry, Current approaches in health and environmental protection, 14-18 June 2021, Turin (Italy), online event.

Poster Presentation: Enantiodiscrimination ability of different inherently chiral selectors with DOPA and other chiral probes of pharmaceutical interest.

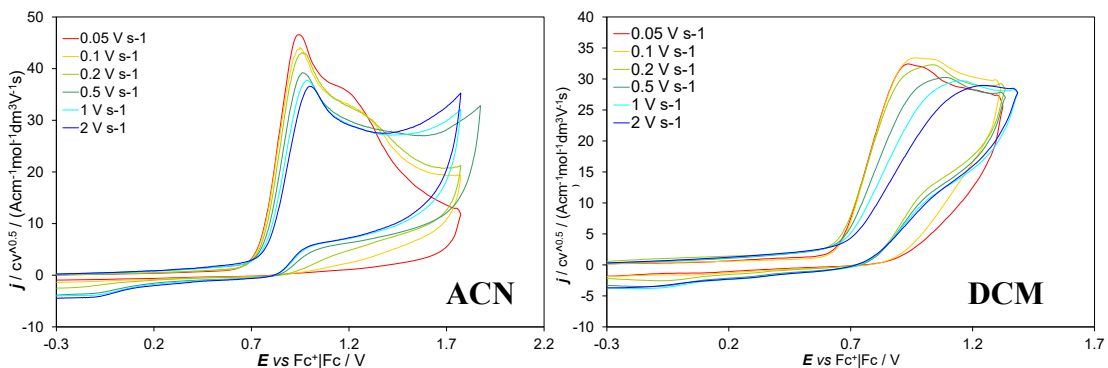
I was awarded with the “Best Poster Award” with this presentation

Chapter 7

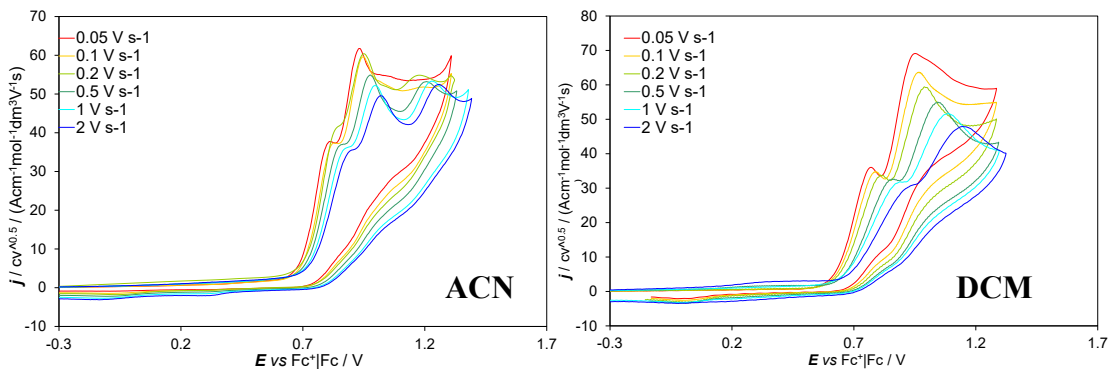
Gallery

1. Electrochemical characterization of the bi-naphthyl systems

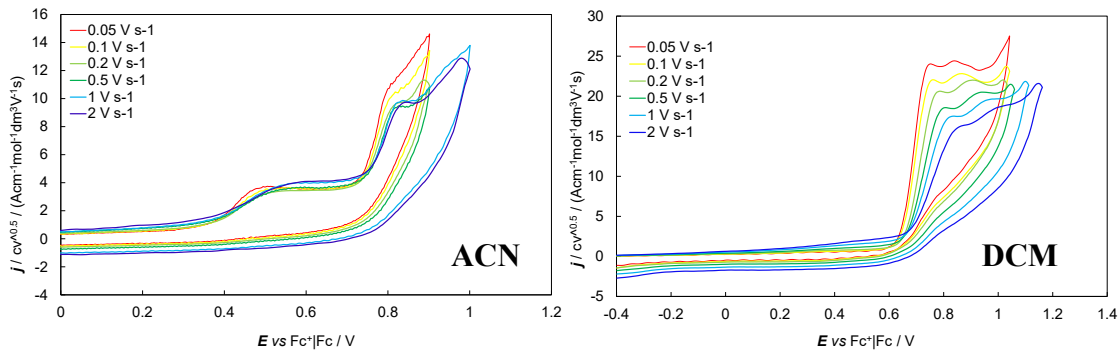
2-Naphtol



BINOL



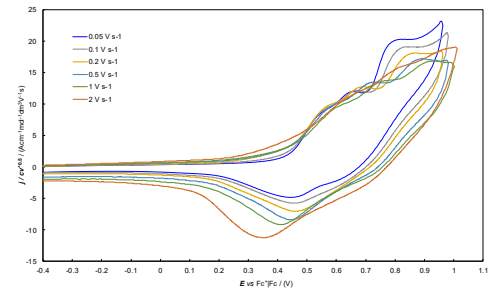
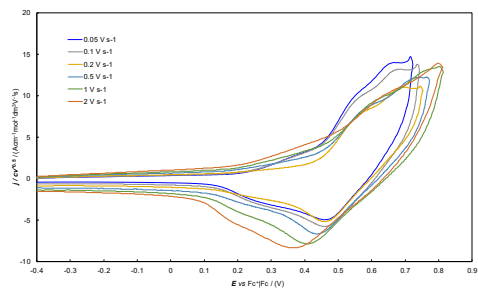
SP26



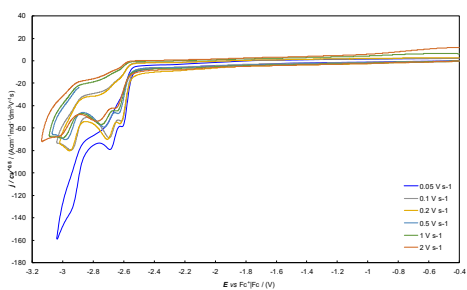
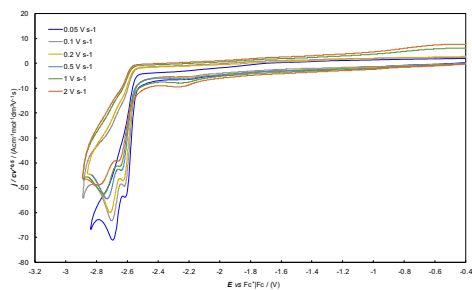
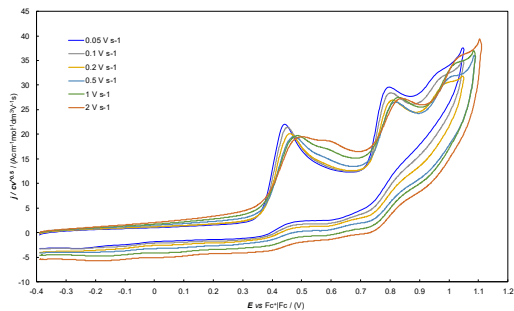
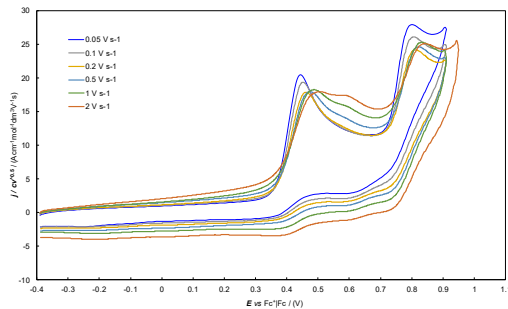
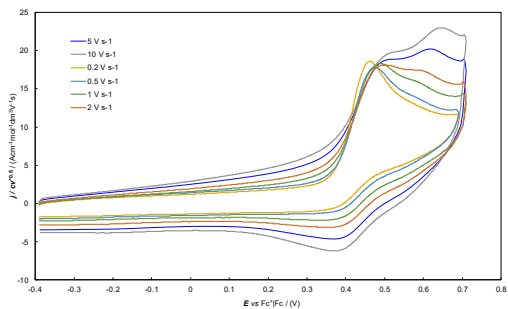
2. Electrochemical characterization of the inherently chiral family with phenyl spacer

(N-Me)-Ind₂Ph₂T₄

DCM

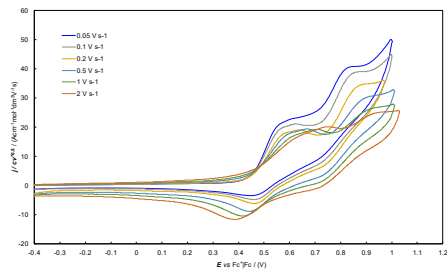
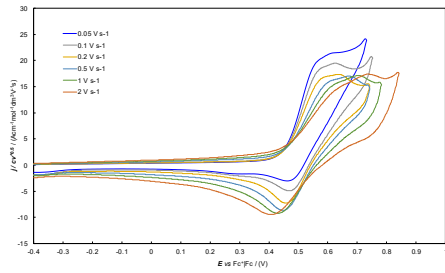


ACN

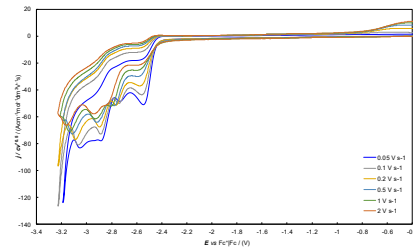
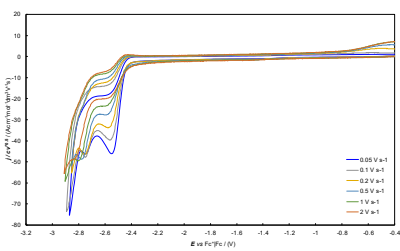
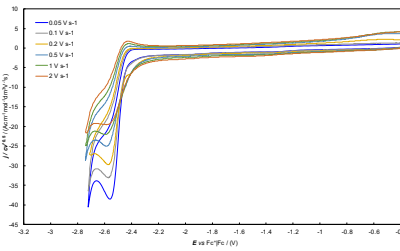
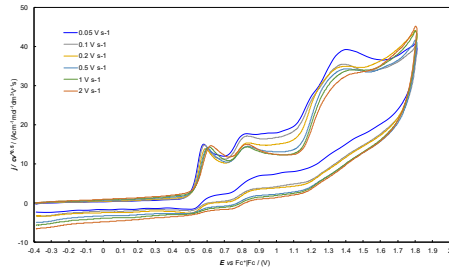
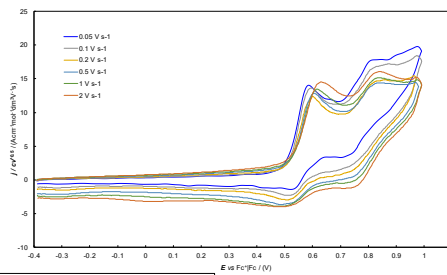
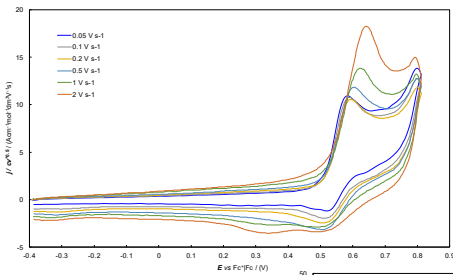


(N-Pr)-Ind₂Ph₂T₄

DCM

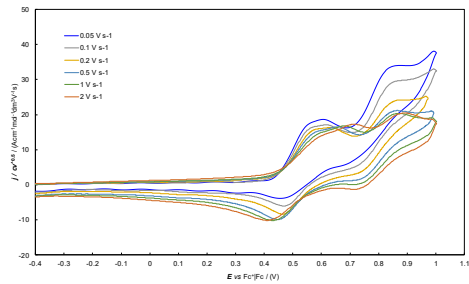
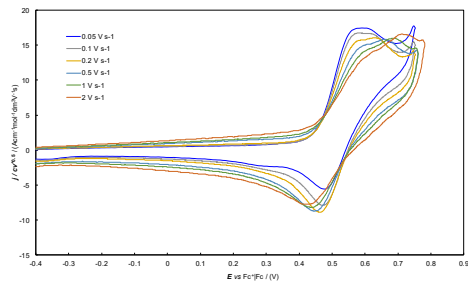


ACN

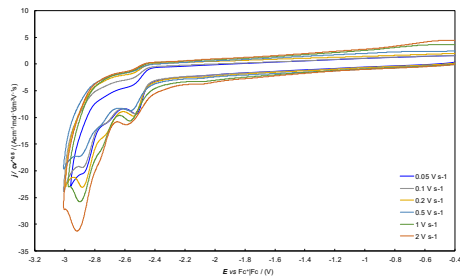
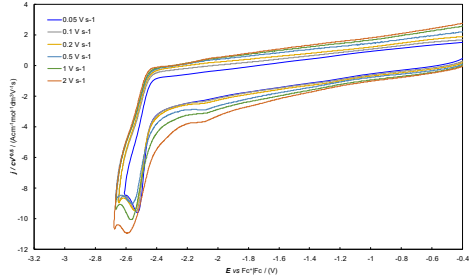
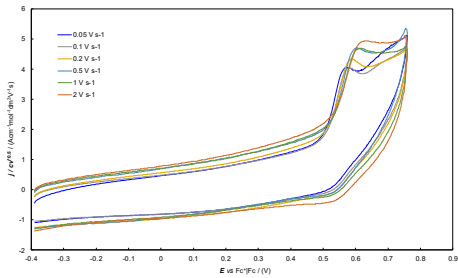


(N-Hex)-Ind₂Ph₂T₄

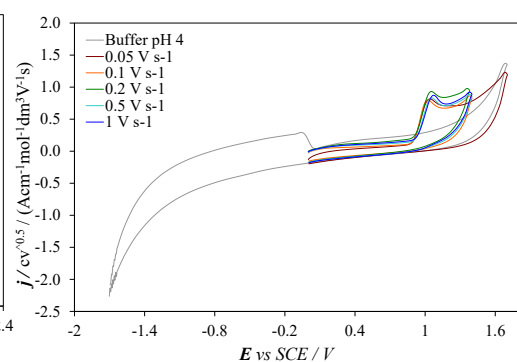
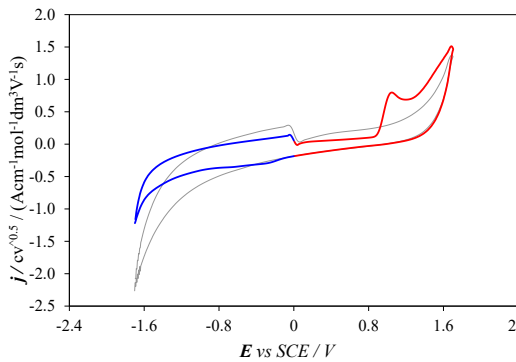
DCM



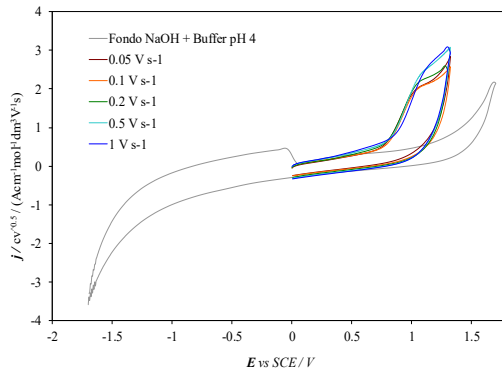
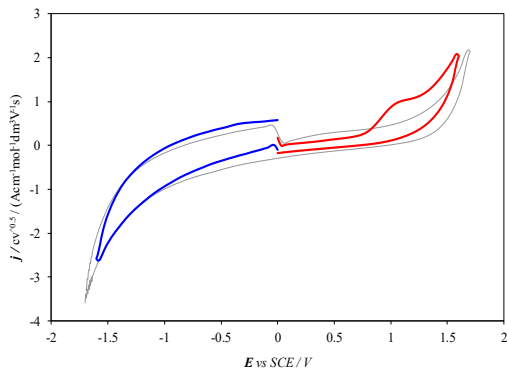
ACN



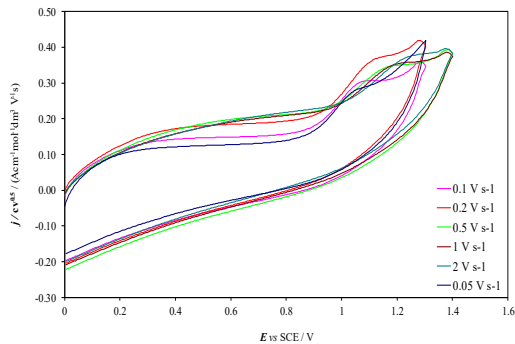
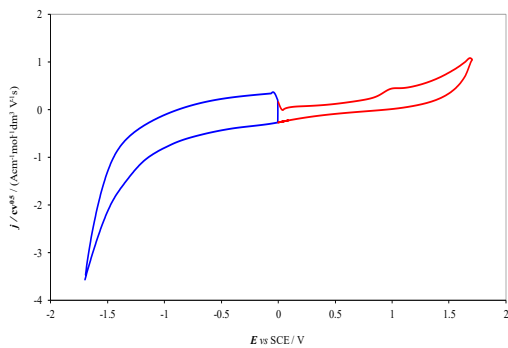
3. Electrochemical characterization of terazosin in pH4 buffer solution



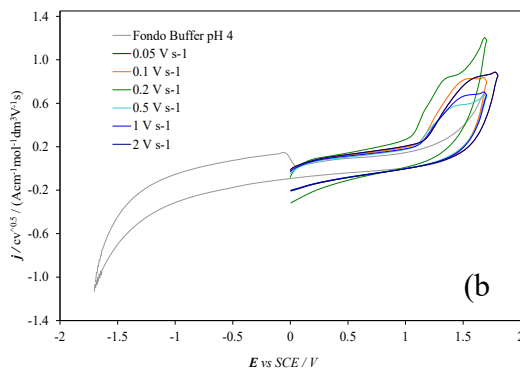
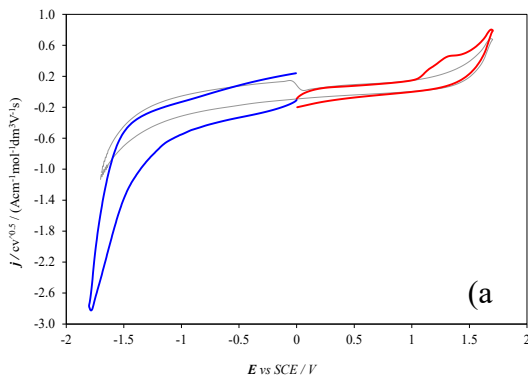
4. Electrochemical characterization of lansoprazole in NaOH 0.1 M + buffer pH 4 (ratio 3:2)



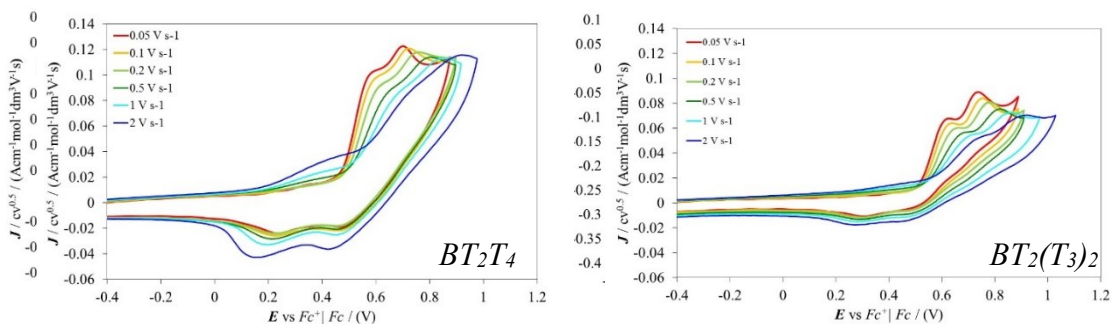
5. Electrochemical characterization of clopidogrel in buffer pH 4



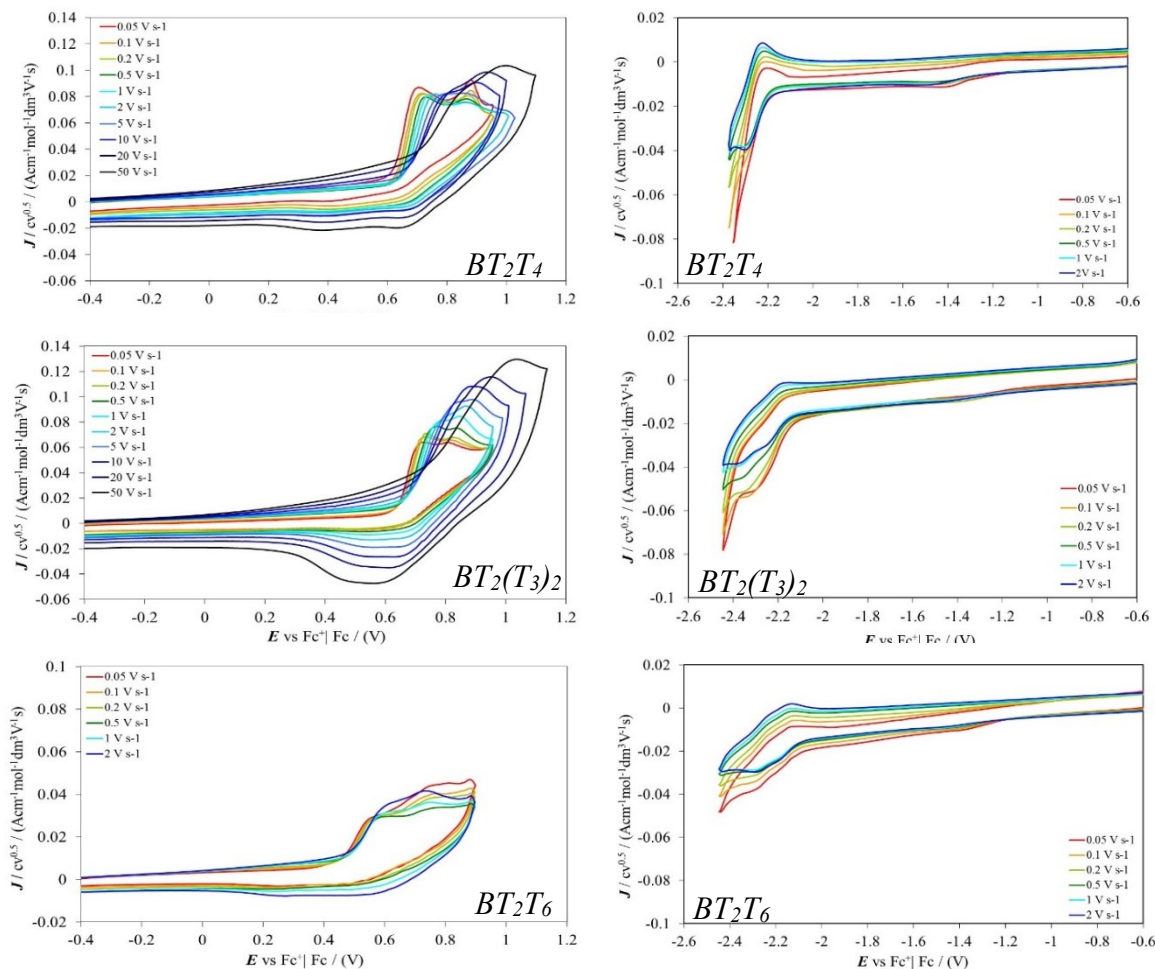
6. Electrochemical characterization of ramosetron in buffer pH 4



7. Electrochemical characterization of BT_2T_4 and $BT_2(T_3)_2$ in DCM



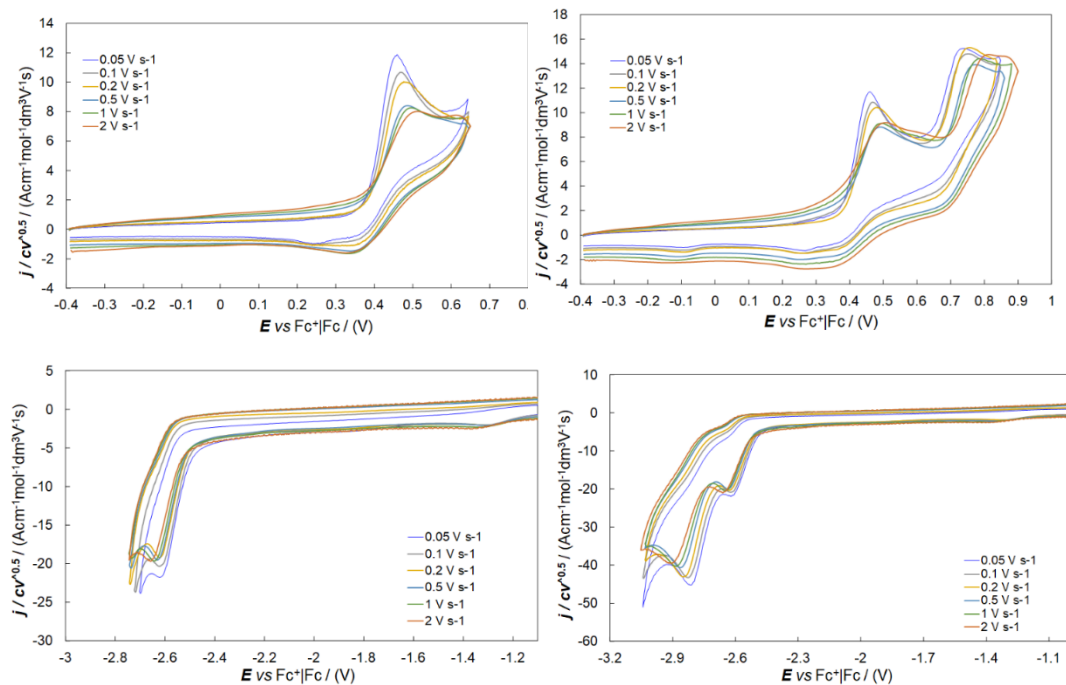
8. Electrochemical characterization of BT_2T_4 , BT_2T_6 and $BT_2(T_3)_2$ in ACN



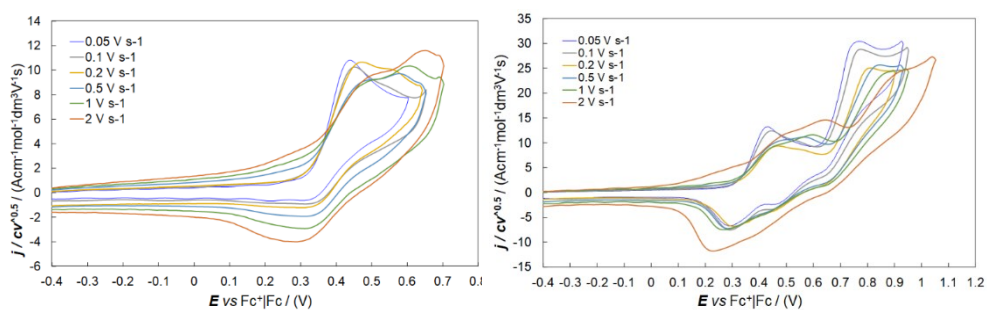
9. Electrochemical characterization of the inherently chiral family EN-OH, EN-OCH₃ and EN-Et

EN-OH

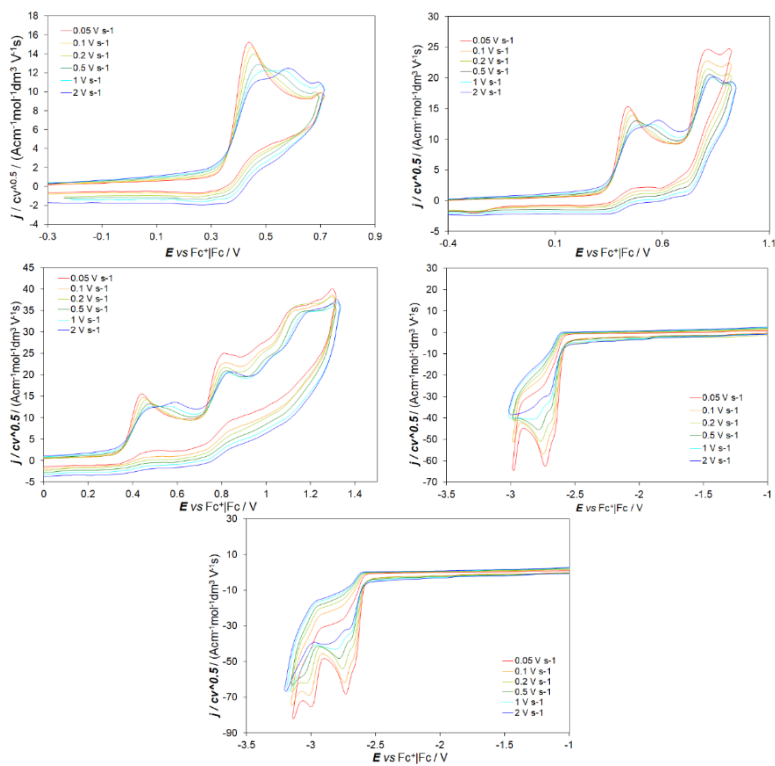
ACN



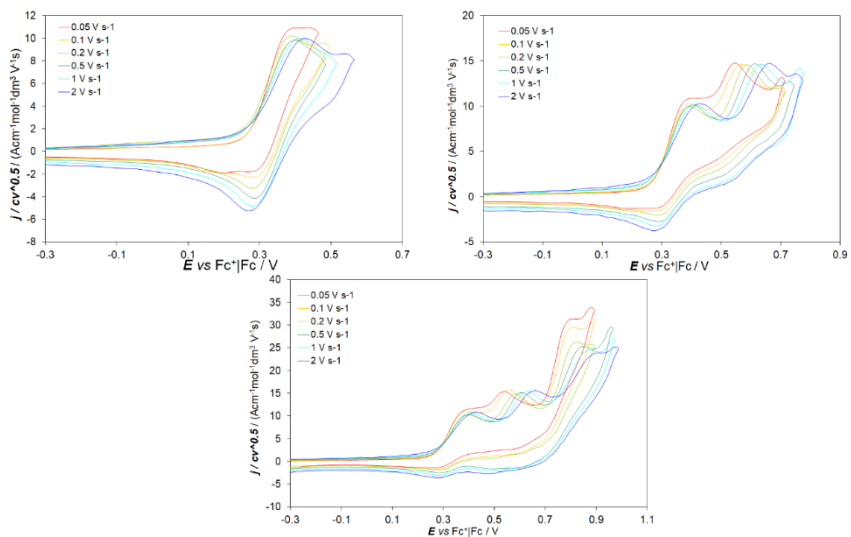
DCM



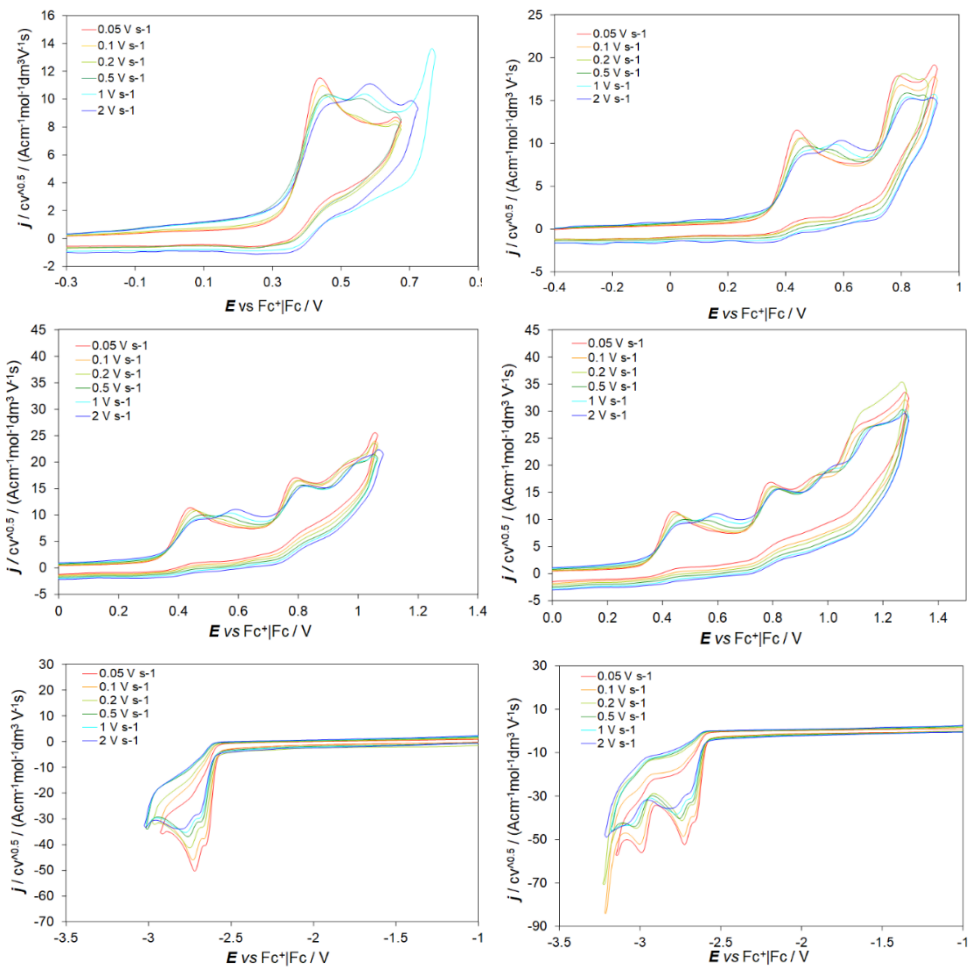
EN-OCH₃
ACN



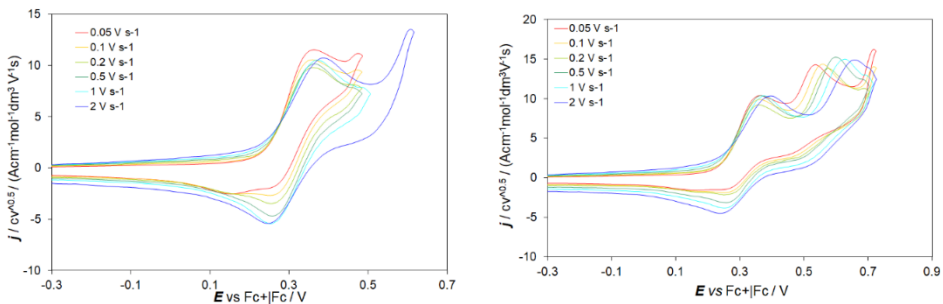
DCM



EN-Et
ACN

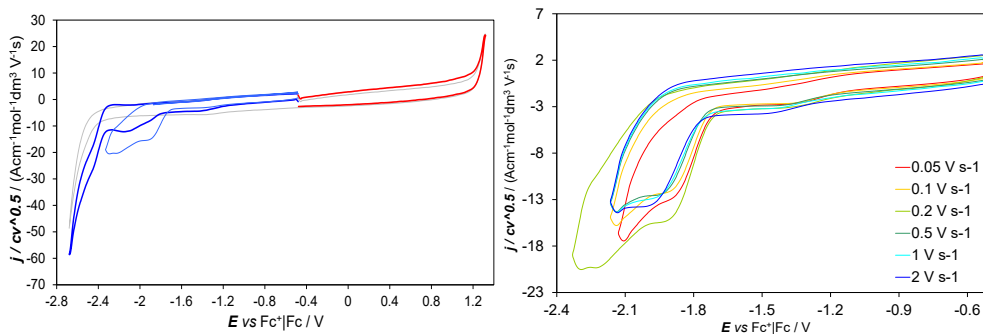


DCM

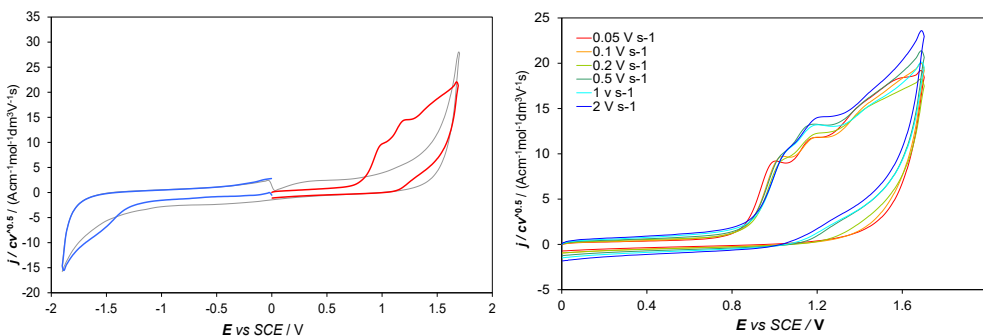


10. Electrochemical characterization of NSAIDs

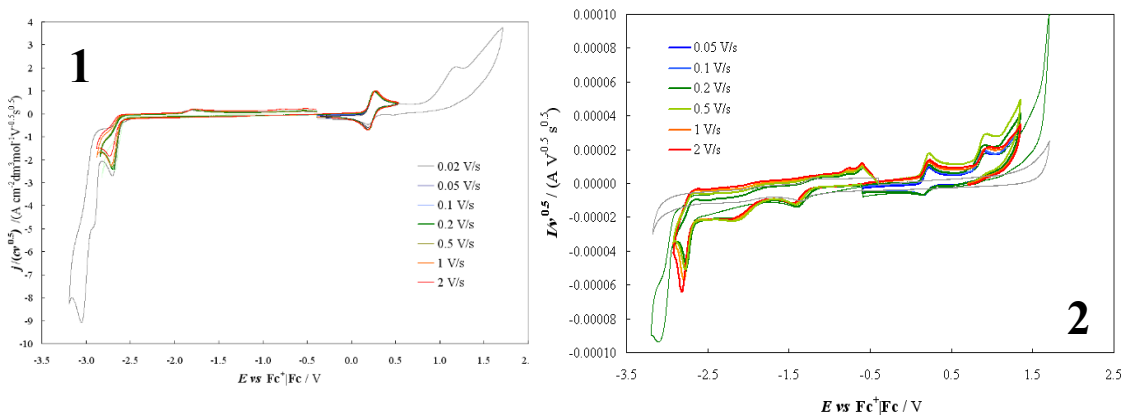
(S)-Ketoprofen in DCM + TBAPF₆ 0.1M

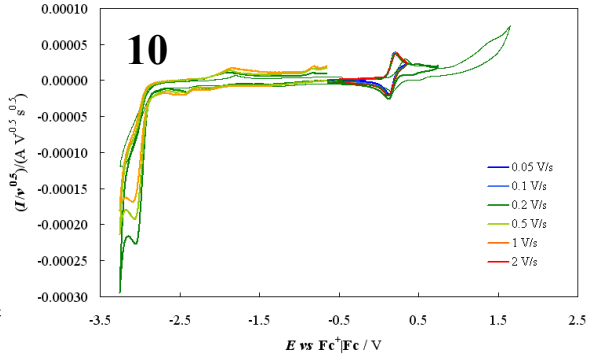
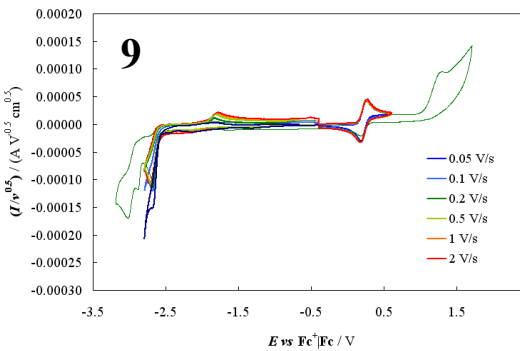
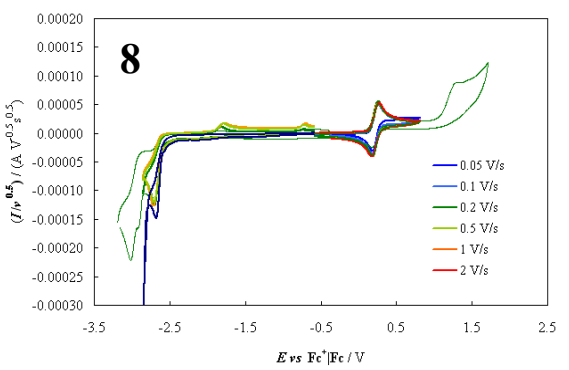
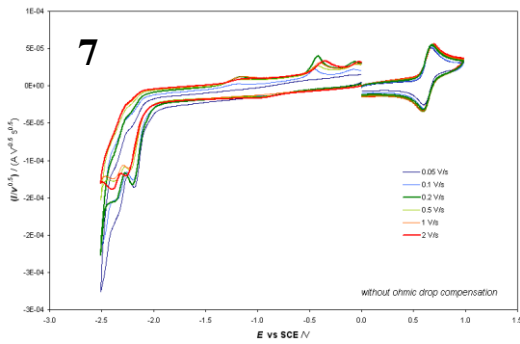
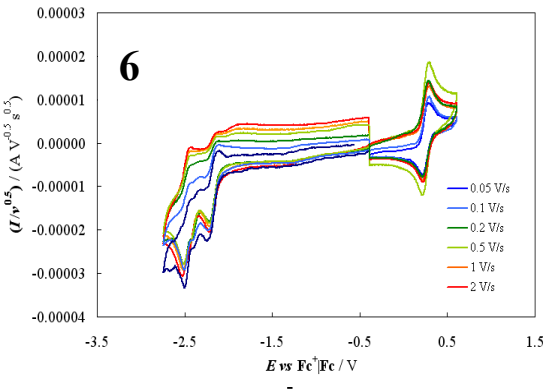
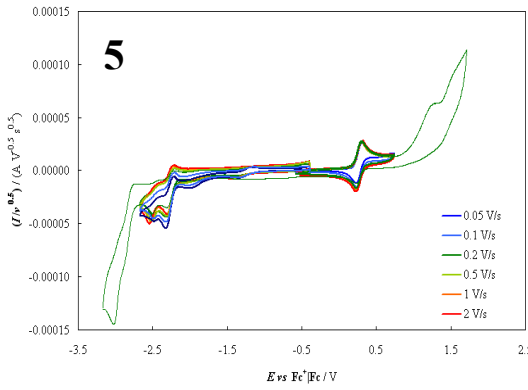
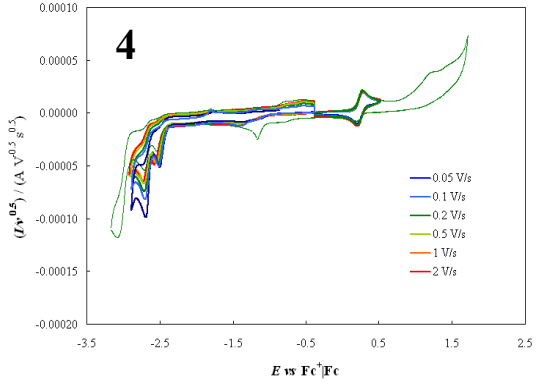
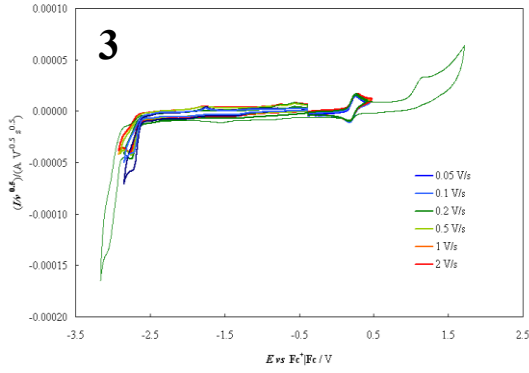


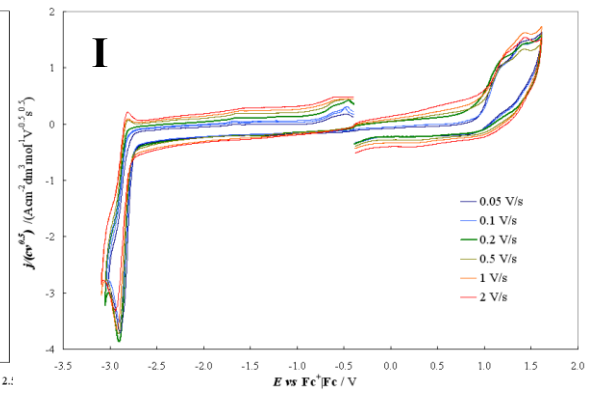
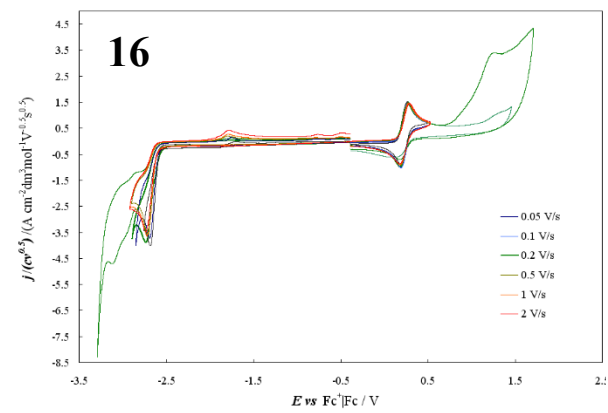
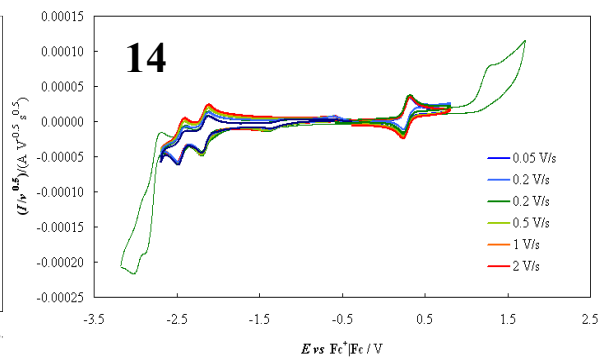
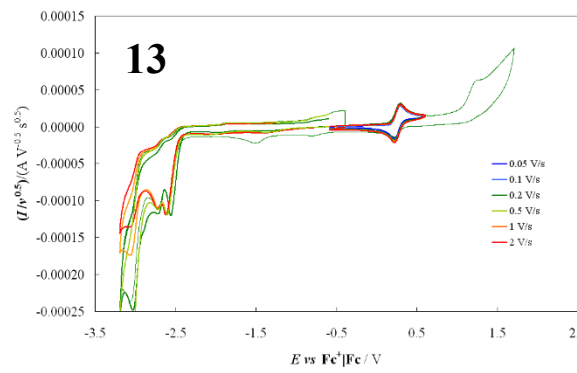
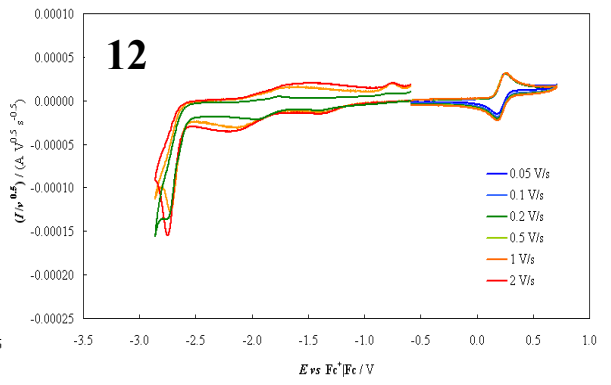
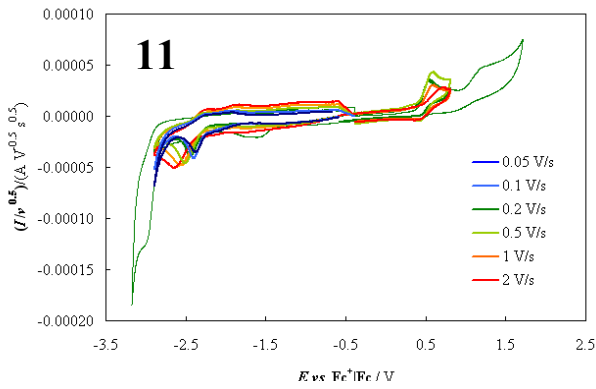
(S)-Naproxen in buffer pH7 solution



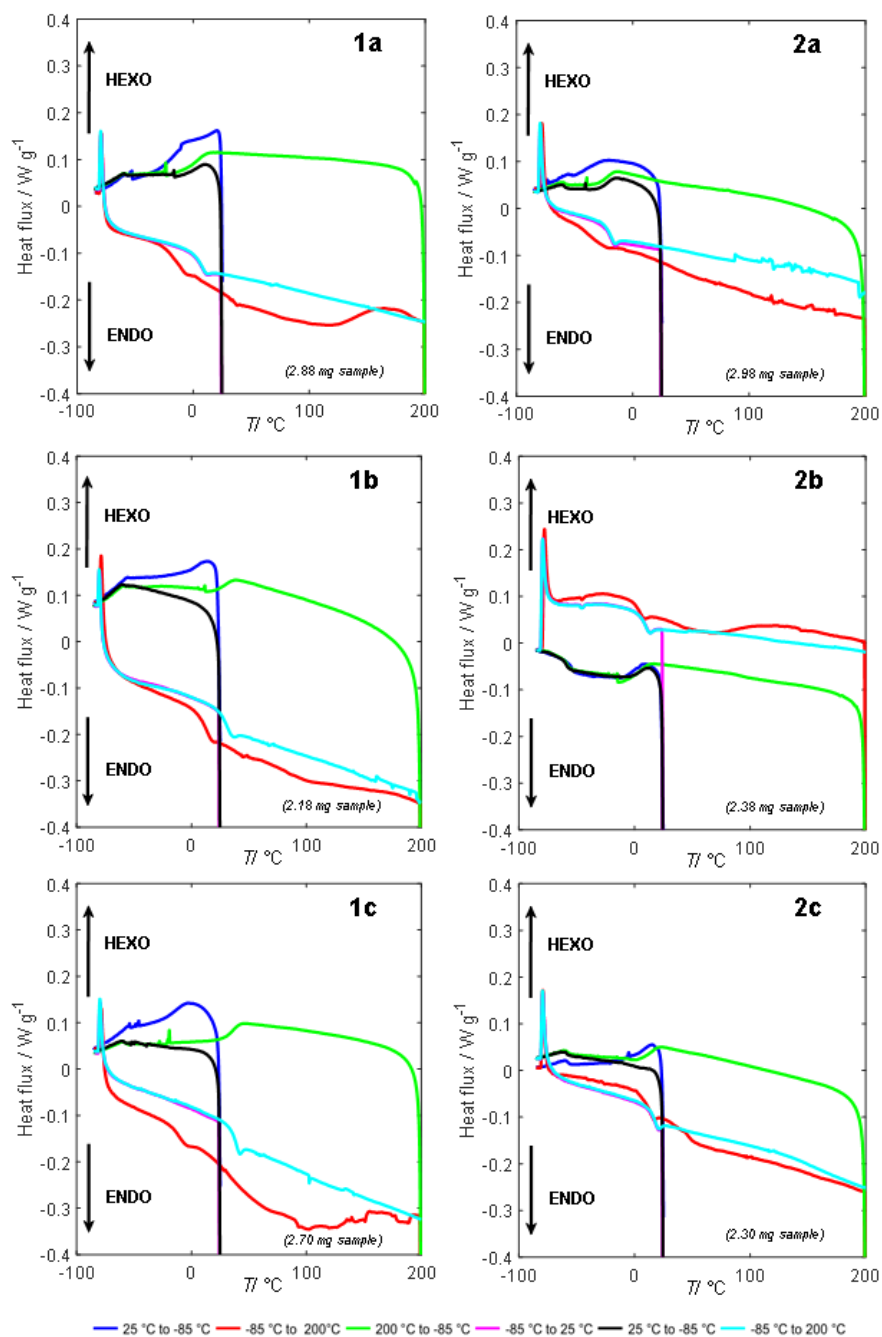
11. Electrochemical characterizations of planar stereogenicity ferrocenes



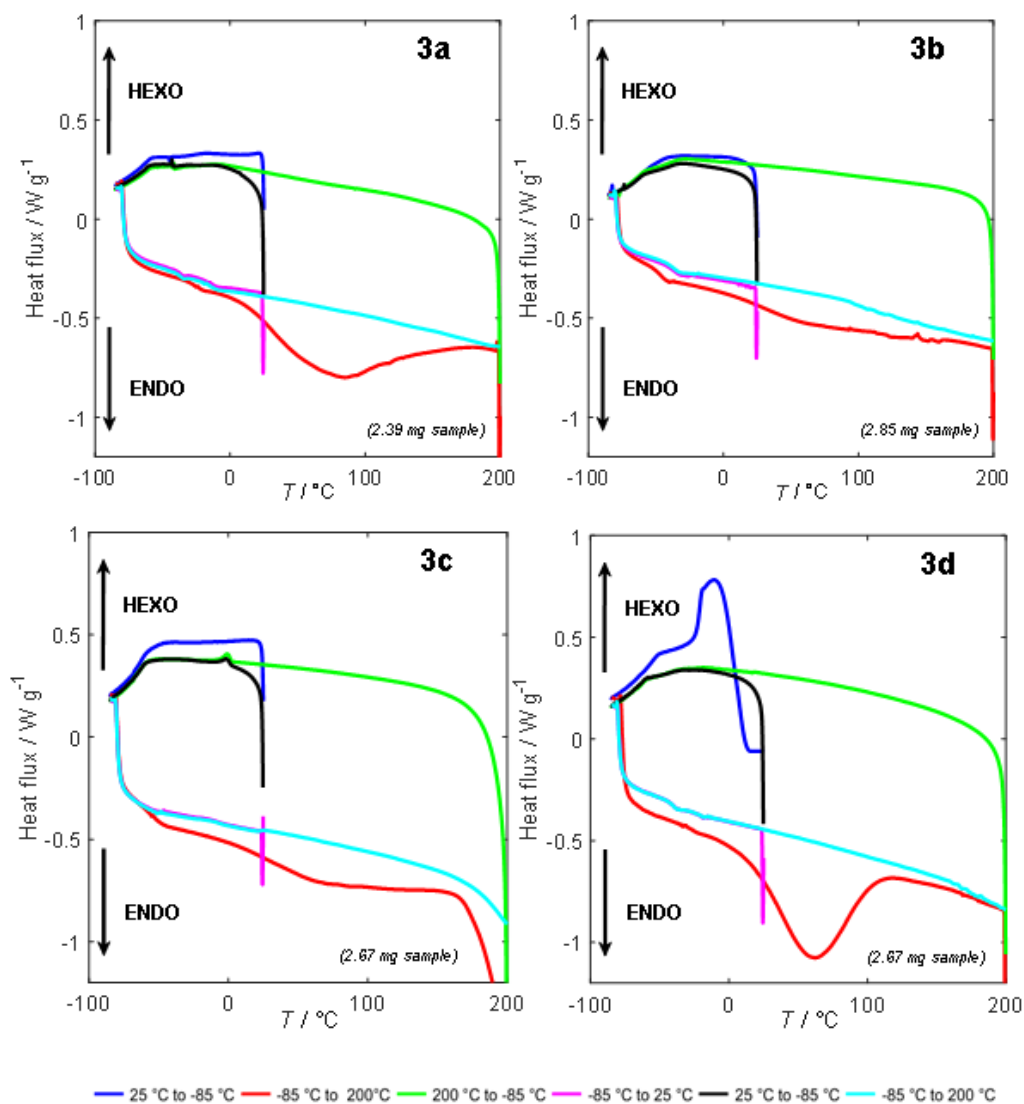




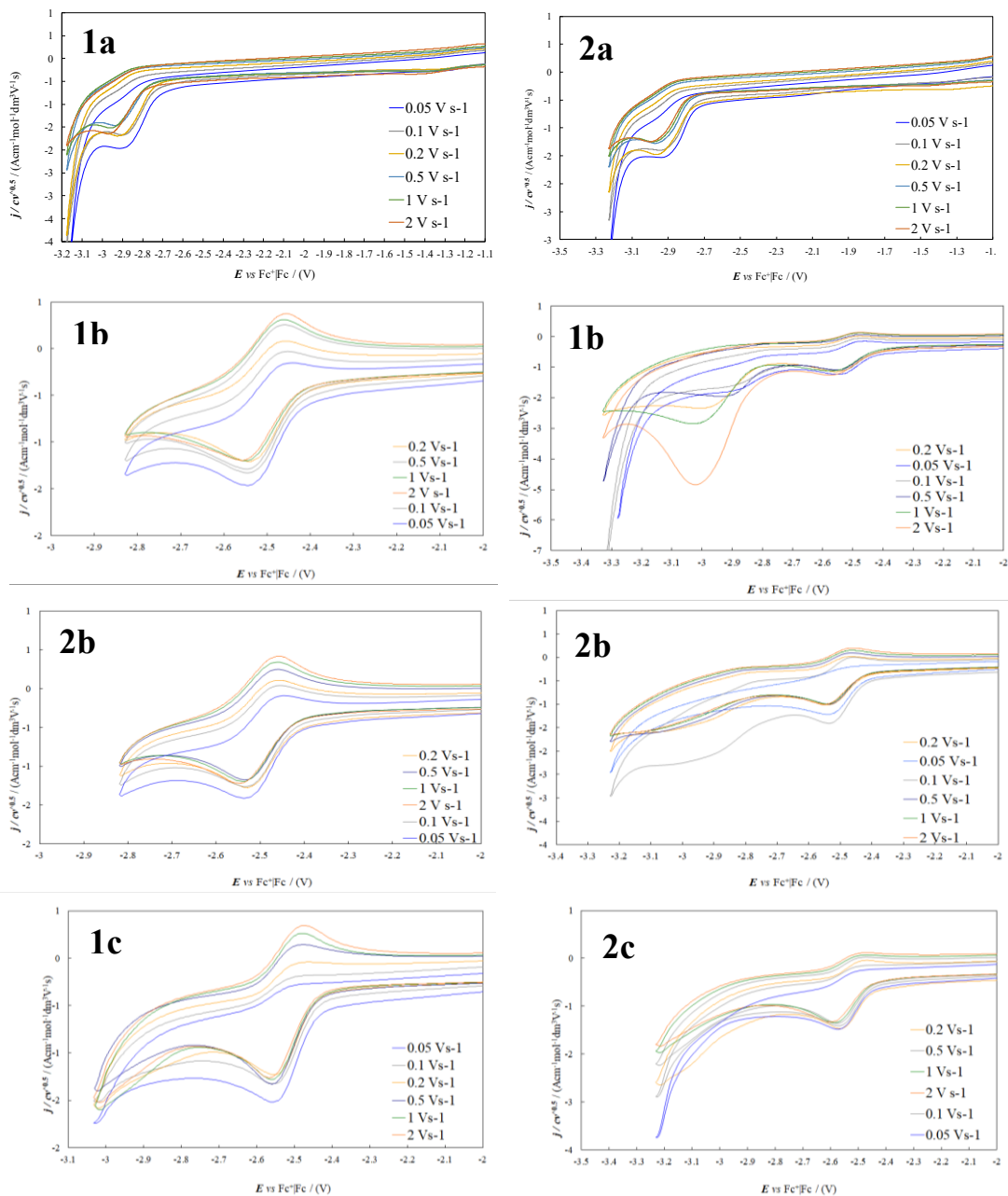
12. DSC features of CILs with chiral cations 1a-c (left column, from top to bottom) and 2a-c



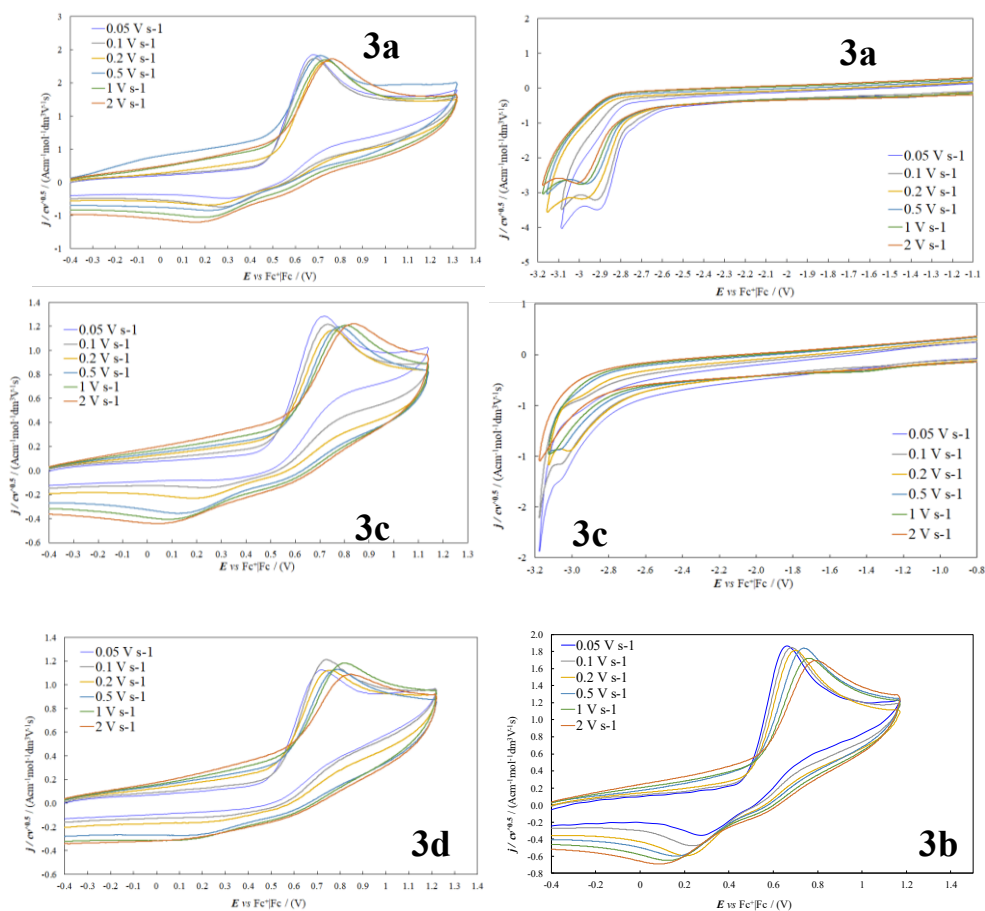
13. DSC features of CILs with chiral anions 3a-d



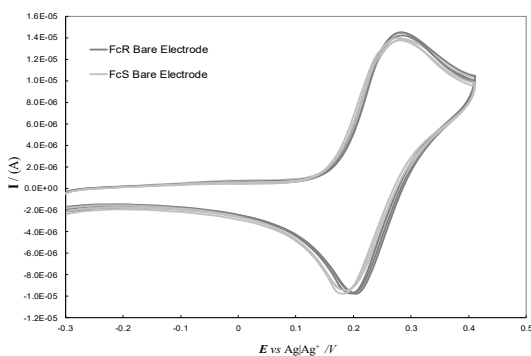
14. Scan rate effect on the CV reduction patterns of the five salts with chiral cation



15. Scan rate effect on the CV reduction patterns of the three salts with chiral anion



16. CV tests of chiral electroactive probe enantiomers (R)-Fc and (S)-Fc in achiral commercial ionic liquid with no chiral additives

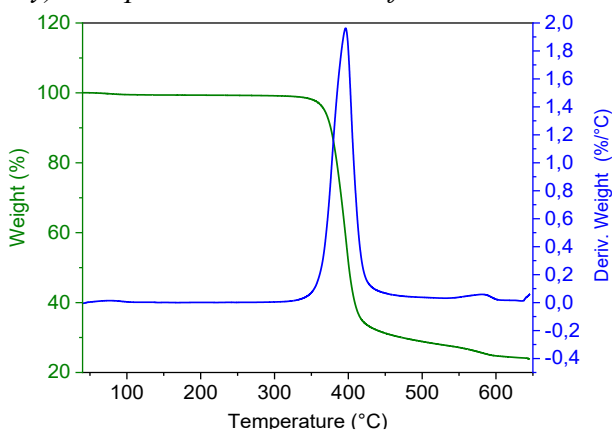


17. Thermal analyses of the new tweezers

TGA

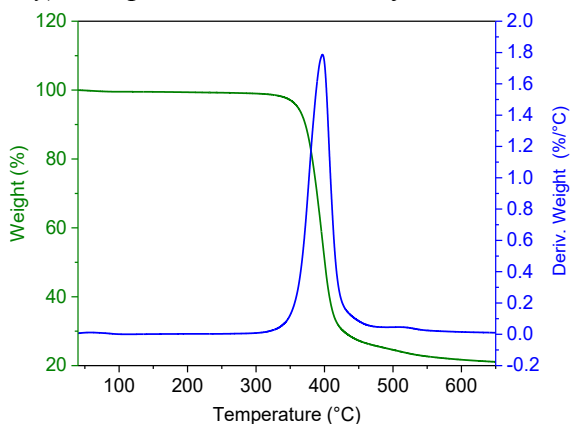
Decomposition temperatures were measured by a TGA Q500 V20.13 Build 39 thermogravimetric analyser (TA Instruments). The samples were measured in a platinum pan (100 μ L), at a heating rate of 10 $^{\circ}$ C/min starting from 40 $^{\circ}$ C to 900 $^{\circ}$ C under a nitrogen atmosphere. Every sample was dried in the furnace at 60 $^{\circ}$ C for 10 minutes under a nitrogen atmosphere prior to measurement. The onset of the weight loss, the temperature at 5% weight loss and 10% weight loss were used as a measure of the decomposition temperatures.

(3R,3aR,6R,6aR)-hexahydrofuro[3,2-b]furan-3,6-di-6-(2-N-methylimidazolium-ethoxy)-2-naphthoate methanesulfonate 3mM



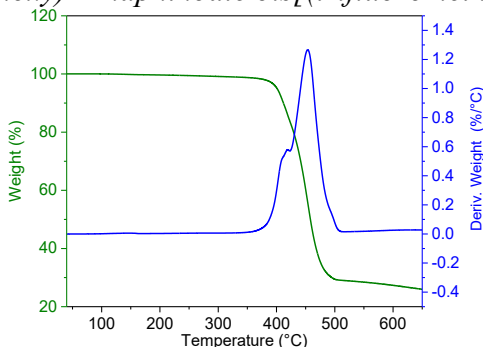
TG (green line) and DTG (blue line) curves of compound **3mM**. (10 $^{\circ}$ C/min; 40 $^{\circ}$ C to 650 $^{\circ}$ C)

(3R,3aR,6S,6aR)-hexahydrofuro[3,2-b]furan-3,6-di-6-(2-N-methylimidazolium-ethoxy)-2-naphthoate methanesulfonate 3sM



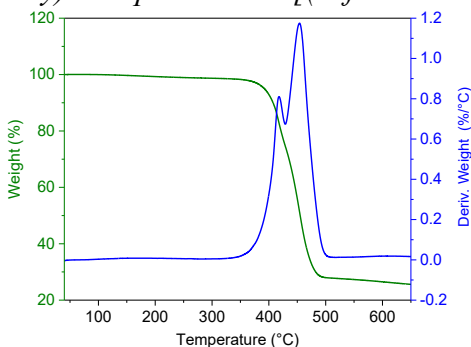
TG (green line) and DTG (blue line) curves of compound **3sM**. (10 $^{\circ}$ C/min; 40 $^{\circ}$ C to 650 $^{\circ}$ C)

3R,3aR,6R,6aR-hexahydrofuro[3,2-*b*]furan-3,6-di-6-(2-*N*-methylimidazolium-ethoxy)-2-naphthoate bis[(trifluoromethyl)sulfonyl]imide **3mT**



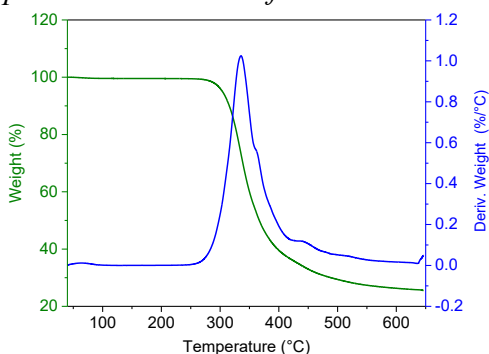
TG (green line) and DTG (blue line) curves of compound 3mT. (10°C/min; 40°C to 650°C)

(3R,3aR,6S,6aR)-hexahydrofuro[3,2-*b*]furan-3,6-di-6-(2-*N*-methylimidazolium-ethoxy)-2-naphthoate bis[(trifluoromethyl)sulfonyl]imide **3sT**



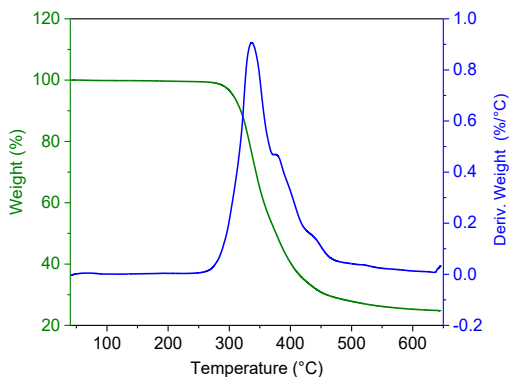
TG (green line) and DTG (blue line) curves of compound 3sT. (10°C/min; 40°C to 650°C)

(3R,3aR,6R,6aR)-hexahydrofuro[3,2-*b*]furan-3,6-di-6-(2-pyridiniumethoxy)-2-naphthoate methanesulfonate **4mM**



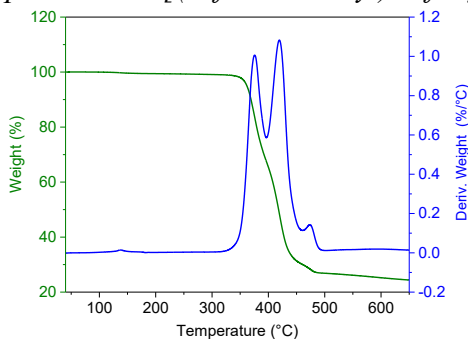
TG (green line) and DTG (blue line) curves of compound 4mM. (10°C/min; 40°C to 650°C)

(3R,3aR,6S,6aR)-hexahydrofuro[3,2-*b*]furan-3,6-di-6-(2-pyridiniummethoxy)-2-naphthoate methanesulfonate **4sM**



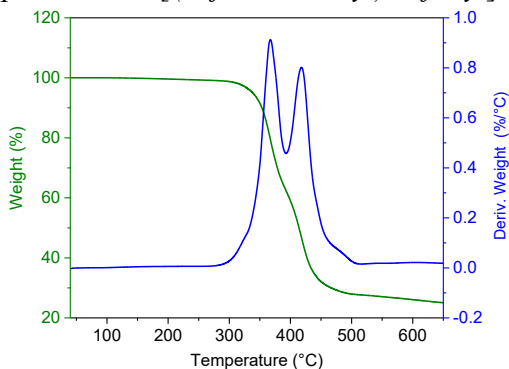
TG (green line) and DTG (blue line) curves of compound **4sM**. (10°C/min; 40°C to 650°C)

(3R,3aR,6R,6aR)-hexahydrofuro[3,2-*b*]furan-3,6-di-6-(2-pyridiniummethoxy)-2-naphthoate bis[(trifluoromethyl)sulfonyl]imide **4mT**



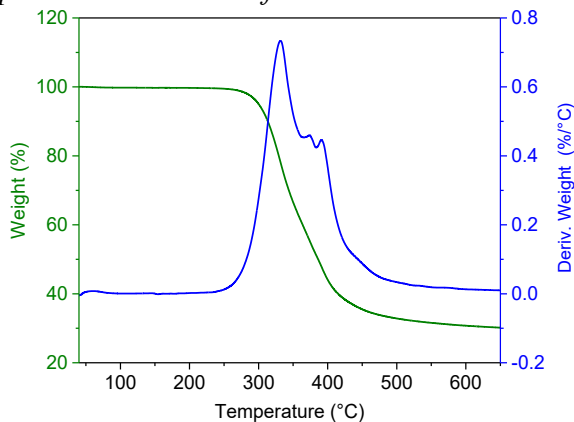
TG (green line) and DTG (blue line) curves of compound **4mT**. (10°C/min; 40°C to 650°C)

(3R,3aR,6S,6aR)-hexahydrofuro[3,2-*b*]furan-3,6-di-6-(2-pyridiniummethoxy)-2-naphthoate bis[(trifluoromethyl)sulfonyl]imide **4sT**



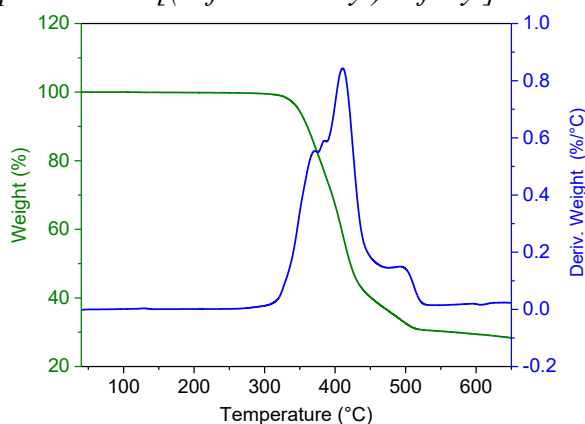
TG (green line) and DTG (blue line) curves of compound **4sT**. (10°C/min; 40°C to 650°C)

(3R,3aR,6R,6aR)-hexahydrofuro[3,2-b]furan-3,6-di-6-(2-quinoliniumethoxy)-2-naphthoate methanesulfonate **5mM**



TG (green line) and DTG (blue line) curves of compound 5mM. (10°C/min; 40°C to 650°C)

(3R,3aR,6R,6aR)-hexahydrofuro[3,2-b]furan-3,6-di-6-(2-quinoliniumethoxy)-2-naphthoate bis[(trifluoromethyl)sulfonyl]imide **5mT**

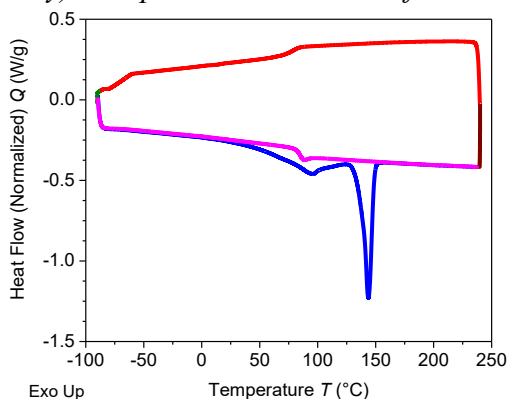


TG (green line) and DTG (blue line) curves of compound 5mT. (10°C/min; 40°C to 650°C)

Differential Scanning Calorimetry (DSC)

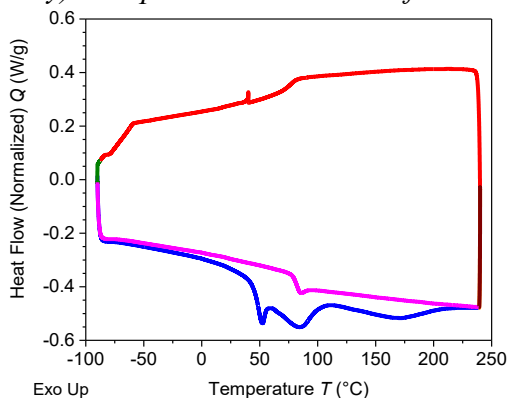
The melting points, crystallization temperatures and glass transitions were measured by a DSC250 (TA Instruments) equipped with a RSC90 refrigerated cooling system. Dry nitrogen gas was purged through the DSC cell at a flow rate of 30 cm³/min. Each sample (1.44-7.21 mg) was sealed in an aluminium pan (T_{zero} , TA instruments) with a pinhole on the cap. The samples were heated to the maximal temperature (10 °C/min) to remove thermal history, then cooled to -90 °C (5 °C/min) and heated from -90 °C to the maximal temperature (10 °C/min).

(3R,3aR,6R,6aR)-hexahydrofuro[3,2-b]furan-3,6-di-6-(2-N-methylimidazolium-ethoxy)-2-naphthoate methanesulfonate 3mM



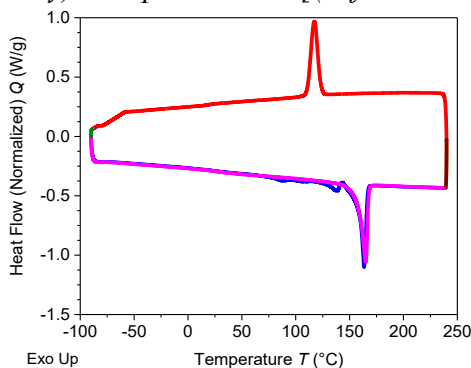
DSC of compound 3mM (Heating ramp at 10°C/min (blue line); Cooling ramp at 10°C/min (red line); Heating ramp at 10°C/min (magenta line)).

(3R,3aR,6S,6aR)-hexahydrofuro[3,2-b]furan-3,6-di-6-(2-N-methylimidazolium-ethoxy)-2-naphthoate methanesulfonate 3sM



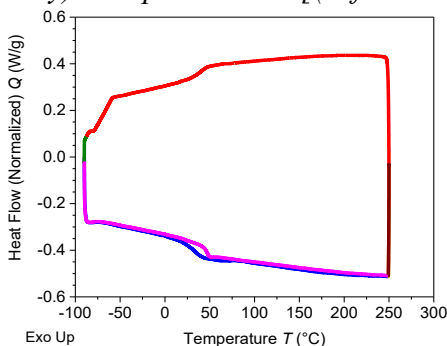
DSC of compound 3sM (Heating ramp at 10°C/min (blue line); Cooling ramp at 10°C/min (red line); Heating ramp at 10°C/min (magenta line)).

(3R,3aR,6R,6aR)-hexahydrofuro[3,2-b]furan-3,6-di-6-(2-N-methylimidazolium-ethoxy)-2-naphthoate bis[(trifluoromethyl)sulfonyl]imide 3mT



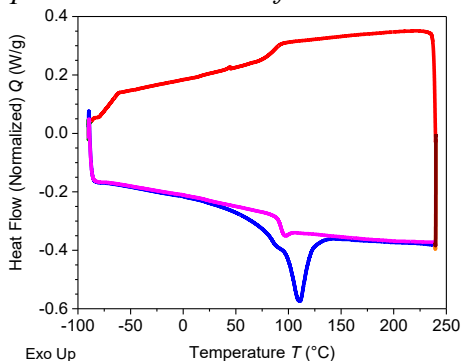
DSC of compound 3mT (Heating ramp at 10°C/min (blue line); Cooling ramp at 10°C/min (red line); Heating ramp at 10°C/min (magenta line)).

(3R,3aR,6S,6aR)-hexahydrofuro[3,2-b]furan-3,6-di-6-(2-N-methylimidazolium-ethoxy)-2-naphthoate bis[(trifluoromethyl)sulfonyl]imide 3sT



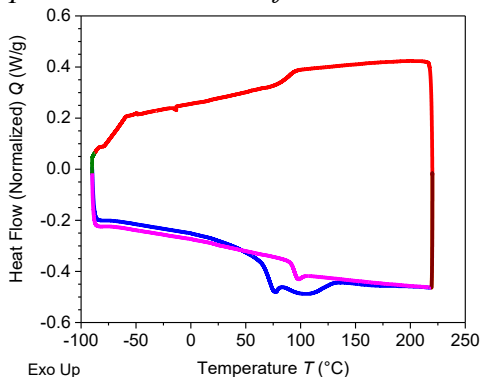
DSC of compound 3sT (Heating ramp at 10°C/min (blue line); Cooling ramp at 10°C/min (red line); Heating ramp at 10°C/min (magenta line)).

(3R,3aR,6R,6aR)-hexahydrofuro[3,2-b]furan-3,6-di-6-(2-pyridiniummethoxy)-2-naphthoate methanesulfonate 4mM



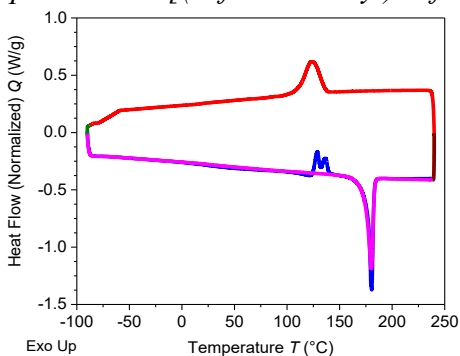
DSC of compound 4mM (Heating ramp at 10°C/min (blue line); Cooling ramp at 10°C/min (red line); Heating ramp at 10°C/min (magenta line)).

(3R,3aR,6S,6aR)-hexahydrofuro[3,2-*b*]furan-3,6-di-6-(2-pyridiniumethoxy)-2-naphthoate methanesulfonate **4sM**



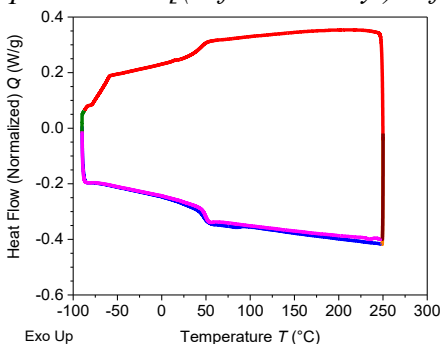
DSC of compound **4sM** (Heating ramp at 10°C/min (blue line); Cooling ramp at 10°C/min (red line); Heating ramp at 10°C/min (magenta line)).

(3R,3aR,6R,6aR)-hexahydrofuro[3,2-*b*]furan-3,6-di-6-(2-pyridiniumethoxy)-2-naphthoate bis[(trifluoromethyl)sulfonyl]imide **4mT**

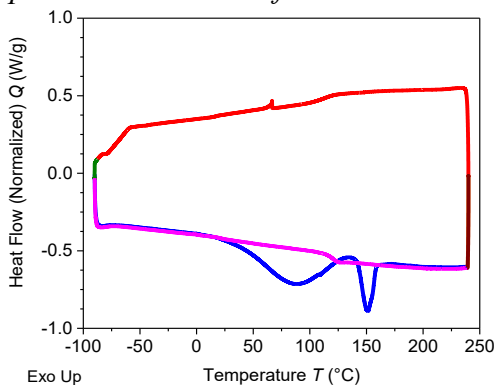


DSC of compound **4mT** (Heating ramp at 10°C/min (blue line); Cooling ramp at 10°C/min (red line); Heating ramp at 10°C/min (magenta line)).

(3R,3aR,6S,6aR)-hexahydrofuro[3,2-*b*]furan-3,6-di-6-(2-pyridiniumethoxy)-2-naphthoate bis[(trifluoromethyl)sulfonyl]imide **4sT**

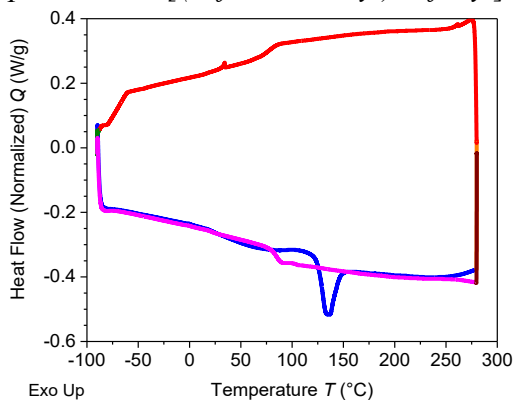


DSC of compound **4sT** (Heating ramp at 10°C/min (blue line); Cooling ramp at 10°C/min (red line); Heating ramp at 10°C/min (magenta line)).
(3R,3aR,6R,6aR)-hexahydrofuro[3,2-b]furan-3,6-di-6-(2-quinoliniumethoxy)-2-naphthoate methanesulfonate 5mM



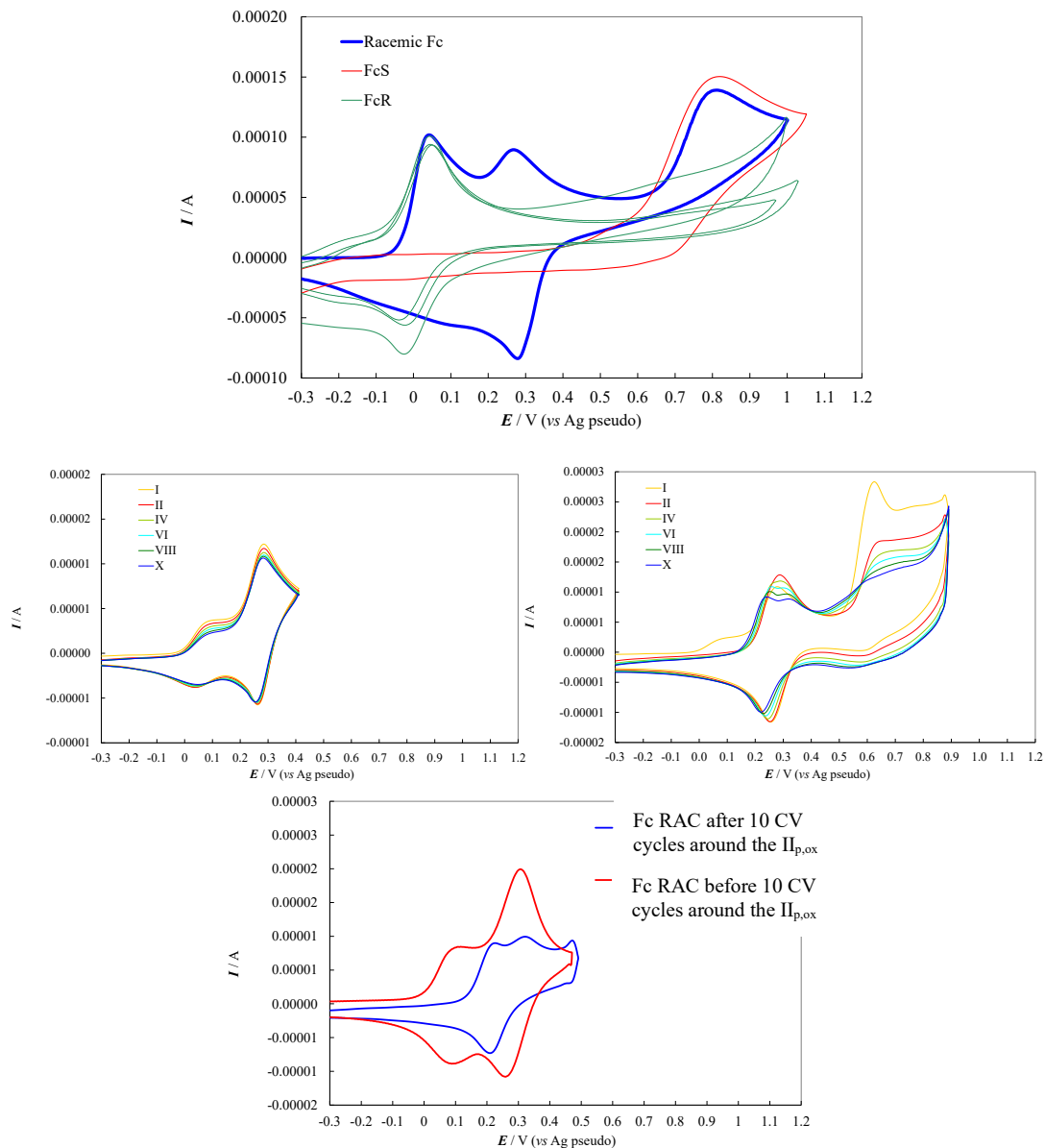
DSC of compound **5mM** (Heating ramp at 10°C/min (blue line); Cooling ramp at 10°C/min (red line); Heating ramp at 10°C/min (magenta line)).

(3R,3aR,6R,6aR)-hexahydrofuro[3,2-b]furan-3,6-di-6-(2-quinoliniumethoxy)-2-naphthoate bis[(trifluoromethyl)sulfonyl]imide 5mT

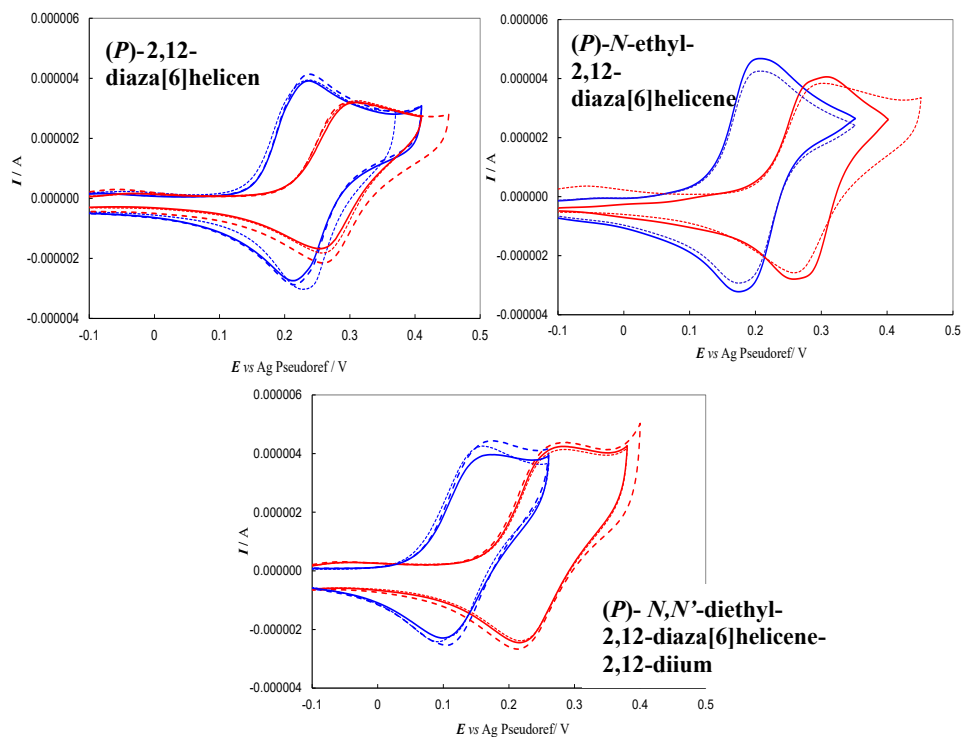


DSC of compound **5mT** (Heating ramp at 10°C/min (blue line); Cooling ramp at 10°C/min (red line); Heating ramp at 10°C/min (magenta line)).

18. CV enantioselection tests with racemic ferrocene in bulk (R)-3mO₂NTf₂

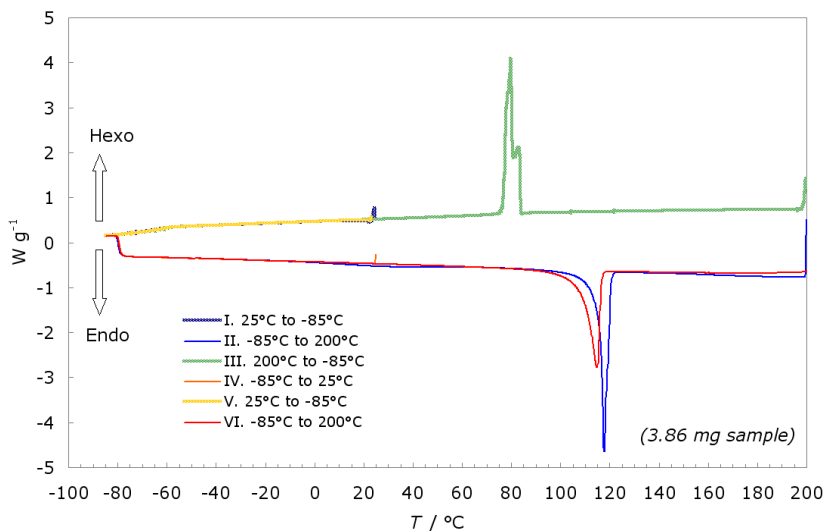


19. CV enantioselection tests with racemic ferrocene in bulk (R)-3mO₂NTf₂

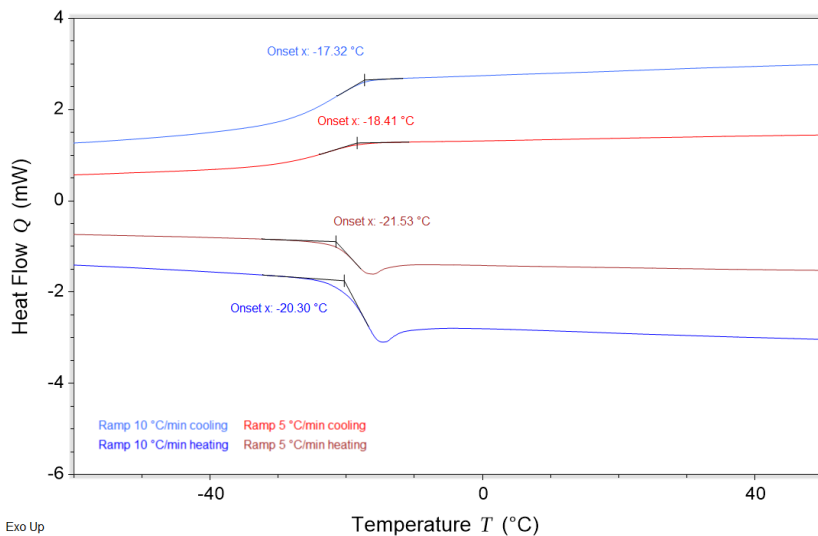


20. DSC thermograms

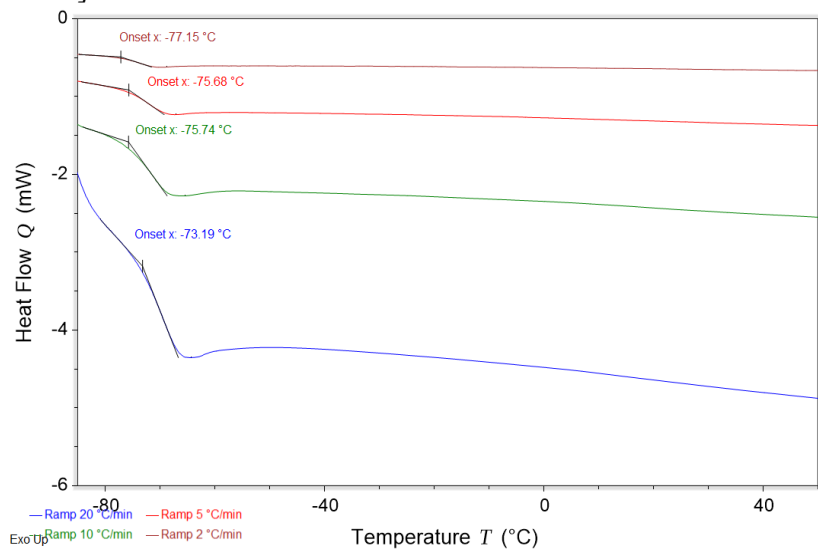
DSC features of [NOPOLMIM]Mes



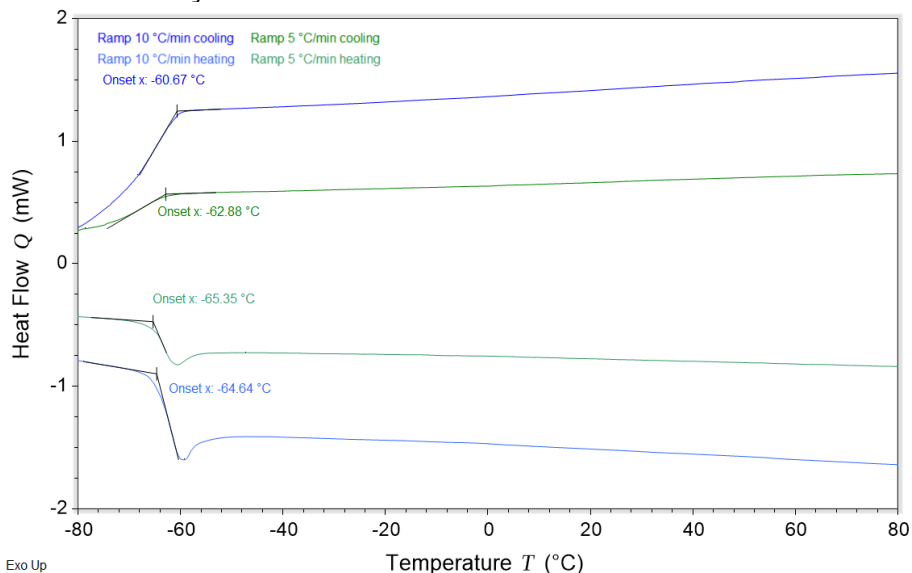
DSC features of the DES U employed in the DPV tests [NOPOLMIM]Mes + Urea 1:2]



DSC features of the DES G employed in the DPV tests [NOPOLMIM]Mes + Glycerol 1:2]



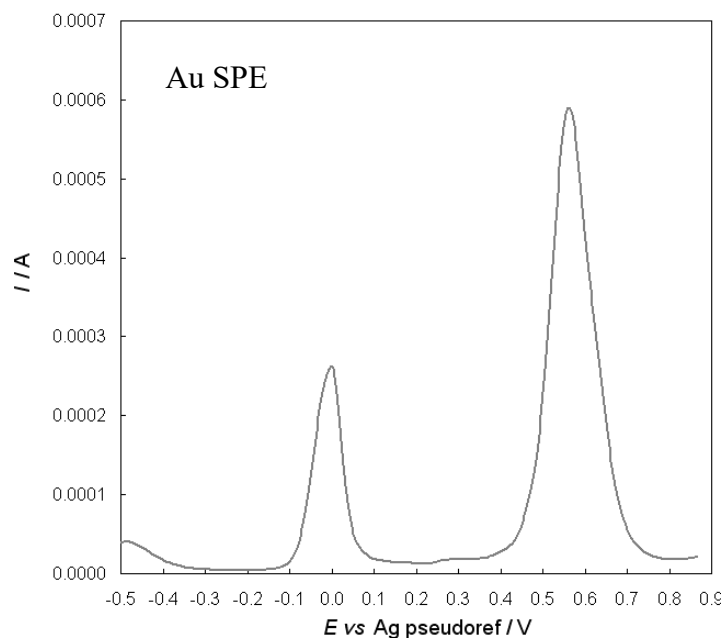
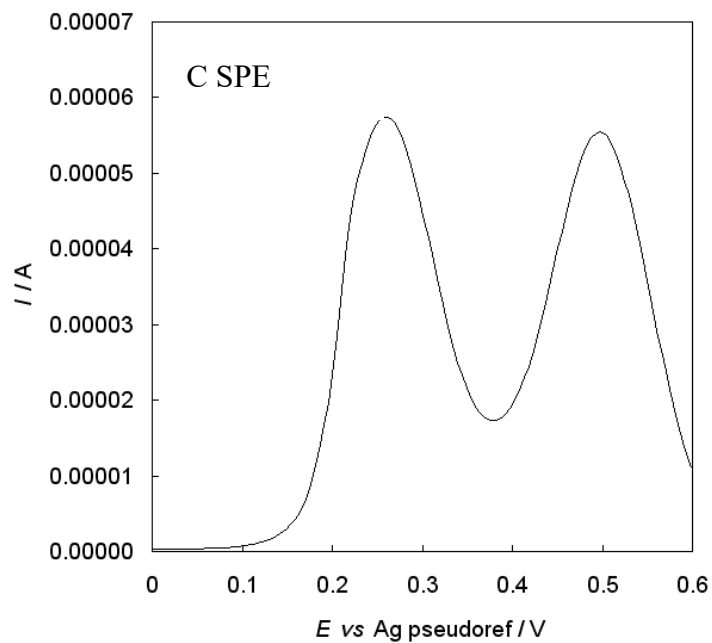
DSC features of the DES A employed in the DPV tests [NOPOLMIM]Mes + Levulinic Acid 1:2



21. EIS equivalent circuit fitting on experimental data

	<i>C</i> electrolyte	<i>R</i> electrolyte	$Q_1 \rightarrow W$ diffuse double layer	$Q_2 \rightarrow C$ double layer	χ^2
KCl 0.1 m ($\kappa_{25^\circ\text{C}} = 12.8247 \text{ mS/cm}$ [46])		0.068 k Ω ($\rightarrow L/S = 0.87 \text{ cm}^{-1}$)			
BMIMTFSI	285 pF 285 pF	0.368 k Ω 0.358 k Ω ($\kappa = 2.4 \text{ mS/cm}$)	$X_{Q1} = 1/(0.0090^{0.30})$ $X_{Q1} = 1/(0.0090^{0.31})$	$X_{Q2} = 1/(0.000198^{0.90})$ $X_{Q2} = 1/(0.000203^{0.91})$	0.0072 0.0088
BMIMTFSI + 0.05 M [NopolMim]Mes	291 pF 286 pF	0.916 k Ω 0.961 Ω ($\kappa = 0.95 \text{ mS/cm}$)	$X_{Q1} = 1/(0.00292^{0.36})$ $W = 0.00145$	$X_{Q2} = 1/(0.000243^{0.97})$ $C = 26.8 \mu\text{F}$	0.020 0.066
DES G	296 pF	3.48 k Ω ($\kappa = 0.25 \text{ mS/cm}$)	$X_{Q1} = 1/(0.00113^{0.40})$	$X_{Q2} = 1/(0.000246^{0.98})$	0.024
DES A	298 pF 296 pF	7.52 k Ω 5.84 k Ω ($\kappa = 0.13 \text{ mS/cm}$)	$X_{Q1} = 1/(0.000550^{0.40})$ $X_{Q1} = 1/(0.000805^{0.41})$	$X_{Q2} = 1/(0.000306^{1.00})$ $X_{Q2} = 1/(0.000321^{1.00})$	0.013 0.020

22. Enantiodiscrimination examples with mixed solutions of (R)- and (S)-enantiomer on C SPE and Au SPE cells



Chapter 8

Acknowledgments

My 3-year thesis project allowed to collaborate with many people and different research group, and I would like to gratefully acknowledges all of them:

- Dr. Roberto Cirilli (Istituto Superiore di Sanità, Rome, Italy), for chiral HPLC and circular dichroism experiments.
- Prof. Francesco Orsini (Università degli Studi di Milano) for AFM images.
- Prof. Tiziana Benincori and her research group (Dr. Luca Scapinello and Giorgia Bonetti, Università degli Studi dell'Insubria, Como, Italy) for providing me the inherently chiral monomers.
- Prof. Heinrich Lang (Technische Universität Chemnitz), for providing me the planar stereogenicity ferrocenes family.
- Prof. Dario Pasini (Università degli Studi di Pavia), for providing me the SP26 inherently chiral monomer.
- Prof. Lorenzo Guazzelli, Prof. Anna Iuliano and Dr. Andrea Mezzetta (Università di Pisa) for providing me the CILs based on bile-acid building blocks, the chiral tweezers family and chiral DESs.
- Dr. Simona Rizzo (CNR Istituto di Scienze e Tecnologie Chimiche "Giulio Natta") for providing me inherently chiral ionic liquid.
- Prof. Francesca Fontana (Università di Bergamo) for providing me the inherently chiral 2,12-diazahelicene family.
- Dr. Marco Pappini for MALDI facilities at UNITECH COSPECT (Università degli Studi di Milano).
- Prof. Fabiana Arduini and Prof Laura Micheli (Università Tor Vergata, Rome, Italy) for providing me SPE cells printed on plastic sheet.
- Prof. Jiří Ludvík and Dr. Magdaléna Hromadová (J. Heyrovský Institute of Physical Chemistry, Prague, Czech Republic) and Elisa Emanuele for ATR measurements.

My deepest and heartfelt acknowledgments also go to Prof Patrizia R. Mussini, my supervisor, Prof. Tiziana Benincori, my co-supervisor and Dr. Serena Arnaboldi, my co-supervisor and dear friend.